Lab Experiences for Teaching Undergraduate Dynamics

by

Katherine Ann Lilienkamp

Abstract

This thesis describes several projects developed to teach undergraduate dynamics and controls. The materials were developed primarily for the class 2.003 Modeling Dynamics and Control I. These include (1) a set of *ActivLab* modular experiments that illustrate the dynamics of linear time-invariant (LTI) systems and (2) a two-wheeled mobile inverted pendulum. The ActivLab equipment has been designed as shareware, and plans for it are available on the web. The inverted pendulum robot developed here is largely inspired by the iBOT and Segway transportation devices invented by Dean Kamen.

Thesis Supervisor: David L. Trumper
Title: Associate Professor of Mechanical Engineering

Acknowledgments

First, I'd like to thank Prof. David Trumper for his support and guidance throughout this thesis. Prof. Trumper is an incredibly knowledgable resource, and he has given me invaluable support and advice throughout the last several years: initially as an undergraduate, then during the consulting and masters degree work I have done with him. He is a gifted educator and genuinely motivated to teach students how to think. This has been inspirational both in my own choice to work on this project to develop educational tools and in getting through a masters thesis at all.

Joe Cattell and Andrew Wilson helped design and build the first generation of ActivLab experiments during the summer of 2001. We could not have developed an entire set of new laboratory experiments without their devotion to the project. Thanks particularly to Joe for the late nights spent machining in the graduate machine shop and the missed vacation days that summer.

Joe and Andrew also worked with me as teaching assistants when the equipment was first used (in the fall of 2001). They insured the lab sessions ran smoothly, showing both the students and faculty how to operate the new equipment. Andrew also put in a huge effort under the guidance of Prof. Samir Nayfeh to create the laboratory write-ups. His patience going through multiple, last-minute iterations of the pre-lab and lab assignment documentation was heroic, and I have included several of his elegant pro-E drawings of the laboratory hardware in the pages of my thesis.

Willem Hijmans, an exchange student from Delft University in the Netherlands, played a substantial role in insuring that the labs ran smoothly during this first term, as well. He created our ActivLab website [1] and was always on hand to help set up and calibrate equipment for class. Thanks also to Professor Jan van Eijk (also of Delft) for arranging Mr. Hijmans internship with us at MIT and for his support and advice throughout this project.

Special thanks to Prof. Ely Sachs for his suggestions and advice on hardware design. Prof. Dave Gossard, Prof. Samir Nayfeh and Prof. Neville Hogan taught the

---

[1]http://web.mit.edu/2.003/www/activlab/activlab.html

4

machine shop. Mark and Gerry in particular have taught me most of what I know about getting around a machine shop. They have always been generous with their time, and I modified several designs based on their advice. They often provided more than a little "help" in actually manufacturing specific parts, too! I believe I'm typing this now with all ten digits, thanks in no small part to their supervision and guidance.

Contents

List of Figures

List of Tables

Chapter 1

Introduction

1.1 Overview

The purpose of this thesis is to develop experiences for teaching undergraduates about dynamic systems and controls. These experiences include (1) several sets of *ActivLab* laboratory hardware and associated experiments investigating system dynamics and (2) a mobile inverted pendulum to be used as a classroom demonstration in controls.

This thesis can be divided into two halves. One half focuses on learning and education, and it includes a description of the ActivLab projects. The second half focuses on a variety of design issues relating to the development of an inverted pendulum system.

The half which focuses on learning and education consists of the second half of Chapter 2, along with Chapters 3 and 4. These "two and a half" chapters together aim to illustrate methods for implementing the following philosophy for teaching undergraduates dynamics: that we should provide hands-on experiences that promote critical thinking, and that "learning how to learn" is an important skill that can then be applied more broadly in engineering specialty our students eventually gravitate toward. This part of the thesis presents some general ideas about how to teach problem solving skills and also describes specific laboratory hardware, demos and other projects that all aim to establish a strong foundation for design and controls.

The second part of the thesis, consisting of the first half of Chapter 2 and Chap-

ters 5, 6, and 7, discusses a specific design problem: building an inverted pendulum as a classroom demonstration illustrating modeling, dynamics and control. The inverted pendulum project is related to the other half of the thesis, since it focuses on the details of designing and implementing one particular educational demo.

This introductory chapter outlines the goals in developing both the laboratory equipment and the inverted pendulum demo. Details of the hardware developed are also summarized, highlighting the successes and failures of attaining these motivating goals. Below is a brief outline of the remaining chapters in this thesis.

Chapter 2 provides a survey of several other recent projects for teaching dynamics and mechatronics. Because the basic design of my inverted pendulum robot is directly inspired by both the iBOT™ and Segway™ human transportation devices, details and images of each of these devices are also presented.[1] The purposes of Chapter 2 are (1) to make the reader aware of related projects and ideas in teaching dynamics, controls and mechatronics and (2) to credit work done by others which was influential in developing this thesis.

Chapter 3 describes the hardware and experiments developed at MIT as *ActivLab* projects for the class 2.003 Modeling Dynamics and Control I. Both the underlying philosophy and specific details of the hardware and laboratory exercises are outlined.

Chapter 4 provides some additional ideas for in-class and laboratory demonstrations useful in teaching undergraduate dynamics. These include both hardware we have built, considered and/or tested in 2.003 and projects used in Prof. Trumper's Mechatronics course (2.737) at MIT. Chapter 4 also describes some variations of the ActivLab experiments in Chapter 3.

An existing driven-cart inverted pendulum is discussed in Chapter 5. This demo hardware was used to test the filtering and calibration of the gyro and accelerometer later used in the robotic inverted pendulum. Chapter 5 also compares the utility of

---

[1]Dean Kamen and his colleagues at *DEKA Research and Development Corporation* invented and developed the iBOT Mobility System, which is now a registered trademark of *Independence Technology*, a Johnson & Johnson company. The Segway Human Transporter is a product of Segway LLC. Both DEKA and Segway LLC are companies founded by Dean Kamen.

the cart and robotic pendulums as classroom demonstrations.

Tilt sensing for an inverted pendulum robot is a particularly interesting problem, and Chapter 6 discusses some of the issues involved. These issues are subdivided into two broad topics, both of which relate to the use of gyros in obtaining an absolute measurement of the angle of tilt of the pendulum body of an IP robot. First, it discusses redundant gyro sensor arrays. My DIPR robot, described in Chapter 7 uses only a single gyro, but the Segway human transport (on which the DIPR is based) uses a 5-sensor array of gyros to enable "fail-operational" performance. The design issues involved in creating such an array are sufficiently interesting to warrant some analysis.

The second half of Chapter 6 describes complementary filtering. If one simply integrates the velocity measurement from a gyro to obtain a position measurement, the DC bias in the gyro will produce a ramping error in position over time. Complementary filtering can reduce the effects of this DC bias by blending a gyro signal with a second measurement of tilt which measures angle instead of velocity, such an accelerometer or electrolytic tilt sensor.

Chapter 7 describes a two-wheeled inverted pendulum robot which I designed as a classroom demo. That chapter discusses the design of both the mechanical hardware and control algorithms. The device is nicknamed the "demo inverted pendulum robot" (DIPR). The specifications of the robot, langrangian equations of motion of the system, theory and implementation of controller, and data evaluating its performance are presented.

Finally, Chapter 8 outlines potential directions for future development of the equipment described in this thesis. I also provide a qualitative assessment of the effectiveness of the various hardware previously described.

The appendices include more details about 2.003, including a summary of the course content and a list of parts and vendors used to construct the ActivLab hardware for 2.003. Also contained in the appendices are diagrams of the Simulink models used to implement the dSPACE controller for the inverted pendulum robot, MATLAB code to simulate the predicted time response of the robot, and a summary of the

robot's components and specifications.

1.2   General Motivations

All of the work done in this thesis is motivated by the following two principles: First, we intend to provide a strong foundation for future study in the integration of mechanical engineering, electrical engineering, design, controls, and other disciplines which can be loosely categorized together as "mechatronics". Second, we hope to present experiences for the students which inspire interest and curiosity primarily about investigating system dynamics but also about any scientifically explainable phenomena in general. In short, we want to provide students with both the requisite academic foundation and personal interest to pursue future studies in the broad range of dynamic systems they are likely to encounter in engineering practice.

Over time, it is becoming increasingly economical to incorporate microcontrollers into a wide variety of mechanical devices. Therefore, mechanical engineers now need to be proficient in a variety of skills often summarized as mechatronics. The undergraduate curriculum in mechanical engineering at MIT currently offers classical controls as a (non-required) elective subject. This has typically been the point at which many of the basic tools used in studying controls are first used in earnest. These include Laplace notation, root locus, block diagram algebra, step and impulse responses in the time domain, and Bode and Nyquist diagrams of frequency response.

Students will be more self-confident and productive in studying controls if they have already become familiar with many of these basic tools. Also, since controlling a system essentially amounts to modifying its dynamics, we believe that it is appropriate to introduce such concepts in the study of dynamic systems. The study of controls provides strong motivation for the study of dynamics.

The overriding objective of this thesis can thus be summarized as the creation of hardware to make both dynamics and controls more interesting and intuitive to students. The Laboratory exercises in 2.003 provide hands-on experience with mechanical and electrical systems, as discussed further in the next section. Classroom

demos provide an opportunity for exposure to interesting and inspirational systems at a less-intensive level than the laboratory projects. As mentioned, the demo developed for this thesis is a robotic inverted pendulum. Inverted pendulums are familiar demos in teaching controls, and the robotic version has a timely resemblance to the recently developed Segway human transport.

1.3 Goals for the ActivLab Experiments

The *ActivLab* project is a part of the restructuring of a sophomore-level course in the Mechanical Engineering Department at MIT: 2.003 Modeling Dynamics and Control I. This course forms a 2-part sequence with 2.004 Modeling Dynamics and Control II. Descriptions of each class from the MIT course catalog can be found in Appendix A. This section provides an overview of our design philosophy in creating the labs and describes general goals in developing the mechanical hardware. Details on the specific laboratory projects can be found in Chapter 3.

Prior to the restructuring, the undergraduate mechanical engineering curriculum in dynamics did not include a laboratory component. The hardware and experiments which comprise our labware were developed during the summer of 2001. The new labs are intended to solidify the students' understanding of dynamic systems. A second goal is to incorporate a *mechatronics* viewpoint in presenting introductory dynamics. As previously noted, there is a growing need for work-ready mechanical engineering graduates with expertise in electronics and controls. Many universities have responded by offering course work and degree programs in mechatronics, but typically such classes are not offered until the junior or senior year. To address this need, 2.003 has been restructured to introduce controller design and basic electronics to students at the sophomore level. By familiarizing students with Bode plots, block diagrams, transfer functions and other tools for designing and analyzing control systems, it is hoped that students will be both better prepared and more motivated to pursue a wide range of dynamics topics in more detail later in their education.

Mechanical systems frequently have significant non-linear effects. A challenge in

designing the labware was to reduce any non-linearities which might dominate the linear behaviors we intend to demonstrate. Creating a nearly-ideal electrical circuit is comparatively trivial. Since mechanical engineering students are typically more comfortable with mechanical systems, however, we have elected to introduce the less-ideal *mechanical* dynamic systems initially and then to present their analogous *electrical* counterparts. The remainder of the section addresses several key issues presented in trying to create the mechanical hardware.

1.3.1   Motivation for Using Low-Friction Air Bearings

One key goal in developing ActivLab labware is to provide students with hands-on experiences to develop an intuition about the behavior of dynamic systems which can be described by *linear, constant-coefficient, differential equations.* Real-world physical systems however often exhibit significant non-linearities in response. For example, both viscous damping and Coulomb friction act to convert mechanical energy into waste heat, but the time response of a system dominated by each is distinctly different, as illustrated in Figure 1-1 and Figure 1-2, respectively.
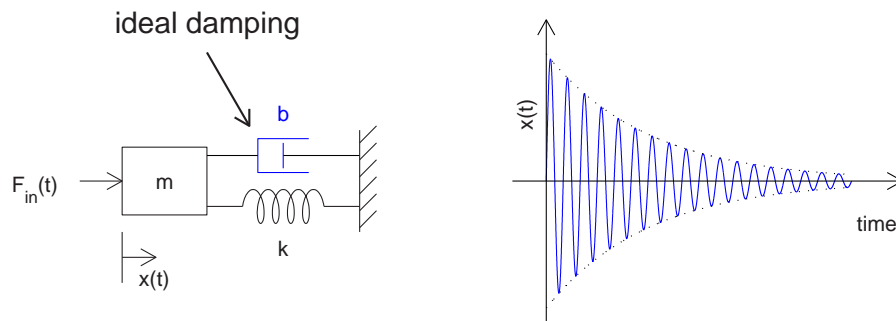
Figure 1-1: Impulse response of a spring-mass system with viscous damping. Response simulated using MATLAB (ode solver).

The second-order system shown in Figure 1-1 can be described by the force balance represented by the differential equation shown below in Equation 1.1,
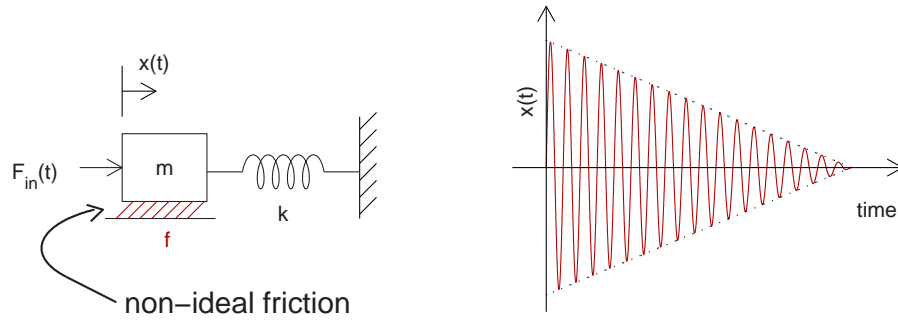
Figure 1-2: Impulse response for a spring-mass system with Coulomb friction, simulated in MATLAB.

$$m\frac{d^2x}{dt} = -b\frac{dx}{dt} - kx + F_{in}(t) \tag{1.1}$$

where $F_{in}(t)$ is a forcing function acting on the mass, as depicted in Figure 1-1. The viscous damping acts to decelerate the mass. That is, it acts *against* the direction of motion, as indicated by the negative sign in the damping force term in Equation 1.1. Note that the force contribution from damping, $b\frac{dx}{dt}$, is linearly proportional to the first derivative of position variable x. (i.e. It is proportional to *velocity*).

In contrast, the force due to Coulomb friction is most simply modeled as a constant magnitude value equal to a friction coefficient, μ, times the normal force against the ground due to gravity, mg. As with damping, this force acts against the direction of motion of the mass:

$$F_{friction} = +\mu mg \quad , \quad \dot{x} < 0 \tag{1.2}$$

$$= -\mu mg \quad , \quad \dot{x} > 0 \tag{1.3}$$

However, the friction force is *not* proportional to the position variable or any of its derivatives. Therefore, a system with non-negligible Coulomb friction cannot be modeled using only linear, constant-coefficient differential equations.

Most mechanical systems exhibit losses due to both viscous damping *and* Coulomb friction. Of course, all real hardware has nonideality at some level. As described in the next section, this can actually inspire open-ended inquiry during the lab sessions.

However, a more fundamental goal is to foster familiarity with basic system dynamics by allowing students to observe relatively clean first- and second- order impulse and step responses.[2] The laboratory equipment should therefore have a minimal amount of Coulomb friction, so that the effects of loss due to viscous damping are not obfuscated by the effects of friction. This goal is achieved in most of the mechanical ActivLab setups by using porous carbon air bearings.[3]
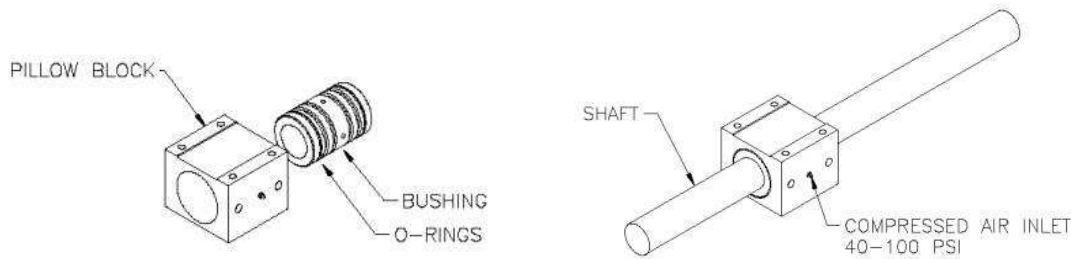
Figure 1-3: Porous carbon New Way air bearings. Images are from the New Way Machine Components website [146]. http://www.newwaybearings.com

Figure 1-3 shows an air bearing in detail. Each bearing consists of two parts, as depicted on the left-hand side of the figure. The inner bushing is press-fit into the pillow block housing to comprise a complete bearing. Note that a length of precision ground shafting would normally be mounted within two such bearings - *not* in a single bearing as depicted in the righthand illustration in Figure 1-3.

Compressed air enters the pillow block through a brass fitting and seeps through the porous carbon inner surface of the bushing. This provides a cushion of air between the bushing and the shafting. If the mating surfaces of the shafting and bearing are clean, smooth, and well-toleranced, the effects of friction are negligible, as desired.

The construction of the bushing can be seen more clearly in Figure 1-4. The o-rings serve two functions. They provide a seal to trap the compressed air, forcing it into the air inlet hole in the bushing's aluminum housing, and they also allow for minor misalignments when mounting the pillow blocks. This allowance for misalignment

---

[2]Analogous first- or second-order electrical circuits typically show comparatively little deviation from their expected, theoretical responses.

[3]Air bearings were supplied to us at substantial discount by New Way Machine Components.
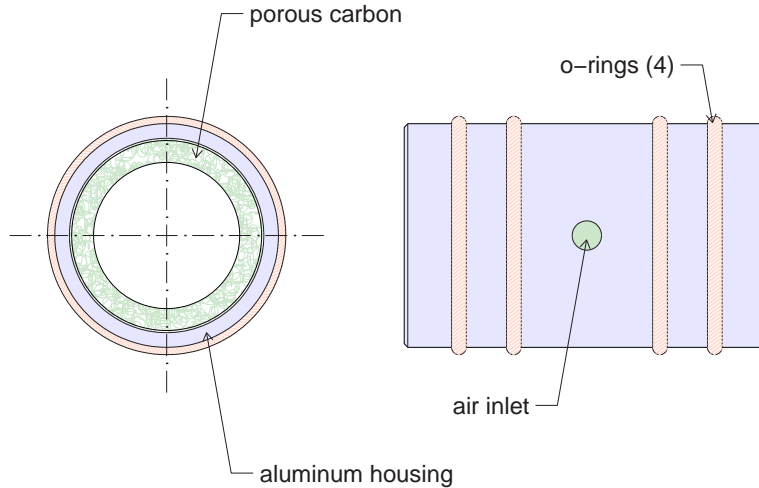
Figure 1-4: Detailed drawing of a New Way air bearing bushing

is important. The air gap between the shaft and the inner surface of the bushing is approximately half a thousandth of an inch.[4] Figure 1-5 depicts the range of acceptable diameter for the shafting and bearing, demonstrating the minimal and maximal air gaps (assuming the components are concentric).

It would not be economically feasible for us to align the two bearings supporting a length of shafting with such tight tolerances. Figure 1-6 illustrates how the o-rings provide flexibility to allow for minor misalignments in mounting the bearing pillow blocks. The deformation of the o-rings allows for minor misalignments between the pillow blocks in their 4 critical degrees of freedom, as well as allowing for minor bending of the shaft.[5]

1.3.2 Presenting Non-Ideal Real World Behaviors

As mentioned, the mechanical hardware is designed to exhibit predominantly first- and second-order behavior. A main goal in all of the laboratory assignments is to

---

[4]The ActivLab equipment uses shafting and bearings with a nominal $3/4''$ diameter. The allowable tolerances given by New Way Machine Components, Inc. are $\phi_{shaft} = 0.7500''^{+.0000''}_{-.0003''}$ and $\phi_{bushing} = 0.7508''^{+.0002''}_{-.0000''}$. The air gap between mating surfaces is the difference in radii: $gap_{min} = \frac{1}{2}(0.7508'' - 0.7500'') = 0.0040''$ and $gap_{max} = \frac{1}{2}(0.7510'' - 0.7497'') = 0.0065''$.

[5]A cantilever formed from a 12-inch length of $3/4''$ diameter steel shafting with a one-kilogram mass at its end would produce about a tip deflection of about $0.0012''$.
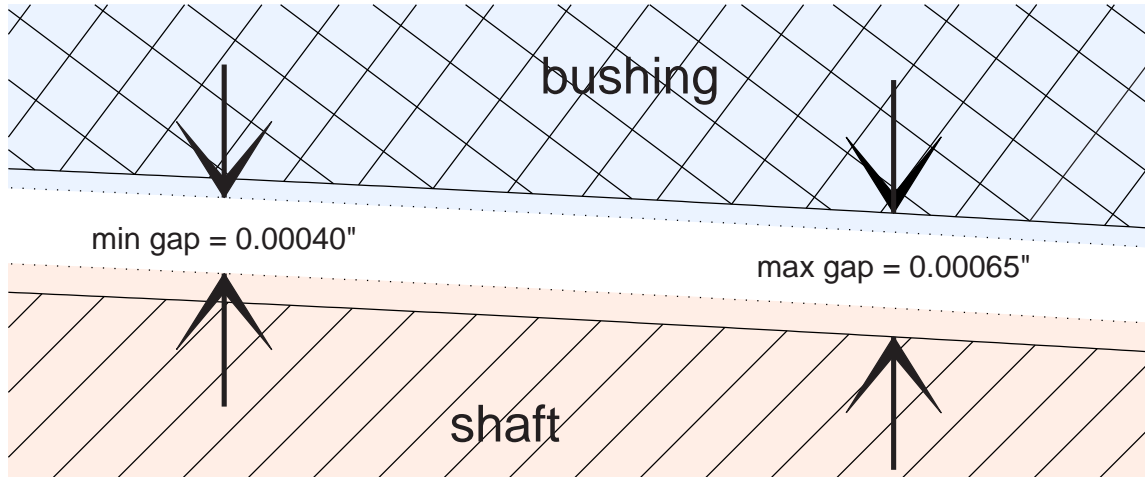
Figure 1-5: Allowable tolerances for shaft-bearing air gap

$$\left(\phi_{shaft} = 0.7500''{}^{+.0000''}_{-.0003''} \quad ; \quad \phi_{bushing} = 0.7508''{}^{+.0002''}_{-.0000''} \right)$$

build familiarity with the real, imaginary, and complex exponential time responses of linear, constant-coefficient differential equations of motion. Non-linear behaviors can potentially distract students from this goal, if the effects are too large.

However, eliminating all non-idealities is impractical - and arguably even undesirable. It is impractical because of cost and time constraints in creating such mechanical systems. In fact, unexpected and unmodeled system dynamics provide a launching point for inquiry and exploration during the lab sessions. That dynamical systems are so commonly plagued by such anomalous behaviors is itself an important lesson for an engineer.

More importantly, these unmodeled aspects of the hardware present an opportunity to ask students to analyze their data, to hypothesize about plausible explanations, and to design simple experiments to test their theories. One always hopes that laboratory experiences will both inspire creative problem solving and demonstrate to the students the utility of the scientific method. Ideally, lab projects will be inherently interesting enough to encourage exceptional students to pursue any unexplained phenomena on their own, while other students can be encouraged to explore by questions and comments from staff and their fellow students.

Laboratory sessions must of course have some specific, central objectives to direct
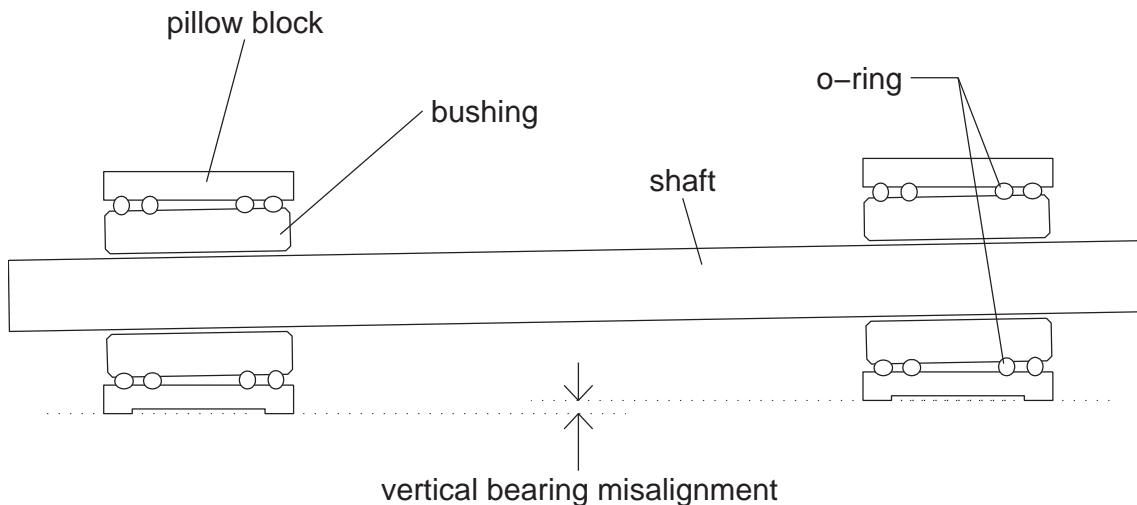
Figure 1-6: Cross-sectional view of vertical bearing misalignment. The magnitude of vertical misalignment is exaggerated for clarity.

students, however. An unfortunate consequence of this is that many students become extremely goal-oriented during labs. Some will literally check off numbered questions as they go, with no initial expectations that anything more open-ended is practical in the limited time frame of a laboratory session. This is likely a result both of years of pre-college laboratory experiences where any labwork is indeed very focused and also of a perceived "optimization" on the part of the students. Students often focus on answering itemized questions and assume this is all that is required to achieve high grades. As a result, they tend to view effort spent on tangential issues as detrimental distractions from their focused goals.

In summary, presenting the students with interesting and unexpected system behaviors is not enough in and of itself to foster curiosity and problem solving during labs. Outlining such anomalous behaviors in the written lab assignments is problematic, because preparing students eliminates the unexpected aspects of the phenomena and much of the potential for independent discovery. Incorporating these secondary explorations effectively into the lab sessions requires devoted staff who can question the students about their results and engage them in thoughtful discussions.

Details on the types of non-ideal behavior we have observed are presented as part

of the relevant laboratory descriptions in Chapter 3. Briefly, some examples include (1) an unmodeled springiness in the air-filled dashpots used in the *first-order spring-damper translational system* (Section 3.3); (2) a slight "recoiling" tendency in the *1st-order inertia-damper rotational system* likely caused by tilting misalignments in the carbide flat bearing surface (Section 3.4); and (3) spring-stiffening of the cantilever used in the *2nd-order spring-mass-damper translational system* which forms the basis for the projects described in Sections 3.5, 3.8, and 3.9.

The voice coils used in this last set-up present a couple of additional, unplanned behaviors. When used merely to provide damping, ideally one might hope to vary the voice coil damping from zero (when the coil circuit is open) to some maximum (when it is short-circuited) by closing the circuit with a finite resistance value. The coils we use are wound on aluminum cups, however, so currents flowing in the aluminum still produce significant damping when the coil is open-circuited. Second, when the voice coil is used as an actuator, a frequency response reveals non-finite-dimensional dynamics.

I would once again like to acknowledge the efforts of Professors Trumper, Nayfeh, Gossard and Hogan and all of the TA's for 2.003 (see Acknowledgements) for prodding the students to explore during the lab sessions. Again, such efforts from the staff are essential in getting most students to pursue understanding in depth in their lab work.

1.3.3   Transparent, Hands-on Operation

As mentioned, the ActivLab projects should foster an intuitive understanding of system dynamics. We intend that much of this intuition will come from encouraging students to touch and play with the mechanical systems. Specifically, the setups have been designed to allow students to change damping, stiffness and/or inertia in a given system and, importantly, to feel the differences created for themselves.

Ideally, the hardware should also be transparent to both students and staff, so that little or no instruction is necessary to figure out how the systems operate. Hopefully, this ease-of-use will also help encourage students to play with the hardware without fear of destroying or misaligning anything.

An important additional principle is that time scales at which any oscillations and decay rates occur should be on the order of a few seconds, so that students can observe these behaviors with their own eyes. By the same reasoning, displacements of at least several millimeters are needed. Otherwise, students cannot relate recorded data from sensors to their own observation to verify that calculations of displacements, frequencies, time constants, or other system parameters actually make sense. They are less likely to remember the lab experience if they cannot easily observe it without sensors, too.

Finally, we would like to minimize the use of "black boxes". To the extent practical, any actuators, sensors and passive components (e.g. springs and dampers) should be easy to understand. We sometimes compromised this goal in favor of simplicity and/or accuracy. For instance, a linear potentiometer is an easier displacement sensor to understand than an LVDT[6], but we chose to use the latter (without much discussion of its operation) because it is frictionless. For other equipment, such as a voice coil actuators or a viscous damper consisting of honey between concentric cylinders, we provide basic explanations of the underlying physics. Only a few components were straight-forward enough that we asked the students to calculate system properties from first principles. These properties include inertia and mass of objects with simple geometries and spring stiffness for a cantilever beam.

1.3.4   Ease of Assembly

Ease of assembly is a practical concern. The TA's putting together the equipment will generally not be the same from term to term, so learning any complicated procedures is not practical. Our strategy was to design each setup to be assembled on *optical breadboard*. The breadboard has a grid of tapped holes, evenly spaced at one-inch intervals.[7] We designed and manufactured our own mounting blocks for various components to make them compatible with the breadboard, so that parts could be

---

[6] "linear variable differential transformer"

[7] Such baseplate surfaces are often used in prototyping optical systems; hence the name "optical breadboard".

assembled from photos of each setup. Generally, the parts can be set loosely in place on the board and then screwed into place with little attention to alignment.

The greatest alignment challenges in the labs are probably in the vertical alignment of the rotational inertia-damping system. The shafting needs to be perpendicular to the base flat, and close to concentric with a tube surrounding it that holds viscous honey. Also, significant force is required to operate a syringe (with a small orifice) to change the level of the honey in the tube. This creates a messy potential failure point: the tubing that channels the honey between the syringe and tubing can become detached from the syringe.

Alignment was also a concern for the translational spring-mass-damper system. As mentioned, air bearings are used to minimize the effects of friction. Also, the range of travel of the mass needed to be on the order of a half an inch (or more) total to be clearly observable to the students. Both the voice coil actuator/damper and the LVDT position sensor involve concentric parts which can potentially scrape against one another as the mass moves. Thus, proper alignment of these parts is important, as described below.

Each voice coil motor consists of a housing with an annular gap (containing a concentrated magnetic field) and a coil assembly which moves within the gap along the axis of the annulus. In our spring-mass-damper lab setup, the coil assembly is mounted at one end of length of shafting. The shafting is constrained within two air bearings to allow only rotations about and linear motion along the axis of the shaft. The housing for the voice coil is mounted on an angle plate of the type shown at the right in Figure 1-11. The angle plate creates a flat surface at a 90 degree angle with the optical baseplate. This is a necessary (though not sufficient) requirement to insure that the walls of the actuator housing remain parallel to the direction of motion of the coil. Of course, misalignment between the housing and coil of the voice coil motor can still occur if (1) the bottom surface of the angle plate mates with the optical breadboard at a skew angle and/or (2) the housing is mounted too high or too low on the vertical surface of the angle plate to allow the coil to move freely inside within scraping. The clearance within the voice coil is sufficient that achieving such

alignment is relatively easy.

.50" outer dia

.25" inner dia
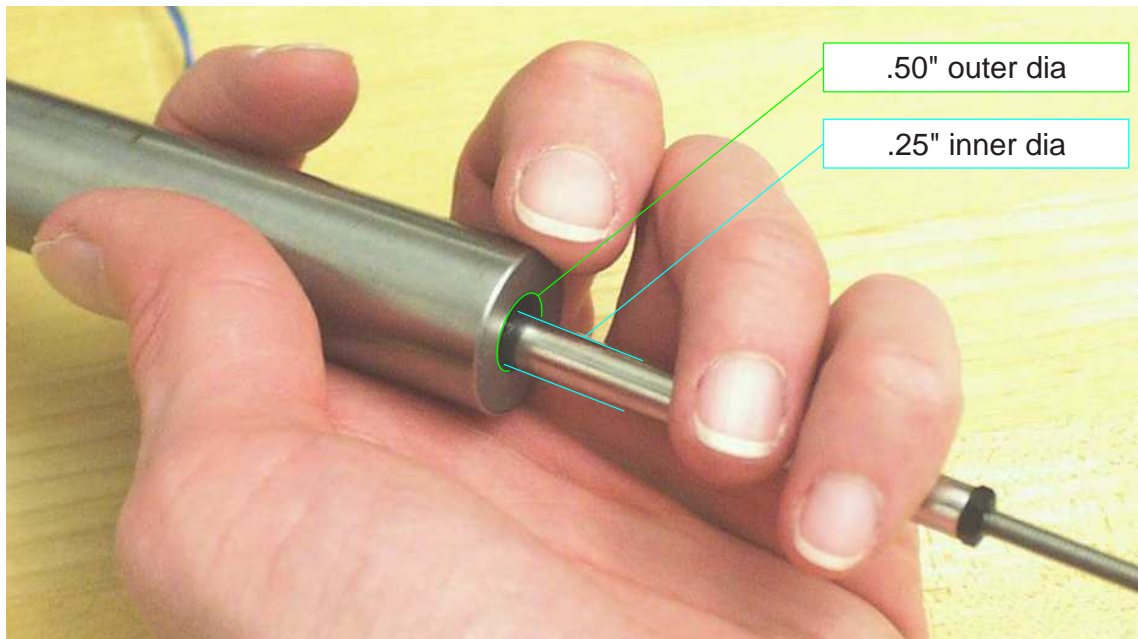
Figure 1-7: Generous LVDT clearance important for ease of alignment of air bearings.

The alignment of the LVDT was a more significant issue for us. Most of the LVDTs we considered purchasing had a clearance of 0.04" or less between the armature and the coil assembly. We tested one such model, and decided it was too difficult to align. The clearance was simply too tight to get repeatable alignment without a lot of fuss. The LVDT sensors we finally chose[8] had about three times this clearance. Figure 1-7 illustrates the generous clearance of the Schaevitz sensors: a bore diameter of 0.5 inches and a core diameter of 0.25 inches means there is 0.125 inches between the core and the housing walls when the parts are aligned concentrically.

The first LVDT we tested was problematic for a second reason, too. In addition to having a tight clearance, the coil housing was only open on one end. Because of this, it was nearly impossible to see how well the armature was aligned within the dark cavity of the housing. The back end of this particular sensor housing contained circuitry for both power and signal conditioning. All LVDTs require signal conditioning to produce a DC voltage representation of position.[9] This can either be performed by

---

[8]manufactured by Schaevitz

[9]There is more information on how an LVDT works on page 211 in Section 4.2.5
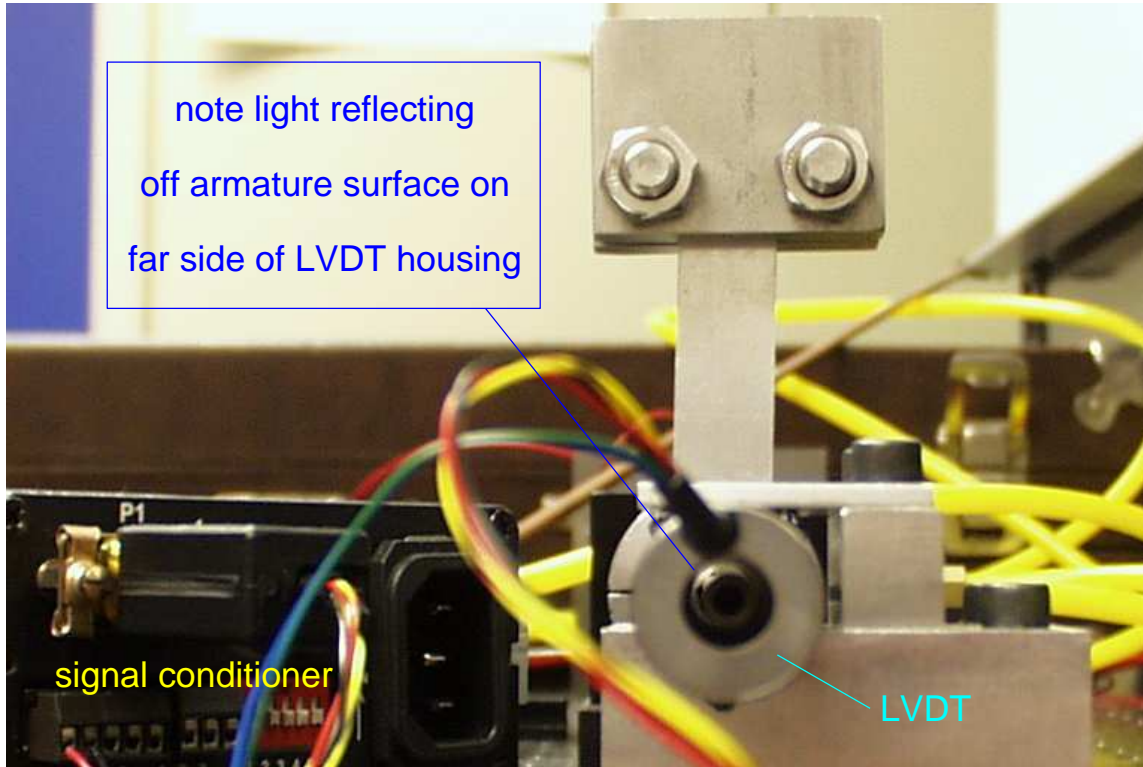
Figure 1-8: Thru hole in LVDT housing aids in alignment. Note the reflected light seen at the far end of the LVDT. You can shine a light through the sensor to test check whether any surfaces are scraping, which is very helpful in alignment.

a separate signal conditioner, as shown at left in Figure 1-8, or by circuitry in the sensor itself. The all-in-one sensor is generally less expensive but also less accurate that the versions sold with separate conditioning units. Another disadvantage of using a separate signal conditioner is that they require calibration with a particular LVDT by the end user. Unfortunately, the only LVDTs we were able to find with that had an end-to-end hole all required separate signal conditioners. As a result, the LVDTs cost almost twice what we had initially expected - around $620 for each sensor-conditioner pair.[10]

Early in the planning of these labs, Prof. Trumper suggested using aluminum split collar clamps to mount various components to the steel shafting. This was an excellent idea: aluminum is easy to machine, and the clamps cost less than one dollar

---

[10]See component prices in Appendix C.

each. We purchased several dozen[11] from Kaman Industrial Technologies[194]. The
Kaman part number is SC-12A, and they are manufactured by Whittet-Higgins[212].
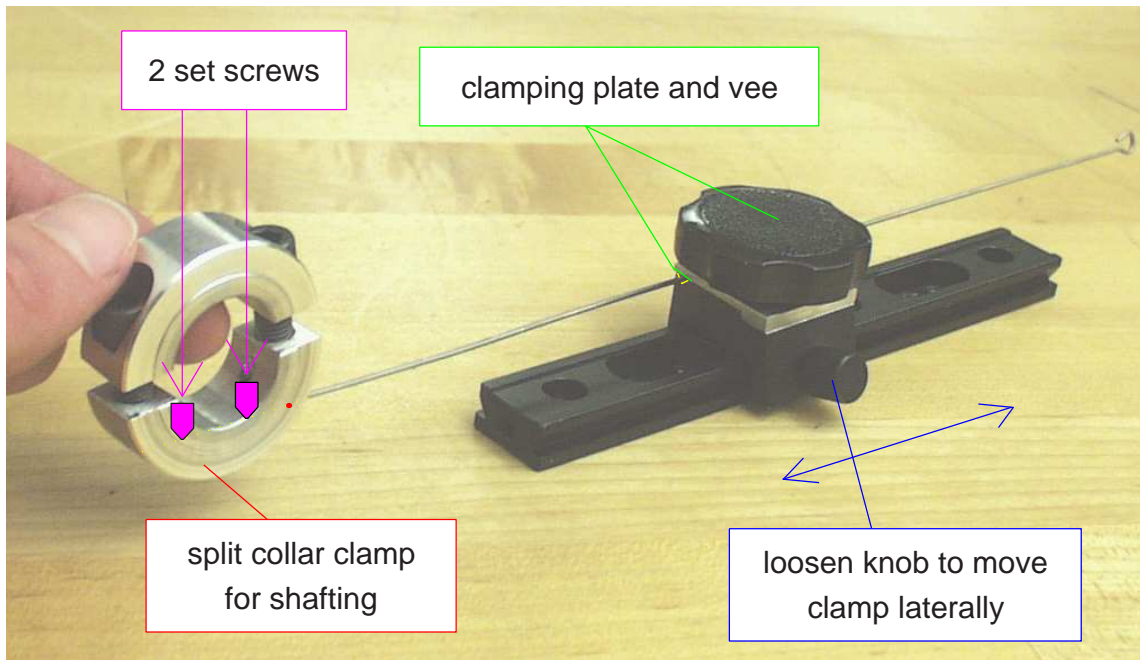
Figure 1-9: Cantilever spring mounting with split collar clamp.

Figure 1-9 shows a split collar clamp that has been modified to securely clamp
one end of a length of welding rod to the stainless steel shafting. In the lab described
on page 170, this rod acts as a translational spring with clamped end conditions.
There are two set screws inside tapped holes within the split collar clamp to fix the
shaft end. The other end is clamped between a vee notch and an aluminum plate,
as shown. The knob at the top of this fixture tightens the clamp, while the one on
the side can be loosened to slide the fixture along the dovetail toward or away from
the shafting. This is a clever design, created by Joe Cattell, that allows students to
adjust the stiffness of spring easily during the labs.

The split collar clamps also appear in many other places through the mechanical
system labs. For instance, they serve as stops to limit the travel of the shafting, and
we adapted a second-order system into a fourth-order system by mounting a blade-
shaped spring with a mass at its end using the split collar clamp. This is depicted

---

[11]with an inner diameter of .75 inches, to mate with the shafting

in Figure 1-8. In another lab (described on page 161), a collar is used to mount a flywheel at the top end of a vertically-mounting length of shafting. Getting the flywheel mounted so that its top surface was square and concentric with the vertical shaft axis was time consuming, requiring some special fixtures to hold the parts in alignment while they were screwed together tightly.

The flywheel was designed to screw into only one half of the two-piece collar. In other words, the halfcollar-flywheel assembly can be taken off the shafting as an intact unit. On subsequent assemblies of the lab, the flywheel will thereby fall into proper alignment once the other half of the collar is used to clamp the structure near the end of a length of precision shafting.

More notes on assembly occur throughout the descriptions of each lab project in Chapter 3. As a final comment, note that considerable time was spent manufacturing mounting blocks in-house, particularly for the air bearings. This was definitely worth the effort for future ease of assembly, however. Using off-the-shelf components whenever possible is also a good strategy, since equipment may need to be replaced over time.

1.3.5 Cost Effectiveness

In any lab setups, cost is of course an issue. We have attempted to keep the necessary components reasonably affordable to enable use by others wishing to copy or adapt ActivLab setups. A list of components, vendors and prices[12] can be found in Appendix C. Note that we were fortunate to be able to use an existing laboratory classroom[13] with 12 lab workstations. Each workstation is equipped with a PC, a dSPACE 1102 controller board, an oscilloscope, a function generator and a power supply. Below is a summary of the most significant costs along with alternatives, where applicable, and the reasoning behind our choices.

As mentioned in the previous section, each of the mechanical ActivLab setups has been designed for assembly on an optical breadboard. We purchased anodized,

---

[12]as of summer, 2001
[13]designed for 2.737, Mechatronics

half-inch thick aluminum baseplates with 1/4"-20 tapped holes at one-inch spacings. Each plate was 18" by 24" and cost about $375. The full 24 inches are required when assembling the translational spring-mass-damper system, as you can see in Figure 3-27.

We realized early in the development of the lab projects that the air bearings would be a costly yet key components for attaining very low friction systems. The bushing and pillow block which comprise each bearing[14] retail for $175 and $85, respectively, and each length of shafting requires two such bearings for support. Our thanks to Drew Devitt of New Way Machine Components who graciously agreed to supply these to us at a substantial discount.

Running the air bearings requires the additional complexity of supplying dry, compressed air to each lab station. Fortunately, our lab space was already equipped with a compressed air supply. We installed filters to dry the air and ran individual lines to each lab station. Each line terminates in a panel-mounted quick disconnect, as shown in Figure 1-10. A valve prevents air flow when the quick disconnect is released. We purchased these small and easy-to-use disconnects along with most of our brass fittings from Beswick Engineering. All together, we spent over a thousand dollars on tubing and brass connectors, which includes a large supply of extra parts.

Swagelok is another good supplier of brass air line fittings and disconnects. However, we preferred the smaller, more elegant (and less expensive) design of the Beswick connectors. One caution about the Beswick quick disconnects: the hollow male plug (labelled "connection to air bearings" in Figure 1-10) and attached tubing can be "shot out" of the quick disconnect housing at high velocity by the pressure of the air line when detaching the line. The heavier, female plug of the connector has a spring-loaded valve, which is needed to shut off air flow when the connection in the line is broken. (The male plug has no such valve, because it is not needed.) Joe Cattell installed the "tubing support" shown in the picture specifically to avoid eye (or other) injuries to the staff when disassembling the hardware.

Of note, we initially considered manufacturing our own baseplates with holes or

---

[14]see Figure 1-3

43
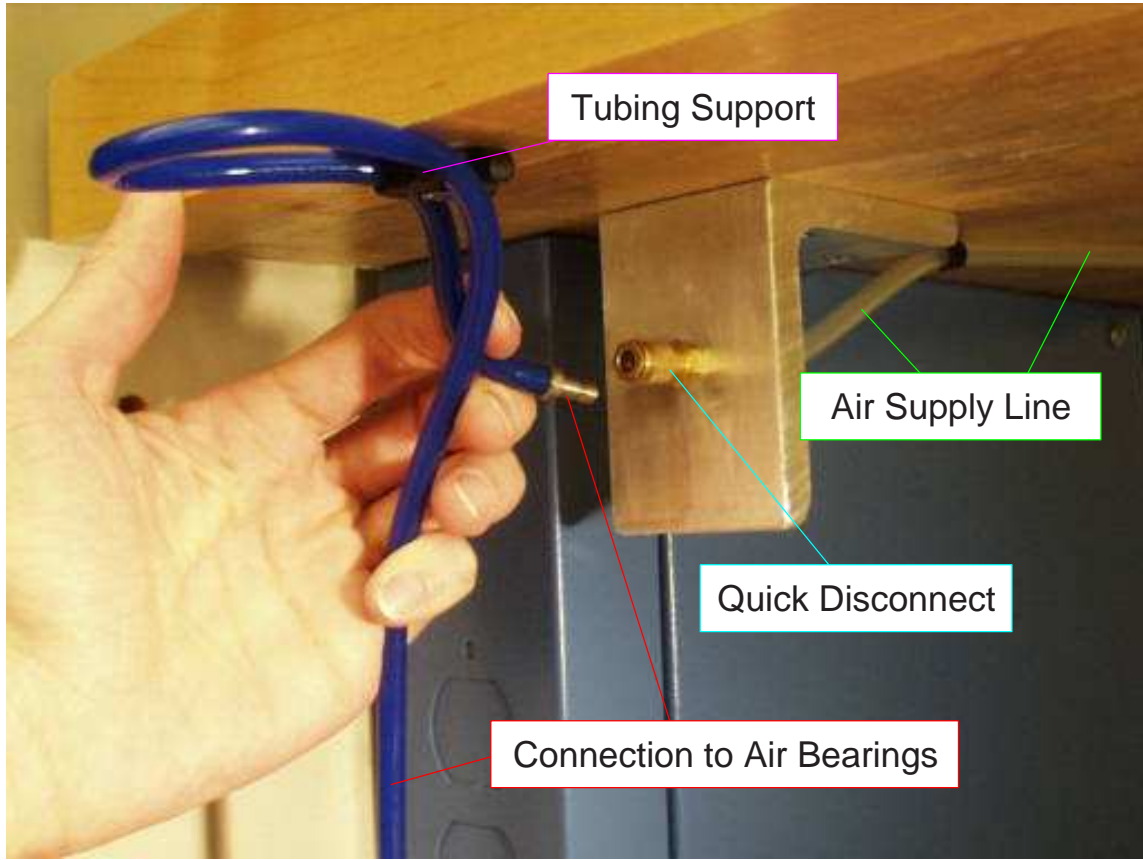
Figure 1-10: Air supply line with quick disconnect fitting.

slots spaced to accommodate the hole alignment in the pillow blocks: 1.5" by 1.562". Our reasoning was that the bearings were known to be constrained to this spacing, and any additional components would either be attached to the breadboard with toe clamps or manufactured in-house to match the unusual spacing. At the time, we envisioned at least one of the lab systems would require two lengths of shafting and therefore four bearings. We also planned to manufacture our own voice coil actuators, which could easily be designed with mounting holes compatible with whatever hole spacing we choose for the baseplates.

Purchasing pre-made breadboards with a standard spacing now seems like the only reasonable option. Either metric or English units can be selected, as convenient. Using toe clamps is not unreasonable, but we chose to manufacture custom mounting blocks to allow the lab components to be linked in place easily like LEGO blocks. The

most essential mounting blocks we built were Delrin[15] adaptor plates which interface between the the pillow blocks and optical breadboard. Figure 1-11 shows adaptors for a voice coil, air bearing and LVDT, respectively. A CAD drawing of the Delrin adaptor plate designed for the New Way bearings is shown in Appendix D.

We have had some issues with the clearance of the bolt holes in these Delrin adapter plates. As a result, the bearings are over-constrained when the bolts through the plates are fully tightened into place on the breadboard. The clearance holes themselves were drilled with appropriate clearance to provide enough slack during alignment. However, the clearance between the counterbore for each hole and the head of the bolt attaching the adapter plate to the breadboard is too tight. The selection of drill diameters available in a machine shop is generally much wider than that of end mills, and we simply chose a mill diameter that was a little too small. We have previously addressed this over-constraint by bolting the adapter somewhat loosely to the breadboard during labs. We have yet to modify the Delrin plates to increase the diameter of the counterbores, which we believe will solve the problem. We therefore cannot yet confirm that this is the sole source of over-constraint in the hardware.

The LVDTs were the single most expensive component we used. As previously noted, we wanted to reduce any friction to a minimum, and therefore wanted a non-contact position sensor. We tested less-expensive LVDT's which had built in signal conditioning (to provide DC output of position directly), but they did not have adequate clearance. The sensors we finally choose (from Shaevitz) provided ample clearance. This clearance was only available for a two-part package including the sensor and a separate signal conditioner[16], however, which consequently meant they were more accurate (although we did not need this accuracy) and more expensive. A partial list of supplies and vendors appears in the appendix on page 417.

---

[15]Delrin is a registered trademark of DuPont.

[16]The cost of the sensor and signal conditioner for one lab set-up was just over \$600.
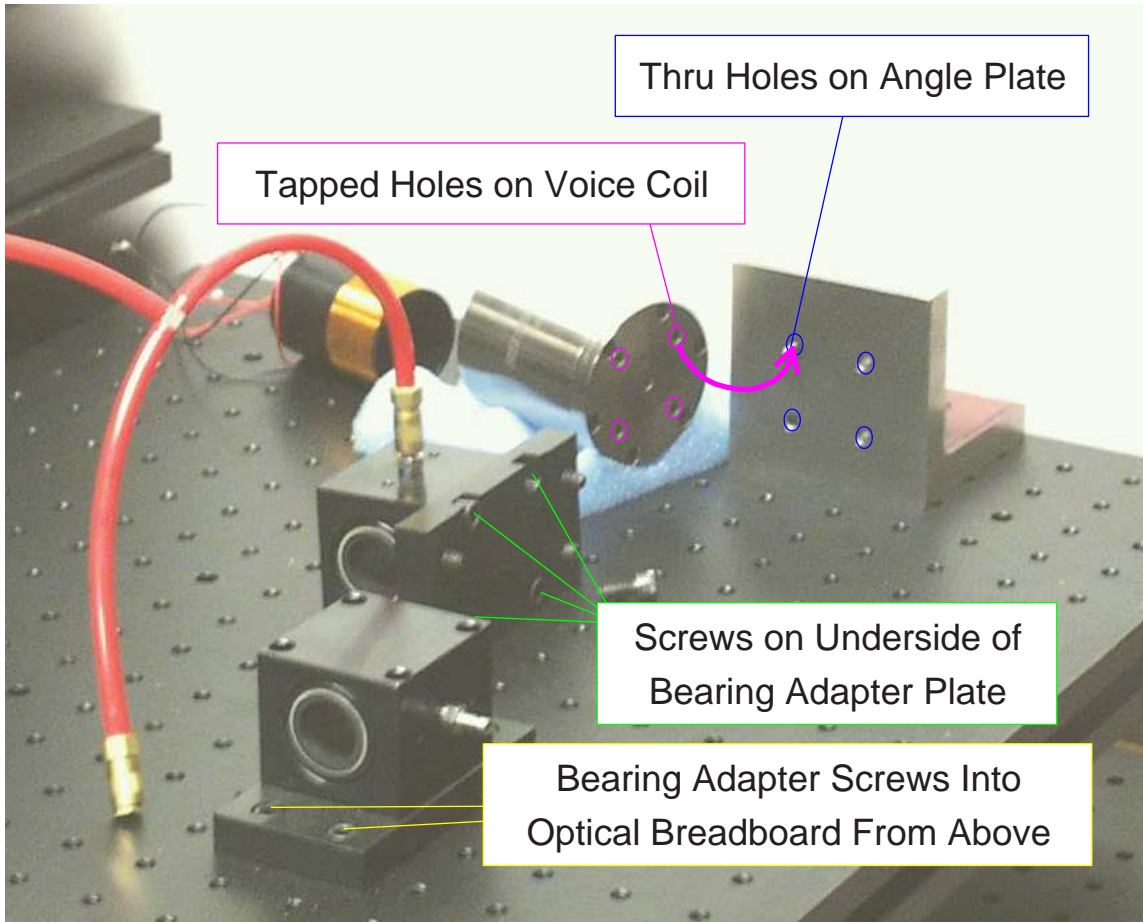
Figure 1-11: Mounting blocks for voice coil and air bearings. One bearing is tipped on its side to show how the Delrin plate is fixed to the bearing pillow block on the underside.

1.4 Summary of the Inverted Pendulum Project
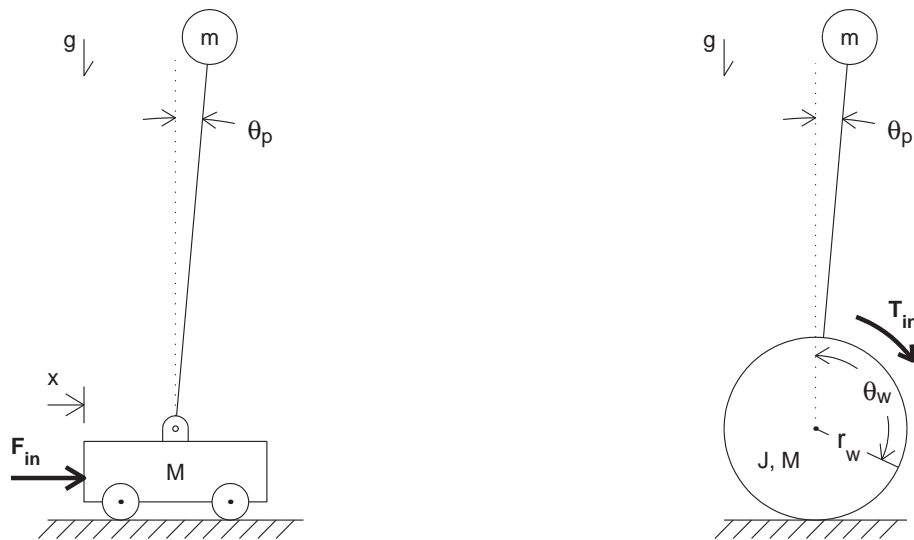
Figure 1-12: Two types of inverted pendulums

An *inverted pendulum* is a familiar classroom demonstration for teaching dynamics and controls at both the undergraduate and graduate level. Topics which can be illustrated include:

- the concept of an unstable equilibrium point

- derivation of equations of motion

- linearization about an operating point

- classical and/or state space controller design

- the relationships between analytical tools such as root locus, and time and frequency response

The most common versions of the inverted pendulum (IP) presented to students incorporate a wheeled cart with a free-hanging pendulum arm. In this type of configuration, shown at the left in Figure 1-12, the pendulum is balanced in the upright (unstable) equilibrium position by moving the cart back and forth.

The inverted pendulum robot developed in this thesis operates somewhat differently. It is depicted at the right in Figure 1-12. In this "robotic" version, the body and pendulum arm of the vehicle form a rigid unit. Motors mounted on either side of this rigid body actuate each of two wheels. Here, the pendulum-body is kept vertical by applying torque to the motors to rotate the wheels and pendulum-body with respect to one another. More details on the operation of the cart and robotic inverted pendulums can be found in Chapters 5 and 7, respectively.

The robotic version developed in this thesis is a two-wheeled robot, inspired by both the iBOT and Segway human transports invented by Dean Kamen[99, 100]. Figure 1-13 shows each of these vehicles. Note how the vehicles in both images balance on two wheels as inverted pendulums. Sections 2.1.1 and 2.1.2 provide more details on each of these devices.

Figure 1-13: IBOT (left) and Segway Human Transports. The rendering of the iBOT comes from a gallery of industrial designs on the "Rhinoceros NURBS modeling for Windows" website (http://www.rhino3d.com/gallery/images/ibotchair.jpg). The photo of the Segway transport was provided at the "Press Kit" section of the Segway website (http://www.segway.com/aboutus/press_releases/pr_062602.html).

1.4.1 Ideal and Actual Hardware Implementation

To function as a practical classroom demo, the IP robot should be large enough to be clearly visible yet also reasonably portable. Since our lecture room must typically be free for other classes before and after the lecture period, the required set-up and disassembly times should each be less than about five minutes. Ideally, the robot would be autonomous, carrying it's own power, microcontroller, and a receiver to allow remote steering.

The robot I created is not autonomous. The robot uses four power supplies: one for each of two motors (36 volts at up to 1.5 Amps for continuous operation, 9 Amps peak), a 12-volt supply for the gyroscope (to measure the absolute pendulum velocity), and a 5-volt supply[17] for a two-axis accelerometer (used as a tilt sensor to compensate for gyro drift). These power supplies are so heavy and bulky[18], one would need to transport them on a separate cart.

The controller is implemented on a dSPACE board, which runs on a PC. This means the equipment cart must also carry a desktop computer (or a laptop with a dSPACE expansion box). In addition to the inconvenience of the bulk of this additional equipment, the lack of autonomy means the robot needs umbilical cords. The vehicle dynamics are affected quite significantly by these cords.

I have tried two mounting schemes for the umbilical cabling. Initially, the cables were attached about five inches directly above the wheel axis. The weight of the cords creates a (disturbance) torque on the pendulum-body, so that its upright equilibrium is offset from vertical (i.e. such that the torque created by the gravity at this angle offsets the disturbance torque). Maneuvering the robot[19] is difficult, both because the cords get in the way and because shifting the position of the robot shifts the disturbance torque.

I also tested the robot with the cables attached about four inches *below* the wheel

---

[17] The dSPACE controller board currently provides the 5-volt supply.

[18] The Lambda power supplies for the motors are shown in Figure 1-14 on page 1-14. They weigh over 50 pounds, together.

[19] Two rotary pots provide steering inputs. One sets the forward/reverse velocity and the other controls turning radius.

axis. This creates a smaller disturbance torque, since there is a much shorter length of cable. Unfortunately, the cable helps stabilize the pendulum-body, however! This makes it more difficult to evaluate the performance of the controller objectively (in stabilizing the robot). The vehicle is also less responsive to commanded velocity. For this type of inverted pendulum, a constant (linear) velocity corresponds to a constant pendulum offset angle. Picture the cables as a "tail" dragging behind (or ahead of) the robot. The static friction between the ground and cables allows a range of "stable" pendulum angles, rather than a single equilibrium angle. For low velocity commands, the robot will stabilize about an angle somewhat off of vertical, but the static friction balances the (constant) torque to the wheels and prevents it from rolling. The controller was designed with the umbilical in the first configuration (mounted above the wheel axis), but the data in Chapter 7 were obtained with the second umbilical configuration. (When operating near equilibrium and at zero forward velocity, the response of the system in each of the two configurations did not differ significantly.)

1.4.2   Challenges and Control Strategy

The most significant challenges in implementing the robot fall into one or more of the following three categories: (1) the mechanical design (i.e. scaling and packaging components appropriately); (2) filtering the sensor signals; and (3) modelling, controlling and/or attenuating higher order dynamics (resonances) in the system.

Mechanical Design

The robot is both more visible and more impressive as a classroom demo if it stands at least a meter or so high. The size of the robot has a huge influence on the complexity of the design. Two extreme examples (described in more detail in Chapter 2) which make this point are the LegWay inverted pendulum robot (described on page 80) and the robotic unicycles described on page 84. The LegWay stands just a few inches tall. Its low weight and inertia allow it to run with standard, Lego (9-volt) motors and to

carry batteries and processor onboard.

The robotic unicycles have enormous inertia by comparison.[20] The motors for such a vehicle need to provide much more torque, and this in turn significantly increases the complexity of providing onboard power. The large inertia will also be inherently more "sluggish" to control. Finally, the sensors for the unicycle are both more numerous and more complex, which again adds to the hassle of packaging everthing.

I designed the chassis of the demo inverted pendulum robot ("DIPR") to be somewhat versatile for future modifications, with the expectation that it would eventually carry its own power and controller. As of this writing, however, the robot still uses umbilicals. Unfortunately, the umbilical cords greatly influence the dynamics of the robot. They are heavy and put a substantial offset torque on the pendulum (for which one compensate reasonably well by offsetting the equilibrium angle of the pendulum away from vertical). More importantly, when they scrape the ground, this causes substantial friction, as mentioned, and can even provide a stabilizing force against the ground. Making the robot autonomous would also improve the steering capability.

Selecting or manufacturing appropriate wheels was (surprisingly for me) another notable concern. One needs to keep the robot "dynamically interesting" as a control problem. That is, if you make the wheel inertia too large, the wheels essentially become fixed objects ("rocks"). Also, using wheel bearings introduces additional issues and potential pitfalls (friction, alignment, etc), so a direct drive system (attaching a wheel directly to the motor's output shaft) is appealing. Each motor gearhead is rated for 120 N radial force at 12mm from the mounting plane, or 1.44 N-m of torque. The pendulum-body has a mass of 8 kg, divided (symmetrically) over the two wheels. In order to meet the side-load spec, this limits the distance of the wheel from the gearhead flange to no more than about 36mm (1.4 inches). Commercially available wheels with a large enough diameter (12 inches) were generally too wide (2+ inches), too heavy and too difficult to mount, so I finally decided to manufacture my own wheels. They are cut from 1/4 inch aluminum plate and have rubber o-rings epoxied to the circumference for traction. This is not the most elegant solution, but it works.

---

[20]See Figure 2-13 on page 85.

(The centerline of the wheel is about 1 inch from the flange of the gearhead.)

Sensors

Sensor issues are discussed in detail in Section 7.1. The two main challenges were: (1) compensating for drift in the gyro (to measure pendulum angle in an inertial reference frame), and (2) filtering the differentiated motor encoder signals to obtain a smooth measurement of motor velocity.

The gyro signal represents angular velocity. It is accurate at high frequency, but it has a DC bias which leads to low frequency angular errors. It is currently combined with a 2-axis accelerometer (more accurate at low frequency) through complementary filtering. Section 6.2 discusses complementary filtering in more detail.

Filtering the encoders to obtain velocity involved a trade-off between accuracy and smoothness of the resulting output. Quantization of the encoder and backlash in the gearhead are of particular concern here. Section 7.1.4 describes this in more detail.

Controller Design

Initially, I modelled the known parameters of the robot in state space and attempted to design an LQR (linear-quadratic regulator) controller.[21] This controller did successfully balance the robot, but it also excited a significant *resonance*! State-space controller methods depend on accurate modelling of system dynamics, and there were clearly important higher order dynamics in the system that I had not modelled.

My advisor, Prof. Trumper, suggested a different approach, which I successfully used to control the robot (with no significant excitation of resonances). The controller is structured with an inner loop to control wheel velocity and an outer loop to stabilize the pendulum. The resulting controller still amounts to a state-space controller (i.e. it multiplies some gain times the filtered signals of each of the same, four state variables previously mentioned; then adds these four values to create a control signal). However,

---

[21] The four state variables were pendulum angle, pendulum velocity, motor position, and motor velocity. Of these, the cost weighting on pendulum angle was clearly the greatest.

the methodology used to design the controller essentially involved loop-shaping (not state-space methods).

Vibration of the *pendulum arm* was particularly noticeable during the LQR-induced resonance. I therefore replaced this arm with a stiffer version. The chassis consists largely of rectangular aluminum extrusions. These were also vibrating significantly, so I added damping layers to the rest of the structure. There is now rubber where the pendulum arm attaches to the body and constrained-layer damping where structural members meet in the chassis. The changes seemed to help reduce the effects of resonances, but since all changes were made simultaneously, I am not sure which were most useful. I still suspect it might prove difficult to create an accurate enough state-space model of the system dynamics to design a satisfactory LQR controller, both because the magnitude of the vibrations observed with the original LQR control implementation were so significant, particularly along the length of the pendulum, and also because I have subsequently found that measurements of transfer functions for the system are not highly repeatable above 100 Hz. I choose to focus my efforts on a loop-shaping approach instead. The initial LQR controller is not discussed further in this thesis.

1.4.3   Results

Figure 1-14 shows the inverted pendulum robot and supporting hardware. The robot stands about 42 inches tall and weighs just over 23 pounds. The transient response (to a disturbance torque and/or force on the pendulum body) is somewhat underdamped, as seen in Figure 1-15. Achieving a significantly faster response[22] would be difficult, given the large inertia of the robot. The frequency response plots and discussion in Section 7.6 aim to explain this in more detail. Stated briefly, there are unmodelled (and not robustly repeatable) higher-order dynamics in the transfer functions from commanded voltage[23] to the sensor outputs (i.e. to pendulum angle [and velocity]

---

[22]It takes roughly 2 seconds for the transient response to essentially die away

[23]Note, the transfer functions obtained using current command do not differ much from those with voltage control of the motors. The choice between voltage and current control is discussed in

and to motor angle [and velocity]).

Since both motors are commanded together in tandem (with a sign difference, because they are oriented in opposite directions), we can break the control loop at this point (where we have a single, commanded output value). Figure 1-16 shows the loop transmission.[24] The peak near 50 Hz occurs in the measurement of pendulum angle and velocity, while the peak just about 100 Hz appears only in the measurements of motor angle and velocity. The loop transmission shown includes low-pass filtering of the motor output to push these two resonances (and anything else at higher frequencies) below unity.

Crossover for the control loop (i.e. broken at a single motor output) is at 9.2 Hz.[25] The controlled robot is a multi-input multi-output system, since it acts on errors in both pendulum angle and wheel position (and their derivatives). The state-space controller begins to lose control authority over *pendulum angle* after 0.5 Hz. This can be noted both in the transient response in Figure 1-15 and the closed-loop transfer function to pendulum angle, shown in Figure 1-17. Figure 1-15 overlays theoretical impulse response plots on the actual data which correspond to a second order system with a natural frequency of 0.5 Hz, with $\zeta = 0.25$, and the magnitude of closed-loop transfer function from voltage to pendulum angle, shown in Figure 1-17, begins to dip below unity after about 0.5 Hz.

The response of the DIPR to either a commanded step in pendulum angle or an impulsive disturbance (both shown in Figure 1-15) seem qualitatively quite smooth and stable at this bandwidth. Increasing the inertia of an inverted pendulum slows the response of the system to imbalancing disturbances. Therefore, the larger the inertia of the vehicle, the lower the required bandwidth necessary to maintain stability. This is the same phenomenon which enables a man to balance more easily on a tightrope[26] if he uses the large inertia of a balancing bar, or which makes it easier to balance a vertical broomstick on the palm of the hand than than it is to balance a shorter

---

more detail in Sections 7.5.4 and 7.8.3.

[24]This figure is identical to the lower half of Figure 7-42 on page 386.

[25]The resulting closed-loop TF falls to -3dB at 7.3 Hz.

[26]A tightrope walker is in fact an inverted pendulum system.

Steering Input

dSPACE Box

Gyro Power

Power Supplies

Inv. Pend. Robot
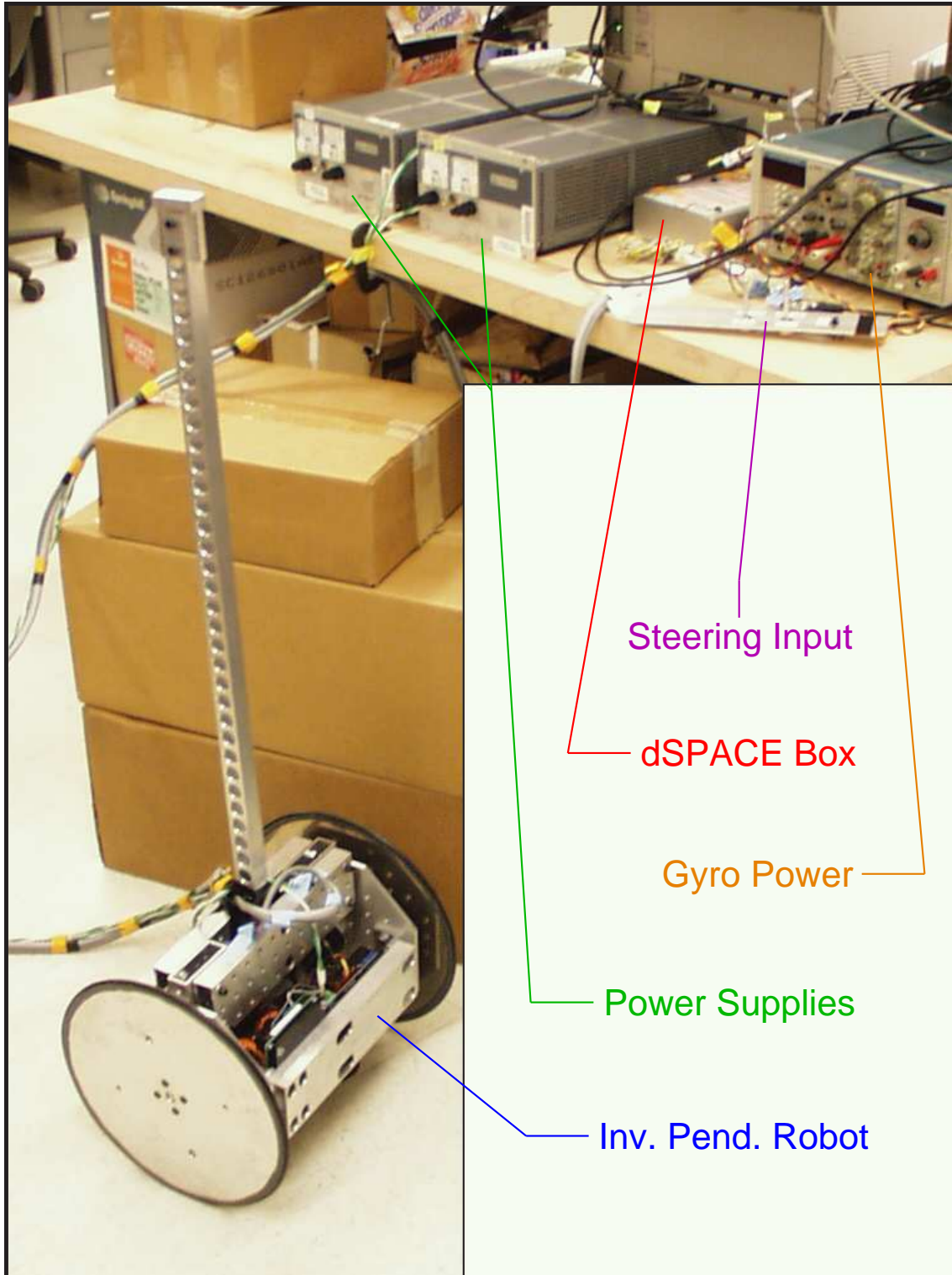
Figure 1-14: Inverted pendulum robot set-up
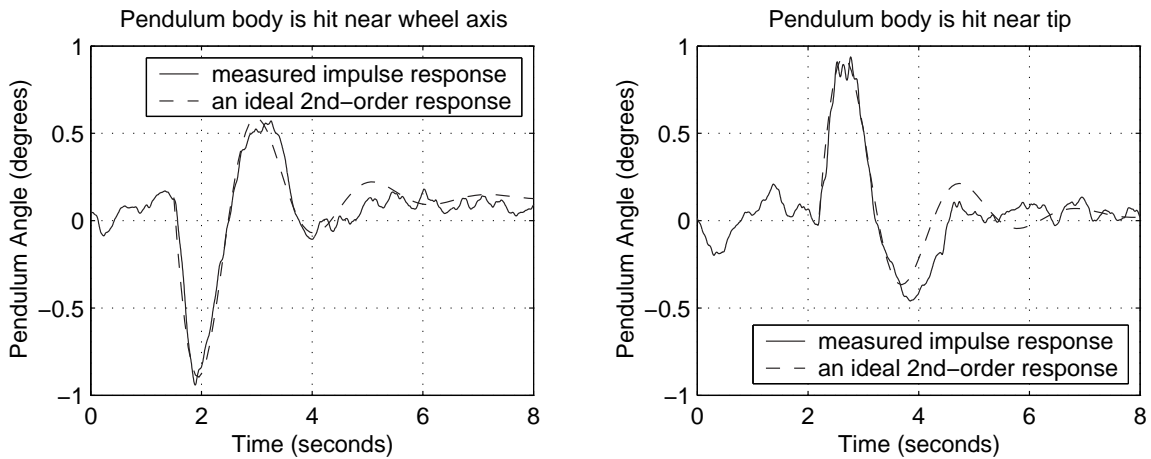
Figure 1-15: Impulse response of IP robot. At left is the response of the IP robot to a sharp nudge applied at the height of the wheel axis. This essentially creates an impulsive disturbance *force* on the robot body. At right is the response to a quick nudge applied near the pendulum tip, creating a disturbance *torque*. The two responses are quite similar in shape (as expected), aside from a difference in the sign of the response. Overlaid on each data set is an ideal (theoretical) impulse response for a system with an undamped natural frequency $\omega_n = 0.5$ Hz (3.1 rad/sec) and a damping ratio $\zeta = 0.25$.
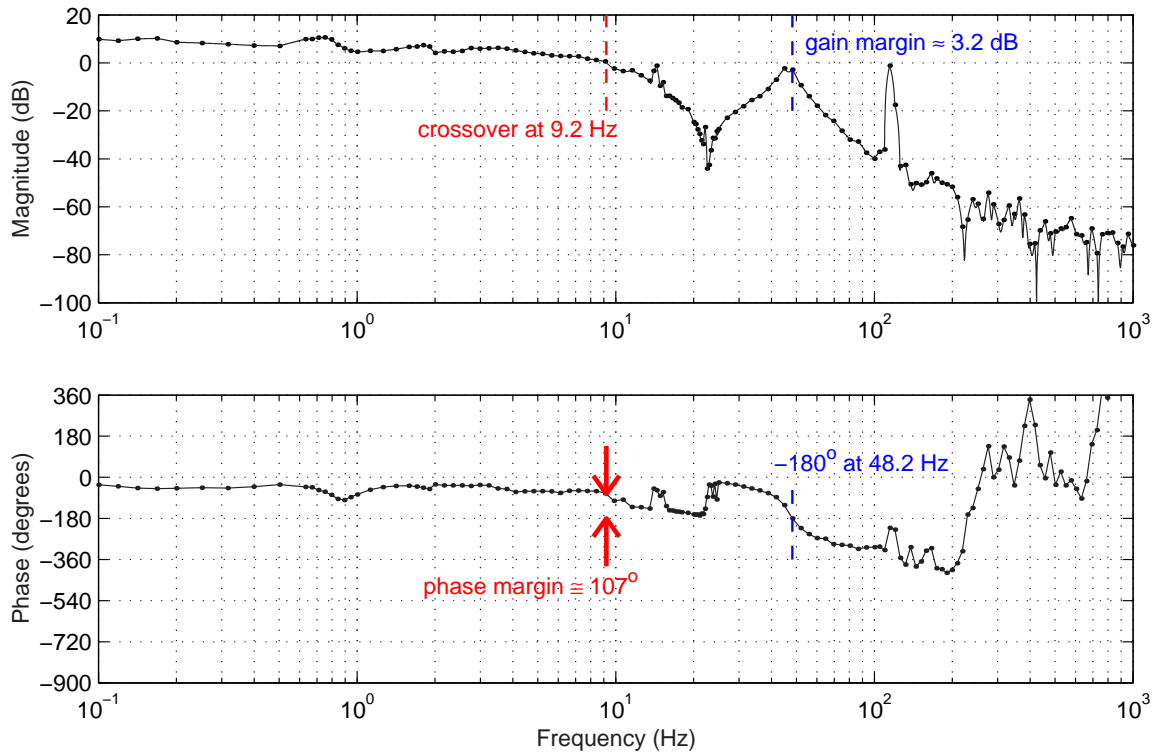
Figure 1-16: Loop transmission for robot and controller

stick. The system has more inherent stability with the larger inertia, and a human is correspondingly allowed to respond more slowly (i.e. with lower bandwidth) to keep the system stable. There is an inherent trade-off, however, because a large inertia also lowers the achievable bandwidth of a controller.

Figure 1-18 compares the performance of the DIPR with that of a similar, two-wheeled inverted pendulum robot named Joe, which was created by researchers at the Swiss Federal Institute of Technology in 2001[75, 74]. Joe is described in more detail in Section 2.1.3. Joe has a mass of 12 kg and stands 0.65 meters tall, while the DIPR is 10.5 kg and 1.15 meters tall. Unfortunately, I do not know the effective inertia of Joe's pendulum body or wheels compares with that of the DIPR. The response of the DIPR is notably hampered by its umbilical cords, and the impulse response shown at the top of Figure 1-18 is not entirely repeatable. In particular, the transient response of the system changes if the initial alignment of the umbilical is changed. I believe this partly explains why the data for the DIPR look less ideal than those Joe, and
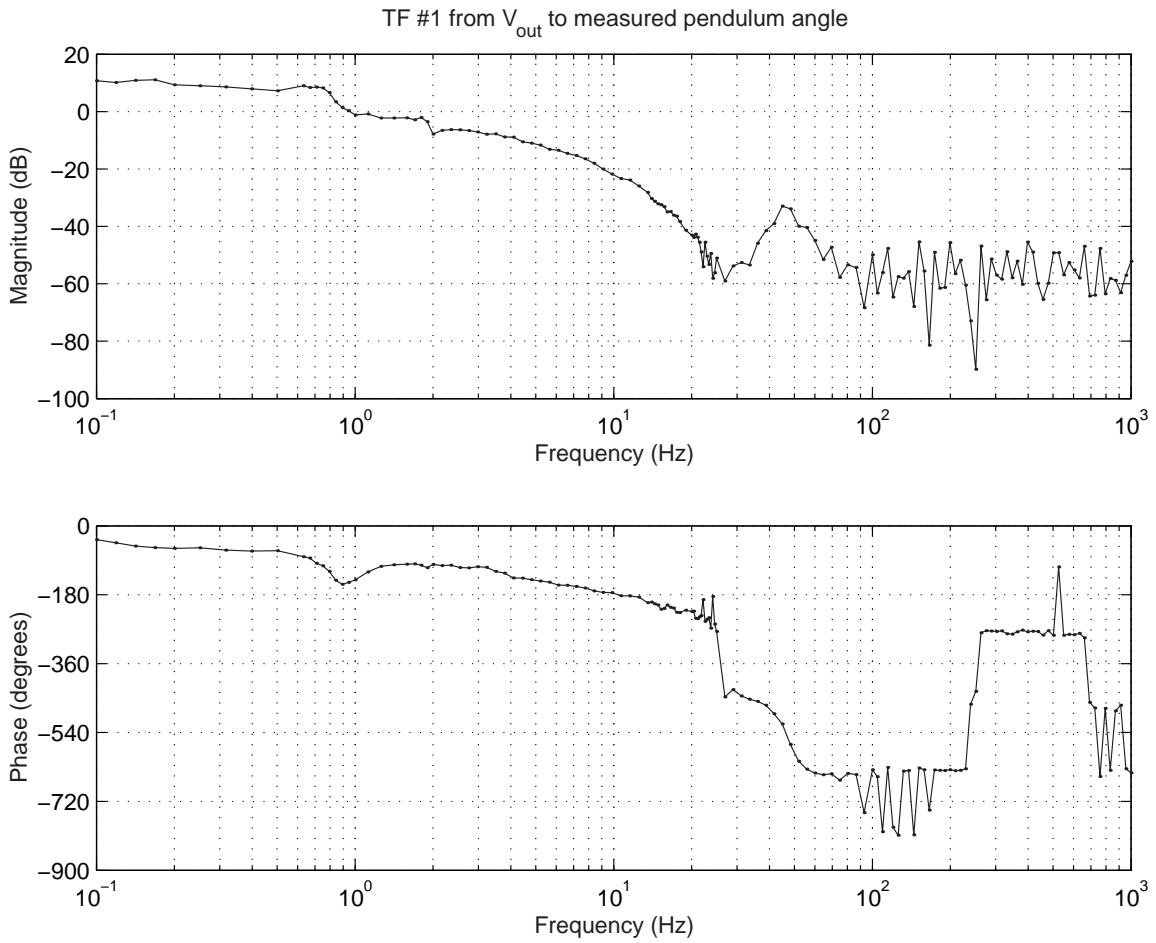
Figure 1-17: Experimental transfer function : $\theta_p(s)/V_o(s)$. This is the transfer function from commanded voltage to the motor, $V_o(s)$, to measured pendulum angle, $\theta_p(s)$ (in units of degrees).
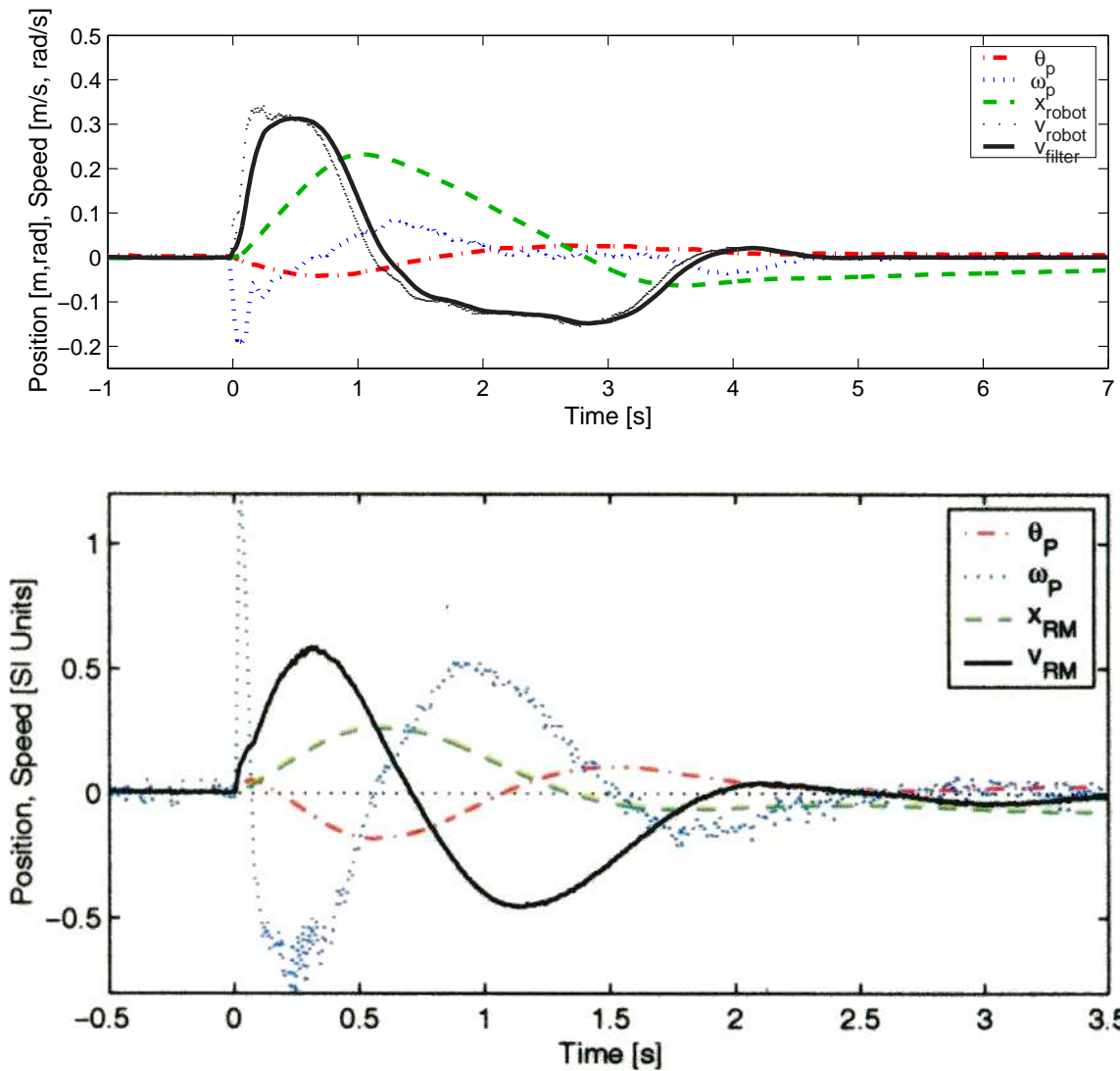
Figure 1-18: Impulse response of IP robots. Shown at top are data for the DIPR, the robot developed as part of this thesis and described in Chapter 7. Impulse response data for a similar robot named "Joe" (which is described in Section 2.1.3) are shown below this, for comparison. Note that the x-axes differ by a factor of two. The data for Joe come from a scanned image in an unpublished version of a paper about the robot by Grasser, D'Arrigo, Colombi and Rufer[74].

that the DIPR's response might look more like that of Joe if it were autonomous.

The impulse response data shown in Figure 1-18 for the two vehicles are similar, with a few noteworthy differences. First, Joe responds about twice as quickly as the DIPR.[27] Next, the data for Joe show a larger angular displacement in pendulum angle and were (I believe) taken under current control[28], while the DIPR commanded voltage to the motors for this particular data set. The difference in response when the DIPR is run under current or voltage control is not significant, however. Finally, Joe uses a first-order filter with a cutoff frequency of 10 rad/s to smooth the differentiated motor encoder output[29], while the DIPR uses a first-order filter with a cutoff at 200 rad/s. Therefore it is difficult to compare the velocity response of the robot (v_{RM} in Joe, labelled more clearly as v_{robot} in the data for the DIPR).

To address this final issue, I have included two plots of the robot velocity for the DIPR in the impulse response at the top of Figure 1-18. One, labelled v_{robot}, shows the response using the DIPR's filter with a breakpoint at 200 rad/s, and the second, labelled v_{filter}, uses a breakpoint at 10 rad/s, to correspond more closely with the data for Joe. Figure 1-19 shows data for an early implementation of the control system for the DIPR which suffered from vibration problems similar to ones cited in early versions of Joe. Joe's vibrations, which were attributed to the effects of backlash[75, p. 111], were eliminated by filtering the measurement of motor velocity.[30]. In the DIPR control system, vibration was greatly reduced by applying a 1st-order low-pass filter with a breakpoint at 20 rad/s to the commanded motor output.

The next chapter provides descriptions of several steerable inverted pendulum vehicles, including "Joe". Chapter 2 also surveys a variety of viewpoints and projects related to teaching undergraduate-level dynamics, control and design. This is followed by descriptions of the ActivLab projects in Chapter 3 and some related demos

---

[27]Note the time axes differ by a factor of two on the plots.

[28]Grasser et al do not explicitly state that they use current control, but they do state, "the vehicle is controlled by applying a torque C_L and C_R to the corresponding wheels."[75]

[29]The filter reportedly eliminates limit cycling due to effects of backlash in Joe[75].

[30]A 1st-order filter with a breakpoint frequency of 10 rad/s is used to filter Joe's motor velocity, as cited earlier.
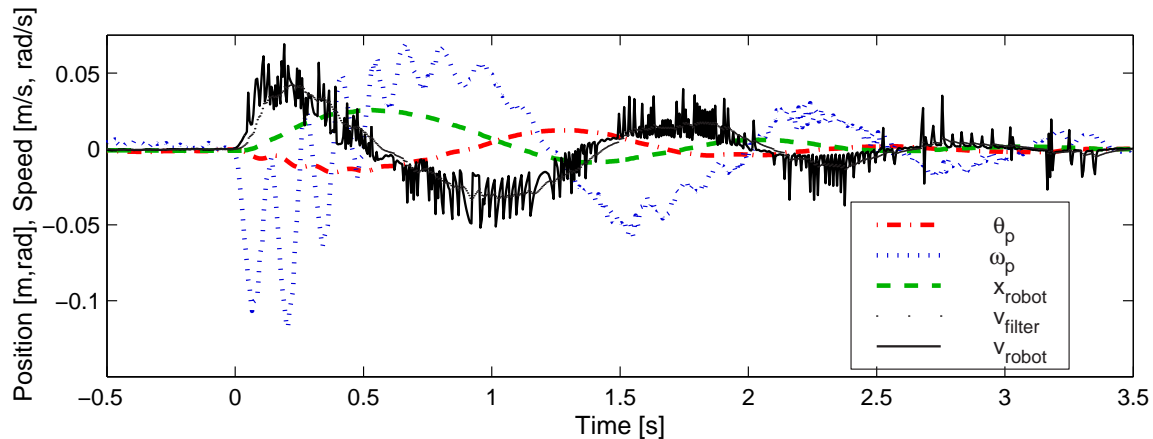
Figure 1-19: Vibration in an early implementation of the DIPR. The plots above show impulse response data for an early implementation of the filtering and control system for the DIPR. The vibrations are due to the poor filtering of the differentiated motor encoder signals. These vibrations were reduced significantly by filtered the commanded output to the motor with a first-order low-pass filter with a breakpoint of 20 rad/s.

for teaching 2.003, described in Chapter refchap:dynpro. Chapter 5 describes an existing cart-driven inverted pendulum used at MIT, and Chapter 7 finally discusses the DIPR, providing details on its hardware, system dynamics, control algorithm and performance. Chapter 8 summarizes both the ActivLab and DIPR projects. At this time, we do not plan to use the DIPR as a classroom demo. The conclusion in Chapter 8 describes some of the difficulties in using the DIPR as a portable classroom demo and suggests improvements.

Chapter 2

Survey of Related Projects

This chapter reviews a variety of projects related to the demo inverted pendulum robot (DIPR) (described in Chapter 7) and the ActivLab experiments (in Chapter 3). The Segway and iBOT are both human transports which operate as inverted pendulums. Both were direct inspirations for the design of the DIPR. In contrast, the other projects described here were generally not direct influences. They are instead included because they illustrate a variety of potential directions one can take in accomplishing the two primary goals of this thesis: namely, (1) the creation of an inverted pendulum robot and (2) the development of hands-on experiences that both illustrate system dynamics and specifically provide a foundation for controls and mechatronic design.

The control algorithms for the pendulum robots surveyed in this chapter are by and large quite similar to one another and to the control strategy I implemented for the robot discussed in Chapter 7. Specifically, most are essentially state-space controllers that multiply some gain matrix, K, times the estimated state vector. Figure 2-1, taken from a DEKA patent that appears to relate to both the Segway and iBOT, shows a schematic of this structure.[1]

Paraphrasing Dean Kamen at a lecture on the iBOT at MIT in Fall of 2000,

---

[1]The patent describes several "embodiments" of inverted pendulum transportation devices, with the passenger either seated (similar to the iBOT) or standing (as on the Segway), although none look quite like either the Segway or iBOT.
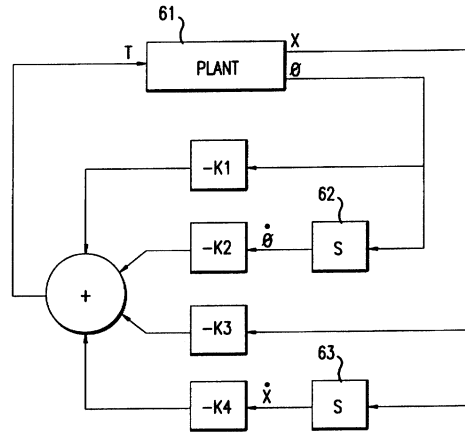
Figure 2-1: DEKA control loop for inverted pendulum vehicle. Image obtained from U.S. Patent 5,792,425: "Control Loop for Transportation Vehicle" [97].

creating a controller that can balance as an inverted pendulum is not one of the more difficult tasks in designing a human transport like the iBOT: the inverted pendulum is a standard problem in undergraduate controls. Creating an electro-mechanical system that is robust enough to balance human cargo in real applications, however, involves many significant challenges.[2] In particular, one must design redundancy into the sensors, actuators, power and processor to create a fail-operational vehicle. A "fail-safe" device is one which will gracefully enter a safe, non-operational state when failure is detected. Because the inverted pendulum vehicles described here are inherently unstable system, they cannot enter such a state. They must instead be "fail-operational"; that is, they must be able to continue operating normally after one (or possibly more than one) sensor, actuator or processor failure is detected. The redundancy requirements necessary for fail-safe operation are discussed in more detail in Section 6.1.

My descriptions of the iBOT, the Segway, and my DIPR robot reflect my own interest in and respect for the importance of the sensors and signal processing in these vehicles. Filtering of the gyro, accelerometer, and encoder signals were significant

---

[2]The iBOT has particularly stringent requirements for robustness, because it is classified as a medical device (similar to a wheelchair).

issues in successfully controlling the DIPR, and the gyro was a substantial portion of its total cost. MEMS gyros are beginning to provide a more affordable alternative however. Over the past ten years, much of the research and advancement in MEMS sensor technology has been motivated by the automotive industry, who have created a substantial market for high-volume, low-cost accelerometers and gyros, used (for instance) in triggering airbags and providing traction control, respectively. The iBOT and Segway rely on rate gyros of this type.[3]

I discuss the current trends making MEMS gyros more accurate and cost-effective in some detail, because the Segway and iBOT clearly demonstrate that these sensors are an adequate alternative to the more expensive Watson VSG gyro I used. In other words, I expect these gyros will find other applications, as they become even more accurate. The issues involved in correction for gyro drift and failure detection are fascinating, educational, and relevant to future technological developments. For all these reasons, I suggest incorporating MEMS gyros into a mechatronic laboratory project. Hopefully, the information in Sections 6.1, 6.2, and 7.1.5 makes a case for this to the reader.

The second half of this chapter (Section 2.2) describes several projects at other institutions which give students hands-on experiences relevant to system dynamics and mechatronics. Note that Chapter 4 surveys a variety of potential projects tested or considered in teaching 2.003: Modeling, Dynamics and Control I. The projects in Chapter 4 generally consist of either alternatives to the present ActivLab laboratories or complimentary in-class demos. In contrast, the projects described in Section 2.2 show various directions taken in teaching classes at other universities or in other disciplines.

---

[3]The bias and rms noise figures for the CRS-03 MEMS gyro used in the Segway are roughly 25x greater (worse) than those for the Watson VSG ("vibrating structure gyro" with a cylindrical, piezoelectric shell). The latter has a resolution of .025 $^o/s$ at a 100Hz BW and run-to-run bias stability of 0.1 $^o/s$. Silicon Sensing does not publicize the price for their MEMS sensor, but it is almost certainly less than 1/25 the \$1000 price of the higher-quality Watson gyro [40, 85, 19, 24].

2.1   Inverted Pendulum Vehicles

As mentioned in Chapter 1, the DIPR robot was inspired by the iBOT and Segway human transports. Since both devices balance a human being in an unstable pendulum equilibrium position, each must have a high level of robustness and redundancy. Sections 2.1.1, 2.1.2 and 6.1 focus on these unique and demanding requirements.

While working on this project, I discovered a group at the Swiss Federal Institute of Technology had already built an autonomous, steerable robot (named "Joe") which is very similar to the one planned for my own project [75]. I include data in Section 2.1.3 comparing the performance of Joe to that of the DIPR in Section 1.4.3 of the introduction. The umbilical cords on the DIPR affect its response significantly. For instance, the transient response of the system changes if the initial alignment of the umbilical is changed. I suspect making the DIPR autonomous may make help the DIPR perform comparably. Section 2.1.3 summarizes the design of and results for Joe.[4]

Many robot enthusiasts and clubs have clearly been inspired by Dean Kamen's Segway human transport. I learned about each of the inverted pendulum robots described in the Sections 2.1.4, 2.1.5 and 2.1.6 while finishing my thesis in February, 2003. They are of interest because together they survey a fairly wide range of complexity both in construction, sensor capabilities, and control algorithms. Finally, I mention two robot unicycles in Section 2.1.7. A robotic unicycle is quite impressive, since it must actively stabilize its pitch (like the Segway) and roll (i.e. lateral stability, which is provided passively on the Segway-type vehicles by having two side-by-side wheels) to remain upright. Each of the two unicycles described can even steer to some extent (thereby controlling yaw) by pivoting an reaction mass mounted within the vehicle.

---

[4]As of this writing, the Joe's creators maintain a website with more information about their device. This site also contains images and movies of the robot. *http://leiwww.epfl.ch/joe/*

2.1.1 The iBOT

The iBOT is an inverted pendulum vehicle developed by Dean Kamen and other engineers at DEKA research in the 1990's[5] as a medical device similar to a wheelchair. The iBOT provides several unique advantages over a traditional electric wheelchair. These advantages are aimed at allowing a more "normal" and independent day-to-day lifestyle for the handicapped.

The iBOT attained widespread publicity on June 30, 1999, following an NBC Dateline television presentation. Johnson & Johnson now owns the rights to the "Independence iBOT 3000 Mobility System" and hopes to market it worldwide. The FDA granted "expedited review status" to a pre-market approval (PMA) application in the fall of 2002 [179]. While this does not guarantee approval, it is a significant landmark, granting the iBOT a fast-track status "reserved for important new medical technology, meaning a decision could come in a few months" [10].

Figure 2-2: The iBOT in action. Image of Dean Kamen (at left) obtained from MSN Dateline website [142]. Image of person climbing stairs at a tradeshow taken from John Williamson's personal website [215].

---

[5]The earliest of Kamen's patent applications for related vehicles and technology seems to date back to May of 1994 (for US Pat. No. 5,701,965 awarded in 1997)[98].
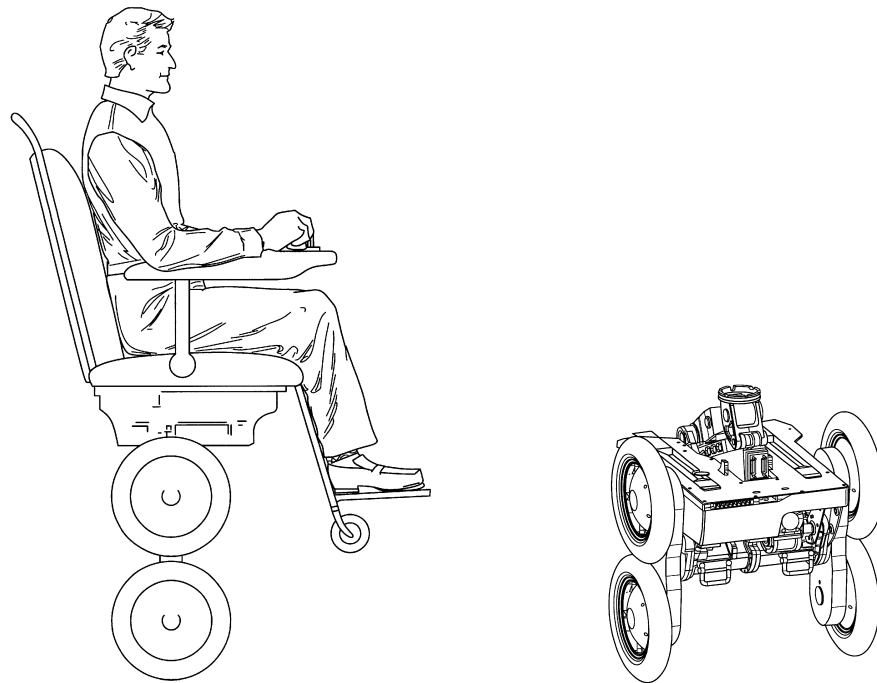
Figure 2-3: iBOT balancing as an inverted pendulum. Source: U.S. Patents 6,405,816 and 6,415,879 [99, 100].
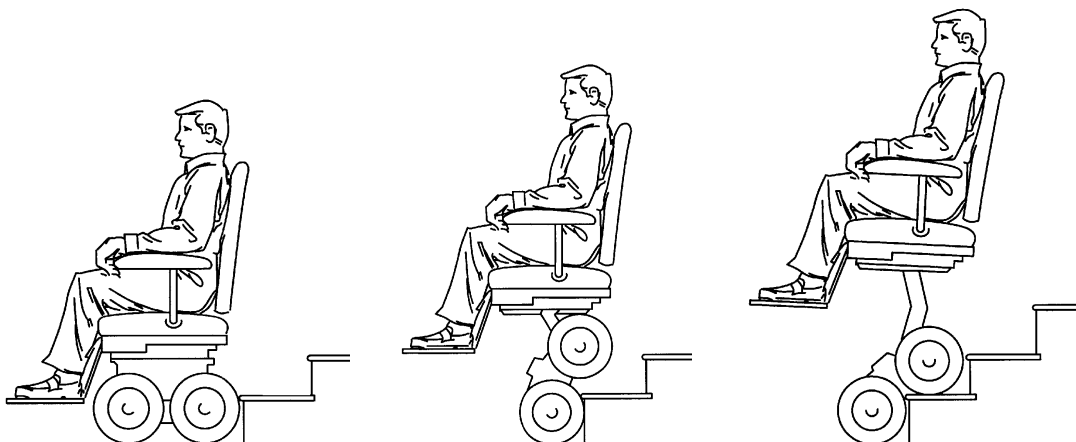
Figure 2-4: iBOT climbing stairs. Use of a support/handrail is required but not shown. Source: U.S. Patents 6,405,816 and 6,415,879 [99, 100].

2.1.2 Segway Human Transport

Figure 2-5: The Segway human transport. Images depict (left to right) a postal worker in San Francisco (source: The San Francisco Chronicle website [177]); use during the Boston Marathon by Boston EMS (source: Boston EMS website [36]); inventor Dean Kamen (source: The Associated Press [14])

The Segway human transporter, shown in Figure 2-5, is essentially a spin-off of the inverted pendulum technology used in the iBOT. While the iBOT is a medical device, designed to provide mobility for a seated handicapped passenger, the Segway carries a standing passenger and is marketed to a broader audience as a high-tech scooter.

The Segway was "unveiled" in December of 2001 after months of speculation about a mysterious new invention commonly referred to as "Ginger" (or simply "It"). In an interview with Dean Kamen for Time magazine, Kamen gives the following explanation for the nickname "Ginger":

> "Watching the IBOT, we used to say, 'Look at that light, graceful robot,
> dancing up the stairs'–so we started referring to it as Fred Upstairs, after

Fred Astaire," Kamen recalls. "After we built Fred, it was only natural to name its smaller partner Ginger." [82]

The Segway is designed with a "footprint" similar to a standing human (19"×25"), with the intention that it can be used as an extension of the human body [79, 82]. That is, it should be not be any more intrusive than a fellow pedestrian on walkways, and the interface should feel as effortless as walking.

Top speed of the Segway is 12.5 mph. It can travel about 10-15 miles on a single battery charge and can negotiate up to a 20° angle of incline [111]. The Segway weighs 65 or 80 lbs (depending on the model). Initial models (engineered for "industrial" markets, like the U. S. Postal Service) sold for $8000. A consumer version was expected to be available in early 2003 for around $3000 [82, 111, 43], but the current price at Amazon is just under $5000 [8].

Several companies have worked in partnership with Segway LLC to develop the technology for the Segway. As with the iBOT, redundancy is important (to allow fail-operational behavior). The design also needs to be efficient (to minimize weight and size), quiet and elegant (i.e. appealingly simple and not intimidating, from an industrial design perspective).

Two notable technological developments in the Segway (and iBOT) are the gyros and motors. The MEMS gyros used are manufactured by Silicon Sensing, a company created as a joint venture between Sumitomo (a Japanese company with expertise in MEMS fab) and British Aerospace (designers of piezoelectric ring-resonator gyros). These gyros are discussed further in Section 6.1.7 of Chapter 6. The rest of Section 6.1 in that chapter discusses issues related to the geometric orientation of sensors in a redundant array.

Pacific Scientific Company designed the motors for the Segway.[6] They developed several innovations aimed at increasing reliability, efficiency, and ease of assembly. First, they developed (and patented) a fault-tolerant winding.[7] The motor is wound in two, isolated stator hemispheres, as depicted in Figure 2-6. The motor can continue

---

[6]The Segway uses two 2-horsepower brushless permanent magnet DC servo motors.
[7]U. S. Patent #5,929,549 - "Fault Tolerant Electric Machine" [196].
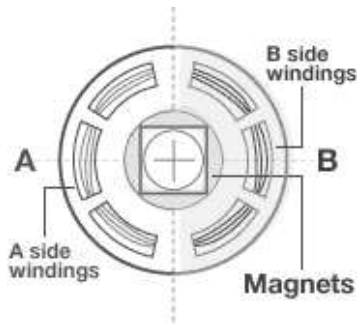
Figure 2-6: Schematic of fault-tolerant motor windings in the Segway. GIF obtained from Segway sales site at amazon.com [8]

to operate if either half fails. This gives the Segway actuator redundancy without the need to equip the vehicle with a duplicate pair of motors.

The motor also uses a single pitch wiring, aimed at minimizing the number of wire crossings (and in particular, phase crossings). According to patent claims, "individual phase coils cross only at the intra-pole loops, and not at the endturns of each coil thereby reducing the number of phase wire crossings, increasing the isolation between each of the individual phase coils, and reducing the potential for inter-phase short circuits". They claim a typical implementation of the "prior art" in redundantly-wired motors include "30,252 wire crossings", while their own winding scheme generates only 9 crossings (thus significantly reducing the probability of a short circuit). This efficient winding also "provides higher performance due to the decreased I^2R losses in the endturns. Additionally, unlike electric machines constructed in accordance with the teachings of the prior art, there is no need to cut notches in the laminations to allow for wire routing. This allows for better performance per unit volume and unit mass of the machine." [196]

Pacific Scientific claims this motor attains "40 percent more torque per unit volume than comparably sized motors", and they have successfully marketed and adapted the new motor for an existing customer (True Fitness Technology) for use in the True Fitness ZTX treadmill [20].

Pacific Scientific also developed a novel injection molding process for the motors.[8]

---

[8]U.S. Patent #6,020,661 - "Injection Molded Motor Assembly" [195]

The "entire stator assembly is potted to unitize the lamination stack and fill voids between the stator poles". The process also mates the potted windings directly to an aluminum end cap (put in place before the potting compound is injected). This reduces the thermal resistance (compared with having a small air gap), which improves heat dissipation. The injection process also binds an electrical connector into place, further reducing assembly time and cost [195].
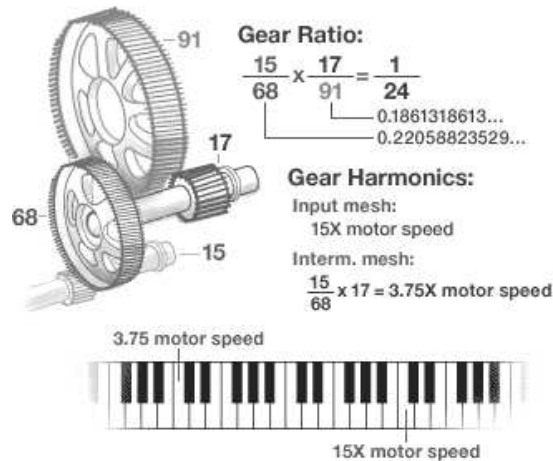
Figure 2-7: Harmonic (two-octave) gear meshing in the Segway. GIF obtained from Segway sales site at amazon.com [8].

The motor is also designed to be quiet. Axicon Techonologies developed the transmission for the Segway. They use helical gears for low noise. The two stages of the transmission even mesh at rates differing by exactly a factor of four (two octaves), to make the transmission sound harmonious [79]. Figure 2-7 illustrates this. I do not recall exactly what the Segway sounded like (when I test rode one in 2002), so I believe it *was* unobtrusive. (By comparison, someone in my neighborhood occasionally rides down the street in a "conventional" motorized scooter, and it sounds almost as loud as a motorcycle!)

In addition to sensor and actuator redundancy, the Segway has two Texas Instruments TMS320LF2406A DSP's [20]. It is not clear how affordable, practical or popular the Segway will ultimately become, but the technology behind it is definitely impressive and well-designed. Many of the trade details behind the technology have

not been published, to my knowledge. The lack of information about processing orientation and signal processing of the gyros and tilt sensors inspired a more detailed analysis of the issues involved in providing redundant sensing of the pendulum angle. This information is presented in Section 6.1 of Chapter 6

Figure 2-8 shows some purely theoretical "embodiments" which were proposed in DEKA patents relating to the iBOT and Segway human transport [98, 97]. The next few sections describe mobile inverted pendulums which have been developed by a variety of other inventors. Some of these robots are directly inspired by the Segway human transport.
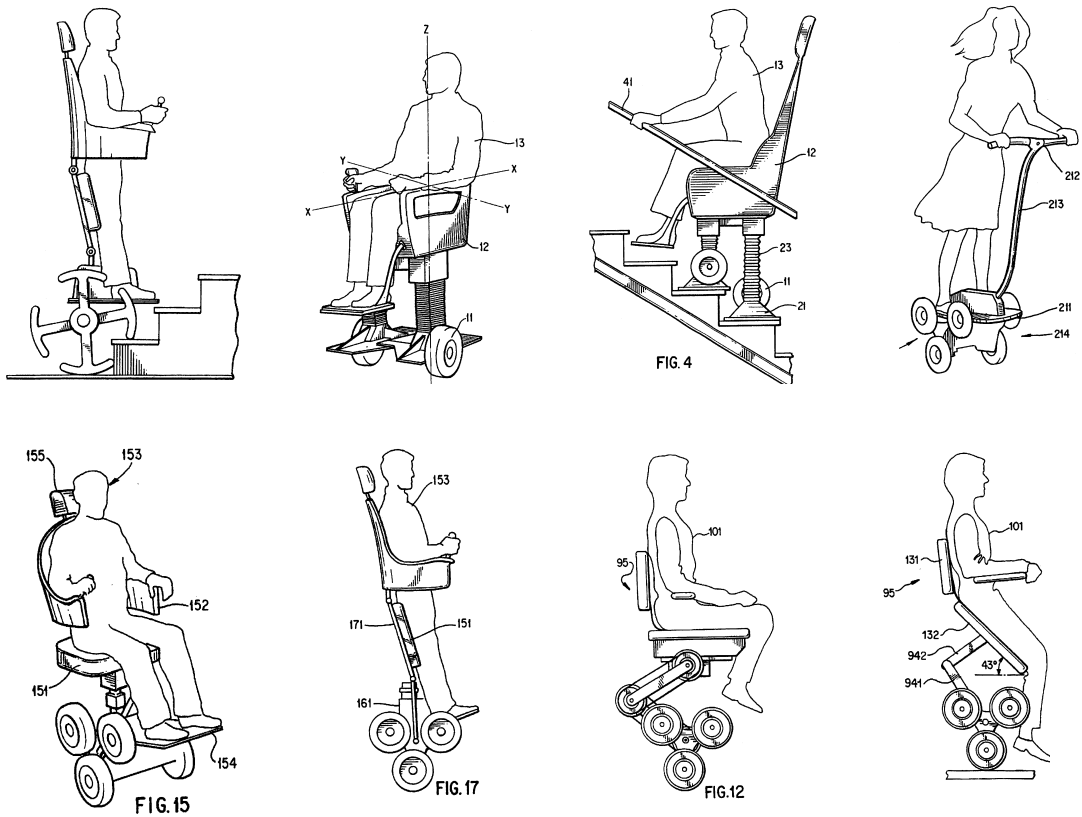
Figure 2-8: Other conceptual personal transport vehicles. These images, from DEKA patents 5,701,965 [98] and 5,791,425 [97], show alternative embodiments for human transports similar to the iBOT and Segway inverted pendulum vehicles.[98]

2.1.3 "Joe": An Autonomous IP Robot

The Industrial Electronic Laboratory at the Swiss Federal Institute of Technology has created an autonomous inverted pendulum similar to my own "DIPR" robot, described in Chapter 7 of this thesis. "Joe", shown in Figure 2-9, uses two decoupled state-space controllers to control the 3-DOF system. One controls the upright stability (pitch of the pendulum from vertical) and the second is used to drive the vehicle (controlling both forward velocity and yaw about the vertical axis). The vehicle is not "self-standing". Sensor readings are reset at each start-up, with the pendulum arm resting on the ground. The vehicle must then be lifted close to its upright equilibrium to begin balancing.

The upright vehicle stands just over two feet high, and weighs approximately 26 lbs. Its maximum speed is 3.4 mph, which is about human walking speed. The controller is implemented autonomously on the robot using a DSP board designed in-house by the Industrial Electronics Lab group. A battery is mounted on Joe's steel pendulum and provides enough power for about one hour of driving. The vehicle receives steering inputs from a human via remote control.

Joe has two actuators and three sensors. Each wheel is mounted directly to the output shaft of a planetary gearbox on each of two DC motors, powered through on-board power amplifiers. The sensors are the two incremental encoders on the motors and a rate gyroscope which measures the angular velocity (pitch) of the chassis. The gyro can measure a maximum velocity of $100^o/s$. The encoders measure the rotation of the motor and not of gearbox. The position of the wheel is therefore not measured directly. Backlash in the gearbox consequently resulted in limit cycling which excited significant mechanical resonance in initial implementations of Joe's controller. The Lausanne group eliminated the worst of the effects of backlash by filtering their speed measurement with a pole at 10 rad/s.

Limit cycling was also a significant problem in the initial (state-space) control system for the "demo inverted pendulum robot" (DIPR) presented in Chapter 7. This problem was adequately addressed by implementing an inner, velocity loop in
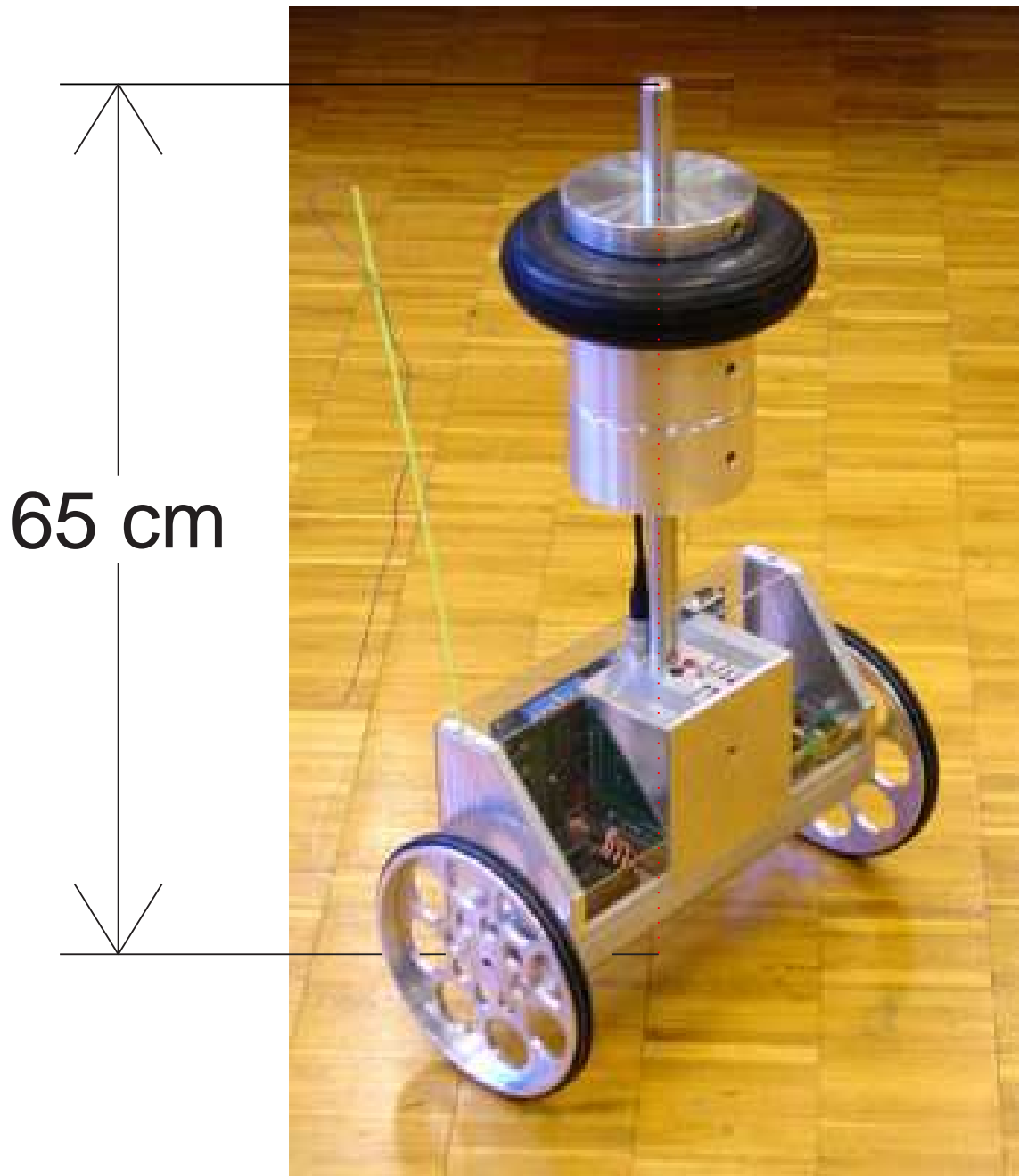
Figure 2-9: "JOE" inverted pendulum robot. Image obtained from "Joe: a Mobile, Inverted Pendulum", by Felix Grasser and Aldo D'Arrigo and Silvio Colombi and Alfred Rufer [75].

the controller for the robot. Section 7.7 describes these issues in controller design in much more detail.

Drift is always an issue when obtaining angular position from a rate gyro. There is a DC bias to the rate gyro output at zero velocity which will change due both to environmental effects (temperature, vibration, humidity, etc) and to small changes in the sensor itself ("aging"). This bias results in a ramping error in angle when the velocity signal is integrated to obtain a position measurement. Drift can be eliminated by blending the high frequency gyro measurement with a low frequency sensor measurement of angle which is not prone to ramping error. Section 6.2 describes how a 2-axis accelerometer is used to compensate for drift in the DIPR.

Joe's creators acknowledge the problem of gyro drift briefly and seem to deal with it in two ways. First, the gyroscope is recalibrated at each start-up, eliminating run-to-run changes in bias at zero velocity. Day to day changes in bias will tend to be more significant than those seen over the course of an hour or two, as illustrated in the data in Figure 6-16 on page 300. Figure 7-20 on page 347 demonstrates how the bias is particular apt to drift as it literally "warms up" during the first few minutes after it is powered up.

Second, Joe's in-run drift will have the effect of a ramping disturbance angle input to the system. The vehicle will compensate by starting to roll forward (or backward) as it attempts to catch itself from falling. The one-hour battery life limits the total drift possible, and presumably, a human driver can compensate[9] for the drift by adjusting the velocity command to the robot from the remote controller.[10]

---

[9]Perhaps subconsciously!

[10]No details are given to quantify the magnitude of the drift seen in the vehicle.

2.1.4 "nBot": Segway-inspired IP Robot
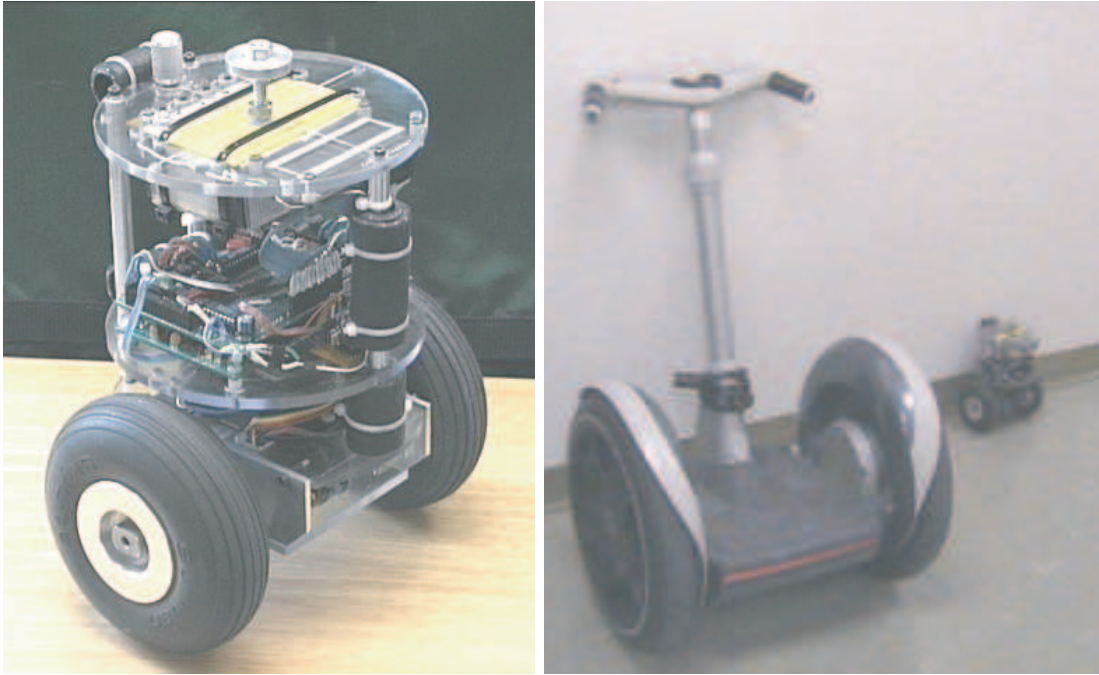
Figure 2-10: "nBot" two-wheeled IP robot. Created by David P. Anderson. At left, this version of the nBot is autonomous and steerable through remote control. It stands approximately ten inches tall. The image at right, which shows the nBot next to the Segway human transport, give a better idea of scale. Images obtained from http://www.geology.smu.edu/ dpa-www/robo/nbot/

The next sections discuss three related IP robots. These are the nBOT, the Legway, and the GyroBot. Both the nBot and GyroBot use a control strategy essentially identical to one I developed (independently) to control the DIPR robot described in Chapter 7. The LegWay is constructed from a LEGO MindStorms kit and achieves stability by optically sensing the pendulum angle.

For almost a year preceding this announcement, there were rumors across the internet and in the popular press about a new invention by Dean Kamen, nicknamed "Ginger" or simply "It".[11] The nBOT, GyroBot, and Legway each seem to be directly

---

[11]The older iBOT, although also an inverted pendulum, has never inspired nearly the level of fascination with the general public that the Segway now enjoys.

inspired by the Segway.

By contrast, the inverted pendulum robot described in the preceding section, Joe, was conceived of in 1996 and functional (initially as a tethered robot) in 1998. This clearly predates the widespread press release, on December 3, 2001, unveiling the Segway.

The nBot is one of several robots developed by David Anderson of Southern Methodist University. He initially created a three-wheeled robotic cart which balanced an inverted pendulum about a pivot mounted on its platform. This version is similar to the cart-style inverted pendulum described in Chapter 5. By contrast, intermediate and final versions of the robot are similar to Joe and to the DIPR, in that a torque is applied directly between a pendulum body and each of two, independently steerable wheels. The intermediate version had a lower pendulum-body center of mass and therefore a low pendulum inertia. In the final version, shown in figure 2-10, the weight of the onboard batteries was moved further from the axis. The increased inertia of the pendulum-body makes the system easier to stabilize. The physical explanation of this phenomenon is to compare balancing a broom-length pole vertically on the palm of your hand versus a shorter stick. It does require more effort to move the larger inertia. However, the larger inertia also rotates away from equilibrium more slowly, which means you do not need to react as quickly (i.e. you do not require as high a bandwidth) to stabilize the longer stick.

Anderson uses a commercially available inclinometer, the FAS-G, to sense pendulum angle [137]. This sensor uses onboard complimentary filtering[12] to combine an integrated rate gyro output with two orthogonal accelerometers. It outputs single-axis angular rotation over a full 360° range. The manufacturer, MicroStrain, claims a typical accuracy of 1.0 degrees, with angle resolution and repeatability of 0.10 degrees. The bandwidth of the sensor is about 50 Hz. This sensor costs just under $700 (plus another ∼$100 for necessary peripherals like power cables and power supplies).

---

[12]See section 6.2 on page 295 for more details on complimentary filtering.

The control strategy used for the nBot can be summarized as:

$$V_x \;=\; K_1\,\theta_{p,x} + K_2\left[\theta_{p,x} - \theta_{p,x-1}\right] + K_3\theta_{m,x} + K_4\left[\theta_{m,x} - \theta_{m,x-1}\right] \tag{2.1}$$

$$\approx\; K_1\,\theta_{p,x} + K_2\,\dot{\theta}_{p,x}\cdot\Delta t + K_3\,\theta_{m,x} + K_4\,\dot{\theta}_{m,x}\cdot\Delta t \tag{2.2}$$

where $\theta_{p,x}$ and $\theta_{p,x-1}$ are the pendulum angles away from vertical at the current and previous algorithm step, respectively, and θ_m represents the averaged angle of rotation of each of the two motors as compared with the commanded wheel rotation. A corresponding notation is used to describe angular velocities. Here, Δt is the controller sampling interval. The microcontroller used is the 68HC11-based Handy Board (described in Section 2.4.1 on page 120). The commanded voltage for each motor is sent to an H-bridge which outputs an amplified pwm signal. Note that the angular velocities of the pendulum (measured with the FAS-G) and motor rotation are estimated simply by subtracting the last measured position from the current position.[13] The algorithm executes 25 times per second (i.e. a step size of $\Delta t = 40\,\mathrm{ms}$).

This control algorithm is similar to the one I use to control the DIPR inverted pendulum robot, although the sensing is different in a few ways. First, the pendulum's angular rate is detected directly from the rate gyro. The rate gyro and accelerometer signals are blended inside the Simulink controller, not onboard the sensor itself. The DC gyro offset bias can be reset automatically at any time (when the angular velocity of the pendulum is zero), to improve measurement of the pendulum angle. Also, the motor encoder signals of the DIPR are filtered a bit more to provide a smoother velocity signal. (The DIPR uses a first-order discrete-time filter with a bandwidth of 50 Hz to smooth the quantized estimate of motor velocity.)

---

[13]The FAS-G sensor can output either angle or angular rate, but surprisingly, it cannot output both simultaneously.

2.1.5 "LegWay": Mindstorms Robot with Single-Sensor Balancing

The "LegWay" inverted pendulum robot, shown in Figure 2-11, is notable because it balances by using an optical sensor instead of a gyro [80]. The optical sensor sends out pulses of light (directed downward, toward the floor) and outputs a value between 0 and 100 to indicate the level of reflected light it receives. The output value is a function of the distance, angle, color and reflectivity of the floor. The robot is designed to operate on a flat, level, monochromatic (white) surface, however, so the sensor works well as a distance measurement.[14] For small tilt angles, the relationship between this distance measurement and the angle of tilt will be approximately linear $(\sin\theta \approx \theta)$, and the sensor output therefore corresponds to the relative angle between the robot axis and the normal to the floor. For a flat floor, this provides an absolute measurement of pendulum angle without the bias issues of a gyro.

The optical sensor used in the LegWay was manufactured by a company called "HiTechnic", which marketed a variety of robotic sensors compatible with the Lego MindStorms line.[15] The company claims their EOPD (electro-optical proximity detector) light sensor are "up to 50 times more sensitive than the standard Lego light sensor" [84] by compensating for ambient light. (The sensors sold for about $40 each.)

Steve Hassenplug created the LegWay, and he designed it as a line-following robot. Note in Figure 2-11 that the Legway is designed with two light sensors, side-by-side. If one of the sensors passes over the (black) path line, its output will drop to zero (or nearly zero). Steve's control algorithm tests for such a "blackout" (a signal less than 3 on the 0-100 scale) of either sensor. If no blackout is detected, the robot averages to the sensor outputs and sets both motors in unison to balance the robot at some

---

[14] One would expect the intensity of the reflected light to be inversely proportional to distance (intensity = reflectance / distance). The sensor output is substantially linear with distance over a limited range, however, according to the data HiTechnic provide on their website.

[15] Apparently the market for Lego-specific sensors was not particularly profitable. HiTechnic stopped manufacturing Lego-compatible sensors around April of 2003, saying they will now concentrate on "developing technology for industry" [84].
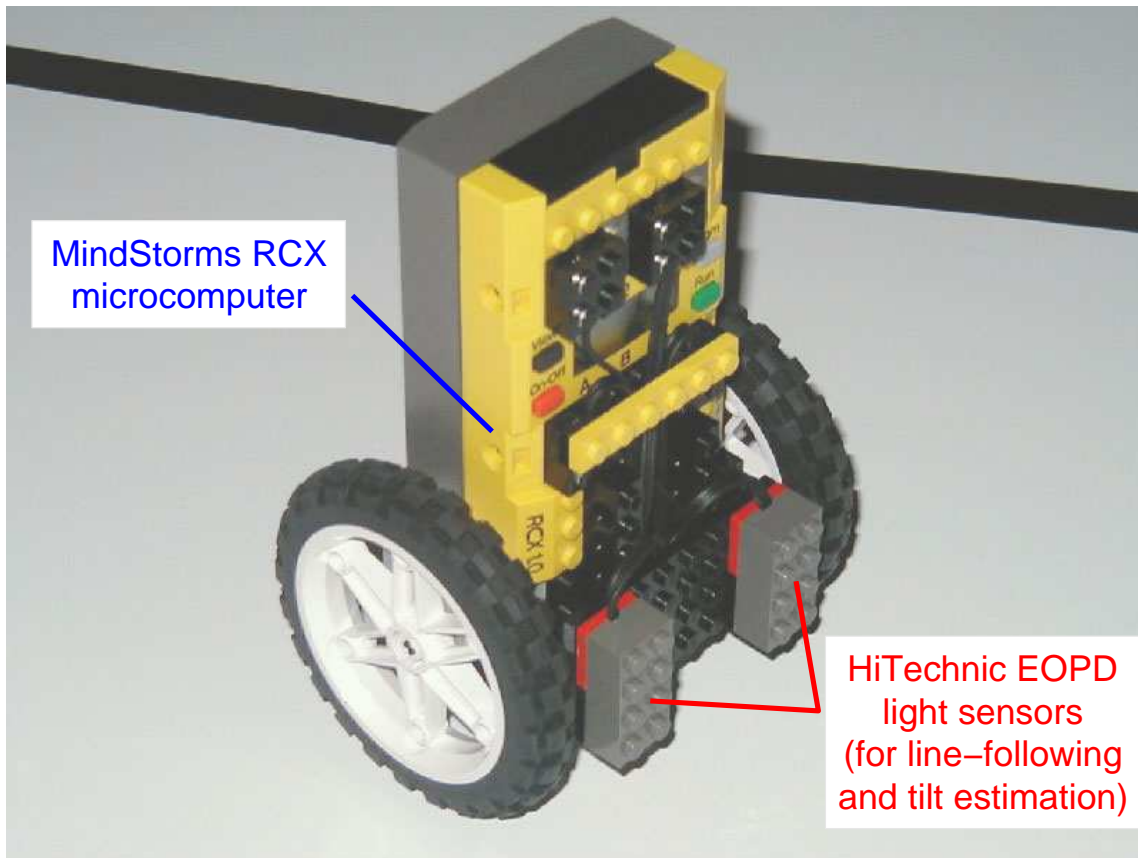
Figure 2-11: "LegWay" LEGO MindStorms IP robot. This robot uses the EOPD sensors shown to estimate tilt angle. The sensors emit pulses of red light and detect the intensity of the light reflected back. (Visible light is used instead of IR to provide better resolution and accuracy for line detection/following.) The robot is held upright at startup for calibration. The initial output from the sensors at startup then sets the desired equilibrium point. Legway was created by Steve Hassenplug, and the image above was obtained from his website: http://perso.freelug.org/legway/LegWay.html

offset angle, resulting in a constant, forward velocity.[16] When one sensor detects a blackout, the algorithm sets the motor output on this side of the robot to zero and uses only the second sensor output for balancing. The second motor output is still set to balance with a net forward velocity, and this causes the robot to turn toward the blackout direction.

As the name implies, the Legway was directly inspired by the Segway. Legway runs autonomously. The bulk of the pendulum body consists of the MindStorms RCX block itself, which provides both the controller (with an execution rate of 50 ms) and power (6 AA batteries).

2.1.6   "GyroBot": IP Robot with Integral Action

The GyroBot, shown in Figure 2-12, was created by Larry Barello. Larry's background is in designing "embedded processors for industrial, medical and communications industries" [25]. He uses a version of the AVR 8-bit RISC, manufactured by Amtel, as the microcontroller.[17] A gyro (manufactured by BEI/Donner System) detects tilt. Larry discusses the use of an accelerometer as a tilt sensor to compensate for gyro drift, but the robot itself does not implement any bias compensation. (The in-run bias drift is rated as less than $.05^o$/sec in 100 seconds.)

The motors have quadrature encoders and use a pwm drive. The controller structure is similar to that of the Segway, iBOT, nBOT and my own robot (the DIPR). The motor output is determined by multiplying measured values of each of four states (pendulum angle and velocity; motor angle and velocity) by a particular gain and summing the result. The gains were determined through "trial and error".

---

[16]Steve describes this as follows: "To move forward (for line following) LegWay actually sets the motors to run backward, causing a tilt, which it automaticly [sic] corrects, by moving forward." [80] Adding a constant "negative velocity" value to the motor outputs is equivalent to adding an offset to the sensor value (or to setting the "zero point" for the sensors to correspond to an angle tilting somewhat forward from vertical). The relationship between detected angle and motor output is a proportional gain (i.e. linear).

[17]The chip is designed for consumer products such as anti-lock brakes, airbags, answering machines, etc. The version used in the GyroBot is the ATMEGA32.

Figure 2-12: "GyroBot" two-wheeled IP platform robot. Created by Larry Barello. The taller version of this robot (at right) is reported to be more stable that the earlier prototype (left). (http://www.barello.net/Robots/gyrobot/index.htm)

Larry has developed several home-grown robots (organizing high students for the First [16] competition, for instance). Interestingly, he says his goal in building at inverted pendulum robot is "to forever eliminate the caster on robotic bases." [25]

2.1.7 Robotic Unicycles

One-wheeled versions of an autonomous inverted pendulum robot have also been studied and successfully controlled [145, 206, 205, 178]. David Vos built and controlled the robot shown in Figure 2-13 under the guidance of Prof. Andreas von Flotow at MIT. The project, which formed the Masters (1989) and Ph.D. (1992) theses for Vos, was inspired and largely modeled on a similar unicycle created and studied as a Ph.D. thesis by Arnoldus Schoonwinkel at Stanford in 1988. Both were autonomous vehicles, carrying onboard power, signal processing, and control.

As with the two-wheeled inverted pendulum, there are two rotary actuators to provide pitch stability and steering capability. Recall that two-wheeled vehicles of the type described in the preceeding section have two co-axial wheels which allow steering (control of yaw) and also provide lateral stability, to prevent tipping over sideways. The one-wheeled vehicles created by Schoonwinkel and Vos use one wheel for forward velocity control and as a primary means of providing pitch stability. In addition, each has a reaction wheel, mounted coaxial with the vertical pendulum body. The reaction wheel essentially mimics the action of a unicyclist's torso, which twists with respect to his lower body to steer and provide lateral stability. There are seven measured states on the unicycle: all three angular velocities of the robot body (pitch, roll and yaw), roll and pitch angles, and angular velocities of both the turntable and drive wheel.

The turntable generates gyroscopic forces which complicate the dynamics of this system and make it difficult to decouple the problems of longitudinal and lateral control. Schoonwinkel's 404-page doctoral thesis concentrates primarily on the construction of the vehicle and sensor testing. He achieved only limited pitch stability, and constructed additional "training wheels" to provide lateral stability. Vos linearized the system dynamics about a "zero turntable velocity" operating point to create two, decoupled systems which were each controlled separately. The primary non-linearly effect he addresses in his research was the highly non-linear surface friction between the drive wheel and floor during yaw motion (turning). This was ap-

Robotic Unicycle

Motor #2 pivots turntable for roll and yaw control

Motor #1 turns wheel for forward velocity and pitch control
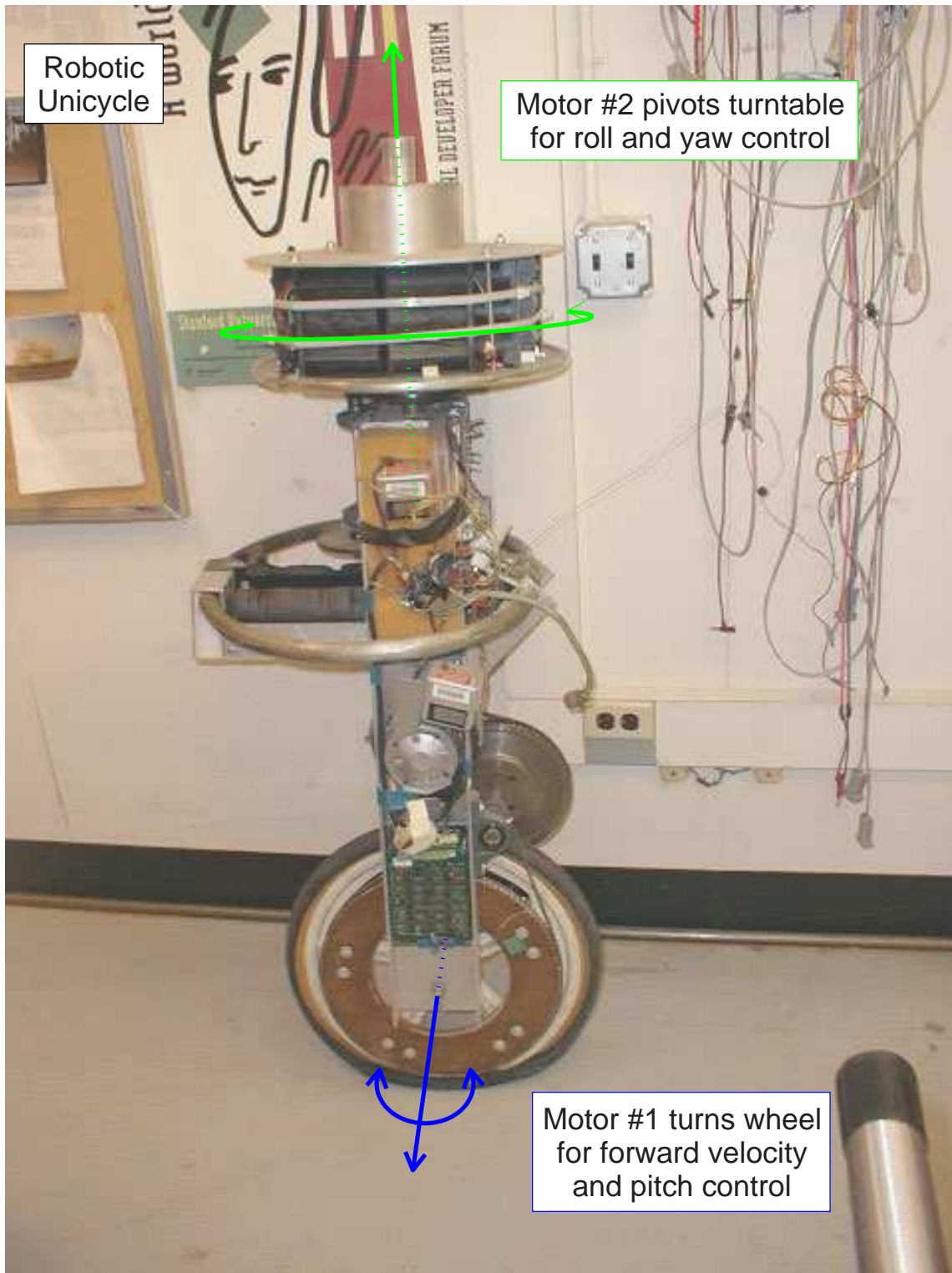
Figure 2-13: Robotic unicycle created by David Vos [206, 205].

parently the most troubling aspect in control of the actual hardware. Summarizing the one-wheeled system in the words of David Vos: "From the control point of view, these dynamics present a particularly challenging problem in that all of the following adjectives apply: unstable, non-minimum phase, time-varying and nonlinear" [206].

2.2 Hands-On Experiences in Undergraduate System Dynamics

The rest of this chapter surveys some creative approaches to undergraduate engineering education. In the paragraphs immediately following the present one, I outline and compare the general philosophies driving the development of our ActivLab experiment and the other projects described here. This is followed by a selective survey (Section 2.2.1) of literature on learning and teaching engineering (particular dynamics and design), with the goal of providing some thought-provoking perspectives on education. Project descriptions begin in Section 2.2.2. Only the two projects described in that section strictly involve the inclusion of a laboratory component in an introductory dynamics course (E161 at Stanford); however, *all* of the remaining programs have goals in common with our own development of the ActivLab projects for MIT course 2.003 (Modeling Dynamics and Control I) and/or with the supplementary classroom and lab demos for 2.003. The ActivLab hardware is described in detail in Chapter 3, and that Chapter 4 includes several examples of lab and lecture demonstrations for 2.003.

The ActivLab experiments and the related demos in dynamics we have developed aim to reinforce students' comprehension of dynamic systems with visual and tactile experiences. We feel it is important to allow students to see and feel physical systems for several reasons. First, we hope it will build a stronger intuition about dynamic systems. For instance, students can apply forces to a system by hand and observe first-hand the effects of varying physical properties such as viscous damping or inertia. Such intuition is highly useful for applying knowledge in dynamics to later course work

in mechanical design or controls, and in engineering practice.

Hands-on laboratories and demos also promote curiosity and exploration. We encourage students to poke and prod most of the hardware, both to lower their inhibitions about "playing with" labware and to encourage them to explore (or at least to note) anomalous behaviors in "real world" systems. Likewise, well-designed classroom demos generally illustrate specific phenomena, but they are also intended to spark broader interest in a subject.

The projects described in the remainder of this chapter aim both to reinforce an understanding of dynamic systems and to foster interest in topics like mechatronics, robotics and modeling of physical systems for which knowledge of dynamic systems is critical. The examples below are certainly not comprehensive. My aim is to survey a variety of approaches and thereby provide the reader with some reference points to compare with our efforts in restructuring 2.003.

For instance, we felt it was particularly important to give students real labware and to encourage them to explore and to become fully engaged in the material, but other educators have touted other alternative to traditional laboratory sessions. Laboratories are expensive, for one thing. Aside from the cost of developing and implementing the hardware itself, including a laboratory component in a class requires additional staff and a devoted laboratory classroom (equipped with necessary instruments, computers, internet access, lab benches, etc). Similarly, live lecture demos require the overhead of maintenance, storage and transportation.

Section 2.3 presents several projects at MIT that replace traditional lab experience or lecture demos with an "alternative media" solution. One alternative to the conventional laboratory is a "studio" approach, which has recently been adopted in teaching introductory physics at RPI, MIT and other universities. An MIT studio physics program is currently used to teach second-term freshman the physics of electricity and magnetism (E&M). This program, called "TEAL", is described in more detail in Subsection 2.3.2. Other multi-media supplements to the standard lecture format include *video recordings* (used in MIT courses 8.01 and 6.013, which are described in Subsections 2.3.1 and 2.3.3, respectively) and *online materials* (for instance, MIT's

school-wide OpenCourseWare program, described in Subsection 2.3.4 and a physics tutorial website for 8.01, described in Subsection 2.3.1).

I conclude this chapter by describing two other broad categories of projects. Section 2.4 describes robot competitions that have been used as design projects in university courses, and Section 2.5 provides examples of laboratory courses in mechatronics. Robot competitions provide as inspiring way to apply and to develop skills in modeling and designing dynamic systems. Similarly, mechatronics requires a solid understanding of how to model and modify system dynamics.

2.2.1 Literature on Learning and Teaching

Much has been written about learning and epistemology. The goal of this section is not to provide a comprehensive survey of the varying viewpoints. Instead, I have compiled a selection of theories, quotations and anecdotes on learning which I find particularly interested, enlightening and (admittedly) preferentially in agreement with my own experiences and thoughts on engineering education. To summarize those thoughts briefly, I have found that I only truly master some body of knowledge when I want to create something (a computer game, or a robot, or a digital controller, etc.) or when I try to teach it to someone else. The key factors seem to be (1) a significantly higher motivation (i.e. trying to accomplish something, versus trying to attain a particular grade or "learning for its own sake") and (2) the human ability to recall direct physical experiences more effectively than abstract ones.

Although I did not initially plan to focus so heavily on anecdotal evidence in this section, it is, upon reflection, both appropriate and telling that my natural inclination has led me in this direction: One common thread throughout this survey is the importance of real experiences, as compared with a recitation or lecturing of lists of facts, in creating intuitive (self-evident) understanding of a subject.

Piaget (and Papert)

I'll begin this survey with Jean Piaget, since his work is seminal to most of the other educational perspectives I will later discuss. Piaget was born just before the close of the 19th century and remained engaged and influential in research until his death in 1980. He moved to Zurich briefly to attend lectures on experimental psychology by Carl Jung (after WWI) and soon after studied with Theodore Simon and Alfred Binet (famous for their innovations in testing human intelligence) [155].

One of Piaget's most influential theories is that children *think differently* than adults. It is an idea that Einstein famously described as "so simple only a genius could have thought of it." [155] A child's mind processes information differently than a mature mind, and in fact observing the way her mind evolves[18], according to Piaget, *might*, logically enough, hold the key to understanding human knowledge more generally [155]. According to Seymour Papert, "his (Piaget's) real interest was epistemology - the theory of knowledge... The core of Piaget is his belief that looking carefully at how knowledge develops in children will elucidate the nature of knowledge in general." [155]

Seymour Papert, mentioned above, founded the Epistemology and Learning group (more commonly known as the "LEGO Lab" in the late 80's and early 90's) at MIT's Media Lab. Papert worked with Jean Piaget in Switzerland in the late 1950's and early 1960's, which inspired his own interest in epistemology and the study of how children learn. Piaget's work focuses on the (famously four [155]) *stages* of mental development in a child (i.e. how they think), while Papert is particularly interested in the *dynamic processes* by which children progress from one stage to the next (i.e. how they learn) [3, 154, 165]. Papert invented the "Logo" programming language, which is designed to be compatible with LEGO robot-building and accessible to young children. Logo is designed to foster learning from the perspective that we learn best by *doing* and, more particularly, by *making* [154].

I have some experience with Logo. I assisted, with Fred Martin, and later taught

---

[18]Piaget received his PhD in evolutionary biology.

classes in LEGO/Logo robot-building intermittently for a couple of years in the early 1990's at Boston's Museum of Science. The kids (various levels of elementary age, depending on the session) were always incredibly motivated and engaged, despite the fact that classes ran up to six hours a day, in two solid, 3-hour blocks. They could indeed pick up the Logo language rapidly, and LEGO blocks are a wonderful medium, allowing one to begin building simple structures and yet providing a well-planned flexibility that allows for surprisingly sophisticated or clever designs.[19]

The educational philosophy behind Logo is essentially Piaget's concept of "constructivism" or, more precisely, what Papert has coined "constructionism" [155, 3]. So what are constructivism and constructionism? And how do they relate to our discussion engineering education?

Constructivism: To Learn by Doing

Piaget describes constructivism as the "use of active methods" so that "every new truth to be learned be rediscovered or at least reconstructed by the student" [165, p. 15]. A constructivist believes, in other words, that we naturally construct our own self-consistent frameworks (theories) to explain and to predict the world around us. Often, the intuitions we form are incomplete or simply flawed, but they work adequately (perhaps) to aide us in most day-to-day reasoning. Since specific fields of study (organic chemistry, for instance) are built upon the experimentation and observation of generations of researchers, students clearly require some level of intermediation to guide them toward mastery. This, Piaget argues, suggests two basic roles for the instructor. First, writes Piaget:

> The teacher as organizer remains indispensable in order to create the
> situations and construct the initial devices which present useful problems
> to the child. Secondly, he is needed to provide counter-examples that

---

[19]I once built a small, rubber-band-powered LEGO hopper that could perform a back flip and land on its feet, for instance, and my 6.270 [123] partner David Hogg actually constructed a working *clock escapement* as a UROP at the LEGO lab!

compel reflection and reconsideration of over-hasty solutions. ...his role should be that of a mentor stimulating initiative and research [165, p. 16].

Piaget's research focuses on *childhood* learning, but he and others [70, 184, 104, 68, 117, 139] postulate that further learning at the university level (and specifically scientific and engineering education) will be most effective if we customize our style of teaching to match the natural processes which orchestrated development of the logical structure of our minds (as humans) in the first place. In Piaget's words:

> ...if there is any area in which active methods will probably become imperative in the full sense of the term, it is that in which experimental procedures are learned, for an experiment not carried out by the individual himself with all freedom of initiative is by definition not an experiment but mere drill with no educational value: the details of the successive steps are not adequately understood [165, p. 20].

He states later:

> What is needed at both the university and secondary level are teachers who indeed know their subject but who approach it from a constantly interdisciplinary point of view... In other words, instructors should be sufficiently penetrated with the spirit of epistemology to be able to make their students constantly aware of the relations between their special province and the sciences as a whole. Such men are rare today [165, p. 30].

All right: so from a Piagetian perspective, we should construct physical learning environments (e.g. laboratories or design projects) where students can and will experiment. But at the same time, we must take care that such an experience is not so overly structured or "canned" that it degrades into a mechanical drill. On one hand, an instructor must clearly design the experience with some sort of goals in mind, and yet (s)he needs to be able to react spontaneously to (and indeed even encourage) deviations from the "planned" path. It's a sticky situation!

Constructionism: To Learn by Making

"There are two basic ideas of education," Papert asserts. "One is instructionism; people who subscribe to that idea look for better ways to teach. The other is constructionism; we look for better things for children to do, and assume that they will learn by doing" [159].

Papert's term "constructionism" is clearly a play on Piaget's constructivism. The two philosophies are similar: Essentially, constructionism accepts the constructivist premise that we learn by building *mental constructs*, but it also places importance quite literally on the *construction of artifacts*. "The principle of getting things done," Papert claims, "of making things - and of making them work - is important enough, and different enough from any prevalent ideas about education, that it really needs another name." [154, p. viii] Perhaps; at any rate, any subtle linguistic distinctions should not distract from his real point here. Design and creation are the ultimate goals in putting knowledge to use, and I think most people would agree that the acts of doing *and* building are both powerful methods for learning. We are motivated to learn by a desire to create things, and the process of creating in turn helps us learn.

Finally, Papert feels too much of education focuses on the concepts of right or wrong answers: it's *solutions* that matter. "Discipline means commmitment to the principle that once you start a project you sweat and slave to get it to work... Life is not about 'knowing the right answer' - or at least it should not be - it is about getting things to work!" [154].

Cautionary Advice to the Would-be Piagetian

Many people try to reduce Piaget's ideas to create a tidy approach to learning. For instance, an instructor may reason, "in the first lab, I will present a situation where the students discover Principle 1-A. The second lab will then be structured such that they discover Principle 1-B, and in the third, they will discover that two phenomena are really instances of the same general rule..." The problem lies in the meaning of

"discovery"![20] How can you predict the activation energy (if you will) it will take for a student to truly discover something? (Particularly anything worth learning.) One may indeed create laboratories soundly based on the principles of interest, and one may in turn guarantee that, hell or high water, the students will hear about the relationship between the physical demonstrations and those "underlying principles". But there is no guarantee either that they will fully comprehend at the level we expect or that they will have "discovered" something for themselves (which is the key to Piaget's ideas).

As Seymour Papert noted at a symposium on computer in education at MIT in 2002, stating:

> The essence of Piaget was how much learning occurs without being planned or organized by teachers or schools. His whole point was that children develop intellectually without being taught! A Piagetian curriculum is a contradiction in terms! [220].

Papert's point is that many of Piaget's observations and principles have been trivialized and reduced to a point where their meaning is completely lost. Certainly, he is not opposed to Piaget's ideas. The following quotation (Papert writing on Logo three years earlier) illustrates this:

> Choosing constructivism as a basis for teaching traditional subjects is a matter for professional educators to decide. I personally think that the evidence is very strongly in favor of it, but many teachers think otherwise and I respect their views. [154, p.viii]

Marvin Minsky on Education and Development

In his book "The Society of Mind", Marvin Minsky provides an amusing anecdote which illustrates how the application of Piaget's ideas about learning can go wrong [139]. Minsky is perhaps most famous as the co-founder (in 1959) of the MIT Artificial Intelligence Project (now commonly known as "the AI Lab" at MIT). He

---

[20]Or "rediscovery", if you prefer.
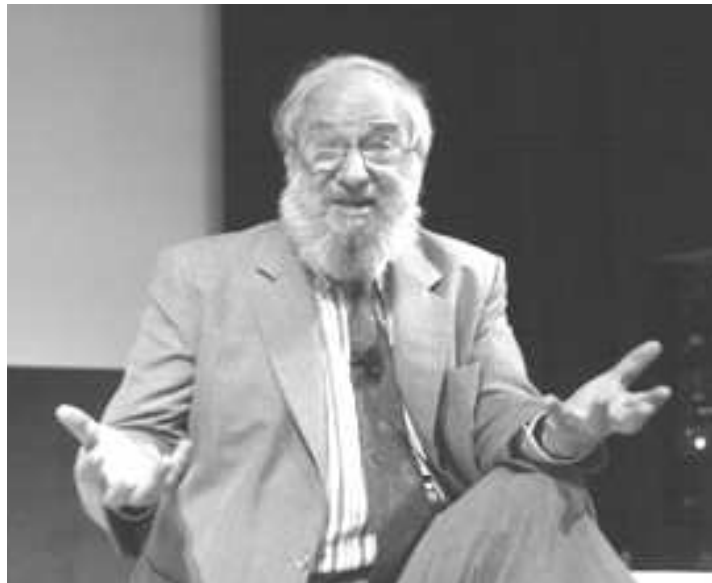
Figure 2-14: Piaget, Minsky and Papert. Starting top left : Swiss philosopher and psychologist Jean Piaget [57], co-founder of the MIT AI Lab Marvin Minsky [138], and Seymour Papert, founder of the Epistemology and Learning group at the MIT Media Lab [50, 220].

emerged from the "golden age of mathematics at Princeton" [139, p. 323]. His teachers included John Tukey (who later worked at Bell Labs and famously introduced the fast Fourier transform) and the incomparable John von Neumann, and his fellow students included John McCarthy (the other co-founder of the MIT AI Lab) and John Nash [139, p. 323]. The study of machine learning (AI) is intricately entwined with that of human learning; each provides insights on the other. Thus, like Piaget and Papert, Minsky is also a keen theoretician on how humans (and particularly children) learn, and in fact Seymour Papert and Marvin Minsky have collaborated in the field of AI.

Let me introduce the anecdote with some key background on Piaget's work. Piaget applied a scientific approach in studying how children think. He designed a variety of experiments to test whether a child had developed an understanding of concepts like mass or volume conservation. A famous Piaget test for an understanding of volume conservation, for instance, goes as follows: Present two identical (short, wide) jars of water to children and all will agree they hold the same amount of liquid. Now, have them watch as you pour the liquid from one of these jars into a taller, thinner jar. A typical 5-year-old will reply that the taller jar has more that the shorter one, but a 7-year-old is likely to reason each jar holds the same amount. "These experiments have been repeated in many ways and in many countries - and always with the same results: each normal child eventually acquires an adult view of quantity - and apparently without adult help!" [139, p. 99].

Thanks to Piaget, we can identify specific stages or concepts in the development of learning, but it is difficult to preempt (i.e. shortcut) the complete process by which such information is ultimately absorbed. This is because we must, in the end, build our own hierarchical structures in the mind which help us interpret the world around us - to solve (and indeed also to formulate) problems, for instance. The development of such structures in our minds need not be conscious, but before such a hierarchy is fully developed, a child (and I would argue any learner) is essentially treating the information as a set of "special rules, and so many exceptions to them" [139, p. 106]. Let me describe the dilemma (briefly) in a second way, before we launch into Minsky's

story. Suppose one reasons: "If we know key *benchmarks* of the stages in the mental development of a child, can't we then focus on teaching each benchmark to accelerate learning?" Stated in this way, perhaps it is easier to realize where this strategy may go wrong. We may be successful in communicating a set of declarative facts to a child, but the connections that link these facts can only be made in his own mind. This is why, as Minsky put is:

> ...educational programs allegedly designed "according to Piaget" often appear to succeed from one moment to the next, but the structures that result from this are so fragile and specialized that children can apply them only to contexts almost exactly like those in which they were learned [139, p. 106].

He continues:

> All this reminds me of a visit to my home from my friend Gilbert Voyat, who was then a student of Papert and Piaget and later became a distinguished child psychologist. On meeting our five-year-old twins, his eyes sparkled, and he quickly improvised some experiments in the kitchen. Gilbert engaged Julie first, planning to ask her about whether a potato would balance best on one, two, three or four toothpicks. First, in order to assess her general development, he began by performing the water jar experiment. The conversation went like this:
>
> Gilbert: "'Is there more water in this jar or in that jar?"
>
> Julie: "'It looks like there's more in that one. But you should ask my brother, Henry. He has conservation already."
>
> Gilbert paled and fled. I always wondered what Henry would have said. In any case, this anecdote illustrates how a young child may possess many of the ingredients of perception, knowledge, and ability needed for this kind of judgment - yet still not have suitably organized those components.

Herbert Simon (CMU)

Prof. Herbert Simon of the psychology department at CMU offers the anecdote below in an essay on teaching and learning in universities. The story is about Bob Doherty, president of CMU around 1949, when Simon came to CMU as a student. I feel this excerpt provides a perspective for the rest of this literature survey on the higher level thought processes educators ultimately hope their students will develop, particularly through mentorship.

> Doherty came from General Electric via Yale, and had been one of the bright young men who were taken under the wing of the famous engineer Stiglitz. Every Saturday, Stiglitz would hold a session with these talented young men whom General Electric had recruited and who were trying to learn more advanced engineering theory and problem-solving techinques. Typically, Bob Doherty would sometimes get really stuck while working on a problem. On those occasions, he would walk down the hall, knock on Stiglitz's door, talk to him - and by golly, after a few minutes or maybe a quarter of an hour, the problem would be solved.
>
> One morning Doherty, on his way to Stiglitz's office, said to himself, "Now what do we really talk about? What's the nature of our conversation?" And his next thought was, "Well Stiglitz never says anything; he just asks me questions. And I don't know the answer to the problem or I wouldn't be down there; and yet after fifteen minutes I know the answer." So instead of continuing to Stiglitz's office, he went to the nearest men's room and sat down for a while and asked himself, "What questions would Stiglitz ask me about this?" And lo and behold, after ten minutes he had the answer to the problem and went down to Stiglitz's office and proudly announced that he knew how to solve it. [184, p. 344]

Prof. Simon's premise is that "the emphasis in engineering education should not be placed on knowledge, but should focus attention on the learning processes solving processes of the students" [184, p. 343].

"Design is a special kind of problem solving...we call ill-structured" [184, p. 345], Simon says, because "the goals are never completely defined until the design is almost finished" [184, p. 345]. Expert designers seem to rely heavily on intuition to sort through this cycle of defining and solving problems, and "Intuition is essentially synonymous with recognition." [184, p. 345] More precisely, it involves recognizing patterns, accessing related information (in your brain), and then making decisions about which information is most relevant and how it can be used. And the more efficient you get at doing this, the more effortless and subconscious ("intuitive") the whole process becomes. Simon notes that this pattern recognition approach is essentially the process researchers in A.I. use in algorithms for expert system and chess-playing programs. I would make an analogy with many physical processes, like playing tennis or sight-reading piano music, where experts are able to respond efficiently to familiar (yet unique) situations because they have years of experience practicing.

"Learning has to occur in the students," Simon finally warns, and whatever ideas you try to impart to your students, "doesn't make a whit of difference unless it causes a change in [their] behavior" [184, p. 346]. "The beginning of the design of any educational procedure is dreaming up experiences for students" [184, p. 346] to help them learn. Even so, providing students with relevant demonstrations and hands-on labs is not enough; ultimately the students have to do the work of learning.

Teaching to Match Students' "Learning Styles" at NCSU

Richard Felder and Linda Silverman state that learning in a univerisity is a "two-step process involving the reception and processing of information" and students "select the material they will process and ignore the rest" [70, p. 674]. They suggest that instructors can be more effective by if they adopt a teaching style that is designed to match the preferred learning styles of their students.

They have developed a set of learning traits, similar to the personality traits (introverted vs. extroverted, etc) used in Myers-Briggs-Jung type tests. For instance: "Sensors like solving problems by standard methods and dislike 'surprises'; intuitors

like innovation and dislike repetition" and they claim that "the majority of engineering students are sensors" [70, p. 676].

Another distinction they suggest is one between "active" and "reflective" learners. "Active learners do not learn much in situations that require them to be passive (such as most lectures), and reflective learners do not learn much in situations that provide no opportunity to think about the information being presented (such as most lectures)" [70, p. 678]. Active learners want to experience phenomena first-hand. They "work well in groups" and "tend to be experimentalists". Reflective learners want time to process new information when they encounter it. They "work better by themselves or with at most one other person" and "tend to be theoreticians" [70, p. 678]. "A class in which students are always passive is a class in which neither the active experimenter nor the reflective observer can learn effectively" [70, p. 678]. One suggestion Felder and Silverman list is to "have students organize themselves in groups of three or four and periodically come up with collective answers to questions posed by the instructor" [70, p. 678]. They continue:

> The groups may be given from 30 seconds to five minutes to do so, after which the answers are shared and discussed for as much or as little time as the instructor wishes to spend on the exercise. Besides forcing thought about the course material, such brainstorming exercises can indicate material that students don't understand; provide a more congenial classroom environment than can be achieved with a formal lecture; and involve even the most introverted students, who would never participate in a full class discussion. One such exercise lasting no more than five minutes in the midde of a lecture period can make the entire period a stimulating and rewarding educational experience. [70, p. 678]

Engineering Dynamics at Texas A&M

Prof. Louis Everett of Texas A&M notes that "Engineering Dynamics...is neither easy to teach nor to learn" [68]. He suggests the key is to "teach Dynamics as a problem-solving process" and that "students tend to learn technical subjects by comparing

with examples" [68]. Everett believes, "The current textbooks pose a real problem. Most texts are a collection of facts."

The strategy he suggests for teaching dynamics is to present students with a loosely-structured plan of attack for problem solving. His strategy attempts to provide students with a set of general steps to aide them in approaching new problems without prescribing specific rules.[21] He also notes that the same basic skills for analysis are essential for the design of dynamic systems, as well. The six steps he cites are:

1. "Think about the problem." (e.g. What is being asked? What are the assumptions? How many degrees of freedom are there?)

2. "Choose Coordinates." (e.g. What reference frame makes sense?)

3. "Define the System." (e.g. free body diagram)

4. "Apply a Force-Motion Relation" (applying either Newton's law or a work-energy equation.)

5. "Find 'Extra' Equations." (e.g. kinematics, or additional assumptions that must be made to to make the equations solvable)

6. "Solve and Interpret" (...and reflect of whether it makes sense.)

Prof. Everett cites that it takes time for most students to become comfortable with his "process-oriented" approach. He is hopeful, however, that students can adapt to it. For instance, he cites an example (similar to the anecdote about Bob Doherty on page 97) where, after an exam, a student approached him to comment that he was completely lost on a particular problem. "I didn't have a clue," the student said, "so I applied the process and it worked out real easy" [68].

Everett also notes that students typically come into a dynamics class with mistaken intuition that needs to be addressed by investigating why students errors are made and correcting faulty reasoning. Students can also fall into the pitfall of applying rules too blindly, when their own experience and common sense should be able to

---

[21]a tricky balance, it would seem...

100

guide them. As one example, he has shown students a car engine (running at constant speed): Show the students a pulley running a fan or pump and another which is an idler, and ask them to draw free body diagrams of the two pulleys. Everett's experience is that most students will say the tension is equal on both sides of the pulley in either case. If you ask them why, students typically respond by saying something like, "Tension on either side of a massless frictionless pulley is the same" [68]. This approximation may be appropriate for an idler, but it certainly will not be for the pulley driving the pump. What is missing from the student solution is an analysis of the equilibrium conditions necessary at the pulley which is driving the pump.

Student-designed labs at USC

Jed Lyons, Jeffrey Morehouse and Edward Young of the University of South Carolina have developed a capstone lab course in mechanical engineering that focuses on the process of *designing* laboratory experiments focusing on thermodynamics, heat transfer, mechanics, dynamics and control. The authors specifically cite that their approach derives from "constructivist learning theory" [117].

They have structured laboratory experiences for the class around the analysis of a 5/8-scale replica "Legends" race car (which typically grabs student interest). Wireless telemetry is used, so that sensors can be monitored remotely while the car is being driven. The first weeks of the course involves more structured "learning modules", where students learn to use a variety of sensors and the wireless data acquisition system and gain experience in reducing the data obtained. The course culminates in an open-ended project, in which students spend five weeks on an experiment they must design completely:

> For example, the students may be asked to determine what effects a steady-state turn has on the suspension and tires. The experiment they develop could consist of using a circular or oval track to study steady state cornering, quantified by lateral acceleration. Both lateral and front-to-back shifts in suspension could be measured as functions of lateral acceleration. Using wheel encoders, the difference in distance travelled

101

by each wheel could be compared to theoretical predictions, and how this distance changes with cornering effort could be examined. The effects of cornering on tire temperature could be correlated with different turn radii and vehicle speeds (etc.) [117, p. 5].

Students would then need to model the system to estimate the order of magnitude of the expected response and choose appropriate sensors[22] from the stockroom for the course and calibrate them.

Other Work of Note

A couple of other outlooks on engineering education are worth mentioning briefly. One involves a project at the University of Alberta to create a suite of hands-on experiments in fluid dynamics. The experiments are used in the recitations, which are taught by graduate TAs, rather than in lecture. In addition to giving the students a more intimate interaction with the demos, the demos provide a focus for the recitations. As a result, "the teaching experience is a very structured one, which allows the beginning teacher to focus on presentation, use of time, and interactions with the students." [104, p. 9]

In a second (remarkable) example, Professors Donald Woods & Cameron Crowe at McMaster University actually entered their departmental programs as "freshmen" and continued through the four-year program, observing lectures, interacting with students, and evaluating what the strengths and pitfalls of their curriculum were. They note that the freshmen and sophomores with whom they interacted seemed to rely largely on "intuition" [219] rather than a self-aware problem-solving strategy. Intuition may be appropriate once you have developed a high level of skill, as described in Section 2.2.1, but to develop the right intuition requires critical thinking. They have found that relying so heavily on pattern matching presents potential pitfalls for the students. "For example, they consider two problems similar if they involve a ladder rather than because the problems ask about the force-mass-movement

---

[22]Sensors available in the class which are appropriate in this example include encoders, accelerometers, LVDTs, infrared pyrometers, a GPS system, and load bolts [117].

relationship." [219, p. 292]

In concluding this survey part of survey on how to teach engineers, I include some remarks from Prof. James Roberge, who notes: "Many designers mention one or two mentors...who had a major impact on their careers." If this is so, then a good instructor in dynamic modeling[23] can clearly have a much more global impact in a student's education than simply building a strong foundation in dynamics alone. Roberge continues: "The abilities required for effective design, while hard to quantify, are common to all disciplines. I believe that a good analog circuit designer could also become a good designer of airplane wings or steam turbines after a relatively short internship in the new field. (It may be fortunate for frequent flyers that this hypothesis is infrequently tested.)" [174, p. 79] With this perspective in mind, the next section describes a variety of approaches educators have taken in teaching dynamics and the design of dynamic systems.

2.2.2   Stanford Course ME161: Dynamic Systems

ME161 is a ten-week junior- and senior-level course in dynamics and introductory controls with a laboratory component. The course is taught once a year at Stanford (in the Fall) with a class size of around 60 [169]. Staff for the class have designed and implemented two project-based themes as a focus for the lab sessions. In both cases, students studied the same dynamic system in each of a series of separate laboratory exercises. Both of these device-centered laboratory innovations are described briefly below. One is a single-degree-of-freedom "haptic paddle" [169, 170], which was used from 1996-1998, and the second (used only in the Fall of 2000) is a pneumatically-actuated, one-legged hopping machine called the "Dashpod" [47]. These two devices are shown in Figures 2-15 and 2-16, respectively.
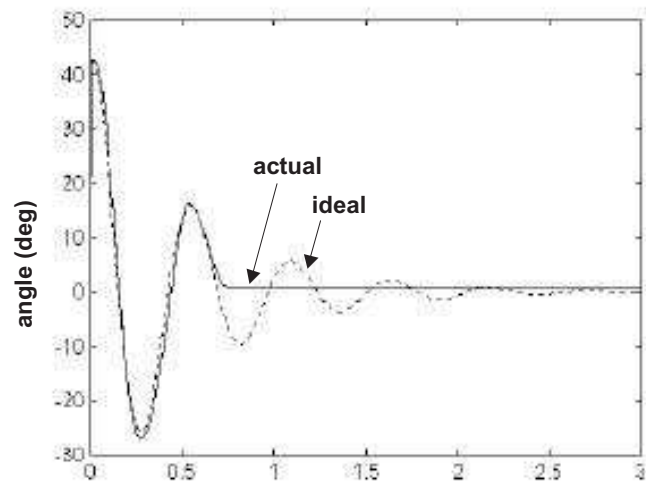
Figure 2-15: The Stanford haptic paddle [152] with step response data [169]. Students in Stanford class ME161 were asked to tune the haptic paddle system to obtain a lightly damped response. In the representative data shown above, the haptic paddle "sticks" due to Coulomb friction, causing the actual data to vary noticeably from an ideal, 2nd-order response.

The Haptic Paddle

The "haptic paddle", shown in Figure 2-15, is a low-cost[24], single-axis force reflecting[25] joystick developed by Christopher Richard, Allison Okamura and Prof. Mark Cutkosky at Stanford for use in a sequence of laboratories on dynamics. It is similar in principle to (and motivated by) the haptic interfaces developed at companies such as SensAble Devices [181] and Immersion [91]. The paddle consists of an acrylic handle, connected through a cable (with a 25:1 ratio) to a low-inertia, low-friction DC servomotor. A Hall effect sensor and cylindrical magnet (glued at the pivot) provide position sensing [170]. Student groups of 2 or 3 students shared a single paddle through the term.

Exercises students performed include the following: determining the equivalent

---

[23]or any other problem-solving subject in engineering

[24]Parts for one haptic paddle cost under $30 [170, p. 3].

[25]a.k.a force feedback

inertia of the motor and handle, calculation of torque and speed constants for the motors, calibration of the Hall effect sensors, and feedback control of the system. Some typical data of the haptic paddle under proportional plus derivative (PD) control is shown in Figure 2-15. Note that the paddle sticks, due to Coulomb friction. Students learned to tune their controllers to adjust the stiffness and damping in the response of the paddle. Staff for course also developed two software environments for the students to explore with their paddles, "haptic tetherball" and "excite the model frequencies". In the tetherball game, four students cooperate to balance a two d.o.f. inverted pendulum, using 4 individual paddles (oriented with 90 degree spacing about the pendulum). In the second program, the goal is to drive a 4th-order system such that only one mode is excited.

Many of the goals of the haptic paddle project are similar to our own goals in developeing the ActivLab labware described in Chapter 3. Richards, Okamura and Cutkosky note, for instance, that "students not only learned to model and analyze dynamic systems, but by using their sense of touch, they were able to feel the effects of phenomena such as viscous damping, stiffness and inertia" [170, p. 1]. In addition to this, they found the device sparked student interest (as intended). The instructors do note that designing and implementing new labs is always "challenging and time consuming" and that some students were "frustrated when things did not run smoothly" during their first run of the class [170]. In subsequent terms, the running the labs was somewhat demanding for the staff, but constant refinements "still made using the haptic paddles a significant amount of extra work" [170].

The Dashpod

Figure 2-16 shows the Dashpod, "a simple, pneumatically-actuated, self-stabilizing, dynamic hopping machine" [47] which was developed by Jorge Cham for ME161 at Stanford. The dynamics of the Dashpod (which is essentially a spring-mass-damper system) provide a unifying theme for a sequence of laboratory exercises. The topics covered in the labs include: first- and second-order system response, simulation of nonlinear dynamics, time and frequency response, stable and unstable behavior, cou-
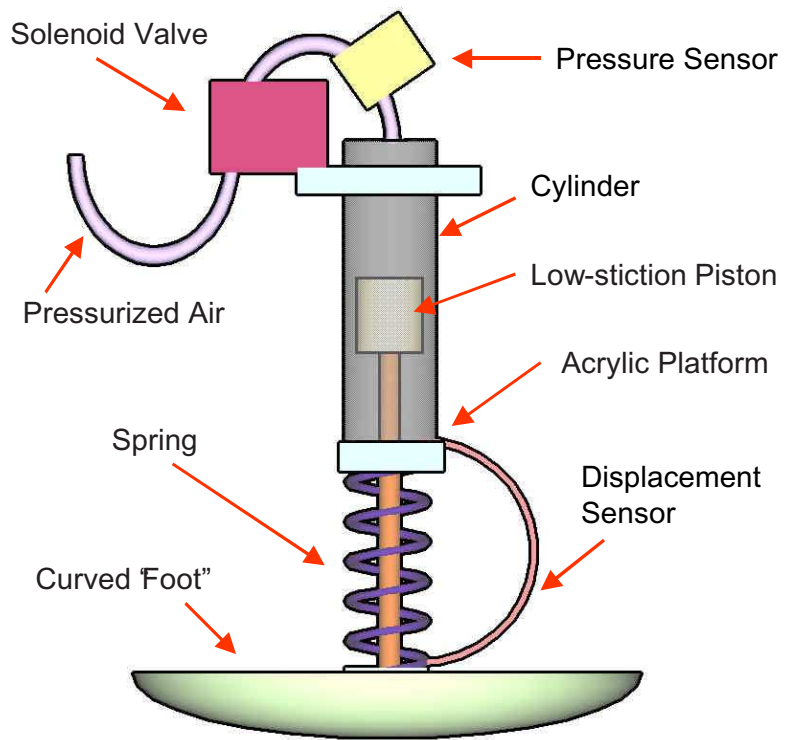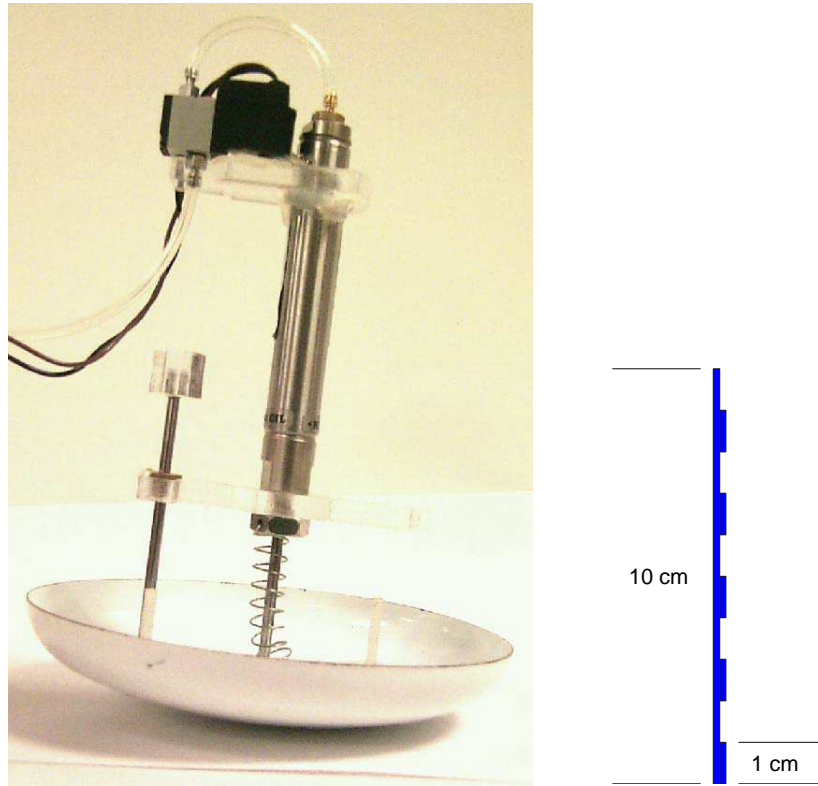
Figure 2-16: Jorge Cham's Dashpod. Images provided courtesy of Jorge Cham [47].

pled dynamics and state-space methods. The course concludes with a contest in which students modify their Dashpods to hop forward as fast as possible. Presenting the students with this design goal provides motivation for learning the course material.
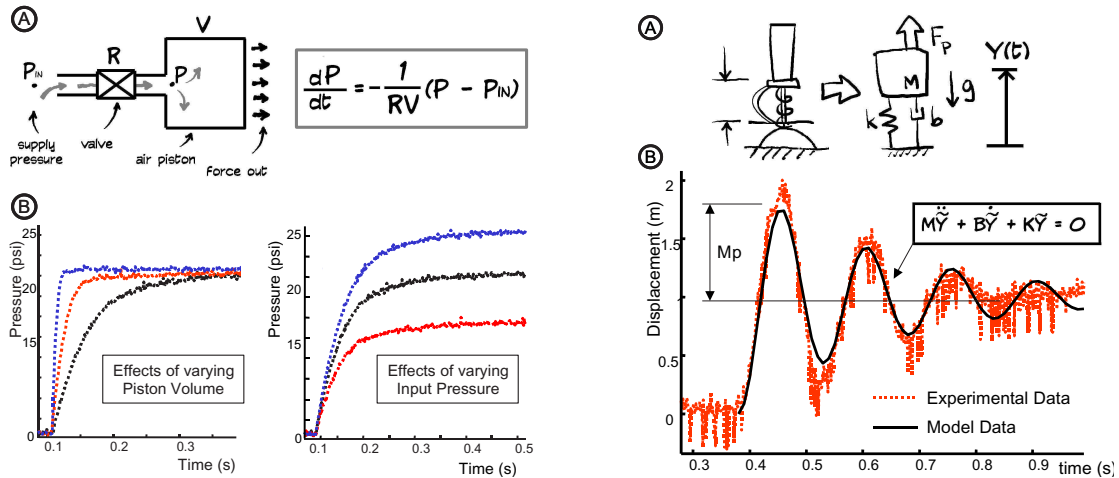
Figure 2-17: Typical Dashpod data. At left are plots of first-order system response from the air piston component of Dashpod, alone. The data at right show the second-order response of the entire Dashpod machine. These plots come from Jorge Cham's paper "See Labs Run: A Design-oriented laboratory for teaching dynamic systems" [47].

Jorge Cham provides some examples of typical data from the Dashpod system in a paper on the class [47]. Some of the data are shown in Figure 2-17. The second-order response shown at the right in this figure is relatively noisy, compared with data from the ActivLab systems described in Chapter 3. This is not surprising, since the Dashpod is intended to represent a real-world system, presenting a "mechanical device that the students can assemble, touch, play with, re-design and modify results in" [47]. In contrast, one of the main goals for the ActivLab project for 2.003 was to present nearly-ideal first- and second-order responses from mechanical systems. Typical 2nd-order response data from the ActivLab hardware can be found in Figure 3-31 on page 176, for comparison.

2.3 Multi-Media Simulations of Dynamic Systems at MIT

This section discusses current projects at MIT which make various educational media (e.g. simulated demos, textbooks, and video) available to students (and typically the general public) on the web. MIT is currently working on a project to make online materials for virtually every course at MIT freely available to educators at other universities and to the general public. This project, called OpenCourseWare (OCW), is described in more detail in Section 2.3.4.

2.3.1 PiVOT/PT tutor for 8.01 Physics I

Over the last years, the physics department at MIT has spent considerable effort revamping their introductory freshman subjects to try to improve upon the traditional lecture format. The physics department at MIT now offers several "flavors" of its two introductory (freshman) classes. To cover classical mechanics, they offer a traditional lecture course (8.01), a longer version which extends into the Independent Activities Period in January[26] (8.01L), a theoretical version aimed at physics majors (8.012), and one taught in a "studio" environment (8.01T). The mainstream course for teaching electromagnetism and electrostatics, 8.02, is now taught using this same studio environment (described in more detail in the next section), with a minority of students (a few dozen) taking a more theoretical option (8.022).

One notable project in the department is the "Physics Interactive Video Tutor" (PIVoT), which currently provides an online text with links to other supplementary materials. The PIVoT "Personal Tutor" (PT) keeps track of the topics and keywords each student accesses most often, to suggest additional related materials. PIVoT is not available to individuals outside of the MIT community, and students at the university must register for a PIVoT account.[27] Figure 2-18 shows a frame from one

---

[26]The MIT fall term ends before Christmas each year, and the second semester does not begin until the first week of February.

[27]I am not sure why it is not publicly available, but I suspect it may be because of copyright issues

of a library of 35 recorded lectures by Prof. Walter Lewin which are available to students from the PiVOT website.
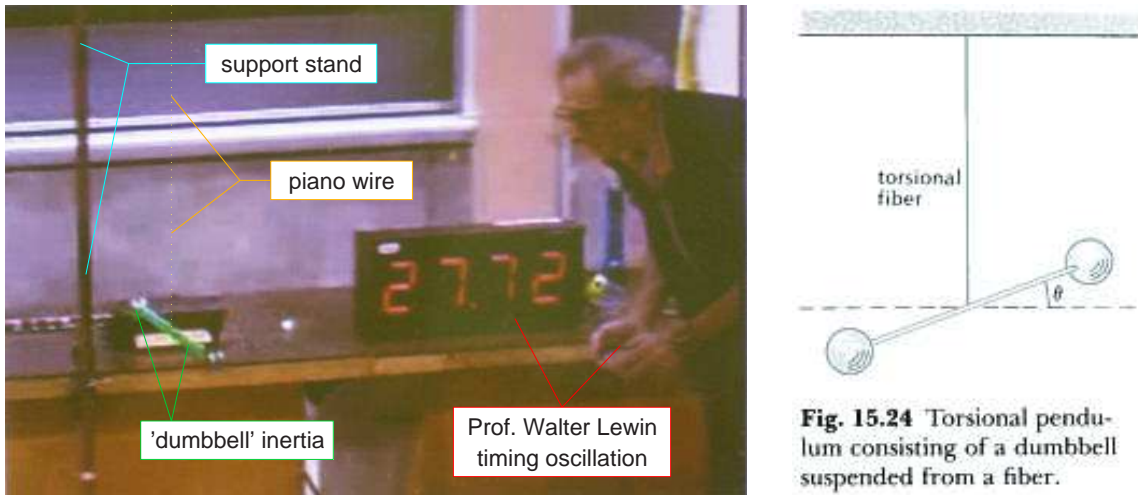
Figure 2-18: PIVoT 8.01 torsional spring demonstration - Prof. Lewin presenting a torsional spring demo during a recorded lecture (left) and a figure from the related materials in the online text [151] (right). A dashed line has been added on top of the piano wire, since it is not otherwise clearly visible. Images obtained from the PIVoT online tutorial [110]

Figure 2-18 shows Prof. Lewin conducting a demonstration in the course of one of the recorded lectures. In the demo, Prof. Lewin times the period (really "half-period") of oscillation for a second-order system. The system consists of a torsional spring, constructed from a length of piano wire (hung from a tall support stand) and a dumbbell inertia. In the demonstration, the inertia is "pre-wound" by varying amounts and then released. A large LED display shows the ellapsed time after the release of the inertia, and Prof. Lewin stops the timer by hand once the inertia comes to rest (just about to reverse direction and spin the other way). During the demo, Lewin emphasizes that we expect it must take the *same amount of time* to complete one oscillation, regardless of the degree to which the pendulum is initially wound. By the end of the demo, he winds the system over a dozen turns, counting the turns

---

involving the online text by Ohanian (published W.W. Norton and adapted into on online version byEspriTEC) [151].

out loud. When he releases the pendulum, he comments to the student to note how rapidly the inertia must spin - it needs to make all of those rotations in the same span of time they have previously timed (for less aggressive windings).

The course 6.013 ("Electromagnetics and Applications", described later in Section 2.3.3 and page 117) has also accumulated a library of such video presentations. Recordings like those used in both 8.01 and 6.013 reduce the overhead in providing demos to supplement lectures or recitations (which may only have a dozen students, each). The MIT recordings described also capture unique and inspirational people for future generations of students. For instance Walter Lewin, who appears in the 8.01 footage, is an excellent lecturer. His enthusiasm for physics is clear, and his teaching style has been refined over many years.

Both the PIVoT project described here and a project studio physics project called TEAL (described in the next section) are attempts to improve the status quo in undergraduate education by revamping or eliminating the large lecture format for required, introductory courses. As Prof. John Belcher noted (in a department News Letter in Fall 2001), "Even with an outstandingly effective and charismatic lecturer like Professor Walter Lewin, lecture attendance at the end of the term in our introductory courses hovers around 50%. No matter how strongly one feels about the intrinsic worth of the lecture format, it is hard to argue that it is broadly effective when half of the students do not attend lecture." [29]

2.3.2 TEAL/Studio Physics Project for 8.02 Physics II

Figure 2-19: The TEAL/Studio Physics classroom at MIT. 3-D rendering by Mark Bessette [29].

The TEAL Project (Technology Enabled Active Learning) at MIT has developed a "studio" environment for teaching introductory physics to replace the more traditional "large lecture" format. The studio approach for teaching introductory physics was originally developed at RPI in the early 1990's as a part of the CUPLE[28] project [29, 217]. It is taught in a unconventional classroom setting (see Figure 2-19). Prof. Jack Wilson (of the RPI CUPLE initiative) describes this as "a 'theater in the round' classroom that encourages extensive interaction among students and between students, faculty, graduate student assistants, and undergraduate student

---

[28]Comprehensive Unified Physics Learning Environment

assistants" [217]. A typical studio classroom has multiple white and/or blackboards, overhead projector(s), and tables which seat subgroups of systems. There are laptop computers and lab experiments on the tables, which are periodically integrated into the studio experience. Part of the TEAL studio project at MIT involves visual simulations of electromagnetic phenomena, which students can view online. Figure 2-21 shows examples of these simulations.

Figure 2-19 show a rendering of the TEAL classroom, which is now being used at MIT to teach introductory electromagnetism and electrostatics (8.02). Studio physics attempts to integrate aspects from lecture, laboratory, recitation and tutorial environments,[29] and the design of the room is meant to facilitate this. The TEAL classroom has twelve large circular tables which each seat nine students. Classes involve a mixture of lecture and table-top experiments, which are performed in groups of three. Each student attends two 2-hr and one 1-hr sessions each week, each in this classroom environment.

Figure 2-20 shows similar rooms for teaching studio physics which are used at North Carolina State University and at the University of Western Kentucky. Universities which have currently adopted the studio physics approach include: North Carolina State University, University of Central Florida, University of Alabama, American University, Coastal Carolina University, MIT, University of New Hampshire, Rochester Institute of Technology, Wake Tech Community College and Western Kentucky University [202].

The effectiveness of the program at MIT is hard to gage at this time. The TEAL program was used on with relatively small groups of students beginning in the Fall of 2001 [29] and was tested on a large scale (with over 600 students [107]) for the first time in the Spring of 2002. In March of 2003, over 150 students in 8.02 signed the following petition [107]:

> 8.02 TEAL does not provide us with the intellectual challenge and
> stimulation that can be expected from a course at MIT. We feel that
> the quality of our education has been compromised for the sake of trying

---

[29]All instruction occurs in the studio; there are no additional labs or tutorials.

something different. We strongly advise that the traditional 8.02 course be reinstated as soon as possible. 8.02 TEAL could remain as an option, which will give TEAL an opportunity to evolve. However, it should not be forced upon the majority of the student body.

Responding to questions about the student protest, Prof. Walter Lewin (mentioned in the preceding section) is quoted as saying:

Many students are really angry. Most complain that TEAL is not helping them to learn, so they are on their own. Without recitation, the students are missing the ins and outs of problem solving...In a few years, TEAL may evolve into a very wonderful program. It may turn out to be wonderful, but right now, it is not working [107].

I do not know enough about the program to comment on its value personally. I will note that the lecture-style freshman courses in physics at MIT traditionally contained *no* laboratory component. The TEAL project at MIT provides students with hands-on experience, and promotes interaction of the students among one another and with staff in learning. The Physics department at MIT plans to expand the use of TEAL in 8.01 Physics in Fall 2003 and to make it the mainstream course option in the fall of 2005 [107]. (It is interesting to note, however, that they have no plans to convert either 8.012 or 8.022, the versions intended for physics majors, to a studio format [29, p. 9].)

As mentioned earlier, the studio approach is being used at several universities now. It should be noted that "economic necessity" [28] is often cited as the driving force for this. NCSU, for instance, reports that their program[30] hopes to "provide an economical alternative to traditional lecture-oriented instruction" [27]. Prof. Jack Wilson also emphasizes cost savings among the motivations for originally developing the CUPLE studio physics approach at RPI, which include the follow: "to reduce the emphasis on the lecture, to improve the relationship between the course and

---

[30]NCSU's studio program is part of a coalition effort called SCALE-UP (Student-Centered Activities for Large Enrollment University Physics).

the laboratory, to scale up the amount of doing while scaling back the watching, to include team and cooperative learning experiences, to integrate rather than overlay technology into all of the courses, and above all to do while reducing costs!" [217] He notes that in the traditional introductory physics course "the lectures are team taught by two or more faculty, labs are taught by teaching assistant, and the recitations use a mix of faculty and teaching assistants...We have two laboratory support staff and one lecture demonstration support person...I was surprised to see just how expensive this course was." [217]

In contrast, the TEAL program at MIT is expected to have "a steady state cost that is the same at the present[31] lecture/recitation mode of instruction, exclusive of start-up costs" [29]. Then again, the traditional MIT freshman courses did not have a laboratory component, while many of the other universities cited did. My own final comment is that it seems a shame to destroy a traditional laboratory, like the one shown in the lower left of Figure 2-20 in favor of what appears to be a primarily computer-based laboratory. (The images at the bottom of this figure depict the same room, before and after conversion to a studio classroom.)

---

[31]Note this was written in fall 2001; TEAL is now the present form in which 8.02 is taught.

Figure 2-20: SCALE-UP renovations of classrooms for physics. At top is a classroom at North Carolina State University before (left) and after (right) renovation (circa 1999). Below, a traditional laboratory at University of Western Kentucky (left) was converted to the SCALE-UP round-table structure (2001). Images obtained from the SCALE-UP homepage at NCSU [150].
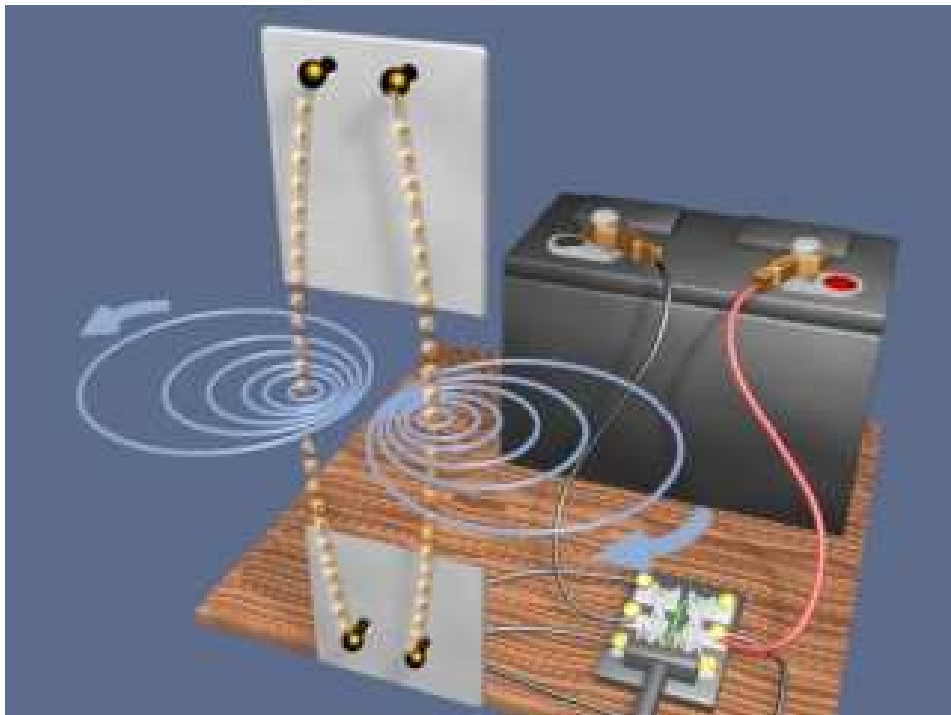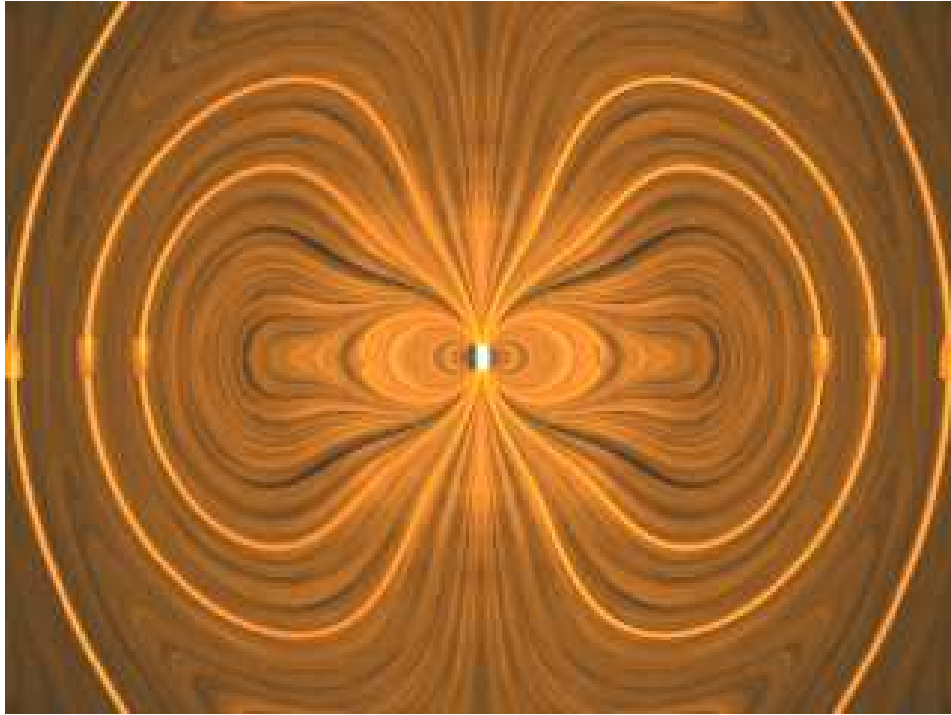
Figure 2-21: TEAL visualizations of electrodynamic phenomena [135]. Electric Dipole Radiation (top). Deflection of parallel wires with opposing current flow direction (bottom).

116

2.3.3 6.013 E & M Simulations and Movies

6.013 is a junior/senior level elective in the department of Electrical Engineering and Computer Science at MIT. The course has recently been revamped, and is now called "Electromagnetics and Applications". The description in this section refers to the previous version of the course ("Electromagnetic Fields and Energy"), which was taught for years at MIT. Curricula for both versions of the course cover "quasistatic and dynamic solutions to Maxwell's equations" [124, p. 391].

The course is worth mentioning here because of the large library of demonstrations they have accumulated. As with many courses in the department, the recitations are taught by full professors (who often alternate from year to year in their roles as lecturer or recitation instructor). Recitation sections focus on problem solving and also include additional demonstrations, allowing students to observe the hardware more closely than is possible in a large lecture hall.
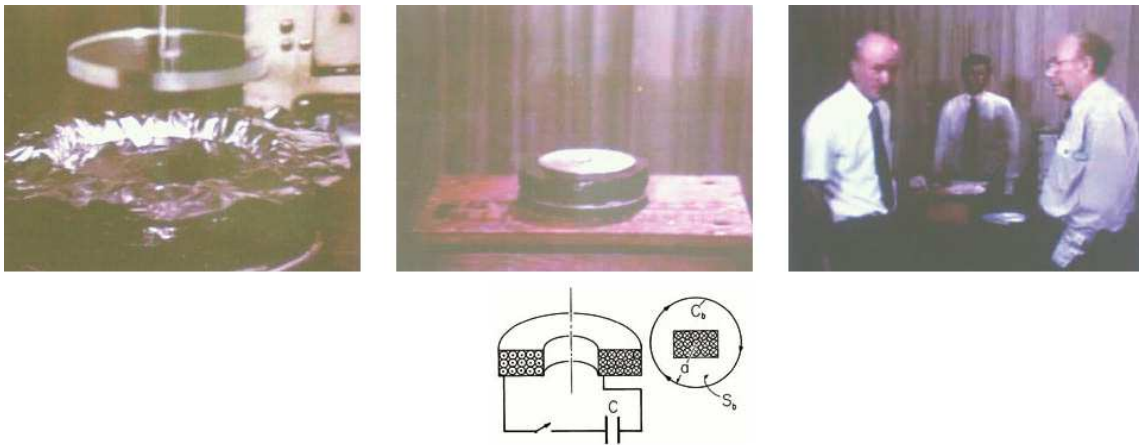
Figure 2-22: "Edgerton's Boomer" video demonstration for 6.013. At left, the force from Edgerton's Boomer has deformed a piece of foil. The "boomer" itself is shown in the middle (with a schematic just below). At right are Professors Melcher, Zahn and Edgerton [136].

The text for the course is available (free of charge) at the course website (it is no longer in print), along with recorded video of many of the demonstrations. Video for 6.013 includes many of the faculty who developed the text and curriculum for
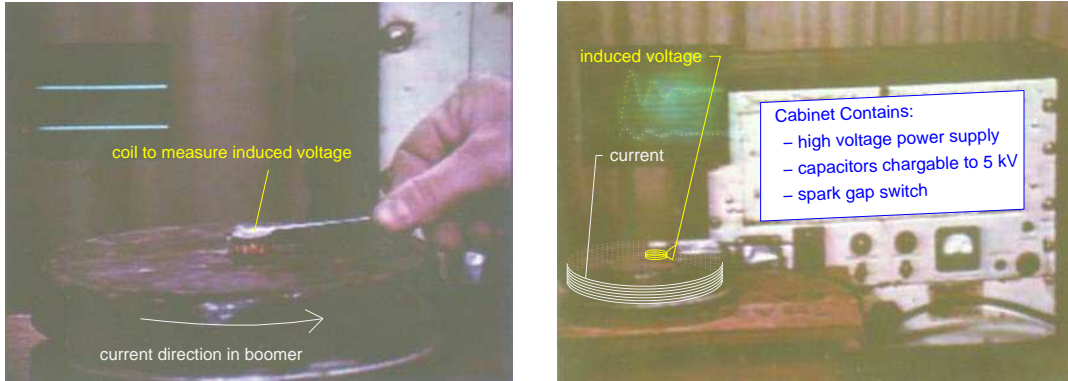
Figure 2-23: Time-varying current and field for Edgerton's Boomer. The induced voltage measured by the small sensor coil is proportional to the time rate of change of magnetic field. Note that I have "enhanced" the oscilloscope traces in the image at right because otherwise this image from the video was too blurry to make out the 2nd-order response (voltage at top, with current below). I brought the image at right into MATLAB and used that environment to plot fitted 2nd order traces, based on the pieces of the image I could still make out. [136]

the course (e.g. Prof.'s Haus, Melcher and Zahn) and, as shown in Figure **??**, even includes a cameo by Prof. Harold ("Doc") Edgerton. Doc Edgerton was still a familiar figure in halls of MIT in the late 1980's (when I first came to MIT). He is perhaps most famous for his innovations in high-speed photography (capturing a bullet as it emerges after piercing an apple, for instance). Doc Edgerton passed away in 1990. The MIT Tech's obituary includes the following comments from Prof. Paul Penfield Jr. (ScD '60) [183]:

> His strobe lab has been a haven for generations of students, who simultaneously learn, mature, and get infected with Doc's enthusiastic approach to science, engineering and life. Doc was always carrying around a pocketful of postcards with one of his famous photographs, to give to children (and those of us still children at heart).

The video captures a small taste of his openness, brilliance, and (in particular) playfulness.

"Edgerton's Boomer" can essentially be modelled as a second-order LRC circuit. The schematic at the bottom of Figure 2-22 shows a cross-section of the coil, which can be modeled as an inductance and resistance in series. This coil is then connected in series to a capacitor to form an LRC circuit. The scope traces in the image on the right half of Figure 2-23 have been "touched up" to more clearly emphasize the decaying oscillatory voltage and current responses (which are 90 degrees out of phase).

2.3.4   The OpenCourseWare Project

MIT is currently engaged in a program to make online course materials available to the general public. This program is called "OpenCourseWare" (OCW). What the project aims to accomplish, as cited on their website, is as follows:

1. "Provide free searchable, coherent access to MIT's course materials for educators in the non-profit sector, students, and individual learners around the world." [125]

2. "Create an efficient, standards-based model that other universities may emulate to publish their own course materials." [125]

The project is funded by the William and Flora Hewlett Foundation, the Andrew W. Mellon Foundation, and MIT. OCW should provide online access to materials for nearly all of MIT's courses (about 2000) by the summer of 2007 [125]. As of Spring 2003, OCW consists of materials from about 60 courses, including 2.003 Modeling Dynamics and Control I. Links to descriptions of our ActivLab projects are provided through OCW.

Much of the material at OCW will presumably consist of documentation of the syllabus, homework and lab assignments in each class. Online (web) materials can also include virtual laboratory experiences and demonstrations, however. For example The videos for 8.01 and 6.013 are available as an online reference for students (independent of the OCW project), and the TEAL simulations in Figure 2-21 are already a part of the suite of OCW materials.

Another example currently on OCW is a complete, downloadable copy of a textbook on heat transfer (by John H. Lienhard IV and John H. Lienhard V). This is the text I used (in hardcover) at MIT as an undergraduate (over ten years ago), which is currently out of print. The authors now hold all rights to the work, and have decided to make it publicly available, free of charge. They give the following explanation: "First, in electronic format, textbooks can be continually corrected and updated, without the delays inherent in printed books (second and later editions are typically published on a five-year cycle). Second, free textbooks hold the potential for fundamentally altering the economics of higher education, particularly in those environments where money is scarce." [112]

2.4   Robot Contests

Over the past ten years, an increasing number of classes in mechatronic design have been structured around autonomous robot competitions. Such contests typically use either the BASIC Stamp (manufactured by Parallax, Inc.), or the 68HC11-based "Handy Board" (developed for 6.270 at MIT). These two microcontrollers are described in more detail in Sections 2.4.2 and 2.4.1, respectively.

2.4.1   6.270 Lego Robots and the Handy Board at MIT

The Handy Board, shown in Figure 2-24, emerged out of a project in the early 1990's to develop a microcontroller for the 6.270 autonomous LEGO robot contest at MIT. The name *6.270* derives from the inspiration for the contest: the popular Mechanical Engineering design class *2.70* developed by Prof. Woody Flowers at MIT.

MIT's 6.270 contest was instituted and developed by a group of LEGO-fanatical students in the Electrical Engineering and Computer Science department who include Fred Martin, Randy Sargent, and Panjak (PK) Oberoi. They put together the hardware, software and funding necessary, and the contest has continued as an annual event each January at MIT ever since. Many universities and high schools now use the Handy Board for similar robot competitions. Related research by Sey-

mour Papert's Epistemology and Learning Group[32] at the MIT Media Lab to create the Programable LEGO Brick inspired the development of the LEGO MindStorms robotics system [67, 109].

Handy Board specifications include 32K of static RAM. There are inputs for 7 analog and 9 digital sensors, and an expansion bus makes additional digital I/O latches possible. The board operates on internal NiCad batteries, has a built-in recharging circuit, and uses two L293D motor driver chips capable of driving a total of four 9-volt DC motors.

The boards are particularly well-suited for teaching higher-level design skills due in large part to the Interactive C (IC) programming language, developed for the 68HC11 by Randy Sargent [147]. IC compiles into pseudo-code (p-code), which is then interpreted by the machine language. As a result, users do not need to wait for lengthy compiles and can test code at the command line. This makes the environment particularly useful for learning higher-level skills, so that robot-builders can focus on algorithms and good design practice rather than on details of low-level implementation.

Figure 2-25 shows two LEGO robots built for the 6.270 autonomous robot contest at MIT. Themes for the contest vary from year to year, and students work together in teams of 2-4 to build their robots. The class is always over-subscribed, and participants are chosen by lottery. The Handy Board (assembled or in parts) can be purchased from several retailers. More details about the board can be found at the following website: http://handyboard.com

---

[32]mentioned earlier in Section 2.2.1
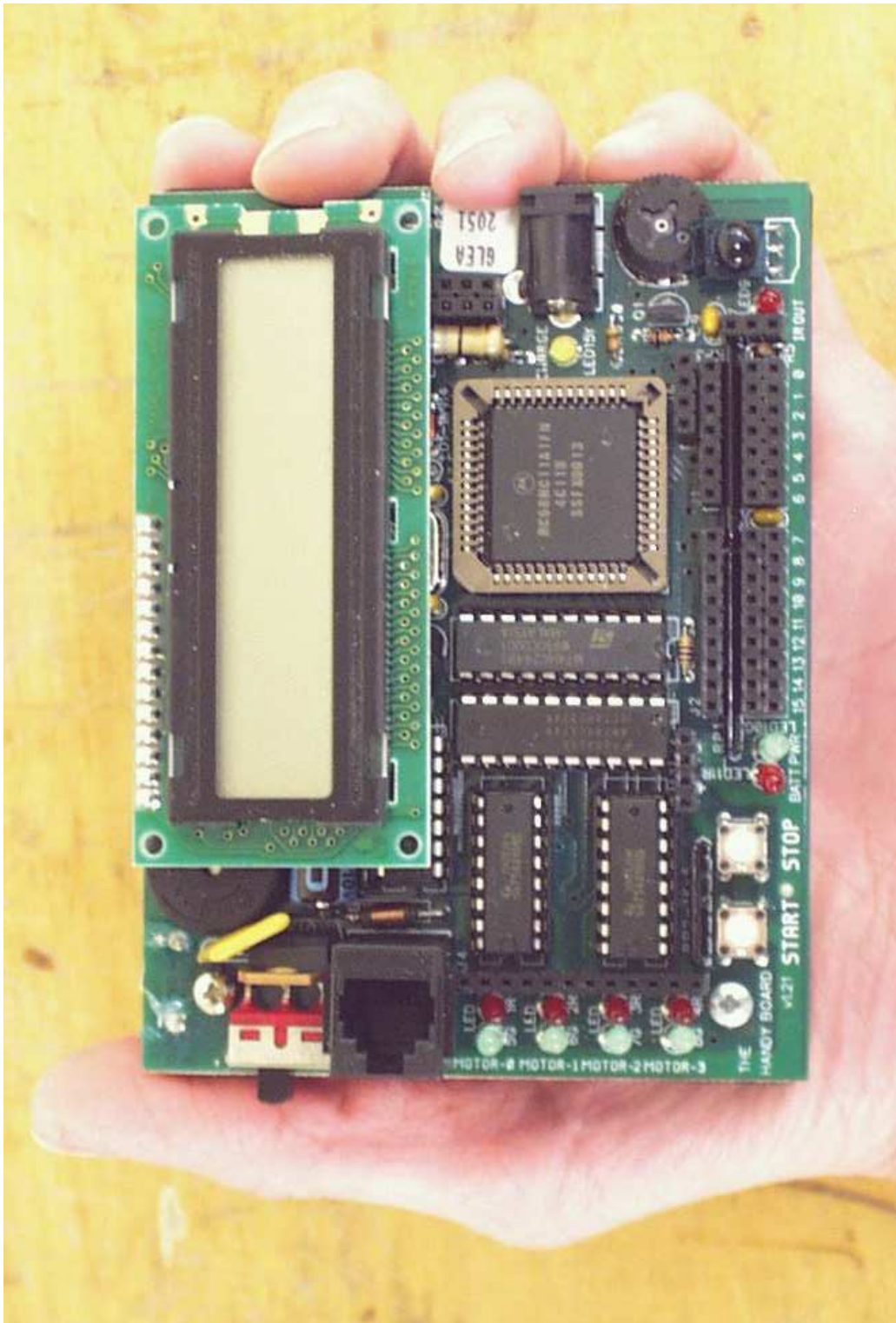
Figure 2-24: The Handy Board [121].
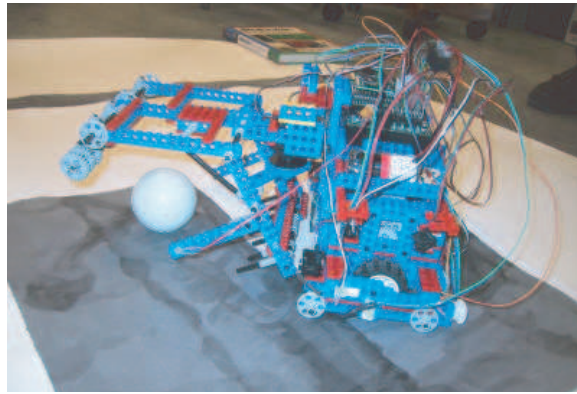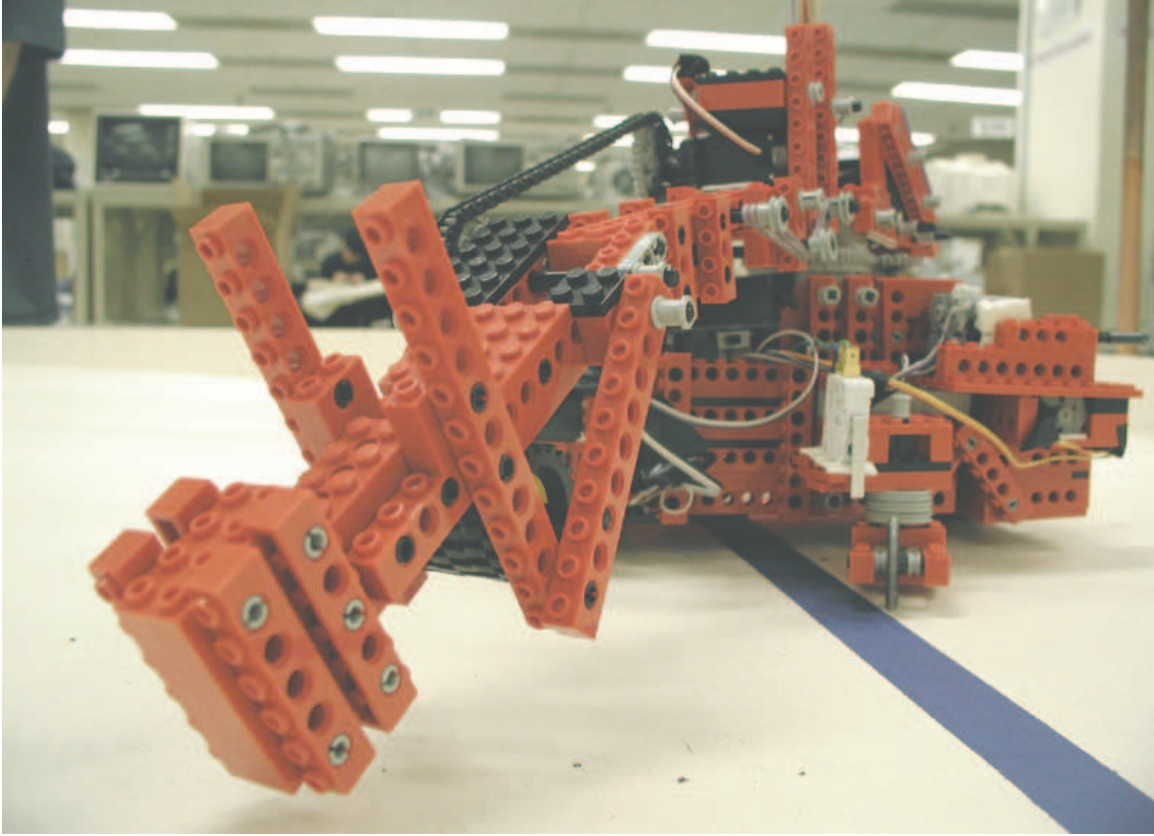
Figure 2-25: Lego ball-collecting robots from MIT 6.270 contests [123] - At top is "Dr. Whackenscore", created by Garrett Barter, Elie Krevat, and Dan Kwon in 2001 [26]. At bottom is "SoZoomy", created by the Microsoft corporate sponsor team consisting of Mike Koss, Walter vonKoch, Kevin Stoltz, Chris Koss, and Zak Stoltzin in 2002 [103].

2.4.2 The BASIC Stamp Robot Controller

The BASIC Stamp, shown in Figure 2-26, is another popular microcontroller used in many robot competitions and design classes, both at the university and high school level. More information and specifications of the BASIC Stamp can be found at: http://www.parallax.com/

One example of a university program using the Basic Stamp is a sophomore course in design at the Woodruff School of Mechanical Engineering at Georgia Tech, taught by Professors Thomas Kurfess and John Witzel. Kurfess states that the course is motivated by the fact that typically "electromechanical system design and implementation is not taught until advanced courses in the undergraduate curriculum" [106]. He further notes that, "the reality is that most engineers work in the world of mechatronics as there are relatively few systems that are purely mechanical or electronic" [106].

Approximately 300 sophomores take the course each year. Material costs are kept "minimal" (about $350 per group, with 50 groups per sememster [105]), but the course is very labor intensive. Running the course requires the equivalent of "one full-time technician and 8 TA's" [105].

Actuators used include stepper and DC motors, solenoids and shape memory alloy actuators, and the sensors available to the students are micro switches, IR range finders with a range of 10 - 100 cm, and a variable resistance flex sensor.

The goals of the contest vary from year to year. One competition involved placing a CD ROM on a target [105]. In another year, the contest was essentially a triathlon, where the machines performed three different tasks with a collection of ping pong balls: pushing them out from underneath a low platform ("bowling"), retrieving them from same platform ("fishing"), and depositing them into a basket above the platform ("basketball"). The machines could perform these tasks individually or simultaneously, and defensive "goal keeping" was allowed. The only power energy sources allowed in this competition were two 6-volt lead acid batteries, 5 mouse traps, and gravity [106].
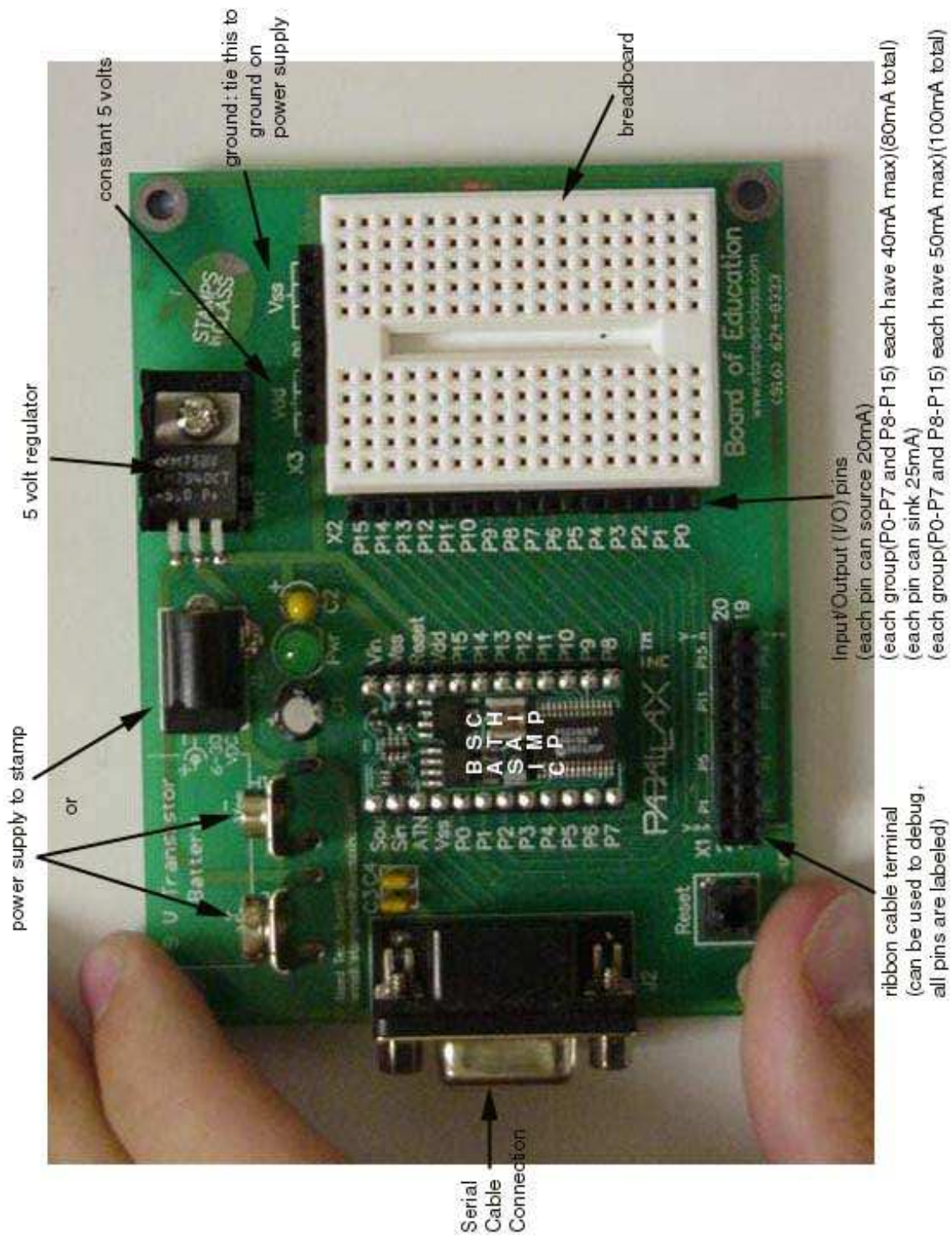
Figure 2-26: The Basic Stamp. Image obtained from the Parallax website [156].

2.4.3 Stanford SPDL March Madness duel

Prof. Ed Carryer of the Smart Product Design Lab (SPDL) at Stanford University has created a contest-driven mechatronic design course for seniors and graduate students in the department of mechanical engineering. This course, "ME118/318 Introduction to Mechatronics"[33], originated in 1998 with a "March Madness" basketball-style robot competitive [46]. Figure 2-27 gives an idea of the types of the robots students create. Robots use umbilical cords for power, but they use on-board microprocessors to provide autonomous control during the contest.
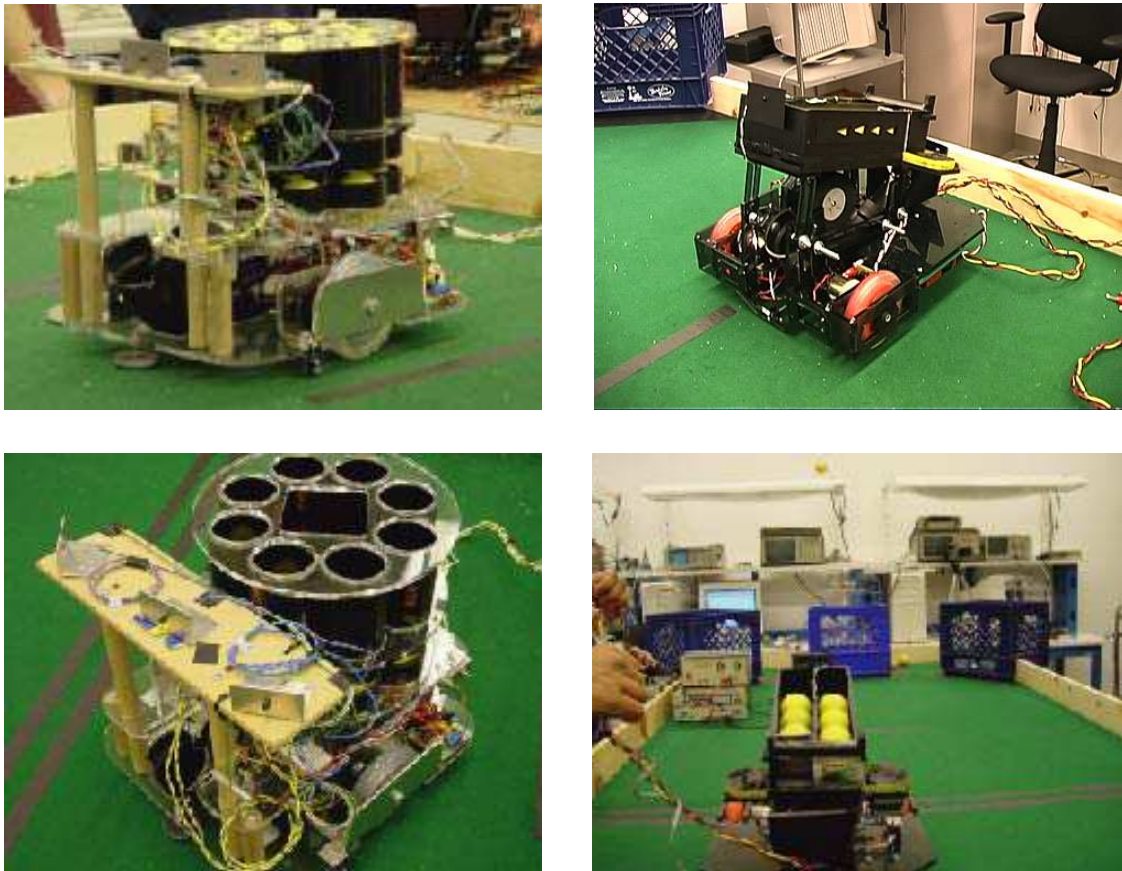
Figure 2-27: Stanford March Madness duel [46]. Images obtained from the website for the class [35, 126].

---

[33]formerly EE118

Over the years, the theme of the contest has varied[34], but the goal of the course is always the same: to provide students with an open-ended team project that requires designing and building an electro-mechanical device with an embedded microprocessor. The class runs for ten weeks, with twice-weekly lectures on topics that include sensors, op-amps, power drivers, solenoids and DC motors, stepper motors, A/D and D/A, microprocessors (including both the BASIC Stamp and the 86HC11), and noise, grounding and isolation issues. During the first four or fives weeks, there is a weekly lab. Lab topics include programming state machines, analog signal conditioning, mechanical prototyping with foamcore, and DC and stepper motors.

The texts for ME118/3118 are the classic "The Art of Electronics" by Horowitz & Hill and "Mobile Robots: Inspiration to Implementation" by Joseph Jones, Bruce Seiger and Anita Flynn. This second book "has grown out of research at the MIT Artificial Intelligence (AI) Laboratory under Rodney Brooks and his mobile robot group."[35] It is an excellent resource for robot builders, covering a gamut of topics including (but not limited to) sensor and motor selection, power systems and isolation, microprocessors, legged locomotion, and mechanical design principles. The authors also include lists of suggested parts suppliers, data books and trade magazines.

---

[34]In 2002, the Winter Olympics inspired a contest based (loosely) on the sport of "curling".

[35]from the book's Preface [96, p. xx].

2.4.4   Micromouse Competition

In Micromouse competitions, autonomous robots must navigate through a maze as quickly as possible. Many Micromouse contests are held throughout the year and across the world, involving participants from the high school students to seasoned analog circuit designers.[36] IEEE organizes regional competitions in the United States for undergraduate students. Several universities now offer courses in which students build a Micromouse as a capstone project. Figure 2-28 shows two views of mouse build by students at California State University at Northridge (CSUN).

IEEE Region 6 (covering much of the south-western US and Hawaii) is particularly active in such competitions. Participating schools in this region include the following: Berkeley, Cal Poly Pomona, U.C. Davis, U.C. Santa Barbara, U.C.L.A., U.C. Santa Cruz, Chico State and the University of Hawaii. The IEEE website at U.C Davis notes: "Micromouse is an official course offered at U.C. Davis under EEC-194ABC. It is one of the few undergraduate courses that integrates several different disciplines of engineering, ranging from electrical to mechanical to computer science - it can offer a valuable learning experience. In addition to various regional and national events for Micromouse competition, one of our fondest events at U.C. Davis is the Picnic Day competition," held annually each Spring [93].

The EEC-194A,B,C Micromouse sequence at U.C. Davis, currently taught by Prof. Tak Auyeung, runs through all three terms (fall, winter and spring) of the academic year to comprise a single, 5-unit elective. The Micromouse projects are student-run. Each team consists of approximately five students, each of whom is responsible for a particular subsystem (electronics, power and motor, software, system integration, and sensors). Topics covered include gears, bearings, wheels, traction, chassis construction, stepper and DC motors, differential steering, sensors, noise issues, PID control, high level algorithms and project management [17].

---

[36]Dave Otten, who currently works a few feet away from me in the Precision Motion Control (PMC) lab at MIT is such a "seasoned analog circuit designer" who has won accolades at several international Micromouse competitions.
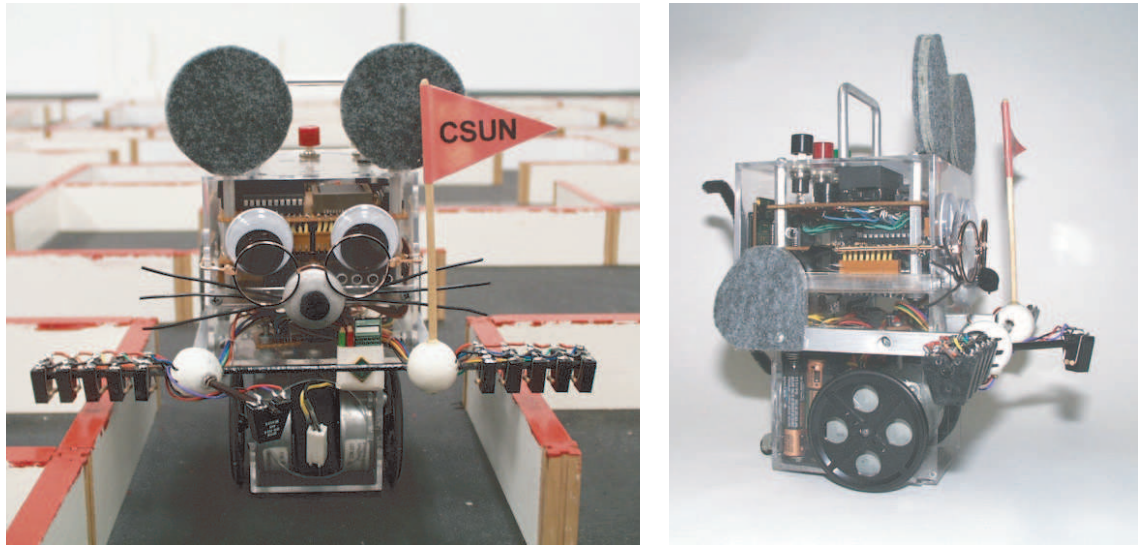
Figure 2-28: "Dexter" the MicroMouse. This robot was built by Steve Benkovic, Steven Uyetanaka and Meng Cheng Hsieh as a senior project at California State University at Northridge (CSUN). Note that the wall (in the lefthand photo) is 5 cm high. These images come from Steve Benkovic's website:

http://homepage.mac.com/SBenkovic/MicroMouse/index.html

2.4.5 Intercollegiate NATCAR Competition

The NATCAR race is an annual competition, sponsored by National Semiconductor, which has involved teams of students from up to eight universities. There are typically 2-3 undergraduates per team. The five universities participating in May 2003 are U. C. Davis, Berkeley, Stanford, San Jose State University, and Oklahoma State University [187]. The objective of the contest is to design and build an autonomous car that can complete a preset course in the shortest time. The race course is traced out on black carpeting with shiny, white vinyl tape with a wire beneath it that produces a 75 kHz signal. The curving path can cross over on itself. The smallest allowable angle at any intersection is 60 degrees [187]. The vehicles can elect to use either optical or magnetic sensors. Students are allowed to begin their designs with the chassis of a radio-controlled car, but all sensing and control electronics must be built by the students. The vehicles often achieve speeds greater than 10 mph - significantly faster than a typical human could control an RC car over the curving path.

Several universities incorporate the contest as the focus of a course in design. Figure 2-29 shows two views of a U.C. Davis entry. Prof. Richard Spencer initially organized the competition with the cooperation of engineers at National Semiconductor [175]. He now teaches "EEC195, Autonomous Race Car Project" at U.C. Davis (where the NATCAR competition is headquartered) and coordinates the official NAT-CAR website (outlining the rules of the competition) [187]. Berkeley offers a similar course which focuses on the design of cars for the competition called "EE192: Mechatronics Design Lab". U.C.Davis and Berkeley are typically the strongest competitors in NATCAR each year. NATCAR courses at other universities include "EE192G: Electronic Dynamic Control Systems Laboratory" at Stanford, and "EEE192 Electrical Engineering Design" at U.C. San Diego.

The competition forms a focal point for covering topics such as DC motor control, analog circuitry, microcontrollers, PID control, optical and magnetic sensors, A/D's, noise and shielding concerns, H-bridges and PWM, and design principles [128, 69].

Figure 2-29: NATCAR autonomous robot race. In the annual NATCAR competition, 1/10 scale autonomous cars compete to complete a curving and self-crossing path in the shortest time. Penalties are assigned for deviations from the prescribed track. [187]

Competitions like this also generate enthusiasm and interest among students outside of the class, as well. U.C. Davis annually holds a well-attended run-off among the in-school teams as a part of their annual "Picnic Day"[37] events each May [175].

2.5 Laboratory Courses in Mechatronics

This section describes two undergraduate-level laboratory courses in mechatronics. Hands-on laboratory experience is vital for learning mechatronics, and many of the basic goals in developing laboratory projects for mechatronics are similar to those we had in developing the labs for 2.003 Modeling and Dynamics I. Specifically, both types of lab projects aim to give students a real "feel" for how dynamic systems behave. One difference is that in mechatronics, students typically concentrate more on how to modify (i.e. control) the dynamics of a physical system by using feedback and on the details of how sensors, actuators and signal processing all work. In a sophomore-level dynamics course like 2.003, the emphasis is weighted toward gaining familiarity with the fundamental characteristics of first- and second-order system dynamics.

In teaching 2.003, we seek to instill in students a basic understanding that controllers are designed in order to the modify system dynamics - but to do so without introducing formal control design such as root locus, the Nyquist criterion, etc. To

---

[37]Picnic Day is mentioned in the preceding section on the Micromouse, as well.

achieve this, we have elected to introduce some of the basic concepts of classical control and introductory op-amp feedback circuits. Many aspects from some of the lab projects originally designed for 2.737 Mechatronics (discussed below) are therefore also relevant projects for the sophomores in 2.003.

2.5.1   2.737 Mechatronics at MIT

2.737 Mechatronics is a hands-on laboratory course developed during the 1990's by Prof. David Trumper and his graduate students. The class teaches essential concepts related to the design of devices which integrate electromechanical components, electronics, and control. Most of the term is spent working through a series of closed-ended laboratory projects. Figures 2-30 and 2-31 show examples of the topics covered. Each project is aimed at developing some well-defined set of skills related to electromechanical systems and control. There are also a number of open-ended projects which have been used as final projects in the class.
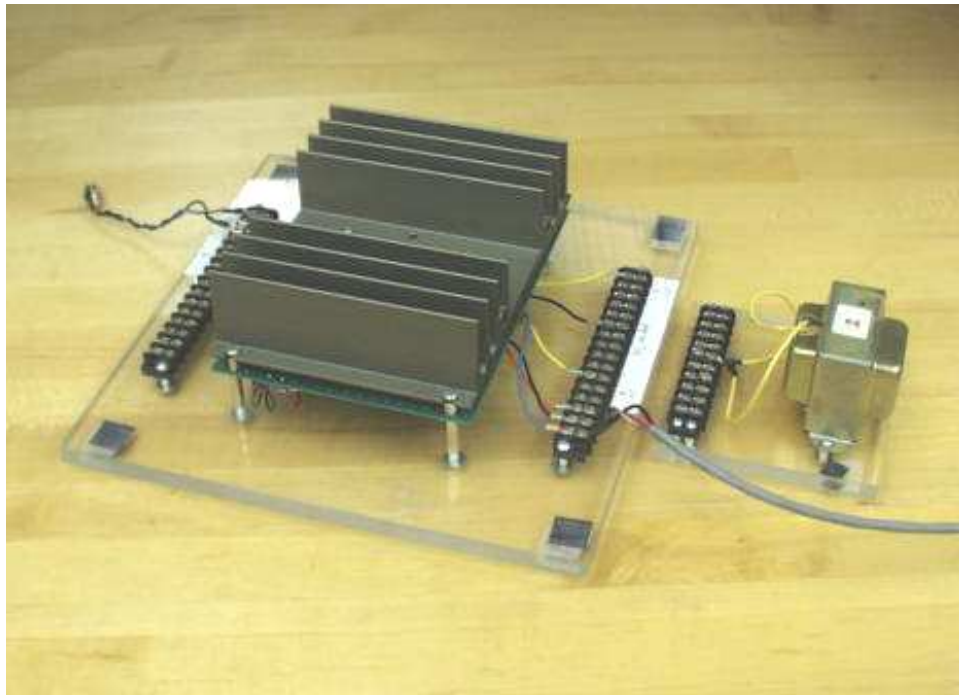
Figure 2-30: Current controller lab for 2.737 Mechatronics. A large heat sink for a power amp (hidden behind the fins) is shown at left; transformer load at right.
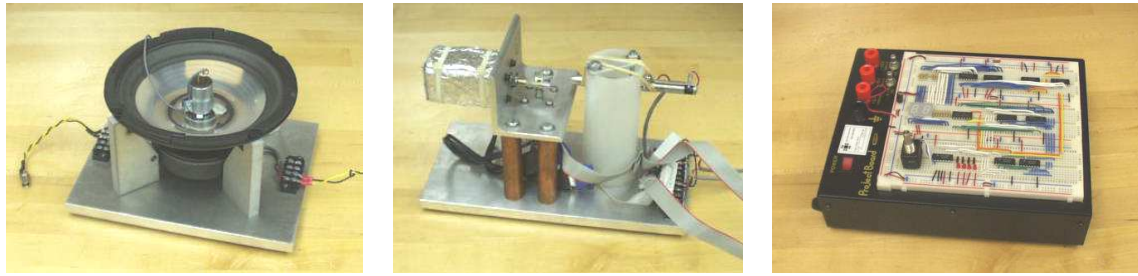
Figure 2-31: Additional projects for 2.737 Mechatronics. From left to right: vibration isolation, laser light show, and encoder lab

Figure 2-32: The 2.737 Mechatronics laboratory

Figure 2-32 show the 2.737 lab. This is currently the same room where the 2.003 labs are taught. Each lab station is equipped with a PC, power supply, signal generator and scope. Digital control is implemented on an 1102 dSPACE controller board, installed on each computer. The dSPACE board operates on Simulink models compiled into C code and then into executables. The Simulink models are essentially block diagrams, with ports for various I/O devices. In earlier years, students were required to write their own computer code directly to implement a controller. The adoption of the dSPACE system allows students to focus on control algorithms and optimization, rather than on learning to program.

The course aims to "teach design in a mechatronic context" from the viewpoint that "design is a subject which, once understood, can be readily executed within other disciplines after learning the governing physics" [197]. This perspective is consistent with those expressed throughout the literature survey in Section 2.2.1, which largely proclaims, as Herbert Simon puts it, "...that the emphasis in engineering education should not be placed on knowledge, but should focus attention on the learning processes and the problem solving processes of the students" [184]. More details about 2.737 can be found in the paper, "Development of 2.737 Mechatronics at MIT" by Trumper and Ludwick [197].

2.5.2 RPI Mechatronics Teaching Lab

The mechatronics program at Rochester Polytechnic Institute (RPI), developed by Kevin Craig, is a well-known model for other universities [52, 53, 54]. Many laboratory experiences have been developed over the years, and they are central in teaching mechatronics at RPI. Figure 2-33 gives a flavor for the types of projects students investigate and the hardware involved.

Prof. Craig has developed two complementary, senior-level elective courses. The first course, "Mechatronics" (MEAE 4490, offered in the Fall term), teaches fundamental skills for mechatronic design. Four hours each week are spent in studio-style lectures. The class is limited to 36 students, which allows for interactive classes that include hands-on exercises. There are also ten two-hour laboratories during the 14-

Figure 2-33: RPI mechatronics teaching lab hardware. At top, left each station is equipped with a 'scope, function generator, multi-meter, powered protoboard and a PC (with a dSPACE controller board and MATLAB/Simulink to implement real-time control). Top right: A two-mass, three-spring system demonstrates free and forced vibrations, colocated and non-colocated control, and principles of dynamic vibration absorption. The hardware includes two DC motors (with tachs), optical encoder, and two infrared position sensors. The lower left picture shows an inverted pendulum that is mounted with a universal joint and actuated through two belt-driven linear slides. The system is controlled in dSPACE using full state LQR feedback. In the final project shown, a 1/2-inch steel ball is magnetically levitated using an analog lead controller (to command current). Light from an infrared diode emitter is detected with a phototransitor. Images were obtained from the RPI Mechatronics website [51].

week class. Both lectures and labs are held a specially-designed classroom, "The Mechatronics Studio", which is equipped with lab stations and multi-media capabilities. Laboratory topics include the following: analog electronics, digital electronics, A/D and D/A, stepper motor control, DC motor control, control of a thermal system, pneumatic servomechanism, and magnetic levitation.

The Spring-term elective in mechatronics is "Mechatronic System Design" (MEAE 4250). This course is more open-ended than the former. Students work in groups of four to complete a central term project and presentation. The project may involve reverse engineering a mechatronic device, for instance, or creating new hardware for the lab. The class has four hours of lecture each week and unlimited open lab access.

Both classes focus on developing essential skills in mechatronic design. As Prof. Craig writes, "while there is certainly a need for controls experts and advanced control techniques, most control designs used in industry today are of the classical lead-lag type, and mechanical engineers need to know how to design and implement these as an integral part of their design and not as after-thought add-ons." [52, 53, 54] Craig's premises are that controls are taught too late (if at all) in most mechanical engineering curricula and that mechatronic design is a relevant skill for all mechanical engineers in today's world.

2.5.3 Other Programs of Note

Traditionally, most mechatronics programs have been aimed at the graduate level. This thesis is specifically concerned with undergraduate programs that give students hands-on (laboratory) experience in dynamics and mechatronics. Over the past ten years, many universities have begun to offer curricula and course degree programs in mechatronics at the undergraduate level. Several such programs, both in the U.S. and abroad, are listed in Tables B.1 and B.2 of Appendix B. I am surely not even aware of many excellent programs worth noting. The lists in this Appendix do not claim to be comprehensive, but they do give a survey of the current approaches used for teaching mechatronics.

Chapter 3

ActivLab Hardware

This chapter describes the hardware and experiments developed for 2.003 Introduction to Modeling, Dynamics, and Control I, which is a required undergraduate course in the Department of Mechanical Engineering. The course focuses largely on deriving linear constant-coefficient differential equations to model linear time-invariant (LTI) mechanical and electrical system and then representing these differential relations in the Laplace domain (e.g. as transfer functions). Such skills are fundamental to controller design, and controller design is in turn an increasingly fundamental skill for mechanical engineers.

In other words, because the goal of a control system is essentially *to alter the dynamics of a system*, designers of control systems need to understand both (1) how to model a real-world system they wish to control and (2) how they can (and should) modify those dynamics using active control. Classical control methods have traditionally been taught as an area of specialization in mechanical engineering programs. Even today, undergraduates do not typically encounter controls until the senior year (if at all). Because it is becoming increasingly practical (i.e. affordable) to incorporate microcontrollers, sensors, and actuators in a wide variety mechanical designs, many educators now recognize that the skill set generally referred to as "mechatronics" is relevant to all mechanical engineers [15, 31, 45, 54, 64, 71, 77, 89, 106, 115, 143, 197, 203, 221].

The lectures, coursework and laboratories in 2.003 are aimed both at teaching

system dynamics and at providing a solid foundation for further study in control. We designed the ActivLab laboratory projects to provide hands-on experiences to reinforce students' understanding of these new concepts.

3.1 ActivLab Labware for Teaching Dynamics

Prof. David Trumper has coined the name *ActivLab* to refer to the set of hardware and experiments we developed during the summer of 2001 for 2.003 Modeling Dynamics and Control I. These lab projects have been developed as shareware, and we are in the process of providing web-accessible documentation to allow instructors at other universities to adapt these labs to their own efforts [83].

3.2 Philosophy for Designing Labs

The laboratories for the 2.003 class were designed with a few basic goals in mind. One particular concern was that the students should be able to directly observe the relevant dynamics in the mechanical systems firsthand. Thus the motions should be tangible, and the time constants and/or oscillations should be on the order of a second, so they are directly perceivable. In these systems, it is also important that students are able to observe the linear effects of damping with a minimal amount of nonlinear friction. To achieve this, we use porous carbon cylindrical air bearings (manufactured by New Way Machine Components, Inc. [146]) to implement both rotational and translational mechanical systems.

We also believe the laboratory hardware and data acquisition should be as transparent as practical to the students. For this reason, we have avoided introducing tachometers, encoders or other sensor technology in the first two laboratories to allow students to observe dynamic systems which evolve on a human-perceivable time scale. The above ideas were catalyzed by discussions with Prof. Ely Sachs in our Mechanical Engineering Department [176].

For these reasons the labs utilize flexures and air bearings to constrain motion,

as these behave in a near-ideal fashion. They allow time constants and oscillation periods on the order of one second, and thus at a time scale directly perceivable to the students. Finally, in the early labs, motion is measured with a video camera. Time resolution is taken by single-stepping through the video frames, which are typically acquired at 20 Hz.

Also, the equipment should be modular in nature, to allow extensions to the setups to be developed with a minimum of effort and to reduce the needed investment in space and money to develop a full set of laboratory hardware. All hardware is mounted on an optical breadboard, which allows us to assemble the labs easily and to disassemble the components for efficient storage.

3.3   1st-Order Spring-Damper Translational System

The first lab in 2.003 demonstrates a first-order response with position as the variable of interest. Student evaluations of the class report that Labs 1 and 2 are more straightforward (i.e. less difficult) than subsequent labs, which is not surprising. Both labs focus on simple, first-order system dynamics, and an emphasis is placed on observing and recording the response visually.

While the system for Lab 1 is designed to be relatively straight-forward, however, the actual system dynamics can also be modeled with much more complexity than we expect from our sophomore-level students. Some of the phenomena we neglect to incorporate in the system model are presented in this section and include (briefly) modeling flow through an orifice, thermodynamic expansion or compression of an ideal gas, and modal vibrations of a 4th-order Bernoulli-Euler beam. These phenomena illustrate that the mechanical system hardware for 2.003 involves complicated dynamics, just as most real-world systems do. Like many real-world systems, however, the system response can be approximated reasonably well using low-order, constant-coefficient linear differential equations. The main point of this lab is to study
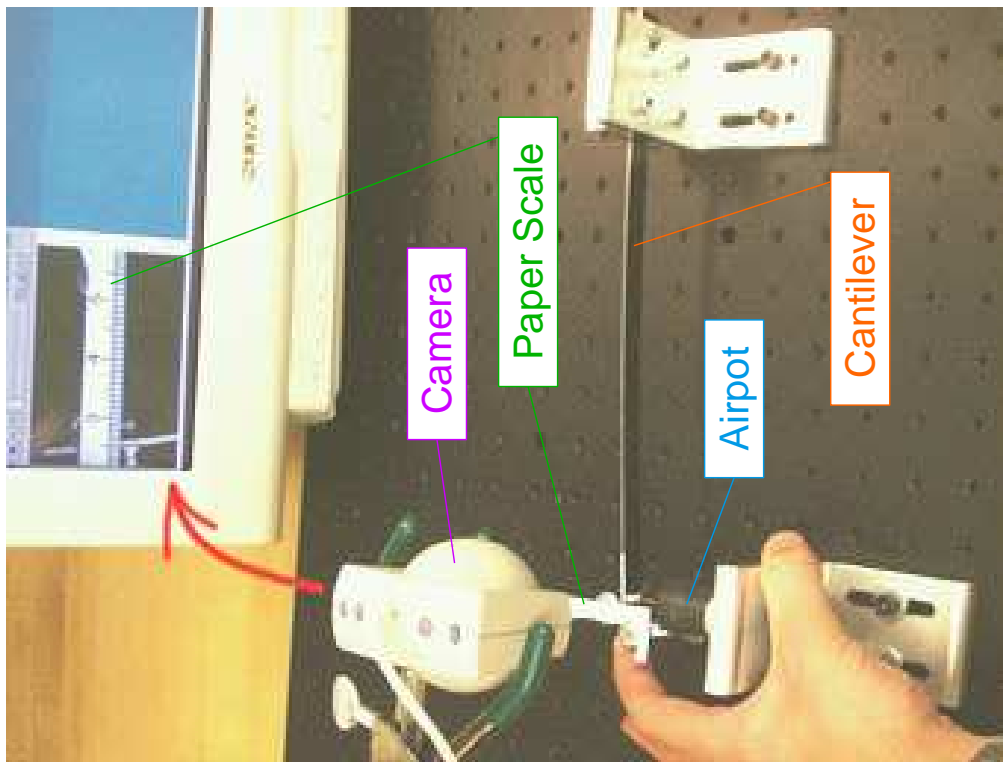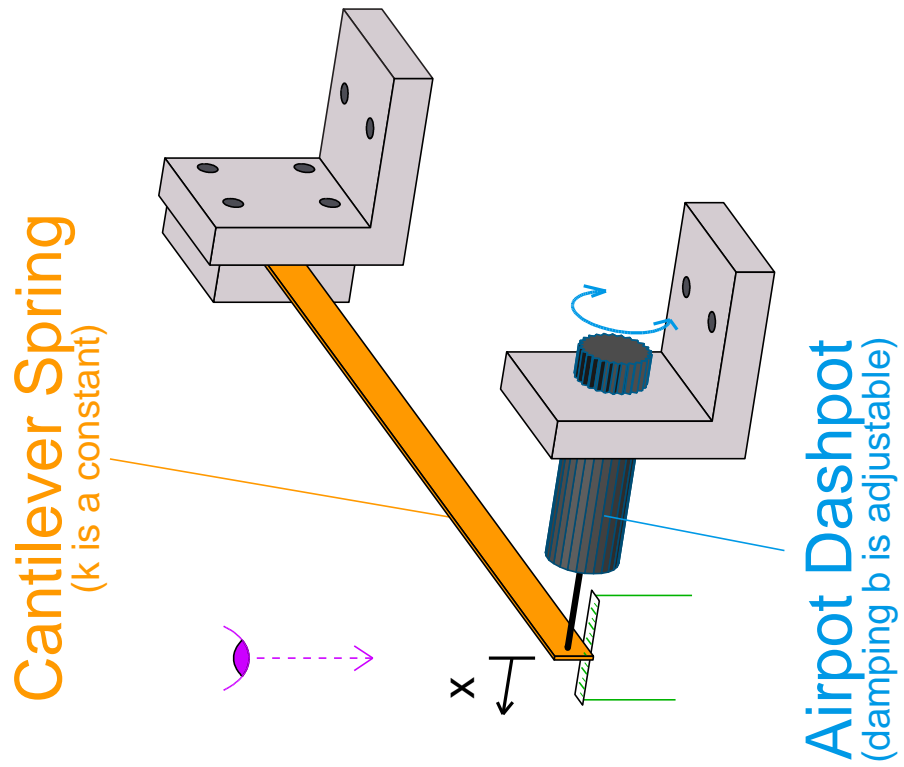
Figure 3-1: 2.003 Lab 1 - 1st-order translational spring-damper system

nearly-ideal first-order system dynamics, but Lab 1 also demonstrates that low-order linear approximations can often provide quite accurate models of more complex real-world phenomena.

The hardware for this lab, shown in Figure 3-1, consists of a flat spring steel cantilever which is clamped at one end by an aluminum bracket and acts as a spring. An Airpot [6] dashpot is connected between the other end of the cantilever and a second fixed aluminum bracket. Damping occurs as a piston forces air through an adjustable orifice in the dashpot. Figure 3-2 shows an Airpot with its protective rubber coating removed to show the cylinder and piston inside. The dashpots in the lab are used with the manufacturer's rubber coating in place to prevent injury from glass shards if the glass cylinder shatters.
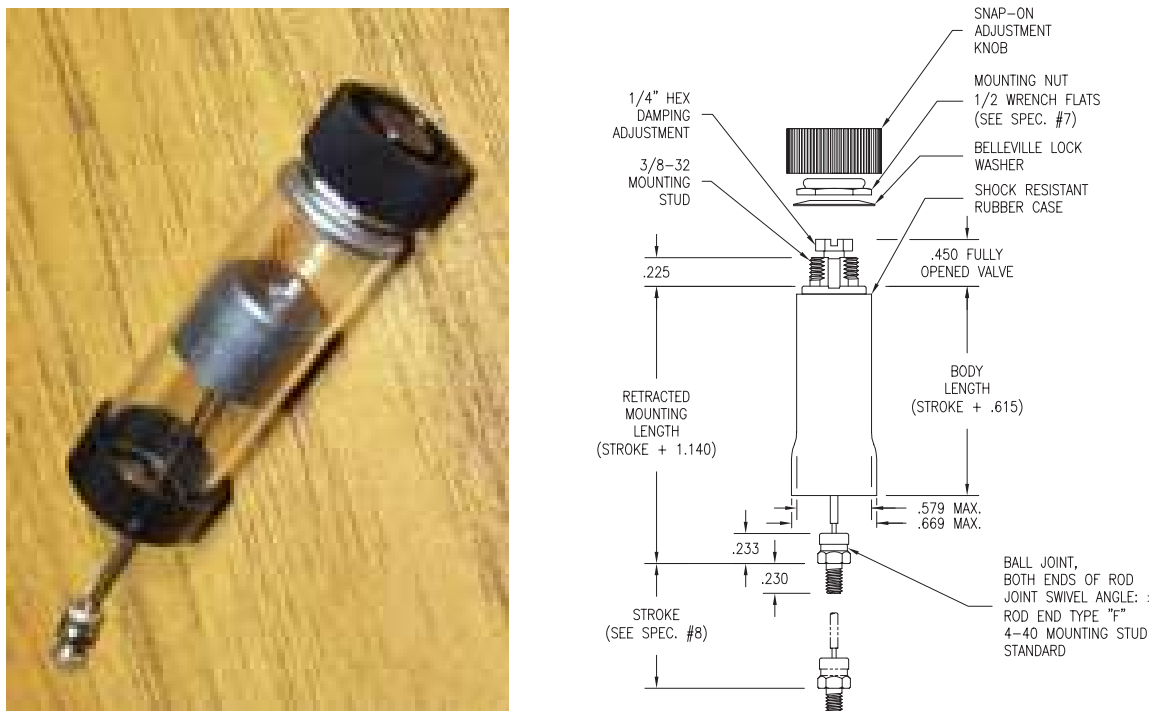
Figure 3-2: Airpot dashpot. Airpot photo by Willem Hijmans. CAD drawing from Airpot Corporation website [6].

We ask students to neglect the combined effective mass of the cantilever and moveable piston assembly in the dashpot when analyzing the dynamic response of

the system. The stiffness of the spring is about 170 N/m, while the effective mass of the system is ∼ 0.01 kg. If the damping is high enough, the poles of this second-order spring-mass-damper system will differ by a factor of 10,000 or more, and the response is strongly dominated by the slower of the two poles. The response in this case looks like that of the first-order system obtained by ignoring the mass.
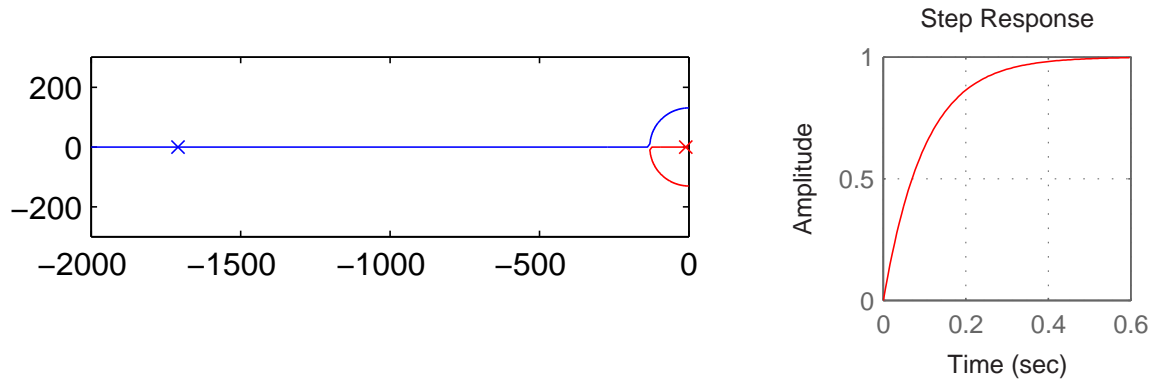
Figure 3-3: Theoretical pole-zero and step response plots for Lab 1.

We have students adjust the orifice of the dashpot so that the system response is well-modelled as first-order, with a time constant on the order of 1/4 to 1 second. For such high damping, the system transfer function from force to displacement can be approximated as:

$$\frac{X(s)}{F(s)} = \frac{1}{ms^2 + cs + k} \approx \frac{1}{cs + k} \tag{3.1}$$

Figure 3-3 shows a root locus of the system poles as the damping of the Airpot dashpot is increased. To obtain a first-order system response with a time constant of 0.1 s, we need the dashpot to provide damping of $c = k \times 0.1s = 17$ [N-s/m]. The resulting system poles for this value of c are superimposed on the root locus in Figure 3-3. The pole locations differ by about a factor of 17,000 in this case. This difference becomes even more pronounced as the damping is increased to provide time constants in the range of 1/4 to 1 second, as desired. At the right in Figure 3-3 is the theoretical step response of this highly over-damped second-order system, which is provided to emphasize that the response can be well-modelled as first-order using the dominant pole approximation.
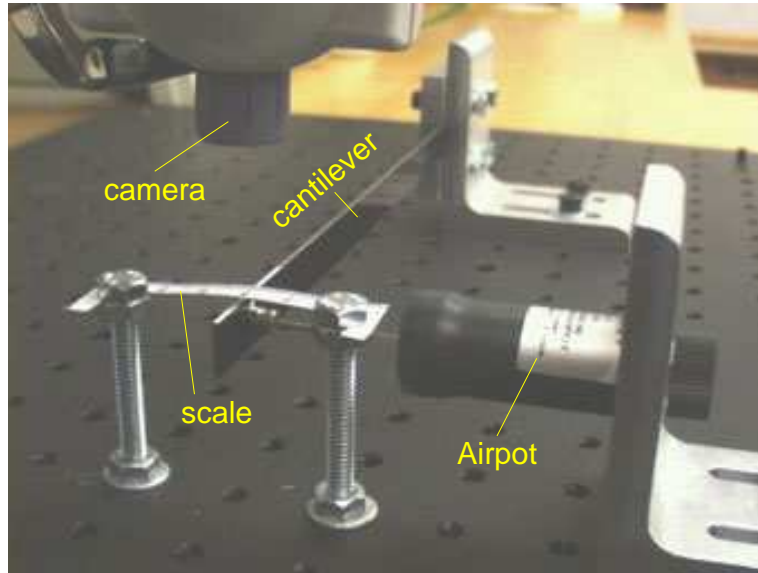
Figure 3-4: Close-up of cantilever and Airpot in first-order lab

The data for the lab are collected using a digital video camera with a nominal capture rate of 20 frames per second. (The actual frame spacing is not exactly constant in practice.) A scale is mounted above the cantilever to allow students to observe the position of the cantilever visually in each frame. Figure 3-4 shows the relative positions of the camera, scale, and cantilever in more detail. Students use MATLAB to plot their data points and estimate the time constant of the system response. They are then asked to determine the damping coefficient empirically using the known spring constant of the cantilever which they calculate in the pre-lab assignment using the analytical result from beam theory, which they encounter in MIT course 2.001.

A secondary effect is that the air-filled cylinder of the dashpot also creates a second, less-significant spring, which is initially ignored in presenting the model of the system to the students in this lab. Figure 3-5 illustrates some details in the construction of the Airpot. The mechanism is a cylindrical cavity with a plunger moving in its base (to which the cantilever in lab 1 is mounted) and an adjustable orifice at one end. Moving the piston creates a pressure differential between the air inside and outside the cylinder. The resistance of the air as it travels through the orifice represents an energy dissipation mechanism and essentially makes the device

a damper.

The Airpot acts is primarily a dissipative device, but it also stores some energy. Rapid movement of the piston results in a change in the stored energy of the air within the cylinder. In other words, the Airpot also acts as a spring. Because pressure, temperature and volume are coupled in an ideal gas, the expansion or compression of the air inside results in a change in both the mechanical and thermal energy. The exact relationship depends on how much heat is exchanged through the walls of the cylinder, that is, on how closely the process comes to being adiabatic and therefore reversible. At the end of this section, I discuss a model which approximately describes the non-linear dynamics of both orifice flow and the energy storage relationships in the air.

Because of the spring effect of the Airport, the relative positioning of the Airpot and cantilever will have a minor effect on the time constant of the first-order fit to the response. Figure 3-5 shows the L-bracket fixture which holds the Airpot in place. This bracket is bolted down through two slots, allowing one to position the fixture as desired. Moving the mounting for the Airpot to the left of right will change the final volume in the Airpot, which in turn affects the time constant of the response. Whether the piston acts to expand or compress the air in the Airpot will also affect the time constant. The theoretical model of the system predicts that neither effect should be significant, however, and the data in Figure 3-6 verify that this is the case.

The springiness of the Airpot becomes significant only as both the size of the orifice is reduced to provide maximal damping and the cantilever is released such that it compresses the air. If it is released in the other direction, the cylinder is initially starting with virtually no air inside. The initial movement of the piston therefore causes a large pressure differential (with nearly a vacuum inside the cylinder) and thus the air spring is quite stiff. When the cylinder instead starts out with the piston fully extended, and thus with a large initial volume of air in the cylinder, a much larger displacement must occur to balance the force of the cantilever. The camera snapshots shown in Figure 3-7 show clear evidence of these phenomena. When the cantilever is at rest (as shown at the bottom of this figure), the image is crisp. The faster the

144
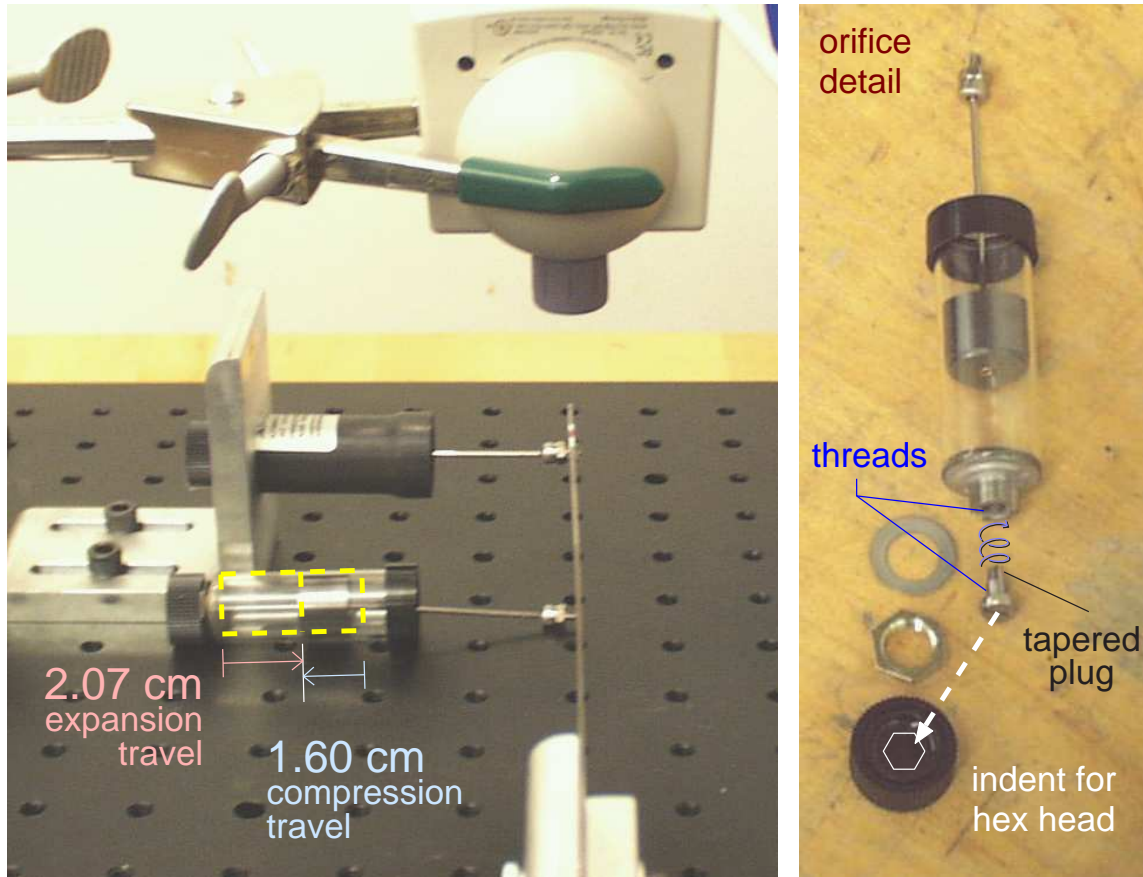
Figure 3-5: Hardware details for cantilever-Airpot lab. At left, an Airpot is mounted on an L-shaped aluminum bracket which can be repositioned by about 1 cm to the left of right of its current position. The position of the L-bracket affects the range of travel of the cantilever. For instance, if the cantilever is pushed to the left before release, the air in the Airpot will expand and the piston will travel about 2.07 cm before returning to the final resting position shown. The piston need not be precisely centered, but its positioning will have a minor effect on how well-matched the measured time constants are in the compression and expansion directions, as shown in Figure 3-6. At the right above is an Airpot which has been disassembled to show how the orifice operates. A cap with a hexagonal indentation (highlighted for visibility) snaps onto the hex head of threaded plug. The mating threads in the cylinder are cut into a square cross-section, to allow them to engage the threads of the plug while also allowing air past. Turning the cap adjusts the width of an annular orifice created between the tapered plug and a round hole just inside the threads of the cylinder.
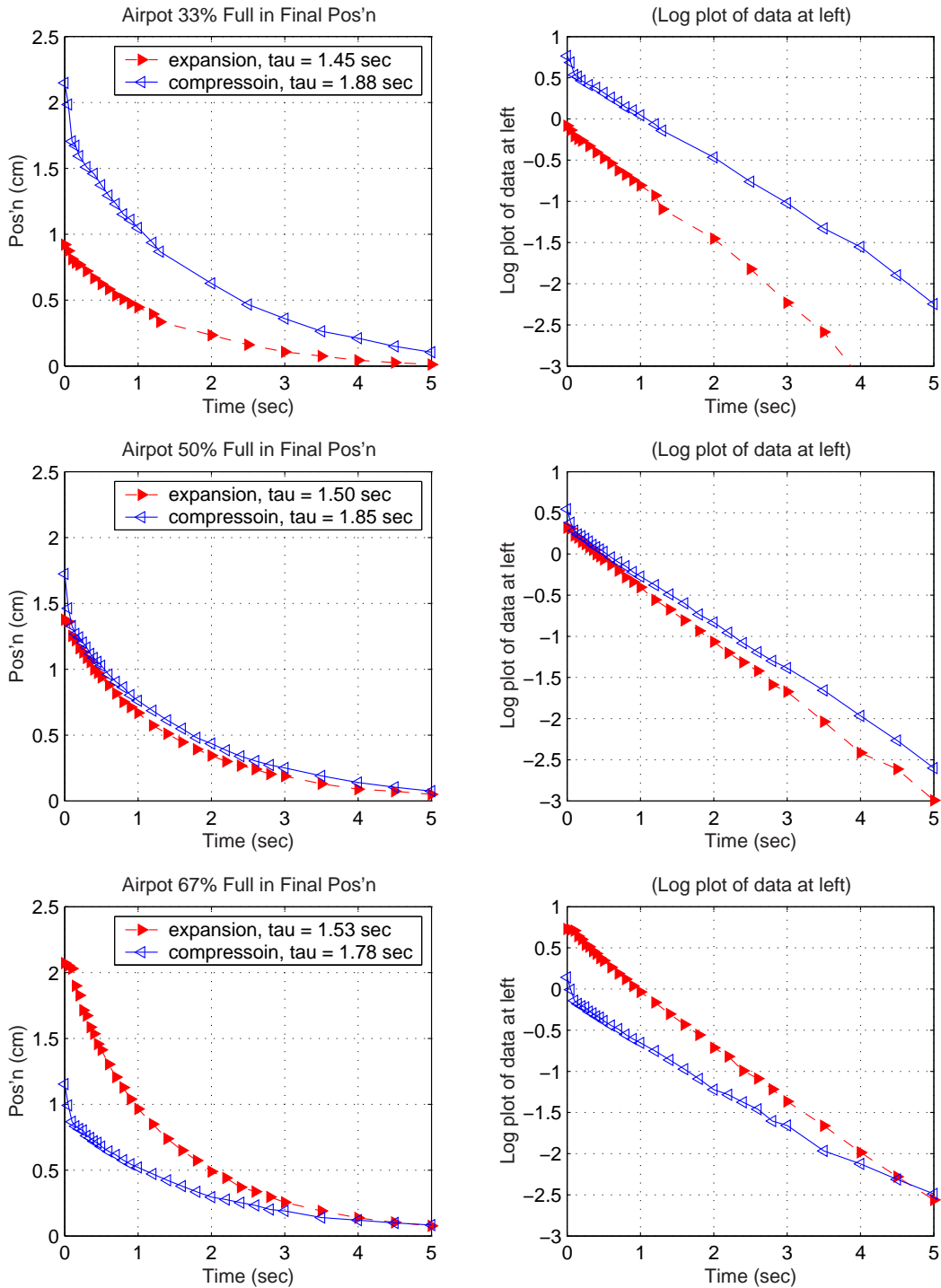
Figure 3-6: Cantilever-Airpot data for different final volumes in the Airpot. The Airpot orifice setting was the same for all three data sets, but the Airpot was mounted to provide a different final volume in each case. The effect on the time constant is not significant.

cantilever is moving, the more the image will appear blurred. At the top, the blur is more opaque at the extremes of travel and transparent at the center, indicating an oscillation (with velocity highest at the center and lowest as it reverses direction at the ends). This evidence of oscillation was obtained with a highly damped (small) orifice and with the cantilever released such that it *compresses* the large volume of air in the cylinder associated with this position. By contrast, the image in the middle of this figure was taken with the piston nearly fully into the bore, and thus with a small contained volume. That is, the cylinder started essentially empty and drew air in upon release. Note that this image does not show the same hallmarks of oscillation; it has an evenly-toned blur (indicating a fairly constant velocity of the cantilever).

Figure 3-8 again shows evidence of the vibration of the cantilever immediately after its release. Note that the oscillations die down after the first three frames or so (about 1/10 of a second), and also that the cantilever experiences an initial "jump" in (average) position immediately after release (as air is suddenly compressed). We do not have the students look at the camera data in this level of detail in the lab, since these details are not central to the purpose of the lab. However, I have noticed that many students (subconsciously?) tend to try to "damp" the spring as they release it in the oscillation-prone configuration in an attempt to attain "cleaner" data. I have also noted that student data do not tend to show the characteristic "jump" as the highly-damped system is released in compression, perhaps because they tend to start the data set after this initial jump. One can see this jump in most of the "compression" direction data sets in Figures 3-13 through 3-18. A more complex ode model of the orifice flow and PVT relations in the gas predicts both the initial "jump" and subsequent oscillations when the cantilever is released with high damping and an initially full cylinder of air. This ode model is discussed in more detail at the end of this section, and the MATLAB code which models the dynamics appears in Appendix E. The frequency of the oscillations due to these phenomena are predicted to be on the order of 30-40 Hz.

Recorded audio provide a second piece of evidence that there are vibrations of some sort after the cantilever is released from this configuration (with a large volume of air
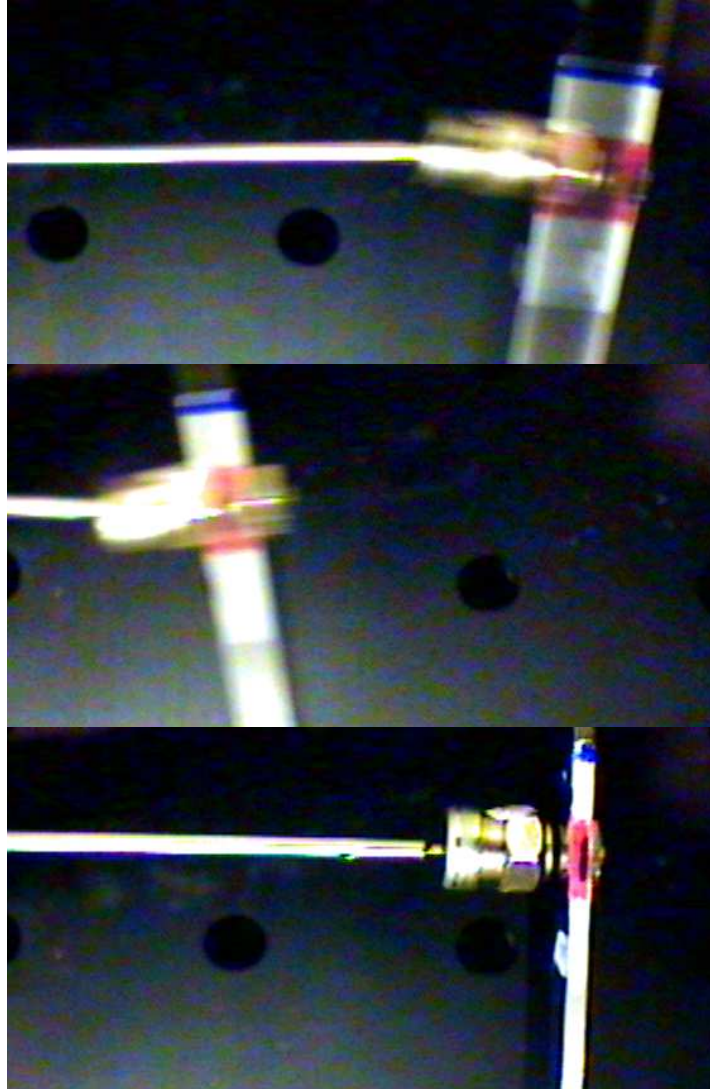
Figure 3-7: Deciphering video blurring. Above are three video frames of the cantilever. 1: The topmost frame has captured the cantilever during vibration. The image is most opaque at the extremes of oscillation, where the velocity was the slowest, but it is virtually transparent in the center, where the velocity was much faster. This frame was captured after the cantilever was released from the righthand side of the image, resulting in rapid compression of the air within the Airpot. Vibrations at 30-40 Hertz are predicted by the MATLAB ode model of the system presented in Appendix E. 2: The middle frame captures the cantilever soon after its release from the lefthand side. The evenly-toned blur is caused by the high velocity of the system, which just been adjusted for low damping. 3: The crisp image at the bottom (of the cantilever at rest) is included for comparison.

final value below:
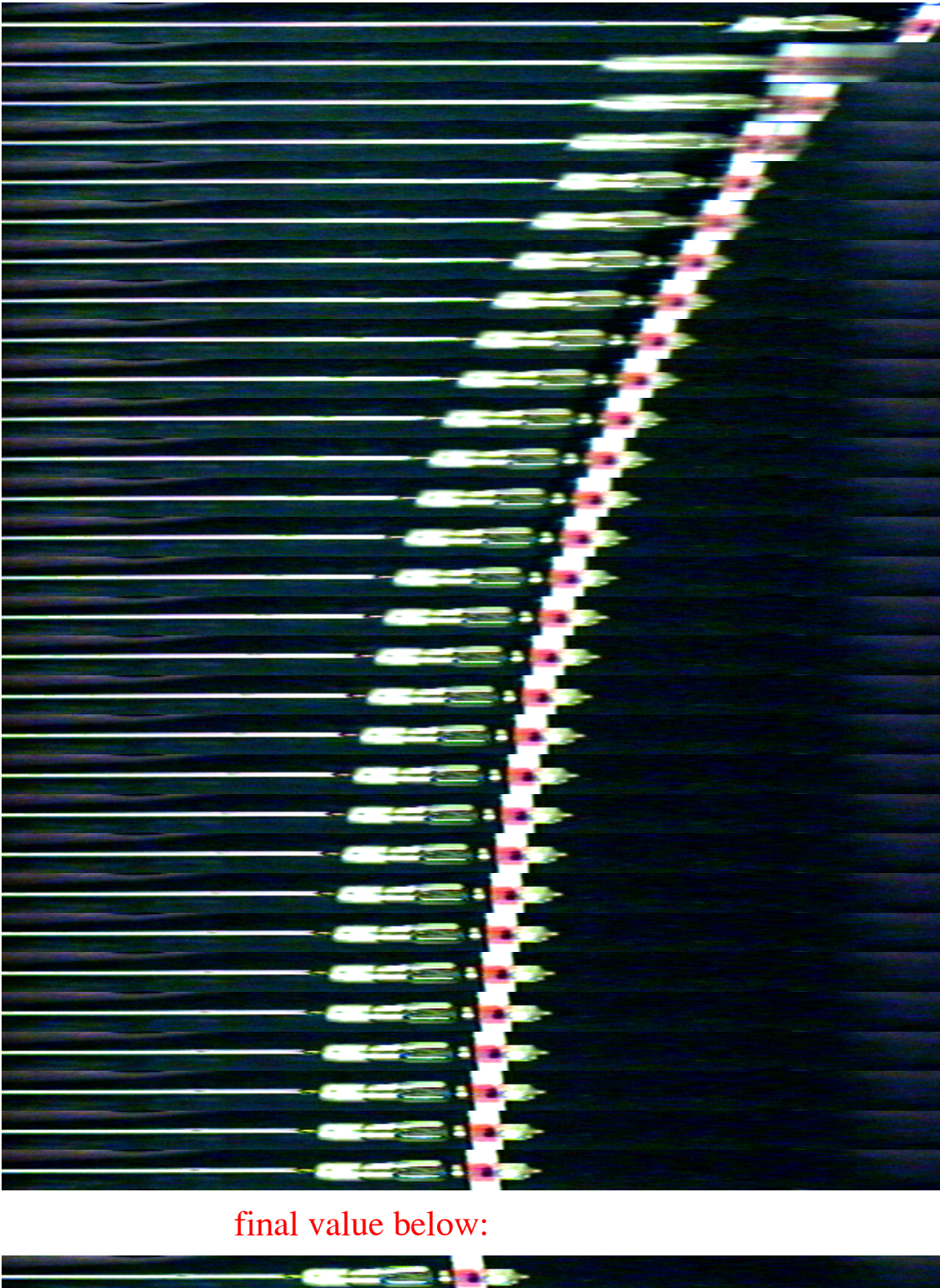
Figure 3-8: Screen shots from cantilever-Airpot lab (more damping)

initially trapped in the cylinder and a large resistance from the orifice). Figure 3-10 shows significant vibration at around 820 Hz, which one can also hear as an audible "twang" when the cantilever is released abruptly. This is a much faster vibration than the 30-40 Hz oscillations predicted by the ode model mentioned in preceding paragraph, and it is likely due to the excitations of higher-order mode shapes in the cantilever beam during its release. Specifically, the 820 Hz oscillations likely correspond to the excitation of the third fundamental frequency for a beam with clamped-free end conditions, which is expected to occur at around 780 Hz, using a Bernoulli-Euler beam model [214, pp. 620-628]. (See Figure 3-9.)

44 Hz   278 Hz   779 Hz   1526 Hz   2522 Hz
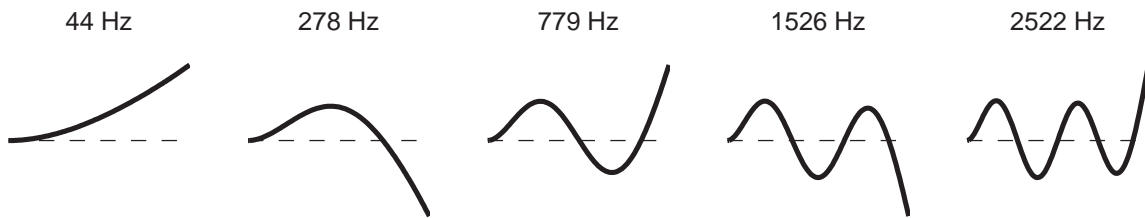
Figure 3-9: First 5 modes for clamped-free beam.

With high damping, the students should observe another unpredicted result in lab 1: the time constant is *not* identical (as predicted by the linear, first-order model presented) when the air in the dashpot is *compressed* versus being *expanded*. Several of the data sets in this section show this to some degree, but it is perhaps most clearly illustrated in Figure 3-16. We have found that students in this lab are consistently reluctant to accept (much less able to explain) that their measured time constant is different in each direction.

I have included data for five different orifice setting to illustrate the variety of responses seen (Figures 3-14 to 3-16). Before analyzing this data, first note that these data were obtained by measuring the position to a mark on the cantilever in each frame of camera data, using a set of calipers, as depicted on the righthand photo in Figure 3-12. One should note that this introduces some error in the data due to parallax, as illustrated in Figures 3-11. Students in the lab do not use this method; they estimate the position using a scale mounted just above the cantilever, which is
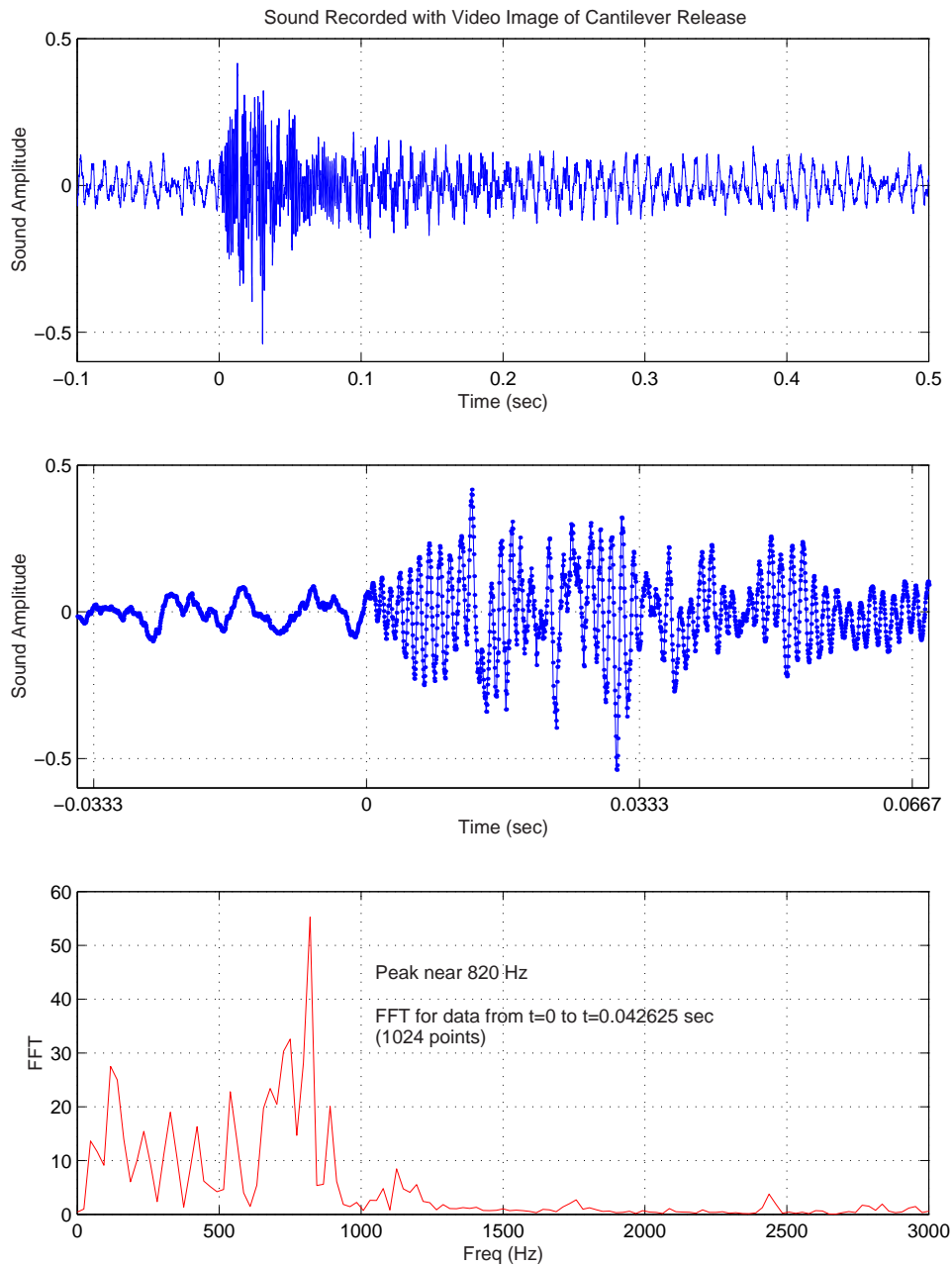
Figure 3-10: Audio indicating higher-order vibrations in the cantilever-Airpot response. The cantilever was released at approximately $t = 0$ and data were sampled at 24 kHz. An FFT of 1024 points (beginning at $t = 0$) shows a spike at around 820 Hz. This is much higher than the vibration of around 30-40 Hz predicted by the ode model of the cantilever and Airpot spring-mass system and most likely represents the excitation of a higher mode in the beam, as described further in the text.

visible in Figure 3-4. The caliper method introduces some parallax at the extremes of travel (for which one could compensate, although I do not), but it has greater resolution than the paper scale.
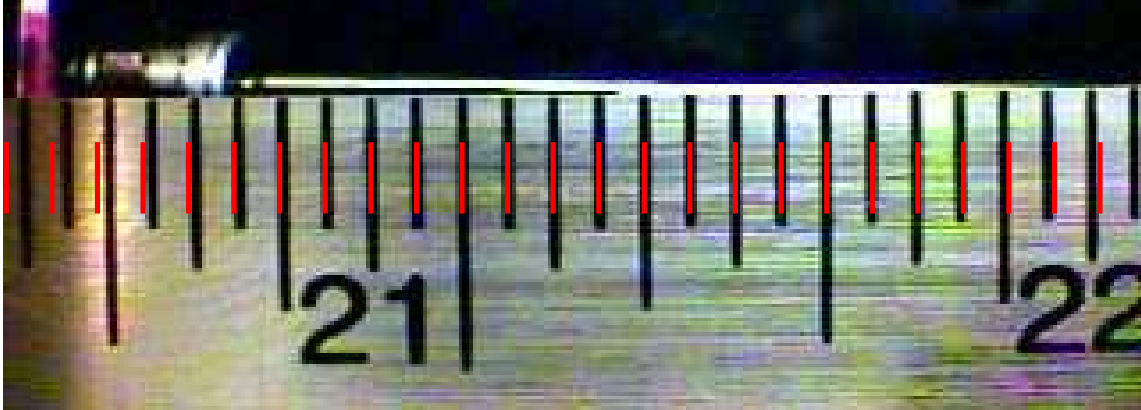
Figure 3-11: Video camera parallax. This figure shows an image of a metal scale, captured by the digital video camera from a distance appropriate for measuring the cantilever displacement (roughly 2 inches). Overlaid on the image is a set of tick marks which are evenly spaced in the reference frame of the piece of paper on which this is printed. The tick marks therefore illustrate a level of parallax typical in the video images for the cantilever-Airpot lab. Students record video with a fixed scale mounted above and photographed with the cantilever, so that the effects of parallax on their measurement are minimized.

Figure 3-13 shows some successive screen shots and the plots (with both linear and logarithmic vertical scaling) of the recorded data. The log plot is included to help the reader estimate how close the response is to ideal. (An ideal 1st-order decay would of course fall on a straight line in a log plot.) Note that it is difficult to estimate the last few points accurately. Data for the five orifice settings, shown in Figures 3-14 through 3-18 are similarly plotted both on linear and semilog axes.

Of the plots of data for each of five orifice settings, shown in Figures 3-14, 3-15 and 3-16, data set 4 (at the bottom of page 157) (with τ equal to about 1/3 of a second) is perhaps the "cleanest", in that it shows nearly-ideal 1st-order behavior, and the calculated time constant for each direction is about the same. Generally speaking, the data look quite good when the orifice is set so that the time constant falls between

Figure 3-12: Data measurement from camera output. The data presented in this section were all recorded using calipers to estimate position on the computer screen, as depicted above. Note that students taking 2.003 simply estimate position with respect to a scale mounted above the cantilever (and also recorded in the video). The caliper measurements are simply more precise, despite the effects of parallax.

about 1/5 and 1 seconds. This range of values for tau also corresponds to the time scales we wish to aim for to allow students to observe the response visually. When τ is less than ~ 0.2 s, the response happens too quickly to obtain more than a few data points, and when it gets greater than about 1 s, the measured time constants in each direction (starting with the dashpot either full of air of empty) begin to differ significantly, as shown in Figure 3-16. This effect is predicted by the nonlinear model of the system and is due to the larger force differential which develops when the piston starts out empty and a near-vacuum is rapidly created inside.

Figure 3-6 shows data for three different mountings of the dashpot, to test how important alignment of the dashpot is when the TA's set up this lab. Obviously, the length of travel possible is different in each direction when the piston in the dashpot is not centered in the cylinder at rest. This explains why the top and bottom plots start at different positions (with respect to the final resting state). Of more concern is how much more or less the measurements of time constant diverge from one another (in compression versus expansion) when for different alignments. The effect on the time constant is not very significant.

Finally, one can provide students with a more complicated model of the dynamics in the system which helps explain some of the unexpected behavior observed in this lab. Specifically, if one both models the PVT (pressure-volume-temperature) relations of the air in the cylinder and uses the equation governing flow through an orifice, the predicted response shows both the initial jump and transient oscillations during compression, as well as deviations from the ideal exponential decay. The model also predicts the small deviations observed in the time constant, depending on whether the piston is released in compression or expansion. This deviation is apparently caused by the asymmetry of the spring effect of the air for the two directions of travel (i.e. with the chamber starting out empty and rapidly forming a near-vacuum vs. starting out full.).

Appendix E provides more details on modeling flow through an orifice and includes a MATLAB function (to be use with one of MATLAB's ode solvers, such as "ode45()") which simulates the dynamics of the Airpot. Plots of simulations using this code are shown along with experimental data sets 4 and 5 in Figures 3-17 and 3-18. In the plots, the valve coefficient for the orifice was selected ("tweaked") by hand until reasonable fits were obtained. I find it satisfying that the *model predicts both transient oscillations and the initial "jump" of the cantilever that occur in the compression direction.* We would not expect nor wish the students (sophomores) to be able to model such dynamics, but it may be worth presenting the model cursorily to demonstrate that despite the complexity of the full non-linear dynamics, the essential features of the response can be captured quite well using a low-order, linear model.
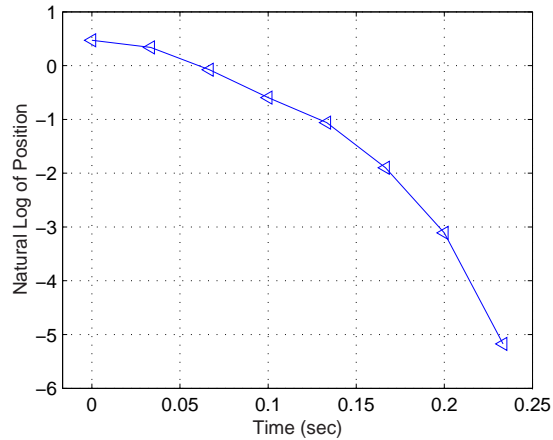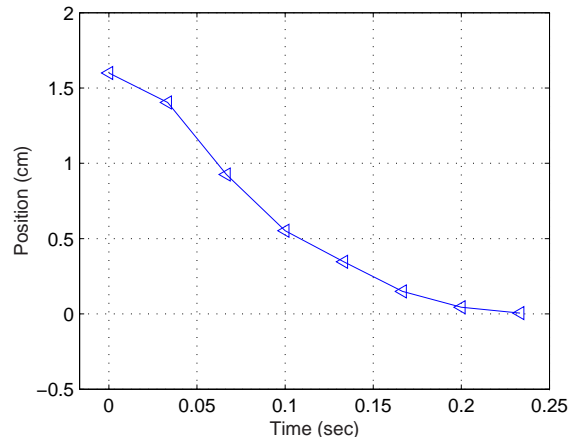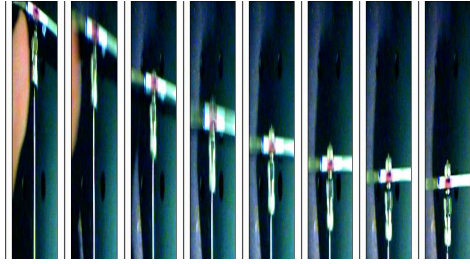
Figure 3-13: Screen shots from cantilever-Airpot lab (less damping). A series of screen shots of recorded video are shown at top, which show the cantilever as it compressed air in the piston. Estimated position values are plotted below this. Data above were taken at 30 fps, while students uses a rate of 20 fps to lessen the chance of dropped frames. (Fortunately, the camera software can detect dropped frames.) The bottom figure, which plots the natural log of position, would be a straight line if the recorded data set represented a perfect exponential decay. The data are relatively flat between the 2nd and 5th frames. The amplitude drops by a factor of e between the 3rd and 5th frames, so $\tau \approx\sim 1/15$ s here.
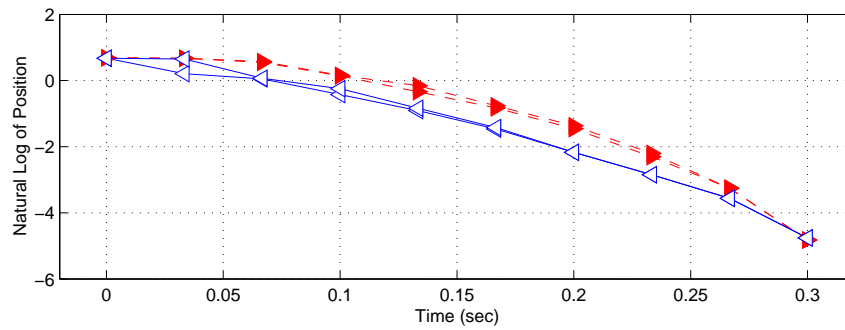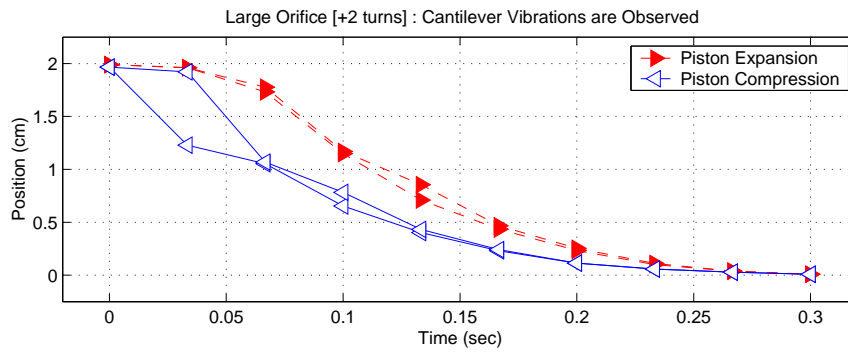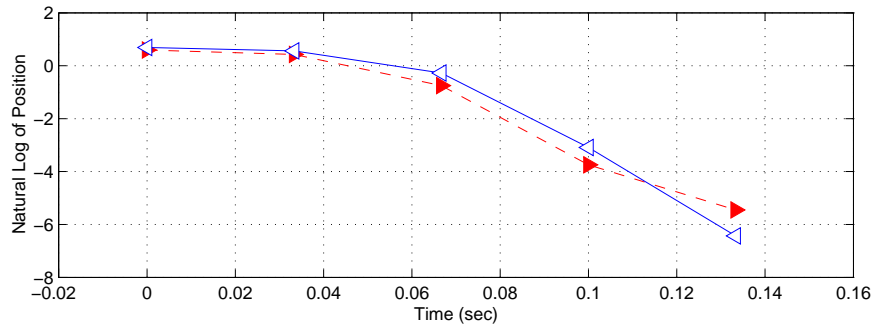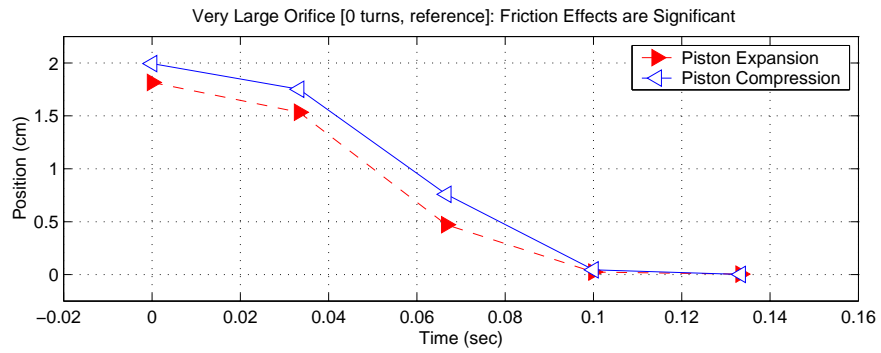
Figure 3-14: Data sets 1 and 2 for cantilever-Airpot Lab.
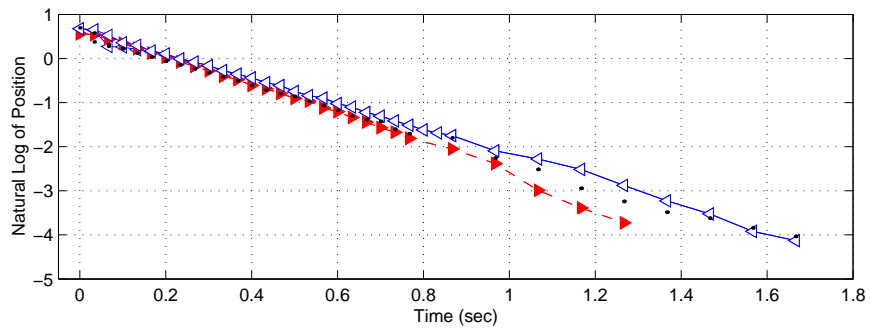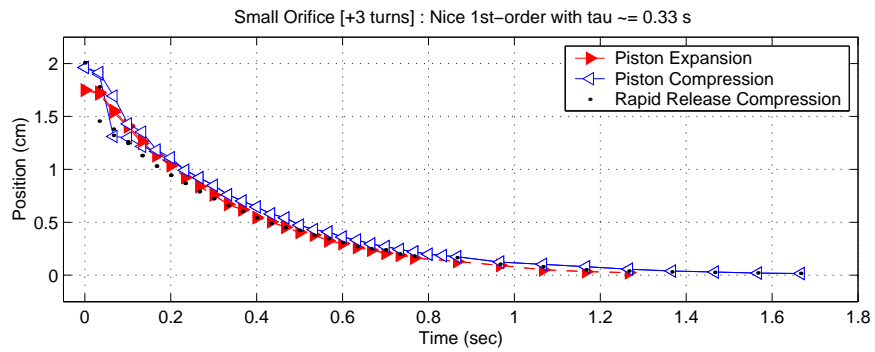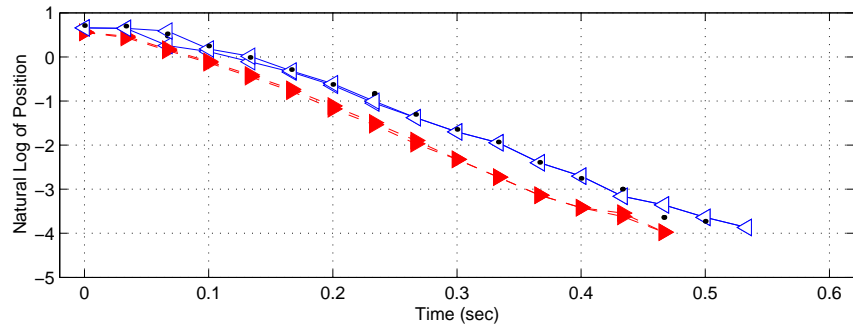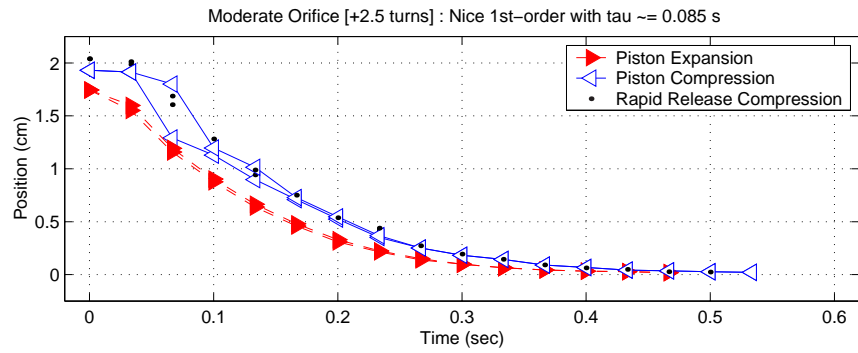
Figure 3-15: Data sets 3 and 4 for cantilever-Airpot Lab.
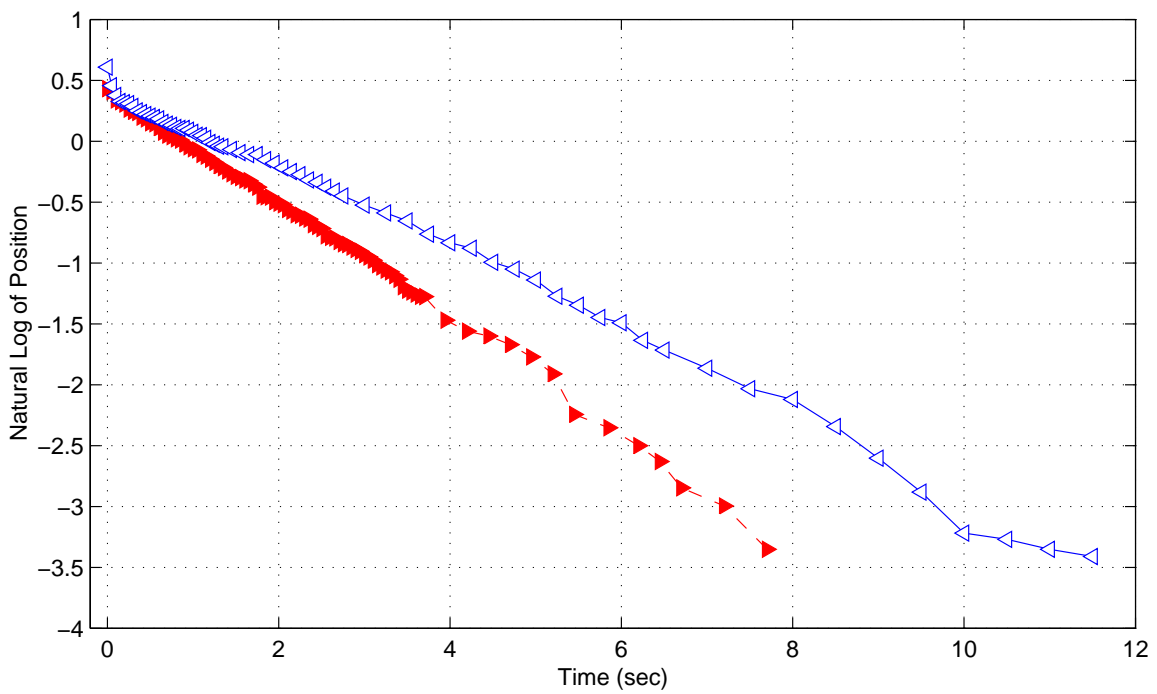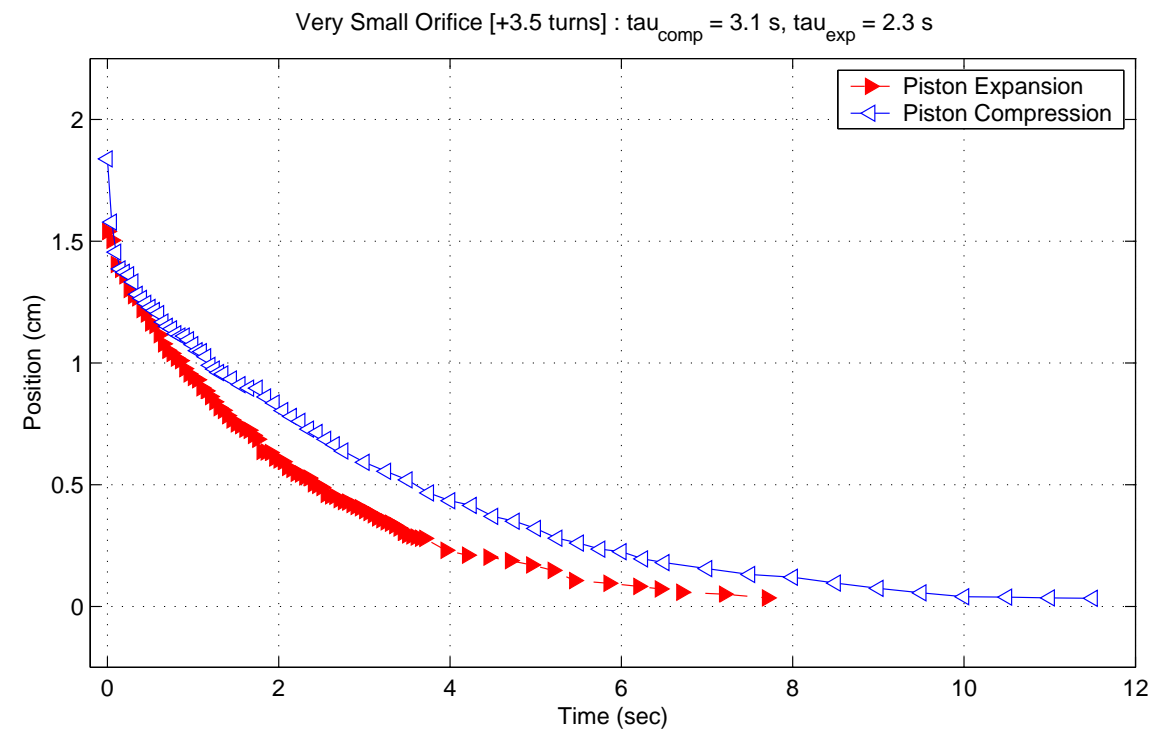
Figure 3-16: Data set 5 for cantilever-Airpot Lab.
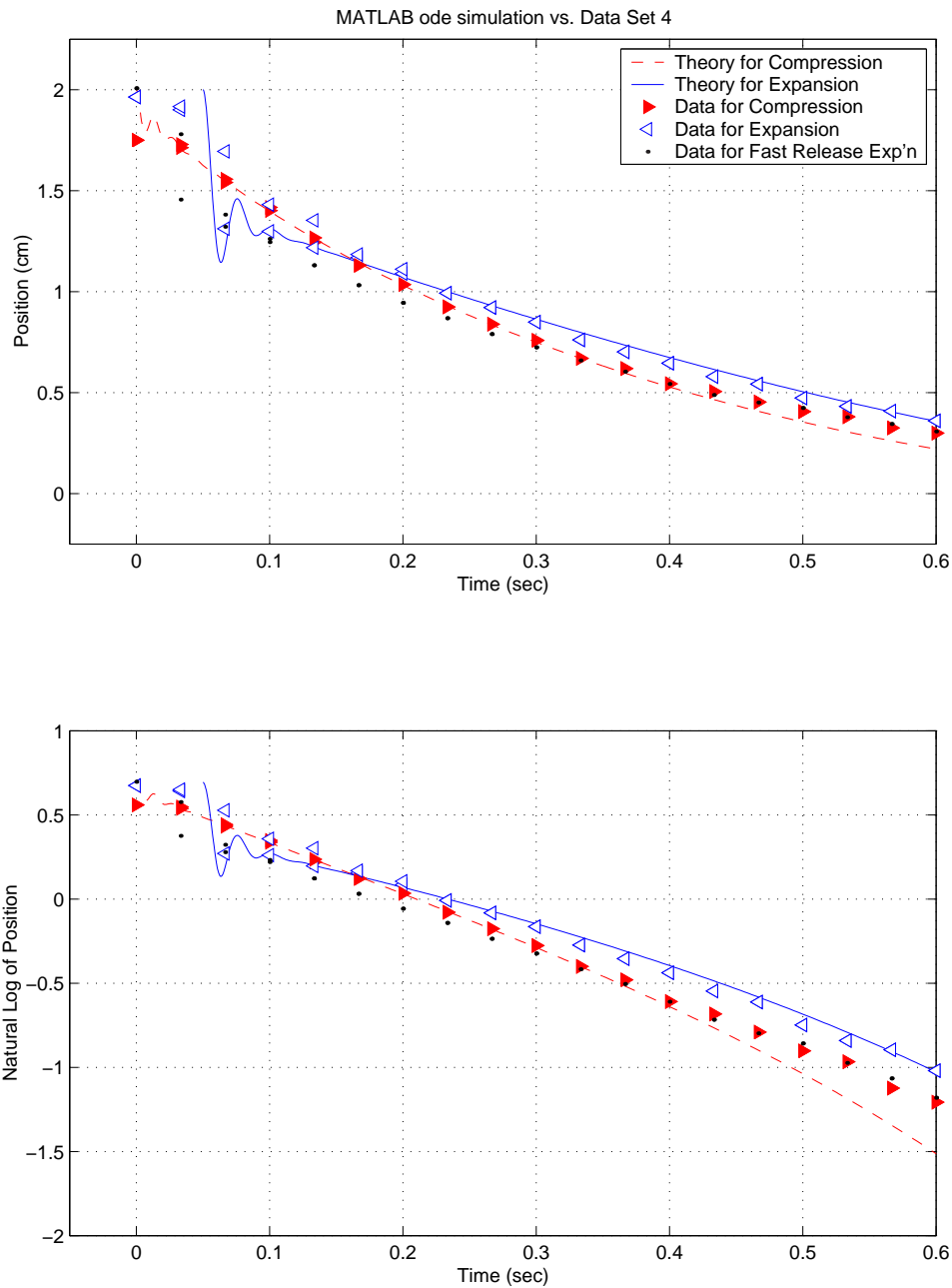
Figure 3-17: MATLAB ode cantilever-Airpot simulation vs. data set 4. The dashed and solid lines represent simulations of the dynamic response of the Airpot. These simulations were run in MATLAB, using the code in Appendix E to model both orifice flow and the PVT relations of the air. (The exact "release time" has been estimated to create a good fit to the experimental data.)

159
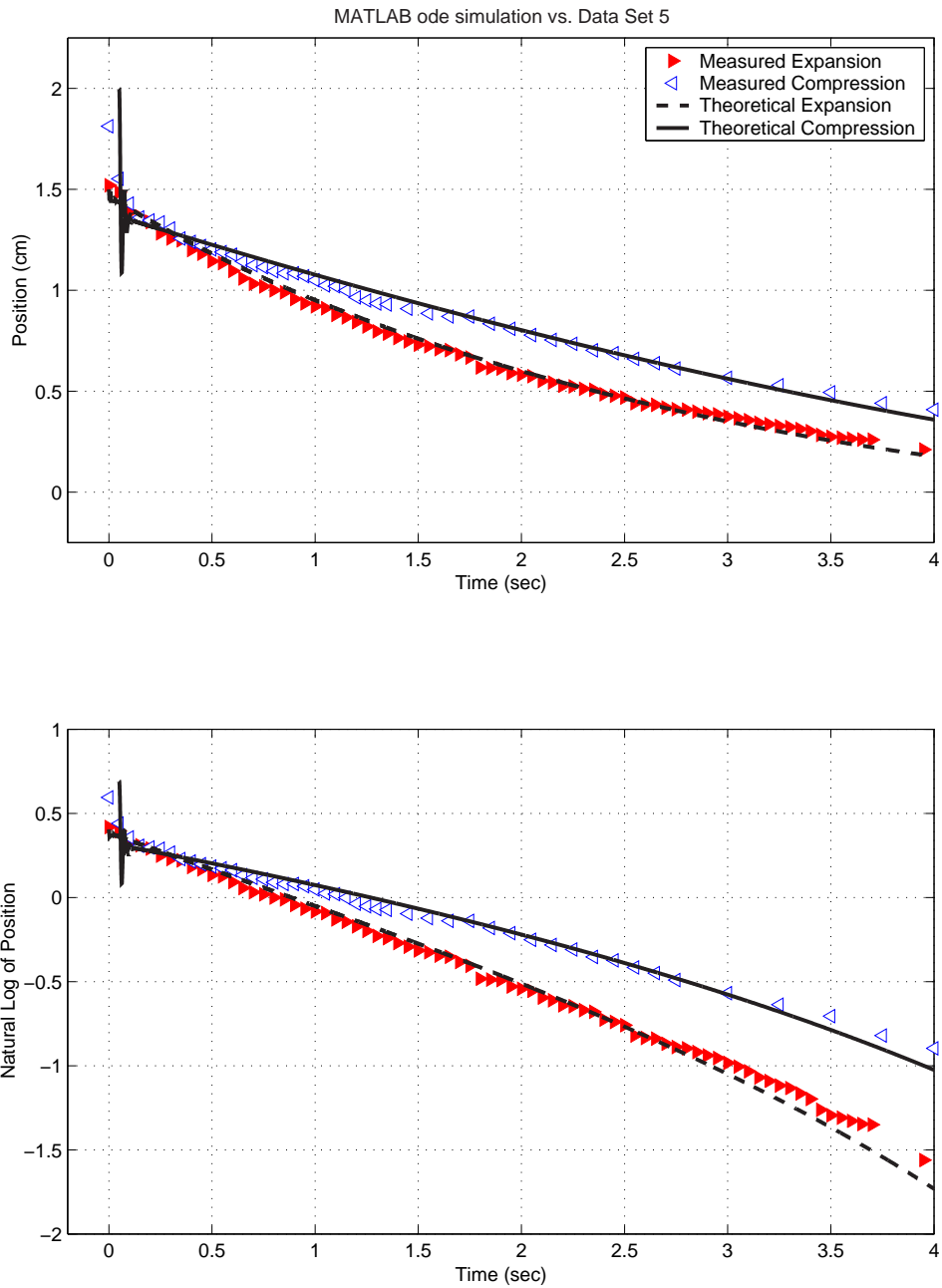
Figure 3-18: MATLAB ode cantilever-Airpot simulation vs. data set 5. The dashed and solid lines represent simulations of the dynamic response of the Airpot. These simulations were run in MATLAB, using the code in Appendix E to model both orifice flow and the PVT relations of the air. (The exact "release time" has been estimated to create a good fit to the experimental data.)

3.4 1st-Order Inertia-Damper Rotational System

In Lab 2, students explore the dynamics of a rotational 1st-order system. Figure 3-19 shows the setup for this lab. A 12-inch length of shafting is mounted vertically within a pair of air bearings, and a ball bearing set into the bottom end of the shaft rests on a tungsten carbide flat, providing a low-friction pivot. A cup at the base of the shaft holds honey to provide damping to the system. We use honey both because of its high viscosity and because it is environmentally benign. The level of the honey is adjusted during the lab exercises with a syringe attached at the base of the cup. An aluminum hub is mounted at the top of the shaft, and a brass ring can be put on or taken off to vary the inertia, as shown in Figure 3-20.

As in Lab 1, students again use the digital cameras to record data. We have placed a radial line at the top of the hub (see Figure 3-20) to allow the students to record the angle at each frame in the recorded data. A clear plastic sheet with angular markings is taped to the computer screen during this lab to provide a scale for angle, as shown in Figure 3-21.

The students record data for two or three levels of honey both with and without the additional inertia of the brass ring. They then use MATLAB to plot their data and use these plots to determine the time constant for each set of system parameters. As part of the pre-lab handout, we present the following equation relating $T_{viscous}$, the viscous torque retarding the rotating shaft in an annulus of fluid, to the viscosity of the fluid (μ), the diameter of the shaft (D), the height of the fluid level (L), and the gap in the annulus (ϵ) [153, p. 263] :

$$T_{viscous} = \frac{\pi D^3 L \mu}{4\epsilon} \, \omega = c \, \omega \tag{3.2}$$

As the students generally have not yet taken a formal course in fluid dynamics, we do not present the derivation of this model. We present students with Equation 3.2 primarily to emphasize that the viscous damping coefficient (c) should be proportional to the height of the honey surrounding the base of the shaft. The lab focuses on the system effects of changing both the viscosity (damping) and inertia of the system.

We feel it is important students both see and feel these effects (i.e. of changing
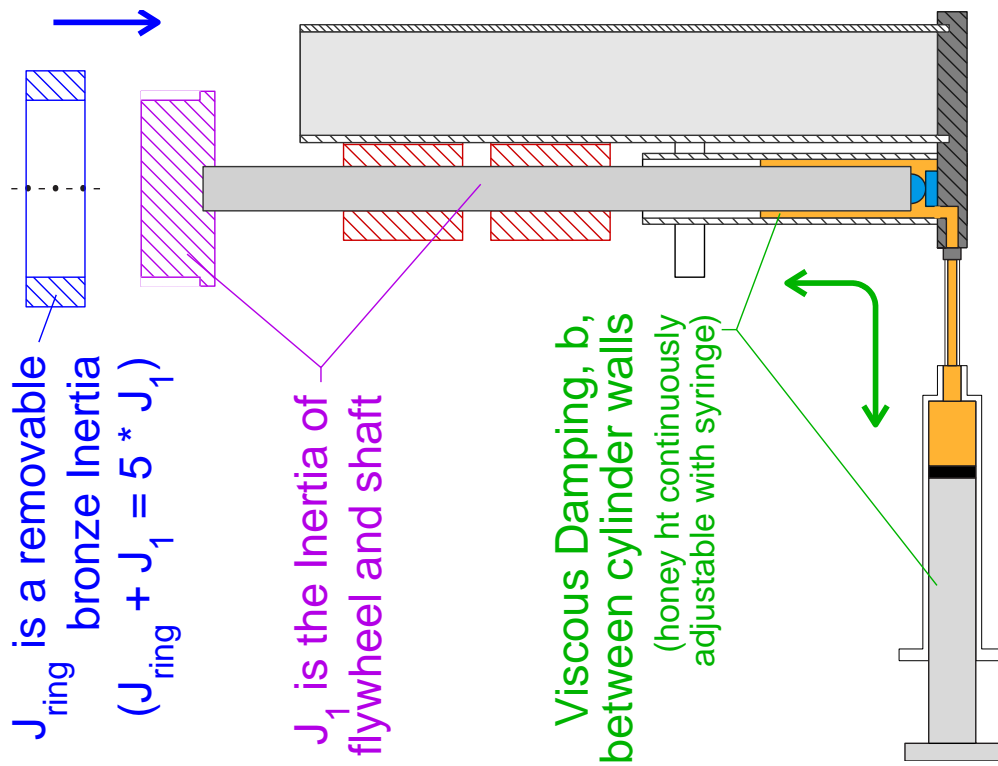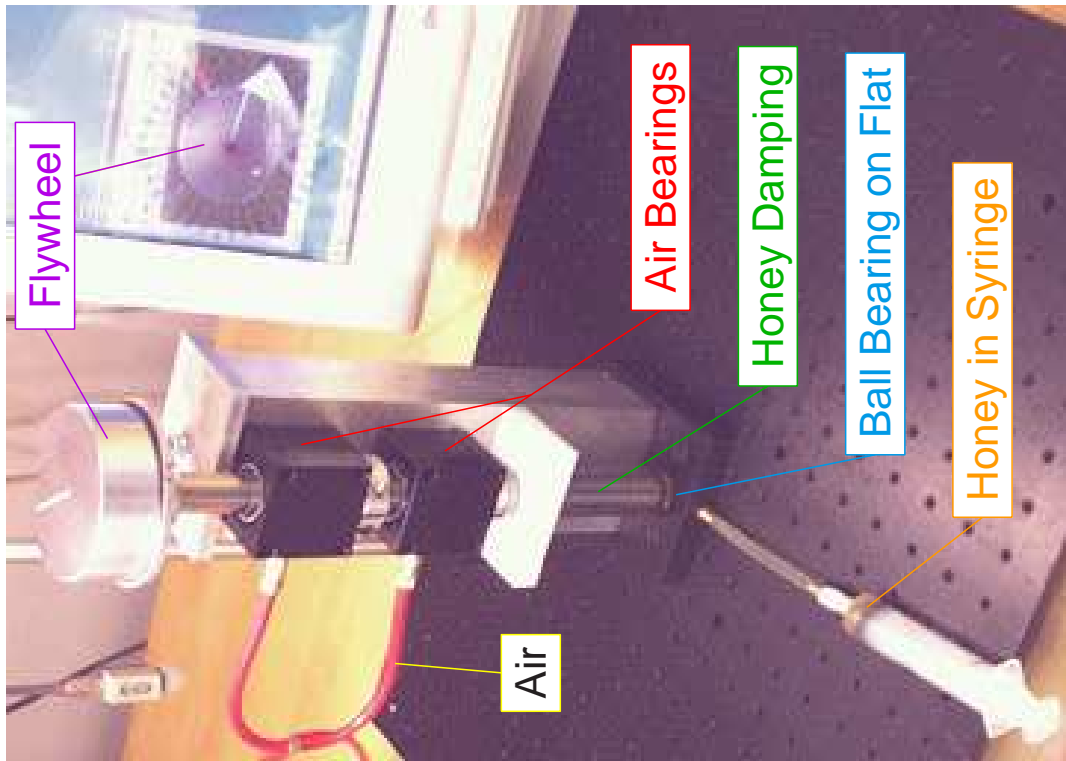
Figure 3-19: Lab 2 - 1st-order rotational inertia-damping system.
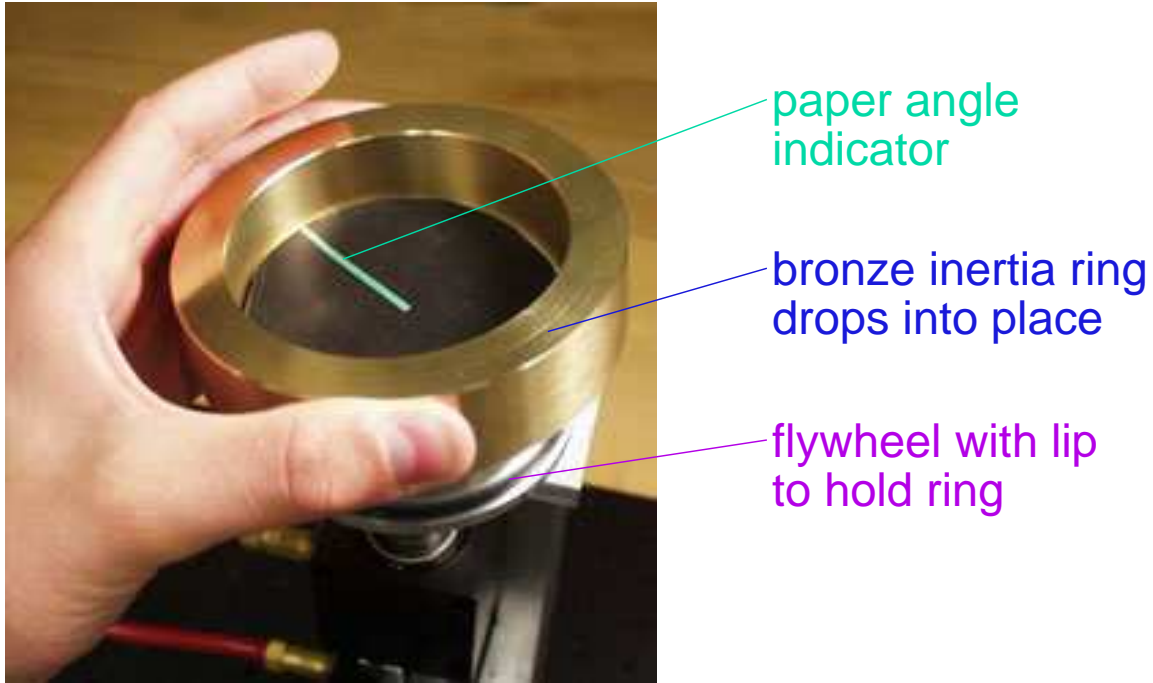
Figure 3-20: Two discrete inertia values are possible for Lab 2. By adding a bronze ring, as shown above, one can increase the system inertia by about a factor of five.

the damping and/or inertia) during the course of the lab. One exercise we use to facilitate this has students pull on a length of string which has been wound about the shafting. Students should be able to feel that the force due to viscous damping increases in proportion to the angular velocity of the shaft.

Figures 3-22 and 3-23 show some representative data for Lab 2. Each figure shows two data sets. Both of the data sets in Figure 3-22 were taken with the level of the honey nominally set to zero, although a thin layer of honey adheres at the contact point between the tungsten carbide flat and the ball bearing at the base of the shafting. The inertia for the system *with* the bronze inertia (represent by the righthand set of data) is about 5.1 times that of the system without it (data at left).

With virtually no honey, $L \approx 0$ in Equation 3.2, and we would therefore expect virtually no viscous damping due to honey. In this configuration, the loss mechanisms by which the system eventually "spins down" seem to be dominated by other (unmodeled) phenomena, as evidenced by the data in Figure 3-22. Two relevant ob-
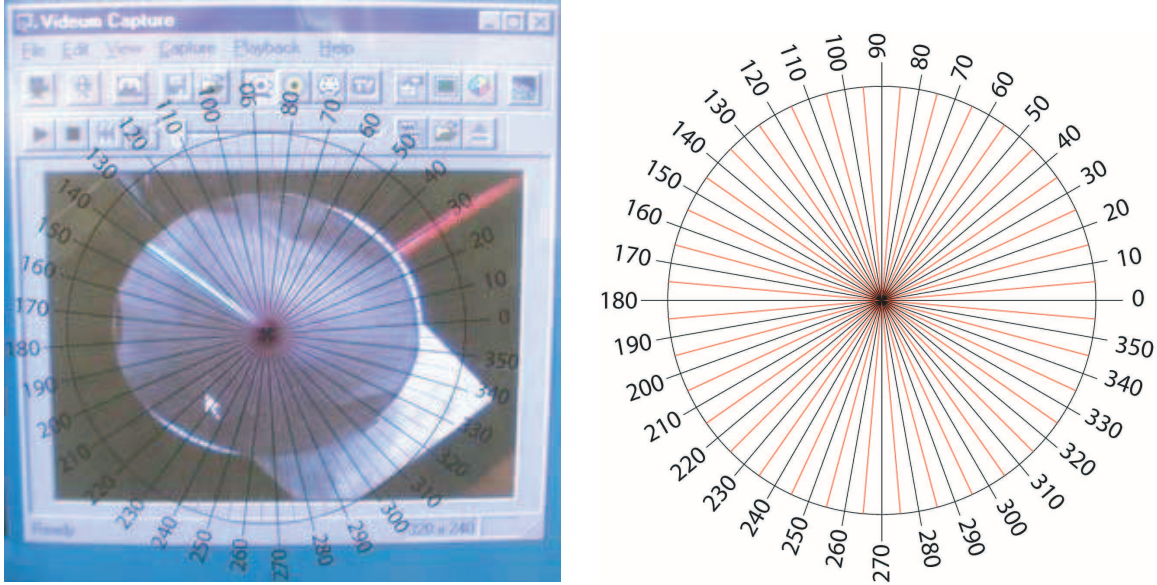
Figure 3-21: Video data collection for rotational 1st-order system. Data are recorded by recording the angle of rotation in particular movie frames (at left). We have students estimate the angle by overlaying a transparent angle gauge (at right) onto captured video.

servations about this data are as follows. First, our idealized first-order model of the system:

$$T_{in} = 0 = J\omega + c\dot{\omega} \tag{3.3}$$

predicts that the time constant should be proportional to the inertia of the system:

$$\frac{\omega(s)}{T_{in}(s)} = \frac{1/c}{(J/c)s + 1} = \frac{K}{\tau s + 1} \tag{3.4}$$

$$\tau = \frac{J}{c} \tag{3.5}$$

The dashed lines in the plots in Figure 3-22 show ideal exponential decays which represents fits to the first few points in each set of data. The viscous damping model predicts that increasing the inertia by a factor of ~ 5 should correspondingly increase the time constant by a factor of five as well, but the fitted time constants instead differ by less than factor of two. A second thing to note about this data is that the actual data are not particularly well-modeled by a first-order decay. In each data set, the experimental data does not decay at a constant exponential rate: the rate of

decay becomes greater as the velocity goes to zero. This is consistent with non-linear effects that would result from Coulomb friction losses.

The dominant loss mechanisms when there is no honey are not well-understood, but they likely include some viscous damping (perhaps from shear in the surrounding air and/or from the residual honey at the bearing interface) and Coulomb friction (predominantly where the ball bearing glued to the shaft end rests on a carbide flat). A more detailed analysis at the end of this section provides further evidence to support this conclusion. In summary, data taken with no honey are not particularly well-modeled as a first-order inertia-damper system.

In contrast, the data taken *with* honey strongly support the system model students develop in the pre-lab assignment. We model the system during rundown as a first-order system with no external applied forces: $J\ddot{\theta} + c\dot{\theta} = 0$. If the damping is a function of the height of the honey, as predicted by Equation 3.2, then "c" is the same in each data set shown in Figure 3-23, and the time constant, $\tau = J/c$, should increase by a factor of 5.1 when the inertia (J) is increased by a factor of 5.1. The data in Figure 3-23 have been carefully plotted to illustrate that they come quite close to this ideal. The axes on which the data have been plotted have been scaled to emphasize that the shape of the decay is essentially the same in both plots: the time axes for the righthand plot span a range five times greater than that of the lefthand plot.

It would probably be desirably to have the students obtain data *with* viscous damping from the honey first, since it supports their first-order model of the dynamics. Unfortunately however, it is a lot easier to push honey into the reservoir than it is to pull it out again! The high viscosity that makes honey such a desirable fluid for the lab (i.e. to get time constants on the order of one second) makes it a real pain when it comes to emptying the reservoirs. Note in Figure 3-19 that the honey must be pulled through a length of narrow tubing (with an orifice connection at either end). If you pull too hard, bubbles are generated or the plunger pulls free of the rubber seal.

There are two issues which make it more difficult to pull honey out than it is to push it in. First, one can at best obtain a vacuum inside the syringe, which limits
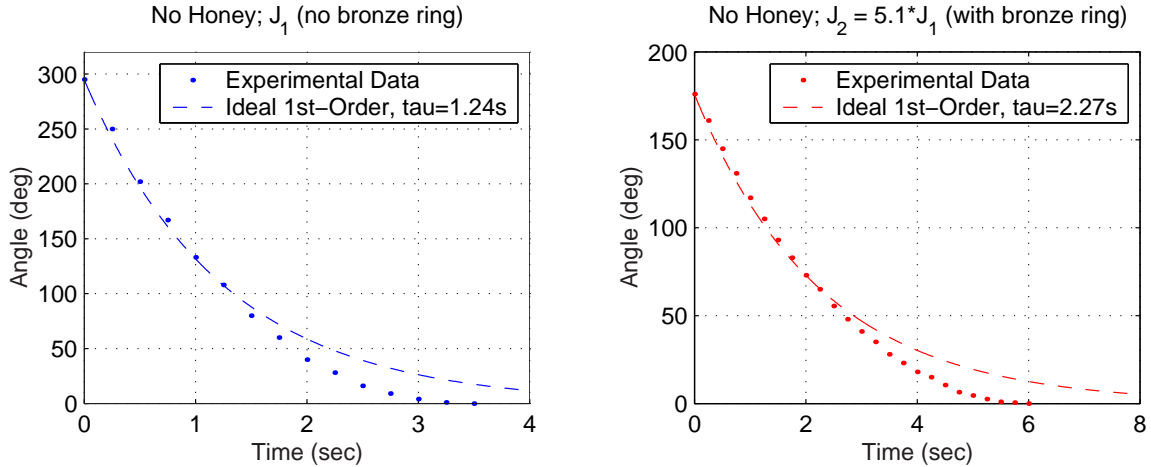
Figure 3-22: Experimental data for 1st-order rotational system (no honey) - These two data sets were taken with no honey, so they give a feel for how significant the losses due to other (non-honey) effects are.

the driving pressure differential (due to atmospheric pressure). Second, if one pulls too hard on the syringe, it is possible to pull the plunger out suddenly. Clearly just "pushing the plunger back in" will introduce air in the syringe. (At this point, one essentially must call the aide of a TA to detach, play around with and then reglue the syringe-tubing-reservoir interface(s) to try to obtain a good interface between the syringe plunger and the honey again.) As a result, we generally have the students begin with *no* honey and then run trials with monotonically increasing amounts throughout the lab. Again, it is unfortunate students encounter the anomalous exception ("What happens with *no* viscous damping from honey?") before the general case ("Honey height and damping are proportional to one another, and inversely proportional to the time constant."). This is not a great concern, since staff can interview the students to reflect on their results after all data are taken, but it is one of the most significant limitations of the lab setup.

As previously mentioned, Coulomb friction is likely a significant loss mechanism in this lab when data are taken with no honey. As the system spins down to rest, the data (shown as points in Figure 3-22) deviate noticeably from an ideal "first-order" decay (overlaid on the plot as a dashed line). If one attempts to calculate a time
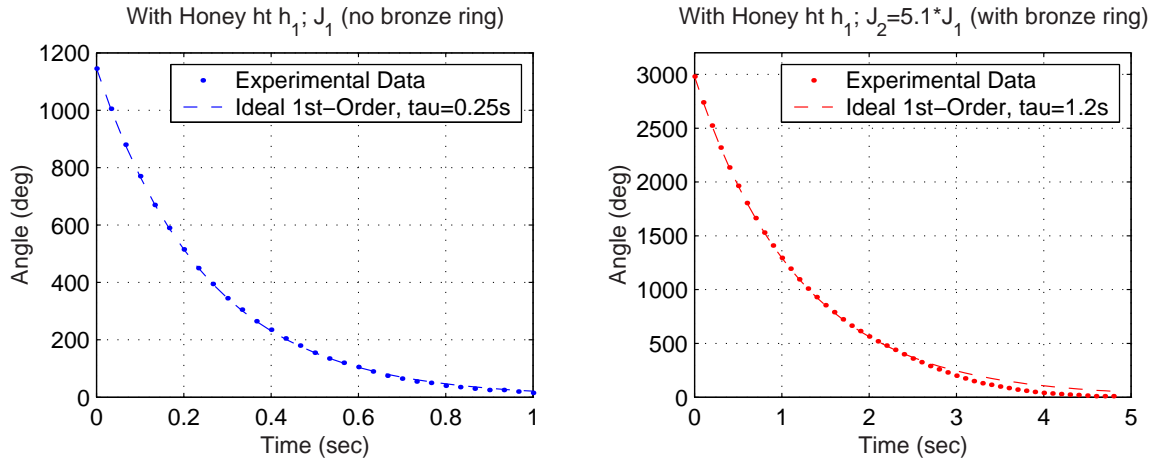
Figure 3-23: Experimental data for 1st-order rotational system (with honey) - The total inertia increases by about a factor of five when an additional bronze ring is added to the system (at right), increasing the time constant by about a factor of five, too, as expected.

constant (based on the first few points of data), "tau" does increase as the inertia increases - but certainly *not* by a factor of five (as one would expect if losses were due only to viscous effects). This implies Coulomb friction is likely a significant loss mechanism.

If the *only* losses in the system were those due to Coulomb friction, the *velocity* as the system spins down would decay linearly (as a straight line). (Friction force and therefore acceleration would be constant, in other words.) Figure 3-24 plots estimates of the velocity over time for data set (shown in Figure 3-22) taken with no honey. Each velocity point is simply the difference between two successive angular position measurements, so the data look pretty noisy (as one might expect).

In Figure 3-24, the righthand velocity data set (with the larger inertia) are plotted along with a straight line fit. If losses are due to Coulomb friction at the tungsten carbide bearing surface (on which the bearing tip of the shafting rests), then a torque balance implies

$$J\ddot{\theta} = -Kmg \tag{3.6}$$

(where K is some constant and mg is the force the mass (m) of the spinning body

167
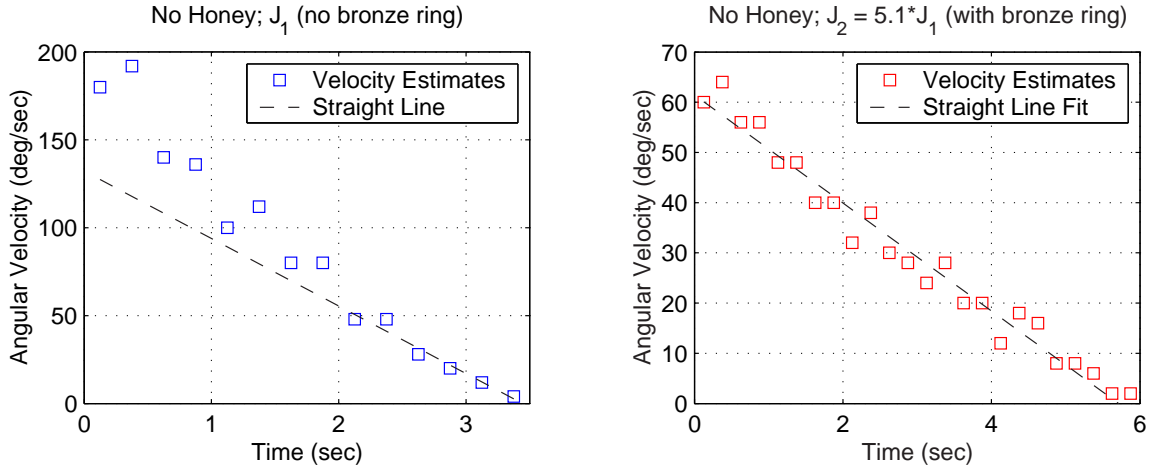
Figure 3-24: Velocity estimates for 1st-order rotational system (no honey) - The plotted boxes show velocity estimates during spin-down, obtained by subtracting sequential values (simple difference method) from the data set shown in Figure 3-22. The dashed lines are overlaid on the data to help determine whether the primary loss mechanism seems to be Coulomb friction (which would result in a linear decay of velocity). *Note there is (virtually) no viscous damping due to honey for these data sets.*

exerts on the bearing surface due to gravity (g)). This means the acceleration will be constant, and the velocity will go to zero as a straight line with the slope given as:

$$s = -Kg \cdot \frac{m}{J} \tag{3.7}$$

The data with the added inertia do indeed see to be nearly (though perhaps not quite) linear. Note that the velocity data would show an *exponential* decay if losses were due to *viscous effects alone*. One can imagine the data shown in fact indicate some combination of Coulomb friction (i.e. they are approximately linear) with a smaller contribution due to viscous effects (the slope at $t = 0$ seems a bit steeper than at $t = 5$, for instance).

If one postulates that Coulomb friction is the most significant loss mechanism in the lefthand data set, then presumably the velocity data in the lefthand plot (without the bronze ring) should also fall on a line. Moreover, if the slope of the velocity is proportional to m/J (equation 3.7), we would expect the slope of lefthand data set

(s_L) to be related to that of the righthand set (s_R) as:

$$s_L = \frac{m_L}{J_L} \cdot s_R \frac{J_R}{m_R} = s_R \cdot \frac{m_L J_r}{m_R J_L} \tag{3.8}$$

Adding the bronze ring increases the inertia by a factor of 5.1 ($J_R/J_L = 5.1$), as mentioned, and increases the mass by a factor of about 1.5 ($m_R/m_L = 1.5$). The slope of the fitted line in the righthand plot is $s_R = -10.8$ (deg/s^2). Thus, we would expect:

$$s_L = s_R \cdot \frac{J_R/J_L}{m_R/m_L} = -10.8 \cdot \frac{5.1}{1.5} = -37 \text{ (deg/s}^2) \tag{3.9}$$

The dashed line plotted with the velocity data at the left of Figure 3-24 is a fit to the *last 6 data points, only*. The slope is -38 (deg/s^2); close to our expected value of -37.

My own conclusion is that we are seeing both viscous damping and Coulomb friction in the data with no bronze ring. Note that the velocities are all substantially lower in the plot with the inertia. Viscous effects seem to be noticeable in the data *without* the bronze ring only for velocities above around $\dot{\theta}_{Lc} = 40$-50 (deg/s^2). Whatever the relationship between the torque due to viscous damping $(B \cdot \dot{\theta})$ and the Coulomb friction $(Kg \cdot m)$ is in this range (when Coulomb friction becomes notably dominant), the velocity at which we expect a *similar* relation between the two contributing torques to exist in the *other* data set should be roughly $\dot{\theta}_{Rc} = \dot{\theta}_{Lc} \cdot m_R/M_L$, or in the range of $\dot{\theta}_{Rc} = 60$-75 (deg/s^2). At any rate, it is not at all surprising that we the data in the righthand plot seem to be dominated more significantly by Coulomb friction. We do not ask students to go into this level of analysis in investigating the effects of Coulomb friction. The labs were in fact designed (as mentioned in the discussion of our use of air bearings on page 30 of the Introduction) to minimize the effects of Coulomb friction, so students could focus on nearly-ideal first- and second-order system behaviors. Because we have students take data for Lab 2 with essentially no honey in the reservoir (except for that which adheres at the bearing interface at the base of the shafting), it is useful to address the effect of Coulomb friction to some extent, however, especially for the most highly motivated students.

3.5   2nd-Order Spring-Mass-Damper Translational System
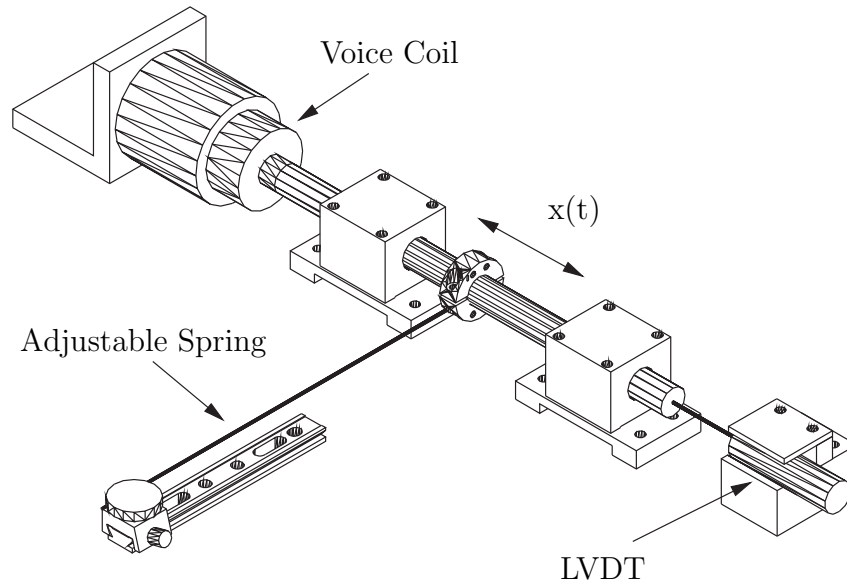
Figure 3-25: Schematic of the spring-mass-damper lab hardware. Drawing by Andrew Wilson.

Air bearings and steel shafting are again used in this lab, but they are now oriented to allow low-friction *translational* movement. Stainless steel welding rod (1.1mm dia) serves as a cantilever spring. The welding rod is mounted off-center of the axis of the shaft to allow the shafting to rotate slightly as the spring is deflected. This allows the spring to remain nearly linear over a deflection of approximately one centimeter.

A voice coil actuator is mounted at the left end of the shaft as shown in Figures 3-25 and 3-27, and an LVDT (linear variable differential transformer) at the other end measures position. In this lab, the voice coil is not used as an actuator; it simply provides a variable system damping. The coil assembly is wound on an aluminum cup. Eddy currents are generated within the aluminum cup as it moves through the magnetic field of the actuator housing. This results in system damping. If the terminals of the actuator are shorted, a back emf is produced in the coils, and the total damping then includes both the eddy current and back emf effects.
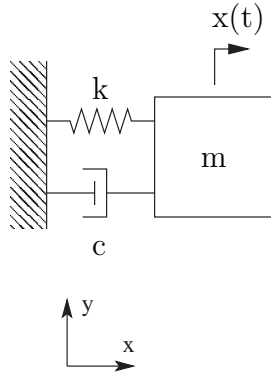
Figure 3-26: Idealized model of the spring-mass-damper system - Drawing by Andrew Wilson.

Students vary both the damping and stiffness of the system in this lab and investigate the resulting system response. The cantilever spring is attached to the optical breadboard baseplate with an adjustable clamp to create a spring of any arbitrary length from about 5 cm to 16 cm. The system damping is varied between its two possible values by either shorting the voice coil with a patch cord or leaving the terminals open-circuited.

Students can deliver an impulse to the system by allowing a brass ball mounted on string to swing into an aluminum target plate. (Ball and target can be seen in the upper right of Figure 3-27.) Impulse response data collected with the oscilloscope can be saved to a floppy disk and then loaded into MATLAB. Students use their data to determine the system poles empirically. They can then replot their data against an ideal, second-order response to compare the two and verify their calculations. Initial position responses can also be taken by displacing the mass by hand.

In lab 4, the same hardware configuration is modified slightly to allow students to investigate the driven response of the system. Figure 3-30 shows these necessary modifications. The voice coil is now used as an actuator. A power amplifier (shown in the bottom left corner of Figure 3-30) drives the voice coil, using a signal from a function generator to create a voltage step input to the system. Protoboards at each station (shown in the upper left corner of Figure 3-30) are used here to make the
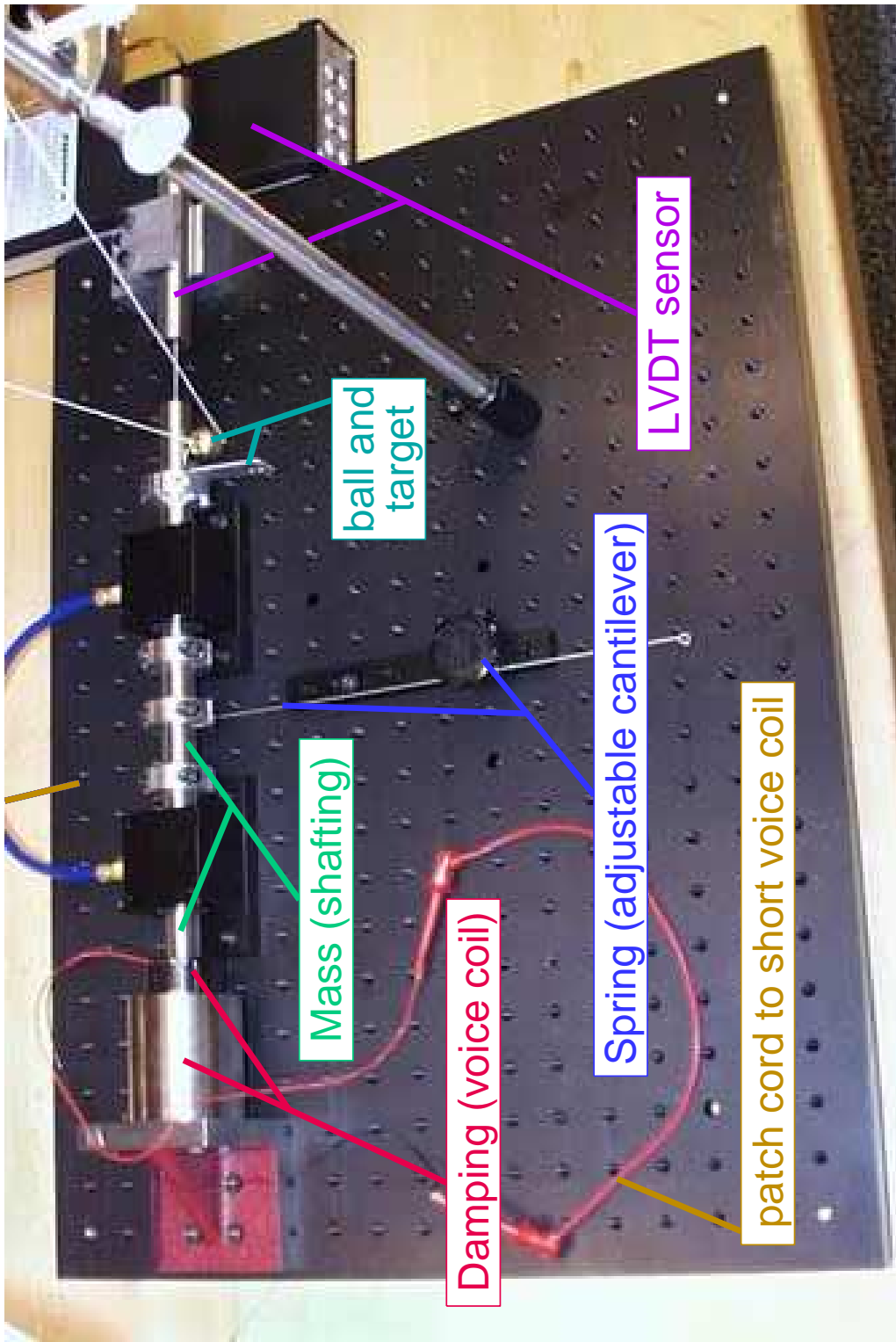
Figure 3-27: Lab 3 - 2nd-order spring-mass-damper system impulse response
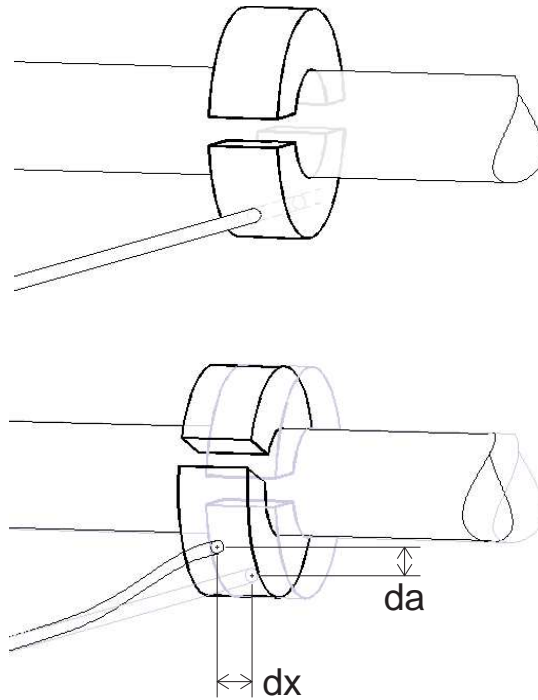
Figure 3-28: Cantilever translation (dx) causing shaft rotation (da).

necessary connections to the oscilloscope and function generator.

Some of the typical data obtained in lab 3 with this second-order system are shown in Figure 3-31. Recall that there are two possible values for the damping in the system; either with the voice coil shorted or open. All of the traces recorded on the subplot at the top of this figure show step responses taken with the voice coil shorted, while the ones in the lower subplot were taken with the voice coil open.

The spring stiffness can be adjusted be changing the length of the cantilever spring. Figure 1-9 on page 41 shows the slidable clamp for the cantilever[1], which can be used to set spring length as desired, within a continuous range from about five to sixteen centimeters.

Note that the spring stiffness, k, is related to its length, L, as:

$$k = \frac{3EI}{L^3} \tag{3.10}$$

---

[1]Designed by Joe Cattell.
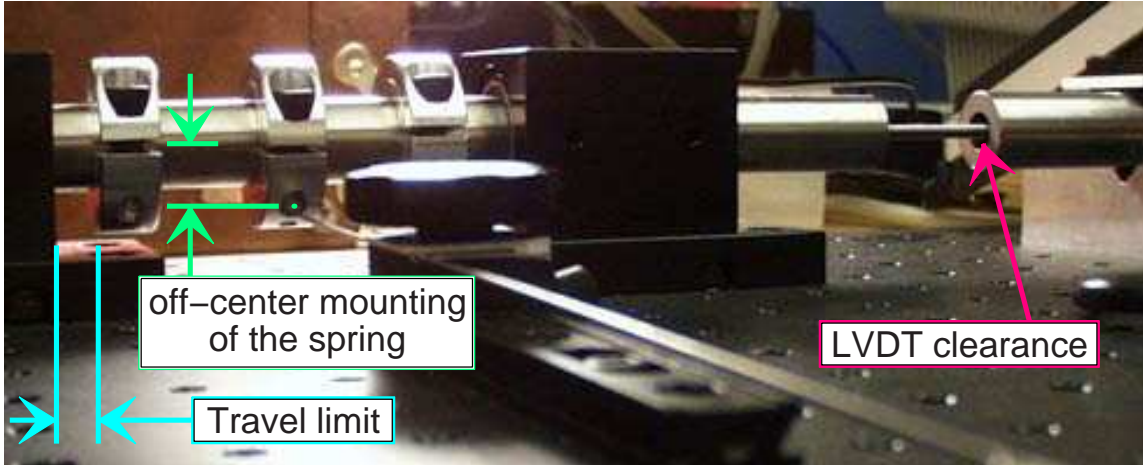
Figure 3-29: Lab 3 - 2nd-order spring-mass-damper system impulse response

where "E" is Young's modulus for the steel cantilever and "I" is its moment of inertia.

The natural frequency of the spring-mass-damper system is:

$$\omega_n = \sqrt{k/m} \tag{3.11}$$

$$\omega_n = \sqrt{\frac{3EI}{mL^3}} \; (rad/sec) \tag{3.12}$$

$$f_n = \frac{1}{2\pi}\sqrt{\frac{3EI}{mL^3}} \; (Hz) \tag{3.13}$$

Lab Station Hardware:

"Nerdkit" protoboard with BNCs to Hardware

PA21 power amp to drive voice coil

signal generator

function generator
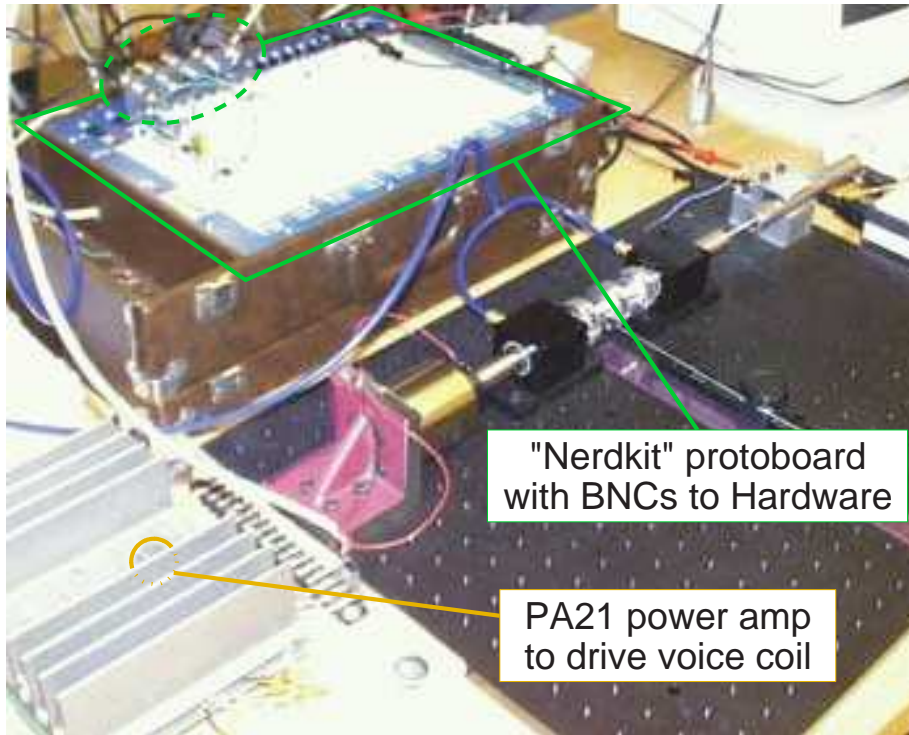
oscilloscope
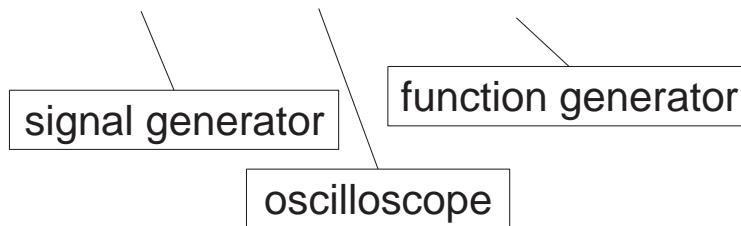
Figure 3-30: Hardware for implementing driven response of 2nd-order system
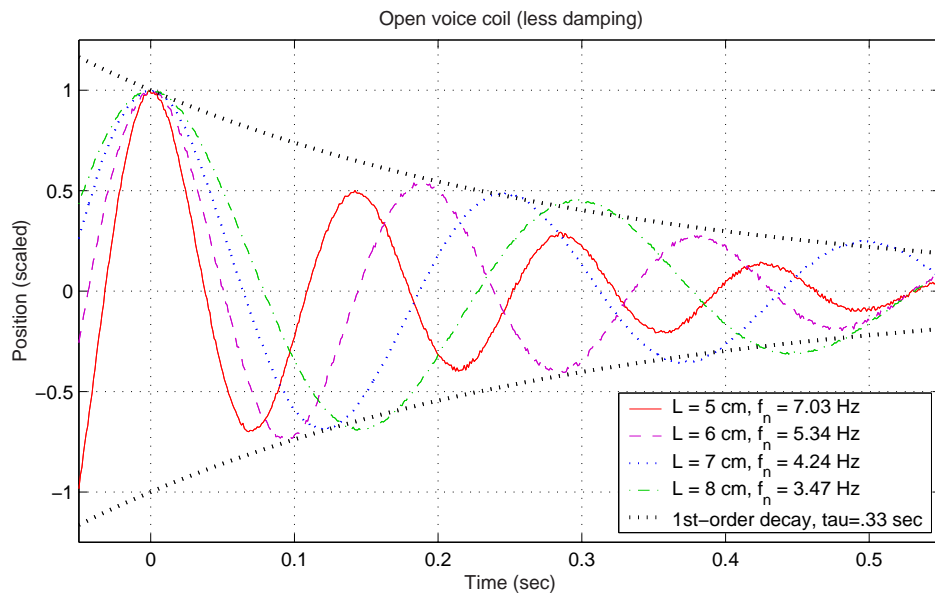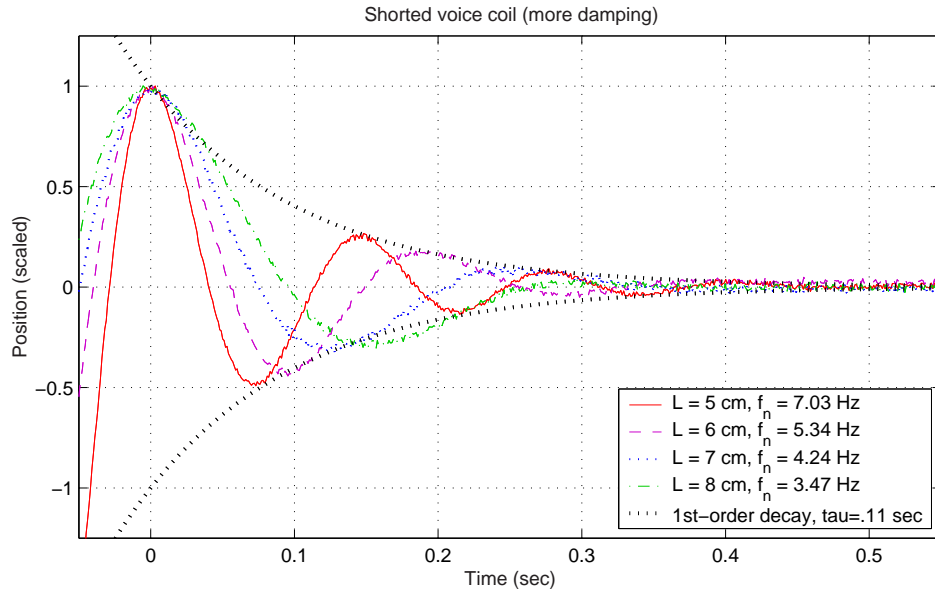
Figure 3-31: Experimental data for 2nd-order translational system in lab 3. At top, the voice coil was shorted. All traces in this set decay with the same decay envelope (approximately), as expected. Conversely, the lower data traces (taken open-circuited) show obvious differences in damping. Student data also reports (unexpected) deviations in damping in this configuration, due to some real-world effects we do not investigate during the lab. Comparing individual traces on the top and bottom plots also illustrate that natural frequency is a function of spring length, but *not* of damping.
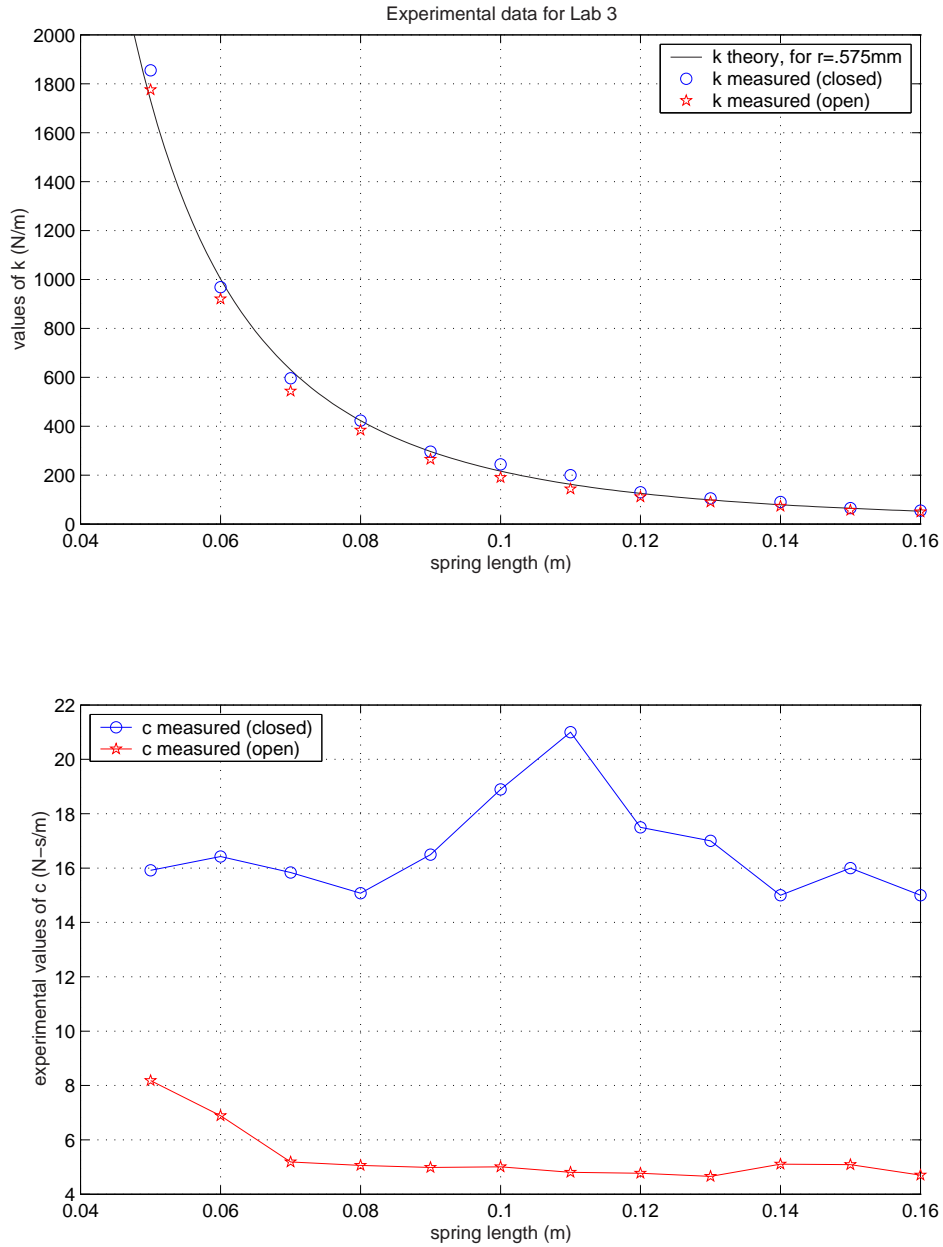
Figure 3-32: Calculated k and c values for 2nd-order translational system. The two plots above show values of k and c as a function of spring length. These values were obtained by fitting successive data sets (including those shown in Figure 3-31). The values of k obtained are all very close to the ideal relationship one would expect. The data in the lower plot are less ideal. One would expect the same damping coefficient for each trial run open-circuit and a second (but consistent) value for all close-circuit data (i.e. Each plot should be a flat, horizontal line). We do not attempt to explain the non-ideality.
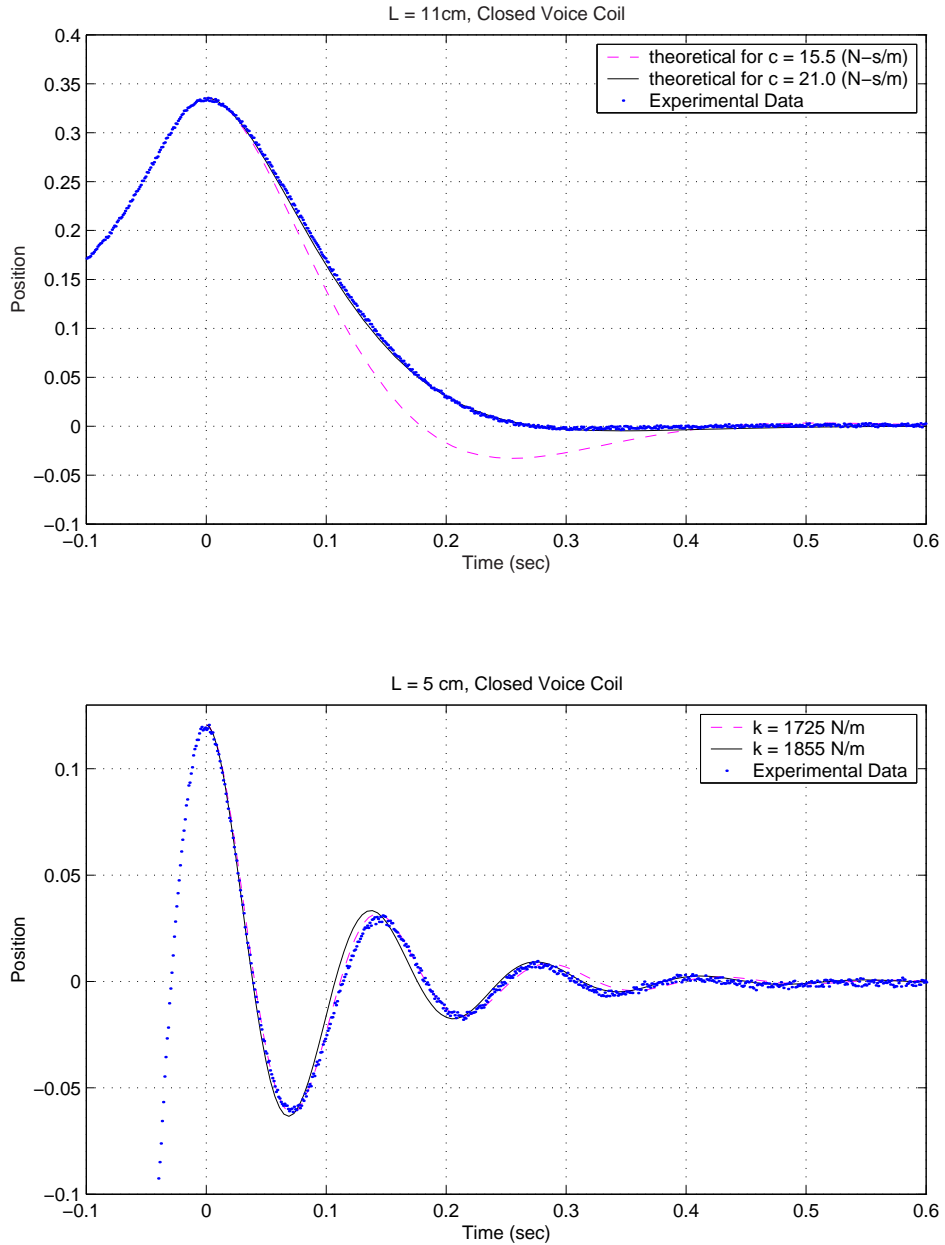
Figure 3-33: Comparisons of c and k values for particular data sets. These data show representative fits to the raw data, used to obtain the plots of k and c shown in Figure 3-32. I provide this data to allow the reader some metric to judge whether deviations from ideal behavior are due to the fitting method or the actual hardware. Above, the solid line corresponds to the value of c (21 Ns/m) I chose as a "best fit", while the dashed one shows a more typical value for the closed circuit configuration. The lower plot matches less convincingly. The solid line again shows my fit, while the dashed one uses the theoretical k value expected, given the spring length.

3.6 First- and Second-Order Electronic Circuits

It is much easier to create a nearly ideal dynamic system using electronic circuits than it is to create a nearly ideal (e.g. low friction) mechanical system. In two laboratories on simple electronic circuits, we have our students create simple RC and LRC circuits on individual prototyping boards at each lab station. The data are again collected on an oscilloscope and then downloaded into MATLAB for further analysis. The previous mechanical laboratories have studied only the system time response. In these labs, we have the students analyze both time and frequency responses.
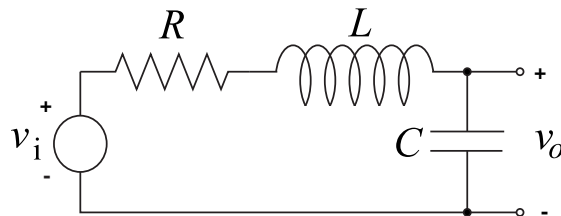
Figure 3-34: RLC circuit. Drawing by Marten Byl.
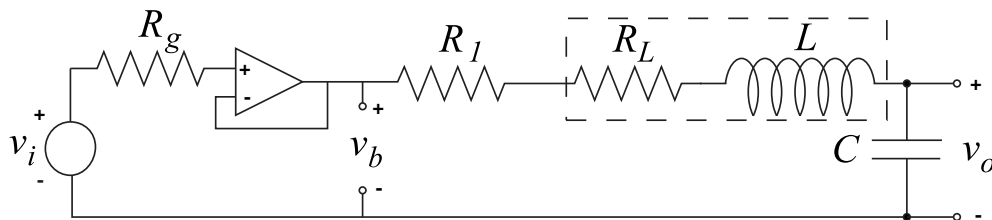
Figure 3-35: Voltage follower and RLC circuit modelling inductor resistance. Drawing by Marten Byl.

One of the goals of the lab is to illustrate how these first- and second-order system dynamics correspond to the dynamics of the mechanical systems the students have previously studied. Mechanical engineering students often find electrical circuits to be less intuitive than mechanical systems, so we have presented the mechanical versions first. In the circuit laboratories, we also begin to emphasize the link between the time response, frequency response, and pole locations of a system.

3.7 Op-Amp Circuit Dynamics

In 2.003 we present three basic models to represent an op-amp: first, as an ideal element with infinite gain, so that a negative feedback connection mathematically forces the positive and negative terminals to be at identical voltages; second, as an element with a finite (but very large) gain; and finally, as an integrator with very large gain (i.e. "G/s") [173]. In this laboratory, we use this third model to represent an op-amp and ask the students to predict system dynamics for two elementary op-amp circuits, shown in Figure 3-36.
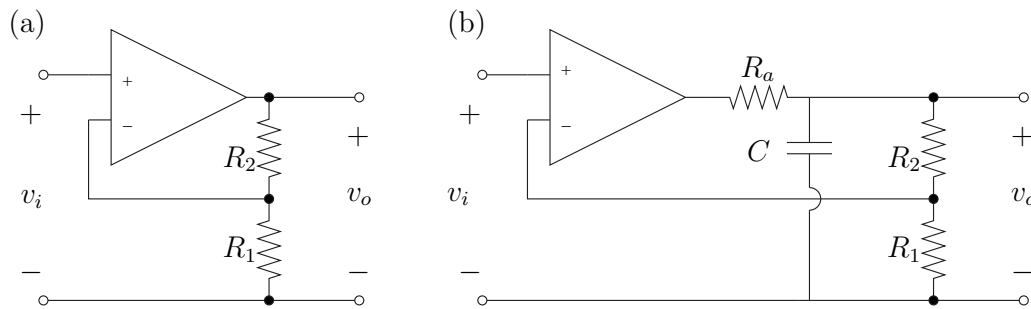
Figure 3-36: Driven response of a second-order system.

The circuit at the left is essentially first-order, while the one at right results in a second-order response. Students predict the system pole locations and then experimentally determine the poles by performing a frequency response test by inputting sinusoids at each of several frequencies and recording the steady-state phase shift and amplitude at each frequency of excitation. The students are shown how to set the digital oscilloscopes to display amplitude and phase directly to expedite this process.

3.8 Effects of Zeros in a Mechanical System

Many undergraduate courses in dynamics do not give much (if any) coverage to the effects of zeros in system response. In this laboratory, we add an additional mass and spring to the translational spring-mass-damper system described in Section 3.5. An aluminum blade and a steel mass mounted at its end provide the additional stiffness and mass (as shown in Figure 3-37). Students observe that the lightly-damped pole pair created by the second spring and mass becomes a lightly-damped complex pair of zeros when both the driving force and position measurement occur at the first mass.
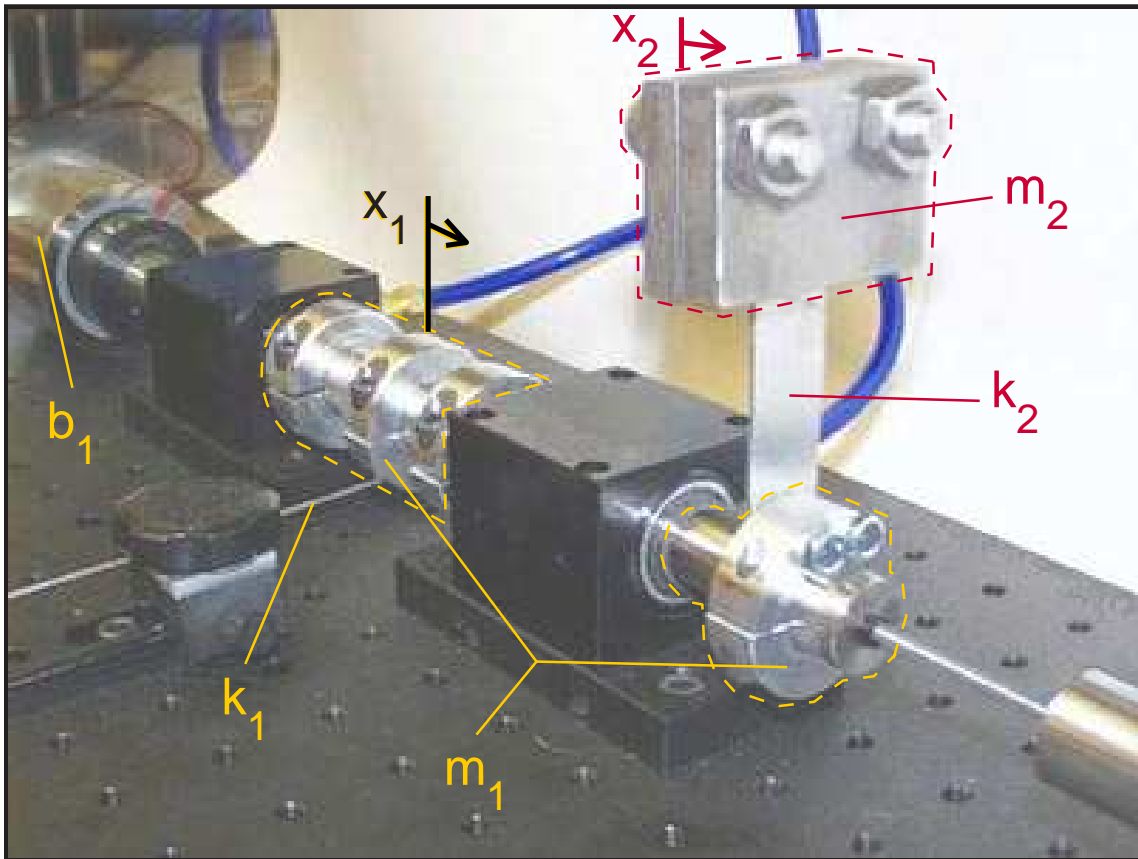
Figure 3-37: 4th-order translational system.
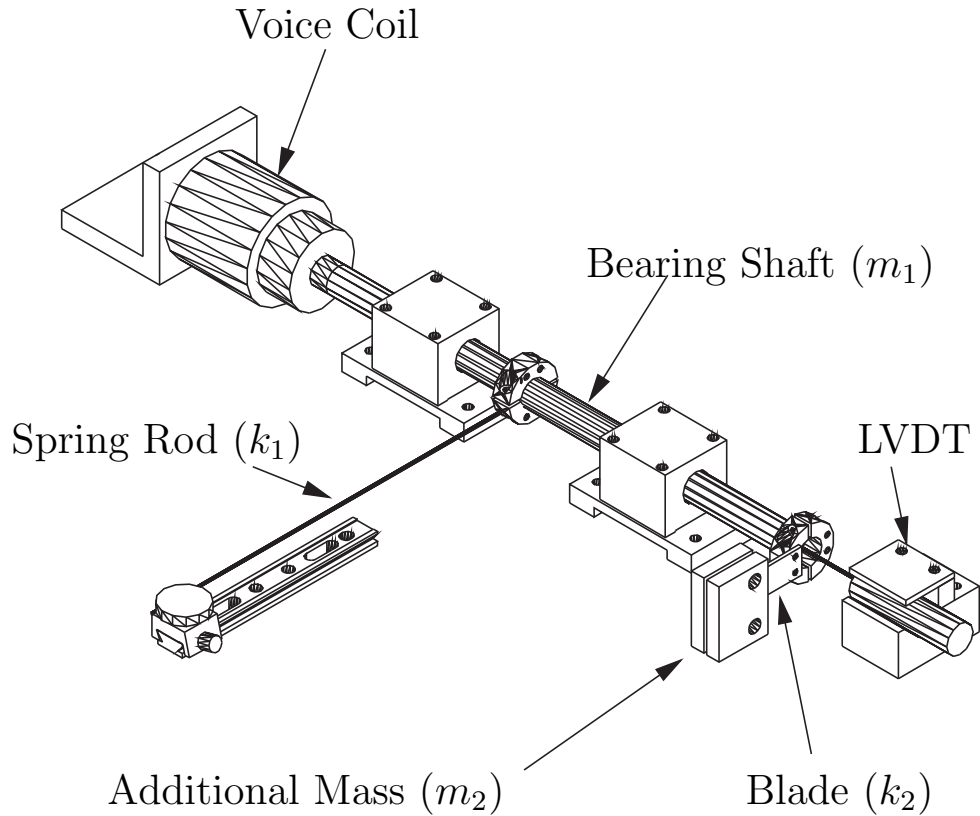
Figure 3-38: Schematic of the 2-mass laboratory hardware. Drawing by Andrew Wilson.

We have the students perform an automated swept sine frequency response using a Simulink model and accompanying MATLAB software which we have developed to run on the dSPACE 1102 boards on the lab computers [114, 113]. Voice coil actuation and LVDT measurement each occur at the larger (shafting) mass. Thus, the transfer function is measured from a voltage input to the voice coil to an output of shaft position. The position of the second mass is not measured directly in this lab.

The students use their experimental frequency response plots to determine the complex poles and zeros of the system. They then generate a theoretical Bode plot to verify their idealized (4th-order) model. Bode plots of both the experimental data and the idealized system model are given in Figure 3-40. It is clear from the phase difference between the two above 10 Hz that the idealized, 4th-order model misses some system dynamics.
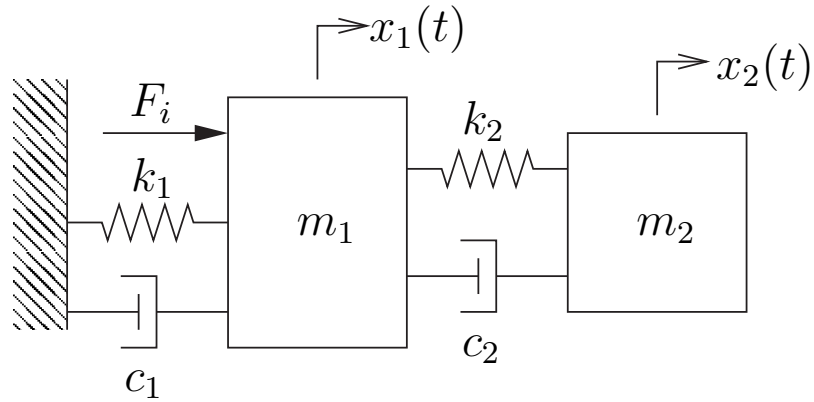
Figure 3-39: Idealized model of the 2-mass system. Drawing by Andrew Wilson.

3.8.1 Unmodeled System Dynamics

As a peripheral exercise, we take advantage of the unexpected (and unmodeled) system dynamics to illustrate to the students the importance of verifying ideal models with experimental data. By including an additional, real-valued (stable) pole at around 30 Hz, students can obtain a much closer fit to the experimental data. Figure 3-41 compares experimental data with a theoretical system including this additional pole.

The additional dynamics (approximated as a "pole at 30 Hz") cannot simply be explained only by the inductance in the coil. The resistance (5 Ω, +/- 12.5%) and inductance (2.3 mH, +/- 30%) of the coiled wire in the BEI voice coil motor result in an electrical time constant of about 0.5 milliseconds. This corresponds to a pole at around 350 Hz (2200 rad/sec), which is an order of magnitude higher than the frequency ($\sim$ 30 Hz) at which the data indicate that another pole seems to appear.

As previously mentioned, the coil is wound on an aluminum cup, and eddy currents are generated as the coil and cup cut through the magnetic field lines inside the voice coil housing. The inductance of the aluminum armature may be responsible for the additional dynamics. We have not verified this, however, and the source of the apparent pole near 30 Hz is still unknown.
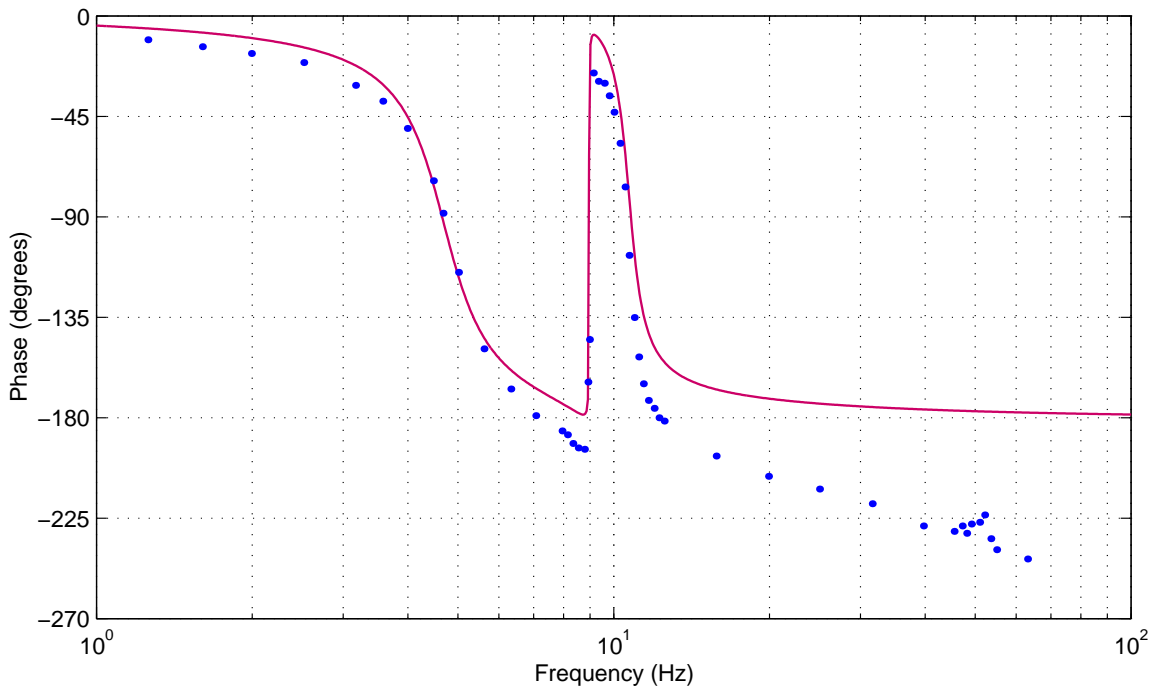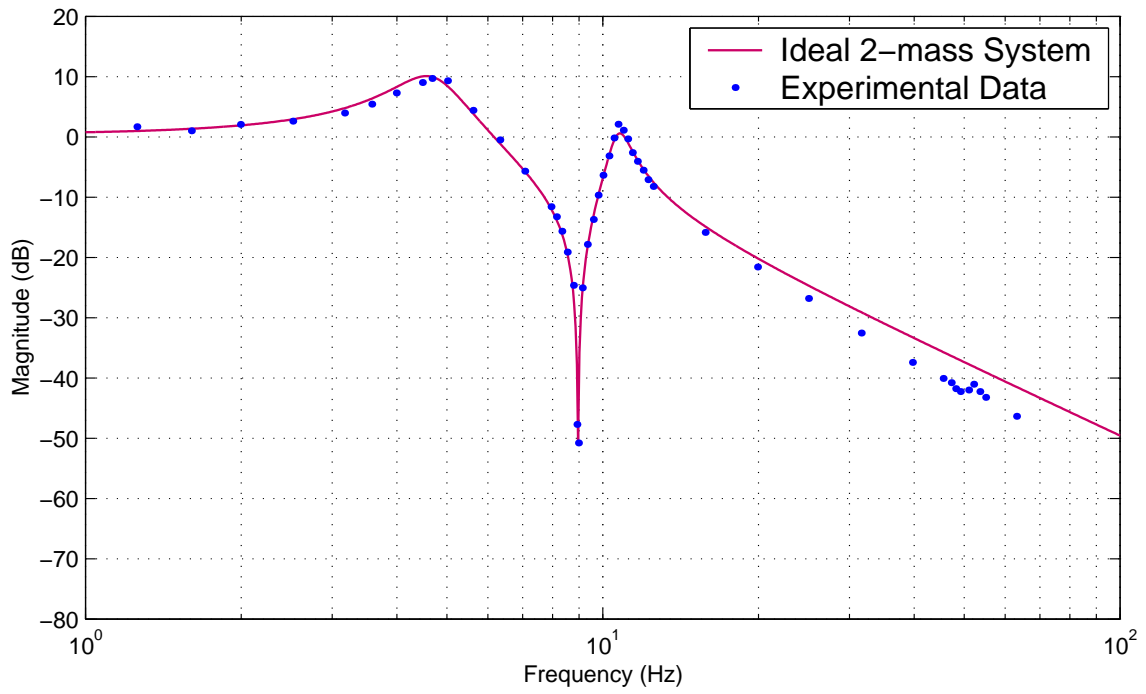
Figure 3-40: Experimental Bode plot for 4th-order system
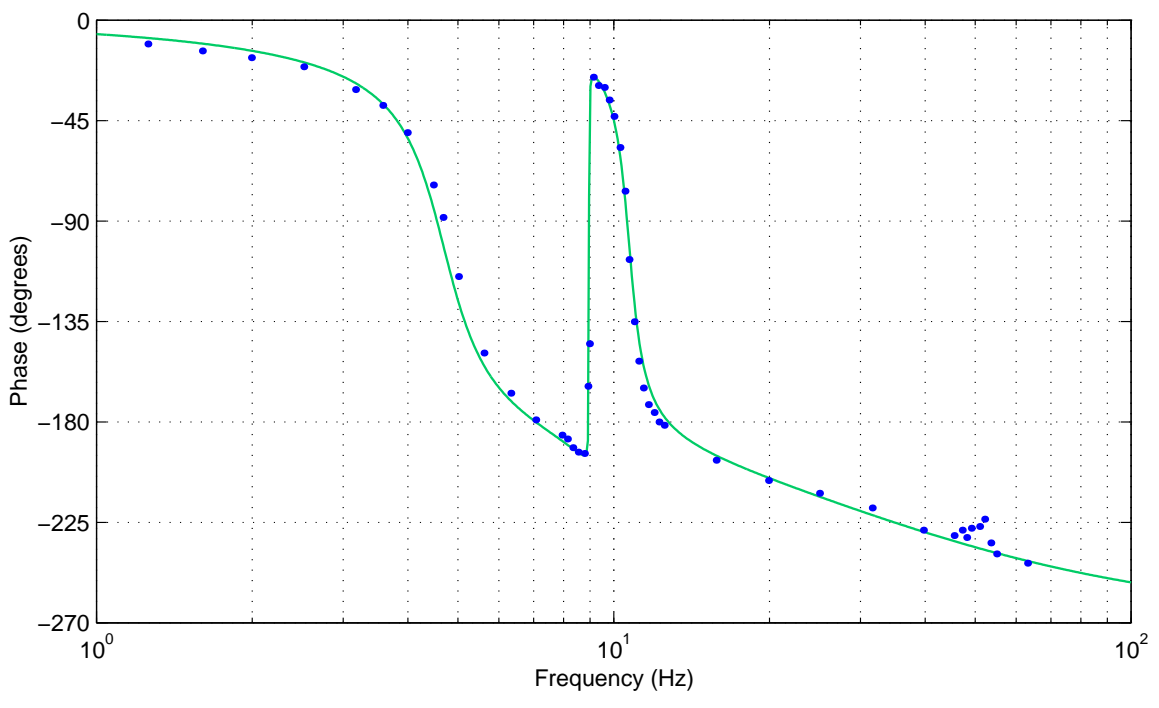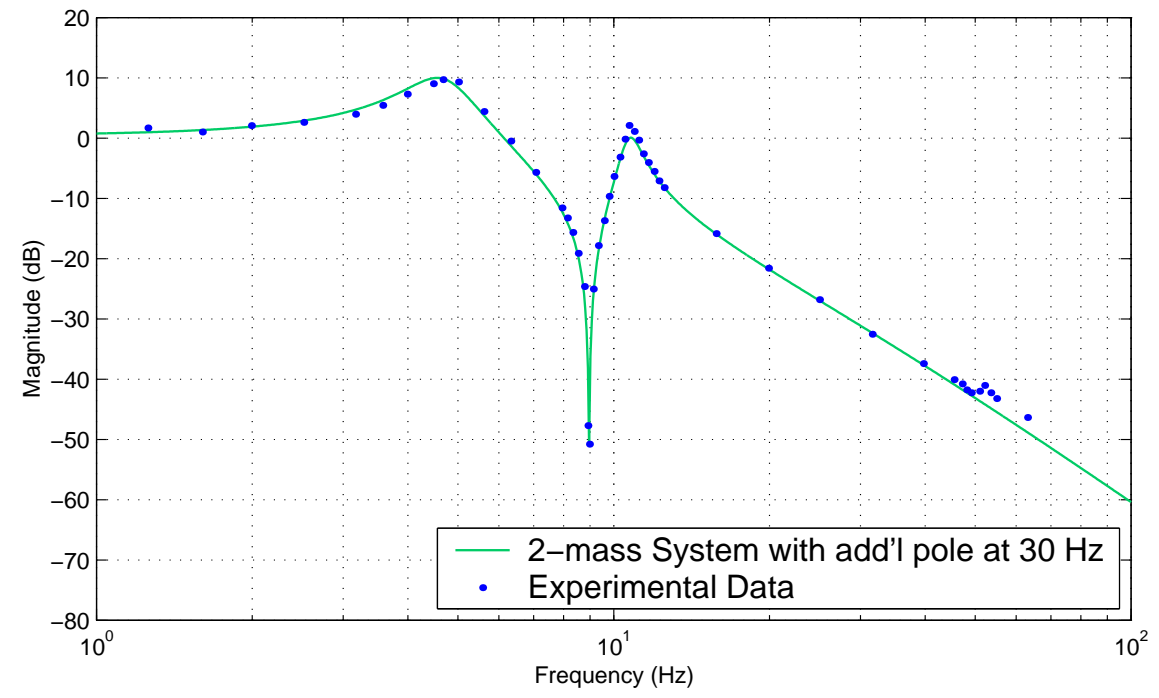
Figure 3-41: Bode plot for 4th-order system with additional pole with break frequency 30 Hz
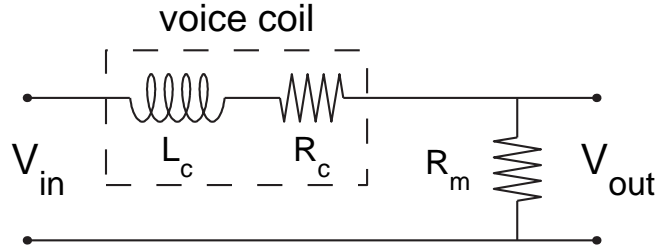
Figure 3-42: Test circuit for measuring voice coil dynamics.

Another aspect missing from the model of the system's dynamics is the magnetic diffusion in the steel core of the voice coil magnetic circuit. We used the circuit shown above in Figure 3-42 and an HP dynamic signal analyzer (model 35665A) to test the frequency response of the voice coil.

The circuit was tested both in open air (essentially in free space) and when fixed (held stationary) inside the magnetic housing. The transfer functions measuring V_{out}/V_{in} in each of these two configurations are shown in Figures 3-43 and 3-44, respectively. Each figure also shows an ideal first-order response based on the inductance given in the specifications for the voice coil ($L = 0.0023$ H) and the measured resistance of the coil (4.7 Ω):

$$\frac{V_{out}(s)}{V_{in}(s)} = \frac{1}{Ls + R} \tag{3.14}$$

The experimental data measured with the coil fixed inside of the magnetic housing shows an apparent fraction-order transfer function, which is indicative of magnetic diffusion. The dashed line in Figure 3-44 represents the following proposed function:

$$\frac{V_{out}(s)}{V_{in}(s)} = \frac{1}{Ls + 0.25s^{0.5} + R} \tag{3.15}$$

The dynamics due to magnetic diffusion are significant only at frequencies well above 30 Hz, and they do not explain the anomalous dynamic behavior seen in the experiment data in Figures 3-40 and 3-41. We do not expect students to have the background in field theory required to directly understand this effect, but an use this example to stress the importance of physical measurement.
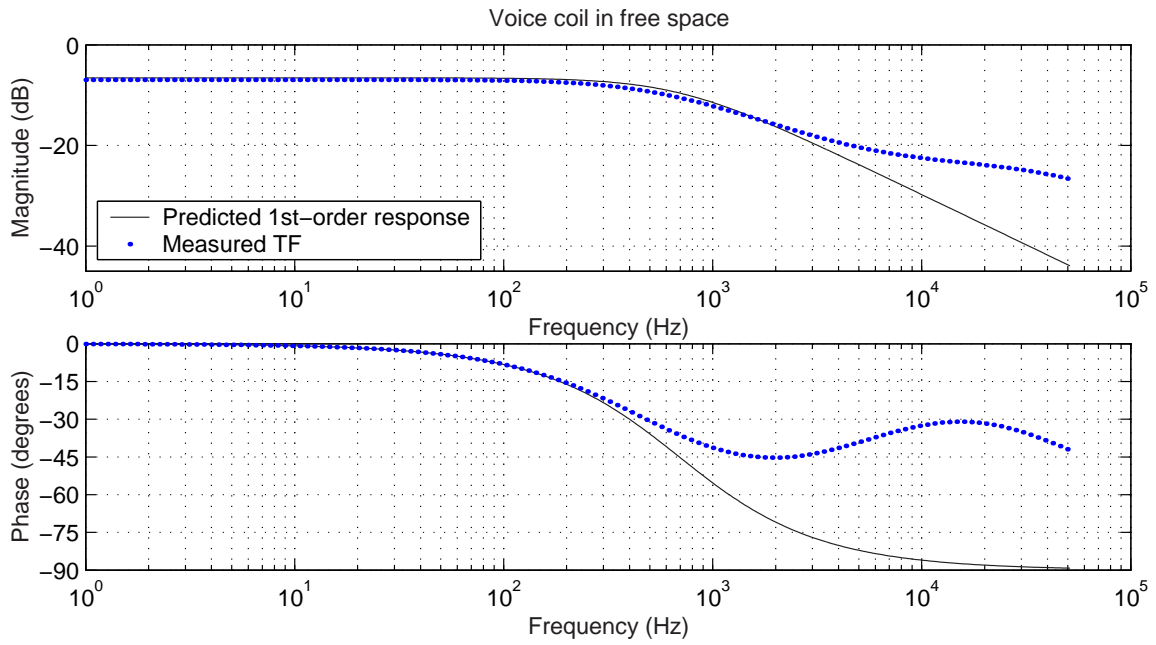
Figure 3-43: Frequency response for voice coil in free space.
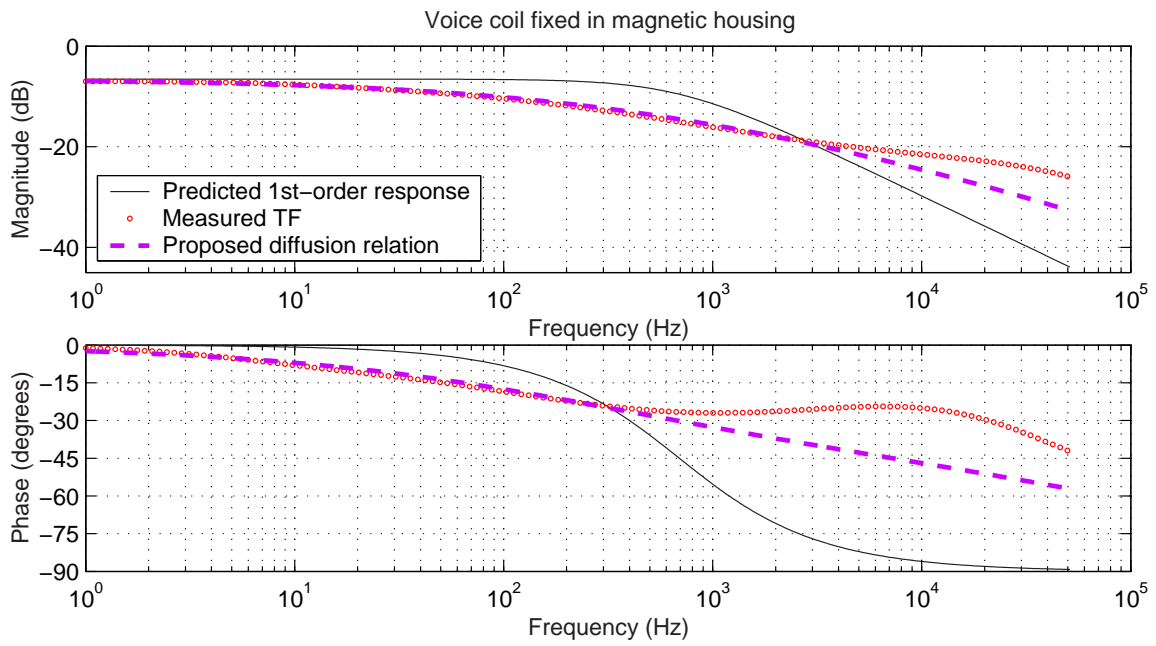
Figure 3-44: Frequency response for voice coil fixed in magnetic housing.

187

3.9 Introduction to Controls

In the final laboratory, students explore the effects of proportional and derivative control action. Students should note that proportional control increases the effective stiffness of the controlled mechanical system and that derivative action adds equivalent damping. Depending on the year, this introduction to controls has used either the spring-mass-damper system used earlier in the term or a DC motor. Each version of the lab is described briefly below.

3.9.1 Control of Translational Spring-Mass-Damper System
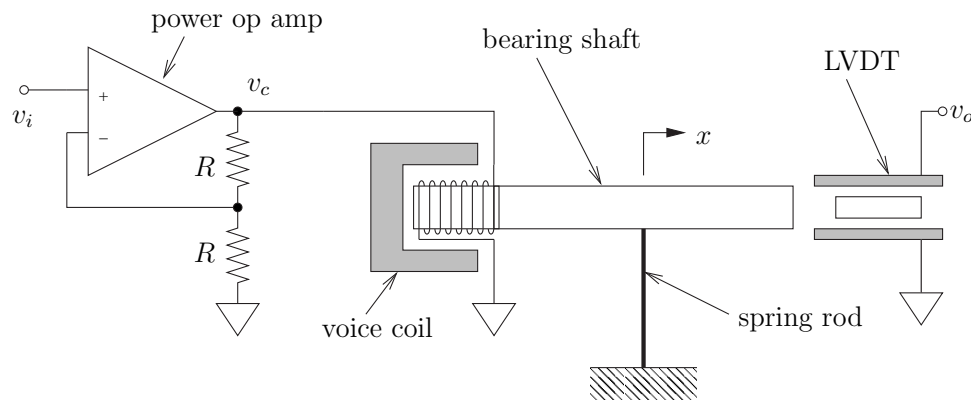
Figure 3-45: Power op-amp used to drive spring-mass-damper system - The desired input voltage, v_i, is generated by the lead (or proportional) controller circuit shown in Figure 3-47. Drawing by Andrew Wilson

In this lab, students use op-amp circuits to implement both proportional and lead compensation to control the translational air bearing set-up described in labs 3 and 4 (shown in Figure 3-27 on page 172). As in lab 4, the voice coil is driven by a power op-amp with a gain of two, as illustrated in Figure 3-45. The LVDT outputs a voltage, v_o, proportional to the position of bearing shaft. The sensor output is subtracted from a reference voltage setting, v_r, using an op-amp circuit. The block diagrams of the two controllers are given in Figure 3-46.

Note that the actual circuit, shown in Figure 3-47, also scales the resulting "error"
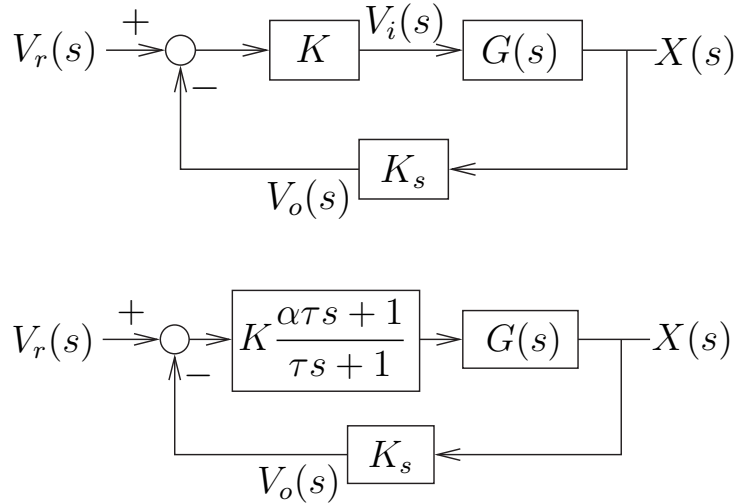
Figure 3-46: Block diagrams of proportional (top) and lead (bottom) controllers for spring-mass-damper system. Drawing by Andrew Wilson

by $1/2$ (i.e. $v_1 = (v_o - v_r)/2$). (This is effectively cancels out the gain of two in the later power op-amp stage mentioned earlier, however.) An additional op-amp circuit, shown in the right half of Figure 3-47, creates an analog lead controller. The circuit is designed so that students can easily convert this into a proportional controller simply by disconnecting the branch with R_3 and C from the circuit.

Students can physically play with the controlled spring-mass-damper system to feel the changes in springiness and damping that result as they adjust proportional
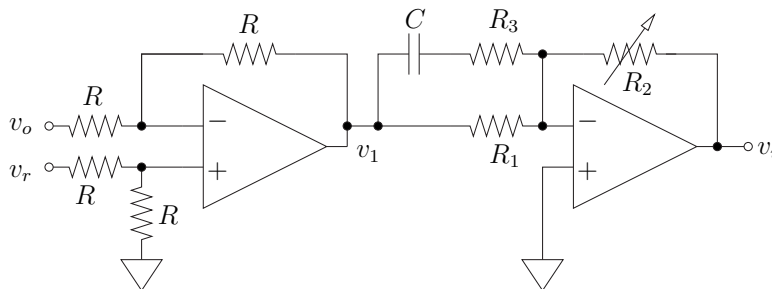
Figure 3-47: Circuit diagram for lead controller. Students can disconnect R_3 and C to compare the dynamics of the resulting proportional controller, instead. Drawing by Andrew Wilson.

and derivative gains. They can disconnect the mechanical spring, for instance, to feel that the controlled system still provides a very similar stiffness. The reference voltage come from a signal generator. Students can set different DC values and watch the equilibrium position of the mass change as a result. They can also drive the system with step or sinusoidal waveforms to analyze transient and frequency response (respectively).

Controller design is often an intimidating subject for undergraduates, and we hope this early hands-on experience will be an aid in developing an intuitive understanding for later courses in control. The lab also provides some introductory circuit experience. Although the students are not asked to design the control circuits used in the actual lab, we do require them to analyze and design op-amp circuits in the pre-lab assignment. Perhaps the most central point we hope students will take away with them is the basic concept that design of a control system essentially amounts to the modification of a system to obtain desired changes in the dynamics.

3.9.2 Control of DC Motor System

The project described in this section has been used to introduce to controls *as an alternative to* the laboratory just described (in Section 3.9.1). This control lab uses a DC motor setup originally created as a laboratory project for 2.737 Mechatronics.[2] A picture of the motor hardware is shown in Figure 3-48. The motor is mounted for 2.737 so that it drives a potentiometer (shown in the foreground), but this (position) output in not used in 2.003. Instead, students use the tach output to command the voltage signal driving the motor.

Figure 3-49 shows a schematic of the DC motor, and Figure 3-50 represents the feedback due to back emf which occurs when one commands voltage (as opposed to current) to drive the motor. Note that the gain of two (at the left in both figures) occurs in the power op-amp stage, as illustrated earlier in Figure 3-47 on page 189. As configured in Figure 3-50, the controller outputs a command voltage proportional

---

[2]More information on other projects for 2.737 can be found on page 132 of Chapter 2

to the measured motor velocity. To create a PI controller, one can replace the proportional gain block, $C(s) = K_{tach}$, with a controller of the form $C(s) = K\tau s + 1/s$.
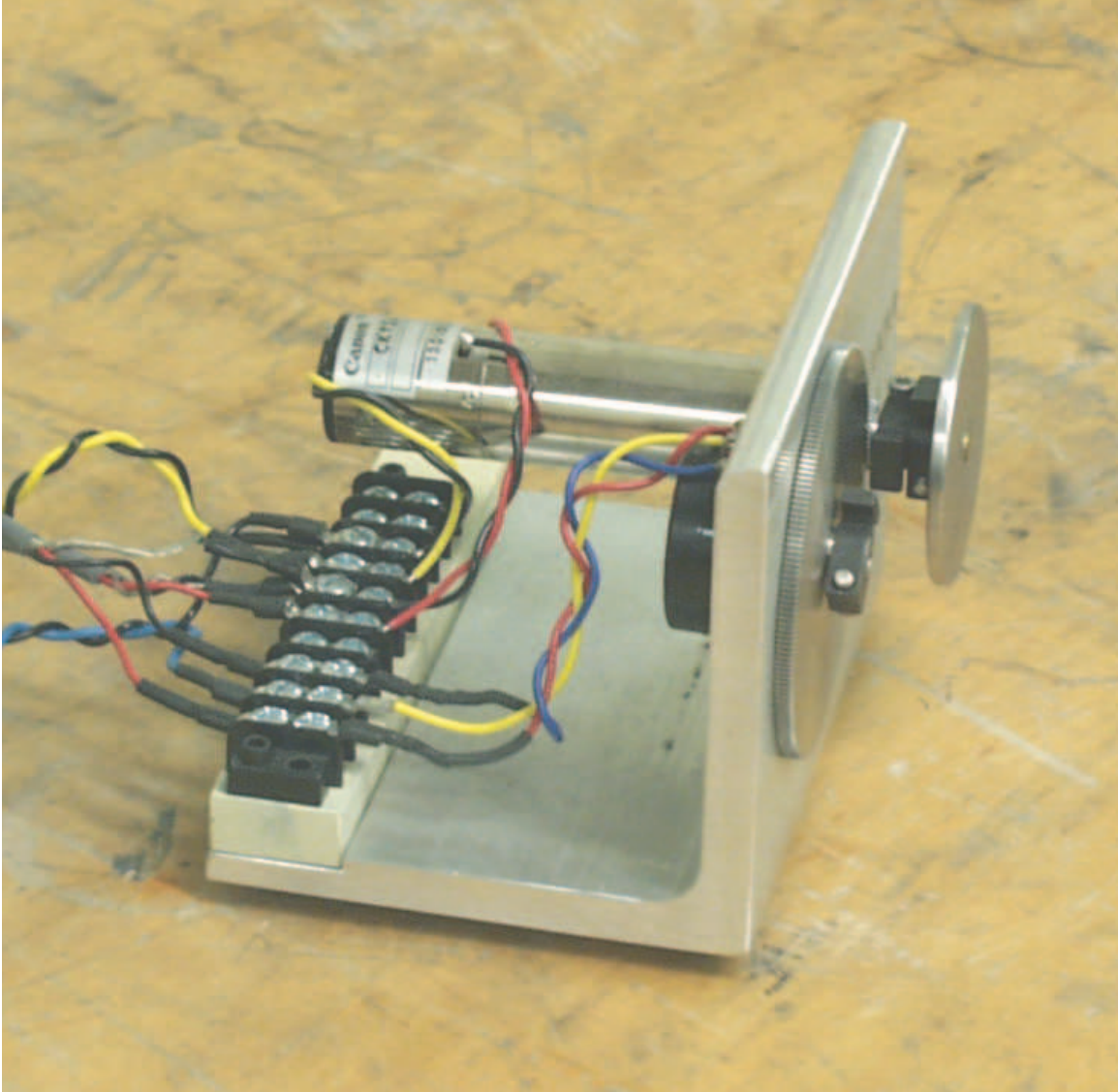
Figure 3-48: DC motor hardware for introduction to controls
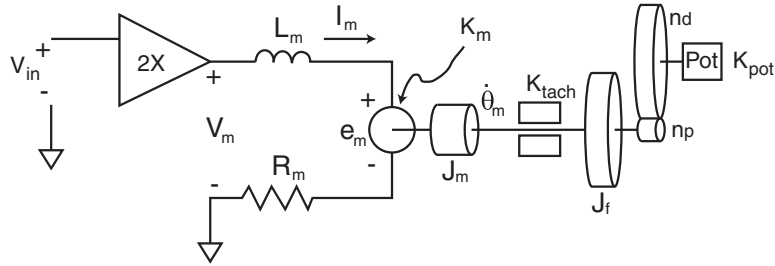
Figure 3-49: Schematic of DC motor system. In this lab, students use only the velocity output of the tachometer (not the position measurement from the potentiometer) for control. Drawing by Marty Byl.
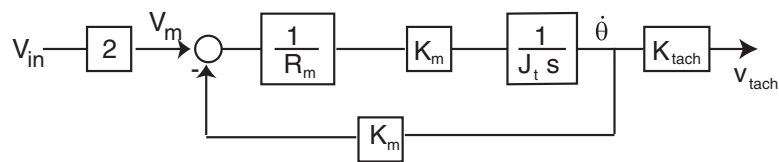
Figure 3-50: Block diagram of a voltage-controlled DC motor system. Note the gain of 2 comes represents the power op-amp stage (as described earlier in the text). Drawing by Marty Byl.

Students use the op-amp circuits shown in Figures 3-51 and 3-52 to implement proportional and PI control, respectively. Students should observe that proportional control adds additional "springiness" to the system response, and that while increasing the proportional gain can reduce steady state error, integral action is needed to drive the steady state error to zero. Velocity control of a rotational system is clearly an advantageous way to demonstrate the effects of a free integrator, since any steady state error without the integrator is not as dramatic when commanding position (and since a motor can spin continuously, while a linear system with finite velocity would just run "off its tracks" - or more likely into a stop of some sort).
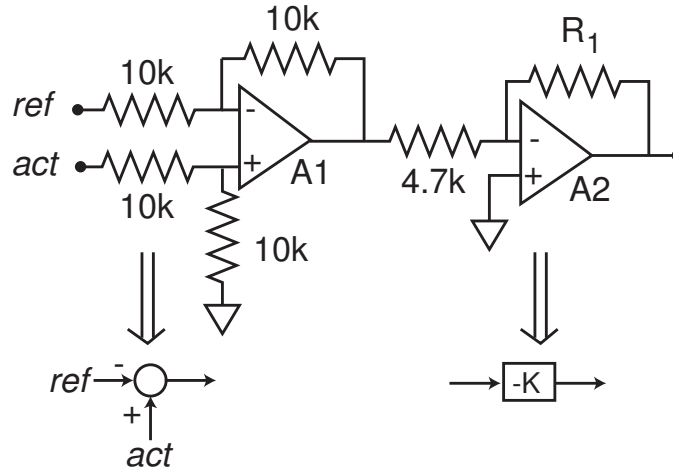
Figure 3-51: Op-amp circuit for proportional control of a DC motor. Drawing by Xiaodong Lu.
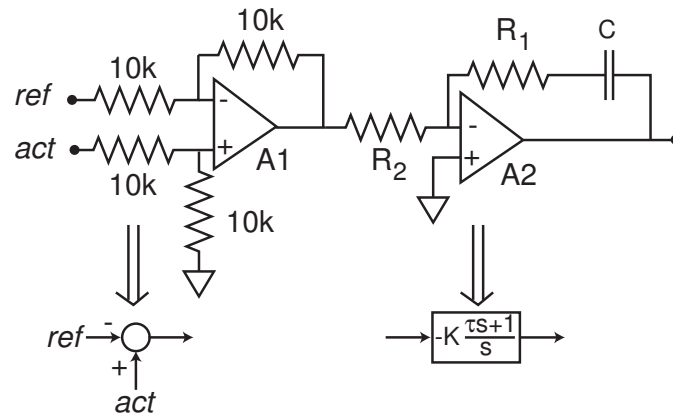
Figure 3-52: Op-amp circuit for PI (proportional-integral) control of a DC motor. Drawing by Xiaodong Lu.

Teaching the controls laboratory with a new set of hardware (i.e. not yet seen by the students in the class in previous labs) also allows us to introduce new concepts. Students can note how the back emf for the rotational motor (more commonly modeled in similar classes) is analogous to that in the linear voice coil motor used in labs 3 and 4. They are also exposed to new sensors (the tach).

Finally, as in the previous control laboratory described, we hope students will begin to appreciate how controllers modify system dynamics. Design of mechatronic devices would corresponding therefore involve *design* of the combined mechanical, electrical and control system dynamics, together.

3.10   Web Documentation of ActivLab Projects

We have documented each of the ActivLab projects on the class website for 2.003 Modeling Dynamics and Control I. Others are welcome to use any of the concepts presented in this thesis or on the ActivLab website, which is currently located here:

http://web.mit.edu/2.003/www/activlab/activlab.html

Web addresses are prone to change, however, and a more reliable method of accessing our site on the web is through the homepage for MIT's OpenCourseWare (OCW) program, which was described on page 119. OCW will eventually document materials for virtually every class offered at MIT. One can presently access the OCW database from the following address:

http://ocw.mit.edu/index.html

2.003 should be listed among the course offered by the Department of Mechanical Engineering.

Chapter 4

Other Project Suggestions in Dynamics

Chapter 3 reviewed the ActivLab experiments we developed and have been used in teaching 2.003 since the Fall of 2001. Chapter 4 describes other projects which may also be useful for teaching dynamics. These are distributed into three categories: (1) additional laboratory projects or variations of existing labs which could be added to the ActivLab curriculum, (2) In-lab demos of phenomena or technology (sensors, actuators, bearings, etc) that are relevant to particular labs, and (3) formal lecture demonstrations (i.e. of the type often seen in introductory college physics). Compared with the survey in Chapter 2, Chapter 4 presents ideas which have been developed at MIT[1] specifically for 2.003, while the Chapter 2 surveys the work of others, including various hands-on projects and demos for teaching dynamics and related disciplines (e.g. mechatronics, robots and physics).

4.1   Possible ActivLab Additions

The next three sections briefly describe some ideas for additional laboratory projects in dynamics. Sections 4.1.1 and 4.1.2 each describe prototypes of rotational and translational 2nd-order systems we built as possible alternatives to the translational

---

[1] by Prof. Trumper and other staff

2nd-order system described in Section 3.5, and Section 4.1.3 discusses the possibility of manufacturing a higher-order dynamic system at the MEMS scale.

4.1.1 2nd-Order Spring-Inertia-Damping Rotational System

We considered including an ActivLab project with a rotational system analogous to the second-order translational system described in Section 3.5 (page 170). Figure 4-1 shows a prototype of the system. The torsional spring is a length of the same stainless steel welding rod used to create the linear spring in the translational second-order system. One end of the spring is clamped to a fixture and the other is attached at the center of the shaft end.

It was quite difficult mounting the spring along the axis of the shaft in the prototype, which involved intermediate fixturing to align everything carefully. Figure 4-2 shows the prototype clamp at the shaft end of the spring. The split collar clamp holding the fixture to the shafting can be taken off and replaced without loosening the clamp on the torsional spring. Once the spring is successfully mounted on center, in other words, it can be reused from term to term (until it fails) without realignment.

We originally intended to notch a vee in one half of the clamp to hold the spring at three points. It proved to be much easier to align the spring if the two clamping surface were simply flat, however. For a prototype showing proof of concept, the clamp was adequate, and the spring is remarkably close to being perfectly concentric.

The aluminum flywheel shown in Figure 4-1 serves two purposes. First, it makes the total inertia of the system approximately three times that of shaft alone. Second, eddy currents generated on the surface of the disk as it moves inside the field of the magnets create damping. The magnet fixture (shown at left in the bottom photograph in Figure 4-1) can be loosened from its mounting and slid into a new position, providing a continuous range of possible damping values for the system. Also, when the magnets are moved away from the shaft to their full extent, the resulting system has an *very* low damping coefficient ($\zeta < .005$).

Recall that the translation lab system has only two possible damping values which differ by about a factor of two. In that lab project, the students can not observe a
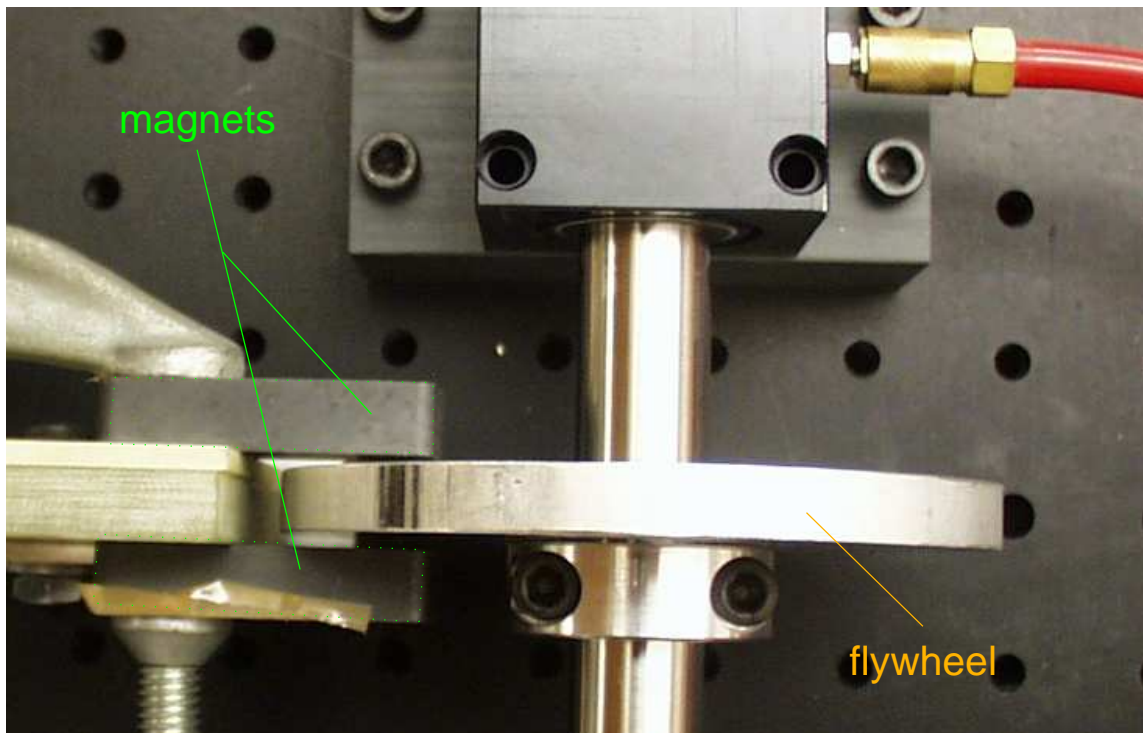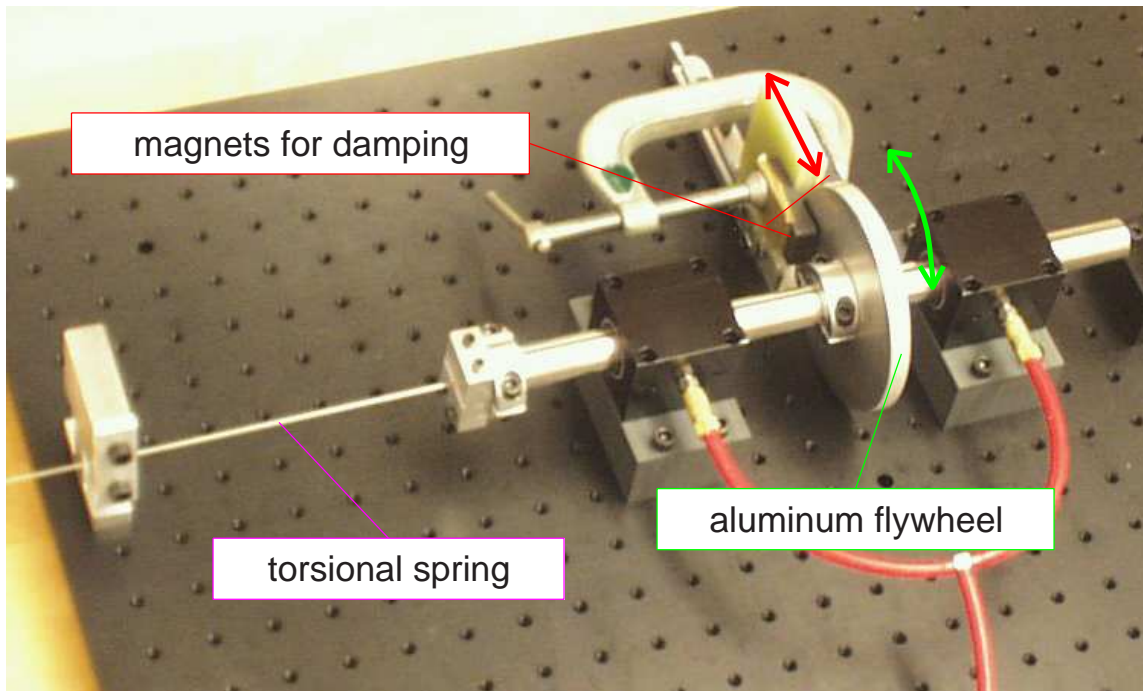
Figure 4-1: Prototype of rotational spring-inertial-damper system - *Detail of the eddy current damping mechanism is shown in the lower picture.*

spring must be mounted concentric with shaft
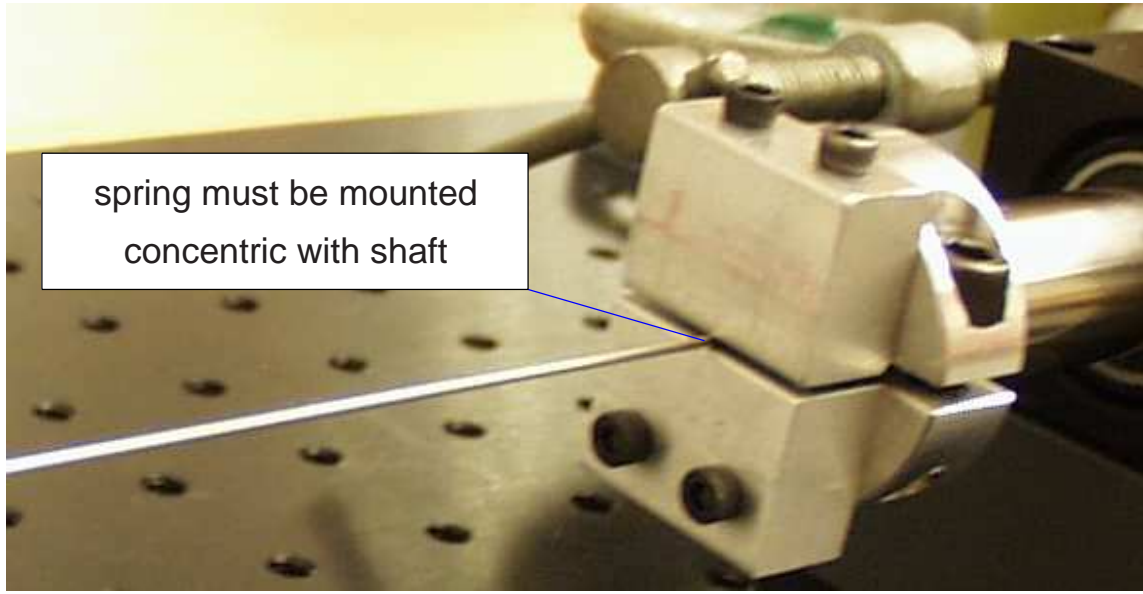
Figure 4-2: Concentric spring mounting in rotational spring-inertial-damper system

system response with virtually no damping. Seeing the rotational system's response without damping is an excellent way to convince the students that friction in the air bearings is extremely low, and it allows the students to compare the damped and undamped natural frequencies of a system.

A final argument for including a rotational lab project is simply that it reinforces an understanding of second-order system dynamics. In general, it has taken two laboratory projects with the translational second-order setup to get across the basic concepts of characterizing a system from its transient (step or impulse) response. Having the second of these labs involve a new setup has advantages and disadvantages. In gives the students greater breadth and exposure to types of physical systems, but lab time might also be wasted in familiarizing the students with a new set of hardware.

4.1.2 Whiskered Spring Cantilever

The lab set-up presented in this section, shown in Figure 4-3, is nearly identical to the 2nd-order system we presently use in 2.003, which is described in Section 3.5 on page 170. The difference between two is the design of the cantilever spring used. The system used in 2.003 uses a single piece of welding rod, while the alternative version

clamp to shafting

shaft oscillation

whiskered spring

clamped clamped
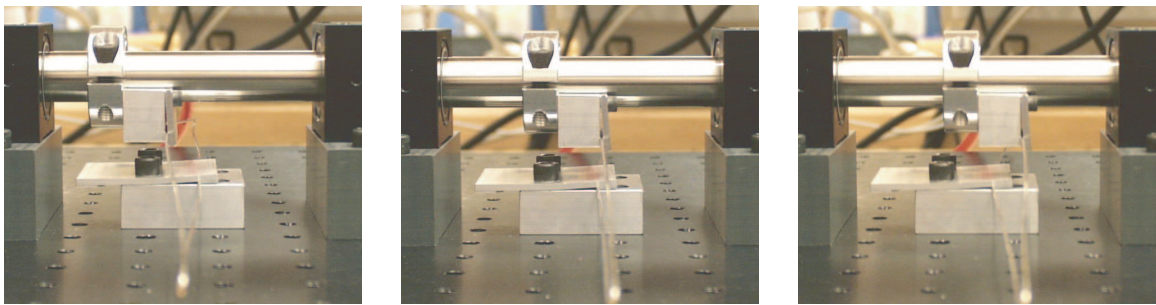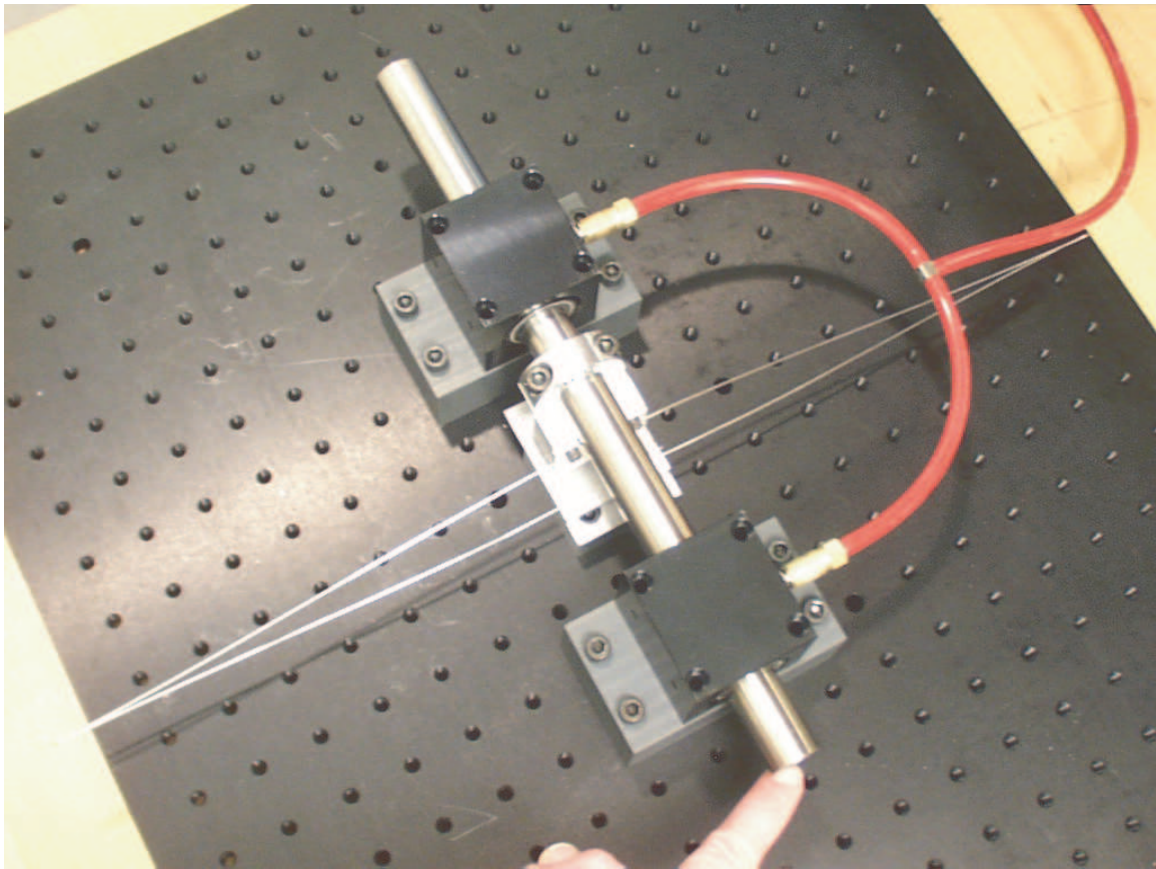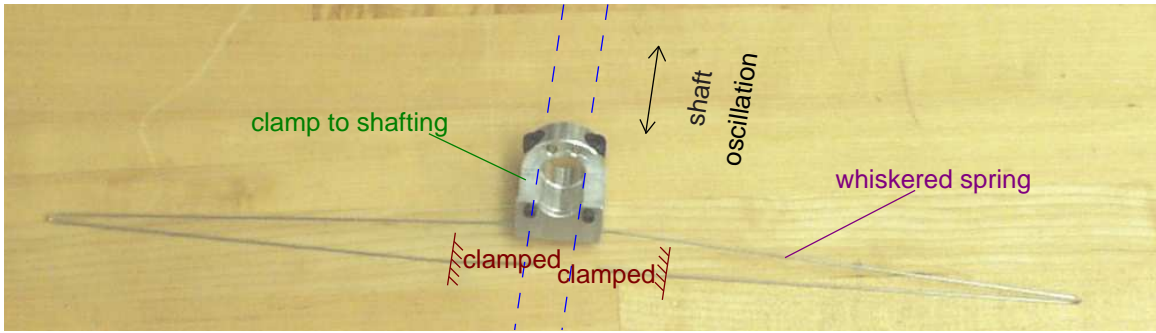
Figure 4-3: Prototype of whiskered spring for translation system

described here would use two lengths of rod, each doubled over into a "whiskered" configuration.

The motivation for the whiskered configuration is to create a more ideal spring which is more nearly linear. The spring we currently use in 2.003 is substantially linear for small displacement, but it stiffens noticeably for larger travel (on the order of a centimeter or so). Section 4.2.6 on page 214 describes this spring stiffening in more detail. The whiskered spring also eliminates rotational coupling of the shaft with translational movement. With the single-rod cantilever we settled on for the labs, the shaft rotates somewhat as it moves back and forth, due to the geometric constraints of the design.

There are several disadvantages of the whiskered spring, however. It would not be as simple to make the spring adjustable. In contrast, the single-cantilever construction now used in 2.003 can be set to different lengths easily by students during the lab. It would also be more difficult for the TA's to align and assemble, and it is not as compact an elegant (so that one can easy picture students bumping into and bending the long whiskers).

4.1.3 MEMS Systems

We have also considered designing and manufacturing MEMS devices which illustrate higher-order system dynamics. Numerous researcher have developed spring-mass systems at the MEMS scale which are driven by parallel-plate capacitors, particularly in developing accelerometers. Many companies (including Analog Devices, Motorola, and Delphi Automotive Systems) currently sell a large volume of MEMS devices to the automotive industry, for instance, and MEMS accelerometers are also being developed as an alternative to using geophones for seismic measurements [130]. *Higher-order* spring-mass structures have also been designed and tested at a few research labs, including Sandia [62], the University of Michigan [148], and National Tsing Hua University in Taiwan [88].[2]

---

[2]Sandia and U. Mich. have designed translational systems, while those developed at the Tsing Hua involve torsional modes.
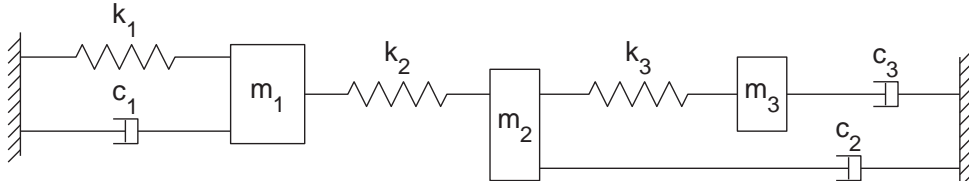
Figure 4-4: Schematic of potential MEMS higher-order system
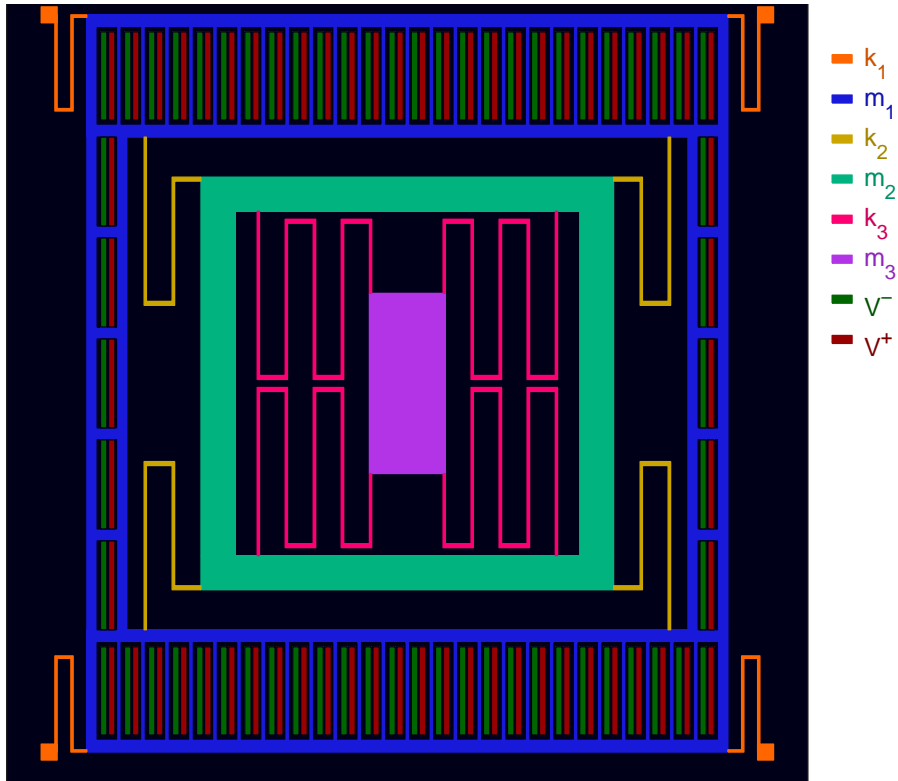
Figure 4-5: MEMS implementation of higher-order spring-mass system

These complex, 3-dimensional systems can be created by depositing alternating layers of polysilicon (polySi) and a sacrificial oxide (e.g. SiO_2). The oxide layers can later be etched away with an appropriate acid (typically buffed HF) which dissolves the oxide rapidly while leaving the polysi features relatively uneffected. This "releases" the features created in polysi. Each layer is partially masked, so that material is deposited on only part of the entire structure. This allows the solid polysilicon structures to mate and bond with one another on various layers, as depicted in Figure 4-6. Creating interesting structures requires the design of multiple, complex masks

of the geometries for the various layers.
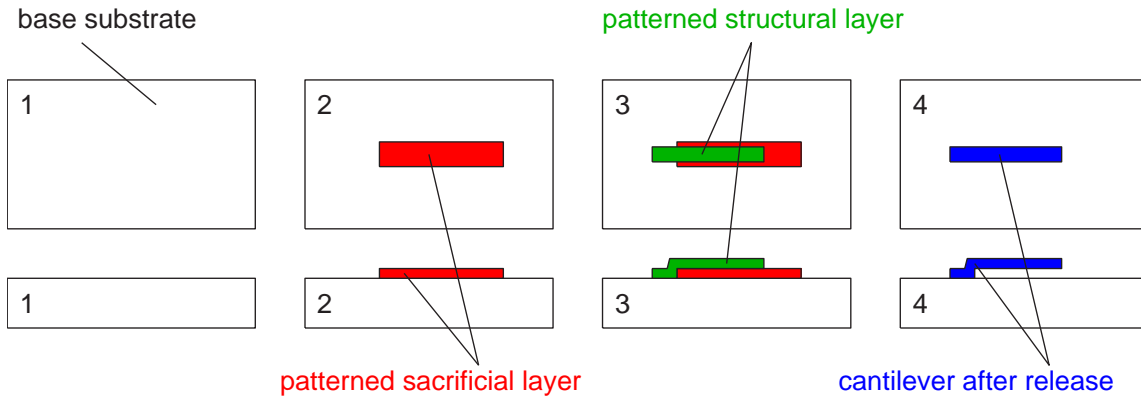
Figure 4-6: MEMS surface machining by release of sacrificial layers. The patterns in steps 2 and 3 are created by masking the nonstructural area in each layer. The structural layer deposited in step 3 carefully overlaps onto the base substrate to create a continuous structure once the sacrificial material has been etched away. This cantilever example is shown on page 59 of Stephen Senturia's book "Microsystem Design" [182].

A layer of silicon nitride can be added to bearing surfaces to reduce friction. The dominant modes of viscous loss in such a system are Couette flow damping and squeeze film damping. Couette flow occurs as fluid shears between parallel plates. At the small scale of most MEMS devices, air provides significant viscous damping as the plates move parallel to one another. Squeeze film damping occurs when parallel plate structures move toward or away from one another, essentially forcing (squeezing) air so it flows between the plates in Poiseulle flow. MEMS structures can easily be manufactured such that there is virtually no damping between one mass and another, - only between each mass and the reference ground.

The springs in this MEMS structure would be folded structures analogous to the whiskered springs shown in Figure 4-3. The folded spring shown in Figure 4-5 is a standard MEMS implementation of a linear spring. Figures 7-21 and 7-22 show the ADXL accelerometer used for complimentary filtering of the gyro drift, which uses a very similar spring. The proof masses would be polysilicon "blocks", linked to one

another and the base substrate through the folded springs.

Many MEMS devices are actuated using capacitive, electrostatic actuators. One type, called a "comb drive", consists of two sets of interlaced combs which pull toward one another when the charges on the two plates are opposite in sign and push away from one another when the plates have the same sign charge. As the interdigitated fingers move parallel to one another, the gap between fingers remains essentially constant; only the amount by which they overlap changes.

The capacitive actuator shown in Figure 4-5 *is not a comb drive* but a parallel plate electrostatic actuator. The parallel plates are simply attracted or repelled, so that here the gap between the plates *does* change. Consequently, this type of actuator is quite nonlinear (compared with the comb drive). The parallel plate actuator is generally capable of higher forces per unit area than the comb actuator, and is easier to manufacture, but it has a very short stroke length.

One could look at the static structure using a low-power microscope, but both the time and geometric scale would clearly make the dynamics of this device unobservable to the naked eye. (The frequencies would be on the order of kiloHertz, with maximum displacements of roughly a micron or so.) MEMS devices supply a host of dynamic effects of interesting dynamics to analyze in class, bringing together many disciplines (fluids, dynamics, thermodynamics, materials, design, etc) for analysis. The higher-order MEMS system described here would also present both an additional example of a dynamic system and a useful introduction to field of microsystem design, which now seems certain to grow in significance over the next couple of decades. Mechanical engineers are particularly well-suited for understanding MEMS design, because it requires expertise in so many engineering disciplines, and a lab project such as this could serve as a useful introduction to interest our students in this growing field.

4.2 In-Lab Demos

The remainder of this chapter documents some demostrations which have been used in teaching 2.003 over the past few terms. While there are multiple sets of hardware for

each of the laboratory projects (described in Chapter 3), each piece of demonstration hardware is typically a one-of-kind apparatus. In general, these demos are designed to further illustrate some particular aspects in one of more of the laboratory projects.

I have made a loose distinction between "laboratory" and "lecture" demonstrations. The first group presented attempt to demonstrate some physical phenomena relating to the laboratory projects that may not be obvious during the course of the lab. These include such things as how a voice coil motor or LVDT sensor works, the viscous damping created by eddy currents, and spring stiffening effects in our cantilever. A critical component in all these demonstrations is that students have the ability to touch and play with the hardware individually - something not typically possible in a large, lecture demo setting. We have set up some of these demonstrations during labs and encouraged students to come over individually at some point during the 3-hour lab to look at them.

The remaining group of "lecture" demonstrations described after this are generally appropriate for demos in a larger, in-class setting, but again, the distinction is very loose! Some of the lecture materials could certainly be used in exercises in laboratory or recitation section, and the lab demos still have use an non-tactile (visual) demonstrations during a lecture.

4.2.1 Purpose of Hands-on Demonstration Hardware

The main purpose of the laboratory demos described here is to isolate particular details and physical phenomena relevant to the lab projects in order to focus student attention to them more clearly. There are many details that become obfuscated (or unobservable) in the fully-assembled hardware for a particular lab.

For instance, when asked about potential sources of error or non-ideality in the equipment, students will often cite the air bearings as a likely source of error. Our purpose in using air bearings was to insure any such issues are miniscule. We find this is not at all obvious to the students, however, because the voice coils in the translational spring-mass-dampers *always* always provide some viscous damping (whether shorted or left open-circuit, because eddy currents are free to flow in the aluminum

housing for the coil). The first demo described below addresses this issue by showing the system response when the voice coil is completely removed from the set-up. Other demonstrations similarly aim to focus attention on particular details about the hardware used in the labs.

4.2.2   2nd-order Translational System with No Damping

As mentioned above, it can be useful to demonstrate that the viscous damping in the 2nd-order system due to the air bearings is small, and any Coulomb friction (from imperfections or dirt along the shaft-bearing interface) is truly miniscule. The data in Figure 4-7 show that the viscous damping for such a system is on the order of 1/100 that of the system with the voice coil mounted, even when it is open-circuit.

If students then disconnect the spring from the damper-less system and either tap or spin the shafting of this system, it becomes viscerally clear that any losses from damping or Couloumb are low. We have also left some unused bearings in the lab. We have allowed curious students to run a finger along the porous carbon surface while it is connected to an air supply, to feel how "slick" the interface feels for themselves, and we have left some bearings disassembled (i.e. the separate pillow block housing and cylindrical core) to show students how they work.

4.2.3   Rectangular Voice Coil

During the development of the ActivLab projects, we considered manufacturing our own voice coil motors. The prototype we developed is shown in Figures 4-8 and 4-9. Ultimately, we were instead able to find a commercially available circular voice coil with a large stroke at a reasonable price from BEI (a little over $300 a piece, in quantity of 30). The circular geometry also allows the shaft to rotate as it translates back and forth, and this in turn allows us to use a simpler cantilever (as illustrated in Figure 3-28 on page 173).

The prototypes of the rectangular voice coil make useful in-lab demos for several reasons. First, students can see the magnets and coil more easily, since the sides of
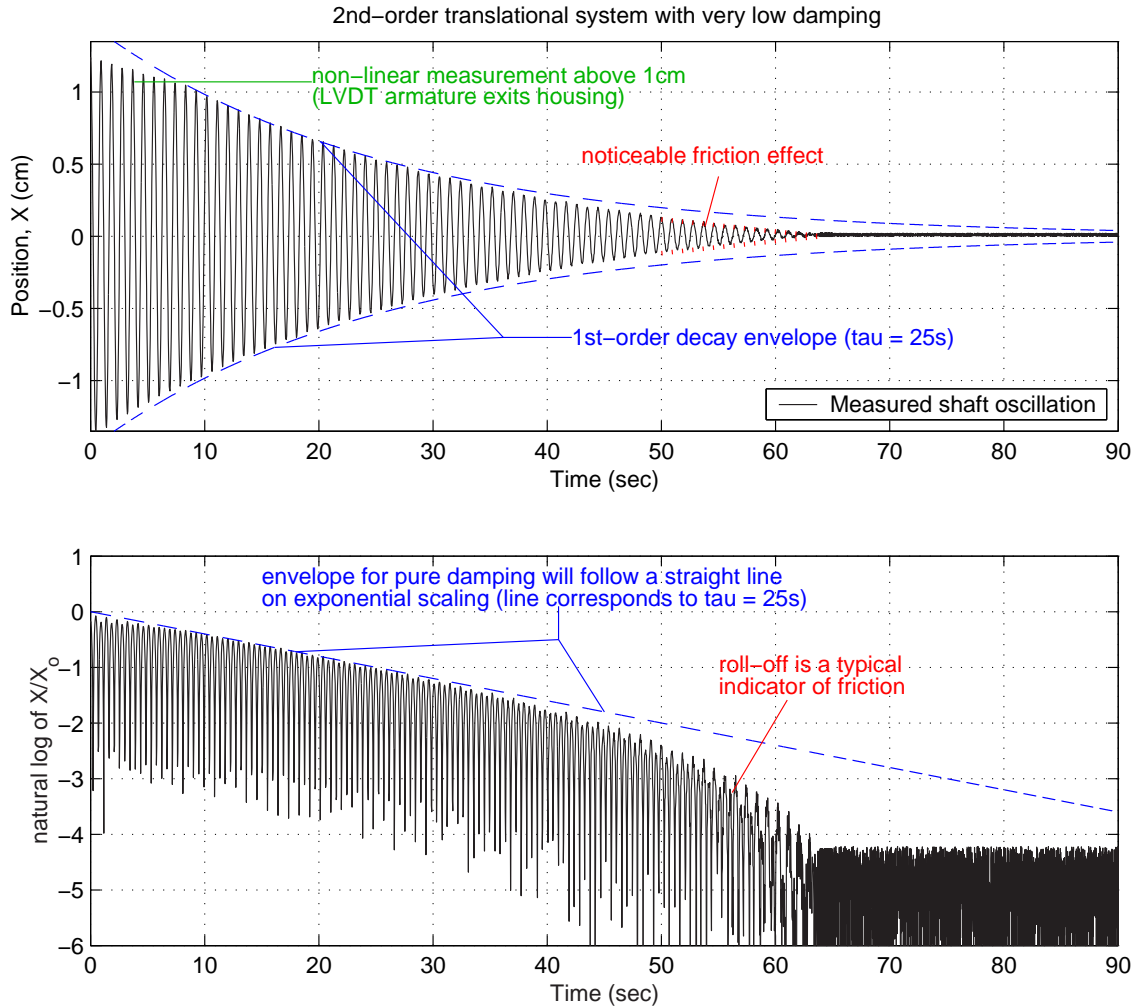
Figure 4-7: 2nd-order system response without eddy current damping. The data above show the response of the second-order translation system with no intentional sources of damping or friction. Here, $m \approx .85$ kg, $k \approx 39$ N/m, and $f_n = \sqrt{k/m}/2\pi = 1.08$ Hz. The decay envelope corresponds to $\zeta \approx 0.005$, so $c \approx 0.05$ N/(m/s). This is $\sim 1/100$th the damping measured with the voice coil in place and open-circuit. (See Figure 3-32 on page 177.) The roll-off seen in the log-scale plot above is indicative of contact friction. Any friction force at the air bearing interface can be approximated as: $F_{friction} = \mu F_{Normal}$. We expect the normal force will be dominated by the force of gravity: $F_{Normal} \approx mg = 8.3$ N. (This neglects any forces due to misalignment of the bearings or tension from the cantilever.) Using MATLAB simulations, the response in the data can be well-modelled using $F_{friction} \approx 0.025$, in which case $\mu \approx 0.025/8.3 = 0.003$
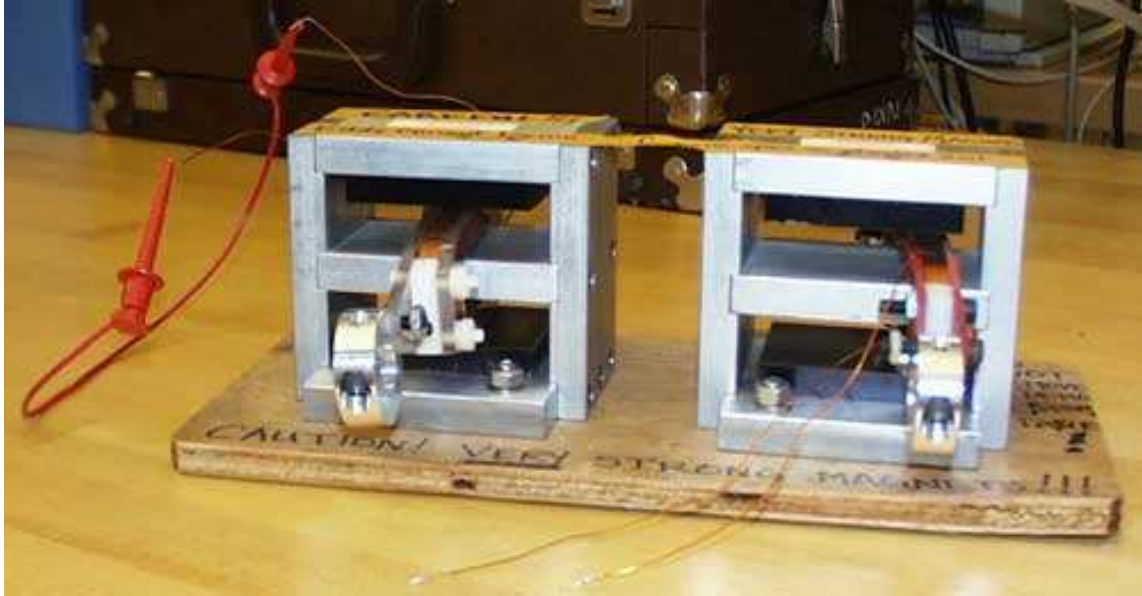
Figure 4-8: Rectangular voice coil motor/generator. These two rectangular voice coils, manufactured in-house, are conveniently transparent for illustrating the vector cross-products involved in describing their function as either a motor or generator. Also, unlike the BEI voice coils, these coils have essentially zero damping when the coil is open. In the BEI actuators, eddy currents travelling on the aluminum support stucture for the coil generate damping whether the coil is open or closed. Image by Willem Hijmans [83]

the actuator are open. The neodymium magnets, seen more clearly in Figure 4-9 in this section, are aligned so that the field lines are essentially vertical (straight) where they intersect the wires in the coil. The sections of the coil between the magnets also run in a straight path. This makes it easier to visualize the vector cross-product of the Lorentz force law [81, page 1.4]:

$$\mathbf{f} = q(\mathbf{E} + \mathbf{v} \times \mu_o \mathbf{H}) \tag{4.1}$$

Putting a current through the coil thus generates a force on the wires:

$$\mathbf{f} = nL\mathbf{I} \times \mu_o \mathbf{H} \tag{4.2}$$

where there are n wires, each of length L.
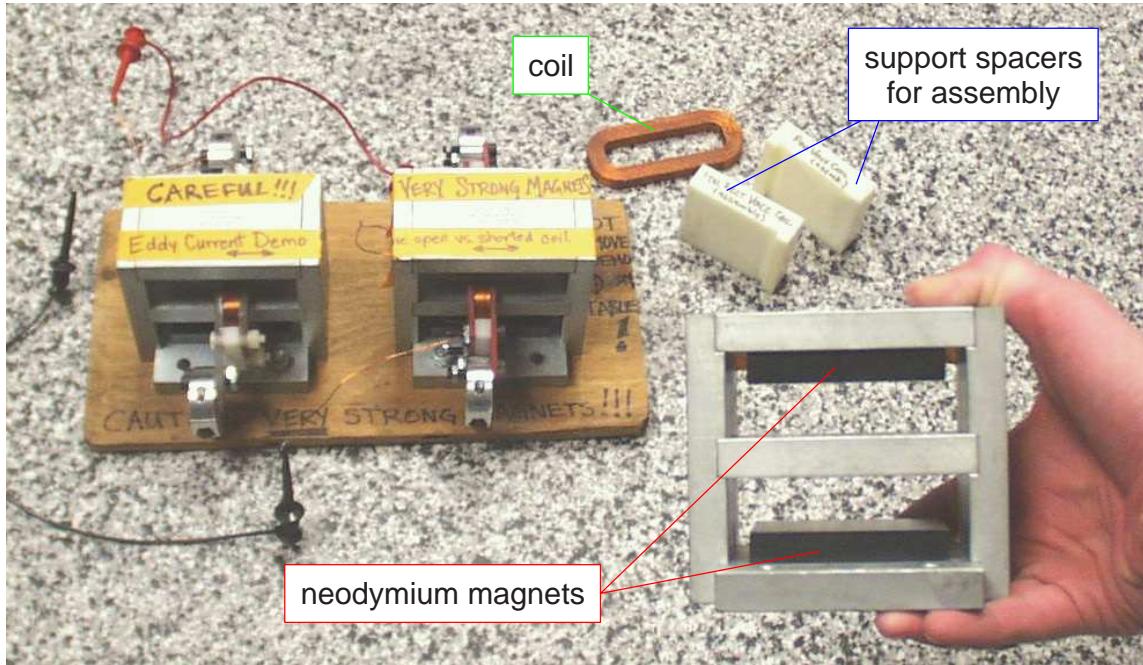
Figure 4-9: Rectangular voice coil components.

If we move the coil through magnetic field lines with some velocity (v) when it is open-circuited, we are obviously moving all the electrons in the wire.[3] The electrons experience a force (as predicted by the Lorentz force law) and accelerate along the length of the wire. The system reaches an equilibrium when there is no longer any force exerted (i.e. acceleration) on the electrons. This happens when the force due to the electric potential across the wire balances the force created by moving the wire at some velocity:

$$\mathbf{E} = -\mathbf{v} \times \mu_o \mathbf{H} \qquad (4.3)$$

At equilibrium, the electrons have no net velocity (i.e. they can not flow in the open-circuited case), and one therefore feels no resisting force as we move the wire.

If the coil is short-circuited, however, the force generated on the electrons will result in a flow of current. Imagine we move the wires in the $+\mathbf{y}$ direction, with the length of each wire parallel to the x axis and the field aligned in the $+\mathbf{z}$ direction. The electrons will flow along the wire in the $+\mathbf{x}$ direction ($\mathbf{y} \times \mathbf{z} = +\mathbf{x}$). This component

---

[3]...and protons and neutrons - we are moving the entire wire, after all!

of the electron velocity then generates a force that *opposes* the movement of the coil, since $\mathbf{x} \times \mathbf{z} = -\mathbf{y}$. (This is the phenomenon we usually refer to as the "back emf" in a linear or rotary motor.)

The result is a force (in the $-\mathbf{y}$ direction) proportional to the velocity at which we move the coil (in the $+\mathbf{y}$ direction). In other words, the system with the short-circuited coil experiences viscous damping as the wires in the coil cut through magnetic field lines, while the open-circuited coil does not. As mentioned in Section 3.5, because the aluminum cup housing the coil of the BEI (circular) voice coil allows eddy currents to flow, one feels viscous damping both when the coil is open- *and* short-circuited. The coils in our prototype rectangular voice coil by contrast have intentionally been mounted in a non-conductive material. (In Figures 4-8 and 4-9, we used clear acrylic for the coil at the left and electrical-grade fiberglass (GP03) for the one at right. Phenolic G10 splintered apart when we tried to water-jet the oval forms which sandwich the coil.) *The rectangular voice coil demo allows students to feel a dramatic difference between the open- and short-circuited coil configurations.*

Finally, students can also connect two voice coils with two patch cords to create a complete circuit. The flow of current generated as the first coil is moved through the field must flow through the second coil as well. This generates a force on the second coil, causing it to move. It allows students to observe how a motor also functions as a generator (in the proper context).

4.2.4 Eddy Current Demos

The eddy current demo described here uses the housing of the voice coil prototype described in the preceding section. The housing hold two very strong (neodymium) magnets. If students move a piece of aluminum through the opening in the housing, they feel significant viscous damping. (Aluminum is an obvious material to use, since it is not magnetic but does allow the flow of current.)

The demonstration is quite dramatic. Students only need to move the aluminum back and forth by hand to feel how significant the viscous damping forces are. However, if one lets an aluminum bar fall through the housing, as shown in Figure 4-10,

the bar quickly reaches a constant (terminal) velocity (such that the force due to gravity balances the viscous force from the eddy currents), moving slowly enough that one can easily let go with one hand and casually reach underneath (with the same hand) to retrieve the bar before it exits the field.
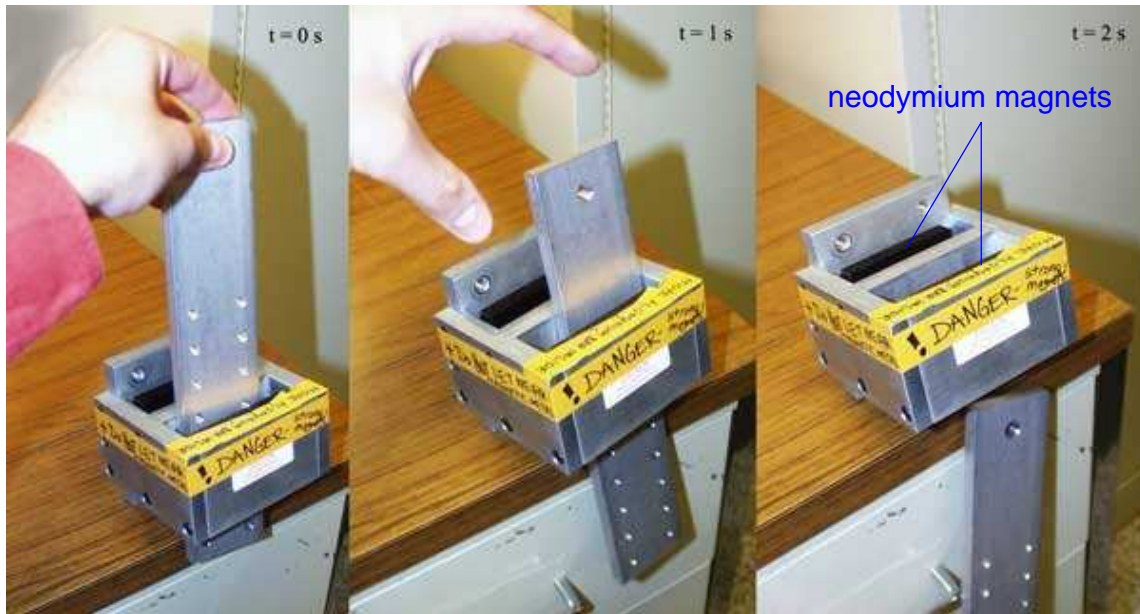
Figure 4-10: Eddy current demonstration. A (conductive) aluminum bar moves through a strong magnetic field created by neodymium magnets, which induces circulating currents on the surface of the bar. These currents in turn generate a magnetic field that opposes the field from the magnets and a corresponding force that retards the motion of the bar. This "eddy current damping" is proportional to the velocity of the bar. Image by Willem Hijmans [83]

4.2.5 Demo of How an LVDT Operates

We do not explain the operation of the LVDT (linear variable differential transducer) sensor used in Labs 3 and 4 (described in Sections 3.5, 3.8, and 3.9). The LVDT is introduced as a convenient transducer which outputs a voltage proportional to the position of its armature within the housing, to allow us to observe and record data on an oscilloscope.

We put together a very simple demo, shown in Figure 4-11, that can be used during the relevant lab sessions to illustrate how an LVDT works. The housing for the LVDT consists of a length of phenolic tubing, shown at left. Thin (motor) wire is wound about the tubing in three sections: a central "primary" coil and two "secondary" coils. The "armature" of the sensor is just a slug of steel that fits nicely within the tubing.
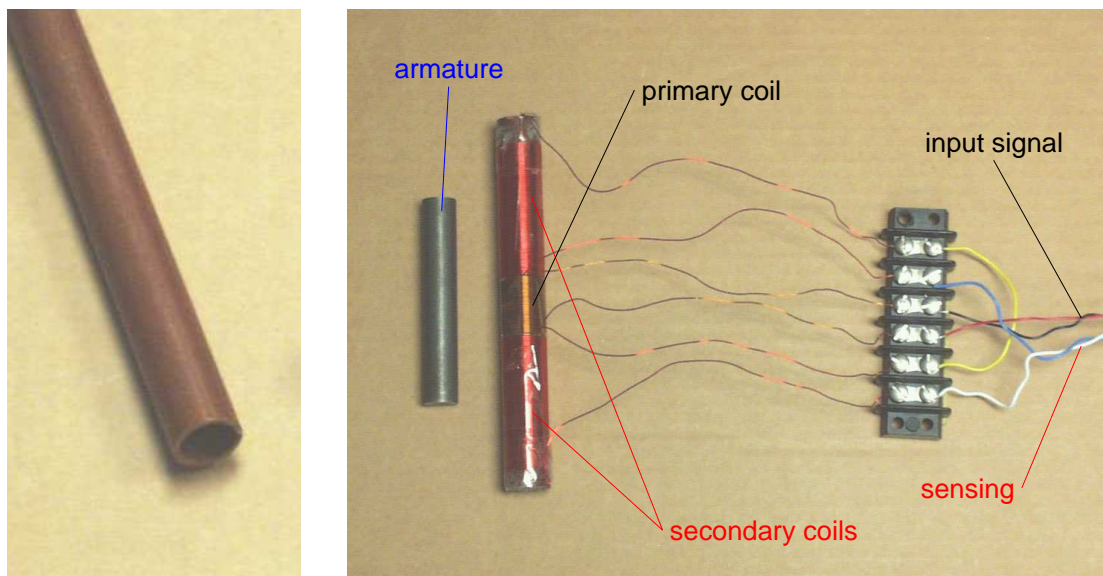
Figure 4-11: Simple LVDT Demo

To operate the LVDT, the primary coil is driven with a sinusoidal input. This generates a time-varying magnetic field. If the metal slug in the tubing overlaps some of the primary and secondary coil(s), it will create a transformer, and current will be induced in the secondary coil(s). By connecting the two secondary coils appropriate, we can make the two "cancel out another one" when the slug is centered within the

tubing. Then, as we displace the slug from this center-point, the currents in each of the secondary coils will become increasing unbalanced. As a result, the *amplitude* of the (net) sinusoidal signal induced in the secondary coils will be proportional to the distance away from the center-point.

This demo does not address the signal processing necessary to extract the amplitude of the sinusoidal signal (to produce a DC voltage output proportional to displacement). However, it does allow students to observe the primary and secondary waveforms as the slug is moved by hand within the tubing. They can observe how the waveform for the secondary coil changes by 180 degrees when the slug moves past the center-point, for instance, that the amplitude grows with the displacement from the center, and that there is a phase lag between the primary and secondary waveforms. All three of these effects are illustrated in Figure 4-12.
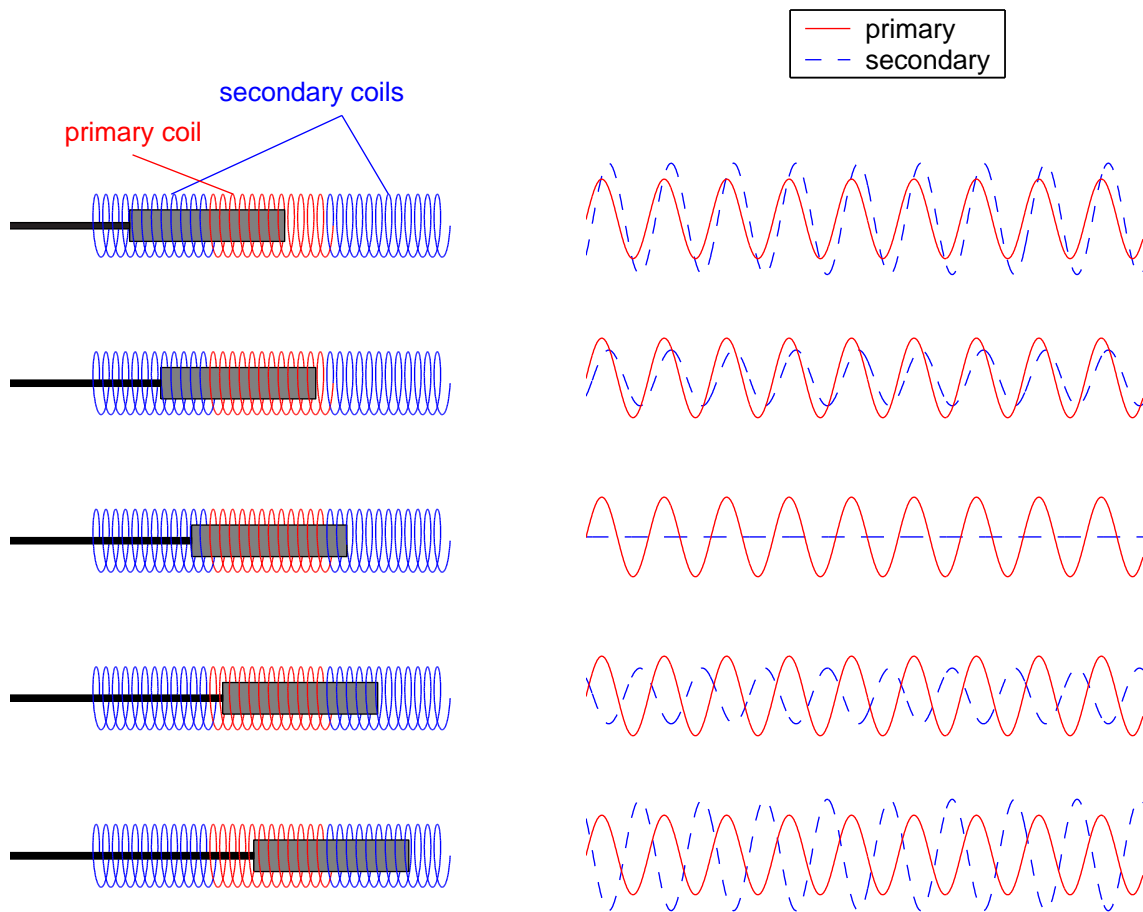
Figure 4-12: LVDT schematic with sinusoidal signals. The primary coil is driven with a sinusoidal excitation of constant amplitude. A time-varying magnetic field is thereby created in a metal slug within the coils. If the slug is perfectly centered, the equal and opposite signals in the secondary coils cancel one another. The differential amplitude of the induced signals in the two secondary coils varies linearly with displacement from the null (centered) position, as shown at right. The sensor (secondary) signal is somewhat delayed with respect to the waveform in the primary coil. The signal conditioner is adjusted to account for this phase lag during calibration to maximize the sensitivity of the LVDT.

4.2.6 Cantilever Spring Stiffening Demonstration

The cantilever we use in Labs 3 and 4 (described in Sections 3.5, 3.8, and 3.9) operates as a nearly-ideal spring at deflections typical for the labs (on the order of a few millimeters). The cantilever depends on the freedom of the shaft to rotate, as illustrate in Figure 3-28 on page 173. Without this rotational degree of freedom to create "slack" in the cantilever, the cantilever would need not only to *bend* but also to *stretch*, which would take considerably more force! The shafting can only provide a finite amount of slack by rotating, however. At some displacement, the shaft will have already rotated so much that it begins to stiffen. That is, it takes a noticeably larger increment in force per increment in displacement after this point.

Figure 4-13 depicts a method for measuring the extent of spring stiffening in the cantilever. The set-up consists of the 2nd-order translational system hardware used in Lab 3 (see Figures 3-25 and 3-27), balanced on the lab table at three points. This has been done in Figure 4-13 by screwing two bolts into the optical breadboard from the underside (at the far corner of the board, from the side view perspective of the figure) and screwing a third bolt with an easily-turnable knob at its head into the board from the top in the center of the near side.

In the upper photograph in Figure 4-13, the board has been carefully balanced on the three bolts so that the breadboard surface is level (in all directions). Turning the knob now allows one to adjust the height of the near side of the board from its initial value, h_1, to some second height, h_2. (Since there are 20 threads per inch on the 1/4-20 bolt, each turn raises or lowers the board by 0.05 inches.) With the board now tilted, the force of gravity will exert a net force along the length of the shafting. For small angles, this component of the force will be proportional to the height, h_2 (since $\sin \theta \approx \theta$ for small θ). One can then measure the displacement of the shaft (say, between a split collar clamp mounted on the shafting and one of the air bearings, fixed to the breadboard) at each of a series of angles (i.e. heights).

The data shown in Figure 4-13 were obtained using the method described above. (The small angle approximation was *not* used in calculating the angle as a function
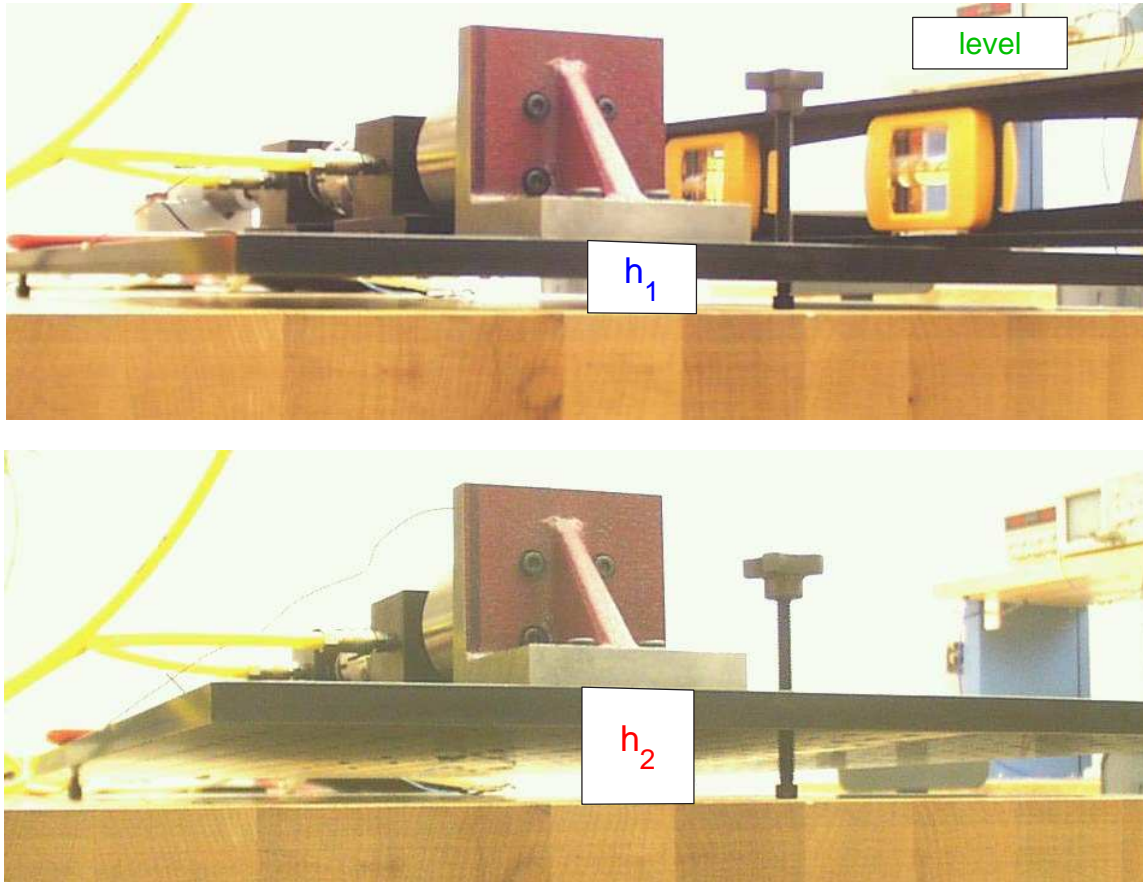
Figure 4-13: Measurement of spring displacement vs. force.

of height, since the spacing between the bolts is known and it is so simple to calculate the angle more precisely.) The smaller plot of the data at the top is included to make it clear that displacement was measured as a function of applied force. The larger plot (in which the same data are plotted with the axes reversed) illustrates the spring stiffening more elegantly, however. Note that the data are quite linear for "small" displacements. For larger displacements, the slope begins to increase (in other words, the spring "stiffens"). The longer the spring length, the greater the "near-linear" region of displacements, as one would expect. (It was too difficult to provide enough force to show any noticeable stiffening for the shortest length tested.)

The data in Figure 4-14 show the effects of stiffening elegantly, but taking enough data to create such plots is quite time consuming and therefore not practical in the context of a "sideline item" in the course of our labs. A clever way to illustrate the
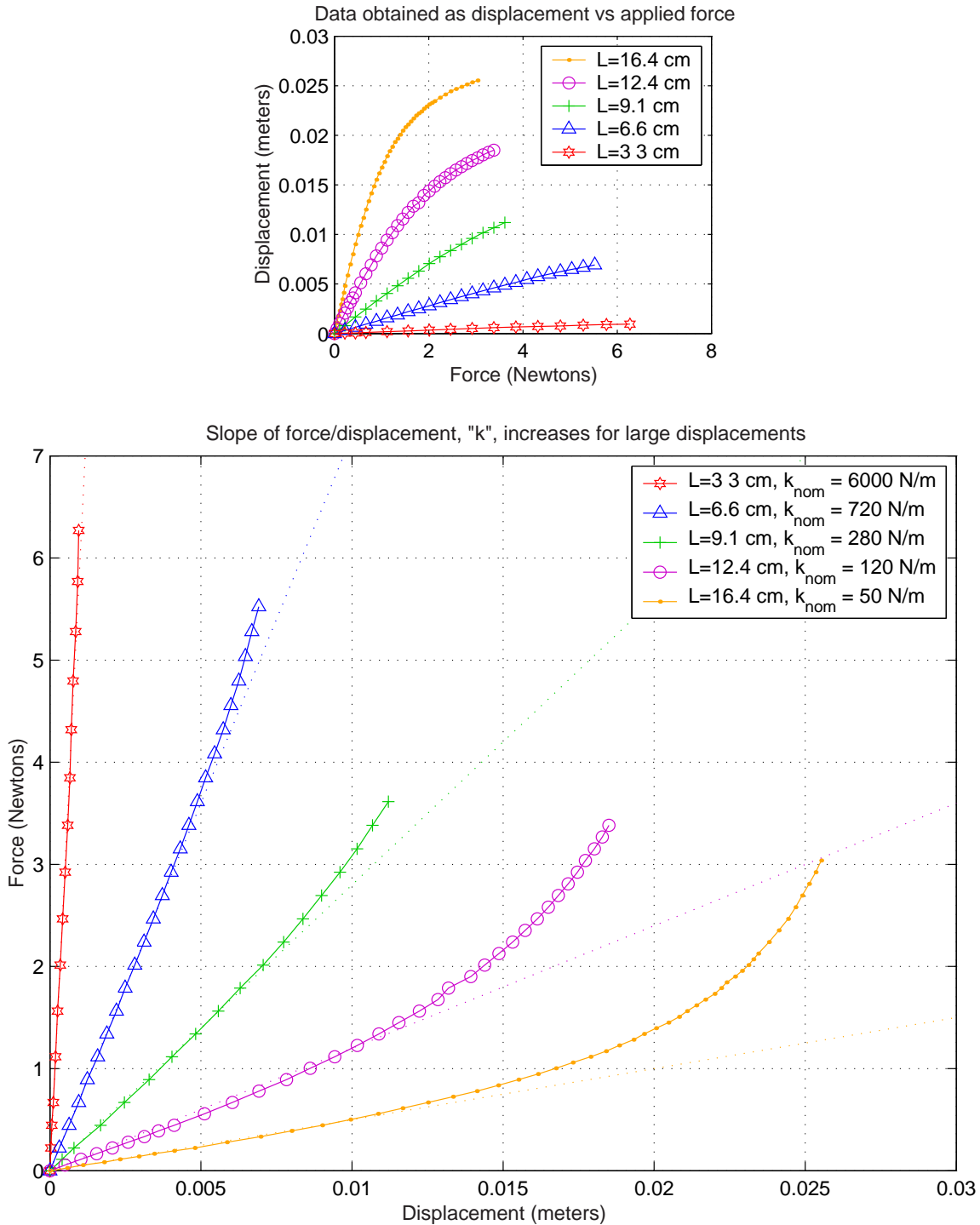
Figure 4-14: Data demonstrating cantilever spring stiffening - *The data shown at top were obtained by applying a known force and recording the resulting displacement. This is described further in the text. The same data are replotted below this with the axes flipped. The slope of force vs. displacement is the spring constant, k, of the cantilever. Note that spring stiffening is more significant for longer cantilever lengths.*

stiffening effect more quickly is as follows: Tip the breadboard by hand and then compare the natural frequency of the system in this orientation with the natural frequency when it is level. The difference can be quite dramatic. For instance, in the data set for a spring length of 16.4 cm, the slope is around 50 N/m when displacements are small, but it is about a factor of 10 greater (500 N/m) at a displacement of an inch (.025 m). Since $\omega_n = \sqrt{k/m}$, we expect the natural frequency would increase by more than a factor of 3. ($\sqrt{10} \approx 3.1$)

I have verified this stiffening behavior occurs by tapping the shafting both when level and at a known angle and recording the frequencies with an oscilloscope. Figure 4-15 illustrates the change in frequency I noted in one particular case. The waveforms plotted at the right in Figure 4-15 do not represent actual recorded data. Instead, they replot decaying oscillations at the frequencies which were recorded by an oscilloscope during this simple test.

One way to incorporate this demonstration into the lab is to come to a lab station near the end of the lab (once students have finished recording data) and show students the phenomenon without explaining it ahead of time. The staff would then ask the students is this makes sense or not, given our model of the system (i.e. constant k and m values). What causes the change in frequency? The way gravity acts on the mass? Or a change in the stiffness of the spring? Or some other phenomenon?

Unfortunately, such exercises potentially lose some "potency" in subsequent offering of the class at a school like MIT, where students collate and lend "bibles" of course materials (and theoretically have access to this thesis!). However, by asking questions such as this casually and "live and in person", it is not nearly as likely the information will be recorded and handed down. The exercise does not correlate directly into a "grade" in the course, either, so there is no overwhelming motivation for communication between busy students in the course of the week the lab is offered (i.e. giving a "heads up" to the next scheduled lab group).
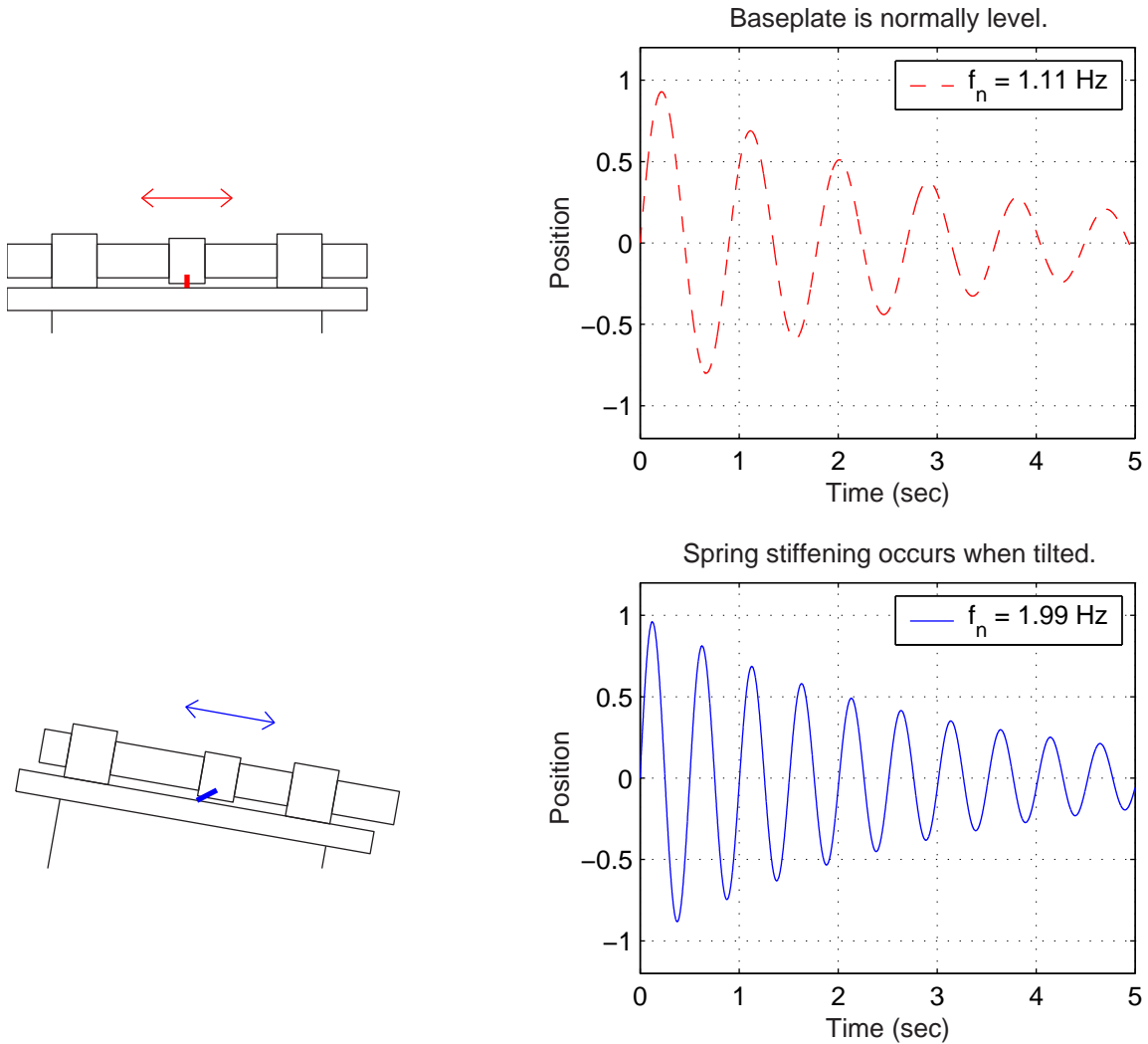
Figure 4-15: Observing an increased natural frequency due to spring stiffening. The force due to gravity when the optical baseplate is tilted changes the operating point about which the spring will oscillate. The example shown here corresponds to a cantilever length of 12.4 cm with a load of 3.4 Newtons. The natural frequency is observed to nearly double, changing from 1.11 Hz on a level baseplate to 1.99 Hz with the offset load. This result agrees well with the data shown in Figure 4-14, where this cantilever experiences an increase in spring constant (slope of force/displacement) from about 120 N/m to 400 N/m: $f_2 = f_1 * \sqrt{k_2/k_1} = 1.11 * \sqrt{400/120} = 2.03$ Hz. The waveforms at right do not represent actual data. They are decaying sinusoids produced in MATLAB which correspond to the oscillation and decay I measured on an oscilloscope output.

4.2.7 Floppy Disk Drive Dissection

Floppy and hard disk drives are both excellent examples of mechatronic design. We obtained used and discarded floppy disk drives for a few dollars a piece on ebay. Students in 2.737 Mechatronics have dissected floppy drives in small groups. The exercise did not involve a formal laboratory procedure nor a write-up; the goals were to illustrate the multi-faceted aspects of the design of the devices and to engage the students in analyzing mechanical devices. This type of experience can be extremely interactive, with students and staff discuss individual elements. Figure 4-16 show several stages in the (destructive) dissection of a floppy drive.

Many universities now offer classes at the freshman or sophomore level where students dissect everyday objects. Such an activity (dissection of floppy or hard disk drives and/or any of a number of other devices) could form the core of an additional laboratory exercise in the class, or a welcome diversion at the end of one of the first two labs (which should take less time than the later labs in the course).

Figure 4-17 shows an Everex hard drive that students dissect in ME 112 "Mechanical Systems" at Stanford, for instance [168]. ME 185 "Introduction to Mechanical Design" includes a dissection exercise involving a floppy drive [211]. Freshman at MIT interested in mechanical engineering[4] are encouraged to take 2.000 "How and Why Things Work", which includes a disk drive dissection as well. Among the other devices which are examined in these classes are the following: sewing machines, radio-controlled cars, automotive transmissions, power drills, kitchen and bathroom scales, and "Furby".

Dissection labs are particularly motivating examples for students at the freshman and sophomore level, since they rely largely on intuitive skills generally produce extremely positive feedback and enthusiasm in the students. In fact, many educators use them for high school students, as well. One example is a class called "Introduction to Engineering", which Berkeley has offered over the summer to high school students (aged 13-16) through their "Academic Talent Development Program" [133].

---

[4]Students do not declare a major at MIT until the sophomore year.
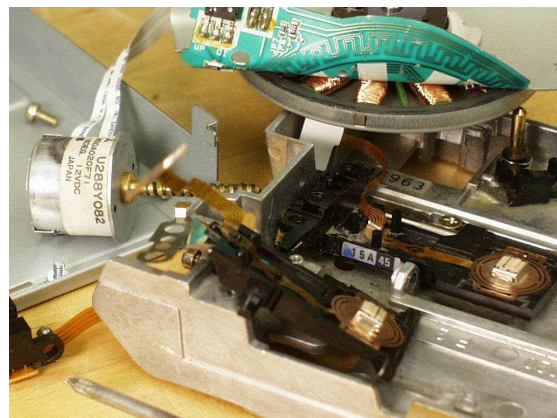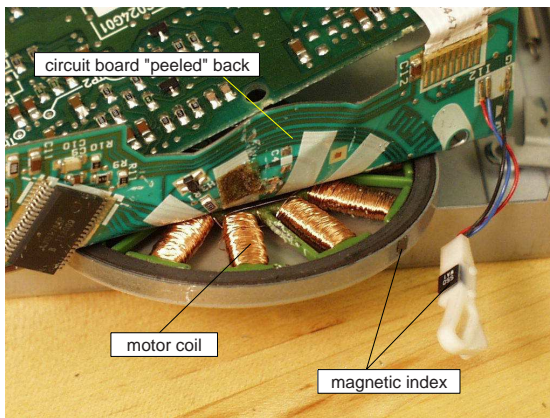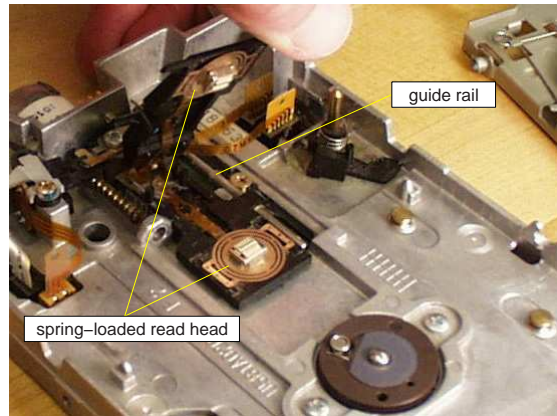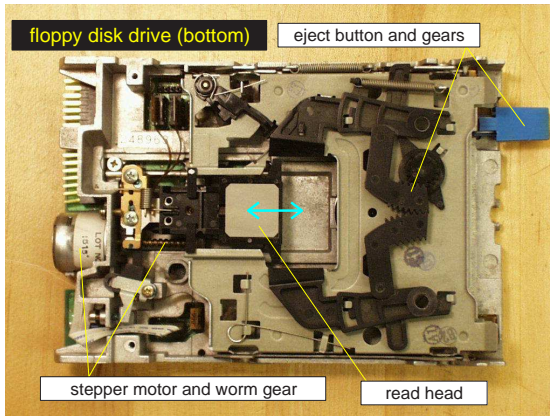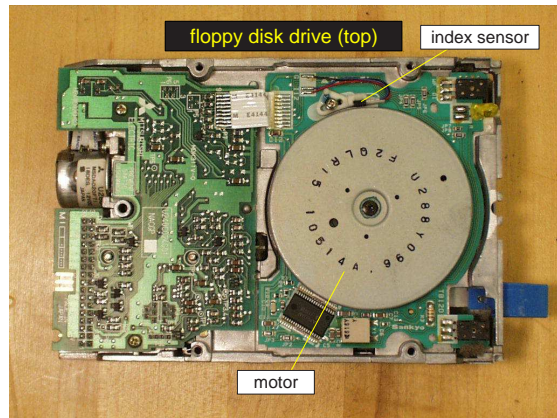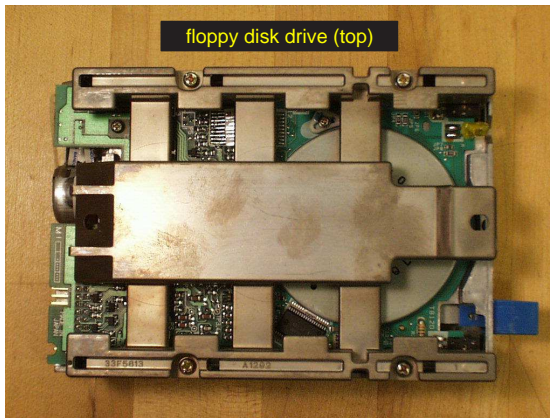
Figure 4-16: Dissection of floppy disk drive

Everex 5 MB Hard Drive
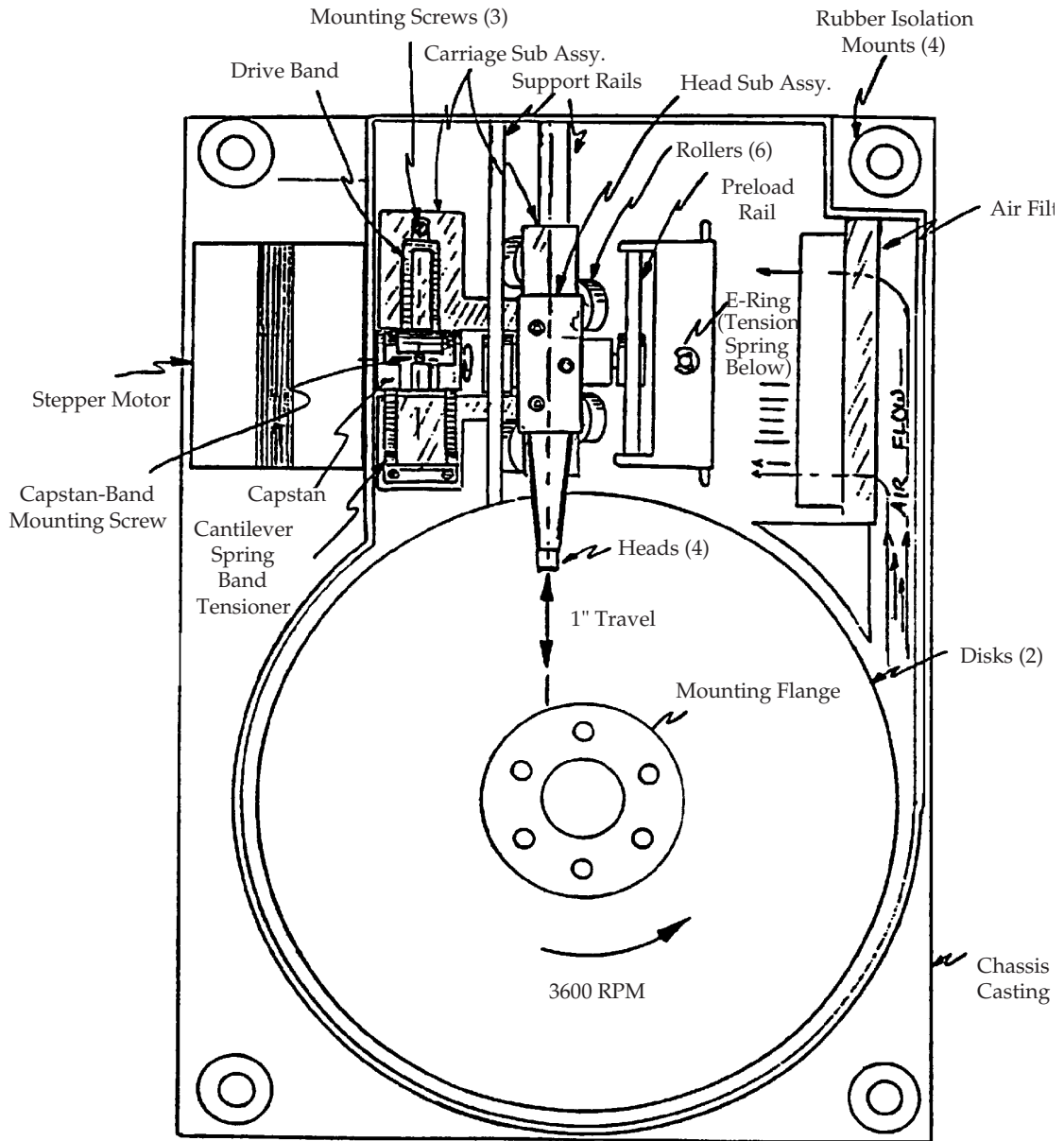
Figure 4-17: Everex hard drive dissected in Stanford ME112 -

The course includes the dissection of an actual disk drive, and the activity is supplemented with a virtual exploration on an interactive CD-ROM that helps describe the various parts and their function [171]. Students can reference the CD-ROM as they take apart the real disk drive in front of them (working in teams of two). This sounds like a great use of technology to me. (I am heartened they did not try to *replace* a real-life dissection with a purely simulated one!)

My own experience indicates that students respond enthusiastically to dissection exercises. I taught a "How Thing Work" class during the January term at an all-girl high school near Boston (The Windsor School). The students seemed mildly receptive to various demos and short lectures I gave in class during first couple of days, but when I began to bring things to us to take apart in class, they became genuinely eager and excited.

The first device we dissected was a broken toaster. The students were interested in exploring how it worked, but their primary "thrill" came from the fact that *we were actually able to fix it*! We just needed to reposition the bimetallic strip so it would properly trigger and release the spring. After this, they began bringing in a variety of broken appliances from home.[5] I don't recall being able to fix any of the rest of the lot, but the students were still excited just to solve the mystery of "what was wrong" (and in the process, learned a bit about mechanical design, I hope).

---

[5]Apparently, I'm not the only one in the world reluctant to throw things out...

4.3 Lecture Demonstrations

This section briefly documents some of the lecture demonstrations Prof. Trumper has used in 2.003. Other potential demos can be found in the survey in Chapter 2. Lecture demos are typically quite popular events in classes. Jack Wilson, professor of physics and dean for Undergraduate and Continuing Education at RPI, gives the following warning that "enjoyable" does not necessarily equate with "educational", however:

> Each meeting of the American Association of Physics Teachers is filled with ideas for how to improve the lecture. One recurring them is the use of lecture demonstrations that range from the spectacular to the humorous. Faculty, students, and even the general public love and remember the best demonstrations and the best demonstrators. Over the years, we have turned to audio, video, and now computers to make lectures more interesting and more instructive. **Unfortunately, later interviews with the students often reveal that the memory of the the demonstration is often not accompanied by an understanding of the physics of the demonstration.**[6] [218]

This last sentence is an excellent comment and a genuine concern. I will, however, rebut the point with the following three points. (1) When lecture demonstrations incite enthusiasm and interest in a class, they are potentially planting seeds of curiosity in the students which may inspire them to pursue a particular discipline (e.g. mechatronic design, biomechanical engineerings, etc) and answer the motivational question, "when would I ever actually *use* this stuff?" ("Stuff" potentially meaning the entire course curriculum!) (2) There is no indication that those students who do not recall and/or understand the details behind their favorite physics *demonstrations* would in fact actually happen to recall and/or understand very much from the *rest* of

---

[6]The italic emphasis is mine, not Prof. Wilson's.

the course.[7] One can argue the demonstration may still be generating a substantially larger "bang for the buck" that an equivalent amount of time spent in typical lecture. (3) Finally, instructors who wish to avoid this potential pitfall should *incorporate complementary exercises (in-class problem solving and/or homework assignments) to reinforce the concepts covered*!

In-class exercises might, for instance, ask that students work with 2 or 3 of their neighbors in class to perform some calculation, develop a model, or answer particular questions that probe their understanding. This gives slower students the opportunity to learn from watching peers solve problems, and it gives the brighter students an opportunity to try to explain phenomena to others. (Everyone knows you learn a subject "best" when you try to teach it to others!)

Homework assignments give students the opportunity to think about the physical phenomena at their own pace (and a graded assignment somehow always seems to provide the most-reliable motivation for learning in our students). When presenting a demo to a large class, it is usually not possible to set a pace which is appropriate for everyone. Supplementary materials can be provided to address this issue, giving the students a reference they can study outside of class and freeing the from the distraction of note taking during the demo. These additional hand-outs (providing equations and text reviewing the concepts covered by the demonstration) "bridge the gap" for students who do not fully comprehend a demo and consequently struggle through the related homework. (TA's can also clearly help to bridge this gap.)

And so, with a mixture of optimism and caution, we proceed to the survey of demos that follows. Note that most of the demonstrations have been used in previous terms by Prof. David Trumper in teaching either 2.003 Modeling Dynamics and Control I or 2.737 Mechatronics.

---

[7]Those principles they do recall have likely been repeated many times throughout the course, too, unlike a demo which they have only seen once and which lasted for perhaps 20 minutes.

4.3.1 Low-Pass and High-Pass Audio Filtering

Everyone has played with the bass and treble adjustments on their home stereos, but students may not have thought about what happens in the system when they tweak those settings. One can demonstrate low- and high-pass filtering in front of the class with simple RC circuits. This is an appropriate demonstration after students have analyzed and experimented with simple first-order circuits in the labs. (The relevant ActivLab experiments can be found in Section 3.6 on page 179.) The analysis of the circuits is straight-forward and should be familiar to the students at this point. (Repetition is still a useful teaching tool, though.)

The circuit can then be used to filter music (e.g. from a CD or MP3 player). The output should be both played aloud for students to hear and shown visually at the front of the room on a scope (preferably projected, so it can be seen easily). Most music conveniently provides components over large spectrum of frequencies (treble and bass), so that students can see and hear significant effects when either a high- or low-pass filter is applied to the waveform.

4.3.2 Camera Flash Charging Circuit

We spend considerable time in the lab sessions[8] investigating the dynamics of a *mechanical* 2nd-order system. The camera flash demo described here presents a 2nd-order electrical (LRC) circuit and provides a context in which such a thing is useful. The circuit charges a capacitor to a high voltage (up to 300 volts). When triggered, the capacitor then discharges at the center of xenon flash tube, generating the "flash" for the camera.

Figure 4-18 shows the simplified model for the circuit which we use in class. With the transistor in position "A", current flows continuously through the inductor. When the transistor is then switched to position "B", the current can not instantaneously *stop* flowing through the inductor, even if the voltage potential across the capacitor already exceeds that of the battery (1.5 volts). Thus, electrons continue to flow, and

---

[8]typically 3 lab sessions, as described in Sections 3.5,3.8, and 3.9
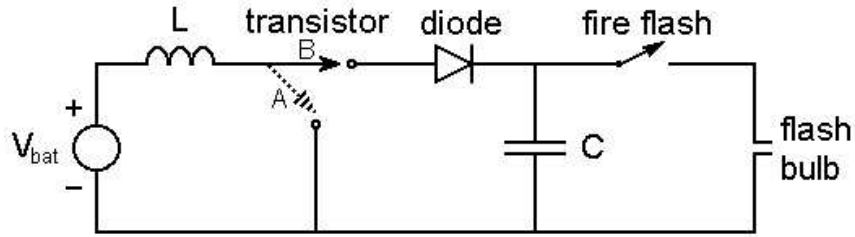
Figure 4-18: Diagram of flash circuit. Drawing by Willem Hijmans [83].

additional charge potential accumulates across the capacitor. The diode prevents the the current from reversing direction, and the process can be repeated until the capacitor has been adequately charged.

Students are given parameters values for L, C, V_{bat} and the maximum current limit for the inductor (e.g. 0.1 Amps) and are then asked such questions as: "How much energy can be transferred to the capacitor in each cycle?", "How many cycles are needed to 'fully' charge the capacitor (to 300 volts)?" and "What is fastest switching frequency possible?" (i.e. How long does it take for the inductor to reach its current limit and then discharge?)

Several other universities have used the disposal flash camera as a laboratory dissection project (with varying levels of sophistication in their circuit analyses). EE498 Consumer Electronics Design at the University of Washington [78] and PHYS345 Electricity and Electronics for Engineers at the University of Delaware [207] are two examples.

There are also a number of analyses of similar charging circuits on the web, often aimed at making the dynamics more intuitive. Prof. Rich Christie at the University of Washington uses the "water flowing in pipes" analogy to explain the dynamics of the charging circuit (e.g. a diode is a valve, etc) [49]. I tried to devise a mechanical analogy when I wrote the solutions to this homework assignment. The introduction to that solution is shown in Figure 4-19. The boxed equations and text next the illustrations for the electrical and mechanical systems are intended to emphasize the analogous relationships.

The analogy between the electrical and mechanical systems in Figure 4-19 is as

Problem 7 Below is the charging circuit. We are asked to analyze what happens during charging (before the flash is ever used) so the flash itself is not shown here (to eschew obfuscation).

There are two states to consider. In what is here called 'state A' (shown below), a switch (transistor) is positioned so that a voltage source pushes current through an inductor at an increasing rate over time. The capacitor is not involved, since it is not connected in this state.

$$L\frac{di}{dt} = V_{in}$$
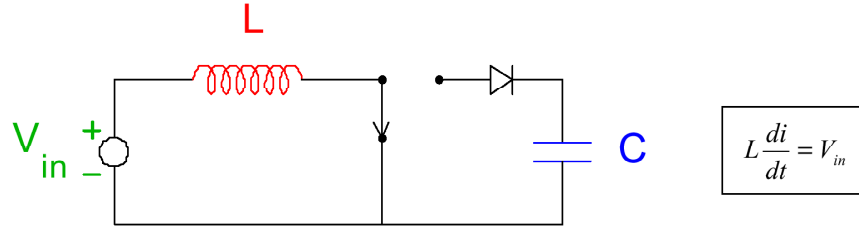
Once the maximum allowed current of 0.1 Amps has been attained, the switch is repositioned (instantaneously) to create state B. Here, the voltage source is still connected, and current flows through both the inductor and capacitor. The diode (triangular thingy) acts as a valve, allowing current to flow clockwise (positive i) in the circuit but preventing any counterclockwise (negative i) flow.

While $i > 0$,

$$L\frac{di}{dt} = V_{in} - \frac{Q}{C}$$

otherwise, $i = 0$ and switch goes to state A again.
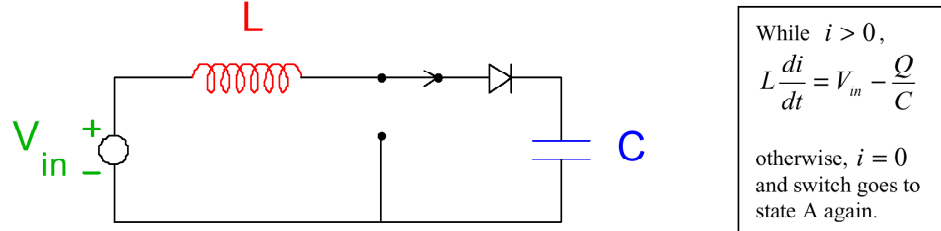
Below is an analogous mechanical system. (The ratchets allow the spring to compress, only.)

$$m\frac{dv}{dt} = mg$$

While $v > 0$,

$$m\frac{dv}{dt} = mg - kx$$

otherwise, $v = 0$ and system returns to state A again.
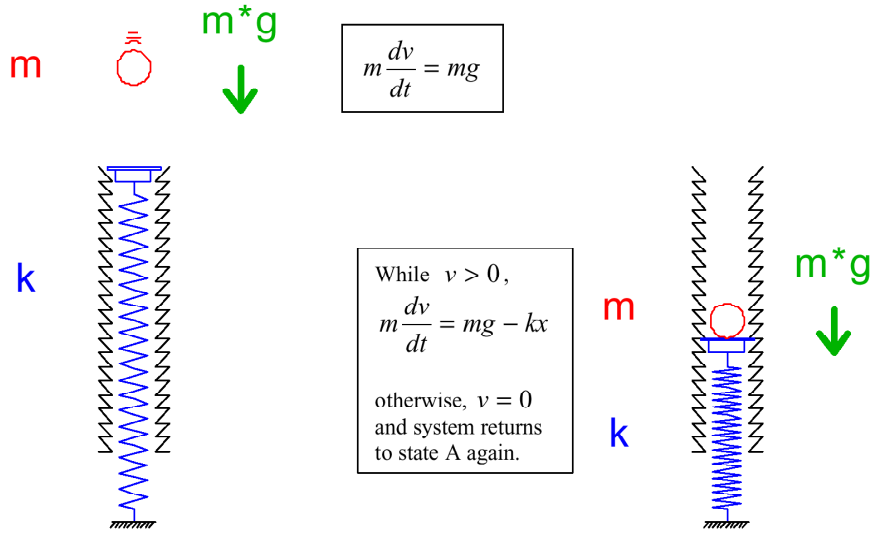
state A: Mass accelerating with a constant force applied.   *state B:* After the mass hits the spring.

Figure 4-19: Mechanical analogy for flash charging circuit. From solutions to Problem Set 7, Fall 2001. (Lilienkamp)

follows: The inductor corresponds to the mass. A voltage applied across the inductor results in an "acceleration" in current, just as a the force of gravity will accelerate the mass during its fall. In the circuit, we let the current in the inductor ramp up to 0.1 Amps and then toggle the switch in the circuit to include the capacitor. This is analogous to raising the mass to some prescribed height above the (massless) platform on the spring and then allowing it to fall under gravity. The constant force of gravity will ramp up (accelerate) the mass to some (calculable) velocity at impact, and when it hits the spring, the kinetic energy ($\frac{1}{2}mv^2$) is converted into potential energy in the compression of the spring. In the electrical system, the energy being transferred from the inductor to the capacitor will (analogously) be $\frac{1}{2}Li^2$. If there were no diode (or ratchet), the system would theoretically oscillate forever after the initial switch of the circuit (or impact of the mass), unless we postulate some loss mechanism(s) in the real system.

Figures 4-20 shows the digital flash camera we use, with the front panel folded down to expose the inside. Figure 4-21 includes images of top and bottom sides of the circuit board inside. Note that the capacitor can hold dangerously high voltage potentials, even if the camera has not been used recently! We are careful to warn the students not to "poke around" with such capacitors at home.
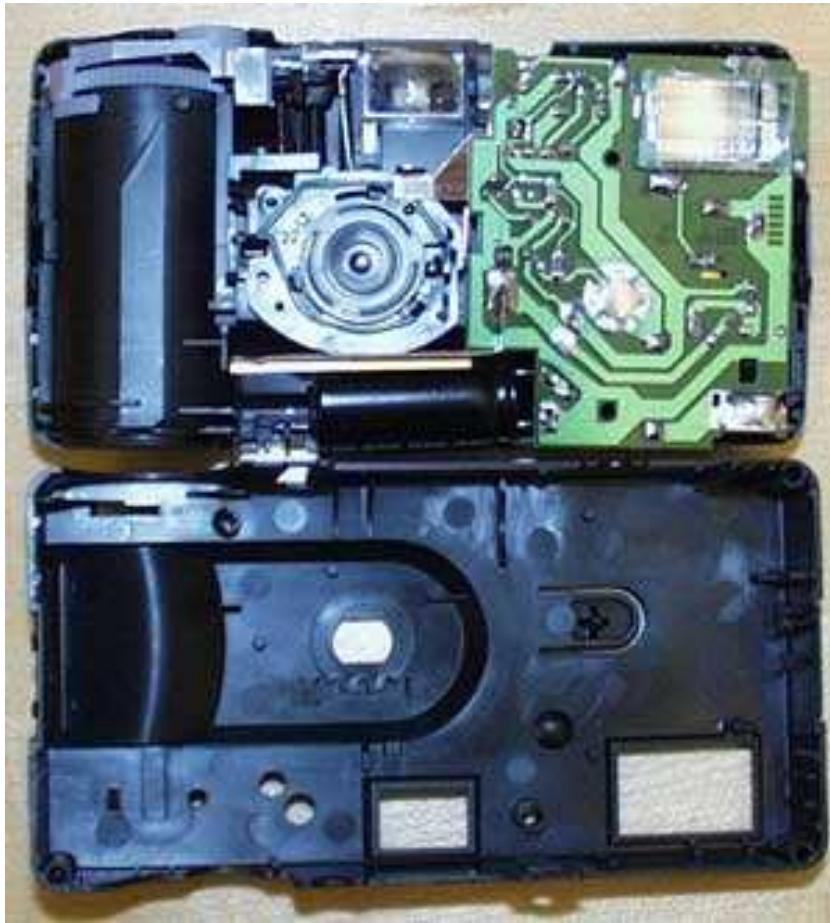
Figure 4-20: Digital flash camera with front panel removed. Photo by Willem Hijmans [83].
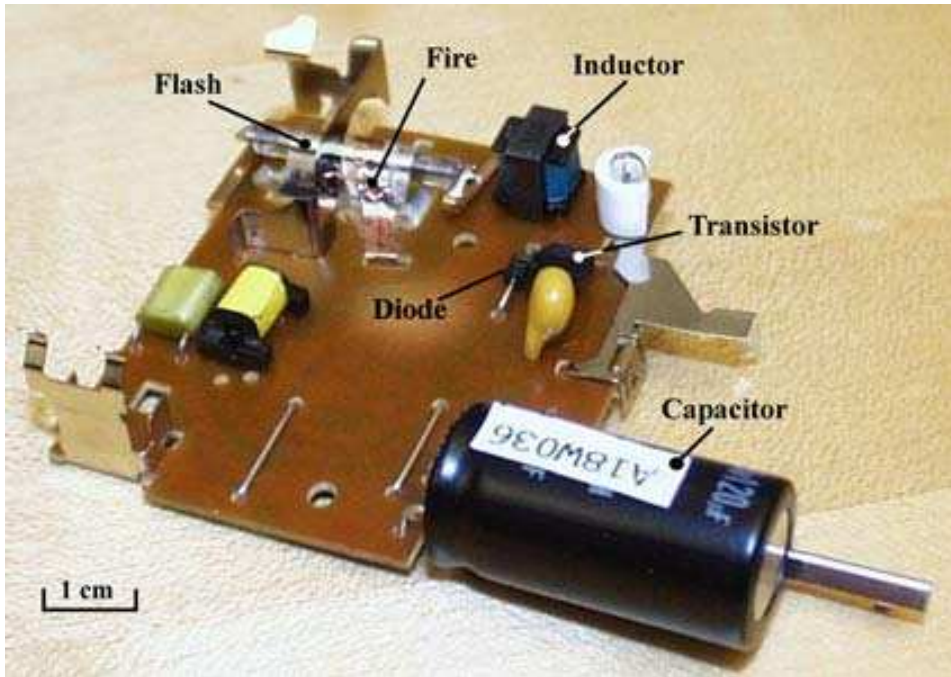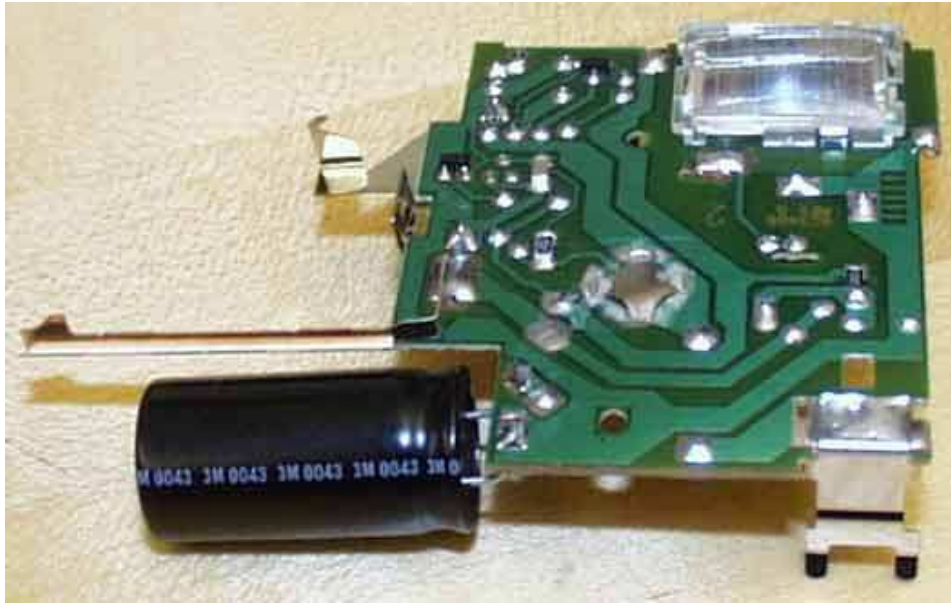
Figure 4-21: Digital camera flash circuit board. Photos taken by Willem Hijmans [83].

4.3.3 MATLAB Tools

MATLAB is a great tool for analyzing dynamic systems and control. Unfortunately however, most of the students who take 2.003 (typically sophomores) have not used MATLAB much (if at all). At MIT, we teach MATLAB basics in a required pass-fail course[9] for mechanical engineering majors. It is offered during IAP[10], and students generally take it in the sophomore year. This means that most students taking 2.003 in the Fall term will need some introduction (a primer) on the basics.

The best way to get started with MATLAB (or any programming language), is to have some simple projects to complete. In 2.003, Prof. Trumper has created an assignment to modify MATLAB code to produce spirograph plots. The students have to describe how the code works and then modify it to try to create interesting patterns.

I have taught the MATLAB section of 2.670 a couple of times. The MATLAB section is taught in three 3-hour sessions. Each session consists of three types of activities. First, the instructor lectures to the entire group (about 12 people), and students sit at individual computers and enter commands from the lecture overheads into MATLAB. Second, the students are asked to write MATLAB functions to perform particular calculations. Third, the lecturer (or other 6.270 staff who wander in during class) talks about some interesting topic, usually with an accompanying demo or pictures. The idea is to flow continuously between the 3 activites throughout the class, spending 20 minutes or so at a time doing any one before changing the format of the class again. This seems to help a lot in keeping student attention throughout the 3-hour class!

Some of the demos relate directly to the programming topics, while others deal more generally with topics related to the Stirling engine. Prof. Hart, who developed

---

[9]The course is "'6.270 Mechanical Engineering Tool". In the class, students build working Stirling engines. This is a motivating project to get them to learn how to use various machine tools. They also learn to use MATLAB and ProE. Roughly 140-150 students take the class each year.

[10]The "Independent Activities Period" (IAP) at MIT occurs in January, between the Fall and Spring semesters.

the class around building a Stirling engine, has purchased several novel toy Stirling engines over the years. Several operate from the heat of a lamp and there is even one that runs from the heat of your hand as you hold it (see Figure 4-22). These are great demos to pass around the classroom. We also teach the students how their Stirling engines work. I've taught the fundamentals of how a standard internal combustion engine and the Wankel engine each work, too. I even created an animation of the engine, drawn entirely with MATLAB as an inspiration (I hope) at how much it can do. A frame from this animation is shown in Figure 4-23.

Many of the MATLAB projects involve implementing some simple numerical method techniques. We also have the students use MATLAB's ordinary differential equation solving functions ode45 and ode23. One project involves predicting how rapidly the heat transfer cylinder of the engine will cool off, once the flame has been extinguished.[11] We brought in an actual engine and used a thermocouple and timer to record it cooling in room temperature air. The resulting data are shown in Figure 4-24, plotted against a theoretical cooling profile calculated with MATLAB's ordinary differential equation solver "ode45()". This figure also includes the m-file "tempdot.m" which provides ode45() with the differential relationship between the current temperature and rate of cooling.

In summary, keeping variety in the class was extremely helpful in turning a rather dull subject into a bearable class.[12] Guided exercises are an efficient way to learn the necessary skills to begin using MATLAB (or similar numerical software).

---

[11]This problem was developed by Prof. Doug Hart and Prof. Kevin Otto. When students bring their engines to the staff to ask for help in adjusting them to run, they almost invariably hand the *hot* end of the engine to the instructor. Thus the inspiration for the problem.

[12]Class evaluations for the sections were quite positive.

Figure 4-22: MM-6 Stirling engine running on the heat of a hand.
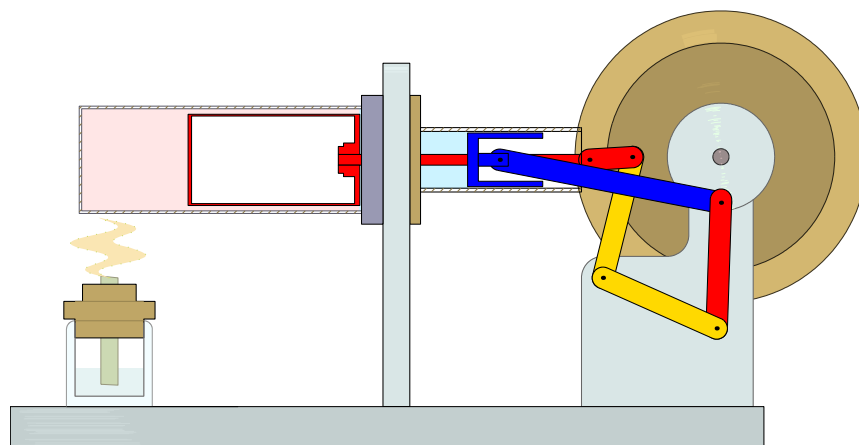
Figure 4-23: MATLAB animation of Stirling engine. This is one frame of an animation I wrote for 2.670 to show how the Stirling engine works. As of this writing, the movie can be found at: http://web.mit.edu/2.670/www/spotlight_2003/engine_anim.html
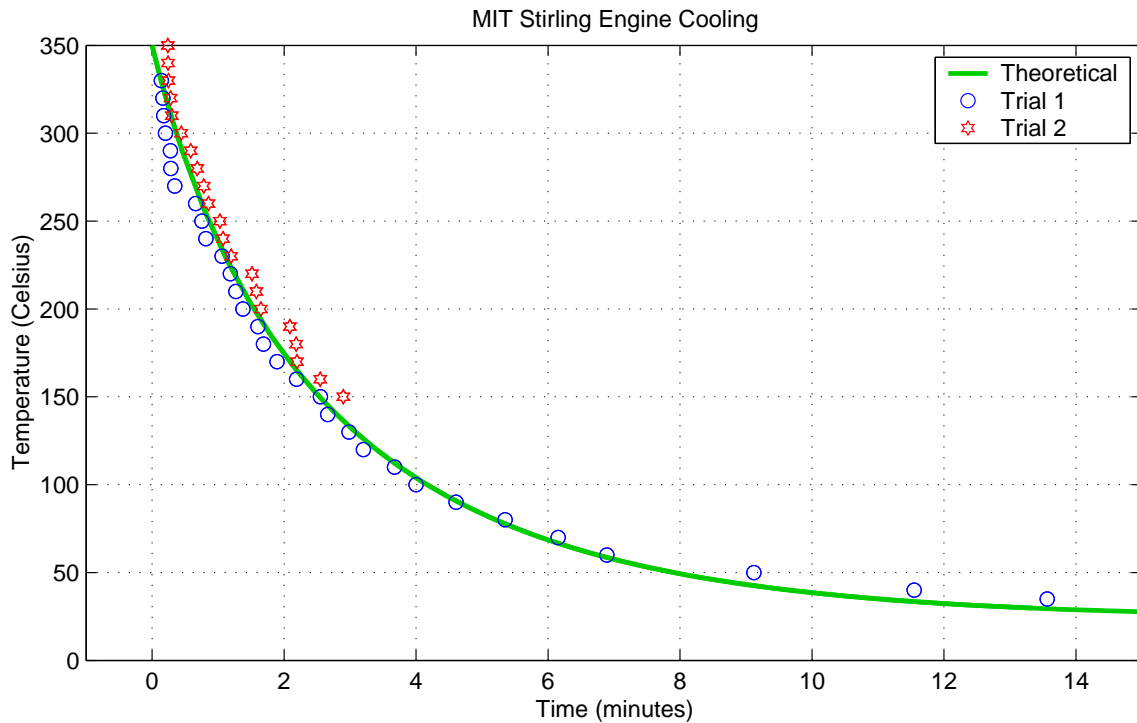
Function "tempdot()" for ode45() to use:

```
function dTemp = tempdot(t,T)

T = T+273;  % Convert input temp from Celsius to Kelvin
h = 18;                              % heat xfer coef
disp_rad = .0254*1.25/2; disp_len = .0254*3; % dimensions
A = 2*pi*disp_rad*disp_len;          % area (m^2)
m = .1;                              % mass (kg)
cp = 400;                            % specific heat
Tinf = 273+(75-32)*5/9;              % room temp
em = .95;                     % emissivity
boltz = 5.67e-8;                     % Boltzman const

dTemp = -(h*A/(m*cp))*(T-Tinf) - (em*boltz*A/(m*cp))*(T.^4-Tinf^4);
```

To run ode45() from the MATLAB command window:

```
>> tfinal = 14*60;
>> init_temp = 350;
>> [t,temp] = ode45('tempdot', [0 tfinal], init_temp);
```

Figure 4-24: MATLAB calculation of engine cooling using ode45().

234

4.3.4 Real-World Dynamic Systems

Real-world systems are a great way to motivate students, who will naturally be curious about how things work. There are many resources in print and on the web which explain the way everyday objects work. Two particularly popular and well-crafted examples worth note are David McCaulay's famous book "The Way Things Work"[13] [118] and the website "howstuffworks.com" [87].

Mountain bike front suspension

A car suspension is a popular system to model in mechanical engineering courses and texts in dynamics. A modern mountain bike fork provides a more modern version of the shock absorber, which is likely to be of interest to many students. As an added bonus, a suspension fork can easily be brought into the classroom, too.

Prof. Trumper has brought such a mountain bike fork into class as a demo in 2.003. Students can put their full weight on the suspension to feel the dynamic response. This system is an excellent candidate for a text or course note example, which can be coupled with a hands-on classroom demonstration. Dorf and Bishop [60] now include such an example in "Modern Control Systems", as shown in Figure 4-25.[14] In this model, the damping (b) can be adjusted by biker to improve performance based on the terrain.

In the description of the demos for 6.013 in Section 2.3.3 (page 117), I described how physical hardware in class can be enhanced by documenting each of a suite of demonstration examples in clear presentations in the course text. Such text descriptions would typically include some information of the how the object or system is used, the essential principles being illustrated, and a derivation of the theoretical equations describing the dynamics. Homework problems can and should be developed which require the students to understand the text example and then extend the principles involved in some way.

---

[13]...and also his 1998 book "The New Way Things Work" [119].

[14]This mountain bike suspension model appears as AP3.4 in the "Advanced Problems" section at the end of Chapter 3 (pp. 165-166).
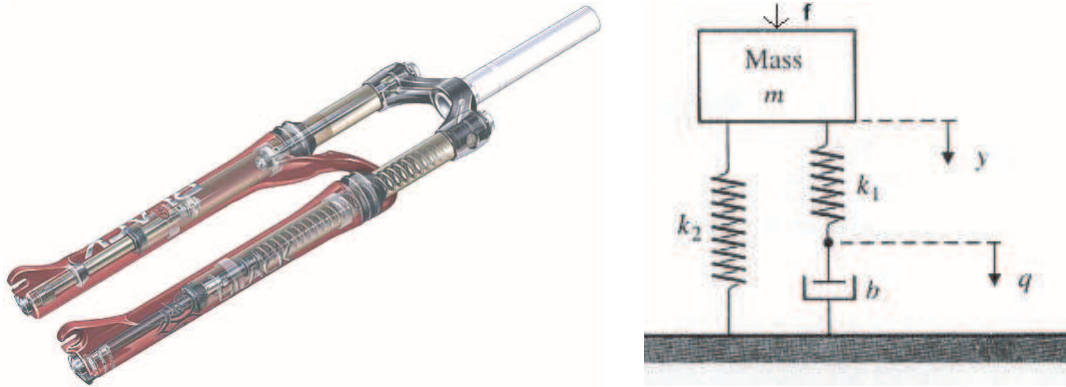
Figure 4-25: Mountain bike suspension fork. A mountain bike suspension fork can be modeled as a second-order system, similar to the shock absorber in an automobile or motorcycle. The Manitou Black fork shown above (at left) is manufactured by Answer Products. The fork has one coil spring, contained in the left leg, which can be replaced to better suit a particular rider's weight and riding style. The right leg contains a fluid damping assembly. The rider can adjust the magnitude of the damping in the compressive and rebound directions independently, using knobs at the top and bottom of the damping leg, respectively. (Image copyrighted by Kevin Hulsey Illustration, Inc. [90].) At right is a simplified model of a variable suspension bike which comes from a textbook example in "Modern Control Systems" by Dorf and Bishop [60]. Here, students are asked to think about how changing the damping will effect the smoothness of ride on different terrains.

This idea is similar to the strategy used in teaching MATLAB, described in the previous section (page 231): variety can be effective in keeping interest and motivation high. A classroom demo sparks interest in real-time. Accompanying lectures describe the phenomena, while a text description gives the students the opportunity to work out details at their own pace. Finally, requiring a related assignment both gives students an immediate "inspiration" for working through the demo explanation and also provides feedback on student comprehension to the instructors. Having these three elements of inspiration, explanation and challenging problem solving is often an impractical ideal, unfortunately, since it clearly requires a lot of time and effort to create such a suite of demonstrations. It's a goal worth aiming toward, at any rate.

Physics toys

In-class demos can very useful for motivating student interest in a particular field of study. There are a number of science toys that aim to "wow" the user by exploiting some particular physical principle(s). Many of these can potentially serve to spark the curiosity of students[15], even if students may not follow all the details of the physics involved during a classroom demonstration. I personally feel students often key on demo time as a signal to sit back and expect entertainment, which can be somewhat frustrating from the point of view of an instructor. When appropriate, further handouts and assignments can be prepared to insure students have gained an understanding of underlying dynamics. However, even if students leave class from only a rudimentary understanding of how a complex phenomenon works, we can still hope a seed is planted which inspires interest in the subject of the class.

Figure 4-26: Euler's Disk (left) and the Levitron (right)

One example of such a toy is "Euler's Disk", shown at the left of Figure 4-26. As the disk spins on a flat surface[16], it looses energy and the frequency of its spin increases. Several papers in recent years have investigated the effects of air viscosity and sliding friction of the behavior of a coin and/or Euler's Disk as it spins down [140, 66, 188].

---

[15]These are often sold at science museums or directly by manufacturers of educational toys.

[16]The disk is oriented nearly parallel to the surface on which it "spins". To picture the orientation, imagine a wayward coin that has rolled away. It will eventually roll over on its side and spin down slowly just before coming to rest, and this is essentially what Euler's disk does.

The Levitron©, shown at right in Figure 4-26, is another intriguing toy that can be used to illustrate that real dynamic system can indeed require more sophistication than the typical first- and second-order models we study throughout the class. The device consists of a magnetic spinning top which levitates over a magnetic base.

Magnetostatic theory predicts that two repellent magnets cannot remain balanced (one above the other), because the equilibrium point is unstable (like an inverted pendulum). The reasoning can be summarized as follows: First, we will model the levitating magnet (the spinning top) as a magnetic dipole with vector moment $\boldsymbol{\mu}$ and mass m. The potential energy of the dipole due to the gravitational and magnetic fields is then:

$$V(r, z) = mgz - \boldsymbol{\mu} \cdot \mathbf{B}(r, z) \tag{4.4}$$

We can then form Lagrange's equation to produce a force balance equation axis the z axis:

$$F_z = -\frac{\partial V(0, z)}{\partial z} = -mg + \boldsymbol{\mu} \cdot \frac{\partial \mathbf{B}(0, z)}{\partial z} \tag{4.5}$$

The dipole is in equilibrium when the net force F_z is zero, meaning we require that $mg = \boldsymbol{\mu} \cdot \partial \mathbf{B}/\partial z$. Now imagine that magnetic field is in the positive z direction, i.e. $B_z > 0$ and therefore $\partial B_z/\partial z < 0$. This means $\boldsymbol{\mu}$ must align antiparallel to $\mathbf{B}$ [132, 33]. Our intuition supports this: the two magnets must be aligned "north-to-north" or "south-to-south" in order for them to provide a repellent force to counteract gravity. However, our intuition (and magnetostatics) also tells us that the dipole $\boldsymbol{\mu}$ will align itself with $\mathbf{B}$. Stability requires that any small perturbation away from equilibrium be opposed by a restoring force (tending to push it back toward equilibrium), and we sense from experience[17] that this is not the case. Earnshaw's Theorem [63] states this more rigorously.

Prof. Kirk McDonald of Princeton University provides analyses of both Euler's Disk and the Levitron at a website which includes numerous other interesting problems and phenomena in physics [132].[18] The most commonly cited paper explaining the physics of the Levitron is by Dr. Michael Berry [33].

---

[17](and can prove by applying Gauss' Integral Theorem [81]

[18]http://www.hep.princeton.edu/~mcdonald/examples/

Viscous damping in syringe with oil drop

Figure 4-27: Viscous damping of thin oil layer between syringe walls

During 2.003 lectures, Prof. Trumper has passed around a ground-glass syringe to demonstrate viscous damping. We have used a 5 mL Yale syringe, shown in Figure 4-27. These are hand-fitted to attain an extremely close fit between the inner (plunger) and outer (barrel) walls.[19] As a result, one can feel the viscous damping as the thin layer of oil is sheared in Couette flow. Note that one can slide the cylindrical surfaces in either translation or rotation.

Automotive transmission

We have a 5-speed transmission, shown in Figure 4-28, that has been cut open to expose its innards.[20] One can turn the input shaft by hand and then watch and feel what the gears and synchros do and you change gears. It is particularly interesting to watch how the synchros disengage from one gear, to put the transmission into neutral, and then lock into a new position. In Figure 4-29, a hand holds the blocking ring of a synchro. Its soft, brass teeth mate with the steel gear assembly below it.

---

[19]The plunger and barrel of a particular syringe are numbered to ensure they remain a matched set.

[20]This nifty demo was rescued by Prof. Trumper during the renovation of the Pappalardo machine shop and lab at MIT. They were just going to pitch it!
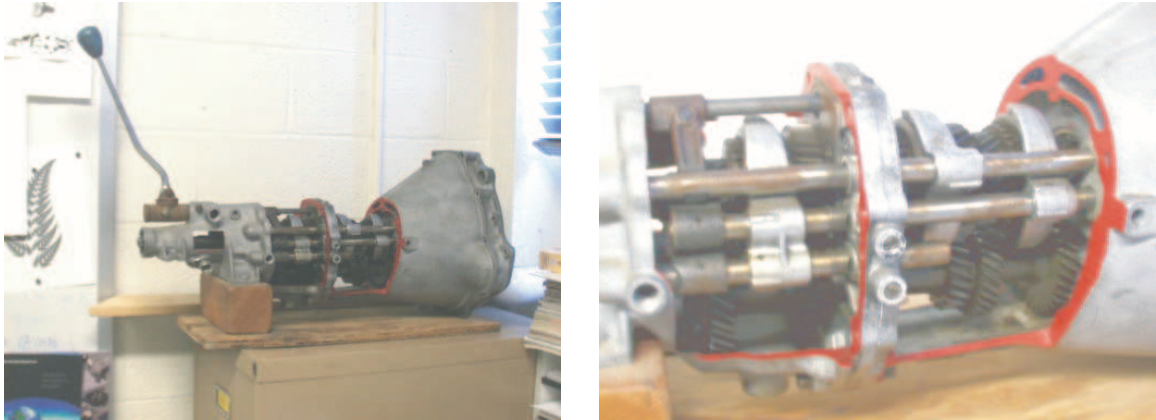
Figure 4-28: Automotive transmission

We have not used this as a demo for 2.003, but I remember it well from my own experience as a student in 2.737, when the transmission sat in a corner of the lab. It is easier to operate with two people: one turning the input shaft and another shifting the gears. I believe this encouraged the students to interact more with one another. When one person would start to try to figure out how it worked, it was very natural for another student to notice and come over to help. Information passed from student to student.
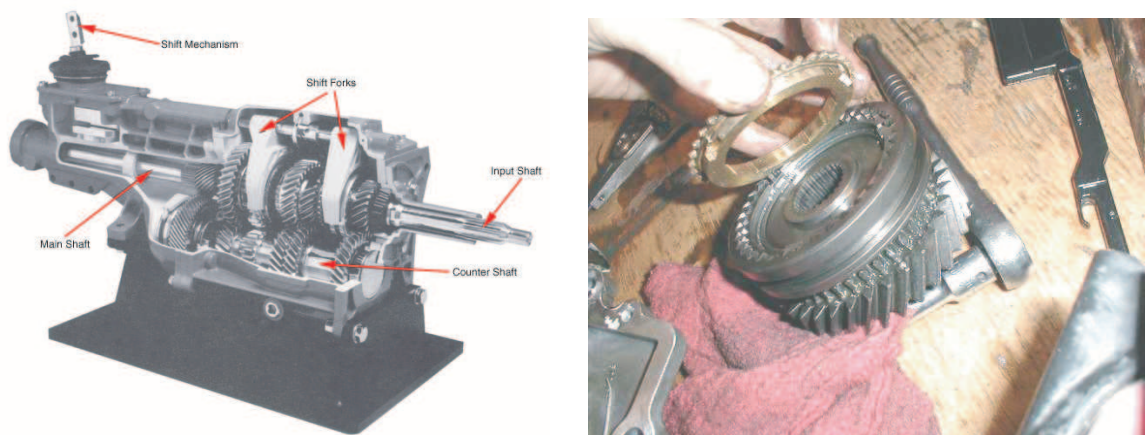
Figure 4-29: Transmission details. The cutaway drawing at left shows the a Borg-Warner T5 5-speed transmission for a Ford Mustang. Image from Edmunds.com [65]. At right is a detailed photo of synchros from the transmission of a Mitsubishi Eclipse GSX. The image comes from the personal website of Andre Cardadeiro [44].

Disassembled motors

We have various types of motors (both intact and disassembled) available around the 2.003 lab for students to examine. One can use such motors to develop a dissection exercise (similar to the disk drive dissection exercises discussed in Section 4.2.7). Alternatively, the motors can be left in the "background" in the laboratory and used from time to time (as relevant) in a less formal way. This is the approach we have taken, and it falls along the lines of how the Automotive Transmission, described in the preceding section, was "used" in the lab when I took 2.737 Mechatronics with Prof. Trumper. Being able to see the innards of the rotary motors also allows students to visualize field lines and torques. The rectangular voice coils described in Section 4.2.3 serve an analogous purpose in illustrate how a voice coil motor operates.

This section is an appropriate way to conclude this chapter: Disassembled motors are particularly well-suited for demonstrating both fundamental physical principles ("What makes a motor work?") and good design practice ("...and why has it been constructed in this particular way?"). Each of the demos surveyed in this chapter is intended to serve a unique set of purposes. Among these various goals, however, nearly all of the seek to demonstrate how and why such artifacts are engineering the way the are, and to develop (and also to motivate) skills in modeling and designing dynamic system system.
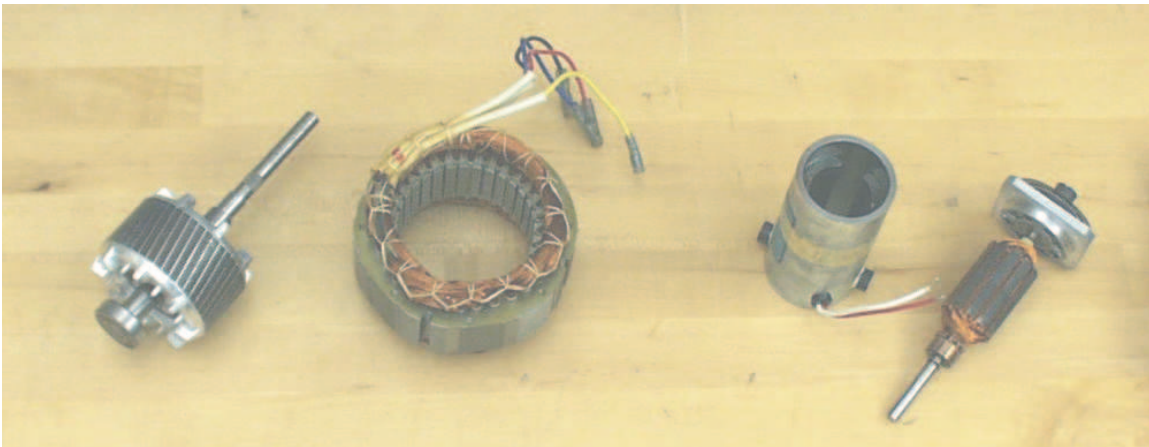
Figure 4-30: Disassembled motors

Chapter 5

Driven-Cart Inverted Pendulum

This chapter describes an existing IP classroom demo first created by Prof. Will Durfee and his students at MIT in the early 1990's. The hardware described here implements a version of the inverted pendulum with a driven cart on a track and a free-hanging pendulum. I review it here for two purposes: (1) to call attention to particular similarities and differences between this cart-type inverted pendulum and the steerable, robotic version described in the next chapter and (2) to discuss the calibration and initial testing of the gyro and accelerometer.

One notable comparison between the driven-cart and robotic inverted pendulums is in the response of each to a step in commanded pendulum angle (or equivalently, to a step error in the measurement of pendulum angle). When the commanded pendulum angle is zero, both systems operate about an equilibrium state where the pendulum angle and cart velocity are both zero. The equilibrium cart position will also be zero in the case of the driven-cart pendulum.

For the cart system, a step in commanded pendulum angle results in a new, non-zero equilibrium cart position, while the steady-state values of both pendulum angle and cart velocity are zero, as before. In the case of the robotic IP, however, a step in commanded pendulum angle results in a steady-state, non-zero velocity of the vehicle and some corresponding, non-zero displacement in pendulum angle. Section 5.1 and Chapter 7 provide more detail on the dynamics of the driven-cart and robotic IP's, respectively, but the principles explaining their most significant differences can be

summarized briefly and are outlined in the next two paragraphs.

The robotic IP is driven by motors which apply torque directly between the pendulum body and the wheels of the vehicle. Consequently, an equilibrium state can exist such that the pendulum angle is non-zero, with the motors providing a constant torque to balance the torque on the pendulum from gravity. With the steady-state motor torque at a constant, non-zero value, the steady-state velocity of the wheels is also constant and non-zero. *A step in reference angle therefore results in both some steady-state velocity of the vehicle and a steady-state change in pendulum angle.*

In a driven-cart inverted pendulum of the type described in this chapter, however, the pendulum hangs freely from a pivot on the cart. No actuator applies a torque directly at the pendulum pivot axis. Therefore, unlike the robotic system, the cart-mounted pendulum cannot find equilibrium states where the pendulum angle is non-zero. Consider a case where the cart moves with a constant velocity, for instance. This provides no torque on pendulum, because there is no acceleration of the cart to produce a force at the pivot. If the pendulum is not exactly vertical, the torque created by gravity will accelerate the pendulum, and it will begin to fall. If this system can find an equilibrium state in response to a commanded step in pendulum angle, the actual pendulum angle in this state must be zero. Section 5.3 explains why the system can in fact find such an equilibrium state (for small values of θ_{ref}) and also why the relationship between the equilibrium position of the cart and the commanded angle, θ_{ref}, is linear.

The second purpose of this chapter is to discuss the initial testing of the calibration and filtering used for the gyro and accelerometer. Together, these two sensors provide tilt sensing which is essential in controlling the free-standing robot. Section 6.2 in the next chapter describes the complementary filtering used to blend the two sensor outputs to measure the pendulum angle.

The gyro and accelerometer were initially tested with the cart setup described in this chapter, which greatly facilitated the development of sensor calibration and filtering. In previous controllers for the cart demo, the pendulum's angular velocity had been obtained by differentiating an encoder signal. Using the gyro to measure

angular velocity directly improved performance notably, as described in Section 5.4. In particular, a significant mechanical vibration around 90 Hz was eliminated by measuring the velocity directly with a rate gyro.

5.1 Cart IP Hardware
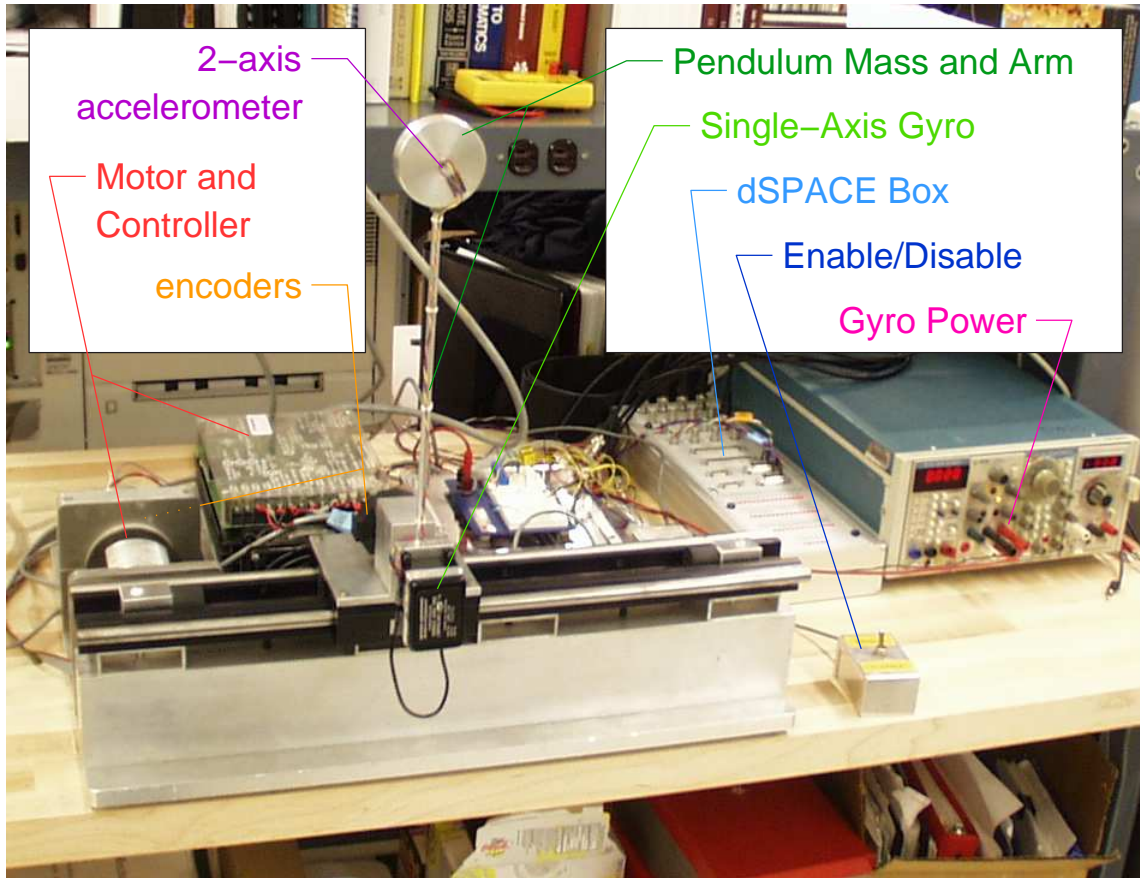
Figure 5-1: Diagram of the cart-driven inverted pendulum

Figure 5-1 shows the cart-type inverted pendulum demo. As built by Prof. Durfee and his students, this demo is capable of standing up on its own, rhythmically exciting the pendulum to attain an upright position. A number of Prof. Trumper's students have subsequently worked with this demo, including Kuo-Shen Chen, Ming-Chih Weng, Steve Ludwick and most recently myself. Andrew Stimac improved the controller for this hardware and refined the stand-up routine to enable the cart to

swing the pendulum from an initial state at rest into the upright equilibrium position more reliably [189].

In this system, the inverted pendulum is stabilized about its vertical equilibrium through the control effort of a single actuator: a current-driven DC servo motor.[1] Force is transmitted from the motor to a cart through a chain drive. The cart rides on two parallel rails and supports the pendulum at one end with a free pivot.

In the original design of the hardware, three sensors are used to estimate four states. An encoder at the back of the motor (hidden behind an aluminum mounting plate in Figure 5-1) gives an output proportional to the cart position, and a second encoder mounted at the pivot of the pendulum measures the pendulum angle. The motor velocity (which is proportional to cart velocity) is measured directly with a tachometer. The angular velocity of the pendulum is estimated by differentiating the pendulum encoder and filtering this output with a first-order low-pass filter with a time constant of 0.005 seconds ($\sim$32 Hz).

I used this system to help design and verify the filtering of the gyro and to calibrate the accelerometers later used in measuring the absolute pendulum angle and angular velocity for the inverted pendulum robot (nicknamed the "DIPR") described in the next chapter. The velocity measurement from the gyro improved the performance of the cart system, eliminating a significant resonance. This is described in more detail in Section 5.4. The next two sections first develop some theory to describe the dynamics of the controlled system adequately enough to compare its behavior with that of the robotic IP in Chapter 7.

One final note on the hardware: Andrew Stimac implemented his controller on the now-outdated DS1102 board which has since been replaced by the DS1104, and there are a few differences between the two boards. In particular, the encoder input on the DS1102 increments by one bit (2^{-23}) for each quadrature count. The advantage of this was that it was easy to tell how close an encoder channel was to overflowing, because the encoder value was always between -1 and +1. The DS1104 has opted for a more intuitive counting scheme. Each quadrature pulse increments the encoder

---

[1]Aerotech Permanent Magnet DC Servo Motor, Model 1135 [189]

by 0.25, so that the encoder channel outputs the number of encoder counts directly. Running Stimac's controller for the IP cart demo on the DS1104 therefore requires re-scaling the encoder gains in the Simulink model for the controller [189].

5.2 Equations of Motion
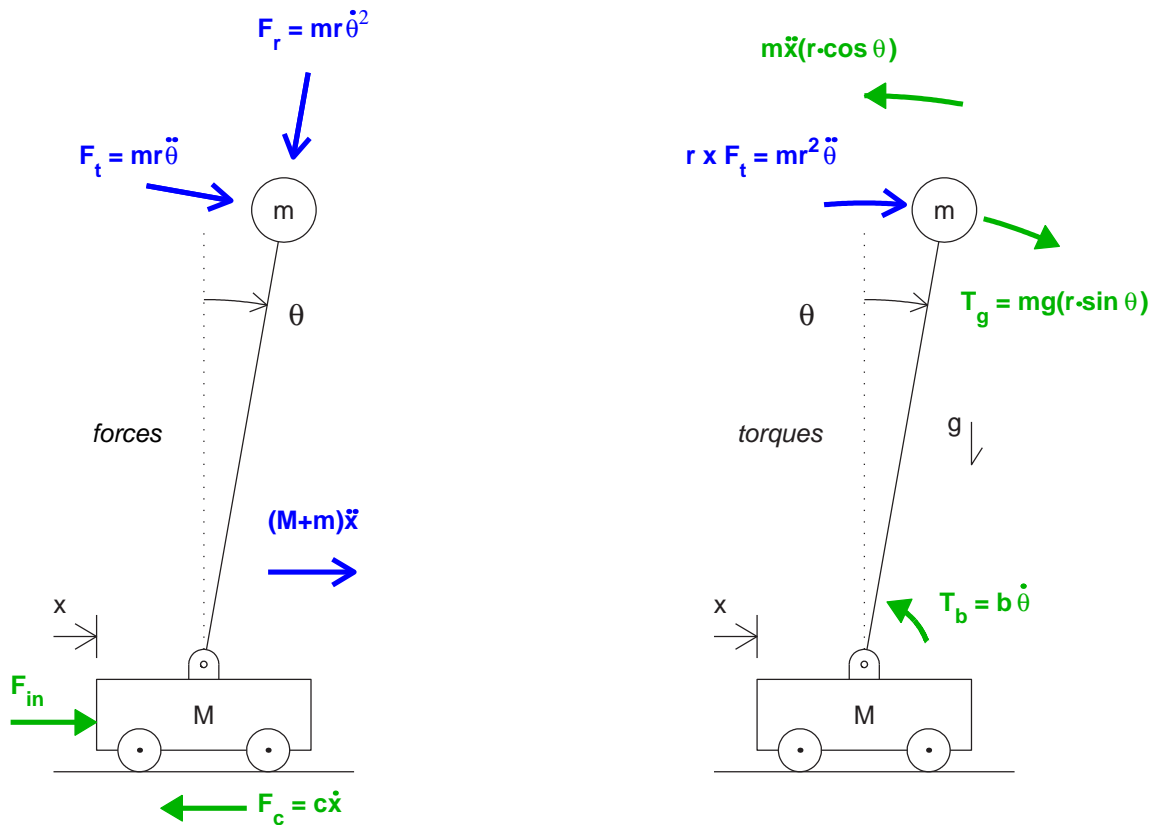
Figure 5-2: Force and torque balances for inverted pendulum on cart. Forces and linear accelerations are shown on the left. Torques and angular accelerations are at the right.

Figure 5-2 gives free body diagrams for both force and torque balances on the cart-type inverted pendulum. The equations of motion can be constructed by inspection, taking careful note of signs and vector directions. Balancing force and linear

acceleration terms in the x direction yields:

$$\Sigma\mathbf{F} = \frac{d\mathbf{P}}{dt}$$

$$F_{in} - c\dot{x} = (M+m)\ddot{x} + mr\ddot{\theta}\cos\theta - mr\dot{\theta}^2\sin\theta \qquad (5.1)$$

where $\mathbf{P} = \sum m\dot{\mathbf{x}}$ is the total (linear) momentum of the system. Equation 5.2 can be obtained similarly, by balancing the net torque on the system with the change in its angular momentum, $\mathbf{L}$:

$$\Sigma\mathbf{T} = \frac{d\mathbf{L}}{dt}$$

$$mgr\sin\theta - b\dot{\theta} - mr\ddot{x}\cos\theta = mr^2\ddot{\theta} \qquad (5.2)$$

where $\mathbf{L} = \sum J\dot{\boldsymbol{\theta}}$. Note that it is assumed here that the moment of inertia of the pendulum neglects any distributed mass along the length of the arm. The mass is modeled as though it is entirely concentrated at a radius, r, from the pivot, so that $J_p = mr^2$.

When the pendulum is balancing upright near its unstable equilibrium position, these equations can be linearized using the approximations $\sin\theta \approx \theta$ and $\cos\theta \approx 1$. Rearranging equations 5.1 and 5.2, the linearized equations of motion become:

$$F_{in} = c\dot{x} + mr\ddot{\theta} + (M+m)\ddot{x} - [mr\dot{\theta}^2\theta]_{[H.O.T.]}$$

$$F_{in} \approx c\dot{x} + mr\ddot{\theta} + (M+m)\ddot{x} \qquad (5.3)$$

$$0 = mgr\theta - b\dot{\theta} - mr^2\ddot{\theta} - mr\ddot{x} \qquad (5.4)$$

When the pendulum is near its stable equilibrium, θ is close to 180° (as defined in Figure 5-2). To write the equations of motion more clearly, we will first define an angle ϕ which is offset from θ by 180° ($\phi = \theta + 180°$) and measures the displacement of the pendulum from the down-pointing equilibrium position.

Since $sin(\theta + 180°) = -sin\theta$ and $cos(\theta + 180°) = -cos\theta$, the linearized equations of motion for the stable equilibrium case are:

$$F_{in} \approx c\dot{x} - mr\ddot{\phi} + (M+m)\ddot{x} \qquad (5.5)$$

$$0 = -mgr\phi - b\dot{\phi} - mr^2\ddot{\phi} + mr\ddot{x} \qquad (5.6)$$

248

5.3 Controller Dynamics

The purpose of this section is to describe some aspects of the dynamic behavior of the controlled cart system. As mentioned in the introduction to this chapter, any steady-state equilibrium positions possible for the cart-driven pendulum are with the pendulum vertical (pointing exactly up or down). The linearized equations of motions demonstrate why this is, as described below.

Any steady-state solution which satisfies Equation 5.4 requires that the pendulum angle be zero ($\theta = 0$, pointing up vertically). For the system to maintain some constant, non-zero pendulum angle the cart must accelerate with a constant acceleration of magnitude $g\theta$. Similarly, any steady equilibrium state which satisfies Equation 5.6 requires that pendulum point exactly downward ($\phi = 0$).

Any friction losses in the cart (represented by the "$c\dot{x}$" term in Equations 5.3 and 5.5) result in a second requirement: that the velocity of the cart be proportional to the net horizontal force on the cart at steady state. If there is no net force on the cart, then there are two possible steady-state solutions. Either the cart is at rest and the pendulum points exactly up (in an unstable equilibrium), or the cart is at rest and the pendulum points exactly down (in a stable equilibrium).

The cart-driven inverted pendulum described in this chapter is stabilized in the upright equilibrium position through a state-space controller which is currently implemented on the dSPACE DS1102 board. The controller uses estimates of the errors between reference and measured values of four states: pendulum angle (θ_e) and angular velocity ($\dot{\theta}_e$) and cart position (x_e) and velocity ($\dot{x}_e$). These states are measured as described in Section 5.1. The commanded control effort, F_{in} (in Newtons), is given below:

$$
F_{in} = \begin{bmatrix} -316 & -276 & -1032 & -1221 \end{bmatrix} \begin{bmatrix} x_e & (m) \\ \dot{x}_e & (m/s) \\ \theta_e & (rad) \\ \dot{\theta}_e & (rad/s) \end{bmatrix} \tag{5.7}
$$

Using Equations 5.3, 5.4 and 5.7, we can make some predictions about the dynamic behavior of this upright driven-cart pendulum system. For instance, if we request an angle of one degree ($\theta_{ref} = 0.017$ rad), the controlled cart system will still operate about an equilibrium state where the actual pendulum angle is precisely vertical (pointing up), as required by Equation 5.4. Now suppose that there are no external disturbance forces exerted on the cart or pendulum. In this case, the cart will operate about an equilibrium position such that the θ_e and x_e terms in Equation 5.7 result in zero net commanded force. The steady-state equilibrium cart position will therefore be proportional to requested reference pendulum angle. Specifically,

$$x_e = \theta_e \cdot \frac{-1032}{316} \frac{(m)}{(rad)} = \theta_e \cdot -3.27(m/rad) \tag{5.8}$$

Since the pendulum continues to operate about vertical, a requested displacement in pendulum angle of 0.017 rad (1° clockwise, as defined in Figure 5-2) will result in a steady-state error in pendulum angle of $\theta_e = -0.017$ rad. The cart position will correspondingly operate about a location 0.057 meters to the right of whatever point is defined as "zero".[2] In other words, the cart's equilibrium position shifts by about 2.2 inches (0.057 m) for each degree change in reference angle for the pendulum.

5.4 Performance

This section briefly discusses some aspects of the dynamic response of the cart-driven. First, it provides data showing improved performance when gyro was used to measure the angular velocity of the pendulum instead of a differentiated encoder signal. Figure 5-3 shows typical data for system demonstrating a significant resonance around 90 Hz which appears when the differentiated encoder signal is used. In Figures 5-4 and 5-5, taken when the gyro was used for control instead, this vibration problem is no longer evident.

---

[2]The encoders are not indexed and reset to zero when the controller is downloaded to the dSPACE board. Therefore, a position of "zero" for the cart corresponds to wherever the cart was resting on the track when the code was generated.
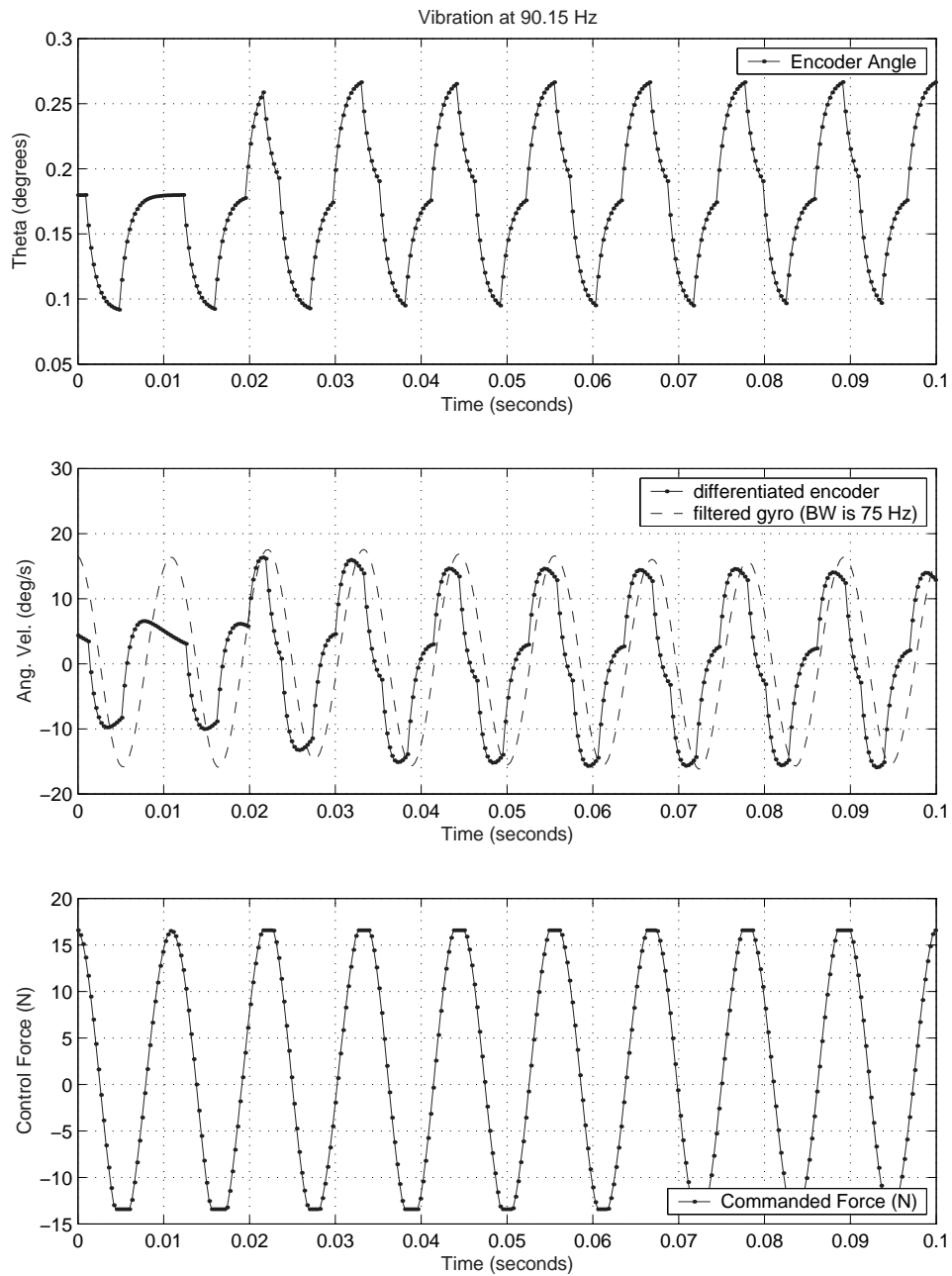
Figure 5-3: Data showing vibration problem near 90 Hz. The differentiated encoder signal was used to estimate pendulum velocity when the data above were collected. Angular velocity data from the gyro was also recorded for comparison, however, and is shown in the middle plot.

Figure 5-4 shows data characterizing the steady-state behavior of the cart-driven pendulum system as it balances upright. The top portion of Figure 5-4 provides data comparing the encoder measurements of pendulum angle to those obtained from complementary filtering of the gyro and accelerometer signals. The encoder measurement in this plot has been offset slightly so that the two measurements line up more closely and can therefore be compared more easily. Below this is data of the cart position, taken during the same time period. The cart has a characteristic oscillation (at a frequency of roughly 0.2 Hz) about its equilibrium position.

The accelerometer provides a low-frequency measurement of the angle of the pendulum with respect to gravity. The 2-axis accelerometer was glued onto the mass at the end of the pendulum by hand, so its alignment was not precise! Any misalignment can be adjusted by adding an offset angle to the pendulum measurement. The locations of both the accelerometer (at the free end of the pendulum) and the gyro (near the pendulum pivot) can be seen in Figure 5-1. The *measured* equilibrium pendulum angle in the top plot of Figure 5-4 is not zero, although presumably the actual equilibrium angle must be zero, for reasons discussed in the previous section. The offset in the measurement appears to be approximately $-1.6°$. The cart position, shown in the lower plot, is offset from zero by about 0.085 meters. This works out to roughly 0.053 meters in the offset of the equilibrium cart position for each degree offset in reference pendulum angle, compared with the predicted ratio of 0.057 m/deg (3.27 m/rad) calculated and the end of the previous section.

Finally, Figure 5-5 shows the transient response of both the cart-driven inverted pendulum and the robotic inverted pendulum (the DIPR) described in Chapter 7. The inertia of the DIPR is much larger than that of the pendulum on the cart-driven system, and the response of the DIPR is correspondingly much slower than the cart system.

The inertia of the pendulum on the cart is primarily due to the 0.15 kg mass, which is mounted 0.314 m from the pivot. The inertia of the cart's pendulum, J_c is therefore approximately:

$$J_c \approx mL^2 = 0.015 \ (kg\,m^2) \tag{5.9}$$
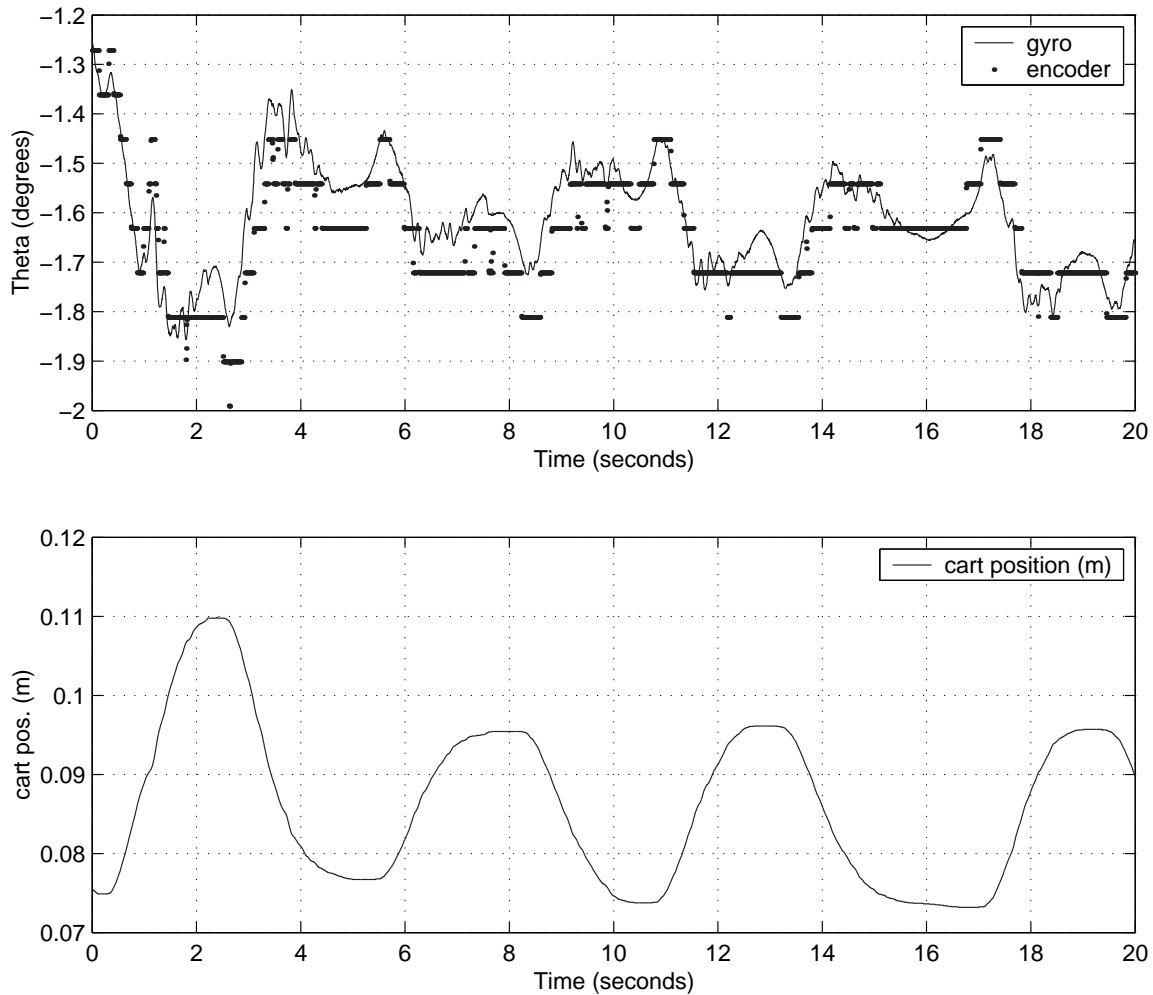
Figure 5-4: Steady-state IP cart response using gyro measurement of $\dot{\theta}$. The figure at the top shows the response of the calibrated gyro-accelerometer estimate of pendulum angle. The gyro and accelerometer signals have been blended using complementary filtering as described in Section 6.2.1 of the next chapter. This data set is overlaid with a simultaneous encoder measurement on the same plot, which has been offset slightly to compare the two more easily. Below this is a plot of cart position during the same time period, measured with the motor encoder. The pendulum encoder signal was *not* used in controlling the system here; it was only recorded for comparison. Note that the 90 Hz resonance seen in Figure 5-3 (i.e. when the controller uses the differentiated encoder signal) is not evident in the data above, using the velocity signal from the gyro and using complementary filtering of the gyro and accelerometer to estimate pendulum angle.
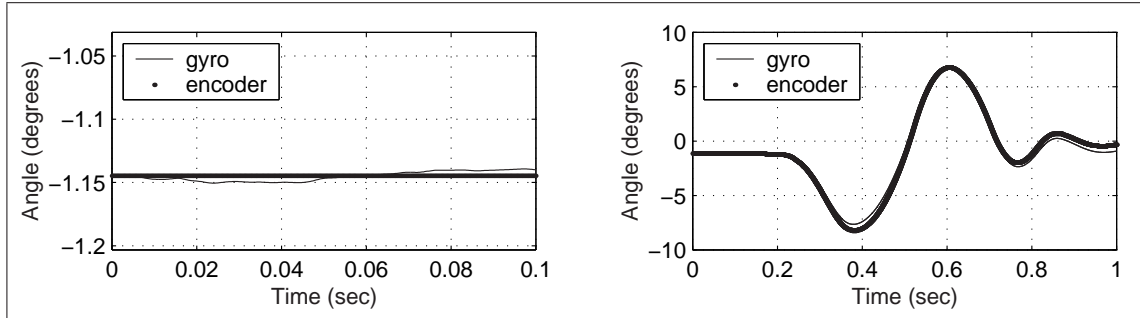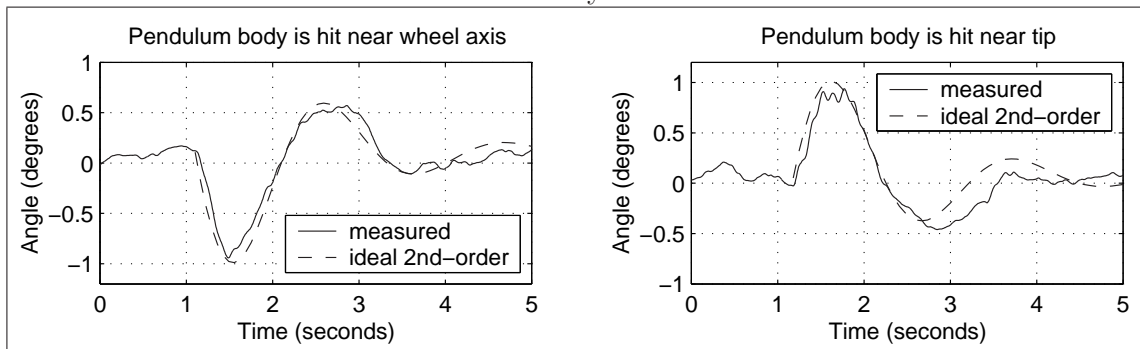
Figure 5-5: Disturbance rejection of the IP cart system. At right, top is the transient response of the pendulum to a disturbance applied at its tip. The controller for the cart system used the gyro (and accelerometer) to estimate pendulum angle and angular velocity when these data were taken. The figure at left, top plots a subset of the same data in the period just before the disturbance is applied, to examine the gyro and encoder measurements of pendulum angle as the pendulum balances in steady state. As in Figure 5-4, the 90 Hz resonance seen in Figures 5-3 is not in evidence here. Each encoder count corresponds to an angle of 0.09^o, as illustrated in the encoder data shown in Figure 5-4, and the gyro data indicate angular deflections on the order of $0.01^o - 0.02^o$ during this time. Thus, it is not surprising the encoder registers a constant value here while the gyro does not.) The lower two data sets show the transient response of the DIPR robot described in Chapter 7 for comparison. (See the text for more detail.) The data shown in the lower plots also appears in Figure 1-15 on page 1-15 of Chapter 1.

The inertia of the "pendulum" in the IP robot is much larger, since it consists of the entire chassis between its two wheels and also the extended pendulum arm. These components are all connected together as a rigid unit and can be seen in the photo which appears on both pages 56 and 319. The total inertia, J_r, of the rigid pendulum-body of the robot (detailed in Section 7.5.2 on page 370) is approximately:

$$J_r = J_p + J_b + mL^2 \approx 0.05 + 0.05 + 1 \cdot 0.4^2 = 0.26 \; (kg \, m^2) \qquad (5.10)$$

This is about 17.6 times larger than the inertia of the pendulum in the cart-based system. The response of the robot is roughly 5 times slower than that of the cart, as shown in the right-hand plots of Figure 5-5.

For the data in Figure 5-5, the disturbances applied to the cart-driven and robotic systems (by tapping each system by hand) were of approximately the same magnitude. One would expect the smaller inertia in the cart-based system would therefore experience a greater deflection, and this is in fact the case. The deflection of cart-driven pendulum is about five times greater than that of the robot.

The next chapter provides more details on the use of gyroscopes in implementing tilt sensing. In particular, Section 6.2 describes a method called complementary filtering in which multiple types of sensors can by blended to provide a single estimate of some desired output. In the case of an inverted pendulum robot, simply integrating the signal from a gyro would result in a ramping error because the gyro has a finite DC bias. To improve the measurement, a gyroscope can be blended with a sensor which measures tilt directly, such as an accelerometer or a tilt sensor which uses electrolytic fluid which has better performance at low frequencies. The "gyro" data shown in the top portions of Figures 5-4 and 5-5 for instance has been blended with an accelerometer signal to create a more accurate estimate of pendulum angle than would obtain by integrating the gyro alone.

Chapter 6

Tilt Sensing for Inverted Pendulum Robots

The cart-driven pendulum system described in Chapter 5 uses an encoder to measure the angle between the pendulum and the cart on which it is mounted. Since the cart rides on a level track, it too remains level, and the encoder therefore provides an absolute measure of the pendulum angle with respect to gravity.

In a robotic inverted pendulum system like the DIPR described in Chapter 7, encoders can measure the relative angle between the body of the robot and each wheel, but the wheels will rotate in inertial space as the vehicle moves. For this reason, such an encoder can not provide an absolute angle of the pendulum body with respect to gravity. This absolute angle measurement is achieved in the DIPR by using gyroscopes.

This chapter describes several issues which relate to the use of gyroscopes for tilt sensing in a two-wheeled inverted pendulum vehicle.

6.1 Tilt Sensing for Segway and iBOT

The implementation of tilt sensing for the Segway is an interesting topic, since cost-effective MEMS sensors will probably make redundant sensing much more widespread in the future. Their low price makes MEMS sensors practical for undergraduate labs,

and the gyro-configuration issue in the Segway is an intriguing design problem. This section briefly analyzes several design issues in configuring multiple gyros for a system like the Segway, where fail-operation behavior is necessary. I begin with a broad review of the key concepts in and brief history of the use of redundant sensor arrays. Necessary mathematical concepts are then developed to explain some basic concepts in sensor redundancy. Finally, I discuss how these results are applicable toward the specific requirements of the Segway.

6.1.1   A Brief Summary of the Use of Redundancy in FDI

Redundant sensors are widely used in implementing "failure detection and isolation" (FDI) for critical systems. "Detection" means signalling a binary alarm [216] when there is a reasonable likelihood that one or more sensors have failed. "Isolation" is the more sophisticated problem of determining which particular sensor(s) are in error. This information must then be used to determine how best to re-weight the outputs of the sensors in the array to estimate the state of the system. For many applications, this simply means excluding information from a bad sensor entirely. More complex algorithms effectively quantify the extent of failure in each sensor to determine if the sensor is completely unusable (referred to as an "off" or "hard-over" failure [216]), or if the output instead suffers from increased noise (e.g. due to a degradation in bias or increased sensor variance). In the latter case, the sensor can still potentially provide useful information about the state of the system (with a reduced weighting, compared to sensors with apparently lower noise levels) [48, 158, 166, 167, 213, 58]. This problem of the "estimation" of system states from noisy sensor data involves more sophistication than that of isolation, just as isolation is a more difficult problem than detection [216].

Methods of FDI have grown significantly in complexity as computing power has increased over the past three decades. The approaches used over the years can be broadly categorized as being based upon either "hardware redundancy" or "analytical redundancy" [158]. These two types of FDI are alternatively referred to as "direct" and "temporal" methods, respectively [48]. Hardware redundancy uses the geomet-

258

ric relationships between the sensors in a fixed array to recognize at any particular moment whether their outputs are mathematically compatible (within given noise thresholds) and, if not, to isolate which sensor(s) disagree with the others. Analytical redundancy, on the other hand, incorporates a model of the dynamics of the system being sensed and analyzes whether the changes in state variables over time are compatible. I prefer using the phrase "geometric redundancy" when discussing hardware redundancy because I believe this more clearly distinguishes it from temporal FDI of a sensor in an array.

The mathematical theory behind geometrical redundancy developed hand-in-hand with the space program in the 1960's and essentially involves creating parity vectors to detect incompatibility in sensor outputs [158, 73, 160]. Parity vectors will be discussed in detail in the next subsection, as they are a central mathematical concept in hardware redundancy systems, and most of this section will focus on geometric (not temporal) FDI.

Once computational power became more available in the 1970's, the state of the art in FDI became much more sophisticated, involving (often complex) state-space models of system dynamics. Based on such models, analytic FDI algorithms analyze and compare the likelihoods of redundant sensor measurements over time. "Fly-by-wire" (FBW) technology strongly motivated the development of this state-space approach. One early example of this type of sensor FDI system was developed at Draper Lab in the 1970's for the F-8 and incorporates data from eleven pairs of sensors [58].[1] The resulting "dual-mode FDI system" evaluates and compares the measurements of both sensors in each pair based on a sequential probability ratio test (SPRT) [58]. A more recent example of temporal analytical redundancy (described in a paper from 1994) is based upon a simplified linearization of a "fully nonlinear thermodynamic" model of a gas turbine jet engine which uses "17 state variables including pressures, air and gas mass flow rates, shaft speeds, absolute temperature,

---

[1]The 11 instrument types includes the following: "longitudinal accelerometer, lateral accelerometer, normal accelerometer, roll rate gyro, pitch rate gyro, yaw rate gyro, vertical gyro, directional gyro, altimeter, Mach meter, and alpha vane" [58].

and static pressures" [158]. Such detection schemes are much more complicated (and computationally intensive) than the purely geometric redundancy checks used in the 1960's moon-landing era.

I find the Segway intriguing because I expect that it simply uses the more primitive, geometric redundancy check (and that this is probably the right choice), and I also suspect they violate a fundamental principle in geometric redundancy (and that this, too, may be an appropriate design choice). Specifically, it appears, from Figure 6-1 that they align three of their five sensors in the same plane. Such a configuration of a five-sensor array would allow fault detection but precludes fault isolation, for reasons discussed in detail in the subsection ahead.
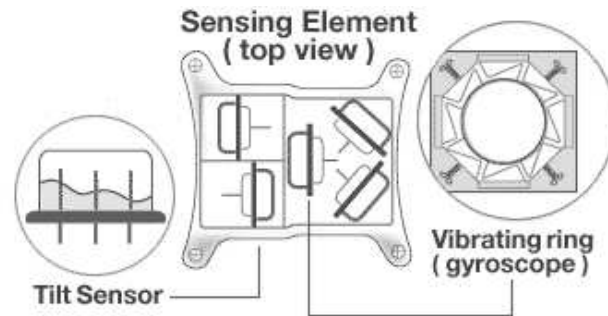
Figure 6-1: Schematic of skew-axis gyros in the Segway. The "Sensing Element" in the Segway contains 5 gyros and 2 tilt sensors. This is the only documentation I have found which gives any hint about the alignment of the gyros, and their exact configuration here is not clear. GIF obtained from Segway sales site at amazon.com [8]

A lot of the seminal work done during the 60's and 70's in both geometric and temporal redundancy occurred at MIT and Draper Lab [58, 48, 216, 167, 73] and at a variety of other companies and institutions working on military and aerospace applications, including Northrop [166], TRW [213], Honeywell [160], Lockheed [210] and Xerox [210]. The mathematical discussion of redundancy in the next section involves only geometrical redundancy, and it owes much to the work done during this seminal period in development of redundant inertial measurement arrays. I focus on hardware (versus temporal) redundancy because (1) the key concepts are so fundamental, (2) I believe that geometric redundancy should be adequate for implementing

fault-operational FDI for the Segway, and (3) I wish to compare the redundancy requirements of the Segway with those of the space program to discuss how applicable such fundamental principles are in this application.

6.1.2 Mathematics of FDI Using Geometric Redundancy

This subsection explains some fundamental mathematical concepts in using geometric redundancy for failure detection and isolation. Summarizing briefly, failure *detection* is typically accomplished through the use of "parity vectors". *Isolation* can be accomplished by creating various subsets from groups of sensors whose axes form a set of linearly dependent vectors and then performing a series of parity checks on each of these subsets to identify the faulty sensor(s) through a process of elimination. The discussion ahead will explain this approach to FDI in detail.

Throughout the analysis that follows, we will be concerned with the case of FDI for a *single sensor failure.* The principles outlined can certainly be expanded to permit FDI in cases with two or more simultaneous sensors faults, but our analysis will be more straight-forward if we limit FDI to single-sensor failure initially. In many hardware situations, single-sensor failure detection is quite sufficient, as well, since the probability of a simultaneous failure of two (or more) sensors will generally be very small.

For instance, suppose we have an array of five sensors which each have an expected average failure rate of once every 10 years, and that we model the failure mechanism of each sensor as a Poisson process (which seem sensible) and assume that failure of one sensor is uncorrelated to that of any other (which may be less likely, but it makes the problem tractable). There is a probability of 39.25% that at least one of the five sensors will fail in a given year (which is quite high). However, the chance of two sensors failing *within an hour of one another* in a given year is approximately 1 in 88,000, and the odds against any two sensors failing *within five minutes of one another* in a particular year are roughly 10,500,000 to 1. Table 6.1 shows what these odds are if we assume other failure rates.

We will also assume throughout this and subsequent discussions that each indi-

261

Table 6.1: Annual failure rates (single and simultaneous dual) in 5-sensor array

average sensor life (years)	Poisson rate (λ)	% chance of some failure in 5-sensor array in 1 year	odds 2+ failures within 1 hr in 1 year ($x = 24$)	odds 2+ failures within 5 min in 1 year ($x = \frac{60}{5}24$)
n	$\lambda = \frac{1}{n}$	$1 - e^{-5\lambda}$	$1/\left(1 - \left[1 - \left(1 - e^{\frac{-\lambda}{365x}}\right)^2\right]^{365x}\right)$	
1	1	99.3%	1/8,800	1/105,000
10	0.1	39.35%	1/880,000	1/10,500,000
100	0.01	4.9%	1/88,000,000	1/1,050,000,000
1000	0.001	0.5%	1/8,800,000,000	1/105,000,000,000

vidual sensor in a redundant array measures some desired quantity with respect to a single axis. For instance, a gyro measures the angular velocity about a particular axis and an accelerometer measures acceleration along an axis.

To begin our discussion, suppose we wish to use sensors aligned along the axes shown in Figure 6-2 to provide measurements along the x and y axes. Any two of the three sensors are sufficient to do so, since each 2-sensor combination spans the desired 2-D space (i.e. the x-y plane). To get an output corresponding to some particular output axis, we would simply combine the individual (scalar) sensor outputs in the same proportions we would combine the vectors of their axes to create a vector in the direction of the desired output axis. For instance, suppose we use the sensors aligned along vectors **a** and **c**. It should be clear that $x = a$ and $y = 1.25\,c - 0.75\,a$, and in turn that these are the weightings we would use to create estimated outputs along the x and y axes.

Detecting sensor failure in our 2-dimensional space requires at least one additional (redundant) sensor output to supplement the two required for measurement alone. Suppose we measure an output of $A = 1$ along the **a** vector and of $B = -1$ along **b**.

3 vectors spanning 2-D space
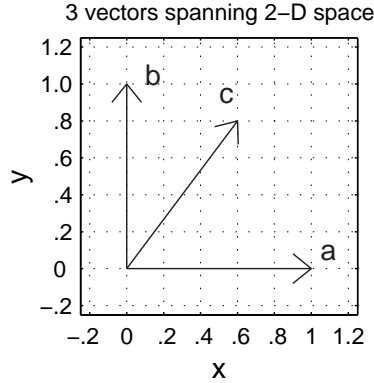
Figure 6-2: A 3-sensor array spanning 2-D space. The three vectors shown point in the directions $\mathbf{a}=[1\ 0]$, $\mathbf{b}=[0\ 1]$, and $\mathbf{c}=[.6\ .8]$. Sensors aligned along these vectors form a sufficient set for fault detection, since the three vectors form a linearly dependent set. Specifically, $\mathbf{c} = .6\,\mathbf{a} + .8\,\mathbf{b}$.

Then the expected value of the remaining sensor output, $\bar{C}$, is:

$$\bar{C} = (0.6 \cdot A + 0.8 \cdot B) = 0.6 - 0.8 = -0.2 \tag{6.1}$$

Sensor noise clearly adds some uncertainty. If there is no gross error in the individual measurements, however, the linear dependence of vectors $\mathbf{a}$, $\mathbf{b}$ and $\mathbf{c}$ is such that we can expect:

$$(0.6 \cdot A + 0.8 \cdot B - C) \approx 0 \tag{6.2}$$

We can use the linear dependence of the sensors in the array to perform a parity check of the system and thereby implement fault detection. First, we must select a threshold "ϵ" based on the whatever we deem as acceptable noise characteristics for the sensors. This threshold defines what we mean by "failure". We can then state that this particular threesome of sensors contains at least one faulty sensor if the absolute value of the parity vector defined by Equation 6.2 exceeds this threshold value.

$$|(0.6 \cdot A + 0.8 \cdot B - C)| \leq \epsilon \quad \rightarrow \quad \text{acceptable} \tag{6.3}$$

$$|(0.6 \cdot A + 0.8 \cdot B - C)| > \epsilon \quad \rightarrow \quad \text{fault detected} \tag{6.4}$$

The 3-sensor array in Figure 6-2 is not sufficient for fault isolation, however. The

method described above can identify when a problem exists within an entire array, but it gives no information about which sensor(s) are broken. Isolation requires at least two redundant sensors (beyond the two required for measurement in a 2-dimensional space). Figure 6-3 shows one of an infinite number of acceptable sets of vectors for isolation in a 2-D sensor array.
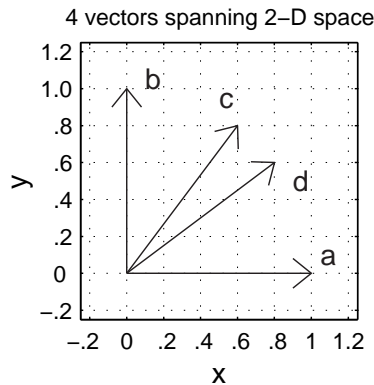
Figure 6-3: A 4-sensor array spanning 2-D space. The four vectors shown point in the directions $\mathbf{a}$=[1 0], $\mathbf{b}$=[0 1], $\mathbf{c}$=[.6 .8], and $\mathbf{d}$=[.8 .6]. Sensors aligned along these vectors form a sufficient set for fault isolation. This can be accomplished by performing parity checks on each of the four possible triads of sensors from this set.

To identify a faulty sensor, we can perform a parity check on each of the four possible triads of sensors. If none of the parity vectors exceed our error threshold, all of the sensors are (probably) fine. If one sensor is bad, it should generally[2] push three of the four triads beyond the acceptable threshold, because it is a member of three of the four triads being tested. Let us suppose we have *already detected a sensor fault exists*. In this case, we can conclude that the sensor which was excluded from the one

---

[2]Of course technically speaking, there is always a finite probability that a bad sensor will "just happen" to output a value which still satisfies the parity check at a particular instant in time! ("Even a broken clock is right twice a day...")

non-faulty triad must be bad one:

$$|(0.6 \cdot A + 0.8 \cdot B - C)| \leq \epsilon \quad \rightarrow \quad \text{D is bad} \tag{6.5}$$

$$|(0.8 \cdot A + 0.6 \cdot B - D)| \leq \epsilon \quad \rightarrow \quad \text{C is bad} \tag{6.6}$$

$$1.09 \cdot |(0.35 \cdot A + 0.75 \cdot C - D)| \leq \epsilon \quad \rightarrow \quad \text{B is bad} \tag{6.7}$$

$$1.09 \cdot |(0.35 \cdot B - C + 0.75 \cdot D)| \leq \epsilon \quad \rightarrow \quad \text{A is bad} \tag{6.8}$$

The parity vectors above are scaled appropriately so that the same value of ϵ is appropriate as the threshold in each check, assuming the acceptable noise characteristics for all four sensors are the same.

Before proceeding to a more formal discussion about parity vectors I will call attention to some additional details which the 2-dimensional examples above can illustrate. First, simply having four sensors is not sufficient for the 2-D fault isolation method above. We also need to make sure the array contains at least one set of four of the sensors *no two of which provide outputs along the same axis.* Referring to the vectors shown in Figures 6-2 and 6-3 again, suppose we use two measurements which point in the direction of vector **c**, C_1 and C_2, along with measurements A and B (in the directions of vectors **a** and **b** respectively, as previously defined). Then we can only create the following three parity checks:

$$|(0.6 \cdot A + 0.8 \cdot B - C_1)| \leq \epsilon \quad \rightarrow \quad C_2 \text{ is bad} \tag{6.9}$$

$$|(0.6 \cdot A + 0.8 \cdot B - C_2)| \leq \epsilon \quad \rightarrow \quad C_1 \text{ is bad} \tag{6.10}$$

$$|(C_1 - C_2)| \leq \epsilon \quad \rightarrow \quad \text{either A or B is bad} \tag{6.11}$$

This means if either A or B fails, we can *detect* that either sensor A or B is at fault , but we can not *isolate* which of the two sensors is the cause. (We *can* isolate a fault of either C_1 or C_2, however.)

The problem in this example is that A and B are the only two sensors which provide any sensitivity along the axis perpendicular to the line on which both C_1 and C_2 lie. Any parity check equation can not exclude either A or B without excluding them both, *because these are the only two sensors which include vector components orthogonal to the space spanned by all the remaining sensors* (i.e. orthogonal to vector

c). As a result, our method of "isolation through a process of elimination" can no longer distinguish a failure in sensor A from a failure in B. Expanding this concept more broadly, if *any* sensor in an array has some sensitivity along a particular axis in space, the isolation method presented here requires that *at least three* sensors in the entire array must have some sensitivity along that axis.

We can now begin to generalize some geometric principles for sensor arrays. To create a sensor array whose outputs span an n-dimensional space, there needs to be at least one (uniaxial) sensor which is aligned at least partially along (i.e. with a non-zero dot product with) each existing vector in the measured n-dimensional space. Stated differently, we can not allow a direction in the n-dimensional space to exist which is not measured with at least some degree of sensitivity by at least one sensor. To provide fault detection, there must be at least two sensors so aligned to provide some sensitivity in each possible direction, and for fault isolation, one must have have three such sensors which provide some level of sensitivity in each possible direction of sensing.

One way of achieving the requirements above for the tasks of measurement, fault detection, and fault isolation is to arrange one, two or three sensors along each of n mutually-orthogonal axes in the n-dimensional space. Detection then involves comparing the outputs of the two sensors along each orthogonal axis. When a discrepancy between two co-linear sensors occurs, we know one of the two is at fault. Isolating which sensor is at fault requires at least three sensors along each of the mutually-orthogonal axes in order to create a majority of "good" sensors to "out-vote" a bad one.

For the 2-d case we have discussed so far, this method (i.e. using a set of mutually-orthogonal axes) requires 2 sensors for measurement, 4 sensors for detection, and 6 for isolation, but as we have already seen, skew-axis orientations allow us to accomplish these tasks with 2, 3, and 4 total sensors, respectively, if such axes are chosen appropriately. For a sensor array whose output spans an n-dimensional space, we can state more generally that:

1. When the sensors in an array are aligned along a set of n mutually orthogonal

axes which span the n-dimensional space of interest, we need to have n, $2n$ and $3n$ sensors for measurement, detection and isolation, respectively.

2. The minimum numbers of measurements required for measurement, detection and isolation are n, $n + 1$, and $n + 2$ (respectively).

3. If we use the minimum numbers of measurements given above, however, we can only be sure of being able to isolate a single sensor failure if each n-sensor subset of sensors spans the full n-dimension space of the sensor array.

As an example, consider the Segway, which uses the a 5-sensor array [180, 8]. This is the minimum number of sensors required for fault isolation in a 3-D sensor array. Complete fault isolation also requires that no three of these five sensors lie in the same plane, however. Otherwise, if either of the non-coplanar sensors fails, we will not be able to distinguish which of the two is bad. At this point, it is useful to remind ourselves that *the real point of isolating a bad sensor is to be able to exclude it so that we can continue to obtain useful output from our sensor array.* If we can not distinguish which of two sensors is bad, we must disregard both of them in our array. For a 3-d sensor array, such as the one used by the Segway, if three of five sensors are oriented within some particular plane ("P"), this means that if either of the non-coplanar sensors fails, the entire array can no longer provide a useful measurement for the axis perpendicular to the plane P.

We will consider the specific case of the Segway in more detail later. In the next section, I will summarize the results we have obtained so far more formally and outline some simple relationships (i.e. linear algebra) one can use to implement this method of FDI. After this, I will discuss sensor alignment. It should be clear by now (and agrees with our intuition) that the alignment of the sensors can affect the sensitivity along each of the output axes of a sensor array. (As an extreme example, aligning all sensors along a single axis clearly provides no information about any other directions in space.) Symmetric orientations are of particular interest. Finally, I will apply all of the concepts covered in this discussion of FDI to the design problem of creating a redundant sensor array for the Segway.

6.1.3 Linear Algebra for FDI

This subsection presents some simple algebraic methods for implementing a parity check on a redundant array of sensors. The method summarized here is sometimes referred to as a "voting scheme" [48, 213, 41]. The linear algebra here simply codifies the general approach discussed over the past several pages for testing whether any of the sensors' outputs violates the geometric requirements defined by its alignment (with respect to the other sensors in the array). The notation used over the years by different authors to describe this method (for the vectors and matrices involved) varies, but the essence of the method is straight-forward [48, 213, 166, 190, 94]. The description below summarizes the goals of the approach and then outlines equations which implement it.

To implement a direct (geometric) redundancy check for the detection and isolation of a single sensor failure in a sensor array, we can create a set of parity equations (i.e. parity checks). To *detect* every possible failure, we need to insure that each sensor is included in at least one parity equation. To *isolate* which sensor has failed, we must also insure that each sensor is excluded in at least one parity equation, and additionally, we must insure that there is a unique (i.e. two-way) functional mapping between the failure of each individual sensor and the resulting set of (binary) alarm statuses produced by the parity checks. This last point was emphasized in the discussion of Equation 6.11 at the end of the preceding subsection. For that configuration of sensors, it was not possible to create a set of parity relations whose statuses could unambiguously identify which particular sensor was bad.

If we have a set of m sensors which span an n-dimensional space, then there exists an space of parity vectors of dimension $m - n$. In the direct (geometric) FDI approach, the extent to which the sensor outputs lie in this $(m - n)$ dimension space is directly related to the incompatibility (i.e. error) in the sensor outputs. Another way to describe this is as follows. Let us consider each sensor output as containing both a dependent component (signal) and an independent component (noise). Then in a worst-case scenario (i.e. with a lot of noise), a set of m sensors will fully span

an m-dimensional space. With no noise at all however, the dependence between the sensors limits the (infinite) set of possible sensor outputs to an n-dimensional space. The parity space approach quantifies the extent to which the set of m sensor outputs lies orthogonal to the limited n-dimensional "space" of sensor combinations we can obtain if the sensors provide perfect (noise-free) output. The parity space represents the $m - n$ dimensional space of sensor combinations which can not exist unless there are errors (noise) in the sensor outputs.

For example, consider the 3-sensor alignment labelled "Set A" in Figure 6-4. The three vectors in this triad are spaced equally in a 2-d plane (i.e. with 120° wrt one another). Specifically, the three are at angles of 40°, 160° and 280°, as measured in a counter-clockwise direction from the +x axis. We will assume each sensor has the same sensitivity, so the three vectors all have the same length. We will use a length of unity for convenience.
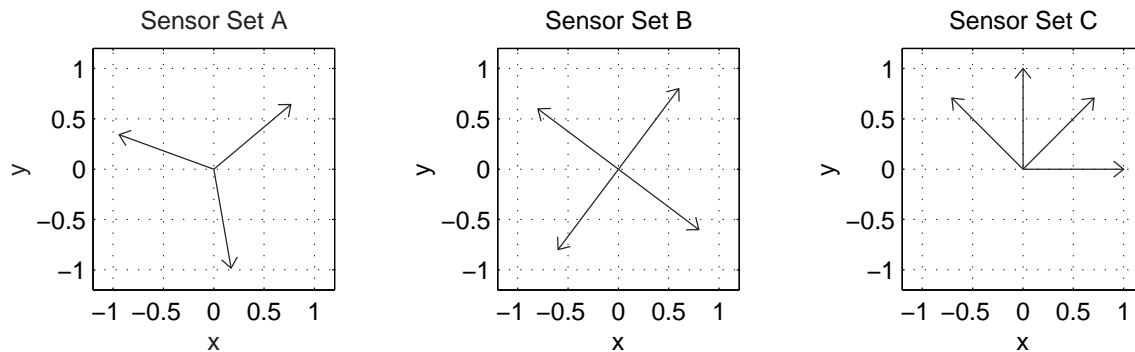
Figure 6-4: Examples of 3-sensor orientations in 2-D space.

The (column) vector of measurements from the three sensors, $\mathbf{y}$, will be related to the actual inputs to the sensor array, $\mathbf{x}$, through the the matrix of direction cosines of the sensors, $\mathbf{M}$:

$$\mathbf{y} = \mathbf{M}\mathbf{x} + \boldsymbol{\epsilon} \tag{6.12}$$

where $\boldsymbol{\epsilon}$ is the vector of noise components for the array. We will assume below that there is no covariance in the noise between any two sensors. We can obtain an estimate

$\hat{\mathbf{x}}$ of the actual states being measured ($\mathbf{x}$) by noting that:

$$(\mathbf{MM}^T)^{-1}\mathbf{M}^T\mathbf{y} = (\mathbf{MM}^T)^{-1}\mathbf{M}^T\mathbf{Mx} + (\mathbf{MM}^T)^{-1}\mathbf{M}^T\boldsymbol{\epsilon} \qquad (6.13)$$

$$= \mathbf{x} + (\mathbf{MM}^T)^{-1}\mathbf{M}^T\boldsymbol{\epsilon} \qquad (6.14)$$

For convenience, we will now define a new matrix $\mathbf{K}$:

$$\mathbf{K} = (\mathbf{MM}^T)^{-1}\mathbf{M}^T \qquad (6.15)$$

so therefore:

$$\mathbf{x} = \mathbf{Ky} - \mathbf{K}\boldsymbol{\epsilon} \qquad (6.16)$$

$$\hat{\mathbf{x}} = \mathbf{Ky} \qquad (6.17)$$

The matrix of direction cosines for the measurement directions in Set A are:

$$\mathbf{M} = \begin{bmatrix} cos(40°) & sin(40°) \\ cos(160°) & sin(160°) \\ cos(280°) & sin(280°) \end{bmatrix} \approx \begin{bmatrix} 0.7660 & 0.6428 \\ -0.9397 & 0.3420 \\ 0.1736 & -0.9848 \end{bmatrix} \qquad (6.18)$$

The rows of $\mathbf{M}$ are the vectors in real space along which the sensor axes lie in the x-y plane. The columns of $\mathbf{M}$ represent the ratios by which the signal component of the sensor outputs will change when the input changes in each of the two input direction (parallel to the x-axis or to the y-axis). If there is no noise ($\epsilon = 0$), then $\mathbf{y}$ must obviously be some linear combination of the columns of $\mathbf{M}$.

Because the vectors in Set A are evenly spaced in the x-y plane, the information content of the array is the same along the x and y axes. We can see this immediately by noting that:

$$\mathbf{M}^T\mathbf{M} = \begin{bmatrix} \frac{3}{2} & 0 \\ 0 & \frac{3}{2} \end{bmatrix} \qquad (6.19)$$

That is, we have the equivalent of 1.5 sensors in information content along each of the axes (x and y) - or in fact along any axis one may choose in the xy plane. If each of the three sensors has a characteristic variance of σ^2, the effective variance in each of the two desired outputs in $\frac{2}{3}\sigma^2$. The magnitude of the noise for the array is

$\sqrt{2/3} = 0.8165$ what it would be with one sensor aligned along each of the axes of interest. (The diagonal terms in Equation 6.19 are zero because the columns of $\mathbf{M}$ happen to be orthogonal to one another in this example.)

In this example, selecting a parity vector is quite straight-forward. The matrix $\mathbf{M}$ already has 2 columns (representing the permissible "directions" which can contribute the sensor array output vector $\mathbf{y}$ in the absence of noise). There is a unique axis which is orthogonal to both of these 2 columns, and we can find it by taking the cross-product of the 2 columns of $\mathbf{M}$ (as defined in Equation 6.18):

$$\begin{bmatrix} 0.7660 \\ -0.9397 \\ 0.1736 \end{bmatrix} \times \begin{bmatrix} 0.6428 \\ 0.3420 \\ -0.9848 \end{bmatrix} = \begin{bmatrix} 0.8660 \\ 0.8660 \\ 0.8660 \end{bmatrix} \tag{6.20}$$

The resulting vector above is comprised of equal portions of each of the three sensor outputs, so our parity check simply involves adding together the three sensor outputs with equal weighting. In the more general case, recall that we will be able to generate a set of "$m - n$" such vectors (given m measurement spanning an n-dimensional space) which will be orthogonal to the columns of $\mathbf{M}$ and mutually orthogonal. It is convenient to group these vector axes into a single matrix, which we will call "$\mathbf{V}$". By convention, these orthogonal vector axes comprise the **columns** of $\mathbf{V}$, and they are scaled to a length of unity so that:

$$\mathbf{V}^T\mathbf{V} = \mathbf{I} \tag{6.21}$$

In our example therefore:

$$\mathbf{V} = \begin{bmatrix} \sqrt{1/3} & \sqrt{1/3} & \sqrt{1/3} \end{bmatrix} = \begin{bmatrix} .5774 & .5774 & .5774 \end{bmatrix} \tag{6.22}$$

The columns of V form our "measurement axes in parity space" [166, p. 10]; each column is associated with a particular sensor in the array.

We can now create a parity vector $\mathbf{p}$ to check the consistency between the sensor outputs:

$$\mathbf{p} = \mathbf{V}\mathbf{y} \tag{6.23}$$

An estimate of the error is

$$\hat{\epsilon} = \mathbf{y} - \hat{\mathbf{y}} \tag{6.24}$$

where

$$\hat{\mathbf{y}} = \mathbf{M}\hat{\mathbf{x}} \tag{6.25}$$

Combining Equations 6.17, 6.24, and 6.25, we find that:

$$\hat{\epsilon} = (\mathbf{I} - \mathbf{MK})\mathbf{y} \tag{6.26}$$

or equivalently,

$$\hat{\epsilon} = \mathbf{V}^T\mathbf{y} \tag{6.27}$$

Importantly, our estimated sensor errors (in $\hat{\epsilon}$) do *not* depend on the magnitudes of the actual inputs in $\mathbf{x}$.

In our example, if $\mathbf{x} = \begin{bmatrix} 10 \\ 100 \end{bmatrix}$ and $\epsilon = \begin{bmatrix} .3 \\ 0 \\ 0 \end{bmatrix}$, then $y = \begin{bmatrix} 72.239 \\ 24.805 \\ -96.744 \end{bmatrix}$. The estimated error in this case is $\hat{\epsilon} = \begin{bmatrix} .1 \\ .1 \\ .1 \end{bmatrix}$, and again this would be the same regardless of the choice of $\mathbf{x}$ and depends only on ϵ. We can not distinguish which sensor is at fault here, and the error estimates are just attributed with equal weight to each sensor. If any of the estimated errors were larger than some defined threshold, it would trigger an alarm that the sensor array contains at least one faulty sensor. We would not be able to isolate which sensor was bad however. Isolation requires at least one additional sensor in the array.

The sensor orientations shown in Set B of Figure 6-4 allow for both detection *and* isolation. The direction cosine matric for this example is:

$$\mathbf{M} = \begin{bmatrix} .6 & .8 \\ -.8 & .6 \\ -.6 & -.8 \\ .8 & -.6 \end{bmatrix} \tag{6.28}$$

272

Since there are 4 sensors spanning 2 dimensions in space, there are an infinite number of possible parity vectors $\mathbf{V}$. One possible choice is:

$$\mathbf{V} = \begin{bmatrix} .5 & .5 & .5 & .5 \\ .5 & -.5 & .5 & -.5 \end{bmatrix} \tag{6.29}$$

Now if $\mathbf{x} = \begin{bmatrix} 10 \\ 100 \end{bmatrix}$ and $\epsilon = \begin{bmatrix} .3 \\ 0 \\ 0 \\ 0 \end{bmatrix}$, then $y = \begin{bmatrix} 86.3 \\ 52.0 \\ -86.0 \\ -52.0 \end{bmatrix}$. The estimated error in

this case is $\hat{\epsilon} = \begin{bmatrix} .15 \\ 0 \\ .15 \\ 0 \end{bmatrix}$. The zeros appear in the sensors which are orthogonal to

sensor number 1 (the "bad" sensor). Since the sensors corresponding to the rows 2 and 4 in $\mathbf{M}$ are co-linear, we can not distinguish between a failure in sensor 1 and a failure in 3. (Clearly, an error in either sensor 2 or 4 would likewise be indistinguishable, since sensors 1 and 3 are co-linear.)

In a final example, depicted as Set C in Figure 6-4, we have a symmetric set of equally-spaced sensors, no two of which are co-linear:

$$\mathbf{M} = \begin{bmatrix} 1 & 0 \\ \sqrt{.5} & \sqrt{.5} \\ 0 & 1 \\ -\sqrt{.5} & \sqrt{.5} \end{bmatrix} \tag{6.30}$$

One of the infinite possible choices for $\mathbf{V}$ is:

$$\mathbf{V} = \begin{bmatrix} 0 & .5 & -\sqrt{.5} & .5 \\ \sqrt{.5} & -.5 & 0 & .5 \end{bmatrix} \tag{6.31}$$

If $\mathbf{x} = \begin{bmatrix} 10 \\ 100 \end{bmatrix}$ and $\epsilon = \begin{bmatrix} .3 \\ 0 \\ 0 \\ 0 \end{bmatrix}$, then $y \approx \begin{bmatrix} 10.30 \\ 77.78 \\ 100.00 \\ 63.64.0 \end{bmatrix}$. The estimated error in this

273

case is $\hat{\epsilon} = \begin{bmatrix} .150 \\ -0.106 \\ 0 \\ 0.106 \end{bmatrix}$. Unlike the 4-sensor array in Set B, we can isolate the fault

within the sensor in Set C. To do so, we would systematically *exclude* a single sensor at a time by setting the corresponding column in $\mathbf{V}$ to zero. Here, we will use the notation $\mathbf{V}_i$ to denote a matrix identical to $\mathbf{V}$, except that all elements in the ith column of $\mathbf{V}_i$ are set to zero. Similarly, we will define a parity vector $\mathbf{p}_i$ associated with each $\mathbf{V}_i$:

$$\mathbf{p}_i = \mathbf{V}_i \mathbf{y} \tag{6.32}$$

We can now perform individual parity checks to identify the faulty sensor through

a process of elimination. We find that $\mathbf{V}_1{}^T \mathbf{p}_1 = \begin{bmatrix} 0 \\ 0 \\ 0 \\ 0 \end{bmatrix}$, $\mathbf{V}_2{}^T \mathbf{p}_2 \approx \begin{bmatrix} 0.15 \\ 0 \\ 0 \\ 0.10607 \end{bmatrix}$,

$\mathbf{V}_3{}^T \mathbf{p}_3 \approx \begin{bmatrix} 0.15 \\ -0.10607 \\ 0 \\ 0.10607 \end{bmatrix}$, and $\mathbf{V}_4{}^T \mathbf{p}_4 \approx \begin{bmatrix} 0.15 \\ -0.10607 \\ 0 \\ 0 \end{bmatrix}$. The one parity check which

"passes" in this case is the one in which we have *excluded* any contribution from sensor 1; therefore, we can isolate the error as being due to sensor 1.

Of course, in a real sensor array, each sensor will have some finite error, and we must set an appropriate threshold which distinguishes a failure from the allowable noise which will exist in the measurements. I will not discuss setting such thresholds, except to say that they clearly depend on the noise characteristics of the sensors and amount to a trade-off, weighing both the probability and cost of triggering false alarms against those of failing to identify actual faults.

To give the reader some feel for the effectiveness of this method, however, consider the sensor alignments in Set C once again. Suppose we instead have errors in all the sensor measurements, with the error in sensor 1 outweighing the others by a factor

of 3. Specifically, let us say that $\epsilon = \begin{bmatrix} .3 \\ .1 \\ .1 \\ .1 \end{bmatrix}$. In this case, the parity relations

will produce the following: $\mathbf{V}_1{}^T\mathbf{p}_1 \approx \begin{bmatrix} 0 \\ 0.01464 \\ -0.02071 \\ 0.01464 \end{bmatrix}$, $\mathbf{V}_2{}^T\mathbf{p}_2 \approx \begin{bmatrix} 0.18535 \\ 0 \\ 0.01464 \\ 0.12071 \end{bmatrix}$,

$\mathbf{V}_3{}^T\mathbf{p}_3 \approx \begin{bmatrix} 0.15 \\ -0.05607 \\ 0 \\ 0.15607 \end{bmatrix}$, and $\mathbf{V}_4{}^T\mathbf{p}_4 \approx \begin{bmatrix} 0.11464 \\ -0.09142 \\ 0.01464 \\ 0 \end{bmatrix}$. The vector first vector,

corresponding to the exclusion of sensor 1, is not of zero length now, but it is still substantially smaller in magnitude than any of the other three vectors.

Symmetry of the sensor array is not required for this FDI method to work, but there are some advantages of choosing axes which are symmetric. In particular, we are often interesting in selecting axes which collectively span each direction in space with equal sensitivity. The next section discusses issues involved in selecting symmetric axes in a 3-dimensional space.

6.1.4 Advantages of Symmetry

There are several considerations when selecting the orientations of the individual sensors in a redundant array. This section focuses on three issues and explains why symmetric configurations are often advantageous. These issues are: (1) Adjusting the relative noise sensitivities of a sensor array in each direction in space, (2) minimizing the overall noise of the array, and (3) minimizing the reduction in performance of the array given the exclusion of any sensor (due to a fault).

First, the alignment of the sensor axes will certainly affect the sensitivity of the sensor array to each direction in space. We have already seen in previous section, for instance, that one can position 3 sensors in a 2-d array to get the equivalent

information of 1.5 sensors in each of 2 orthogonal measurement directions. Suppose more generally that we have m sensors spanning n dimensions. We can position the m sensors to obtain the equivalent of x_i sensors of information in each ith out of n orthogonal measurement directions. Of particular interest, we can define "optimal" configurations as those which satisfy the following restrictions:

$$\sum_{i=1}^{n} x_i = m, \qquad (x_i >= 0, \quad \forall i) \tag{6.33}$$

The equality in the equation above with "m" becomes an inequality in suboptimal configurations, as we will see later.

In some applications, one may wish to distribute the information content of the array equally in each direction in space, although there are other applications where sensitivity is more (or less) critical along a particular axis. For instance, the development of early inertial navigation systems (INS) in the 1960's centered on space (zero-g) navigation, and a lot of emphasis was therefore placed on obtaining equal sensitivity along each direction in 3-d space [210, 166, 213, 73].

The development of Earth-bound INS systems gained importance by the early- to mid-1970's, and this redefined the problem of optimal sensor configuration in at least two significant ways: (1) Azimuthal errors will generally have a lesser importance than those in the horizontal directions (latitude and longitude), and (2) rotating gyros generally have both g-insensitive and g-sensitive noise characteristics in drift rate, and the standard deviation of the gravity-dependent noise term "varies with the cosine of the elevation angle of the output axis" [160]. The configuration of the rate gyros for the Segway is another application where one would probably not assign equal importance to every axis in our 3-space. The most critical axis for the Segway is the rotation of the body of the device about the wheel axis (i.e. pitch).

A second consideration is insuring that sensors are distributed so that we take full advantage of the noise-reducing potential of the m sensors in an array. I noted above that we **can** configure m sensors such that their information content is efficiently divvied up (in whatever proportions we wish) among n dimensions in space, as described by Equation 6.33. However, *it is possible to configure them inefficiently*

in most cases[3], so that:

$$\sum_{i=1}^{n} x_i < m, \qquad (x_i >= 0, \quad \forall i) \tag{6.34}$$

At this point, I should make it clear what I mean by "the equivalent of x_i sensors of information". Suppose we have N sensors with identical (and uncorrelated) Gaussian noise characteristics which are all aligned along the same axis. If we add together the outputs of these N sensors, both the signal and the variance (σ^2) of the total output will be a factor of N greater than that of a single sensor. Therefore, the ratio of the standard deviation (σ) of the noise compared with the signal will go as $N^{-1/2}$:

$$\frac{\sigma_{tot}}{\text{signal}_{tot}} = \frac{\sqrt{N}}{N} = \frac{1}{\sqrt{N}} \tag{6.35}$$

When I say we can obtain 'the equivalent of x_i sensors of information" in a particular direction, I mean that the variance in the measured output in this direction will be $\frac{\sigma^2}{x_i}$ (where σ^2 is the variance of a single sensor).
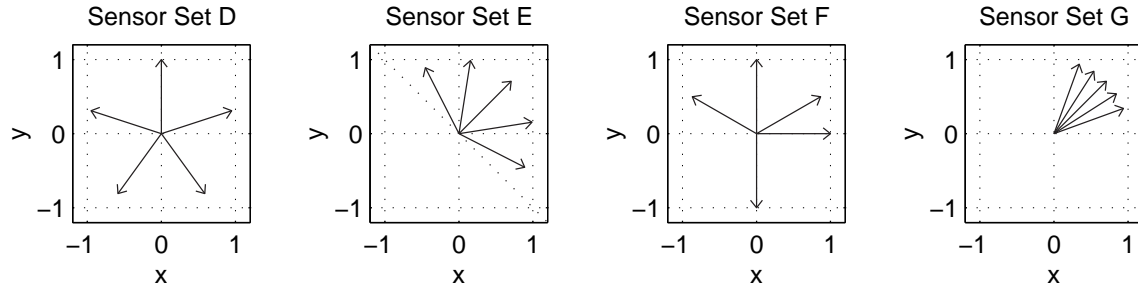
Figure 6-5: Examples of 5-sensor orientations in 2-D space.

To illustrate this point, consider the four 2-dimensional sensor configurations shown in Figure 6-5. In each of the four arrays, the sensors are aligned such that they provide equivalent sensitivity along either the x or y axis. However, in the first three sets on the left (Sets D, E, and F), there are 2.5 sensors of information in each of the two output directions (x and y), while Set G provides only the equivalent of ~ 0.8205 sensors of information in each direction, x and y. We would obtain noisier output signals, in other words, using the 5-sensor configuration shown in Set G to

---

[3]Well, this is not true for the trivial case of 1 sensor aligned along a single axis, for instance...

provide outputs in the x and y directions than we would get by using just 2 mutually-orthogonal sensors (i.e. with 1 sensor of information in each direction)!

The sets in Figure 6-5 illustrate several principles in "optimal" sensor configuration. Both Sets D and E consist of five evenly-spaced sensor axes. We can align such sensors with a spacing of 72° between adjacent sensors, as in Set D, or we can "flip" the signs of some of the vectors so that they all span a half-plane (with a spacing of 36° between adjacent sensors). In either case, the set of lines along which vectors lie are rotationally symmetric: the lines fall into an identical configuration when we rotate the entire set of lines to orient any particular line as vertical. Intuitively, it makes sense that this type of symmetry would result in equal sensitivity in *any* direction in the plane, and this is indeed the case. It is also an "optimal" configuration in the sense that we obtain the maximal information content, as defined by Equation 6.33.

If the outputs of interest are specifically aligned along the x and y axes (and not potentially just "any" directions in the plane), Set D also exhibits a second symmetry of interest. Specifically, it is symmetric about one of the output axes. The matrix of direction cosines for Set D can be written as:

$$
\mathbf{M}_D = \begin{bmatrix}
\cos(90° - 72°) & \sin(90° - 72°) \\
\cos(90°) & \sin(90°) \\
\cos(90° + 72°) & \sin(90° + 72°) \\
\cos(90° + 144°) & \sin(90° + 144°) \\
\cos(90° - 144°) & \sin(90° - 144°)
\end{bmatrix}
\tag{6.36}
$$

The *sin* function is symmetric about 90° while *cos* is antisymmetric. With the notation used in Equation 6.36, we can therefore immediately argue that the two 5-dimensional columns in $\mathbf{M}_D$ will be orthogonal to one another, because:

$$
\cos(90° - x) \cdot \sin(90° - x) + \cos(90° + x) \cdot \sin(90° + x) = 0 \tag{6.37}
$$

$$
\cos(n \cdot 90°) \cdot \sin(n \cdot 90°) = 0 \tag{6.38}
$$

If we take the dot products of the two columns in $\mathbf{M}_D$ (i.e. $\mathbf{M}_D^T \mathbf{M}_D$), terms generated from the rows 1 and 3 cancel, due to the relation in Equation 6.37, as do terms corresponding to row 4 and 5. Equation 6.38 shows that the contribution due to the

278

product of the terms in row 2 is simply zero as well. For Set D, we find that:

$$\mathbf{M}_D^T\mathbf{M}_D = \begin{bmatrix} 2.5 & 0 \\ 0 & 2.5 \end{bmatrix} \tag{6.39}$$

The equivalence of the diagonal terms in Equation 6.39 shows that the information content along the x and y axes is the same, and the off-diagonal terms are zero because of the orthogonality between the columns of $\mathbf{M}$ (as previously discussed). This orthogonality provides proof that we have achieved an "optimal" sensor configuration, as defined by Equation 6.33.

Sets E and F are equivalently optimal, however, since:

$$\mathbf{M}_E^T\mathbf{M}_E = \mathbf{M}_F^T\mathbf{M}_F = \begin{bmatrix} 2.5 & 0 \\ 0 & 2.5 \end{bmatrix} \tag{6.40}$$

Set E provides orthogonality because of the rotational symmetry of the axes. The five axes in Set F can be subdivided into an orthogonal pair (in the +x and +y directions) and a rotationally symmetric triad (at angles of 30°, 150°, and 270° with respect to the x axis). This means that the columns of $\mathbf{M}_F$ can be subdivided (in the same way) into two subgroups which are individually orthogonal, and therefore the *entire* columns in $\mathbf{M}_F$ must also be orthogonal.

As previously mentioned, Set G does *not* satisfy our condition for optimality.[4] The spacing between neighboring vectors in this set is 10°, with the middle vector pointing at a 45° from the x axis. For Set G:

$$\mathbf{M}_G \approx \begin{bmatrix} 2.5 & 2.05 \\ 2.05 & 2.5 \end{bmatrix} \tag{6.41}$$

The off-diagonal terms indicate that the columns in $\mathbf{M}_G$ are not orthogonal. Although this set distributes the information content along the x and y axes equivalently (due to the symmetry about the an axis at a 45° angle from x), it does not do so optimally.

The problem with Set G may seem more intuitive if we consider the simplified problem of selecting a two-sensor configuration. If we wish to provide equivalent

---

[4]again, as defined in Equation 6.33

information along the x and y axes, then the lines on which the sensor axes lie must be symmetric about a line at $45°$.[5] Sets H and I in Figure 6-6 approach two limits, with the vectors nearly orthogonal in Set H and nearly co-linear in Set I. The angle of separation is $80°$ in Set H, resulting in the equivalent of ≈ 0.97 sensors of information along each output axis (x and y). This is not much worse than a perfectly orthogonal pair. In the limit as the two sensors become completely co-linear, the two measure identical values, and we clearly have no way of distinguishing outputs along x and y. The vectors in Set I are only $10°$ apart, and this provides the equivalent of ≈ 0.03 sensors of information along either x or y.
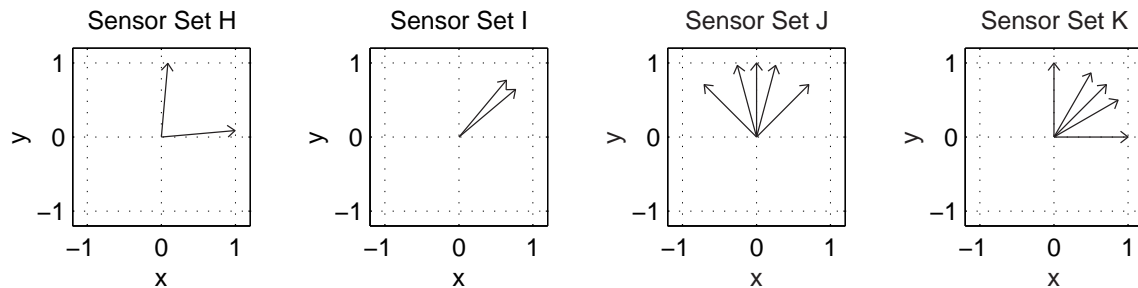
Figure 6-6: More examples of 5-sensor orientations in 2-D space.

Mathematically, we can note that for any array of two sensors in the x-y plane aligned at angles a and b, the matrix of direction cosines is:

$$\mathbf{M} = \begin{bmatrix} cos(a) & sin(a) \\ cos(b) & sin(b) \end{bmatrix} \tag{6.42}$$

Recall that the matrix $\mathbf{K}$ (defined in Equation 6.15) transforms the sensor measurements into estimates of outputs along x and y. This matrix will be:

$$\mathbf{K} = \begin{bmatrix} \frac{sin(b)}{sin(b)cos(a)-sin(a)cos(b)} & \frac{-sin(a)}{sin(b)cos(a)-sin(a)cos(b)} \\ \frac{-cos(b)}{sin(b)cos(a)-sin(a)cos(b)} & \frac{cos(a)}{sin(b)cos(a)-sin(a)cos(b)} \end{bmatrix} \tag{6.43}$$

Recall also that our estimate $\hat{\mathbf{x}}$ (from Equation 6.17) is:

$$\hat{\mathbf{x}} = \mathbf{K}\mathbf{y} \tag{6.44}$$

---

[5]Note that changing the sign of the vector does not change the line on which it lies, so if two lines are symmetric about the line at $+45°$, then they are also symmetric about the line at $-45°$.

which differs from the actual value of $\mathbf{x}$ by some noise component, given by Equation 6.16:

$$\mathbf{x} = \mathbf{Ky} - \mathbf{K\epsilon} \tag{6.45}$$

$$\hat{\mathbf{x}} - \mathbf{x} = \mathbf{K\epsilon} \tag{6.46}$$

If the sensors each have (uncorrelated) Gaussian noise with a standard deviation of σ_s, the standard deviation of the noise in our estimates along the x and y axes will each be:

$$\sigma_x = \begin{bmatrix} \frac{sin^2(a)+sin^2(b)}{(sin(b)cos(a)-sin(a)cos(b))^2} \\ \frac{cos^2(a)+cos^2(b)}{(sin(b)cos(a)-sin(a)cos(b))^2} \end{bmatrix} \cdot \sigma_s \tag{6.47}$$

When the angles are equal $(a = b)$, the denominator (which is the same in the terms corresponding to the x and y directions) goes to zero, and we have infinite noise. If the angles differ by $90°$ (either $a = b + 90°$ or $a = b - 90°$), both the numerator and denominator in each of the two noise components equal unity, and we obtain the equivalent noise of an orthogonal alignment where one sensor is specifically oriented along the x axis and the second lies along y.

We can expand this last principle to the more broad case of m sensors distributed evenly (with equivalent angles separating them) in n dimensions, in which case we will obtain an "optimal" configuration with $\frac{m}{n}$ sensors of information in each of n directions. (The proof of this is not provided here, but will hopefully make intuitive sense to the reader at this point.) This will be an important concept when we expand this analysis (shortly) to consider 3-dimensional sensor arrays.

Sets J and K in Figure 6-6 show symmetric 5-sensor arrays which can be used to reemphasize some of the points covered in the last few pages. Each set consists of a central axis with two axes at $\pm 10°$ and two more at $\pm 45°$. As before, suppose we are concerned with obtaining outputs along the x and y axes. In Set J, the axis of symmetry coincides with an output axis (the y axis), so the columns of $\mathbf{M}_J$ will be orthogonal:

$$\mathbf{M}_J^T\mathbf{M} \approx \begin{bmatrix} 1.06 & 0 \\ 0 & 3.94 \end{bmatrix} \tag{6.48}$$

281

Since the off-diagonal terms above are zero, we can also immediately observe that we have achieved the information equivalent of 1.06 sensors in the x direction and 3.94 sensors in y. $(1.06 + 3.94 = 5.00$, so this is an optimal set.) For Set K,

$$\mathbf{M}_K^T \mathbf{M} \approx \begin{bmatrix} 2.5 & 1.44 \\ 1.44 & 2.5 \end{bmatrix} \tag{6.49}$$

Here, the symmetry of the result above means that we have equivalent information in both x and y. The off-diagonal terms indicate that the configuration is not optimal, however, and in fact we have achieved the equivalent of approximately 1.67 sensors of information each direction (x and y).

Finally, one may wish to expand the concepts in this subsection to consider an array with one (or more) failed elements. The primary concern here is whether fail-operational behavior is required for any or all of the array outputs, in which case one must insure fault isolation is possible (as already discussed). A secondary goal may be to minimize the 'worst-case" deterioration of any channel due to a single sensor. Practically, this is often not a critical design decision. For example, let us once again consider the three optimal 5-sensor arrays previously discussed in Sets D, E, and F, which are shown again in Figure 6-7. For both Sets D and F, the loss of a single sensor would at *worst* degrade one of the outputs (x or y) from the equivalent of 2.5 to 1.5 sensors of information (leaving the other channel unaffected with 2.5 channels of sensitivity).
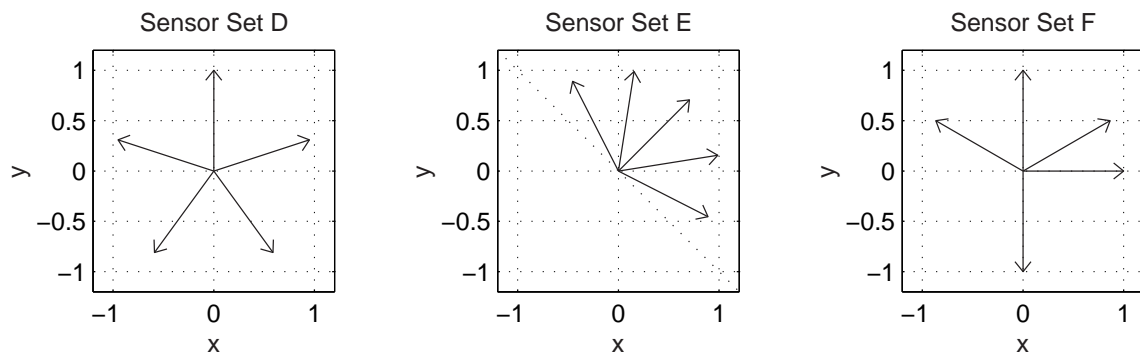
Figure 6-7: Examples of 5-sensor orientations in 2-D space.

Set E provides the least degradation in the case of a "worst case" single sensor

failure (of any optimal 5-sensor array in 2-D), but it is really not much of an improvement over the other two. If either of the two sensors which are closest to the x and y axes were to fail, that nearest output axis would then operate with the equivalent sensitivity of 1.5148 sensors. This is less than 1% greater that the "equivalent sensor value" for the worst case scenarios for Set D and F, and it corresponds to an increase in the standard deviation of the noise on that output of less than 0.5%.

6.1.5 Suggested Geometries for Redundant Sensor Arrays

As outlined in the preceding section, symmetric configurations can be used both to equalize the sensitivities along the desired output axes and to maximize the overall effectiveness of the sensors being used. In 2-dimensional arrays (like the ones shown so far), it is relatively straightforward to identify optimal sensor orientations. The problem is less intuitive for a 3-d array, but it is tractable once one defines optimality for the array. This was defined at length in the preceding subsection and can be summarized as (1) obtaining the desired ratios of sensitivities along the output axes (e.g. equal sensitivity in each direction) and (2) making full, efficient use of all sensors.

One way of achieving symmetric configurations in three dimensions is to use geometric features of the Platonic solids. The Platonic solids are the five regular polyhedra. They are the only convex solids whose faces are comprised of identical regular polygons. Figure 6-8 shows the five Platonic solids.
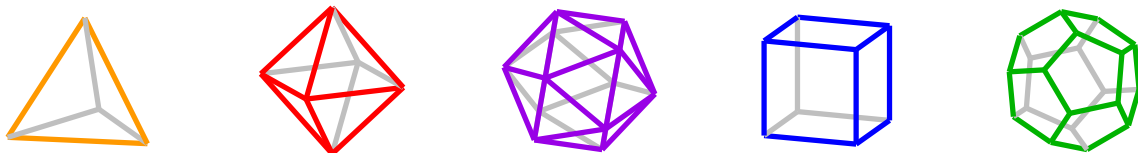
Figure 6-8: The 5 Platonic solids. A Platonic solid is a polyhedron whose faces are congruent regular polygons that meet at equal angles. Only five such solids are geometrically possibly. They are (as depicted from left to right above) the tetrahedron, octahedron, icosahedron, hexahedron (aka cube), and dodecahedron.

We can create a symmetric set of axes for a sensor array by drawing vectors from

the center of one of these regular polyhedra to the center of each side. Such a set of vectors will be symmetric in that the solid can be rotated into an identical position with any one of the vectors pointing directly at the observer. A sensor array using such vectors will span each direction in space with equal sensitivity and will do so efficiently (i.e. satisfying Equation 6.33 on page 276).

We can also create such symmetric sets of axes by drawing vectors from the center of one of the solids to either each vertex or to the mid-point of each edge. Table 6.2 shows the resulting number of vectors created using each method. The numbers shown in parentheses count only "unique axes" - that is, the maximum number of axes one can select such that no other axes are co-linear with any in the subset.

Table 6.2: Geometric Properties of the 5 Platonic Solids

polyhedron	faces (unique axes)	vertices (unique axes)	edges (unique axes)
tetrahedron	4 (4)	4 (4)	6 (3)
octahedron	8 (4)	6 (3)	12 (6)
icosahedron	20 (10)	12 (6)	30 (15)
cube	6 (3)	8 (4)	12 (6)
dodecahedron	12 (6)	20 (10)	30 (15)

To understand (briefly) why there can only be five Platonic solids, consider that at least three regular polygons must meet at each vertex of a regular convex polyhedron. (If there were only two, the two would be coplanar) The interior angle of the type of regular polygon being used must be *less* than 120°, otherwise the sum of the angles of the three (or more) polygons at each vertex would add to more than 360°. This means each regular polygon must have fewer than six sides. If we use a pentagon, we can join three polygons at each vertex, and the resulting shape is a dodecahedron. Using squares, we can again use no more than three polygons at each vertex (forming a cube), otherwise the sum of the interior angles would again be equal to or greater than 360°. If we use equilateral triangles, we can join either three (tetrahedron), four

(octahedron) or five (icosahedron) polygons at each vertex.

The cube and the octahedron are considered "duals" of one another. That is, the two can be aligned in space such that the set of vectors from the center of a cube to the center of each of its faces is identical to the set of vectors from the center of an octahedron to each of its vertices. The drawing in the center of Figure 6-9 shows a cube and an octahedron so aligned with respect to one another. The dodecahedron and icosahedron are also duals, and the tetrahedron is a dual of itself.
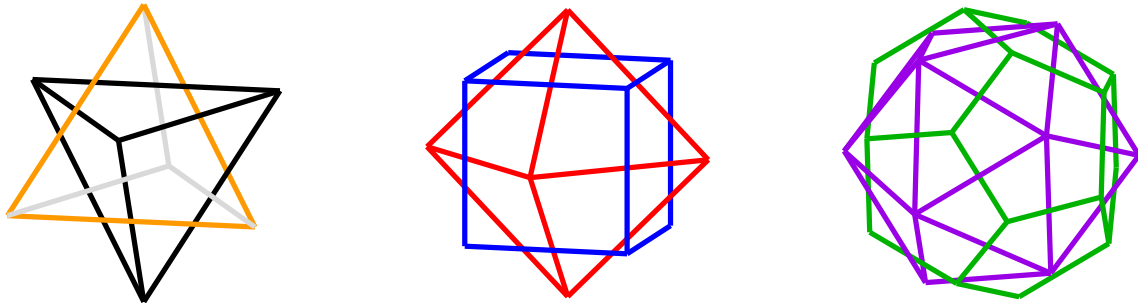
Figure 6-9: Correspondence of edge and face axes for Platonic solids. Each of the Platonic solids has a dual which can be scaled and rotated such that mid-points of the faces of one align to coincide with the vertices of the other. The tetrahedron (at left) is a dual with itself. Other pairings include the cube and octahedron (center), and the dodecahedron and icosahedron (at right).

Although there are 15 entries in Table 6.2, there are only six sets of unique (non-colinear) vector directions. Figure 6-10 depicts each of the six sets. Two of the six sets can be represented as equally spaced vectors about a cone. Another three of the sets can be aligned such that there is one central vector with the remaining vectors evenly spaced on the surface of a cone coaxial with the central vector.

We can use similar configurations to create other sets of vectors which, like those formed from the features of the Platonic solids, also span each direction with equal sensitivity and do so in an optimal fashion. That is, we can create arrangements which place evenly-spaced vectors on the surface of a cone with some particular half-angle either with or without a central vector. Solving for the half-angle of the cone necessary to result in a set of vectors which span each direction with equal sensitivity

is fairly straight-forward.

Consider the first and fourth configurations shown in Figure 6-10, in which there are three vectors about a cone either with or without an additional central vector along the axis of the cone (respectively). The matrix of direction cosines for the "1–3" case, in which there are one central vector and three about a cone with half-angle β, can be written as:

$$M_{1\text{-}3} = \begin{bmatrix} 0 & 0 & 1 \\ \cos(0 \cdot 360°/3) \cdot \sin(\beta) & \sin(0 \cdot 360°/3) \cdot \sin(\beta) & \cos(\beta) \\ \cos(1 \cdot 360°/3) \cdot \sin(\beta) & \sin(1 \cdot 360°/3) \cdot \sin(\beta) & \cos(\beta) \\ \cos(2 \cdot 360°/3) \cdot \sin(\beta) & \sin(2 \cdot 360°/3) \cdot \sin(\beta) & \cos(\beta) \end{bmatrix} \quad (6.50)$$

Each row vector above is of length unity, and therefore the sum of the squares of any single row will be one. The sum of the squares of all the elements of all the rows must therefore be equal to the number of rows in $M_{1\text{-}3}$, which is 4. To span each direction in space equally requires that each *column* vector in $M_{1\text{-}3}$ have identical length. To do so efficiently requires that the column vectors in Equation 6.50 be orthogonal to one another, and therefore that the squares of their lengths will each add to $(n + 1)/3$, where $n + 1$ is the total number of rows in $M_{1\text{-}n}$. The first and second columns will automatically be equal in length if we space the vectors equally about a cone (as done in Equation 6.50). Applying the necessary restrictions on the length of the third column of Equation 6.50, we require that:

$$1^2 + 3 \cdot (\cos(\beta_{1\text{-}3}))^2 = \frac{4}{3} \quad (6.51)$$

Therefore:

$$\cos(\beta_{1\text{-}3}) = \sqrt{\frac{4}{3 \cdot 3} - \frac{1}{3}} \quad (6.52)$$

$$\beta_{1\text{-}3} = 70.529° \quad (6.53)$$

More generally, to generate a set of $n + 1$ vectors arranged with 1 central and n peripheral vectors equally spaced about a cone with half-angle $\beta_{1\text{-}n}$ such that they span each direction in space equally and optimally, the half-angle $\beta_{1\text{-}n}$ must be given

4	4	10	3	6	15
(1–3)	(0–4)	(0–5–5)	(0–3)	(1–5)	(5–5–5)
0°	54.736^o	37.377^o	54.736^o	0°	31.717^o
70.529^o		79.188^o		63.435^o	58.283^o
					90°
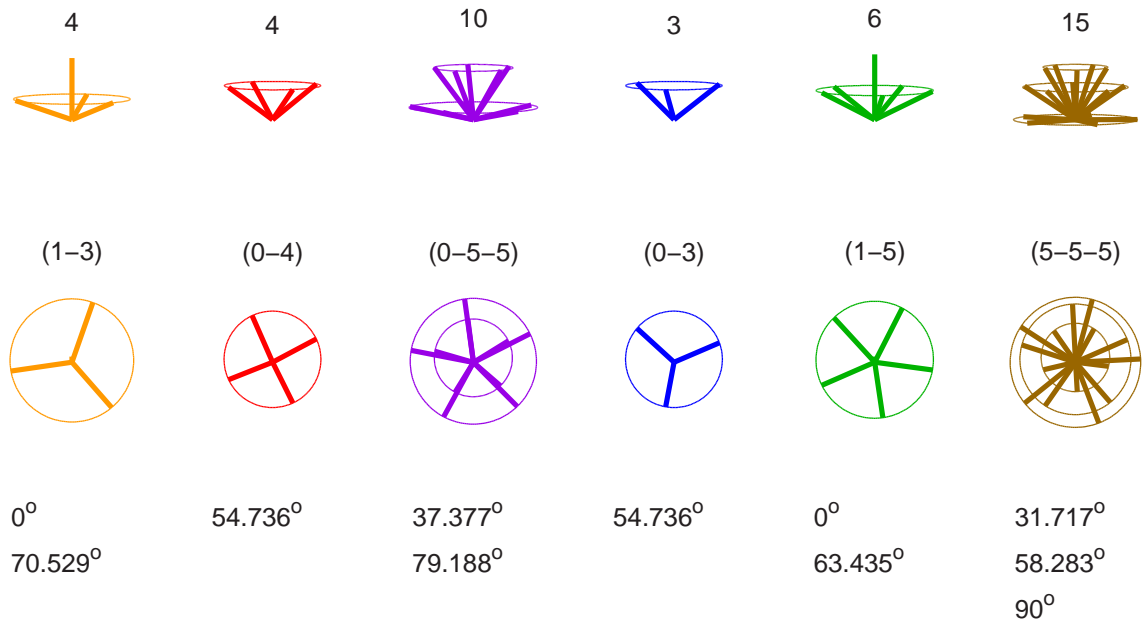
Figure 6-10: Symmetric axes associated with Platonic solids. Each set of axes shown is formed by drawing vectors from the centroid of one of the Platonic solids to one of the following: (1) the center of each side, (2) each vertex, or (3) the mid-point of each edge. When two such resulting vectors are co-linear with one another (i.e. when they point in exactly opposite directions in space), only one of this pair is shown. Each of these six sets can be subdivided into one or more sub-groups of vectors which lie (with equal spacing) on the surface of a vertical cone. The six figures in the top row show side views of these vector sets, while the bottom six look down from above. The circular lines shown are included to help visualize the conical surfaces on which these axes lie. Numbers at top give the total number of non-colinear axes. For the hyphenated sets of nunbers, the first digit indicates how many axes point in the vertical direction. (This is always either 0 or 1.) The remaining numerals show how many axes lie on each successive conical surface. The values beneath the figures show the half-angles for these conical surfaces.

as:

$$\cos(\beta_{1-n}) = \sqrt{\frac{n+1}{3n} - \frac{1}{n}} \tag{6.54}$$

$$\beta_{1-n} = \cos^{-1}\left(\sqrt{\frac{(n+1)-3}{3n}}\right) \tag{6.55}$$

Some of the resulting "optimal" half-angle values are:

$$\beta_{1-3} = 70.529° \tag{6.56}$$

$$\beta_{1-4} = 65.905° \tag{6.57}$$

$$\beta_{1-5} = 63.435° \tag{6.58}$$

$$\beta_{1-6} = 61.874° \tag{6.59}$$

$$\beta_{1-7} = 60.794° \tag{6.60}$$

We can similarly analyze the case with no central angle by first writing the matrix of direction cosines for the "0-3" case (with three vectors equally spaced about a cone but no central vector):

$$M_{0-3} = \begin{bmatrix} \cos(0 \cdot 360°/3) \cdot \sin(\beta) & \sin(0 \cdot 360°/3) \cdot \sin(\beta) & \cos(\beta) \\ \cos(1 \cdot 360°/3) \cdot \sin(\beta) & \sin(1 \cdot 360°/3) \cdot \sin(\beta) & \cos(\beta) \\ \cos(2 \cdot 360°/3) \cdot \sin(\beta) & \sin(2 \cdot 360°/3) \cdot \sin(\beta) & \cos(\beta) \end{bmatrix} \tag{6.61}$$

This geometric configuration corresponds to a set of non-colinear vectors drawn from the center of a cube to centers of three of its faces and is depicted in the fourth image from the left in Figure 6-10.

From the form of Equation 6.61 and our previous reasoning, it follows that in the general "0–n" case, with equal and optimal sensitivity along all axes, we require that the sum of the squares of the elements in the n rows of the third column must add to $n/3$:

$$n \cdot (\cos(\beta_{0-3}))^2 = \frac{n}{3} \tag{6.62}$$

And therefore:

$$\cos(\beta_{0-n}) = \sqrt{\frac{1}{3}} \tag{6.63}$$

$$\beta_{0-n} = 54.736° \tag{6.64}$$

Interestingly, Equation 6.64 does not depend on n! If we wish to align any number of sensors optimally with equal sensitivity in each direction in space, therefore, one way to do so is to distribute all of the sensors equally about a cone with a half-angle of 54.736°.

6.1.6 Redundant Gyro Sensing Array for the Segway
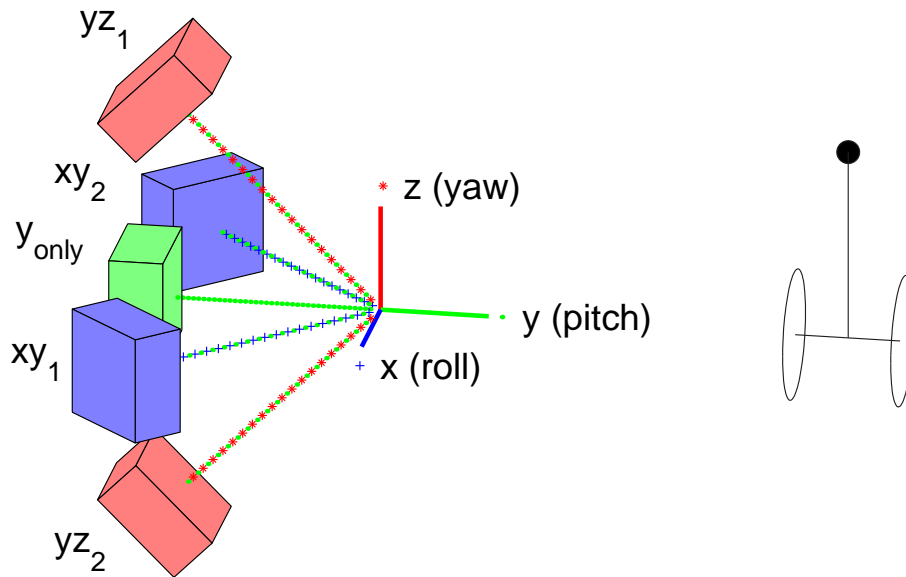
Figure 6-11: Redundant 3-axis angular velocity sensing with 5 rate gyros

I am not sure exactly what alignment the Segway uses. One configuration I would suggest for a device such as the Segway (and which is consistent with the schematic in Figure 6-1) is shown in Figure 6-11. Here, all five sensors are aligned such that each provides some degree of information about rotation about the wheel axis. Specifically, one sensor is aligned exactly along the wheel axis, and the other four are spaced symmetrically about a cone with a half-angle of 45°. This "pitch" axis, about which the inverted pendulum balances, is clearly the most important one for Segway. There are only three sensors aligned along each of the other axes, however.[6] This means that if one of four sensors aligned at 45° with respect to the wheel axis fails,[7] it is

---

[6] yaw (for steering and traction control) and roll (to detect unsafe conditions)

[7] for instance, yz_1 in Figure 6-11

not possible to *isolate* whether it was in fact *this* sensor which is faulty or the one aligned 90° to it (one the opposite side of the central cone axis).[8] If the sensor along the wheel axis fails, in contrast, it can be precisely isolated.

The result of *not being able to precisely isolate* every sensor failure is as follows: First, if the sensor along the wheel axis fails, it can be isolated and normal operation can continue, with the remaining four sensors providing information about the wheel axis, and two sensors each aligned at 45° to each of the other axes. Moreover, the four sensors used in estimating pitch, each 45° off the wheel axis, provide the equivalent information content (with respect to noise) as two aligned exactly along the axis, and therefore result in an output with somewhat lower noise[9] than a single on-axis sensor. For each of the other orthogonal axes, the two remaining sensor outputs provide the equivalent SNR of a single on-axis sensor.

By contrast, if one of the other four sensors fails, we are left with only three usable sensor outputs. As a result, we can only sense rotation about two of the three axes - but importantly, the pitch axis is always one of these two sensed directions. If sensor yz_1 in Figure 6-11 fails, for instance, then we can no longer sense *roll*. There are still one on-axis and two off-axis sensors giving the equivalent of two on-axis sensors' data for pitch (just as in the on-axis failure case), and there are two off-axis sensors for estimating roll (providing the equivalent of a single on-axis sensor, just as in the on-axis failure case).

As a consequence, this alignment allows the Segway to balance given the failure of any gyro in the assembly. However, 4/5 of the possible failures will make it impossible to measure either roll or yaw. Balance is critical for insuring the Segway is "fail-operational", but traction control and roll information is not.[10] If a gyro fails in this configuration, the Segway can warn the user that maintenance is required, yet still remain quite operational. Also, the alignment improves sensitivity along the pitch axis (over the sensitivity of a single gyro) and provides an equivalent SNR along the

---

[8]i.e. yz_2 in Figure 6-11

[9]by a factor of $sqrt.5 = 0.7$

[10]The gyros are necessary to maintain stability about an axis of pitch, but there is no active stabilization in the lateral direction.

pitch axis given any single gyro failure.

6.1.7 MEMS Gyros Used in the Segway

The CRS03 MEMS gyro sensors used in the Segway are manufacturer by a company called "Silicon Sensing" [85, 111]. This company was formed as a joint venture between a Japanese company, Sumitomo, experienced in MEMS fabrication, and British Aerospace (BASE), who have expertise in designing larger resonant ring gyros using piezoelectrics.

At the core of the CRS03 sensor is a thin silicon ring, shown in Figure 6-12, which is driven to excite a wineglass mode. Ring resonators which use the wineglass mode are common among both piezoelectric and MEMS gyros. Section 7.1.5 provides more details about piezoelectric gyros and the wineglass mode shape. The drive and sensing paths along the ring of the CRS03 gyro are shown in Figure 6-13. Care has been taken in this design to reduce capacitive coupling between the sense and drive signals by separating them with a grounded trace (as depicted in the right half of this figure).

MEMS gyros are still orders of magnitude less sensitive than the inertial grade gyros used to send men to the moon. Engineers describe high-grade inertial sensor errors in terms of a few "milli-Earth rate units" (merus) - 0.001 times the rate at which the Earth rotates, or 0.015 deg/hr. Apollo-era precision gyroscopes achieved a bias of less than 30 meru with a drift in bias of around 5 meru [73]. The Hubble space telescope reportedly has the most accurate gyros in use today (as of 2002) [186]. They are manufactured by Allied Signal and have a bias drift of around .4 meru ("20 arc seconds per hour") [5].

MEMS gyros are significantly less accurate, but they are continually improving. Presently, comparable errors associated with MEMS gyros are on the order of 1,000-100,000 meru (typically 0.5 deg/sec, or roughly 2000 deg/hr [19]), with the most aggressive claims of resolution at around 0.01 deg/sec [108].

The level of accuracy typical for a low-cost MEMS gyro is already acceptable for many applications. The most economical gyro currently on the market is manufac-

tured by Analog Devices. Analog Devices currently sells their ADXRS150 for $30, and the price is expected to drop to around $10 in the future [101]. The automotive industry is now the largest market for such devices, which provide feedback for traction control, sensing rollover or spin-out to deploy airbags, and enhancing GPS navigation in tunnels or other areas where satellite communication may be lost temporarily [101].

The issues relating to practical implementation of redundant gyro arrays which have been discussed so far in this chapter seem likely to become more relevant in the future as MEMS technology is making gyros smaller, more accurate and more affordable [223, 18, 19, 191, 86, 85, 32, 137, 108].

dia ≈ 6mm

MAGNETIC CIRCUIT   SILICON

ANODICALLY BONDED GLASS

PRIMARY LOOP

VCO

V_{AGC}

g_{DP}

g_{DS}

SECONDARY
LOOP

g_P

R

X
B FIELD

g_P

V_N

R

Q

R

R = RATE PHASE
Q = QUADRATURE
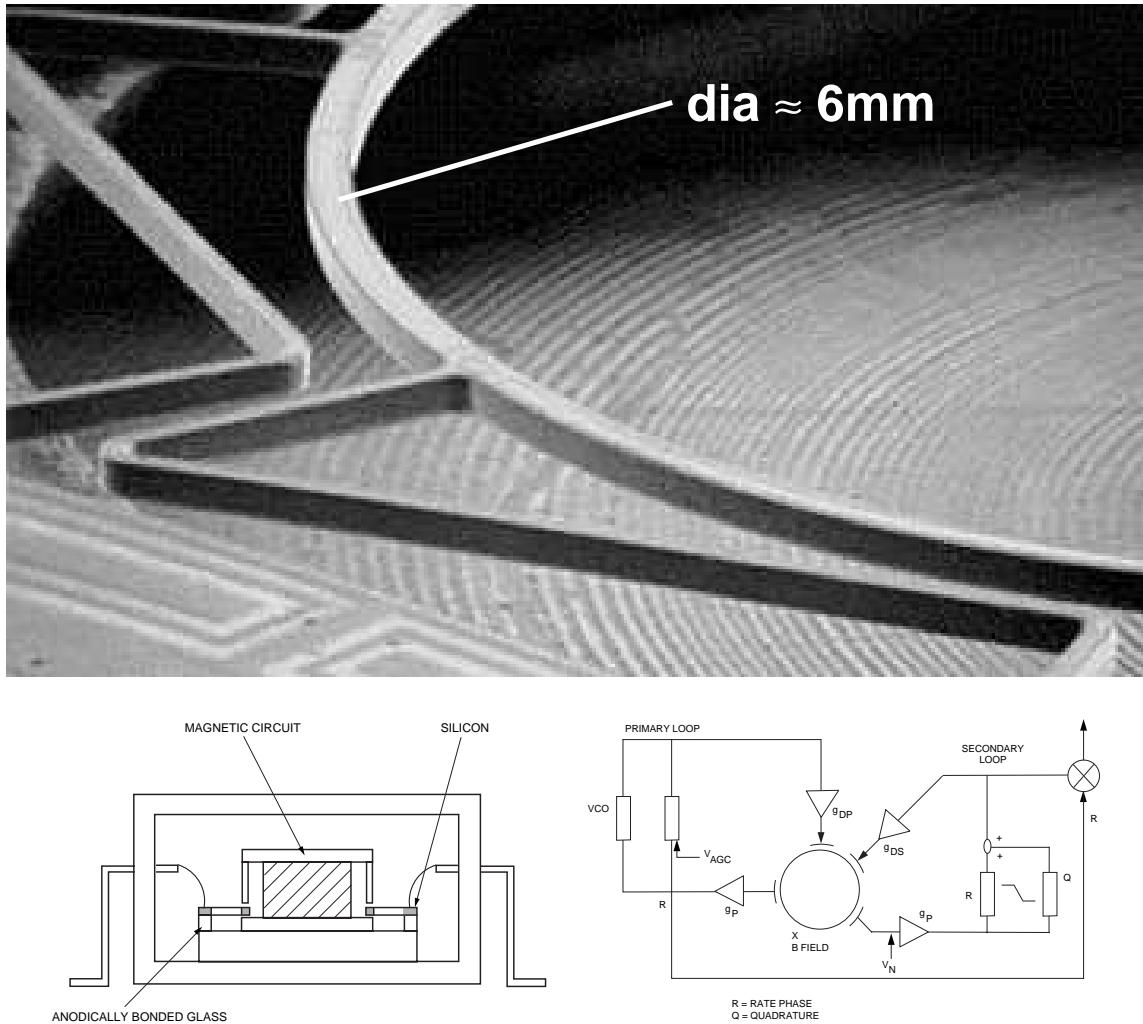
Figure 6-12: Silicon Sensing CRS03 rate gyro. At top is an SEM image of a section of the resonant ring structure used in the CRS03 rate gyro. (A cylindrical magnet to be mounted inside the ring is not shown.) The figure at the lower left shows a cross-section of the magnetic circuit in the gyro; at right is a schematic of the circuit used to maintain constant-amplitude vibration (at a natural frequency near 14.5 kHz). Upper image obtained from Sensor Magazine online [32] : (http://www.sensorsmag.com/articles/0203/14/main.shtml). Lower two images obtained from Silicon Sensing Systems [85] : (http://www.siliconsensing.com/acrobat/AN0199.pdf).
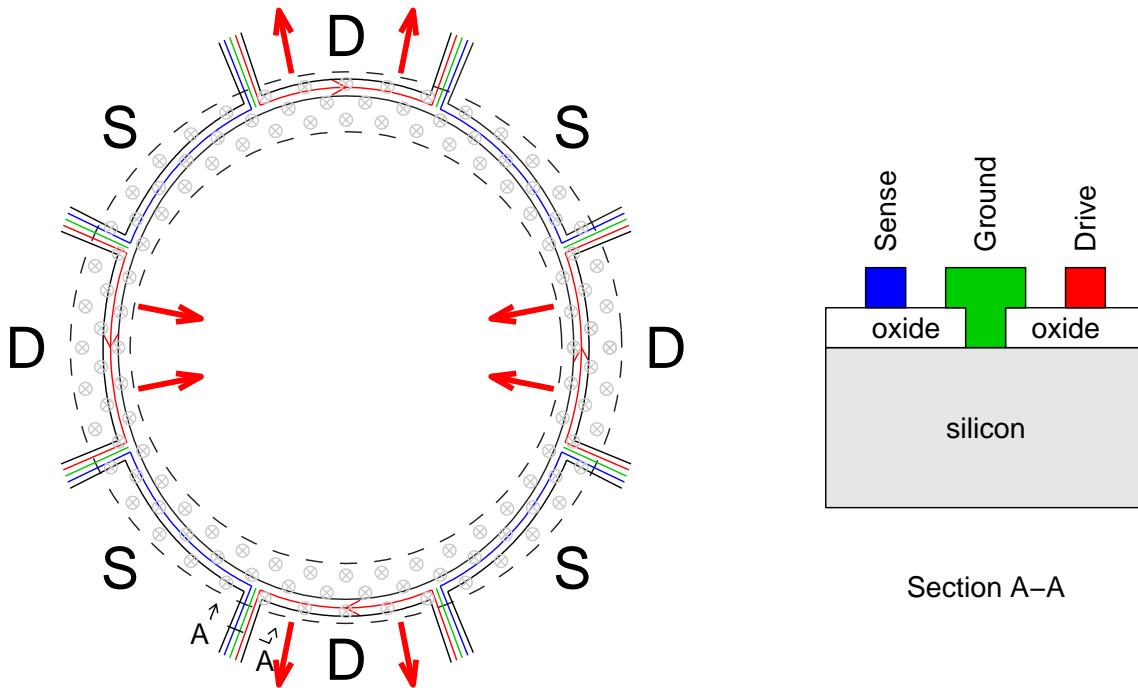
Figure 6-13: Current paths and field orientation in CRS03 gyro. At left is a schematic of the resonant ring structure of the CRS03 gyro. (The deformation of the ring is exaggerated for clarity.) A magnetic circuit concentrates a magnetic field (into the page) in the region about the ring. Current through thin conductive (e.g. aluminum or gold) traces along each of the four sections labelled "D" will produce radial forces. The structure is driven at resonance through VCO (voltage-controlled oscillator) and AGC (automatic gain control) loops. Rotation about the axis of the ring will excite a secondary mode (oriented 45° with respect to the driven mode shape). The rate of rotation can be sensed by measuring the signal in the sensing ("S") sections. The linearity and bias of the sensor can be improved, however, by maintaining a constant mode shape (using the four sensing segments to suppress the secondary mode) and monitoring the amplitude of the signal necessary to do so. At right is a cross-section of one of the eight support beams carrying the conductive traces to the resonator. Each beam carries one drive and one sensing trace, which are separated by a grounded trace to reduce capacitive coupling. The crystalline silicon substrate at the base of each beam is semi-conductive and acts as a ground plane. Silicon oxide insulates the drive and sense traces, as shown [85, 86].

6.2 Complementary Filtering of Gyro and Accelerometer Signals

This section begins by describing why a gyro is a useful sensor for a robotic inverted pendulum vehicle and also why using an integrating a gyro signal introduces ramping errors in position over time. It then presents some theory behind the use of complementary filtering in eliminating ramping errors in angle measurement from a gyro. The section continues by presenting data for the gyro and accelerometer used in the DIPR described in Chapter 7. These data are used to illustrate how complementary filters can be designed to blend outputs from two (or more) sensors to create an estimate with improved noise characteristics over those of either sensor alone.

Control of an inverted pendulum robot requires an accurate measurement of the angle of the pendulum with respect to the earth's gravitation field. A rotary encoder can provide a relative measure of the rotation between two bodies. In a cart-driven inverted pendulum, like the one described in Chapter 5, an encoder which measures the relative angle between the cart and the pendulum will also provide an absolute measure of the pendulum angle, because the cart is constrained on a track so that it can not rotate as it travels.

For a robotic inverted pendulum, like the one described in Chapter 7, an encoder is no longer sufficient for measuring the absolute angle of the pendulum-body, because the pendulum is no longer mounted to a non-rotating body. Encoders can be used to detect the angle between the pendulum-body and each of the two wheels, but the wheels will rotate as the vehicle is stabilized and commanded to travel.

A gyroscope measures absolute angular velocity. A gyroscope which is mounted on the pendulum-body of an IP robot can therefore provide an accurate estimate of the angular velocity of the pendulum. One way of estimating the absolute angle of the pendulum is simply to integrate the angular velocity output from such a gyro. This method will not be adequate over prolonged periods of time, however, because any non-zero DC component to the error (i.e. bias) in the gyro signal will result in a ramping error in the position measurement. This is illustrated in Figure 6-14.

In the figure, the left diagram shows:

$$\theta(s) \rightarrow \boxed{s} \rightarrow \Sigma \rightarrow \boxed{\dfrac{1}{s}} \rightarrow \theta(s) + \dfrac{N_g}{s}$$

with N_g entering the summation.

The right plot is labeled "Error in Angle" versus "Time" with the annotation:

The DC component in gyro noise yields a ramping error after integration
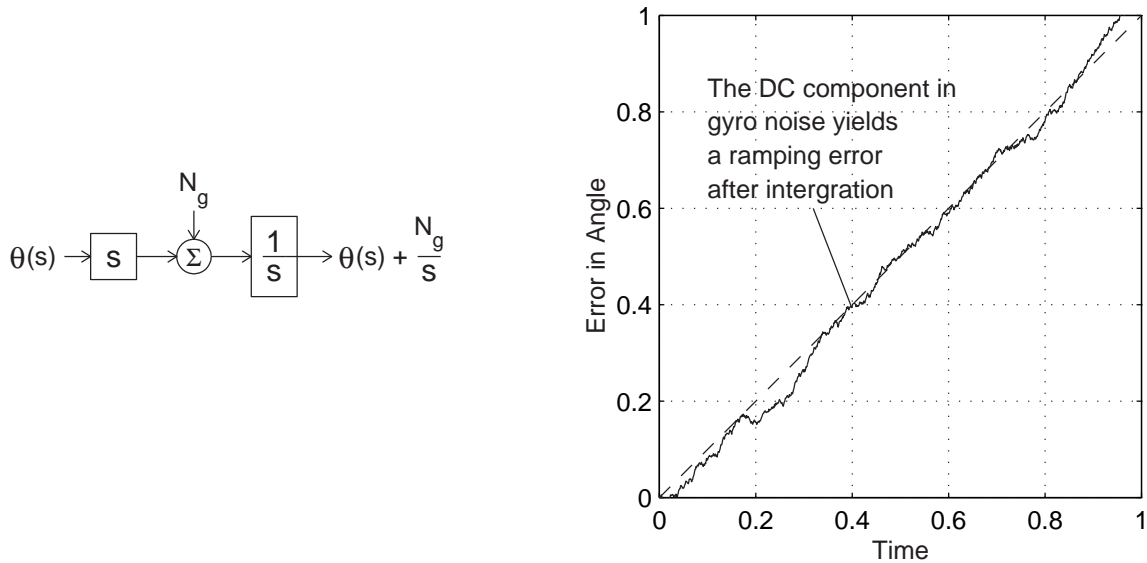
Figure 6-14: Finite DC bias in gyro causes a ramping error in angle measurement after integration. The response shown at right has been simulated using MATLAB.

One way of improving the measurement of absolute pendulum angle is by using the gyro with an additional sensor which provides a better low frequency (DC) estimation of the tilt angle. The two sensor outputs can be blended such that the combined output measurement relies more heavily on the more accurate (i.e. less noisy) of the two sensors at any given frequency. This blending can be achieved through the use of complementary filters.

Complementary filters are, as the name implies, filters which are designed to work together as a set. Each filter in the set operates on a particular sensor measurement. Generally speaking, the filter for a particular sensor attenuates that sensor's response at frequencies which have a low signal-to-noise ratio. The filters in the complete set literally "complement" one another, in that their sum outputs the *signal* unaltered (e.g. with no phase lag) while (uncorrelated) *noise* may be attenuated significantly at particular frequencies. Thus, it provides a signal with better noise characteristics than any one sensor in the set, alone. Designing a set of complementary filters essentially amounts to a Kalman filtering problem, where the typical goal is to minimize the mean-square error for a discrete-time, state-space system [42].

6.2.1 Theory of Complementary Filtering

The basic goal of complementary filtering is to combine multiple types of sensor outputs in a way which takes advantage of their individual frequency response characteristics. For instance, one can compensate for the drift in the gyro by using an accelerometer as a tilt sensor. The accelerometer provides a good low-frequencies estimate of its orientation in gravity, but at higher frequencies, the output from each channel of the accelerometer becomes more significantly influenced by the accelerations of the pendulum body. Combining the gyro and accelerometer outputs with appropriate filtering, one can create an estimate of the pendulum angle which has better frequency characteristics than either individual sensor could provide alone.

Ideally, we would like to blend the sensors such that the total transfer function, $H(s)$, of the blended measurement of pendulum angle is "perfect" and introduces no additional dynamics.

$$\theta(s) \, H(s) = \theta(s) \tag{6.65}$$

and therefore $H(s) = 1$. Suppose we know the dynamic response, $G_i(s)$, of each of n sensors we wish to blend. We then need design a filter, $F_i(s)$, for each sensor such that:

$$H(s) = \sum_{i=1}^{n} G_i(s) \, F_i(s) = 1 \tag{6.66}$$

For now, let us neglect the dynamics of the gyro and accelerometer. The output from the rate gyro then simply consists of the angular velocity $(G_g(s) = s)$, along with whatever noise components there are. If we take the arctangent of the two orthogonal accelerometer channels, the resulting signal component of the accelerometer measurement is the angle of tilt $(G_a(s) = 1)$. We therefore need to create a pair of filters for the two sensors such that:

$$s F_g(s) + F_a(s) = 1 \tag{6.67}$$

The simplest solution is to create a pair of first-order filters:

$$F_g(s) \quad = \quad \frac{\tau}{\tau s + 1} \tag{6.68}$$

$$F_a(s) \quad = \quad \frac{1}{\tau s + 1} \tag{6.69}$$

It is simple to verify that this set of filters indeed outputs the *signal* component of the measurement unaltered (regardless of the value of the time constant):

$$s \cdot \frac{\tau}{\tau s + 1} + \frac{1}{\tau s + 1} = \frac{\tau s + 1}{\tau s + 1} = 1 \tag{6.70}$$

The dynamics of the *noise* which passes through the complementary filters will be affected by the selection of τ, however.

Figure 6-15 models each sensor output as a combination of a perfect (dynamically unaltered) signal component and some additional noise component. Each sensor will have its own, frequency dependent noise characteristics.
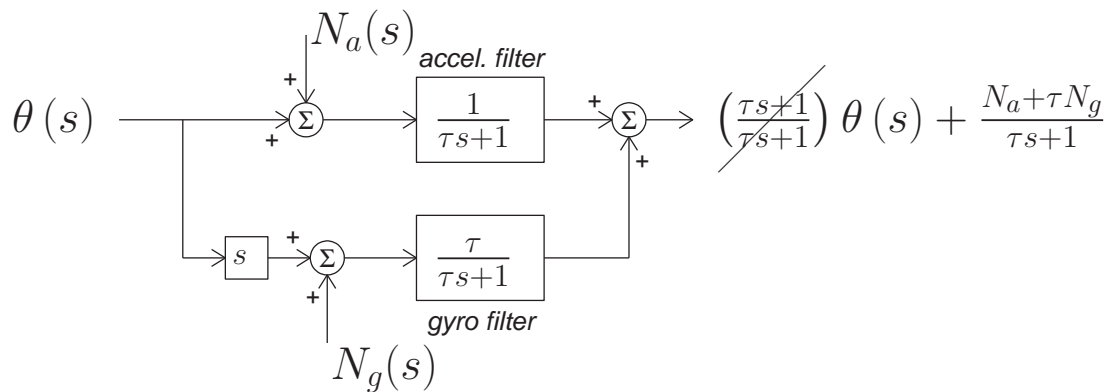
Figure 6-15: Block diagram of gyro-accelerometer complementary filtering

The output of the blended measurement, shown on the righthand side of Figure 6-15, is rewritten below in Equation 6.71. Here, the total estimate of the angle, $\theta_{meas}(s)$, is written in terms of the actual angle, $\theta_{act}(s)$, and the noise in the accelerometer and gyro signals, $N_a(s)$ and $N_g(s)$, respectively.

$$\theta_{meas}(s) = \theta_{act}(s) + \frac{1}{\tau s + 1} \cdot N_a(s) + \frac{\tau}{\tau s + 1} \cdot N_g(s) \tag{6.71}$$

We can make a few general comments based on the form of Equation 6.71. First, while both the accelerometer and gyro signals will have a DC (bias) component, changing τ will affect only the magnitude of the influence of the gyro bias. Any bias in the accelerometer will pass through the filter unaltered. Since the entire output from the gyro is scaled by τ, the shorter this time constant is, the less significant any noise contribution from the gyro will be. In the limit as $\tau \rightarrow 0$, the

measurement $(\theta_{meas}(s))$ simply consists of the estimate from the accelerometer alone. We wish to find an appropriate value for τ which appropriately attenuates both the high-frequency components from the accelerometer (which are corrupted by the accelerations of the robot) and the DC bias from the gyro. Section 6.2.3 discusses in detail how the value of the time constant can be set to attenuate the noise from each sensor significantly.

The complementary filters used to estimate the tilt of the pendulum-body of the inverted pendulum robot described in Chapter 7 are of the form shown in Equations 6.68 and 6.69. However, there are clearly an infinite variety of complementary filter pairings we could use instead. Equations 6.72 and 6.73 provide the form for two possible second-order filters, for instance:

$$F_g(s) = \frac{\tau^2 s}{(\tau s + 1)(\tau s + 1)} \tag{6.72}$$

$$F_a(s) = \frac{2\tau s + 1}{(\tau s + 1)(\tau s + 1)} \tag{6.73}$$

The pair of two-pole filters shown above were used to filter the signals from a rate gyro and an inclinometer for a small autonomous helicopter, where the inclinometer was modeled as having a first-order lag with a time constant of about a half a second [21]. For the gyro-accelerometer sensor blending used in the IP robot, first-order filters provided better performance, as documented in Section 6.2.4.

6.2.2 Noise Characteristics of Accelerometer and Gyro

This section documents the typical noise characteristics for the gyro and accelerometer used in tilt sensing for the inverted pendulum robot described in Chapter 7. The rate gyro is a single-axis Vibrating Structure Gyroscope (VSG, part number 299640-0100) manufactured by British Aerospace which has a range of $\pm 100°$. The accelerometer is a dual axis ADXL202, which is manufactured by Analog Devices and measures up to $2g$. The gyro and accelerometer are described in more detail in the next chapter in Sections 7.1.5 and 7.1.6, respectively.

The signals from both the accelerometer and gyro are each pre-filtered before blending the two. The actual measurement of the pendulum angle therefore expe-

riences some phase lag, unlike the ideal examples presented in the previous section. Figure 6-16 shows the magnitude of the drift typical for the rate gyro. Figure 6-17 provides examples of the unfiltered and filtered accelerometer waveforms, while Figure 6-18 shows the response of the filtered accelerometer channels to a step change in angle of roughly 2°. Finally, Figure 6-19 is included to illustrate that the unfiltered gyro and accelerometer signals look similar in character, with relatively large-amplitude oscillations.
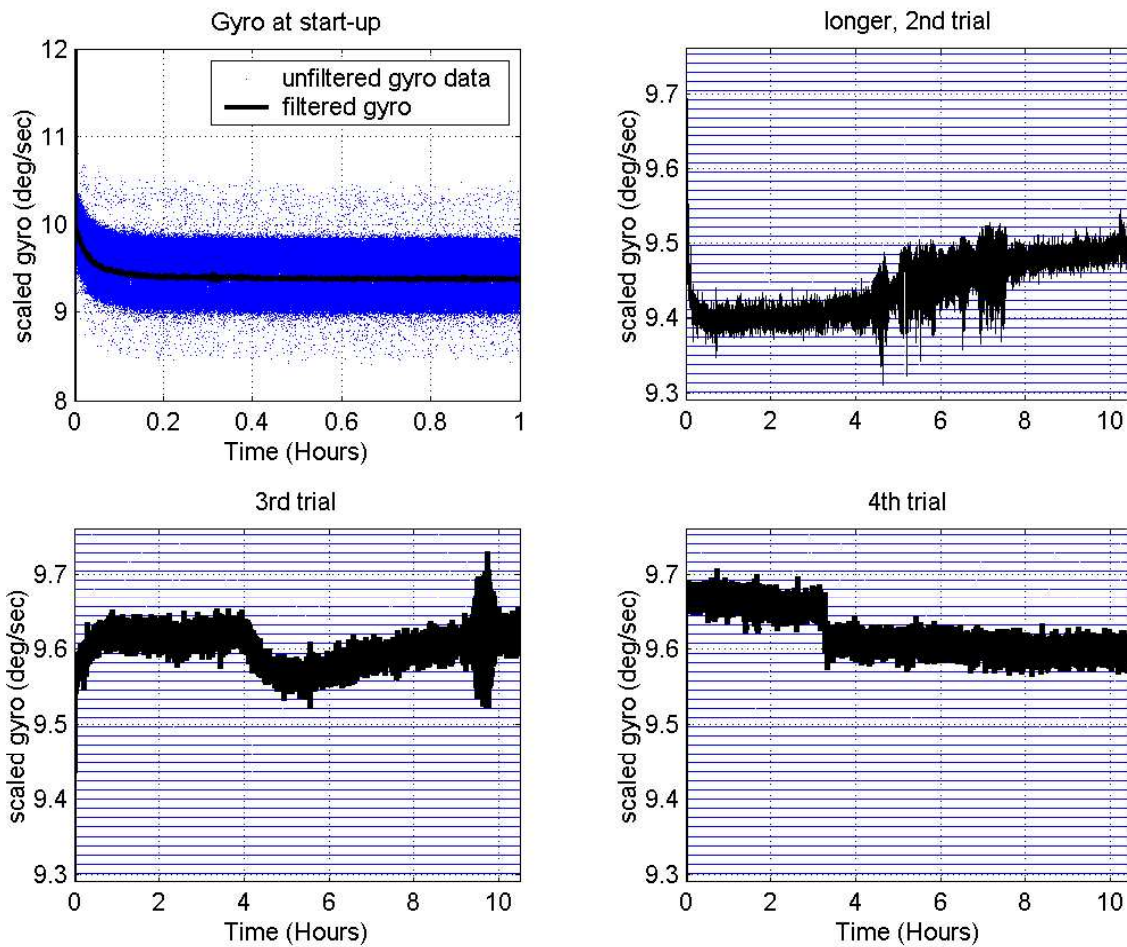
Figure 6-16: Drift of gyro DC bias (offset) over time. These data were taken with the gyro at rest and the ambient temperature steady to within a few degrees Fahrenheit (in our air conditioned laboratory). Temperature has a significant effect on bias. The upper left plot here shows the change in bias typical for the device as it warms up after power is initially sent to it.
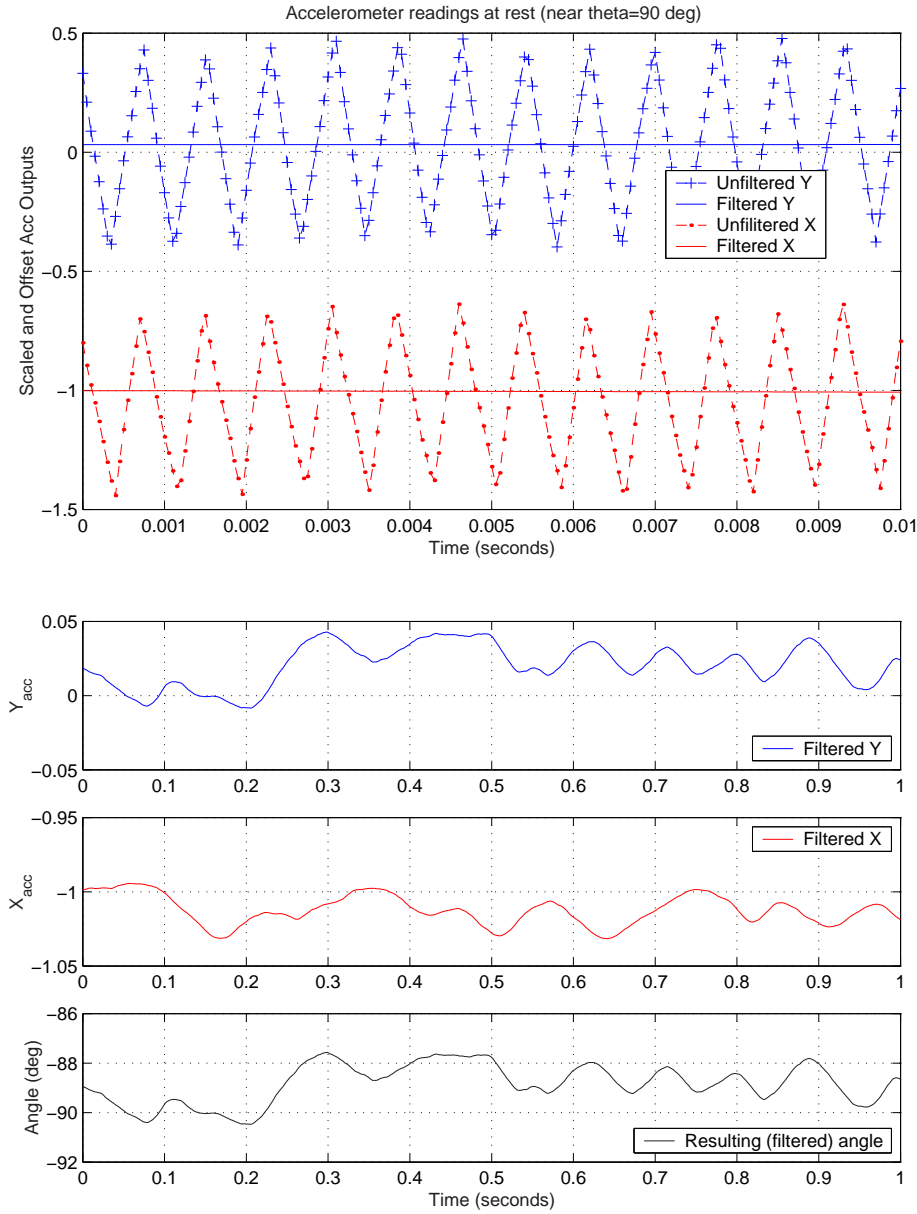
Figure 6-17: Accelerometer signals before and after low-pass filtering. Data were taken with the pendulum resting nearly horizontal (stationary with $\theta \approx -90°$) on the floor. With the pendulum resting on the floor, the accelerometer output is a combination of floor vibrations and noise. The data at top have been scaled such that a value of "1" on the y axis is approximately 1g of acceleration. The amplitude of the high-frequency oscillations (top) is therefore approximately 0.4g (quite large). After filtering (bottom), there is still significant uncertainty in pendulum angle at this time scale.
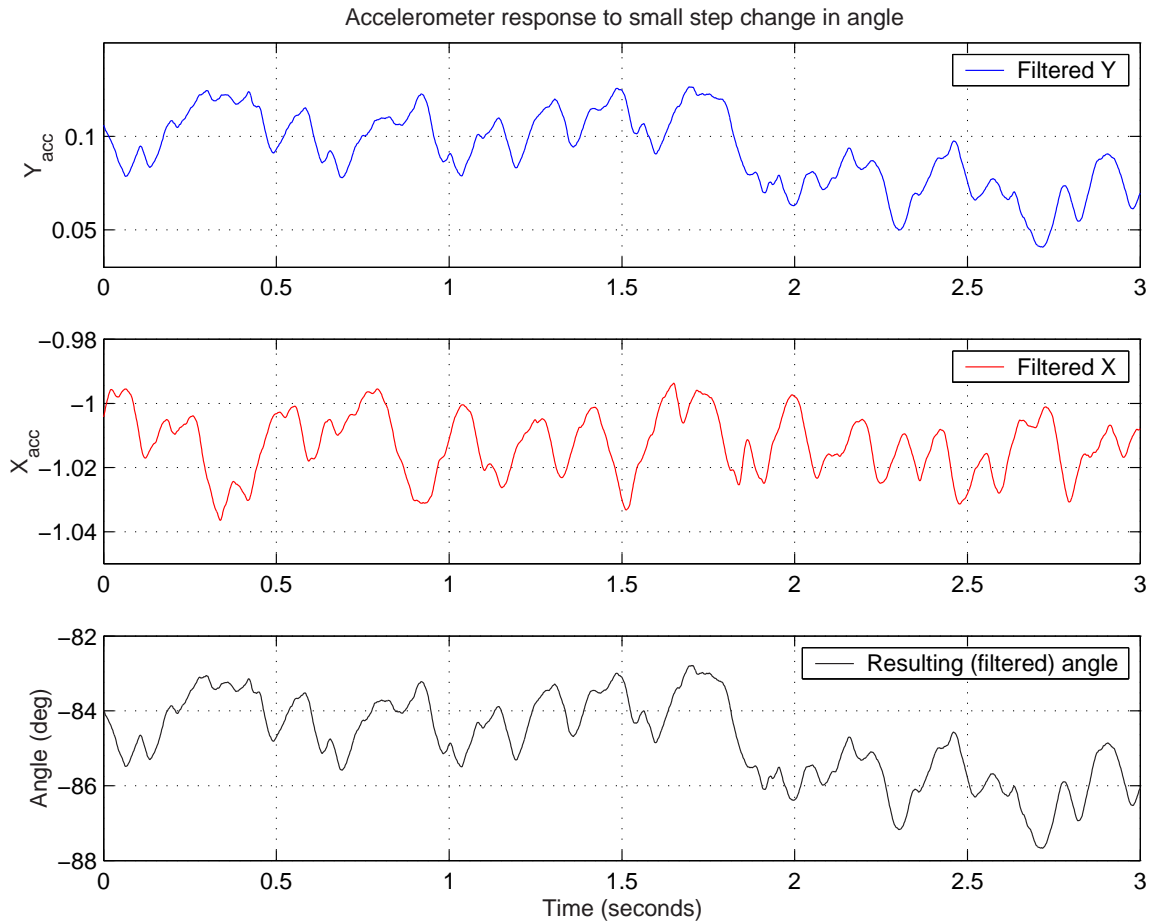
Figure 6-18: Accelerometer signals during a small step change in pendulum angle. The pendulum angle changed by two degrees at $t \approx 1.8$ seconds in the traces shown above. Note the magnitude of the "noise" (consisting of seismic or other vibrations of the floor and any sensor noise) in the accelerometer measurement of pendulum angle at this time scale, as compared with the gyro measurement (with low frequency drift compensation from the accelerometers). The accelerometer is not accurate enough to be used in measuring the pendulum angle directly. Also note that the top and bottom plots are almost identical (through a scaling factor). When the pendulum is within a few degrees of being vertical or horizontal, the output angle is essentially a scaled version of the output of just one of the accelerometer axes, while the other signal essentially serves as a sign bit.
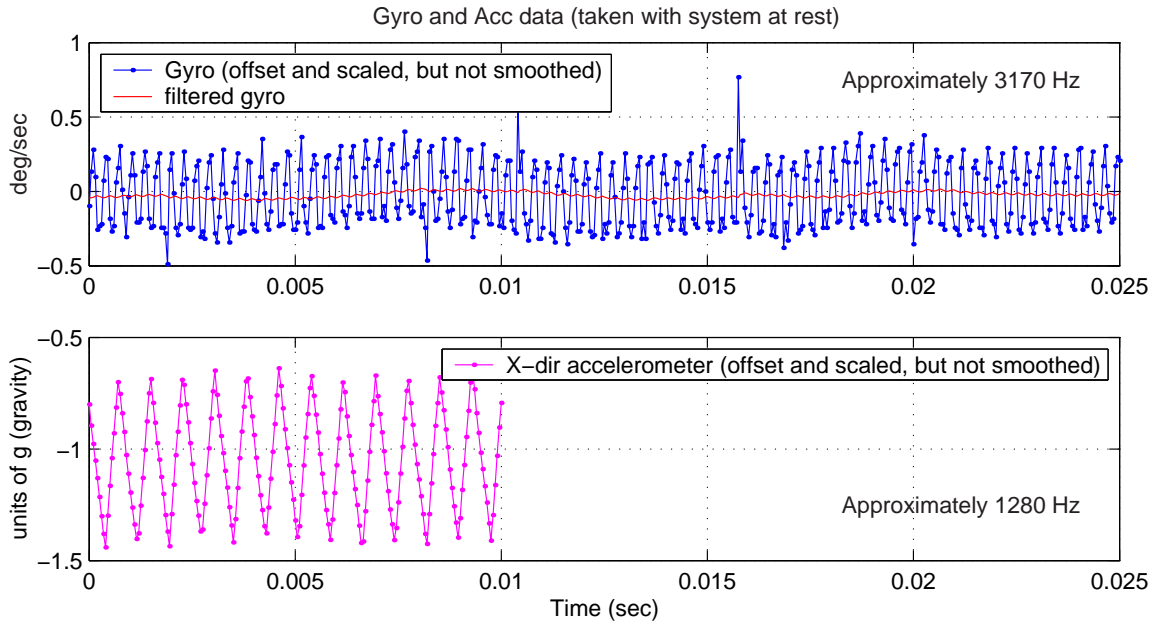
Figure 6-19: Data illustrating relative frequencies of oscillation of unfiltered gyro and accelerometer signals. Both the rate gyro and the accelerometer operate by resonating a mechanical structure and detecting particular forces on that system. (The gyro detects Coriolis forces caused by rotation about a particular axis, and the accelerometer detects the force of acceleration along each of two axes.) The data shown above illustrate both the magnitude and frequency of the oscillations from each sensor. These oscillations are shown on the same time scale to illustrate that they are not noticeably coupled. That is, although the waveforms have similar characteristics, they are clearly independent signals when seen next to one another.

6.2.3 Selecting an Appropriate Time Constant

The choice of the time constant for the two (first-order) complementary filters will affect the magnitude of the total noise in the angle measurement. If we know the noise spectra of the accelerometer and gyro, we can then solve for an optimal time constant which minimizes the mean-square error in the measurement. As an example, imagine the noise in each sensor can be reasonably well-characterized by a "white" component, σ^2, and some larger, DC bias term, B. Below, we can integrate to solve for the mean-square value of the *white noise component* of the accelerometer:

$$N_a(s) = \sigma_a^2$$

$$F_a(s) = \frac{1}{\tau s + 1}$$

Using a standard integral table [42, p. 133], the expected value of the square of the error is:

$$E(e_a^2) = \frac{\sigma_a^2}{2\pi j} \int_{-j\infty}^{j\infty} \frac{1}{\tau s + 1} \cdot \frac{1}{\tau(-s) + 1} \, ds = \frac{\sigma_a^2}{2\tau} \tag{6.74}$$

We can similarly derive the expected noise output from the filter for the gyro. Clearly, the entire output is just scaled by τ, compared with the filter for the accelerometer.

$$N_g(s) = \sigma_g^2$$

$$F_g(s) = \frac{\tau}{\tau s + 1}$$

$$E(e_g^2) = \frac{\sigma_a^2}{2\pi j} \int_{-j\infty}^{j\infty} \frac{\tau}{\tau s + 1} \cdot \frac{\tau}{\tau(-s) + 1} \, ds = \frac{\tau^2 \sigma_g^2}{2\tau} \tag{6.75}$$

The expected variance of the total noise includes contributions from the white and DC components, as shown below.

$$E(e_{tot}^2) = \frac{\sigma_a^2}{2\tau} + B_a + \frac{\tau^2 \sigma_g^2}{2\tau} + \tau^2 B_g \tag{6.76}$$

We can solve for an "optimal" time constant by setting the derivative to zero:

$$0 = \frac{dE(e_{tot}^2)}{d\tau} = \frac{-\sigma_a^2}{2\tau^2} + \frac{\sigma_g^2}{2} + \tau B_g \tag{6.77}$$

$$\sigma_a^2 = \sigma_g^2 \tau_{opt}^2 + 2B_g \tau_{opt}^3 \tag{6.78}$$

If the gyro and accelerometer noise are both truly white (in particular, if there is no predominant DC bias component in the gyro), then $\tau_{opt} = \sigma_a / \sigma_g$. In the limit as $\sigma_g \to 0$ (or as $\sigma_a \to \infty$), then $\tau_{opt} \to \infty$. That is, as the gyro noise gets vanishingly small, there is no longer any reason to compensate with the accelerometer, and we would simply use the integrated gyro signal to estimate the tilt angle. In the other extreme where the accelerometer signal is far superior to the gyro (as $\sigma_g \to \infty$, or as $\sigma_a \to 0$), then $\tau_{opt} \to 0$, and we would use the unfiltered accelerometer signal, alone.

The piezoelectric shell-type resonator used in the BASE gyro is plagued by significant, temperature-dependent bias. There is an (unused) temperature output for the gyro. I have chosen not to use the temperature output, and the measurement of pendulum angle is in fact adequate without it. This temperature effect will have an influence on the noise characteristics of the robot, however, particularly if it is not run in an air-conditioned environment (like out lab). Figure 6-16 shows the drift in bias over a long (10-hr) time scale. For an hour-long run, the magnitude of the drift in bias can be on the order of two or three times the magnitude of the white noise or more, depending on ambient temperature changes - the temperature-dependent drift in bias is on the order of .01 deg/sec/^{o}F of temperature change.

The complementary filters for the DIPR currently use $\tau = 1\,$s. The noise data and captions in Figures 6-20 and 6-21 are included to justify this choice. Both the gyro and accelerometer outputs are pre-filtered in addition to the complementary filtering performed on each signal. The BASE gyro is pre-filtered with a single-pole low-pass filter which matches the bandwidth of 75 Hz of the device. The accelerometer channels are pre-filtered before taking an arctangent to estimate tilt angle.

The accelerometer compensates for the DC bias in the gyro, and the bandwidth of the pre-filtered accelerometer is only a few Hertz. At the lower right of Figure 6-20 is the noise spectrum of the pre-filtered angle measurement from the accelerometer (taken with the pendulum at rest). If this were reasonably flat, one could solve Equation 6.77 explicitly to find the optimal time constant. I have instead used actual data to calculate the magnitude of various noise components as a function of τ. This data is shown in Figure 6-21.
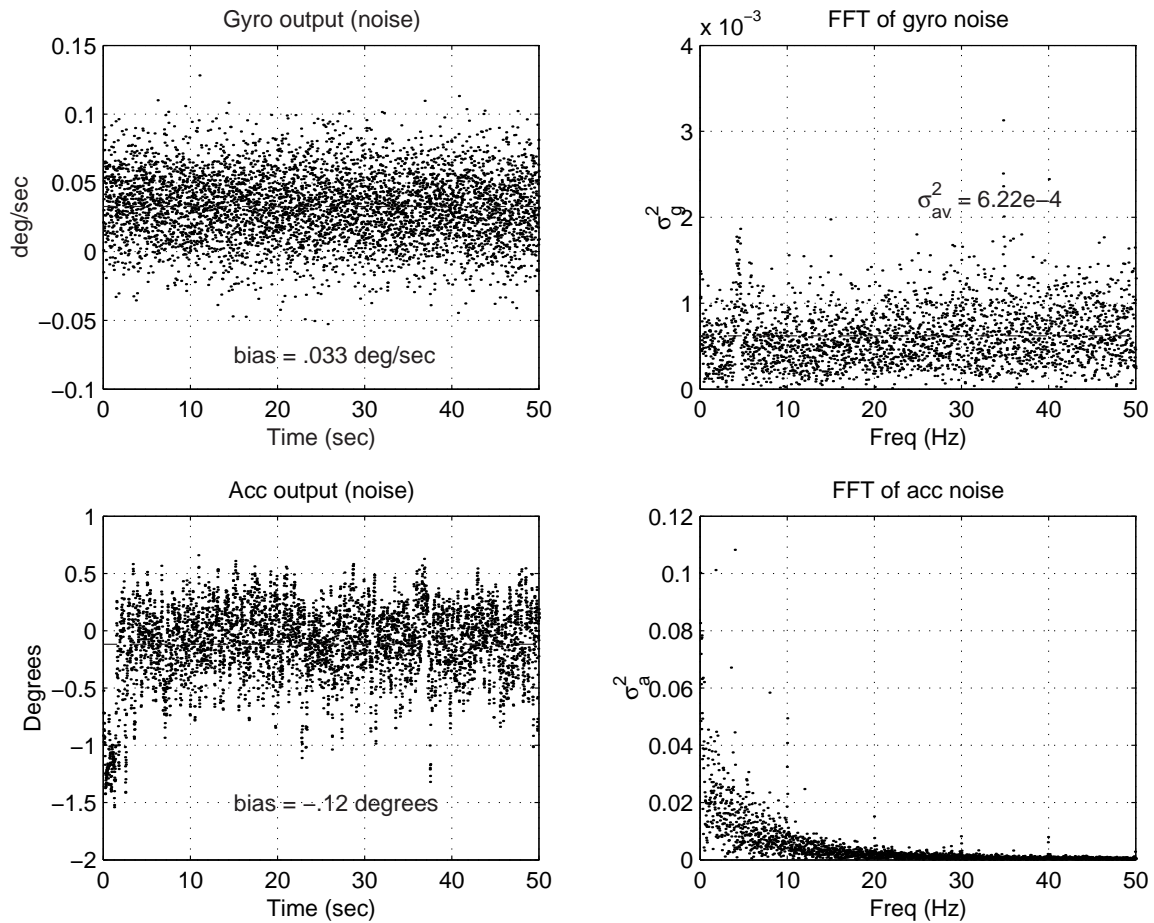
Figure 6-20: Typical gyro and accelerometer noise data. At left are pre-filtered and downsampled data ($\Delta t = 0.01$ sec) collected with the pendulum propped upright (at rest). Each signal is pre-filtered in addition to the filtering provided by the complementary filters, as mentioned in the text. The gyro and accelerometer signals shown are the inputs to the two complementary filters (labelled "drift_comp_gyro" and "drift_comp_acc" in Figure H-3 on p.437 of App. H). Note that the gyro noise (FFT top right) is still relatively white across the frequency range shown, while the accelerometer signal has significantly larger noise below 10 Hz (roughly). (The accelerometer signal is pre-filtered to smooth input to the nonlinear arctan function.) Interestingly, the accelerometer signal always displays a characteristic "jump" when data collection is initially triggered. (The accelerometer is powered off of the 5-volt dSPACE supply, while the gyro runs off of a separate, 12-volt supply.)
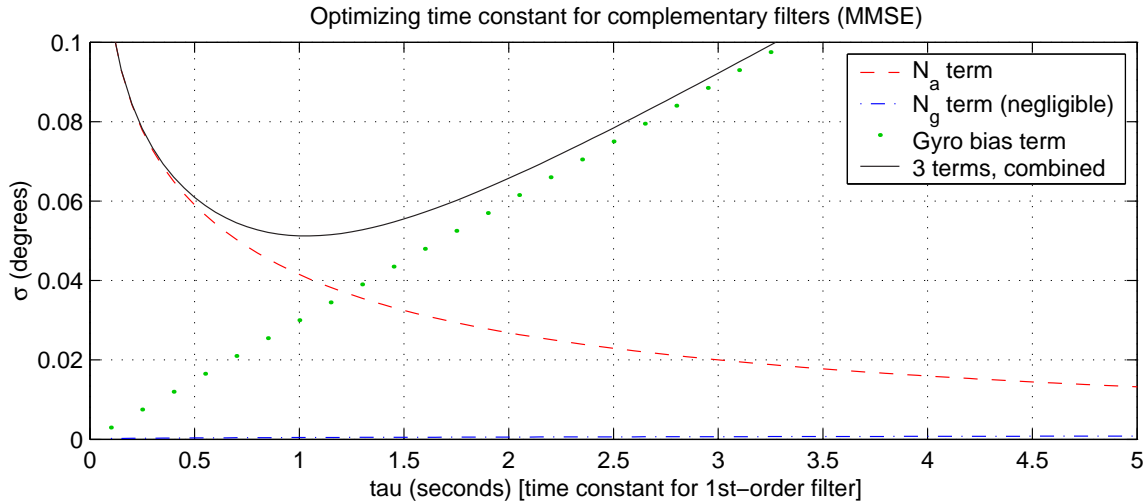
Figure 6-21: Optimal time constant for complementary filters (MMSE). The standard deviations of the gyro and accelerometer noise (shown as dashed lines above) were obtained by filtering actual data (100,000 points with $\Delta t = 0.001$s) with filters of varying bandwidth. Any DC bias in the gyro results in a constant offset in measurement angle which has a linear dependence on the filter time constant. Bias in the accelerometer will also result in a constant error in angle, but this error term has no dependence on the filter time constant. Therefore, it is left out of the plot above for clarity. The bias of the gyro represented above (.03 deg/sec) is typical but approximate. (Product specifications list .02 deg/sec in-run bias at constant temperature, but the bias has a strong dependence on temperature — *roughly* on the order of .01 deg/sec/^{o}F of temperature change). A useful definition of the "optimal" time constant is the value which minimizes mean-square error (MMSE) of the resulting output. The complementary filters in the dSPACE model use a time constant of 1 sec, which is near the minimum (zero derivative) point on the solid-line plot above. The actual variation in gyro bias clearly affects the "optimal" time constant, however, and "$\tau_{opt} = 1$ sec" should be viewed as a ballpark value, only. Finally, recall that accelerometer bias will also add to the total error. The accelerometer bias will add a constant offset to the measurement of tilt angle and can be on the order of 0.1 degrees.

6.2.4 Performance of the Complementary Filters
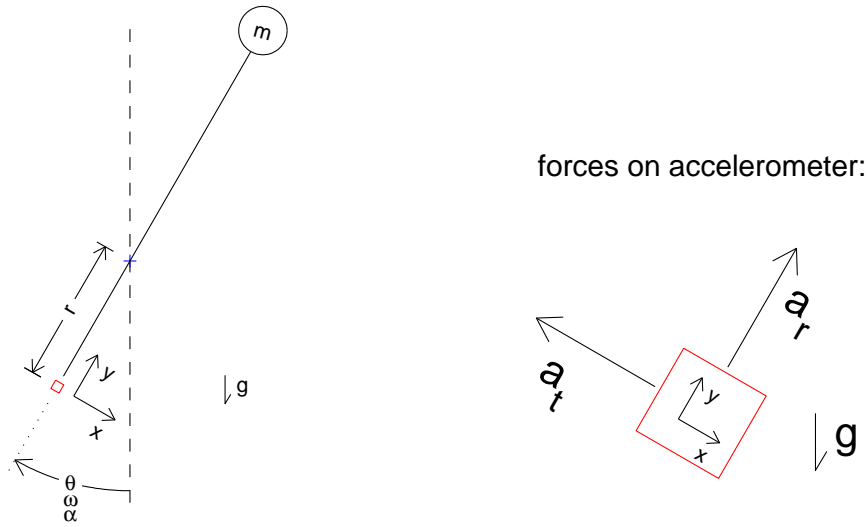
Figure 6-22: Forces on accelerometer as pendulum swings. The pivot point of pendulum is modeled here as fixed, so there are no accelerations due to lateral movements of the robot chassis.

Figure 6-22 shows the accelerations acting on the 2-axis accelerometer as the pendulum arm swings about a *non-accelerating pivot point*. Clearly, additional acceleration of the robot chassis forward or backward will also be sensed by the accelerometer. The analysis below ignors any lateral acceleration simply to allow for a more convenient comparison between theoretical and experimental sensor performance. Data shown in Figure 6-24 were collected with the wheels fixed and the pivot is coaxial with the wheel axis. Since the wheel can not rotate, the encoder reading in this constrained configuration measures the actual pendulum angle. The encoder measurement of the angle can therefore be compared directly against the estimate of angle created through complementary filtering of the gyro and accelerometer signals.

The total acceleration acting upon the sensor can be broken into the following three components, as depicted on the righthand side of Figure 6-22: (1) the acceleration of gravity, g; (2) a radial centripetal acceleration, a_r; and (3) a tangential acceleration, a_t. As the pendulum rotates, a_r is always aligned along the y-axis while a_t is correspondingly sensed solely by the x-axis channel. The acceleration of gravity

is sensed by each axis as the cosine or sine of the pendulum angle:

$$a_y = -a_r - g \cdot \cos(\theta) \tag{6.79}$$

$$a_x = a_t + g \cdot \sin(\theta) \tag{6.80}$$

The centripetal acceleration, a_r, is proportional to the square of the angular velocity. The sign of this component and of gravity will both be negative, with respect to the axis orientation shown in Figure 6-22. If the pendulum is not rotating at a *constant* angular velocity, then its angular acceleration will be sensed along the x-axis. Equations 6.81 and 6.82 summarize these forces.

$$a_r = r\omega^2 = r \left(\frac{d\theta}{dt} \right)^2 \tag{6.81}$$

$$a_t = r\alpha = r \frac{d^2\theta}{dt^2} \tag{6.82}$$

Recall that the entire point of using the accelerometer is to detect the direction of gravity. Therefore, we would like to minimize the detection of any other accelerations and should therefore locate the accelerometer as close as practical to the pendulum pivot (so that $r \approx 0$). The robot has been tested with the ADXL202 located coaxial with the wheel axis. The accelerometer is currently mounted approximately 3" below the pivot point of the pendulum, however, to make the wiring and debugging of the robot more accessible. Any difference in performance between the coaxial and off-center the accelerometer positions was not noticeable. The simulations and data shown here all correspond to an accelerometer mounted 3" below the pivot point.

Figure 6-23 shows simulated estimates of the pendulum angle, while Figure 6-24 provides actual data taken with the wheels of the DIPR fixed in place and the pendulum moved rapidly by hand. Complementary filtering in the DIPR currently uses the single-pole filters shown in Equations 6.68 and 6.69 with a time constant, τ, of one second. This value was determined to be close to "optimal" as defined in the previous section. The lower half of Figure 6-23 compares theoretical outputs with values of τ a factor of four faster and slower than this.
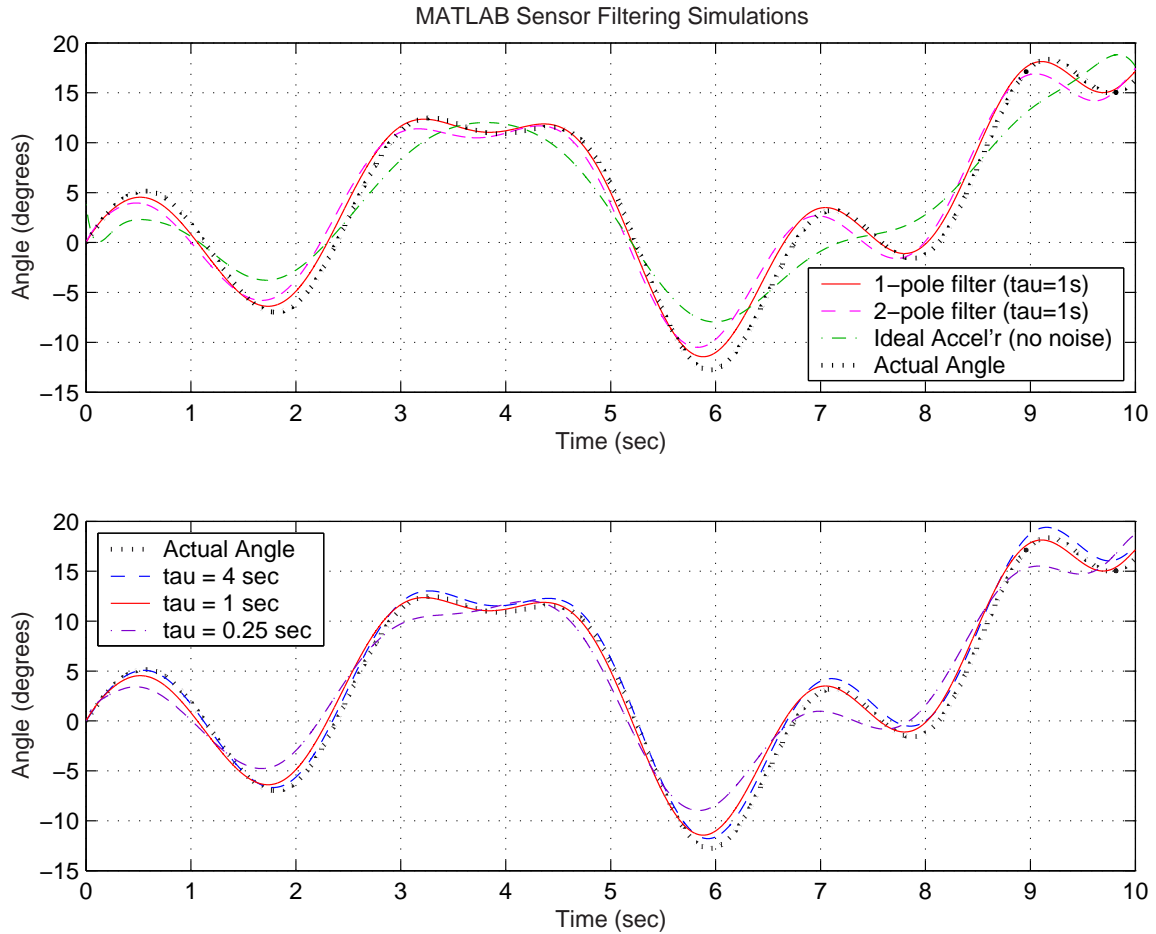
Figure 6-23: MATLAB simulations of filter performance. The theoretical plots above assume a constant bias in gyro the measurement of 0.25 deg/sec and Gaussian noise in accelerometer channels with a standard deviation of 0.01g. The wheel axis of the robot is modeled here as fixed. Plots at the top compare three simulated estimates of pendulum angle with the "actual angle" of the pendulum. The solid line shows the predicted output of a one-pole complementary filter of the form described by Equations 6.68 and 6.69. This is the final filter used in the actual DIPR. A two-pole filter pair described in Equations 6.72 and 6.73 is also shown and seems to introduce additional lag in the measurement. The accelerometer signal alone is also shown, to demonstrate that the blended gyro-accelerometer output is significantly more accurate (particularly at high frequencies) than the accelerometer measurement alone. The traces in the lower plot compare the predicted performance of the single-pole filter design for three values of τ. In the actual filters for the DIPR, $\tau = 1$s.
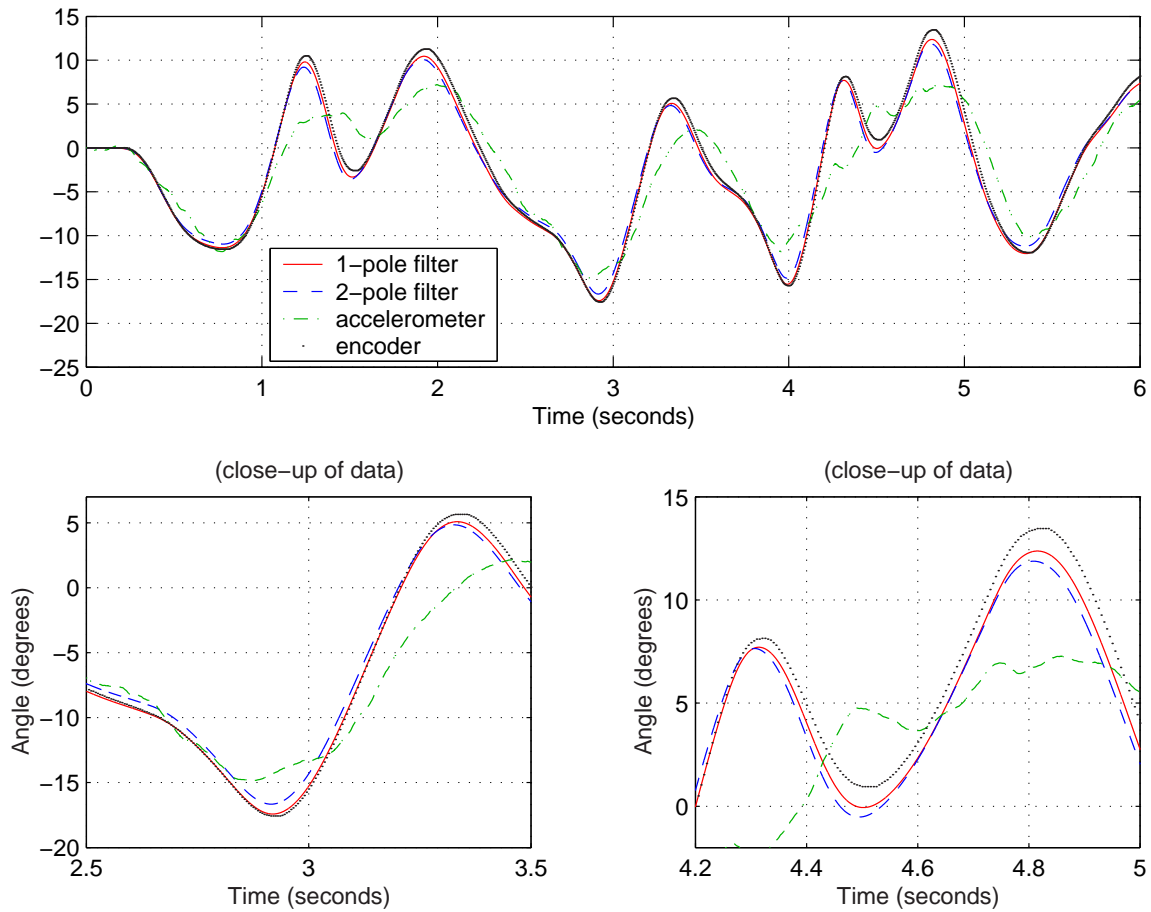
Figure 6-24: Experimental tracking data for drift-compensated gyro signal. The plots above show actual data taken with the wheels of the DIPR held in place while the pendulum was "wiggled" rapidly by hand. A dSPACE model similar to the one documented in Appendix H was used to filter signals, but the system was not under active control when data were taken. The one-pole and two-pole complementary filters used here are identical to those modeled in the plot at the top of Figure 6-23, with $\tau = 1$ sec. The lower two plots above simply focus in on segments of the plot at the top to show more detail.

6.2.5 Minimizing the Effects of the DC Bias in the Gyro

Any DC bias, B_g, of the gyro measurement of angular velocity manifests itself as a steady-state offset in the measurement.

$$\lim_{s \to 0} \left[B_g \frac{\tau}{\tau s + 1} \right] = \tau B_g \qquad (6.83)$$

We would therefore like to minimize any bias in the gyro during each run to the extent practical.

The specifications for the BASE rate gyro used in the DIPR list an "in-run" bias of 0.02 deg/sec at constant ambient temperature and a "run-to-run" bias of 0.1 deg/sec. The specifications do not define the length of a single "run", but the experimental data in Figure 6-16 give some indication of the drift characteristics possible in an air-conditioned (i.e. fairly constant temperature) environment. In these data, the bias is shown to experience slow steady drift, step changes, and also some particularly "noisy" episodes over time. The run-to-run bias shown here (and from experience with the set-up) seems closer to 0.3 deg/sec or more in our laboratory environment.

Ideally, one would like to reduce the magnitude of the error due to the "DC" bias by estimating the zero-velocity bias at the start of a run and then offsetting the sensor output by this amount. Figure 6-25 shows a method used for doing this within the dSPACE controller for the DIPR. The constant labelled "reset1_hold2" in this figure can be reset in real time within the "ControlDesk" dSPACE environment while the model is run on the controller board. The value of this constant determines which of the three signals entering the "Multiport Switch" below this will be output. Initially, the constant has a value of 3, as shown in the figure, and the switch therefore outputs a default gyro offset. When the value of the constant is changed to a value of 1, the switch outputs the current measured gyro value.

The "offset_filter" provides low-pass filtering of the switch output with an effective time constant of around 0.5 seconds. Figure 6-26 shows the transient output of this filter after the "reset1_hold2" constant is set to 1 (at $t/approx 3$s). Figure 6-27 shows the output from the switch as the reset constant is cycled through several values (see caption).
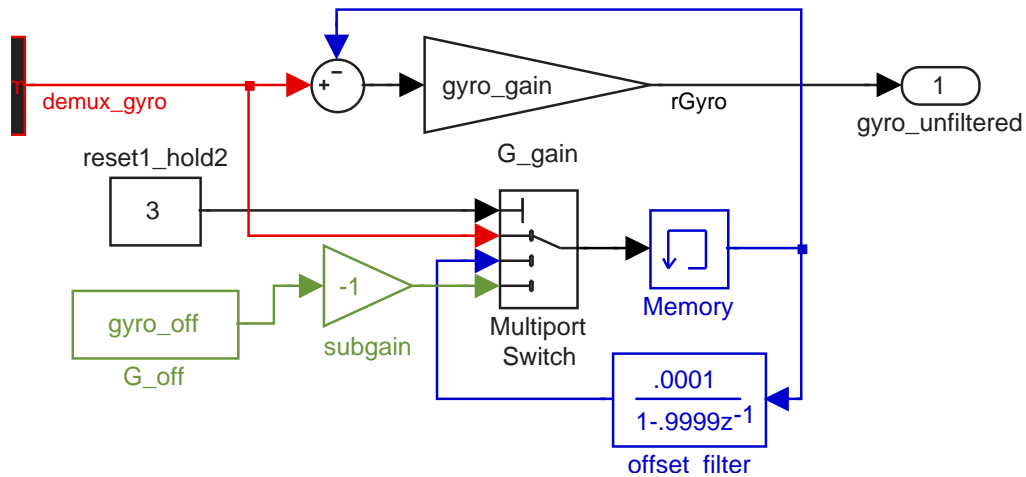
Figure 6-25: Method for resetting DC gyro offset in dSPACE/Simulink model. Above is the subroutine used to reset the DC gyro bias (if desired) when the pendulum sits at rest, before being controlled. The topmost (0th) port-selecting input to the "multiport switch" identifies which of the remaining three input ports (numbered from top to bottom) will be output. When the Simulink model is compiled, the initial value of the variable labelled "reset1_hold2" is three, and the switch therefore outputs the negative of a default bias offset: "gyro_off". The value of the port-selecting variable can be changed using the dSPACE "ControlDesk" environment. When input port #1 is selected, the switch outputs the (unfiltered) rate gyro measurement. The output from the switch goes through a low-pass discrete filter (labelled "offset_filter") with an effect time constant of 0.5 seconds. (The memory block is necessary to allow the input and output of the offset_filter to hold different values.) When the second possible output is selected, the switch simply cycles the same value through at each time iteration. The (delayed) output of the switch is subtracted from the unfiltered gyro signal, "demux_gyro", to compensate for the DC error in the signal. The gyro signal is then scaled and filtered and combined with the accelerometer signal (which has been filtered by a complementary transfer function).
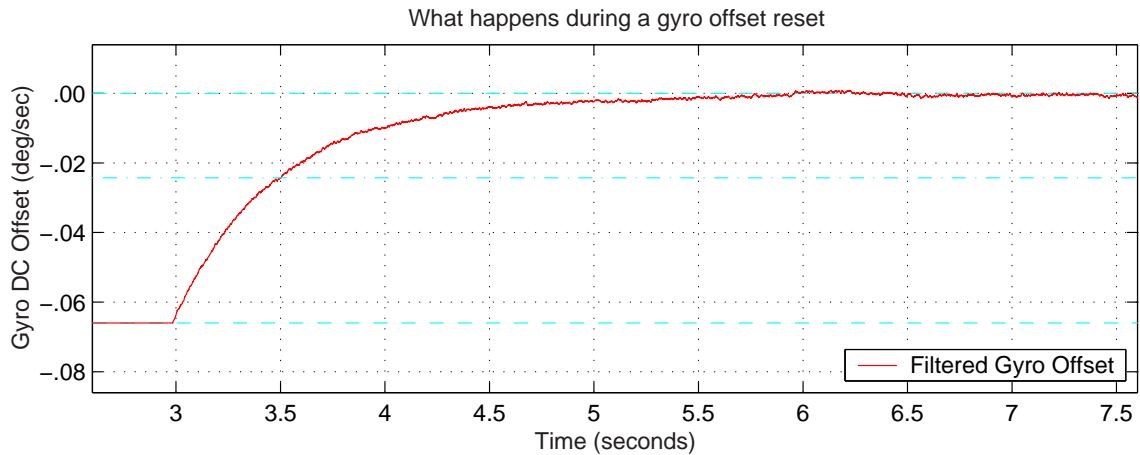
Figure 6-26: Transient response during a reset of the gyro offset. This figure shows data (taken while the pendulum was at rest) of a transition from the default gyro offset to the measured DC bias. The time constant to reach a steady-state measurement of the bias is 0.5 seconds. The output above is scaled to correspond to angular velocity units of degrees per second. The DC offset in the measured pendulum angle will be proportional to the DC bias in the gyro measurement: $\theta_e = \tau_{cf} \cdot \dot{\theta}_{bias}$, where τ_{cf} is the time constant used in the *complementary filters*. For the inverted pendulum robot, $\tau_{cf} = 1.0$ sec. In other words, since the initial bias shown at the lefthand side of this plot is approximately -.065 deg/s, these data indicate the DC error in the measurement of the pendulum angle would be about 1.0[s]·0.065[deg/s]= 0.065 [deg] (quite small) if the default bias value were used.
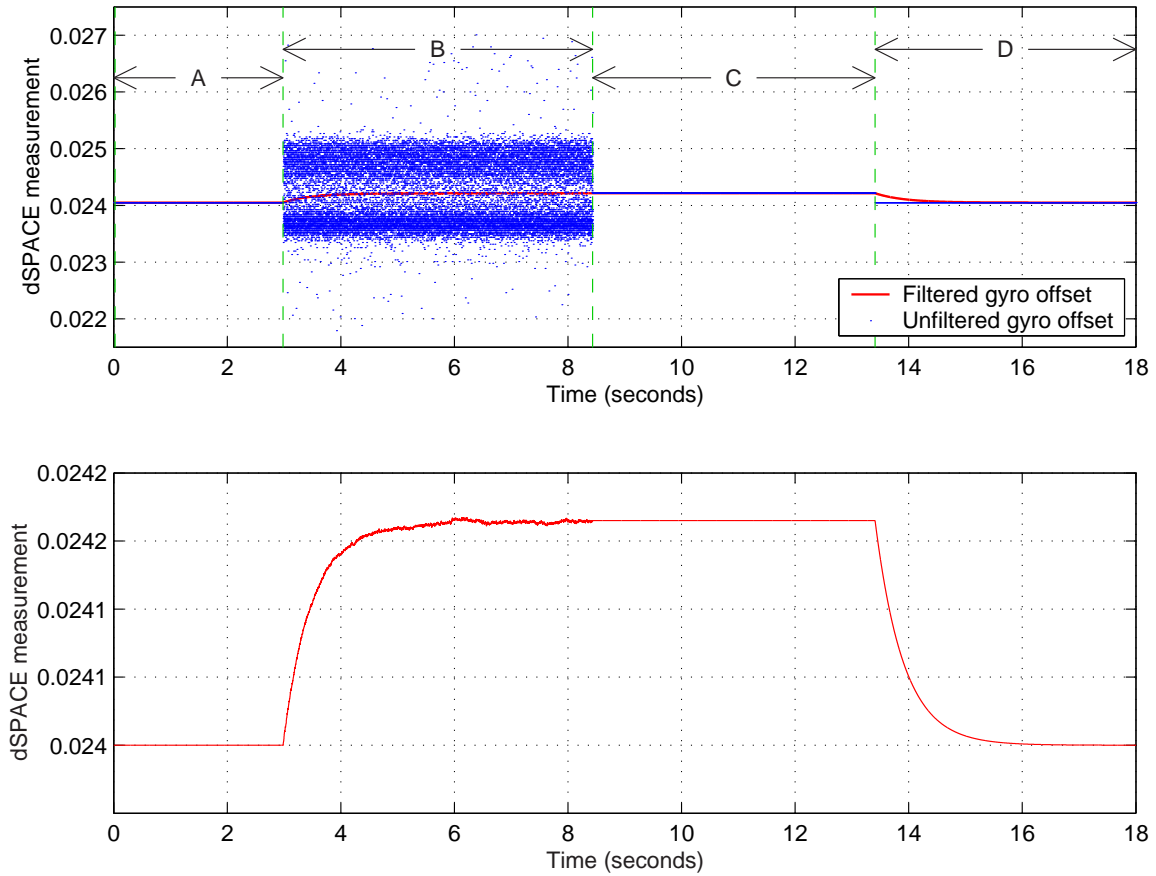
Figure 6-27: Typical signals during reset of the gyro offset. There are four, distinct regions in the signals above, labelled A, B, C and D. In regions A and C, the offset value is simply being held at a constant value. Region B shows a transition from the default offset to a time-averaged measurement of the gyro signal while the pendulum is at rest. The plot at the top shows both the raw, unfiltered gyro input and the time-averaged (smooth) signal which converges to the DC bias value. The time-averaged response can be seen more clearly in the lower plot. Region D shows a transition from the measured (and held) bias value back to the default bias constant.

This simple reset method significantly reduces the bias during a typical run of the DIPR. The inverted pendulum robot named "Joe" which is described on page 74 of Chapter 2 also uses a compensation scheme which measures the initial gyro bias with the system at rest just before running the controller. For Joe, the subsequent in-run bias is small enough that the robot can operate for several minutes without any additional compensation for drift. Joe operates without using a low-frequency tilt sensor (e.g. an accelerometer) or complementary filtering.

6.3   Conclusions

A gyroscope is a key sensor for obtaining an absolute measure of pendulum angle in a robotic inverted pendulum vehicle. Of the inverted pendulum vehicles described in the first half of Chapter 2 for instance, only one - the Legway, described in more detail in Section 2.1.5 on page 80 - does *not* use a gyroscope to detect pendulum angle. Since the Legway instead depends on the intensity of light reflected from the surface beneath it, however, it is limited to operation on a relatively flat and monochromatic surface. A gyro allows for more robustness to environmental conditions.

This chapter discusses several of the issues involved in optimizing the performance of one or more gyros in a tilt sensing application. Specifically, it describes the design of redundant sensor arrays for fail operational devices like the Segway and iBOT, and it reviews complementary filtering to reduce the errors introduced by integrating a velocity sensor to obtain an estimate of position.

Section 6.1.7 also describes some of the advances in MEMS gyro design. As the performance of low cost gyros improves, the issues covered in this chapter may become relevant for a wider variety of devices. The inverted pendulum robot described in the next chapter (the DIPR) uses a gyro based on a piezoelectric shell resonator. The operating principles of both types of gyros are similar, but the piezo device is both more expensive and more accurate than the MEMS gyros described here. Sections 7.1.5 and 7.1.6 of the next chapter describe this piezo gyro and the Analog Devices accelerometer which are used together for tilt sensing in the DIPR.

Chapter 7

Demo IP Robot (DIPR)

This chapter describes a two-wheeled "demo inverted pendulum robot" (DIPR) that was originally designed as a demo for 2.003 Modeling Dynamics and Control I. Figure 7-1 shows a diagram of the robot, and Figure 7-2 provides a photo of the actual hardware.[1] This two-wheeled design is inspired by the iBOT and Segway human transports reviewed in Sections 2.1.1 and 2.1.2 of Chapter 2. A brief outline of the chapter is given below.

The sensors and actuators for the robot are described in Section 7.1. Section 6.2 in the preceding chapter provides more detail on sensor issues relating to the complementary filtering of the gyro and accelerometer signals to provide tilt sensing and has a more general, theoretical focus. In contrast, the sensor discussion in 7.1 relates more directly to the specifications of the devices actually used in the DIPR.

Section 7.2 derives of the equations of motion for the system. Sections 7.3 and 7.4 and then present these equations in both transfer function and state space format for completeness. Section 7.5 discusses some issues related to the sizing of robot and its motors and the choice between current and voltage control of the motors. Section 7.6 provides experimental transfer functions characterizing the plant. Section 7.7 outlines the control loop used, and Section 7.8 gives time and frequency response data which illustrate the performance of the closed-loop system. Finally, the project is summarized briefly in Section 7.9 and in Chapter 8.

---

[1]Figure 7-2 uses the same photo of the robot hardware previously shown in Figure 1-14 on page 56.
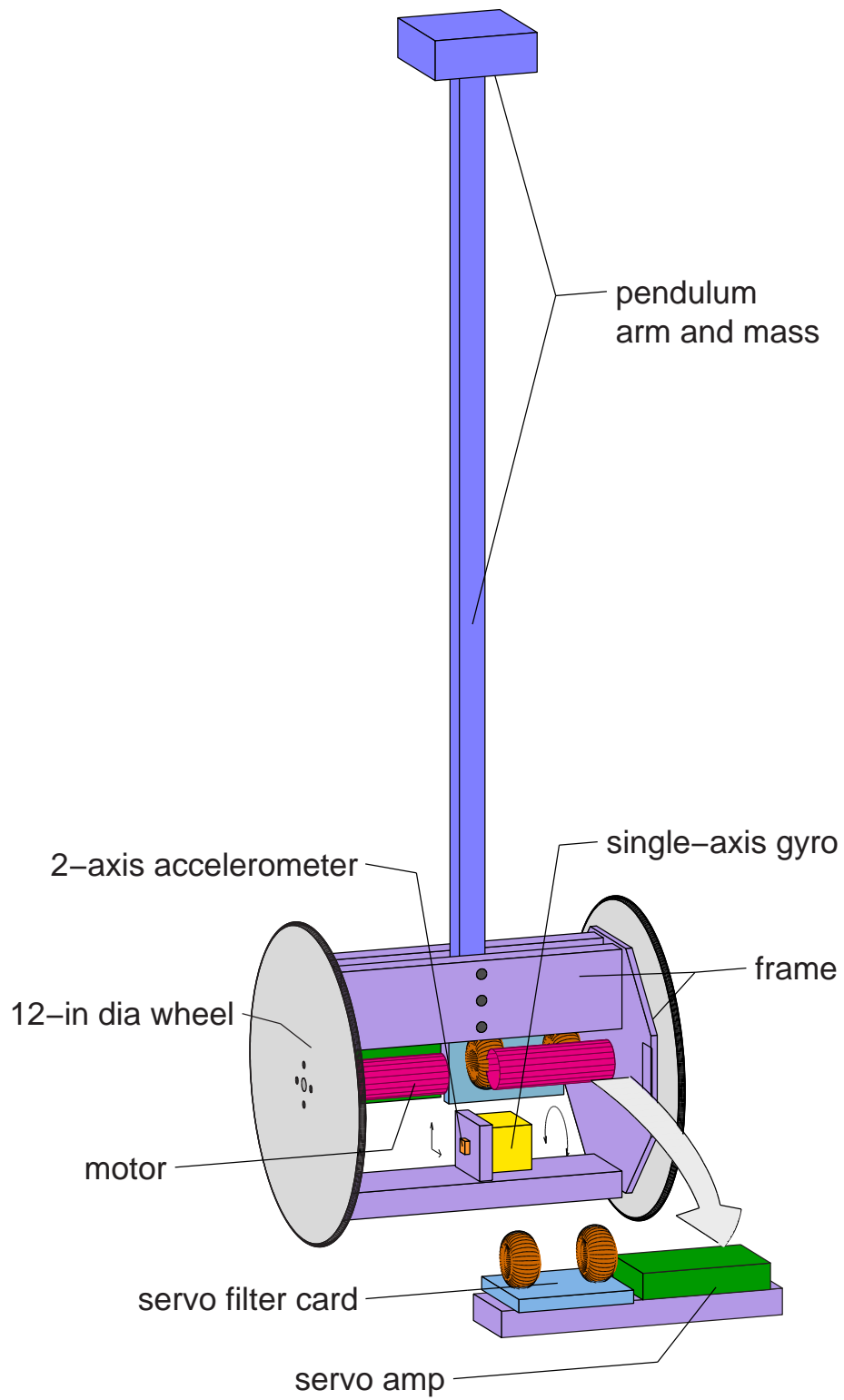
Figure 7-1: Diagram of the inverted pendulum robot
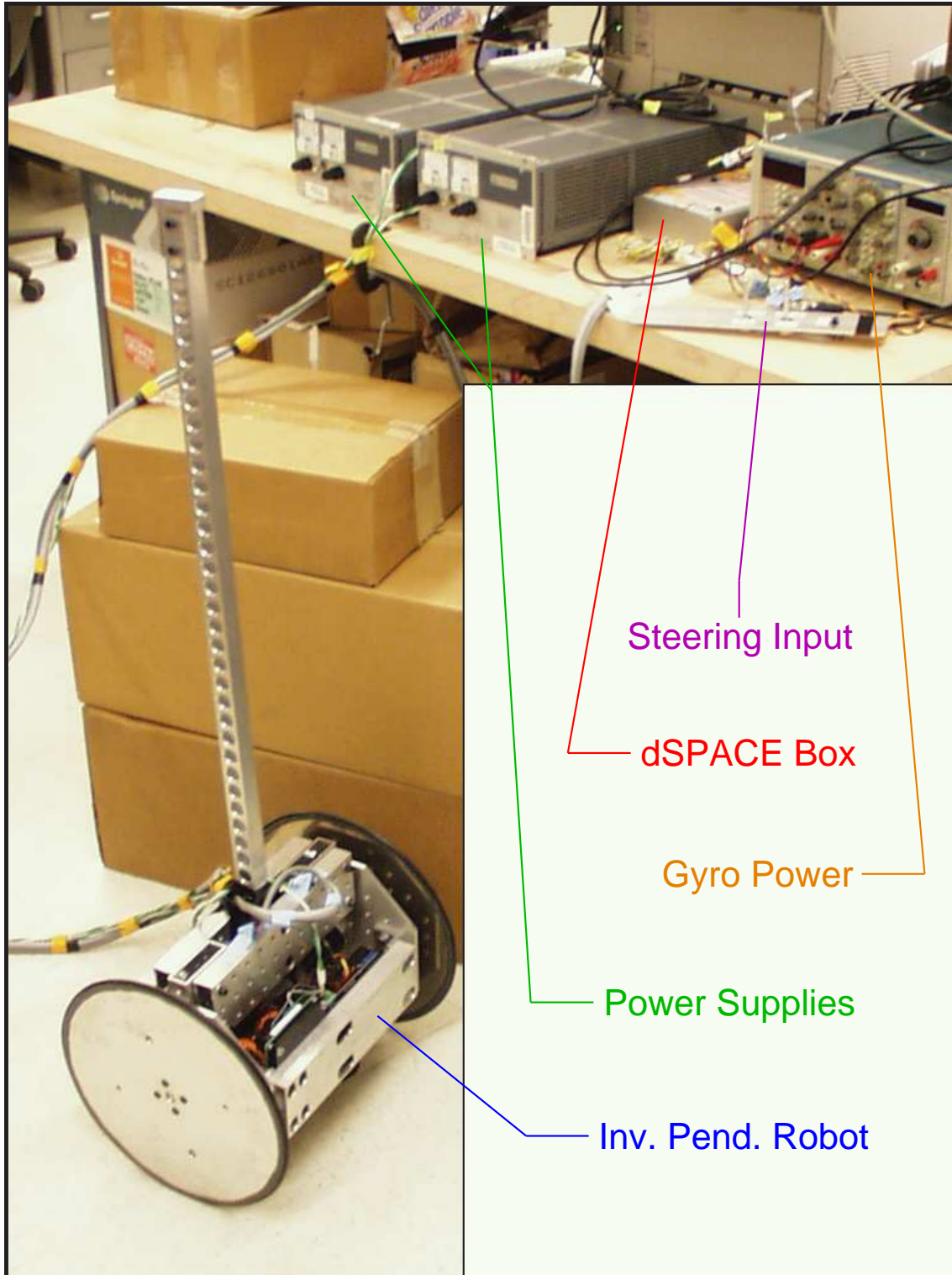
Figure 7-2: Inverted pendulum robot hardware
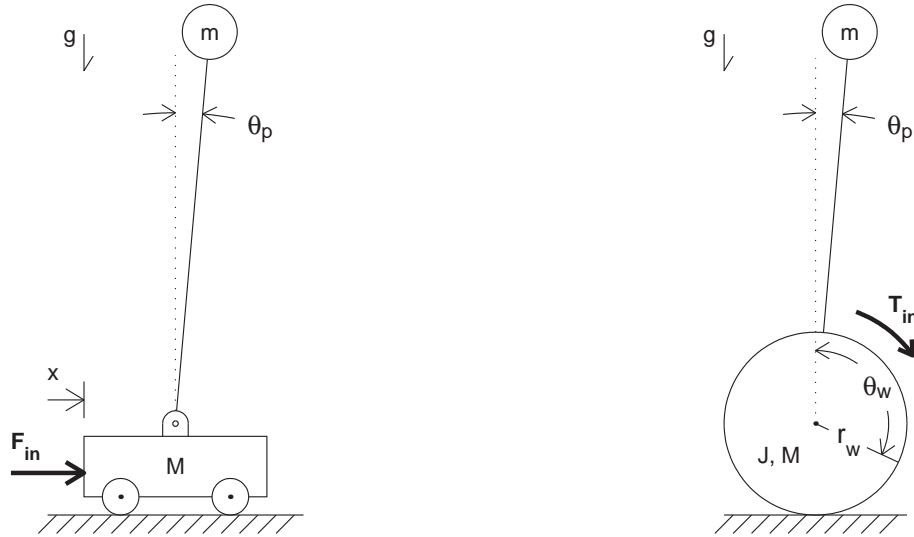
Figure 7-3: Two types of inverted pendulum systems. At left is a cart-driven inverted pendulum. Chapter 5 describes a set-up of this type, which was developed over a number of years by other students and faculty at MIT. At right is a two-wheeled robot of the type described in Chapter 7.

Figure 7-3 provides schematics to compare the essential elements of a cart-driven inverted pendulum, like the one described earlier in Chapter 5, with those of a two-wheeled robotic IP.[2] In the schematic on the left-hand side of this figure, the pendulum is attached to the cart at a free pivot, so that any torques applied to counteract the torque of gravity must come from lateral forces at the pivot point due to the accelerations of the driven cart. As a result, a pendulum mounted on a driven cart can only be in equilibrium when the pendulum is vertical (pointing exactly up or down with respect to the pivot).

By contrast, the robotic inverted pendulum is capable of generating a torque directly between the wheels and pendulum body. The robotic IP can therefore be controlled to find equilibrium positions which are offset from vertical, with the motor providing the necessary steady-state torque to balance the torque from gravity. This difference in the dynamic behaviors of these two types of inverted pendulum was previously outlined in Chapter 5.

---

[2]Figure 7-3 duplicates the schematics shown in Figure 1-12 on page 47.

A constant motor torque in the robotic IP corresponds to a constant steady-state vehicle speed. Since a given motor torque corresponds both to a particular equilibrium pendulum angle and a particular forward velocity for the robot, there is a direct correspondence between commanded pendulum angle and robot velocity. In other words, one can command a particular robot speed by commanding the appropriate desired pendulum angle (or equivalently by offsetting the measurement of pendulum angle by this amount).

Each of the two wheels of the DIPR is controlled by a separate motor. One can therefore steer the robot by offsetting the command signal to each motor by equal and opposite amounts. Technically, they are in fact offset by equal and "same-sign" amounts, because the motor output shafts are aligned 180° with respect to one another. However, it makes more sense semantically to consider each motor as having a "forward" and "reverse" direction. Commanding both motors to move "forward" results in the robot moving forward in a (theoretically) straight line, and adding oppositely-signed outputs causes the vehicle to turn.

As of this writing, the DIPR is not autonomous, and the umbilical cords required to transmit power, sensor measurements and command signals have several disadvantages which do not make the robot practical as a classroom demo. First, the umbilical cords significantly affect the dynamics of the system. They damp the movement of the pendulum, and they also create significant drag on the ground which essentially anchors the wheels of the robot in place to some extent. This drag inhibits the robot from moving forward as the robot tilts forward or backward and allows the robot to balance with moderate offset angles (away from vertical).

The non-autonomous design also reduces the ease with which the equipment can be transported to and set up in a classroom for a demo. The robot requires multiple power supplies: the two servo amps driving the motors each require a power supply, and separate 5- and 12-volt supplies power the accelerometer and gyro, respectively. Redesigning the robot to make it autonomous would require substantial effort, and there are no plans to implement an autonomous version of the robot nor to use the current version as a classroom demo at this time.

7.1 Robot Hardware

Figure 7-1 shows a diagram of the key components of the robotic inverted pendulum developed in this thesis. The vehicle weighs approximately 26 lbs, has two 12-inch diameter wheels which are spaced 14 inches apart, and stands about 44 inches high when balancing upright. Umbilical cords carry power and sensor/actuator signals. Two potentiometers provide steering inputs to command the desired forward velocity and turning rate. The controller for the robot is implemented digitally on a dSPACE 1103 board using an execution step size of 50 microseconds.

The sensors, actuators and robot chassis are described in more detail below. This section also outlines specifications on and advantages of using dSPACE and ControlDesk in implementing the controller. Sections 7.7 and 7.8 present the controller design and performance in detail. Section 6.2 of the previous chapter describes complementary filtering of the gyro and accelerometer and provides data showing the noise characteristics of each of these sensors and of the overall estimate of pendulum tilt angle produced through filtering.

Estimates of the actual robot specifications are used in modeling through the rest of this chapter. Calculating (or simply measuring) the mass of the robot pendulum-body is more straight-forward than estimating its moment of inertia. One simple way to test calculated inertia of the robot chassis (i.e. the rigid structure that forms both the body and extended pendulum arm) is to measure the frequency of oscillation of the pendulum in the downward (stable) configuration, assuming the wheels are fixed. This was done and is described in Section 7.5.2.

7.1.1 Robot Chassis and Wheels

An aluminum frame, shown in Figures 7-1 and 7-2, forms the basis of the robot chassis. The frame is essentially an open box: two $\frac{1}{4}$" thick octagonal plates form the sides and are bolted through a set of aluminum L-brackets to five extruded aluminum tubes which run parallel to the wheel axis.

This design was intended to facilitate prototyping during the planned evolution of

the robot into a fully autonomous device, with additional components being bolted along the aluminum extrusion as necessary. The aluminum tubes also provide some heat dissipation for the motor servo amps. Figure 7-1 is drawn with one extrusion pulled away from the robot, so one can see the component lay-out within the robot more clearly. The DIPR still requires the use of umbilical cords at this time, however, and in retrospect, the chassis design seems unnecessarily inelegant.

The pendulum arm is bolted between two extrusions at the top of the frame, so that the robot chassis and pendulum together form a rigid. A $\frac{1}{16}$-inch layer of rubber was added at the interface between the frame and arm to attenuate significant vibration in the pendulum observed in early versions of the robot. This seemed to reduce vibration along the pendulum, but the chassis was still prone to resonances during development and testing of the control system. I added constrained layer damping ($\sim$ 15 mil thick) at most of the aluminum-aluminum joints in the robot after the pinions on both motors came unglued at a significant resonance near 8 Hz (see Section 7.1.3 and Figure 7-5 on page 326).

Finding appropriate off-the-shelf wheels proved difficult, and I finally decided to manufacture the wheels for the robot myself. There were two key features I wanted for the wheels. First, I wanted thin wheels to keep the torque due to the radial force from the weight of the robot on the output shaft of the motor gearbox within specifications. Commercial wheels of this diameter (12") are typically 3 or 4 inches wide and would therefore necessitate a transmission with additional wheel bearings. The thin wheels allow the robot to operate with a direct drive transmission.

The second feature I wanted for the wheels was a convenient method for attaching them to the motor shaft. The wheel are cut from $\frac{1}{4}$-inch thick aluminum plate. Four bolts near the center attach each wheel connect it to a 2-inch diameter inner aluminum hub. The hub has a keyway which mates with the output shaft of the motor gearbox and is held in place with a set screw. Four additional holes further out on the wheel surface are simply a by-product of manufacturing the wheels (allowing it to be bolted down during machining).

Inertia and traction of the wheels were additional concerns. O-rings are epoxied

at the circumference of each wheel and provide adequate traction. The inertia of the wheels affects the dynamics of the system. Balancing the pendulum become a less interesting problem if the inertia of the wheel gets too large. In an extreme case where the wheels are virtually immovable objects, one is essentially just commanding the motors to remain at a fixed position, and the robot loses (virtually) all of its mobility.

7.1.2 dSPACE/Simulink Control Environment

The controller for the robot is implemented on a dSPACE 1103 board, using an execution step size of 100 ms. The dSPACE environment provides several features which facilitate the development of control systems. Algorithms can be created intuitively using the graphical "block diagram style" Simulink/MATLAB environment. Additional Simulink blocks specific to the dSPACE board enable communication with a set of A/D, DAC and encoder channels. Appendix H shows the Simulink model (with subsystems) used to control the DIPR.

Another feature is the dSPACE ContolDesk environment, which allows users to view data and change variable parameters in real time as the controller runs. One can also access data streams and write to variable addresses directly through a specialized MATLAB function called "mlib()". The experimental transfer functions shown in Sections 7.6 and 7.8 were obtained using a Simulink-driven dynamic signal analyzer based on this mlib() function. The analyzer uses mlib() both to command the frequency and amplitude of a sinusoidal signal generator within the Simulink model and to collect relevant system response(s)[113, 114].

7.1.3 Motors and Power Amps

The DIPR has two 18-volt DC Maxon RE 36 motors, each equipped with a planetary gearhead with a ratio of 13:3 and a 500-count quadrature digital encoder. Figure 7-4 show the motor (left) with the gearhead (right) detached. Appendix F on page 425 provides data sheets for the motor, gearhead and encoder. The motor has a stall torque of .73 Nm (at 27.8 Amps), corresponding to about 2.8 Nm after gear reduction

(assuming 90% efficiency), and its continuous torque rating is 0.082 Nm (at 3.1 Amps; 0.31 Nm at gearhead output).
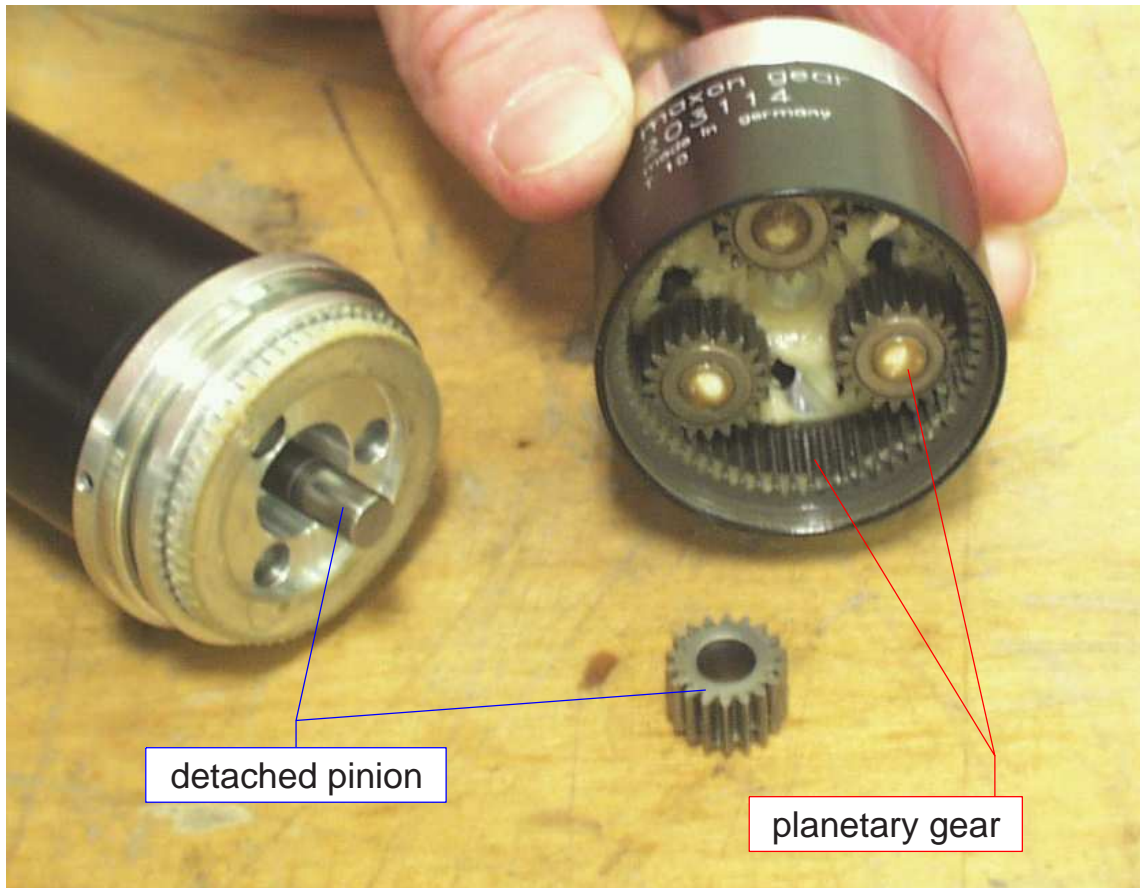
Figure 7-4: Maxon motor and gearhead, with detached pinion. This figure shows one of the Maxon motors used in the DIPR (at left) with the gearhead (at right) removed. The pinion (shown at center) became unglued from the smooth output shaft of the motor during vibration.

Each motor is powered through a model 413 DC Brush Servo Amplifier manufactured by Copley Controls Corporation, which requires a 24-90 VDC single-ended (unregulated) power supply and can supply a peak output of 30 Amps (15 Amps, continuously). I used Lambda LK 343A power supplies capable of outputting 36 Volts and up to 9 Amps of current. Each servo amp was supplied the full 36 Volts but power output was limited to about 2 Amps output during most testing of the robot. This corresponds to a maximum current of about 3.8 Amps to the 18-volt motor

(i.e. approximately 95% efficiency in the servo amp).

The Copley servo amps can be run in either "torque mode" (current control) or in voltage mode. Both current control and voltage control were tested for the DIPR. The dynamics of the system did not differ significantly in each case. Sections 7.5.4 and 7.8.3 discuss the choice between current versus voltage control in more detail.

The pinions at the output shafts of both motor came unglued during documentation of a significant resonance during the development of the controller for the robot. Figure 7-5 shows some of the data recorded during this particular resonance. The data were recorded at the input to a saturation block which limited the actual commanded current level to +/-3 Amps.
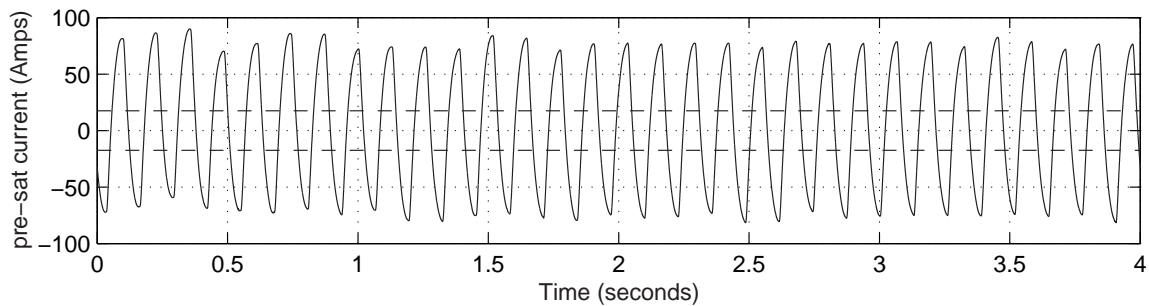
Figure 7-5: Significant mechanical resonance at 7.73 Hz. This plot shows the commanded current to the motors before passing through a saturation limit of +/-17.5 Amps (levels shown as dashed lines above) at the outputs of the Motor Control subsystem. I took this data while tweaking a marginally-stable controller for the robot. The glue joint between the pinions to the motor shaft sheared apart on both motors during this resonance. Thanks to Marty Byl for helping to get the motor-pinion interface reglued and (temporarily) operational once again.

The pinion was successfully reattached, and the system was tested for several weeks until one of the new glue joints finally failed. The new glue joint between the motor shaft and pinion was assumed to be much weaker than the original one. To try to avoid breaking the new glue joints, the current was additionally limited within the Simulink/dSPACE control model. A current limiting cut-off switch labelled

"cont_curr_check" can be seen near the center of the Motor Controller subsystem of the model, shown on page 439 of Appendix H. Figure 7-6 shows the response of the conservative current-limited method implemented for the system after the motors were repaired. Essentially, the commanded current is passed through a first-order filter to create a threshold signal, and when this threshold exceeds a value of one, the actual output to the servo amp is shut off.
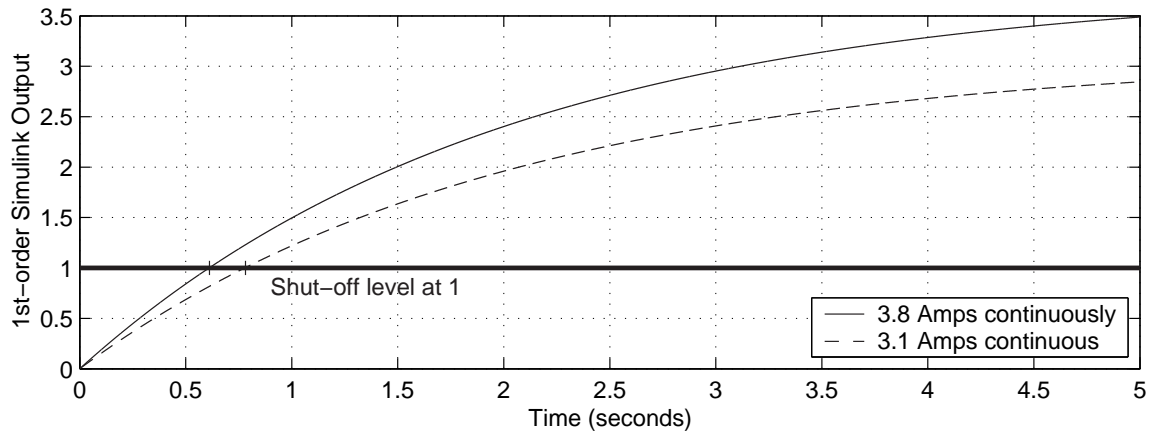
Figure 7-6: Response of current cut-off filter in Simulink model. The control system for the DIPR contains a switch to shut off any output to the motors any time a threshold input to the switch is equal to or greater than 1. The requested current output to the motors is passed through a first-order filter with a time constant of two seconds to provide an unsophisticated method of ensuring the commanded output does not exceed 1 Amp for too long. The continuous current rating is 3.1 Amps, but vibrations at current levels at or below this level cause the output pinion of both motors to detach from the motor shaft. The plot above shows the shut-off characteristics used after this failure (with the pinion temporarily reglued in place). The solid line shows the output of the filter to a step in requested current of 3.8 Amps (the maximum current the Copley servo amp can provide given a current limit of 2 Amps from the Lambda supplies), which results in shut-down after about 0.6 seconds. A step in requested current of 3.1 Amps (which should be safe continuously) results in shut-down after 0.8 seconds.

Because the motors are aligned such that they point in opposite directions (see Figures 7-1 and 7-2 on pages 318 and 319), moving the robot forward in a straight line requires that the output shafts of the two motors rotate at rates which are equal but opposite. The requested current (or voltage) command is scaled appropriately just before the signals are sent to the DACs to account for this. In Figure H-1 on page 435 of Appendix H, the scaling blocks labelled "dac_left" and "dac_right" are equal and opposite in value, as necessary. Each output is also reduced by a factor of 10 at this point, because a (maximum possible) output of 1 actually corresponds to a level of 10 volts at the dSPACE DAC outputs.

7.1.4 Effects of Encoder Quantization and Backlash

The robot is not equipped with motor tachometers or other sensors to measure the velocity of the motor directly. Instead, the motor velocity must be estimated using the output of the digital encoder. Two obvious approaches for doing this are as follows.

One method involves monitoring the cumulative encoder counts at evenly spaced time intervals. In this method, the velocity is recalculated at each time interval to equal the change in the value of the count divided by the (constant) length of the time interval used.

The dSPACE encoder block automatically outputs both the cumulative encoder count and the "delta" in the count since the last iteration of the dSPACE control algorithm, which facilitates this first method of estimating the velocity. The bottom half of Figure 7-7 shows a typical signal from this delta output channel as the pendulum-body of the robot rotates with respect to the wheels. Since the time increment remains constant, this delta output is a scaled estimate of the instantaneous velocity. The spikiness of this plot is to be expected, for reasons outlined below, and the estimate of angular velocity would need to be filtered (smoothed) significantly to obtain a usable measure of velocity.
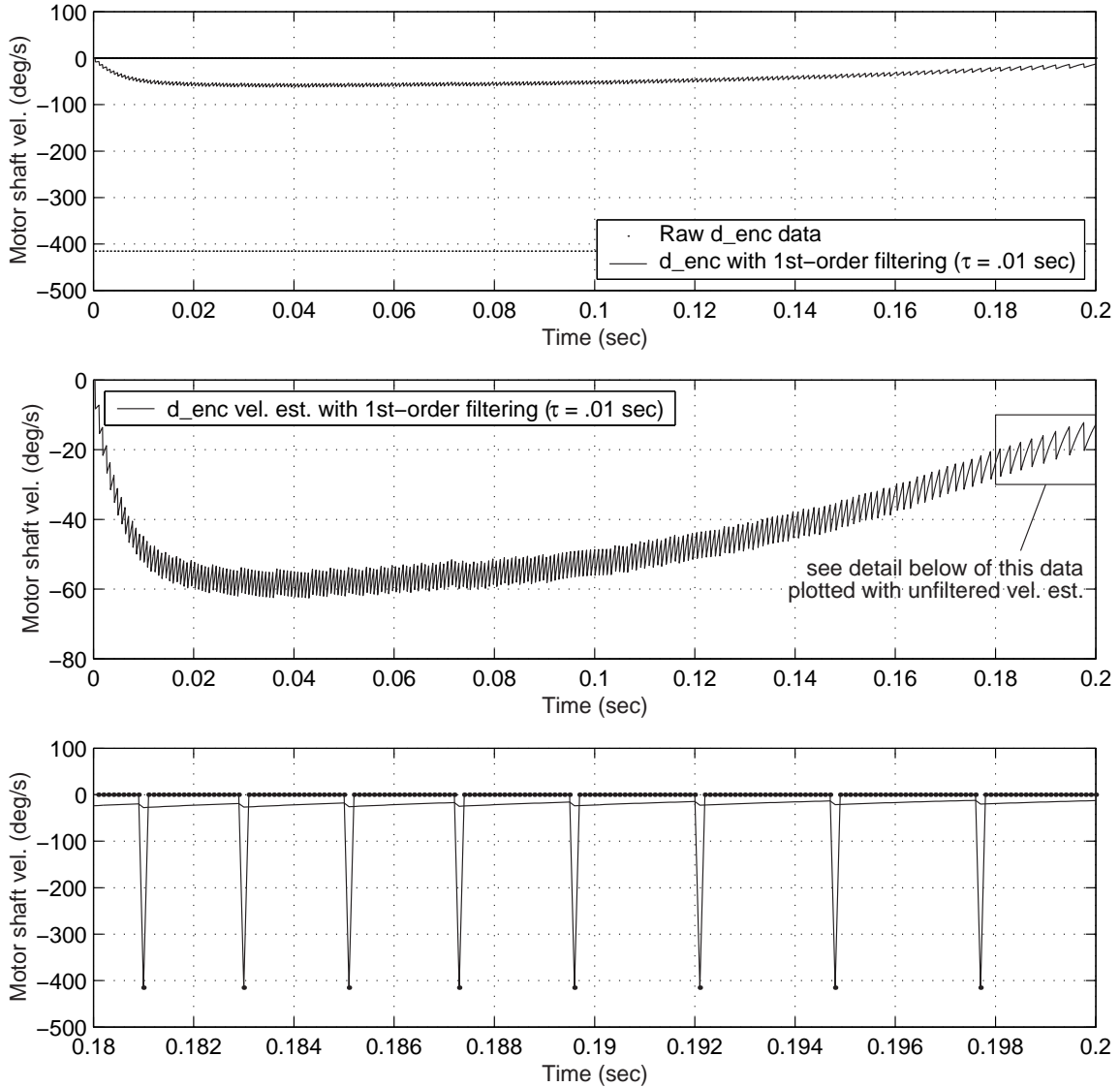
Figure 7-7: Using scaled and filtered delta encoder data for motor velocity. All three plots use the same data set, based on raw delta encoder measurements of the robot as the pendulum-body was moved by hand. The filtered velocity estimate was created in MATLAB after data collection, which explains why the velocity estimates starts (arbitrarily) at zero at $t = 0$. The plots at the top and bottom show both the instantaneous velocity estimate and the filtered estimate at each time step ($\Delta t = 0.1$ ms). For velocities below 415.4 deg/s, the quantization of the encoder allows for only 3 possible values for the instantaneous velocity estimate: 0, -415.4, or +415.4 deg/s. The filtered data is plotted alone in the center plot, to show the choppiness of this signal more clearly.

The smallest increment of the quadrature encoder which can be detected is $\frac{1}{4}$ of a full count, the encoder has 500 quadrature counts per revolution, and the wheel (which is attached to output shaft of the gearbox) completes $\frac{3}{13}$ of a rotation for each full rotation of the encoder (which is attached directly to the motor). The resolution of the encoder is therefore:

$$\Delta\theta_{min} = \frac{3}{13}\frac{360°}{4 \times 500} = 0.0415° \tag{7.1}$$

The step size for dSPACE model is 0.1 ms. The smallest non-zero instantaneous velocity estimate which is possible using this method occurs if the encoder value changes by a quarter count (the smallest change which can be resolved). The minimum non-zero instantaneous motor shaft velocity will therefore be:

$$\dot{\theta}_{min} = \frac{415°}{0.0001s} = 415 \text{ deg/s} \tag{7.2}$$

If the angular velocity is no greater than 415 deg/s, then the "delta" output of the encoder block will output either zero or 0.25. In normal operation, the motor velocity should be below 100 deg/s. Figures 7-43 and 7-44 on pages 388 and 389 show the measured transient responses in motor velocity in response to an impulse disturbance, for example, which peak near 25 and 50 deg/sec, respectively.

The inherent spikiness seen in plot at the bottom of Figure 7-7 is due, in other words, to the quantization of the encoder. Figure 7-8 shows a simulated velocity estimate for the DIPR in response to a step in angular velocity (i.e. a ramp in position). The plot is intended to give the reader a feel for the typical frequency and magnitude of the spikes observed when the signal is filtered at a "reasonable" bandwidth for the DIPR of 32 Hz. (The bandwidth of the gyro is 75 Hz.) The velocity chosen (20.8 deg/s) is a typical value for robot during transient response to a disturbance.

The velocity estimates shown in both Figures 7-7 and 7-8 are "spiky" because the discrete time increments actually provide a more sensitive scale than the angular distance increments at velocities typical for the DIPR. Even at the highest angular

speeds expected during operation of the robot, one will typically see multiple time intervals pass by with no change in the encoder output, interspersed with single-step readings of ± 415 deg/s, as required by Equation 7.2.

Obtaining a "reasonably smooth" signal using this first method of estimating the motor velocity would require significant filtering and would thereby greatly reduce the bandwidth of the sensor. Figure 7-9 illustrates the relationship between the sensor bandwidth and the choppiness of the velocity estimate. The plot at the top of this figure shows a simulated encoder measurement of a sinusoidal angular displacement between the pendulum-body and wheel of the robot. The lower plot shows filtered velocity estimates for three different values of τ. Clearly, there is a trade-off between the smoothness of the signal and the bandwidth of the resulting measurement. We can obtain a smoother signal at a given desired bandwidth by implementing a second, time-based estimate of the velocity instead.
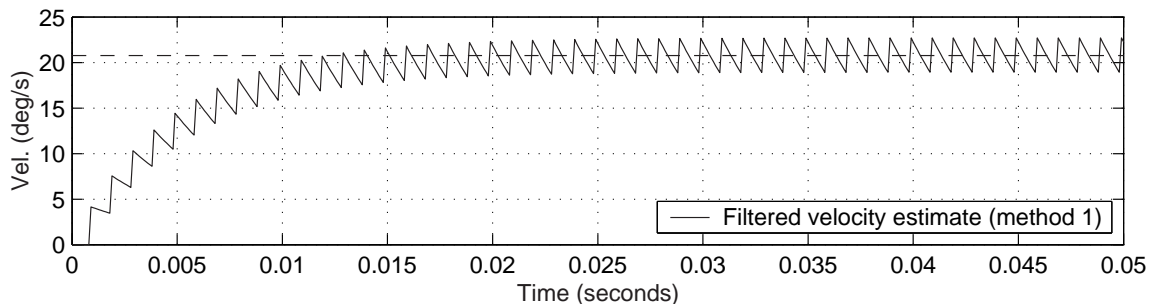
Figure 7-8: Filtered velocity estimate based on the delta encoder output. The spiky nature of the delta encoder output is still evident after passing the signal with a first-order low-pass filter with a time constant of 0.005 seconds (32 Hz). The output above was simulated in MATLAB for a step input in actual velocity of 20.8 deg/sec. At this velocity, the quadrature encoder increments by a quarter of a count (0.25) every millisecond, which explains why the frequency of the spikes is 1000 Hz ($1/.001s$).

331
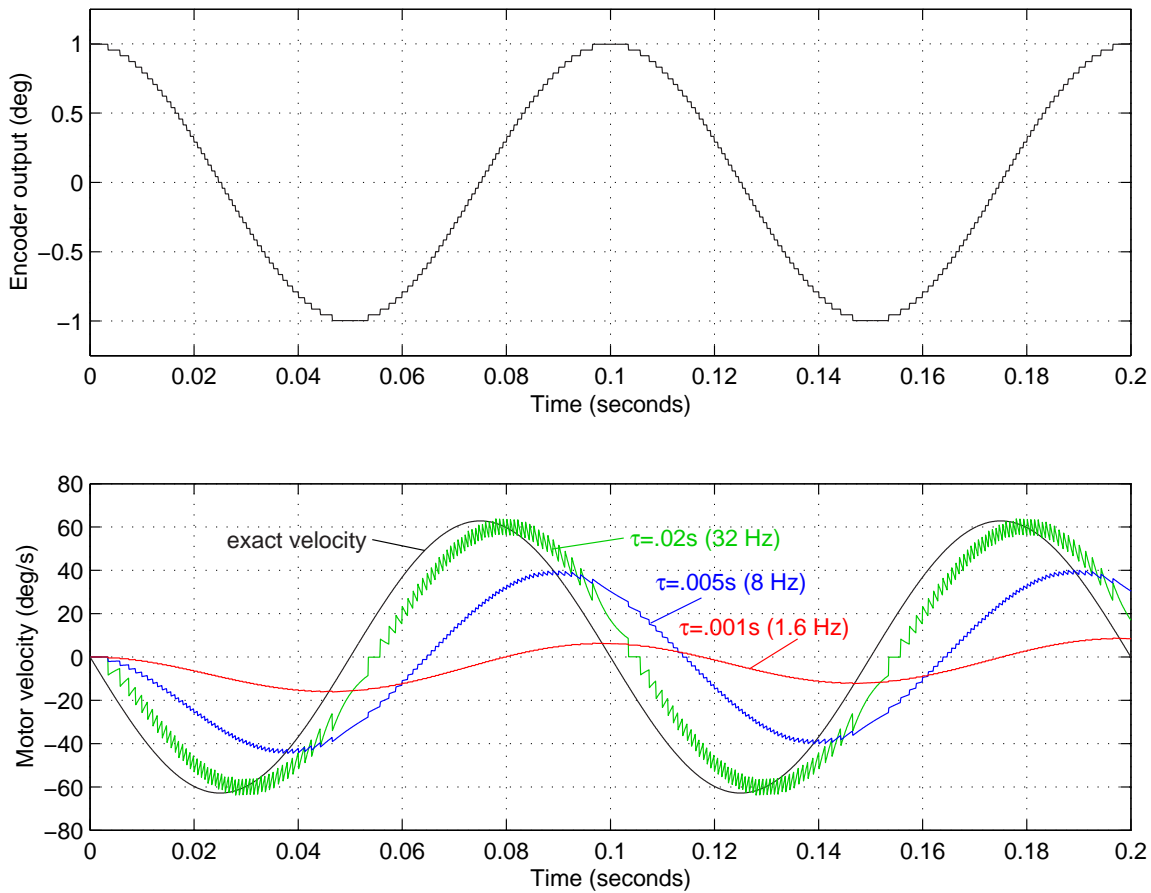
Figure 7-9: Theoretical filtering of the delta encoder signal. The data shown represent simulations of a "count-based" velocity estimation method in which the instantaneous velocity is recalculated at each time step as being equal to the change in measured position from the encoder reading at the last time step divided by the (constant) time step. In other words, the instantaneous velocity estimate is a scaled version of the delta encoder signal. The upper plot shows a quantized encoder measurement of a 10 Hz sinusoidal waveform. The lower plots shows low-pass filtered versions of the count-based velocity estimate for three values of τ. The exact (non-measured, non-quantized) velocity is also shown on this plot, for comparison.

The second method for estimating velocity from an encoder measurement essentially uses a filtered zero-order-hold estimate based on the time between successive encoder counts. The (pre-filtered) zero-order-hold estimate is created by updating the velocity only when the encoder registers a new value. The new velocity estimate is then equal to the change in the encoder signal divided by the time elapsed since the previous change in encoder value.

Both the first (count-based) velocity estimation method and this second (time-based) zero-order-hold estimate produce inherently quantized signals, due to the discrete nature both of the encoder measurement and of the constant time increments of the digital controller. As before, this quantization can be smoothed significantly by passing the signal through a low-pass filter.

This time-based method is more practical than the first (count-based) method when the angular velocities are slow enough that encoder typically registers the same value for multiple time steps in row during typical operation. For the combination of encoder (2000 quadrature counts per revolution), gearhead (3 encoder turns correspond to 13 rotations of the vehicles wheel) and discrete time step (0.1 ms), this threshold velocity of one quarter-count per time step works out to 415 deg/s. ($\frac{360°}{4 \times 2000} \times \frac{13}{3} \div 0.0001$ s ≈ 415 deg/s) As previously mentioned, the data shown later in this chapter (specifically, Figures 7-43 and 7-44 on pages 388 and 389) show typical velocities in response to an impulse disturbance are not likely to exceed the measurement limit of the gyro, which is 200 deg/s, much less twice this value. Therefore, the second, time-based method of calculating the velocity is more appropriate.

Figure 7-10 shows actual data obtained by moving the robot pendulum by hand with the wheels fixed. The plot at the top shows both the quantized zero-order-hold estimate and the smoother signal which results from low-pass filtering of this estimate. Below this plot is a close-up of part of the delta encoder signal used to create the time-based estimate. Figure 7-11 shows simulated data for the robot. This plot also illustrates the significant "steps" in the signal when the encoder measurement reverses direction (and the velocity therefore crosses zero) and shows the results of a "smoothing" technique described next.
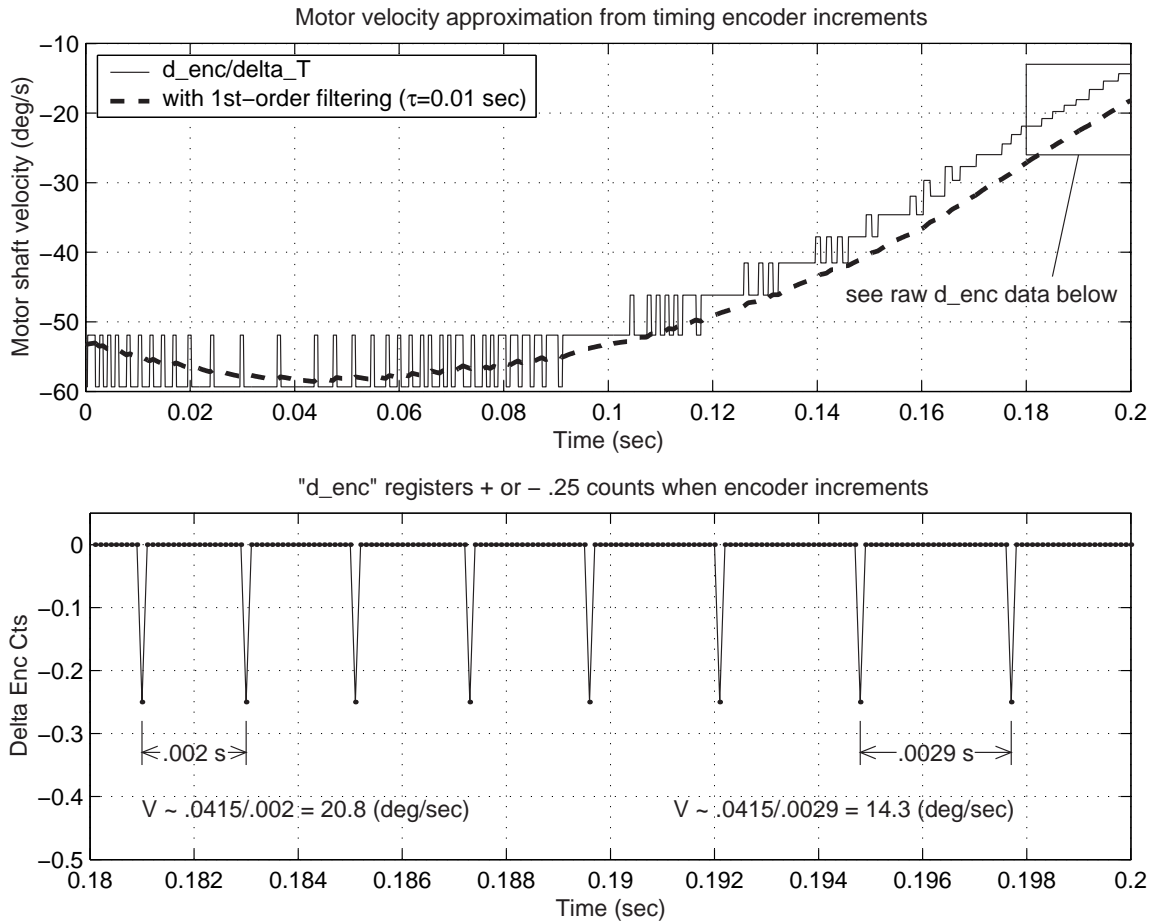
Figure 7-10: Experimental data for encoder velocity calculation and filtering. The plots above show data from the actual robot, taken with the wheels held in place and the pendulum-body wiggled by hand. Only the sensors (not the motors) were active during the trial. The plot at the top shows the zero-order-hold estimates of velocity based on the timed intervals between successive encoder counts both before and after low-pass filtering. Below this is a plot of the "delta encoder" signal which corresponds to the time interval between 0.18 and 0.2 seconds on the upper plot. The delta encoder equals the difference in encoder output between the current and previous time steps. The smallest increment in the encoder output is 0.25. The lower plot illustrates how the updated time-based velocity estimated is calculated. A change of 0.25 in the encoder reading corresponds to a change of $0.0415°$ in the relative angle between the pendulum-body and wheel.
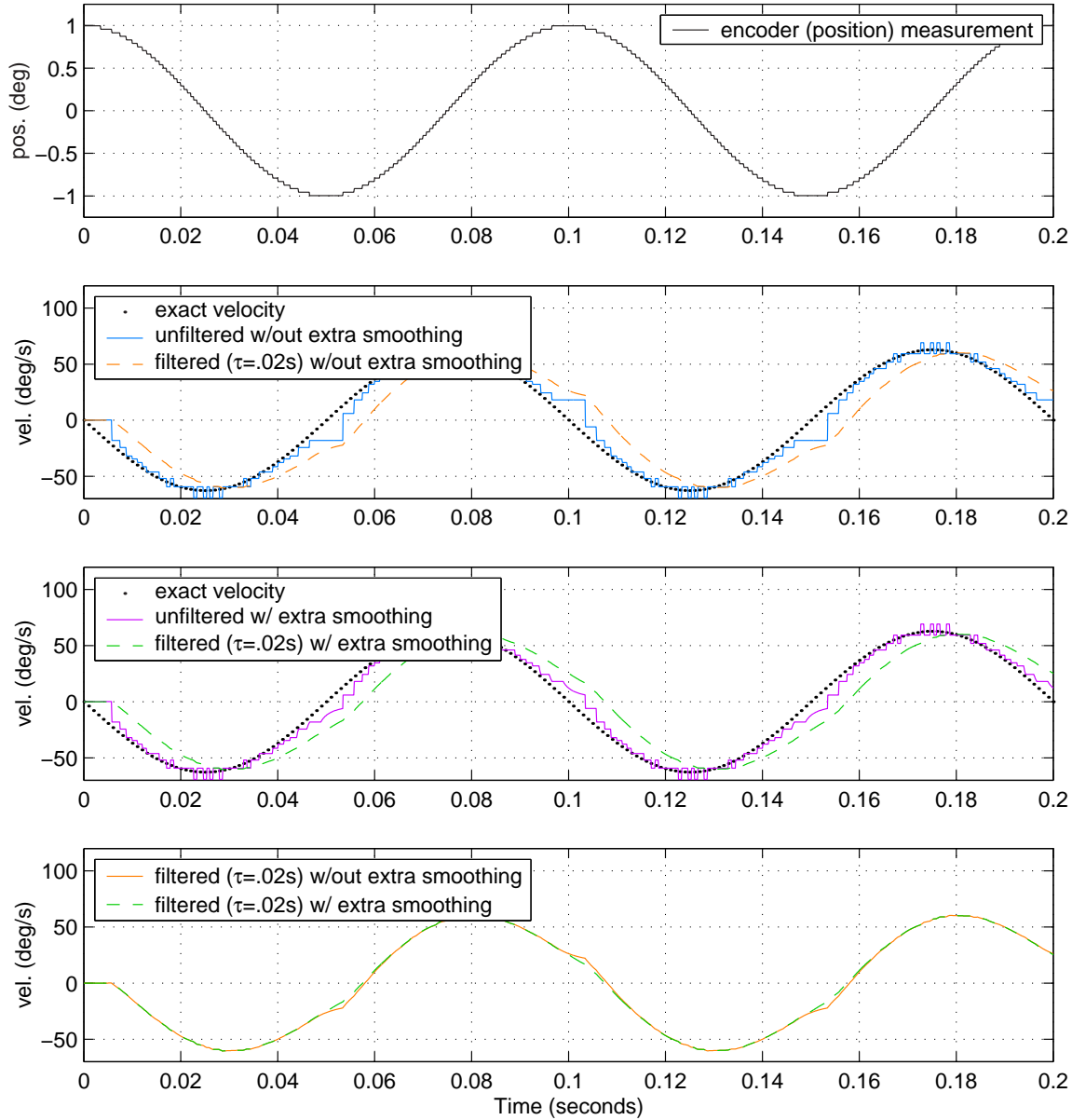
Figure 7-11: Theoretical estimation of velocity based on the time between encoder counts. The data at top show MATLAB simulations of the quantized encoder measurement of a 10 Hz sinusoidal signal. The quantization units (.0415°) correspond to those in measuring the angle between the wheel and pendulum-body in the DIPR. Below this are various estimations of velocity based on the elapsed time between successive encoder counts, which are based on the encoder signal. The exact (theoretical) velocity is also shown in the middle two plots, for comparison. More details are given in the text, particularly about the "extra smoothing" enhancement mentioned in the legends above.
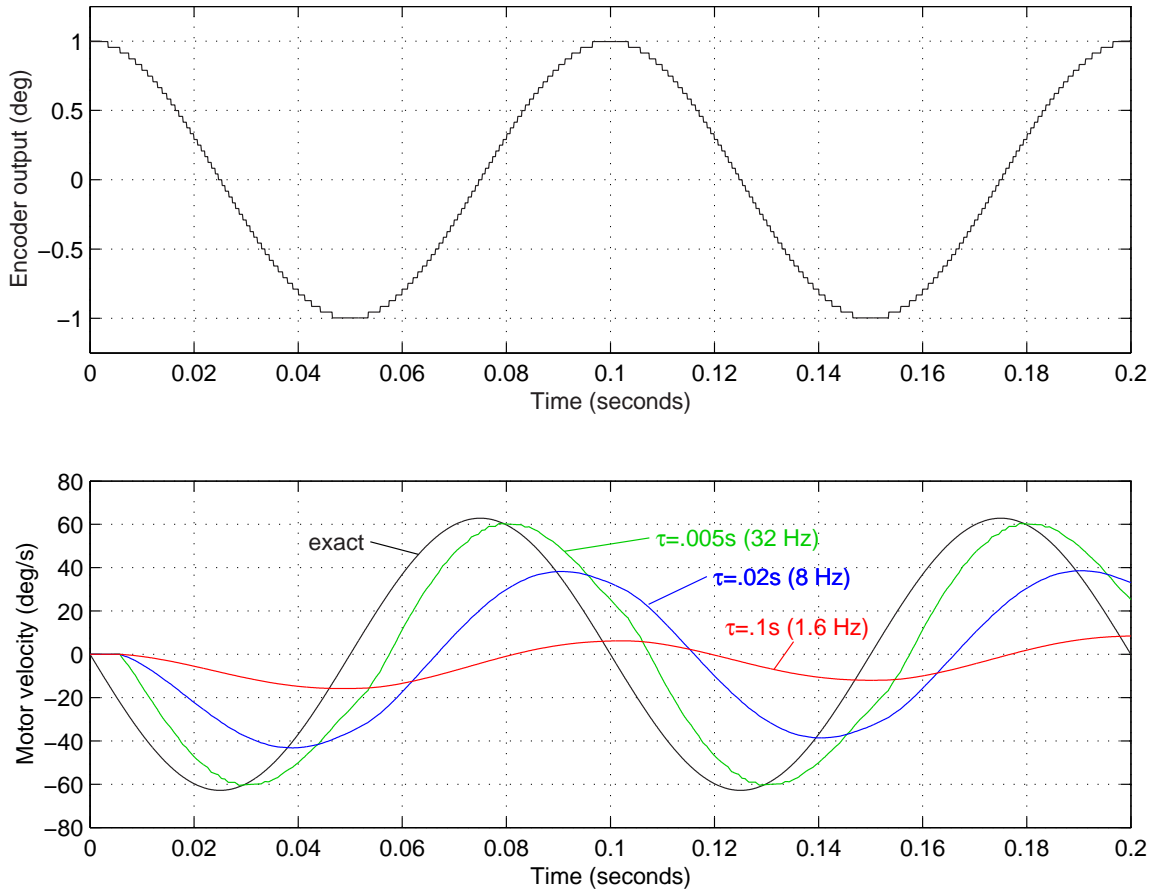
Figure 7-12: Theoretical filtering of time-based velocity estimate. This plot is intentionally formatted to facilitate direct comparison with Figure 7-9 on page 332. The data present simulations of the "time-based" velocity estimation method described in detail in the text, which uses the time interval between encoder counts to estimate the relative velocity between each wheel and the robot chassis. The particular estimation algorithm used to produce the plots above compares any current zero-order-hold estimate with an upper bound on the magnitude of the velocity. This upper bound is a velocity one would obtain by dividing the smallest encoder increment by the time which has so far elapsed since the the previous change in encoder output was measured. This is a conservative adjustment to the estimate and provides what I refer to as "extra smoothing" in the resulting velocity signal. The three estimates on the lower plot use first-order low-pass filtering (corresponding to the labelled values of τ).

The "smoothing" technique uses the following reasoning to update the zero-order-hold measurement after there have been no new encoder readings for some time. If the average velocity currently being held (z.o.h.) since the previous encoder increment estimate is correct, then we can estimate the next time at which the encoder value should change. Therefore, if the waiting period has exceeded this time limit, we know the magnitude of our z.o.h. velocity estimate must be too high. A conservative adjustment is to use the smallest detectable angle divided by the time elapsed so far to create an upper bound on the magnitude of the velocity.
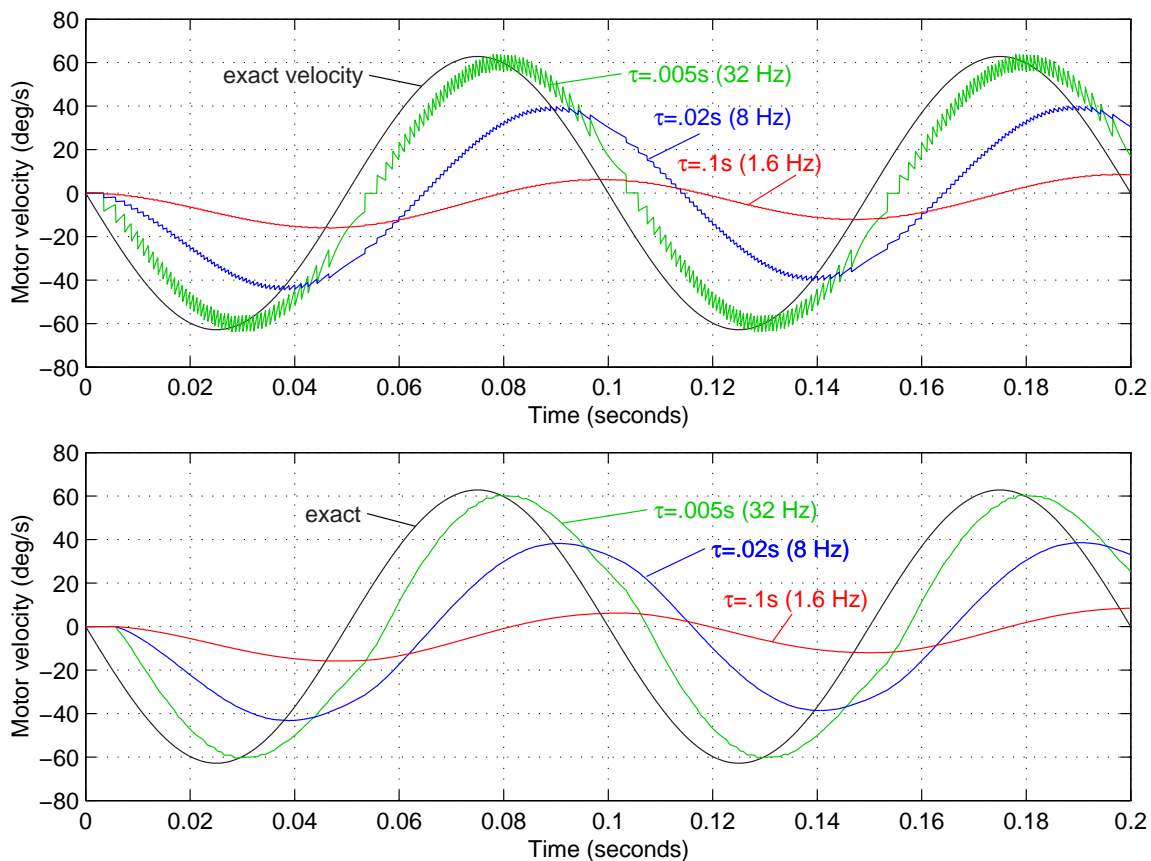
Figure 7-13: Comparison of count- and time-based velocity estimates after filtering

Figure 7-12 shows data from MATLAB simulations which use this smoothing technique along with various first-order low-pass filters. Figure 7-13 simply displays the plots from the bottom halves of Figures 7-9 and 7-13 on top of one another to make it easier to compare the two signals qualitatively. The DIPR uses the time-based

velocity estimate with the extra smoothing technique, with a first-order low-pass filter with a time constant of 0.005 s (32 Hz).

Backlash presents a second difficulty in measuring the relative motion between the pendulum-body and the wheels. Each encoder is mounted directly to the output shaft at the back end of a motor. Each wheel, however, is attached to the output shaft of the gearbox and the front end of a motor. Because the gears will have some play, the encoder measurement will not accurately reflect the relative position between the pendulum-body and the wheel during a brief transition period as the motor reverses direction.

The inverted pendulum robot called "Joe", which is described in Section 2.1.3 on page 74, reportedly suffered from significant vibrations due to the backlash in the transmission to the wheels [75, 74]. I also saw significant vibrations in my own inverted pendulum robot when I initially attempted to control the system by using a state space (LQR) controller, although I cannot explain the cause of the vibration exactly. Joe successfully uses a state-space controller by passing the velocity measurement through a first-order filter with a breakpoint of 10 rad/s (1.6 Hz). (Recall that the breakpoint of the filter used for the velocity estimate from the encoder signals on the DIPR has a breakpoint of 200 rad/s.)

I expected backlash might also be a significant problem for the DIPR. Therefore, when I noticed a repeatable, jagged characteristic during zero crossings in the velocity estimate, I initially attributed this to the effects of backlash. Figure 7-14 shows experimental data documenting these jagged transitions as the relative velocity between the pendulum and the wheels reverses direction.

The step-like nature of the zero-crossings in the separate sets of data shown in the two subplots in this figure is characteristic of backlash, but the reader may recall that they are also similar to zero-crossing observed in the time-based velocity estimate just discussed - particularly with no additional "smoothing" at low velocities. In Figure 7-11 on page 335, the "unfiltered" signal in the second plot from the top demonstrates zero-crossings which are qualitatively similar to those in quantized velocity measurements in Figure 7-14.

The effect of backlash in the system is to lengthen the time during which the encoder registers no new value when direction is reversed. Correspondingly, the predicted velocity measure when backlash is present should include exaggerated versions of the jagged zero-crossings seen in the second plot of Figure 7-11. Looking at Figure 7-14 alone, it would not be obvious how to answer the following question: Can the step-wise transitions seen in the data be explained entirely by the quantization of the encoder, or do they indicate significant backlash?

The simulation results shown in Figure 7-15 are presented next to the experimental data in Figure 7-14 specifically to address this question. The top-most plot in Figure 7-15 compares the encoder signal from a system which includes backlash to the actual angle between the motor and the transmission output. Backlash produces a lag in the measurement. The second plot in Figure 7-15 shows the time-based z.o.h. estimate of velocity based on the encoder measurement shown in the top plot. We see a step in this signal when the direction reverses. The lower two plots are similar to the upper two, except that the simulation producing these data included no backlash.

The magnitude of the backlash used in producing the data for the upper two plots is based on the specifications given for the single-stage Maxon planetary gearhead used with the motors for the DIPR. The no-load backlash is given as approximately 0.3°, which is somewhat over seven times the resolution the encoders provide at the output of the transmission. We would effectively "miss" the first seven encoder counts after the transmission reverses, and this explains why the length of the delay (i.e. the plateau in the plot) is so much longer when backlash is assumed.

The frequency and magnitude of the oscillations simulated in Figure 7-15 were selected and the x- and y-axes scaled to aid in comparing the lowermost plot in Figure 7-15 with the upper plot in Figure 7-14. By my judgement (and initial surprise) the delay seen can be convincingly explained entirely by the quantization of the encoder (i.e. with no backlash). Upon reflection, I think this result does makes sense, however. The armature of the motor has inertia and "keeps going" when the angular acceleration of the pendulum (which was driven by hand in these trials) changes sign, eliminating backlash well before the velocity reaches zero.
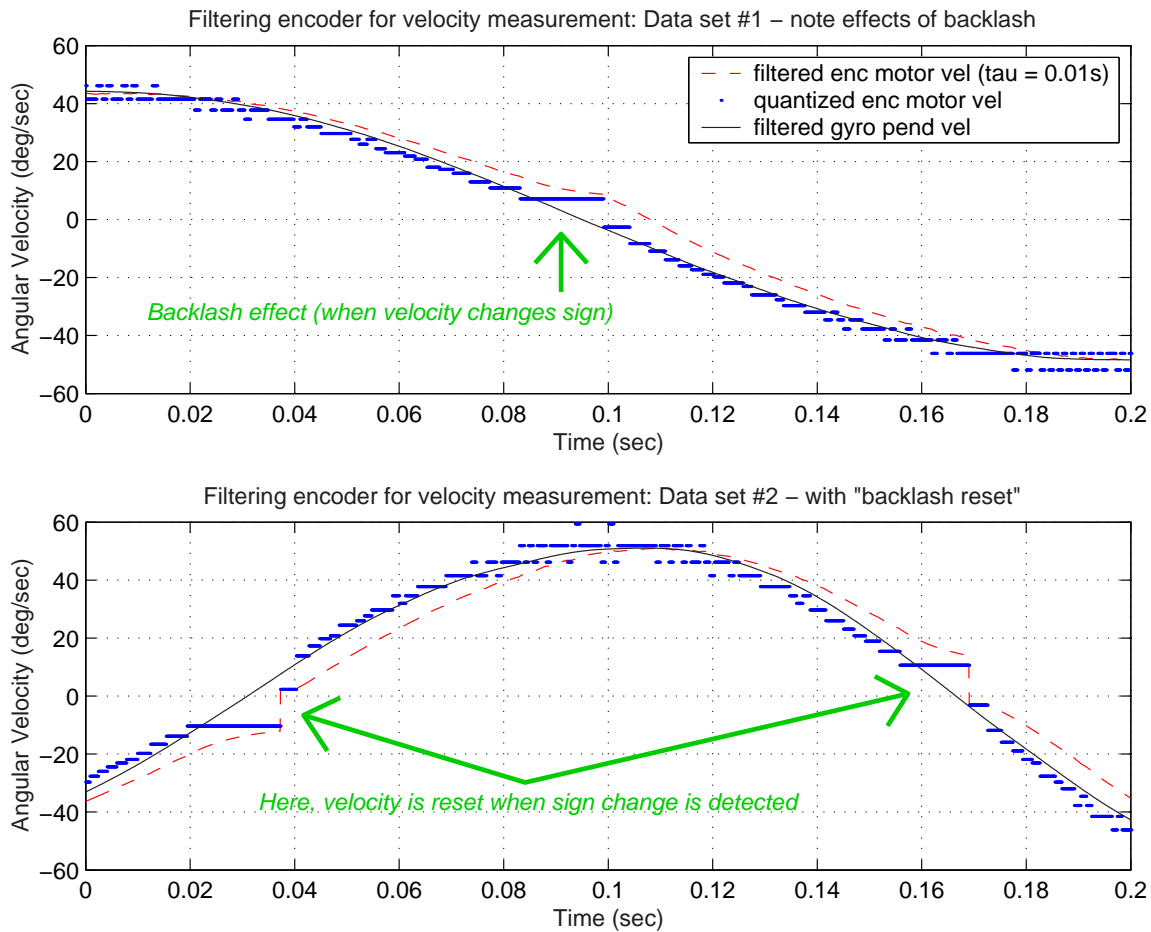
Figure 7-14: Experimental data to test backlash and quantization effects. The plots above show actual data obtained by wiggling the pendulum-body of the DIPR rapidly by hand with the wheels held in place. With the wheels stationary, the encoder measures an absolute angle, which allows one to compare the estimations of velocity from the encoder and from the gyro. Initially, I assumed the jagged delays indicated with the three arrows above were primarily due to the effects of backlash. The no load backlash for the single-stage planetary gearbox at the output of the Maxon motor is specified as approximately $0.3°$. This should be quite noticeable if there were play before the gears when the pendulum reversed direction, as Figure 7-15 indicates. The fact that backlash does not seem to be a factor in the data above is most likely an artifact of the limitations of the test environment and does not mean that backlash is insignificant in normal operation of the robot. (See text for more details.)
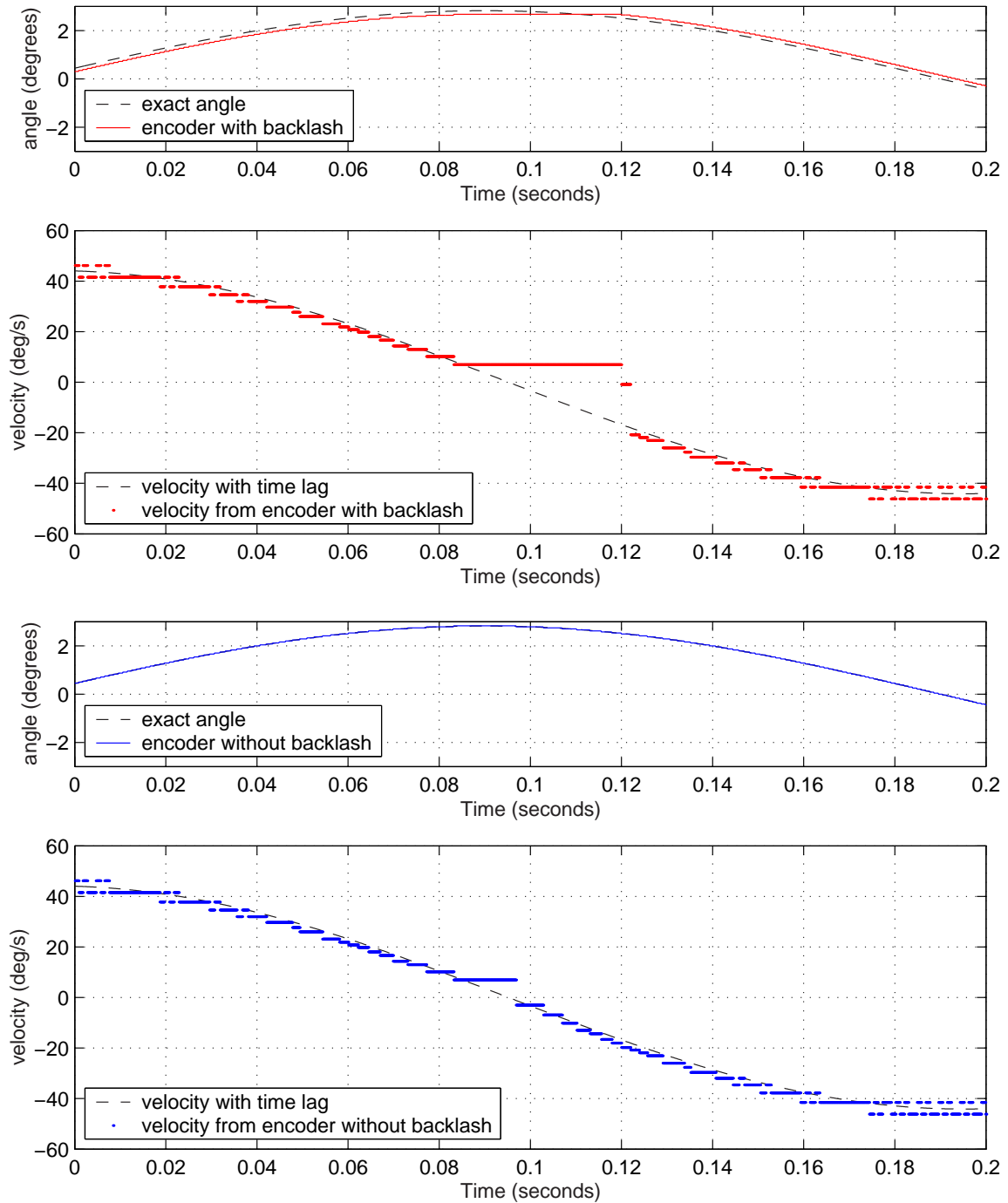
Figure 7-15: Time-based velocity estimates with and without backlash. The plots above are theoretical MATLAB simulations. The bottommost plot above (simulating a system with no backlash) appears more similar to actual data in the upper plot in Figure 7-14 than the plot with backlash (second from top above). (See text for more detail.)

7.1.5 Single-Axis Gyroscope

This section explains why a rate gyro is used in the DIPR and provides a general description of the single-axis gyro used and its specifications. Section 7.1.6 describes a 2-axis accelerometer which is used to compensate for drift in the gyro. Section 6.2 of the previous chapter provides more details on how drift compensation is achieved through complementary filtering.

The controller for the inverted pendulum requires estimates of the absolute angle and angular velocity of the pendulum with respect to gravity. The cart-driven IP system in Chapter 5 used an encoder to detect pendulum angle and differentiated this measurement to estimate velocity, but the same solution is not possible for a robotic IP.
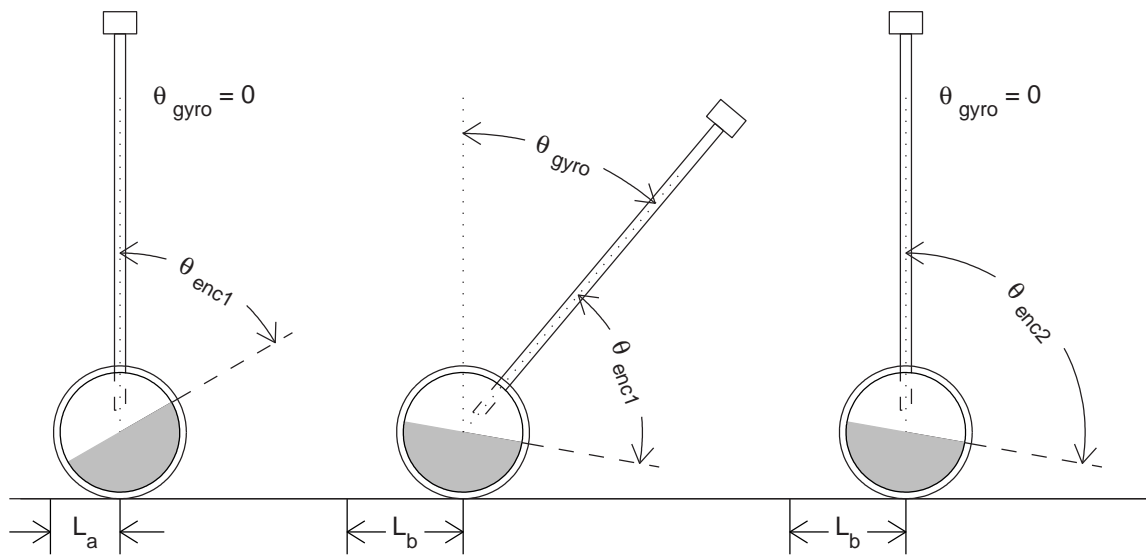
Figure 7-16: Angular measurements of motor rotation and pendulum angle. The diagrams above simplify the dynamics of the robot somewhat by assuming that both wheels of the robot always rotate in unison.

Figure 7-16 illustrates why an encoder measurement of the rotation of the motor is not sufficient for determining the absolute angle of the pendulum. This figure shows schematics of the inverted pendulum robot in three different states. Each schematic in the figure shows two angular measurements: θ_{gyro} is the absolute angle of the

pendulum with respect to vertical, and θ_{enc} is the relative angle between pendulum-body of the robot and the wheels. Also shown is the distance, L, that the robot has travelled with respect to its position when $\theta_{gyro} = 0$ and $\theta_{enc} = 0$. The three measurements form a linearly dependent set:

$$L = R_w \left(\theta_{enc} + \theta_{gyro} \right) \tag{7.3}$$

where R_w is the radius of the wheel.

Because of the dependence shown in Equation 7.3, it is necessary and sufficient to measure any two of these quantities to estimate all three. The three orientations in Figure 7-16 were chosen to emphasize that measuring one of these variables alone is not sufficient. If you select any two, you will find that exactly one of these three variables (θ_{gyro}, θ_{enc} or L) is the same in each of the two diagrams.

In the cart-driven system from Chapter 5, an encoder is mounted at the pivot of the pendulum. This encoder therefore measures the relative angle between the pendulum and the cart, just as the motor encoder on the robot measures the angle between the chassis and wheels. The encoder for the cart-driven pendulum measurement also represents the absolute angle of the pendulum, however, because the cart is constrained so that does not rotate as it travels. This constraint is effectively equivalent to setting $L = 0$ in Equation 7.3.

Since an encoder position alone does not tell us the pendulum angle, we need to include another type of angle sensor to control the robot. Most of the inverted pendulum vehicles I know of use a rate gyroscope to measure the angular velocity of the pendulum and then estimate the angular position from this velocity measurement, although the Legway, described on page 80, is a notable exception.[3] As mentioned, the details on obtaining a good estimate of angular position from the gyro are presented in Section 6.2 of the preceding chapter. The remainder of this section describes the gyro used in the DIPR.

The DIPR uses a VSG-E601[4] rate gyro manufactured British Aerospace Systems and Equipment (BASE). The device operates by driving a shell piezoelectric (specifi-

---

[3]See Section 2.1 of the survey chapter for more details on other IP vehicles.

[4]VSG stands for "vibrating structure gyro".

cally PZT) cylinder to excite the structure at its primary resonance. In fact, because of the symmetry of a ring structure, the shell actual has two degenerate primary resonances, which are depicted (at an exaggerated scale) in Figure 7-17. One can produce a version of this mode shape which is aligned along any arbitrary axis through the center of the shell through the appropriate linear combination of mode 1 and mode 2. This mode shape is often referred to as the "wineglass" mode of a cylindrical structure, because it is the resonance most people have observed at one time or another by encircling the rim of a wineglass with a wet finger tip to produce a clear (nearly pure) tone.
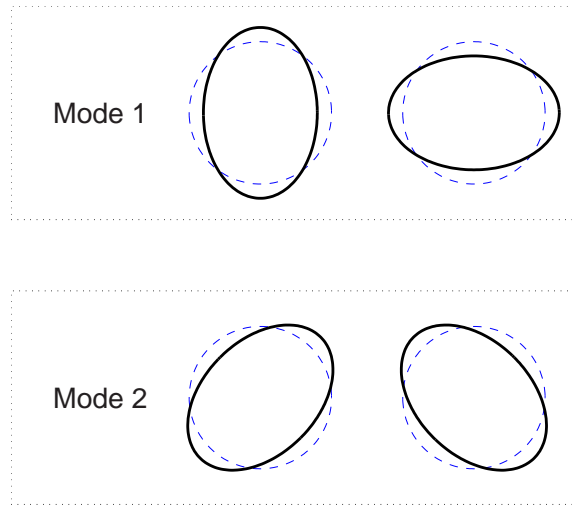
Figure 7-17: Primary (wine glass) modes for gyro resonator.

The outer surface of the resonant shell in the sensor has four drive electrodes and four sensing electrodes, aligned symmetrically as shown in Figure 7-18. The inner surface of the shell forms a continuous ground electrode. Drive electronics in the sensor excite a wineglass resonance in the structure (at around 7.5-8 kHz). When the structure is rotated about the axis of the cylinder, the momentum of the oscillations prevents them from continuing to remain exactly aligned along the same relative axis on the rotating shell. In other words, the degenerate mode becomes excited. Figure 7-19 depicts the effective "lag" in the rotation of the axis of the mode shape (with respect to the reference frame of the shell) which occurs as the cylinder rotates.
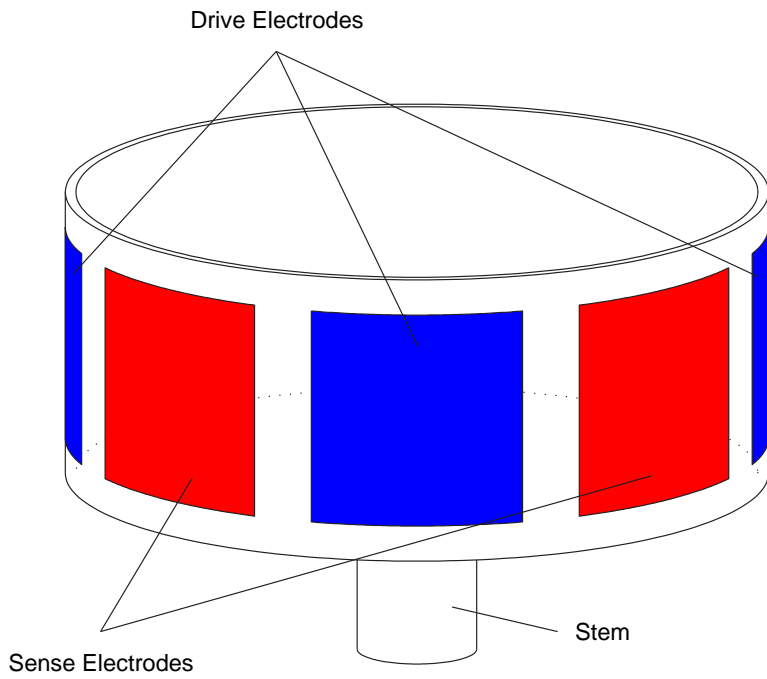
Figure 7-18: Gyroscope electrode placement.
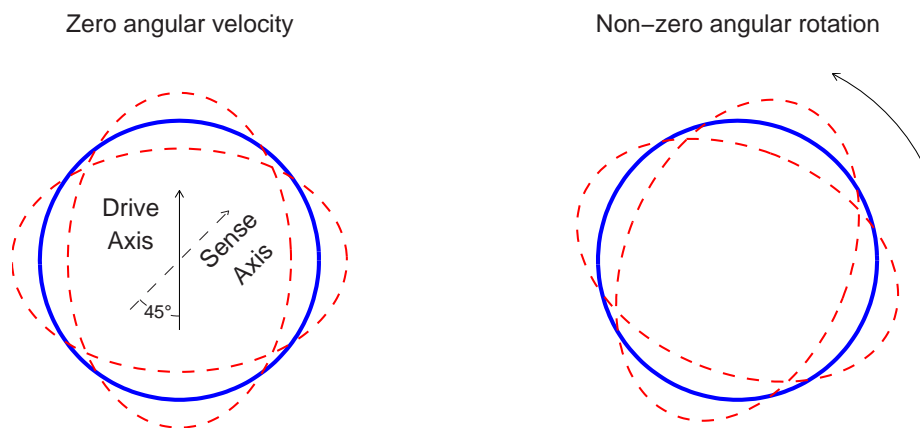
Figure 7-19: Effect of rotation on mode shape.

The sensing electrodes are aligned specifically to detect any excitation of the mode which is degenerate to the drive mode. The sensing electronics include a charge amp and demodulating circuit to measure the amplitude of the oscillating current through the electrodes. This signal is then filtered (low-pass) to provide an output proportional to the angular velocity. The actual shape of the drive and sensing electrodes is more complex than shown in Figure 7-18 and has been optimized based on finite element analysis of the stress distribution in the shell during resonance. [208].

The bandwidth of the VSG-E601 is specified as 75 Hz. The gyro can measure velocities up to ±200 deg/s [40]. The sensor can run on a power input of between 8.5 and 18 volts and provides an output with nominal gain of 40 deg/s/V, regardless of the voltage of the power supplied. In contrast, the less-expensive CRS03 MEMS gyro (described in Section 6.1.7 on page 291) used in the iBOT and Segway provides a ratiometric output (i.e. proportional to the input power) [85].

The specific gyro we purchased was tested by the distributor (Watson Industries), and the actual scale factor they document is approximately 40.04 deg/s/V. We verified the scaling factor as well by mounting the gyro on the pendulum of the cart-driven IP system described in Chapter 5 and comparing the position measurement of the pendulum encoder with the integrated pendulum angle (with the DC bias subtracted out).

When the gyro is initially powered up (from thermal equilibrium with the environment at room temperature), the output (DC bias) exhibits a first-order response. The time constant for the response is about two minutes, as shown in Figure 7-20. The DC bias of the gyro is significantly influenced by temperature, and this transient presumably corresponds to the resistive heating of the device. In fact, the gyro we used provides a temperature measurement as an additional output, although it was not necessary to use this output to obtain sufficient accuracy for the control of the DIPR in our lab (which provides a reasonably stable temperature-controlled environment).

The start-up time for the device is specified as 0.3 seconds, which corresponds to a sharp transient response seen when the gyro is initially powered up. In Figure 7-20,

this initial transient is cut off on the scaling of the plot. To minimize the effects of the DC bias, however, it make more sense to wait several minutes for the output to stabilize before zeroing out the bias (as described in Section 6.2.5 on page 312) and subsequently turning on the controller for the robot.

More details on the noise characteristics of the gyro are provided in Section 6.2.2 on page 299, as they are relevant to the design of the complementary filters for the gyro and accelerometer.
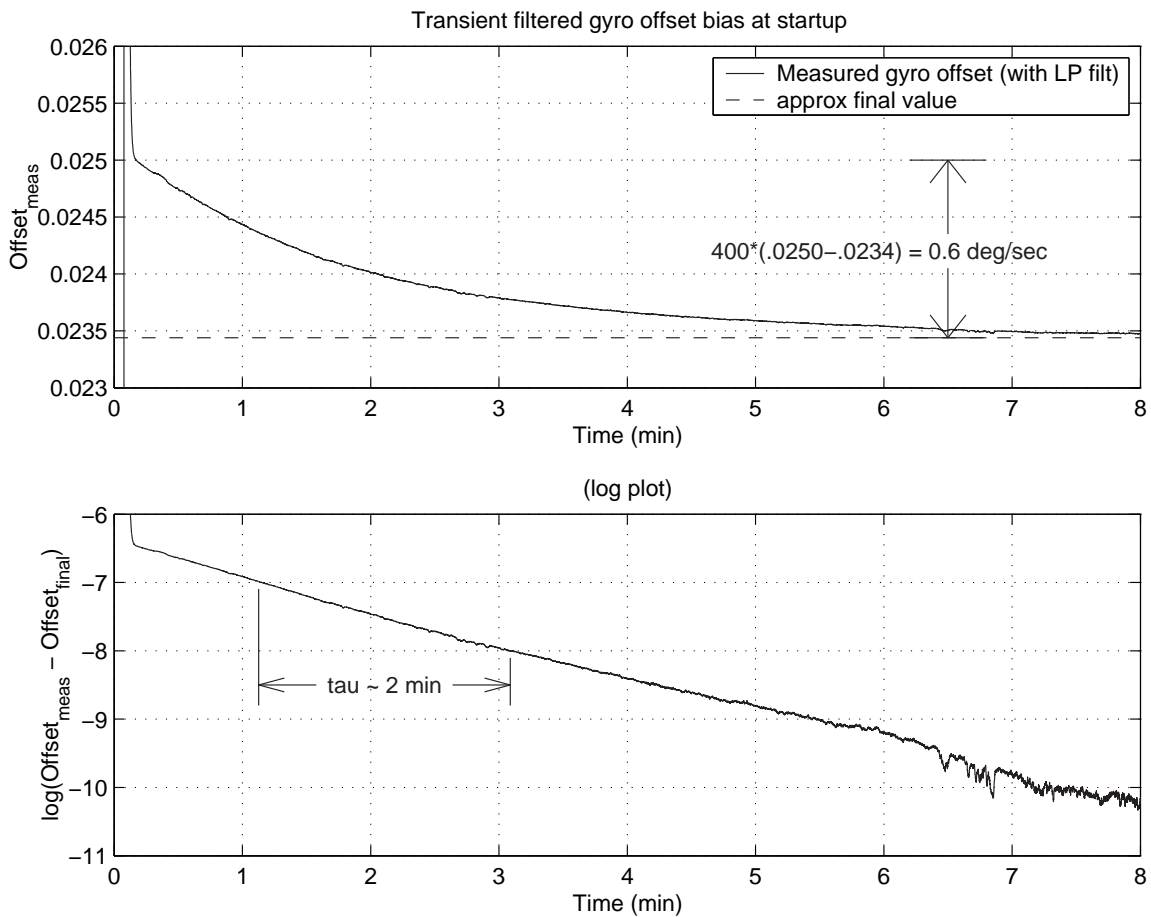
Figure 7-20: Data showing first-order transient response in gyro drift during sensor warm-up

7.1.6   2-Axis Accelerometer

The robot uses a 2-axis accelerometer to compensate for the DC bias of the gyro. The accelerometer is used as a 'tilt sensor' to detect the angle of the pendulum-body with respect to the Earth's gravitational field. Of course, the sensor detects any other accelerations of the robot chassis, in addition to the acceleration of gravity. In normal operation, these accelerations should not be too significant, particularly since only a low-passed component of the accelerometer is needed to compensate the gyro.

Conceptually, the process of converting the gyro and accelerometer signals into an estimate of the pendulum angle can be broken down into three steps. First, the angular rate measurement from gyro is integrated. Then, we subtracte out a low-passed component of the integrated signal to eliminate the noise of the DC bias. Finally, we add in a low-passed estimate of the pendulum angle obtained from the accelerometer, which adds back the low-frequency signal which was lost when we filtered out the low-frequency noise of the gyro.

Mathematically,

$$
\begin{aligned}
\theta_{meas}(s) &= \frac{1}{s} \cdot \left[1 - \frac{1}{\tau s + 1} \right] \cdot \dot{\theta}_{gyro}(s) + \frac{1}{\tau s + 1} \cdot \theta_{acc}(s) \qquad (7.4) \\
&= \frac{\tau}{\tau s + 1} \cdot \dot{\theta}_{gyro}(s) + \frac{1}{\tau s + 1} \cdot \theta_{acc}(s)
\end{aligned}
$$

This is identical to the result which is derived in more detail in Section 6.2 on complementary filtering. Section 6.2 also describes more precisely why it is most logical to use the same time constant in the low-pass filters for the gyro and accelerometer. The time constant for the DIPR's complementary filters is one second.

The accelerometer used in the robot is the Analog Devices ADXL202E, shown in Figures 7-21 and 7-22. This is a low-cost[5], dual axis, MEMS device, which can measure accelerations up to approximately $2g$ [11]. MEMS technology has been advancing rapidly over the past decade [59], and so it seems worthwhile to document the current state-of-the-art as of this writing. (A similar summary is provided documenting the MEMS gyros used in the iBOT and Segway in Section 6.1.7.)

---

[5]Around \$10-\$20 per chip, depending on quantity. The accelerometer used in our robot was a free evaluation part.
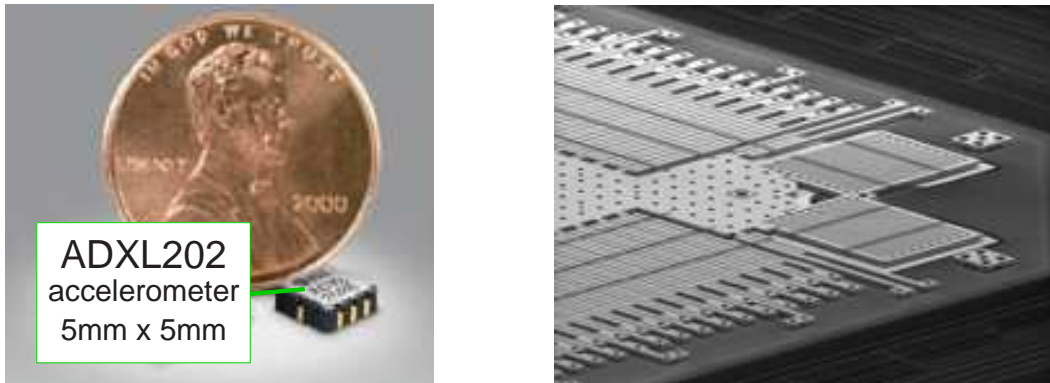
Figure 7-21: ADXL202 2-axis accelerometer. Image at left from Analog Devices[209]. At right is detail at the corner of the proof mass. Righthand image from http://www.memagazine.org/backissues/nov01/features/rattle/rattle.html [59])
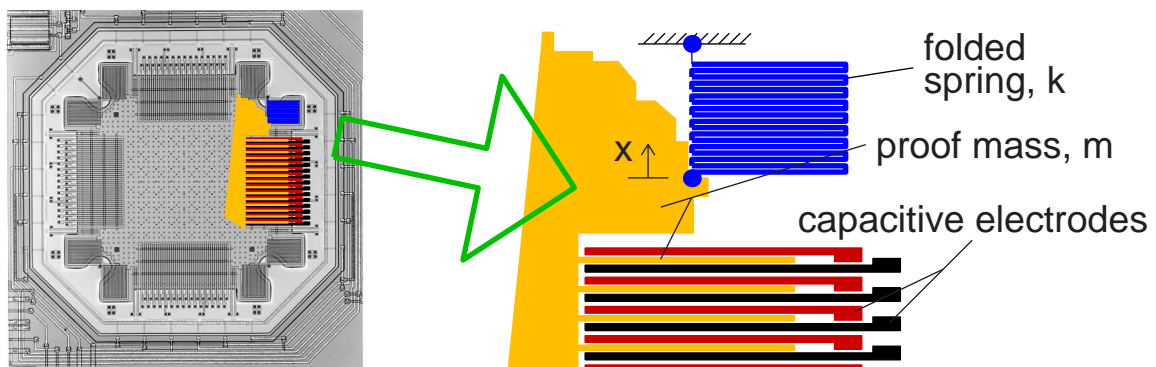
Figure 7-22: Schematic of the ADXL202 accelerometer. Image at left is from the Analog Devices website [209]. At right is an enlarged schematic showing details of the spring, mass and sensors.
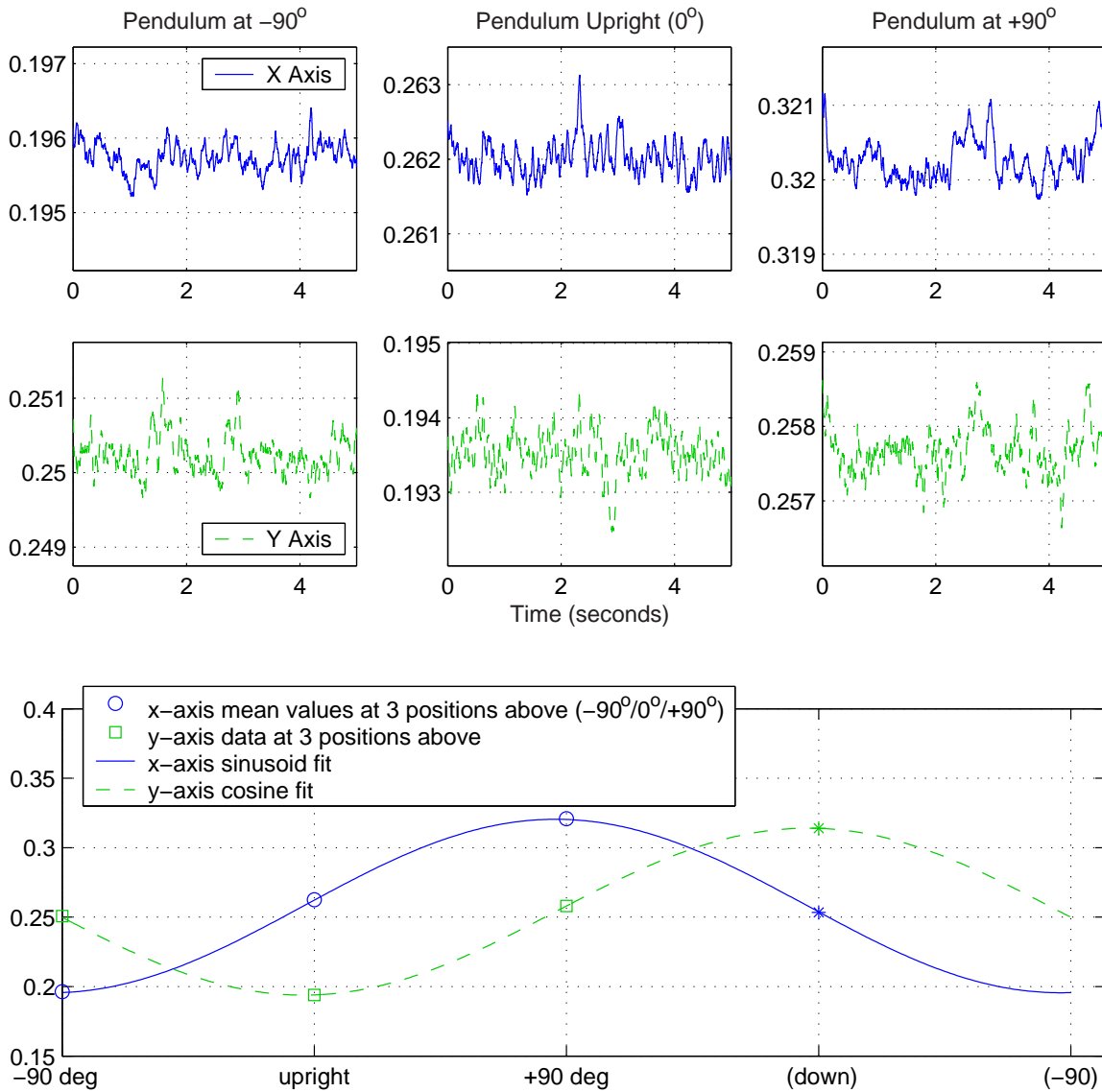
Figure 7-23: Accelerometer calibration and resulting sine and cosine fit. The six data sets at top are filtered but unscaled. Below this, the DC component of the six data sets are fit to sine and cosine functions to estimate the scaling and offset of each channel.

Output when pendulum upright

X_{nom} = 50.0% duty cycle
= 0.2500 A/D input
X_{meas} = 0.2620 A/D input

Y_{nom} = 37.5% duty cycle
= 0.1875 A/D input
Y_{meas} = 0.1935 A/D input

Output at −90° tilt

X_{nom} = 37.5% duty cycle
= 0.1875 A/D input
X_{meas} = 0.1957 A/D input

Y_{nom} = 50.0% duty cycle
= 0.2500 A/D input
Y_{meas} = 0.2503 A/D input

g

(ADXL202AE top view)

Output at +90° tilt

X_{nom} = 62.5% duty cycle
= 0.3125 A/D input
X_{meas} = 0.3203 A/D input

Y_{nom} = 50.0% duty cycle
= 0.2500 A/D input
Y_{meas} = 0.2576 A/D input

Figure 7-24: ADXL202AE output as tilt sensor. This figure is included to explain how data for Figure 7-23 were obtained and to illustrate more clearly how the measured values from the data in that figure compare with nominal outputs specified for the sensor, as described further in the text.

The ADXL202 is a monolithic device, with all mechanical elements and accompanying electronics integrated onto a single chip. It is essentially just a spring-mass system. The force in the spring ($F = kx$) balances the acceleration of the mass ($F = ma$), and therefore the position of the mass is proportional to the acceleration ($x = \frac{m}{k}a$). Folded polysilicon beams form the springs which are attached at the corners of a thin square proof mass to minimize cross-coupling of the x- and y-axis measurements. A series of fingers extend from the periphery of the mass. Each finger is surround by two stationary plates which are fixed to the support structure and driven by square waves which are 180° out of face. These interdigitated plates form a differential capacitor, so that the amplitude of the resulting square wave output is proportional to the displacement of the mass and therefore also to the acceleration on the body [209, 11].

The DIPR uses the two PWM outputs of the ADXL202 which are thenfiltered by a passive low-pass RC circuit with a bandwidth of 50 Hz. At 0 g, the duty cycle should nominally be 50%, or 2.5 V after low-pass filtering. The nominal scaling factor is 12.5% duty cycle change per g. The variance in the device can be huge, however. The zero g bias level is given specified to fall within the range between 25% and 75% duty cycle, and the specified tolerance on the scaling factor goes from 10% duty cycle per g to 15% per g.

Figures 7-23 and 7-24 on previous two pages document the measured zero-g offset and scaling factor for each of the two axes on the accelerometer. The values did not vary significantly on a run-to-run basis.

Figure 7-23 on the left-hand page (p. 350) shows partial segments of six longer streams of data each recorded while the robot was at rest with the pendulum pointing either vertically or horizontally (as indicated on the figure). When the pendulum is at rest, the acceleration of gravity should be the only force or acceleration acting on the sensor. The three data sets shown at the top come from the x-axis channel of the gyro and should therefore correspond to accelerations of -1g, 0g and +1g (going from left to right). The y-axis data below this should ideally correspond to accelerations of 0g, -1g (due to the orientation of the sensor) and 0g.

Because the accelerometer is not aligned perfectly on the robot, the actual angle at which accelerometer is oriented is likely off by a couple of degrees (consistently) from the angle of the pendulum. If you look closely at Figure 7-23, you may note that the sine and cosine fits have been shifted somewhat to the left to take this into account. The data seem to indicate that the alignment error of the accelerometer mounting is approximately 2°.

The figure on the righthand leaf (page 351) summarizes the expected and measured DC outputs in each of the three configurations. Additional information on the noise characteristics for the ADXL202 is given in Section 6.2.2 on page 299.

7.2 Lagrangian Derivation of the Equations of Motion

The equations of motion for the inverted pendulum robot are derived below using the indirect approach (i.e. "variational dynamics"). First, the lagrangian function, $\mathcal{L}$, is formed by subtracting the potential energy, V, from the kinetic coenergy, T^*, as shown in equation 7.5 below:

$$\mathcal{L} = T^* - V \tag{7.5}$$

where T^* and V are written in terms of a set of generalized variables. For the derivation that follows, there are two generalized variables: θ_w, the rotation of the wheels, and θ_p, the angle of the pendulum with respect to vertical.[6] The generalized *forces* acting on the system are denoted as "Ξ_j". Lagrange's equations, shown in equation 7.6, provide a systematic way to balance the systems dynamics with these external forces to form the equations of motion of the system.

$$\frac{d}{dt}\left(\frac{\partial \mathcal{L}}{\partial \dot{\xi}_j}\right) - \frac{\partial \mathcal{L}}{\partial \xi_j} = \Xi_j \qquad (j = 1, 2, \ldots, n) \tag{7.6}$$

The kinetic coenergy of a particle is $\frac{1}{2}m_i v_i \cdot v_i$. For a rigid body, the total coenergy of all particles in the body can be represented as:

$$T^*_{body} = \frac{1}{2}m_b v_b \cdot v_b + \frac{1}{2}J_b \theta_b \cdot \theta_b \tag{7.7}$$

where m_b and J_b are the mass and moment of inertia of the body, respectively. Correspondingly, for a *system* of rigid bodies:

$$T^*_{system} = \sum_{i=1}^{n} \frac{1}{2}m_i v_i \cdot v_i + \sum_{i=1}^{n} \frac{1}{2}J_i \theta_i \cdot \theta_i \tag{7.8}$$

For the inverted pendulum robot, we will consider four rigid bodies in constructing the langrangian. These are illustrated in Figure 7-25. It is a reasonable approximation to assume that the centers of mass of the wheels (M_w), chassis (M_b), and motor

---

[6]Note that this analysis has been simplified by lumping both wheels together, so that they always rotate in unison.
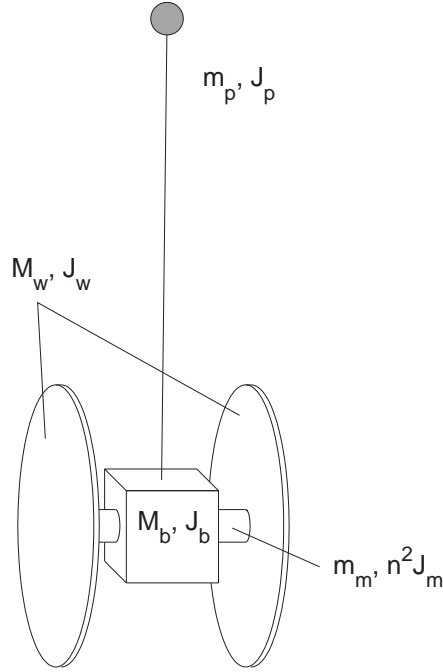
Figure 7-25: Mass and inertia definitions for IP robot equations.

(m_m) all lie on the wheel axis and move at velocity "v_b". The center of mass of the pendulum is a distance L from the wheel axis, and we will define its velocity as "v_p". As mentioned, the wheels are oriented at an angle defined as "θ_w". The body (chassis) and pendulum rotate together as a rigid unit; their angle of rotation is "θ_w". Finally, the angle of the armature in the motor, J_m, is the difference between the wheel and body angles *times* the gear ratio, n. The total kinetic energy is therefore:

$$
\begin{aligned}
T^* &= \frac{1}{2}(M_w + M_b + m_m)\, v_b \cdot v_b + \frac{1}{2} m_p\, v_p \cdot v_p + \dots \\
&\quad \frac{1}{2} J_w \dot{\theta}_w^2 + \frac{1}{2}(J_b + J_p)\dot{\theta}_p^2 + n^2 \frac{1}{2} J_m(\dot{\theta}_p^2 - \dot{\theta}_w^2)
\end{aligned}
\tag{7.9}
$$

while the potential energy is:

$$
V = m_p g L \cos \theta_p
\tag{7.10}
$$

Now, we must rewrite the lagrangian in terms of our generalized variables, θ_w and θ_p. The position of the pendulum mass is:

$$
r_p = (R_w \theta_w + L \sin \theta_p)\, \hat{i} + (L \cos \theta_p)\, \hat{j}
\tag{7.11}
$$

therefore its velocity is:

$$v_p = \frac{dr_p}{dt} = \left(R_w \dot{\theta}_w + \dot{\theta}_p L \cos \theta_p \right) \hat{i} + \left(-\dot{\theta}_p L \sin \theta_p \right) \hat{j} \tag{7.12}$$

and so:

$$\frac{1}{2} m_p \, v_p \cdot v_p = \frac{1}{2} m_p \left[R_w^2 \dot{\theta}_w^2 + 2 R_w L \dot{\theta}_w \dot{\theta}_p \cos \theta_p + L^2 \dot{\theta}_p^2 \cos^2 \theta_p + L^2 \dot{\theta}_p^2 \sin^2 \theta_p \right]$$
$$= \frac{1}{2} m_p \left[R_w^2 \dot{\theta}_w^2 + 2 R_w L \dot{\theta}_w \dot{\theta}_p \cos \theta_p + L^2 \dot{\theta}_p^2 \right] \tag{7.13}$$

Collecting terms:

$$T^* = \frac{1}{2} M R_w^2 \dot{\theta}_w^2 + \frac{1}{2} m_p \left(R_w^2 \dot{\theta}_w^2 + 2 R_w L \dot{\theta}_w \dot{\theta}_p \cos \theta_p + L^2 \dot{\theta}_p^2 \right) + \frac{1}{2} J_w \dot{\theta}_w^2 + \dots$$
$$\frac{1}{2} n^2 J_m \left(\dot{\theta}_p^2 - 2 \dot{\theta}_p \dot{\theta}_w + \dot{\theta}_w^2 \right) + \frac{1}{2} \left(J_p + J_b \right) \dot{\theta}_p^2 \tag{7.14}$$

$$\mathcal{L} = \frac{1}{2} M R_w^2 \dot{\theta}_w^2 + \frac{1}{2} m_p \left(R_w^2 \dot{\theta}_w^2 + 2 R_w L \dot{\theta}_w \dot{\theta}_p \cos \theta_p + L^2 \dot{\theta}_p^2 \right) + \frac{1}{2} J_w \dot{\theta}_w^2 + \dots$$
$$\frac{1}{2} n^2 J_m \left(\dot{\theta}_p^2 - 2 \dot{\theta}_p \dot{\theta}_w + \dot{\theta}_w^2 \right) + \frac{1}{2} \left(J_p + J_b \right) \dot{\theta}_p^2 - m_p g L \cos \theta_p \tag{7.15}$$

where $M = M_b + M_w + m_m$. We can now derive the two equations of motion. First, with respect to the wheel angle,

$$\frac{d}{dt} \left(\frac{\partial L}{\partial \dot{\theta}_w} \right) - \frac{\partial L}{\partial \theta_w} = \Xi_{\theta_w} \tag{7.16}$$

The torques acting to accelerate the wheel angle include the motor torque, $n K_t i$, friction, $f_{fric} \left(\dot{\theta}_p - \dot{\theta}_w \right)$, and any external disturbance force applied at (or near) the motor, $F_m \cdot R_m$:

$$\Xi_{\theta_w} = n K_t i + b_{fric} \left(\dot{\theta}_p - \dot{\theta}_w \right) + F_m \cdot R_m \tag{7.17}$$

$$\frac{\partial L}{\partial \dot{\theta}_w} = M R_w^2 \dot{\theta}_w + m_p R_w^2 \dot{\theta}_w + m_p R_w L \dot{\theta}_p \cos \theta_p + n^2 J_m \left(\dot{\theta}_w - \dot{\theta}_p \right) + J_w \dot{\theta}_w \tag{7.18}$$

$$\frac{d}{dt} \left(\frac{\partial L}{\partial \dot{\theta}_w} \right) = M R_w^2 \ddot{\theta}_w + m_p R_w^2 \ddot{\theta}_w + m_p R_w L \ddot{\theta}_p \cos \theta_p - m_p R_w L \dot{\theta}_p^2 \sin \theta_p + \dots$$
$$n^2 J_m \left(\ddot{\theta}_w - \ddot{\theta}_p \right) + J_w \ddot{\theta}_w \tag{7.19}$$

$$\frac{\partial L}{\partial \theta_w} = 0 \tag{7.20}$$

Combining all these terms and applying equation 7.16, we obtain the **first equation of motion**, shown in equation 7.21:

$$
\begin{aligned}
[(M + m_p)\, R_w^2 + n^2 J_m + J_w]\, \ddot{\theta}_w + [m_p R_w L \cos\theta_p - n^2 J_m]\, \ddot{\theta}_p = \dots \\
m_p R_w L \dot{\theta}_p^2 \sin\theta_p + n K_t i + b_{fric}\left(\dot{\theta}_p - \dot{\theta}_w\right) + F_m \cdot R_w
\end{aligned}
\tag{7.21}
$$

The second equation of motion is derived (below) in the same manner. Again, we begin with the definition of the lagrangian, now with respect to the pendulum angle.

$$
\frac{d}{dt}\left(\frac{\partial L}{\partial \dot{\theta}_p}\right) - \frac{\partial L}{\partial \theta_p} = \Xi_{\theta_p}
\tag{7.22}
$$

The torque contributions from the motor and friction are equal but opposite to those in the previous derivation, and we will now include a disturbance torce applied to the pendulum-body unit.

$$
\Xi_{\theta_p} = -n K_t i - b_{fric}\left(\dot{\theta}_p - \dot{\theta}_w\right) + \tau_p
\tag{7.23}
$$

$$
\frac{\partial L}{\partial \dot{\theta}_p} = m_p L^2 \dot{\theta}_p + m_p R_w L \dot{\theta}_w \cos\theta_p + (J_p + J_b)\, \dot{\theta}_p + n^2 J_m \left(\dot{\theta}_p - \dot{\theta}_w\right)
\tag{7.24}
$$

$$
\frac{d}{dt}\left(\frac{\partial L}{\partial \dot{\theta}_p}\right) = m_p L^2 \ddot{\theta}_p + m_p R_w L \ddot{\theta}_w \cos\theta_p - m_p R_w L \dot{\theta}_w \dot{\theta}_p \sin\theta_p + J_p \ddot{\theta}_p + n^2 J_m \left(\ddot{\theta}_p - \ddot{\theta}_w\right)
\tag{7.25}
$$

$$
\frac{\partial L}{\partial \theta_p} = -m_p R_w \dot{\theta}_w \dot{\theta}_p L \sin\theta_p + m_p g L \sin\theta_p
\tag{7.26}
$$

The **second equation of motion** is shown in equation 7.27:

$$
\begin{aligned}
[m_p L^2 + J_p + J_b + n^2 J_m]\, \ddot{\theta}_p + [m_p R_w L \cos\theta_p - n^2 J_m]\, \ddot{\theta}_w = \dots \\
m g L \sin\theta_p - n K_t i - b_{fric}\left(\dot{\theta}_p - \dot{\theta}_w\right) + \tau_p
\end{aligned}
\tag{7.27}
$$

To linearize the equations of motions about the unstable (upright) equilibrium point, we will make the standard small-angle assumptions that $\theta_p << 1$ and $\dot{\theta}_p << 1$. Therefore, $\sin\theta_p \approx 0$, $\cos\theta_p \approx 1$, and $\dot{\theta}_p^2 \approx 0$. Applying these approximation to equations 7.21 and 7.27 we get the following two **linearized equations of motion**:

$$
\begin{aligned}
[(M + m_p)\, R_w^2 + J_w + n^2 J_m]\, \ddot{\theta}_w + [m_p R_w L - n^2 J_m]\, \ddot{\theta}_p = \dots \\
n K_t i + b_{fric}\left(\dot{\theta}_p - \dot{\theta}_w\right) + F_m \cdot R_w
\end{aligned}
\tag{7.28}
$$

$$\boxed{\begin{aligned}
&[m_p L^2 + J_p + J_b + n^2 J_m]\,\ddot{\theta}_p + [m_p R_w L - n^2 J_m]\,\ddot{\theta}_w = \ldots \\
&m_p g L \theta_p - n K_t i - b_{fric}\left(\dot{\theta}_p - \dot{\theta}_w\right) + \tau_p
\end{aligned}} \tag{7.29}$$

7.3 Transfer Functions and Pole Plots for Plant

This section uses the linearized equations of motion (7.28 and 7.29) to derive some transfer functions of interest for the uncontrolled inverted pendulum robot. Plugging in relevant parameters for the robot (given in Table 7.3), we can then gain insight into the uncontrolled system dynamics based on the locations of the system poles. We begin by adding together the two linearized equations of motion, 7.28 and 7.29:

$$\left[m_p L^2 + J_p + J_b + m_p R_w L\right]\ddot{\theta}_p - m_p g L \theta_p = \ldots$$

$$-\left[(M + m_p)\,R_w^2 + J_w + m_p R_w L\right]\ddot{\theta}_w + F_m \cdot R_w + F_p \cdot L \tag{7.30}$$

The transfer function from wheel angle, θ_w, to pendulum angle, θ_p is then:

$$\frac{\theta_p(s)}{\theta_w(s)} = \frac{-\left[(M + m_p)\,R_w^2 + J_w + m_p R_w L\right]s^2}{\left[m_p L^2 + J_p + J_b + m_p R_w L\right]s^2 - m_p g L} \approx \frac{-1.3 s^2}{s^2 - 14.5} \tag{7.31}$$

To provide more insight into the actual system dynamics, approximate numeric values are shown at right in this equation, using the parameter values given in Table 7.3.

Using equation 7.31 to eliminate θ_w from equation 7.29, we can represent $\theta_p(s)$ in terms of the input current, $I(s)$, and the disturbances, $F_p(s)$ and $F_m(s)$.

$$\theta_p(s) \quad \cdot \quad \left(A_3 s^3 + A_2 s^2 + A_1 s + A_0\right) \quad = \tag{7.32}$$

$$-\left((M + m_p)\,R_w^2 + J_w + m_p R_w L\right)n K_t \quad \cdot \quad s I(s) \ \ldots$$
$$+\left(\left((M + m_p)\,R_w^2 + J_w + n^2 J_m\right)s + b_{fric}\right)L \quad \cdot \quad F_p(s) \ \ldots$$
$$-\left(\left(m_p R_w L - n^2 J_m\right)s - b_{fric}\right)R_w \quad \cdot \quad F_m(s)$$

The new variables defined in this equation are:

$$A_3 = m_p M L^2 R_w^2 + (M + m_p) R_w^2 (J_p + J_b) + m_p L^2 J_w + J_w (J_p + J_b) + \dots$$
$$\dots + n^2 J_m \left[m_p (L + R_w^2)^2 + M R_w^2 + J_w + J_p + J_b \right] \tag{7.33}$$
$$\approx m_p M L^2 R_w^2 + (M + m_p) R_w^2 (J_p + J_b) + m_p L^2 J_w + J_w (J_p + J_b)$$
$$\approx \underline{0.0718}$$

$$A_2 = \left(m_p (L + R_w)^2 + M R_w^2 + J_w + J_p + J_b \right) b_{fric} \tag{7.34}$$
$$\approx \underline{0.00034}$$

$$A_1 = -m_p g L \left((M + m_p) R_w^2 + J_w + n^2 J_m \right) \tag{7.35}$$
$$\approx -m_p g L \left((M + m_p) R_w^2 + J_w \right)$$
$$\approx \underline{-1.14}$$

$$A_0 = -m_p g L b_{fric} \tag{7.36}$$
$$\approx \underline{-0.002}$$

The transfer functions from each input to θ_p are:

$$\frac{\theta_p(s)}{I(s)} = \frac{-\left((M + m_p) R_w^2 + J_w + m_p R_w L \right) n K_t s}{A_3 s^3 + A_2 s^2 + A_1 s + A_0} \tag{7.37}$$
$$\approx \frac{-0.039 s}{0.072 s^3 + 0.00034 s^2 - 1.14 s - 0.002}$$
$$= \frac{-0.33}{(s - 4.0)(s + 4.0)}$$

$$\frac{\theta_p(s)}{F_m(s)} = \frac{-R_w \left((m_p R_w L - n^2 J_m) s - b_{fric} \right)}{A_3 s^3 + A_2 s^2 + A_1 s + A_0} \tag{7.38}$$
$$\approx \frac{-0.0090 s + 0.000075}{0.072 s^3 + 0.00034 s^2 - 1.14 s - 0.002}$$
$$\approx \frac{-0.125}{(s - 4.0)(s + 4.0)}$$

$$\tag{7.39}$$

$$\frac{\theta_p(s)}{F_p(s)} = \frac{L\left(\left((M + m_p)\, R_w^2 + J_w\right) s + b_{fric}\right)}{A_3 s^3 + A_2 s^2 + A_1 s + A_0} \tag{7.40}$$

$$\approx \frac{0.12}{0.072 s^2 + 0.00034 s - 1.14}$$

$$\approx \frac{1.67}{(s - 4.0)(s + 4.0)}$$

Estimated Parameter Values for Inverted Pendulum Robot. Note that each inertia value are taken with respect to the *center of mass* of that object.

Var.		Final robot	Smaller prototype
m_p	$=$	$1.0\ [kg]$	$0.2\ [kg]$
M_w	$=$	$2.6\ [kg]$	$2\ [kg]$
M_b	$=$	$6.5\ [kg]$	$2\ [kg]$
m_m	$=$	$1.3\ [kg]$	(same)
M	$=$	$10.6\ [kg]$	$\sim 5.5\ [kg]$
J_p	$=$	$0.05\ [kg\,m^2]$	$0.02\ [kg\,m^2]$
J_w	$=$	$0.029\ [kg\,m^2]$	$0.009\ [kg\,m^2]$
J_b	$=$	$0.05\ [kg\,m^2]$	$0.016\ [kg\,m^2]$
J_m	$=$	$0.000012\ [kg\,m^2]$	(same)
n	$=$	$13/3$	(same)
$n^2 J_m$	$=$	$0.00023\ [kg\,m^2]$	(same)
R_w	$=$	$0.15\ [m]$	$0.10\ [m]$
L_{eff}	$=$	$0.4\ [m]$	$0.5\ [m]$
b_{fric}	$\approx$	$0.0005\ ?\ [Nms/rad]$	(same)
K_t	$=$	$0.026\ [Nm/A]$	(same)

The numeric solutions to the preceding transfer functions show that the poles of the IP system in the unstable (upright) configuration should be at approximately $s = -4.0$ rad/s and $s = +4.0$ rad/s. This 2-pole approximation neglects the effects of friction ($b_{fric} \approx 0$). The full characteristic equation is:

$$A_3 s^3 + A_2 s^2 + A_1 s + A_0 = 0 \tag{7.41}$$

Neglecting friction simplifies this equation, since both A_2 and A_0 scale linearly with b_{fric} and are therefore approximated in the equation as zero:

$$A_3 s^3 + A_1 s = 0 \tag{7.42}$$

The solution at the origin cancels with a zero at the origin in each of the preceding transfer functions shown. This leaves a symmetric pair of poles which will lie on either the real or imaginary axes. If the signs of A_3 and A_1 differ, the poles are real, and the righthand pole indicates that the system is unstable. If A_3 and A_1 have the same sign, the approximation predicts that the poles will be purely imaginary, and the system should be marginally stable (with undamped oscillations). The actual system will of course be stable, with the finite (viscous) friction terms insuring that the oscillations are damped to some extent.

When the pendulum is in stable (lightly damped) configuration, the effect on the equations of motion is that the sign of gravity (g) will be reversed. In Equations 7.33 through 7.36, changing the sign of gravity will correspondingly change the signs of A_1 and A_0. As a result, all four coefficients of the characteristic equation will now be strictly positive, which is sufficient to show that system is stable. Neglecting friction, we instead obtain a marginally stable approximation of the system dynamics, with predicted poles at $s = \pm\sqrt{\left|\frac{A_1}{A_3}\right|} j \approx \pm 4.0 j$.

This solution is in agreement with measurement of the *stable* pendulum frequency, shown in Figure 7-30 on page 371. With the wheels elevated so that the pendulum-body is allowed to hang down, oscillations about the stable equilibrium have a natural frequency of approximately 3.9 rad/sec (0.62 Hz). Figure 7-26 shows both the predicted locations of the symmetric poles of the idealized (lossless) upright pendulum

vehicle (at left) and (at right) the measured complex pole pair corresponding to the stable pendulum. The magnitude of the distance of each pole from the origin is the same (approximately), as expected.

In fact, the frequency of the oscillations in the stable configuration was used to help determine the inertia of the chassis more precisely (as described further in Section 7.5.2), so it is no accident that the agreement is so close!
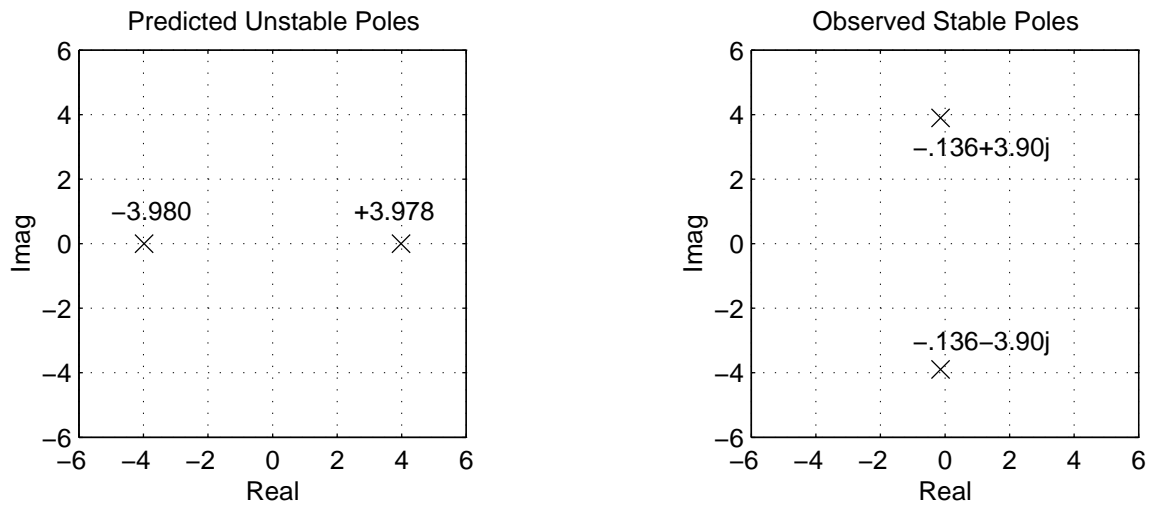
Figure 7-26: Poles for IP system near unstable and stable equilibria. The unstable pole locations at left are those predicted by the transfer functions derived in this section. The stable poles shown are right were obtained from encoder measurements of the pendulum oscillations near its stable equilibrium. These pole plots show that that two results are in agreement. Because the system has little damping, we would expect mathematically that changing the sign of gravity would effectively just change the signs of some terms in the characteristic polynomial for the system and would correspondingly "swap" the axes (Real vs. Imag) on which the poles are located. The distance of the poles from the origin should not change, however.

Finally, we can derive transfer functions for the unstable system with the same inputs as in Equations 7.37, 7.38, and 7.40 but with the *wheel* angle, θ_w, as output. This can be done by multiplying each of the previous transfer function equations by the transfer function from θ_p to θ_w, below:

$$\frac{\theta_w(s)}{\theta_p(s)} = \frac{-\left[m_p L^2 + J_p + J_b + m_p R_w L\right] s^2 - m_p g L}{\left[(M + m_p) R_w^2 + J_w + m_p R_w L\right] s^2} \approx \frac{-0.77(s^2 - 14.5)}{s^2} \tag{7.43}$$

Equation 7.43 is the inverse of Equation 7.31, used in the derivations earlier in this section. The numeric values of each resulting transfer functions are listed below. If the position of the robot is the output of interest, this is of course linearly related to the angular of the wheel as $X(s) = R_w \theta_w(s)$.

$$\frac{\theta_w(s)}{I(s)} \approx \frac{0.25(s + 3.8)(s - 3.8)}{(s + 4.0)(s - 4.0)} \tag{7.44}$$

$$\frac{\theta_w(s)}{F_m(s)} \approx \frac{0.10(s - 3.8)(s + 3.8)}{(s - 4.0)(s + 4.0)} \tag{7.45}$$

$$\frac{\theta_w(s)}{F_p(s)} \approx \frac{-1.3(s + 3.8)(s - 3.8)}{(s - 4.0)(s + 4.0)} \tag{7.46}$$

7.4 System Equations in State Space

This section derives the state and output equations,

$$\dot{\mathbf{x}} = \mathbf{A}\mathbf{x} + \mathbf{B}u \tag{7.47}$$

$$\mathbf{y} = \mathbf{C}\mathbf{x} + \mathbf{D}u \tag{7.48}$$

Here, the only controllable input, u, is the total commanded current, i, to the motors.[7] For the analysis that follows directly, the state variable vector, $\mathbf{x}$, includes both the observable parameters θ_p, θ_w, $\dot{\theta}_p$, and $\dot{\theta}_w$, and the exogenous inputs, τ_p and F_m. The most significant disturbances on the robots come from the effects of the umbilical

---

[7]This analysis continues to assume that both motors act together as a single entity. The results can be generalized for the case of a steerable robot without much difficulty.

cord. To simplify the derivation, we will assume any input disturbances, τ_p (on the pendulum-body) and F_m (on the mass) are constant *states* in the system over time:

$$\dot{F}_p = 0 \tag{7.49}$$

$$\dot{F}_m = 0 \tag{7.50}$$

Another logical way to account for the external forces is to include an additional vector, **w**, of *uncontrolled* system inputs, τ_p and F_m:

$$\dot{\mathbf{x}} = \mathbf{A}\mathbf{x} + \mathbf{B}u + \mathbf{G}\mathbf{w} \tag{7.51}$$

If the uncontrolled forces on the robot were more stochastic in natural (particularly if they could adequately be approximated as zero-mean), I think equation 7.51 would clearly be preferable.[8] Since the forces on the robot are relatively constant now[9], I would argue there are potential advantages to each approach. Below, I will start with the model given by equation 7.47 and then discuss state space approaches on a simplified system that ignores the disturbance forces.

For clarity, the linearized equations of motions, 7.28 and 7.29, are rewritten below:

$$J_1\ddot{\theta}_w + J_2\ddot{\theta}_p = nK_t i + b_f\left(\dot{\theta}_p - \dot{\theta}_w\right) + R_w \cdot F_m \tag{7.52}$$

$$J_3\ddot{\theta}_p + J_4\ddot{\theta}_w = -nK_t i - b_f\left(\dot{\theta}_p - \dot{\theta}_w\right) + \tau_p + m_p gL\theta_p \tag{7.53}$$

where we define the following inertia values:

$$J_1 = (M + m_p) R_w^2 + J_w + n^2 J_m \tag{7.54}$$

$$J_2 = m_p R_w L - n^2 J_m \tag{7.55}$$

$$J_3 = m_p L^2 + J_p + J_b + n^2 J_m \tag{7.56}$$

$$J_4 = m_p R_w L - n^2 J_m \tag{7.57}$$

For the robot, $J_1 \approx 0.29\ [kg\,m^2]$; $J_2 = J_4 \approx 0.060\ [kg\,m^2]$; and $J_3 \approx 0.26\ [kg\,m^2]$.

---

[8]We might then be more inclined to use a Kalman filter to refine our estimates of the states.

[9]The umbilical only allows about 6-8 feet of travel, so much of the analysis focuses on pendulum response while the robot's commanded velocity is zero.

First, we can solve for $\ddot{\theta}_w$ in equation 7.52 and then plug this into equation 7.53 to solve for $\ddot{\theta}_p$ in terms of the state variables and system inputs:

$$\ddot{\theta}_w = -\frac{J_2}{J_1}\ddot{\theta}_p + \frac{nK_t}{J_1}k + \frac{b_f}{J_1}\dot{\theta}_p - \frac{b_f}{J_1}\dot{\theta}_w + \frac{R_w}{J_1}F_m \tag{7.58}$$

$$J_3\ddot{\theta}_p + J_4\left[\frac{-J_2}{J_1}\ddot{\theta}_p + \frac{nK_t}{J_1}k + \frac{b_f}{J_1}\dot{\theta}_p - \frac{b_f}{J_1}\dot{\theta}_w + \frac{R_w}{J_1}F_m\right] = \ldots$$
$$-nK_t i - b_f\left(\dot{\theta}_p - \dot{\theta}_w\right) + L \cdot F_p + m_p g L\theta_p \tag{7.59}$$

$$\boxed{\begin{aligned}\ddot{\theta}_p &= \left(\frac{1}{J_1 J_3 - J_4 J_2}\right) \cdot [J_1 m_p g L\theta_P - (J_1 + J_4)\,b_f\dot{\theta}_p + (J_1 + J_4)\,b_f\dot{\theta}_w \ldots \\ &\quad + J_1\tau_p - J_4 R_w F_m + (J_1 + J_4)\,nK_t i]\end{aligned}} \tag{7.60}$$

Next, we solve explicitly for the angular velocity of the *wheel* in a similar manner:

$$\ddot{\theta}_p = -\frac{J_4}{J_3}\ddot{\theta}_w + \frac{m_p g L}{J_3} - \frac{nK_t}{J_3}i - \frac{b_f}{J_3}\dot{\theta}_p + \frac{b_f}{J_3}\dot{\theta}_w + \frac{L}{J_3}F_p \tag{7.61}$$

$$\boxed{\begin{aligned}\ddot{\theta}_w &= \left(\frac{1}{J_1 J_3 - J_4 J_2}\right) \cdot [-J_2 m_p g L\theta_P + (J_2 + J_3)\,b_f\dot{\theta}_p - (J_2 + J_3)\,b_f\dot{\theta}_w \ldots \\ &\quad - J_2\tau_p + J_3 R_w F_m + (J_2 + J_3)\,nK_t i]\end{aligned}} \tag{7.62}$$

To present these equations in matrix form more concisely, let us define the following set of variables:

$$K_1 = \frac{J_1}{J_1 J_3 - J_4 J_2} \approx 4.0 \quad [1/(kg\ m^2] \tag{7.63}$$

$$K_2 = \frac{J_2}{J_1 J_3 - J_4 J_2} \approx 0.83 \quad [1/(kg\ m^2] \tag{7.64}$$

$$K_3 = \frac{J_3}{J_1 J_3 - J_4 J_2} \approx 3.6 \quad [1/(kg\ m^2] \tag{7.65}$$

$$K_4 = \frac{J_4}{J_1 J_3 - J_4 J_2} \approx 0.83 \quad [1/(kg\ m^2] \tag{7.66}$$

$$K_{14} = \frac{J_1 + J_4}{J_1 J_3 - J_4 J_2} \approx 4.9 \quad [1/(kg\ m^2] \tag{7.67}$$

$$K_{23} = \frac{J_2 + J_3}{J_1 J_3 - J_4 J_2} \approx 4.4 \quad [1/(kg\ m^2] \tag{7.68}$$

Representing equations 7.60 and 7.62 in state space:

$$
\mathbf{x} =
\begin{bmatrix}
\dot{\theta}_p \\
\dot{\theta}_w \\
\ddot{\theta}_p \\
\ddot{\theta}_w \\
\dot{\tau}_p \\
\dot{F}_m
\end{bmatrix}
=
\begin{bmatrix}
0 & 0 & 1 & 0 & 0 & 0 \\
0 & 0 & 0 & 1 & 0 & 0 \\
K_1 m_p g L & 0 & -K_{14} b_f & K_{14} b_f & K_1 & -K_4 R_w \\
-K_2 m_p g L & 0 & K_{23} b_f & -K_{23} b_f & -K_2 & K_3 R_w \\
0 & 0 & 0 & 0 & 0 & 0 \\
0 & 0 & 0 & 0 & 0 & 0
\end{bmatrix}
\begin{bmatrix}
\theta_p \\
\theta_w \\
\dot{\theta}_p \\
\dot{\theta}_w \\
\tau_p \\
F_m
\end{bmatrix}
+ \ldots
$$

$$
\ldots +
\begin{bmatrix}
0 \\
0 \\
K_{14} n K_t \\
-K_{23} n K_t \\
0 \\
0
\end{bmatrix}
\begin{bmatrix} i \end{bmatrix}
\tag{7.69}
$$

The outputs of interest, $\mathbf{y}$, will be the measured states used for control, which are the

angles of rotation of the pendulum and the motor, θ_p and θ_m, and their derivatives.

$$
\mathbf{y} =
\begin{bmatrix}
\dot{\theta}_p \\
\theta_m \\
\theta_p \\
\dot{\theta}_m
\end{bmatrix}
=
\begin{bmatrix}
1 & 0 & 0 & 0 & 0 & 0 \\
-1 & 1 & 0 & 0 & 0 & 0 \\
0 & 0 & 1 & 0 & 0 & 0 \\
0 & 0 & -1 & 1 & 0 & 0
\end{bmatrix}
\begin{bmatrix}
\theta_p \\
\theta_w \\
\dot{\theta}_p \\
\dot{\theta}_w \\
\tau_p \\
F_m
\end{bmatrix}
\tag{7.70}
$$

Plugging in estimated parameter values for the robot, the equation for $\mathbf{x}$ becomes:

$$
\begin{bmatrix} \dot{\theta}_p \\ \dot{\theta}_w \\ \ddot{\theta}_p \\ \ddot{\theta}_w \\ \dot{\tau}_p \\ \dot{F}_m \end{bmatrix} =
\begin{bmatrix}
0 & 0 & 1 & 0 & 0 & 0 \\
0 & 0 & 0 & 1 & 0 & 0 \\
15.8 & 0 & -.024 & .024 & 4.0 & -.12 \\
-3.3 & 0 & .022 & -.022 & -.83 & .54 \\
0 & 0 & 0 & 0 & 0 & 0 \\
0 & 0 & 0 & 0 & 0 & 0
\end{bmatrix}
\begin{bmatrix} \theta_p \\ \theta_w \\ \dot{\theta}_p \\ \dot{\theta}_w \\ \tau_p \\ F_m \end{bmatrix} +
\begin{bmatrix} 0 \\ 0 \\ .27 \\ -.46 \\ 0 \\ 0 \end{bmatrix}
\begin{bmatrix} i \end{bmatrix} \quad (7.71)
$$

Treating the umbilical forces as unknown system inputs, rather than as system states, we get the alternate state space representation:

$$
\mathbf{x} = \begin{bmatrix} \dot{\theta}_p \\ \dot{\theta}_w \\ \ddot{\theta}_p \\ \ddot{\theta}_w \end{bmatrix} =
\begin{bmatrix}
0 & 0 & 1 & 0 \\
0 & 0 & 0 & 1 \\
K_1 m_p g L & 0 & -K_{14} b_f & K_{14} b_f \\
-K_2 m_p g L & 0 & K_{23} b_f & -K_{23} b_f
\end{bmatrix}
\begin{bmatrix} \theta_p \\ \theta_w \\ \dot{\theta}_p \\ \dot{\theta}_w \end{bmatrix} + \dots
$$

$$
\dots + \begin{bmatrix} 0 \\ 0 \\ K_{14} n K_t \\ -K_{23} n K_t \end{bmatrix}
\begin{bmatrix} i \end{bmatrix} +
\begin{bmatrix} 0 & 0 \\ 0 & 0 \\ K_1 & -K_4 R_w \\ -K_2 & K_3 R_w \end{bmatrix}
\begin{bmatrix} \tau_p \\ F_m \end{bmatrix} \quad (7.72)
$$

Or numerically, using the estimated robot parameters:

$$
\begin{bmatrix} \dot{\theta}_p \\ \dot{\theta}_w \\ \ddot{\theta}_p \\ \ddot{\theta}_w \end{bmatrix} =
\begin{bmatrix}
0 & 0 & 1 & 0 \\
0 & 0 & 0 & 1 \\
15.8 & 0 & -.024 & .024 \\
-3.3 & 0 & .022 & -.022
\end{bmatrix}
\begin{bmatrix} \theta_p \\ \theta_w \\ \dot{\theta}_p \\ \dot{\theta}_w \end{bmatrix} +
\begin{bmatrix} 0 \\ 0 \\ .55 \\ -.50 \end{bmatrix}
\begin{bmatrix} i \end{bmatrix} +
\begin{bmatrix} 0 & 0 \\ 0 & 0 \\ 4.0 & -.12 \\ -.83 & .54 \end{bmatrix}
\begin{bmatrix} \tau_p \\ F_m \end{bmatrix} \quad (7.73)
$$

The poles for this system are $s_1 = 0$, $s_2 = +4.0$, $s_3 = -4.0$, and $s_4 = -0.017$. The transfer functions from commanded current, $\mathbf{i}$, to pendulum position, θ_p, motor velocity, $\dot{\theta}_m$ and vehicle velocity, $\dot{\theta}_w$ are:

$$
\frac{\theta_p(s)}{I(s)} \approx \frac{0.55s}{(s - 4.0)(s + 4.0)(s + .017)} \quad (7.74)
$$

$$
\frac{\dot{\theta}_m(s)}{I(s)} \approx \frac{-1.05(s + 2.4)(s - 2.4)}{(s - 4.0)(s + 4.0)(s + .017)} \quad (7.75)
$$

$$\frac{\dot{\theta}_w(s)}{I(s)} = s\frac{\theta_p(s)}{I(s)} + \frac{\dot{\theta}_m(s)}{I(s)} \approx \frac{-.50(s+3.5)(s-3.5)}{(s-4.0)(s+4.0)(s+.017)} \tag{7.76}$$

7.5   Mechanical Design Issues and Simulation

This section discusses some practical issues. The actual system includes dynamics which led me to avoid focusing on state space methods for control, as discussed further below (7.5.1). This section also discusses experimental estimation of the inertia of the chassis (7.5.2), the possibility of creating a self-standing robot (7.5.3), the choice between using current control versus voltage control for the motors (7.5.4), high-pass filtering of the measurement of wheel position (7.5.5), and encoder damage (7.5.6).

7.5.1   State Space Control

If one can obtain an LTI model which captures the dynamics of a plant sufficiently, any of a variety of state space methods can be used to design a controller for the system. The controller for the IP robot named Joe (see page 2.1.3) was designed using pole placement techniques, for instance, and the cart-driven system from Chapter 5 uses a linear-quadratic regulator to minimize a weighted sum of the errors of the measured states in a least-squares sense. MATLAB provides many useful functions for implementing state space techniques including pole placement (acker() and place()) and the design of a linear-quadratic regulator (lqr(), dlqr()), and dare()).

However, the dynamics of the actual system are not well-modeled by the analyses in the preceding sections. I first discovered this when I implemented an lqr controller. The pendulum stayed upright, but the system could easily be set into a resonance in which the pendulum arm (in particular) vibrated significantly.

I changed my strategy for developing a controller after this initial attempt using state space methods, focusing on loop-shaping techniques instead. The new strategy, which is described further in Section 7.7, involves closing an inner loop on wheel velocity and an outer loop on pendulum angle.

The transfer functions in Section 7.6 document the measured plant dynamics. Figure 7-27 shows an example of the measured plant data, which is identical to the data presented in Figure 7-37 on page 380.
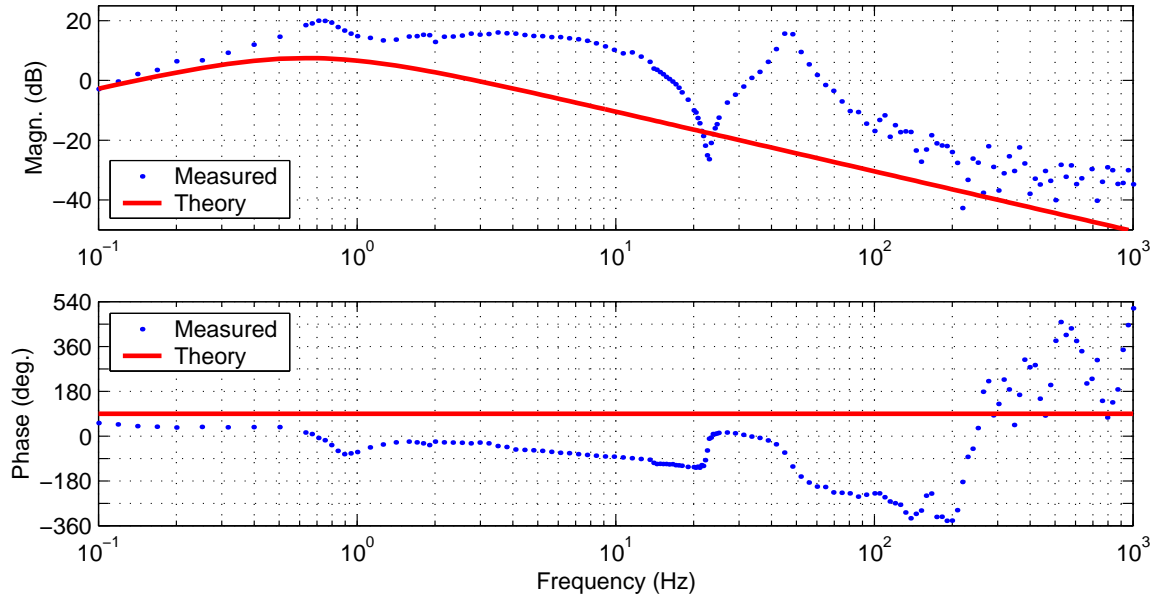
Figure 7-27: Measured plant compared with theoretical TF ($\dot{\theta}_p(s)/V(s)$). The predicted transfer function from voltage to pendulum angle is very close to the TF from current to θ_p, which is given in Equation 7.37. (Section 7.5.4 discusses the differences between current and voltage control.)

Both the theoretical and measured systems have a zero at or near the original and a pair of poles near 4 rad/s. Aside from this, however, the two systems show quite significant disparity! Mostly particularly, the expected dynamics include an unstable pole at $+4$ rad/s, while there seems to be a complex pole pair rather than a real pole pair in the measured transfer function. Moreover, the actual poles seem to lie entirely in the left-half plane, so the pendulum is theoretically stable in upright position, even without control.

Figure 7-28 compares the same measured data shown in Figure 7-27 with a 7th-order plant. This higher-order system was selected to match the general characteristics of the experimental data, but it is not intended to be a close fit. The 7th-order system contains a lightly damped pole pair at around 4.3 rad/s (0.68 Hz) with $\zeta \approx 0.1$.
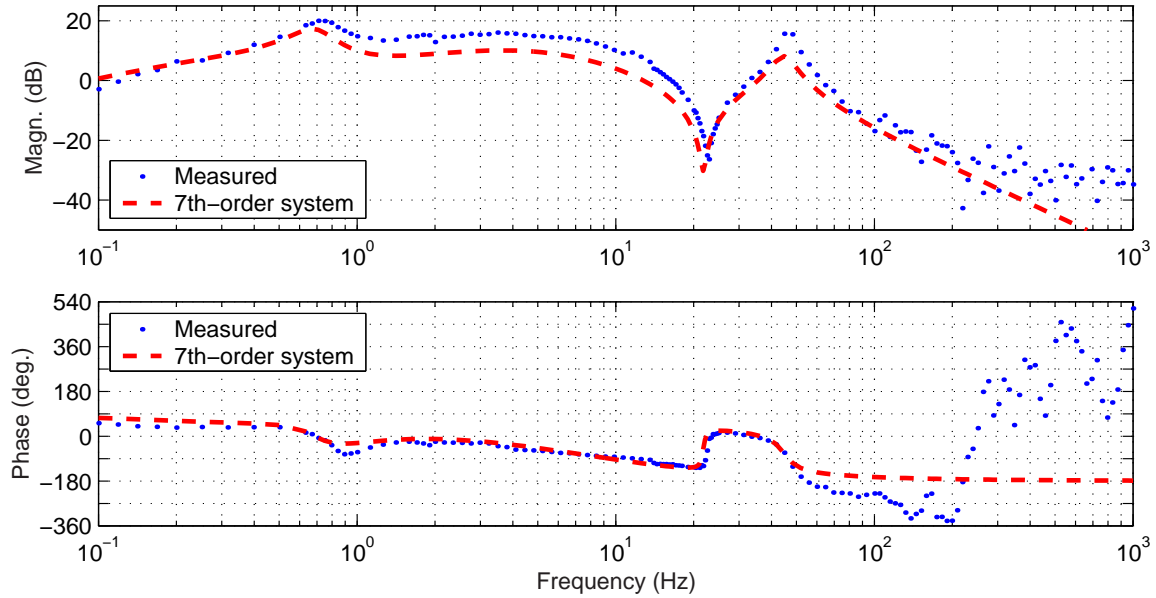
Figure 7-28: Measured dynamics compared with a 7th-order stable system. The measured data, which are identical to those shown in Figure 7-27, represent the transfer function from voltage to pendulum angle $(\dot{\theta}_p(s)/V(s))$. The dashed line represents a stable 7th-order system. The 7th-order system is not meant to match the data as a convincing fit, but it does seem to indicate that the actual plant can be modeled more closely as a stable 7th-order system than as the unstable 2nd-order plant predicted (which was shown in Figure 7-27).

Also of interest are the lightly damped pair of zeros near 22 Hz (140 rad/sec) and the resonant pole pair at about twice this frequency (45 Hz), which present a potential obstacle to attaining high bandwidth. The data above about 100 Hz look largely erroneous. Any controller should roll off significantly by this frequency.

The best possible explanation I have for the unpredicted system dynamics is that the umbilical supports the structure. The measured data shown here were obtained with the umbilical attached at the base of the robot. In the original robot, these cords were attached near the top of the chassis. The robot has been successfully stabilized (with similar resulting dynamics) in both configurations. Each has its own drawbacks and affect the uncontrolled plant dynamics significantly.

7.5.2 Robot Moment of Inertia Estimations and Verification

Calculating (or simply measuring) the mass of the robot pendulum-body is more straight-forward than estimating its moment of inertia. One simple way to test calculated mass and inertia parameters is to measure the frequency of oscillation of the pendulum in the downward (stable) configuration, while holding the wheels fixed. The derivation of the expected frequency given below is straightforward and uses the Lagrangian approach described in Section 7.2. Figure 7-29 below shows the geometry of the robot body, and Figure 7-30 shows data collected with the encoders as the pendulum oscillated in this stable configuration.
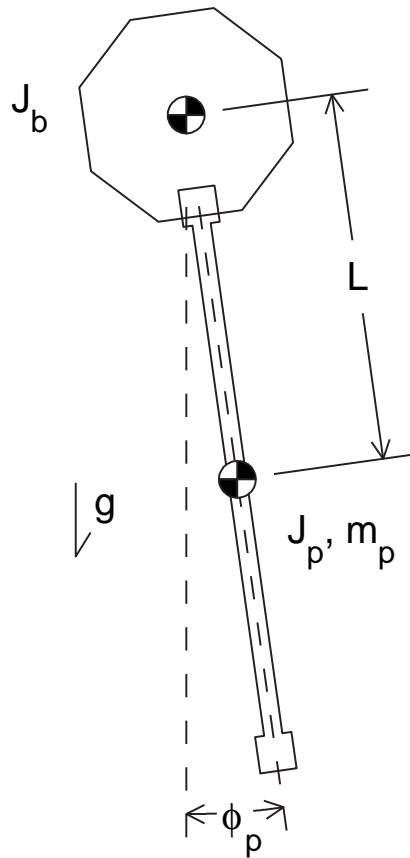
Figure 7-29: Pendulum near stable equilibrium.

The pendulum and chassis of the robot are rigidly fixed to one another. The "chassis" is by definition well-modeled as having three axes of symmetry, so that the center of mass of the chassis, J_b, is collocated with the axis of rotation. The
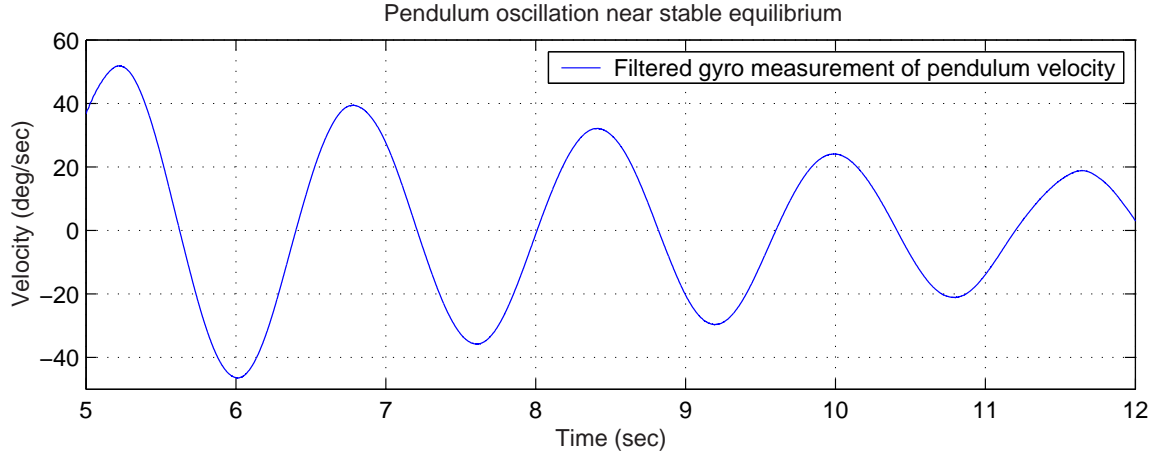
Figure 7-30: Pendulum oscillation at 0.62 Hz. The period of oscillation is about 1.61 seconds. Note that the umbilical (carrying the gyro signal) contributed significantly to the losses seen above; the data are only representative in estimating the natural frequency - not damping.

"pendulum" has a moment of inertia J_p about its center of mass, which is offset from the axis of rotation by a distance L. The kinetic co-energy of the pendulum-body is:

$$T^* = \frac{1}{2} \left(J_b + J_p + m_p L^2 \right) \dot{\phi}_p^2 \tag{7.77}$$

and the potential energy is:

$$V = -mg \cos \phi_p \tag{7.78}$$

The lagrangian, $T^* - V$, is therefore:

$$\mathcal{L} = \frac{1}{2} \left(J_b + J_p + m_p L^2 \right) \dot{\phi}_p^2 + mg \cos \phi_p \tag{7.79}$$

The equation of motion for free oscillation (without any system inputs) is given below.

$$\sum F \; = \; 0 \; = \; \frac{d}{dt} \left(\frac{\partial \mathcal{L}}{\partial \dot{\phi}_p} \right) - \frac{\partial \mathcal{L}}{\partial \phi}$$
$$= \; \left(J_b + J_p + m_p L^2 \right) \ddot{\phi}_p + mg \sin \phi_p \tag{7.80}$$

Linearizing this equation about $\phi_p = 0$:

$$0 = \ddot{\phi}_p + \frac{m_p g L}{\left(J_b + J_p + m_p L^2 \right)} \; \phi_p \tag{7.81}$$

371

Therefore, the natural frequency is:

$$\omega_n = \sqrt{\frac{m_p g L}{(J_b + J_p + m_p L^2)}} \quad [\text{rad/sec}] \tag{7.82}$$

The moment of inertia of the body is the most difficult parameter to estimate. Based on my accounting of the geometry and density of the various components of the chassis, I calculated its inertia should be in the range of $0.053 \pm .005 \; [kg \; m^2]$. We can use the measured natural frequency of approximately 0.62 Hertz (see Figure 7-30) to refine this estimate. A value of $J_b = 0.050 \; [kg \; m^2]$ yields a predicted frequency of 0.62 Hertz, as shown below. Plugging in estimated parameters values (listed in Table 7.3 on page 359), we find:

$$\omega_n = \sqrt{\frac{(1.0 \, [\text{kg}])(9.8 \, [\text{m/s}^2])(0.4 \, [\text{m}])}{(0.05 + 0.05 + (1.0)(0.4)^2) \, [\text{kg m}^2]}} = 3.9 \, [\text{rad/sec}] = 0.62 \, [\text{Hz}] \tag{7.83}$$

The other system parameters for the larger robot in Table 7.3 should be accurate to within $\pm 5\%$.

7.5.3 Matlab Simulations of Self-standing Robot

I created several MATLAB m-files before the IP robot was built to simulate the dynamic response of the robot. Of particular interest at the time were the torque requirements for achieving a self-standing robot which can begin at rest with the pendulum horizontal and lift itself to a stable upright position.

The MATLAB simulations animate the expected response of the robot, assuming perfect sensor data and a discrete execution step size equivalent to that of the dSPACE controller (i.e. 0.1 ms steps). This allowed me to test the feasibility of particular combinations of variables including motor specs, gear ratio, and mass and moment of inertia of both the robot body and wheels.

The initial prototype for the robot, shown on the left-hand side of Figure 7-31 (and in all of the earlier photos of the robot appearing in this chapter), is too large to be self-standing. The large size facilitated prototyping, however.

A smaller prototype, shown at the right of Figure 7-31, was also developed and stabilized. The chassis of this robot is not large enough to hold the servo amps and
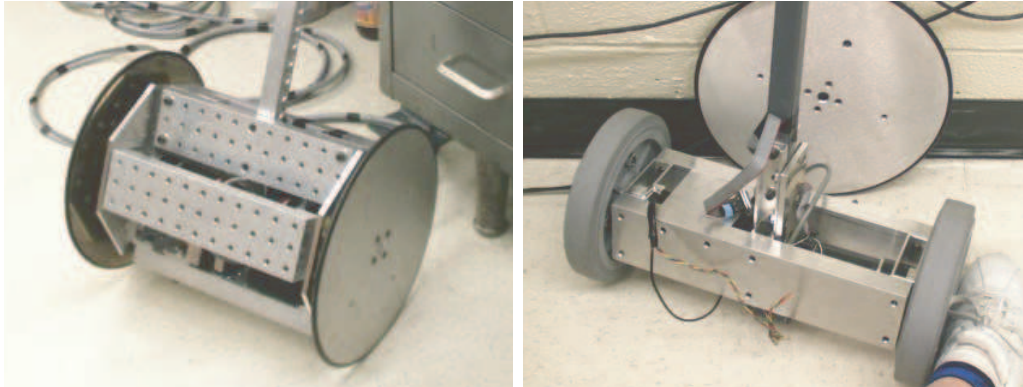
Figure 7-31: "Big DIPR" and "Little DIPR" robots. The larger robot, at left, is the one described and analyzed in the rest of text in this chapter. The smaller prototype, however, more closely matches the specifications assumed in the MATLAB stand-up simulation code described in this section. Both versions have been successfully controlled near the upright (unstable) equilibrium point, while neither is capable of self-standing. The larger chassis is a more realistic size for an autonomous robot, but it is much too large to stand up from rest. The larger robot is not autonomous as of this writing, but its onboard servo amps still require a chassis and wheel size on the order of this (larger) size.

accompanying filter on-board, however. Also, the inertia of the wheels would need to be increased to make the robot self standing. A wheel from the larger robot is shown behind the smaller robot to help the reader gage how the two compare in size.

The final version of the robot uses the same chassis developed for the initial (larger) prototype. It is not designed to stand on its own from rest, and there are no plans at present to modify it to be able to do so. MATLAB code and images from an example animation are presented in Appendix G on page 429.

7.5.4 Commanding Voltage vs. Current

The servo amps which power each motor are capable of commanding either current or voltage. Generally, current control is preferable in most motor control applications, since this simplifies the dynamics of the system.

The torque is directly proportional to current:

$$\tau = K_t \, i \tag{7.84}$$

If we command voltage instead, the total voltage across the armature will include both the commanded voltage and a back electromotive force (back emf). The back emf is proportional to the rotational velocity of the motor armature, and it acts to retard the motion of the armature:

$$
\begin{aligned}
V_{back} &= K_t \, \dot{\theta}_p \\
\tau &= K_t \, \frac{(V_{in} - V_{back})}{R}
\end{aligned}
\tag{7.85}
\tag{7.86}
$$

In other words, the back emf is inherently fed back to the commanded voltage in a system with voltage control, and this adds damping to the system.
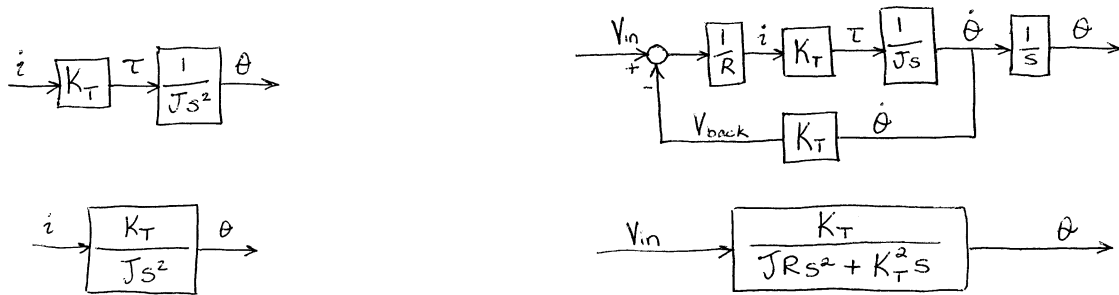
Figure 7-32: Block diagrams of current and voltage control. The inductance of the motor is neglected here.

The block diagrams in Figure 7-32 illustrate the difference between these two control methods for an idealized system which consists of a motor driving an inertial load, J. The diagrams on the left-hand side of Figure 7-32 show the dynamics of the current controlled system. The transfer function from current to motor output angle, θ, indicates that the acceleration of the inertia will be directly proportional to the current:

$$\frac{\theta(s)}{I(s)} = \frac{K_t}{Js^2} \tag{7.87}$$

At the right in Figure 7-32 are block diagrams of the same plant with voltage as the commanded input. For this system, one of the poles of the transfer function from voltage to motor angle is no longer at the origin:

$$\frac{\theta(s)}{I(s)} = \frac{K_t}{(JRs + K_T^2)s} \tag{7.88}$$

The denominator of Equation 7.87 consists solely of an inertial term. By contrast, Equation 7.88 contains both inertial and damping terms. The back emf creates a damping term in the characteristic equation for the system in the voltage-controlled system.

The controller for the IP robot will include damping anyway, however. Also, the quantization of the motor encoders makes it somewhat difficult to estimate the velocity of the motor accurately, as discussed in Section 7.1.4. It is therefore not obvious whether the damping effects of voltage control are unwanted or if the added damping, if properly taken into account, will help the controller run more smoothly.

I initially designed a controller for the system using current control and then tested the same controller (with gains scaled by R) using voltage control. Any difference in performance was not significant. The experimental transfer functions shown in Sections 7.7, 7.6 and 7.8 were all obtained using voltage control.

It is not surprising that the the two control methods result in nearly identical dynamics, since the inertia of the pendulum and wheels are relatively large. The larger the inertia in the system, the larger the time constant ($\frac{JR}{K_T^2}$) of the voltage-controlled system. As the associated pole gets closer and closer to the origin, the dynamics of the voltage-controlled system become closer to those of the current-controlled system (with both poles at the origin).

We can quickly estimate the magnitude of the effects of the plant dynamics by using the numeric solutions to the transfer functions derived in Section 7.3. Below, we will compare the transfer function from commanded current to pendulum velocity ($\dot{\theta}_p(s)/I(s)$) with the TF from commanded voltage to pendulum velocity ($\dot{\theta}_p(s)/V(s)$). We can begin with Equations 7.37 and 7.44, noting that the desired angular velocity

output is just the derivative of angular position:

$$\frac{\dot{\theta}_p(s)}{I(s)} \approx \frac{-0.33s}{(s^2 - 16.0)} \tag{7.89}$$

$$\frac{\dot{\theta}_w(s)}{I(s)} \approx \frac{+0.25(s^2 - 14.5)s}{(s^2 - 16.0)} \tag{7.90}$$

Combining these two equations,

$$\frac{\dot{\theta}_w(s)}{\dot{\theta}_p(s)} \approx \frac{-0.77(s^2 - 14.5)}{s^2} \tag{7.91}$$

Recall that the back emf will be proportional to the motor velocity, $\dot{\theta}_m$:

$$\dot{\theta}_m = \dot{\theta}_w - \dot{\theta}_p \tag{7.92}$$

$$= \left(\frac{\dot{\theta}_w(s)}{\dot{\theta}_p(s)} - 1\right) \dot{\theta}_p \tag{7.93}$$

$$= \left(\frac{-0.77(s^2 - 14.5)}{s^2} - 1\right) \dot{\theta}_p \tag{7.94}$$

$$= \frac{-1.77(s^2 - 6.72)}{s^2} \tag{7.95}$$

Combining the preceding equations, we derive the block diagram for this system which is shown in Figure 7-33.
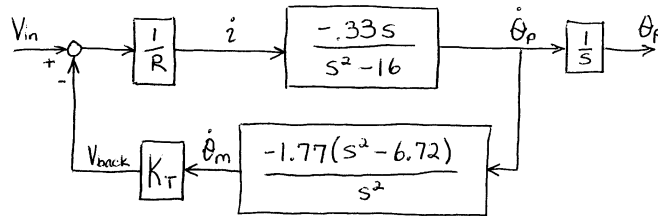
Figure 7-33: Block diagram of predicted voltage-controlled IP robot.

The resistance of the Maxon motor used in the robot is $R = 0.647 \, \Omega$, and the back emf constant is $K_T = 0.0263$ Volt/rad/s. (Motor parameters are listed in Appendix F on page 425.) The block diagram above simplifies to the following transfer function:

$$\frac{\dot{\theta}_p(s)}{V_{in}(s)} = \frac{-0.51s^2}{s^3 + 0.056s^2 - 16.0s - 0.378} \tag{7.96}$$

The poles for this system are at -4.02 rad/s, +3.98 rad/s and 0.02 rad/s. Over the frequency range in which the transfer function was measured (see Figures 7-27 and

??), the theoretical plant dynamics under voltage control should vary little from that under current control. The transfer functions shown in Figure 7-34 vary by a factor of R in magnitude (which should obviously be taken into account by scaling all gains for the control output to the motor), but they are otherwise very similar.
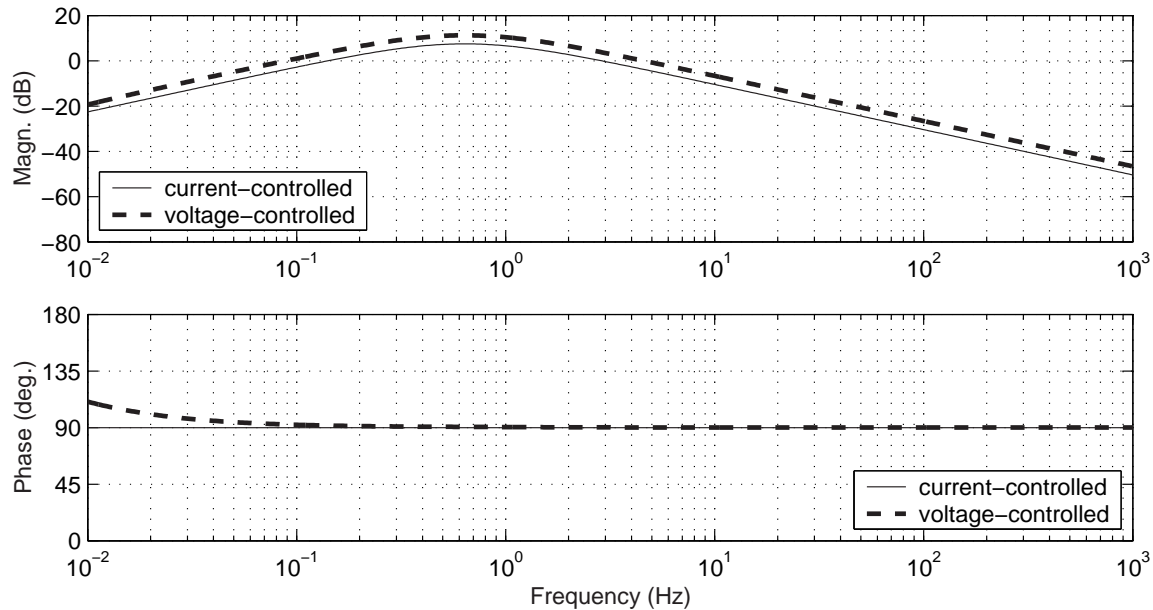
Figure 7-34: Predicted TFs with current vs. voltage control $(\dot{\theta}_p(s)/V(s))$. The predicted transfer function from commanded motor input (current or voltage) to pendulum angle (in degrees) do not differ significantly for the inverted pendulum system.

7.5.5 High-pass filtering of wheel position

The measurement of the motor position includes a first order high-pass digital filter with a time constant of 5 seconds. This in turn affects the estimation of wheel position, since $\theta_w = \theta_m + \theta_p$. (See Equation 7.92.) Recall that the estimation of θ_p comes from complementary filtering of the gyro and accelerometer and is completely independent of the motor encoder measurement.

The high-pass filter was added because the umbilical interferes significantly with the mobility of the robot. As a result, the effect of an error in robot position on the

control effort is that of a spring and dashpot in series, rather than that of a spring alone. This effect is described further in the caption for the transfer function from voltage to wheel position on page 382.
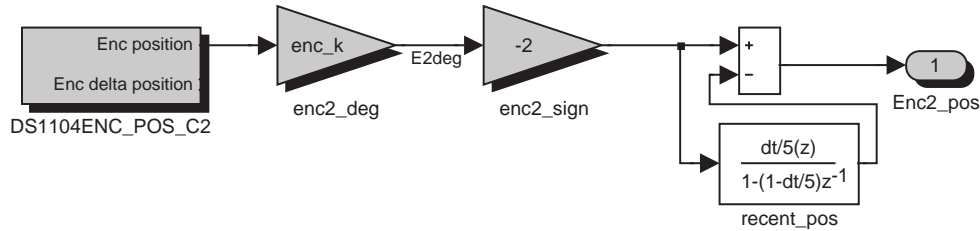
Figure 7-35: High-pass filtering of wheel position.

Figure 7-35 shows the Simulink blocks which implement this filtering in the control model. The entire encoder-filtering subsystem is shown on page 438 of Appendix H.

7.5.6 Damage of Motor Encoder

In the process of repairing the motors, one of the encoders was damaged. As a result, the final version of the controller uses a single encoder to estimate motor position and velocity. The robot has been tested using both encoders, which allows for steering from a potentiometer input. The loss of an encoder has not had a significant effect on performance, although both motors must now be controlled in tandem.

7.6 Experimental Frequency Response Data

The next five pages shows experimental Bode plots for the robot. Data were obtained using a Simulink-driven dynamic signal analyzer within the dSPACE model [114, 113]. The step size for the Simulink model was 0.1 ms, which causes a half-sample delay of 0.05 ms in both the measured transfer functions shown and in the actual dynamics of the system under digital control.

The controller was initially developed without access to such data. The data were all obtained while the plant was controlled, so the system would remain stable. Subsequent fine-tuning was then done once the actual dynamics had been measured.

378

Figure 7-36: Experimental transfer function #1: $\theta_p(s)/V_o(s)$. This is the transfer function from commanded voltage to the motor, $V_o(s)$, to measured pendulum angle, $\theta_p(s)$ (in units of degrees). The pendulum angle measurement is created through complementary filtering of signals from a rate gyro (accurate at high frequency) and an accelerometer (accurate at low frequency). Both the gyro and accelerometer signals are additionally smoothed through low-pass filtering. The output of the transfer function above corresponds to the final, measured pendulum angle: it includes the effects of these filters and of the discretization of the (digital) controller (with a time step of 0.1 ms). The controller for the robot consists of the sum of scaled versions of TF#1, TF#2, TF#3 and TF#4. The scaling factor for this transfer function (TF#1) is: $G \times PDval = 0.05 \times 18 = 0.9$

Figure 7-37: Experimental transfer function #2: $\dot{\theta}_p(s)/V_o(s)$. This is the transfer function from commanded voltage to the motor, $V_o(s)$, to measured pendulum velocity, $\dot{\theta}_p(s)$ (in units of deg/sec). The pendulum angular velocity is measured with a rate gyro. The gyro signal is smoothed through low-pass filtering. The output of the transfer function above corresponds to the final, measured pendulum velocity: it includes the effects of low-pass filtering and of discretization. The controller for the robot consists of the sum of scaled versions of TF#1, TF#2, TF#3 and TF#4. The scaling factor for this transfer function (TF#2) is: $G \times Dval \times PDval = 0.05 \times 0.3 \times 18 = 0.27$
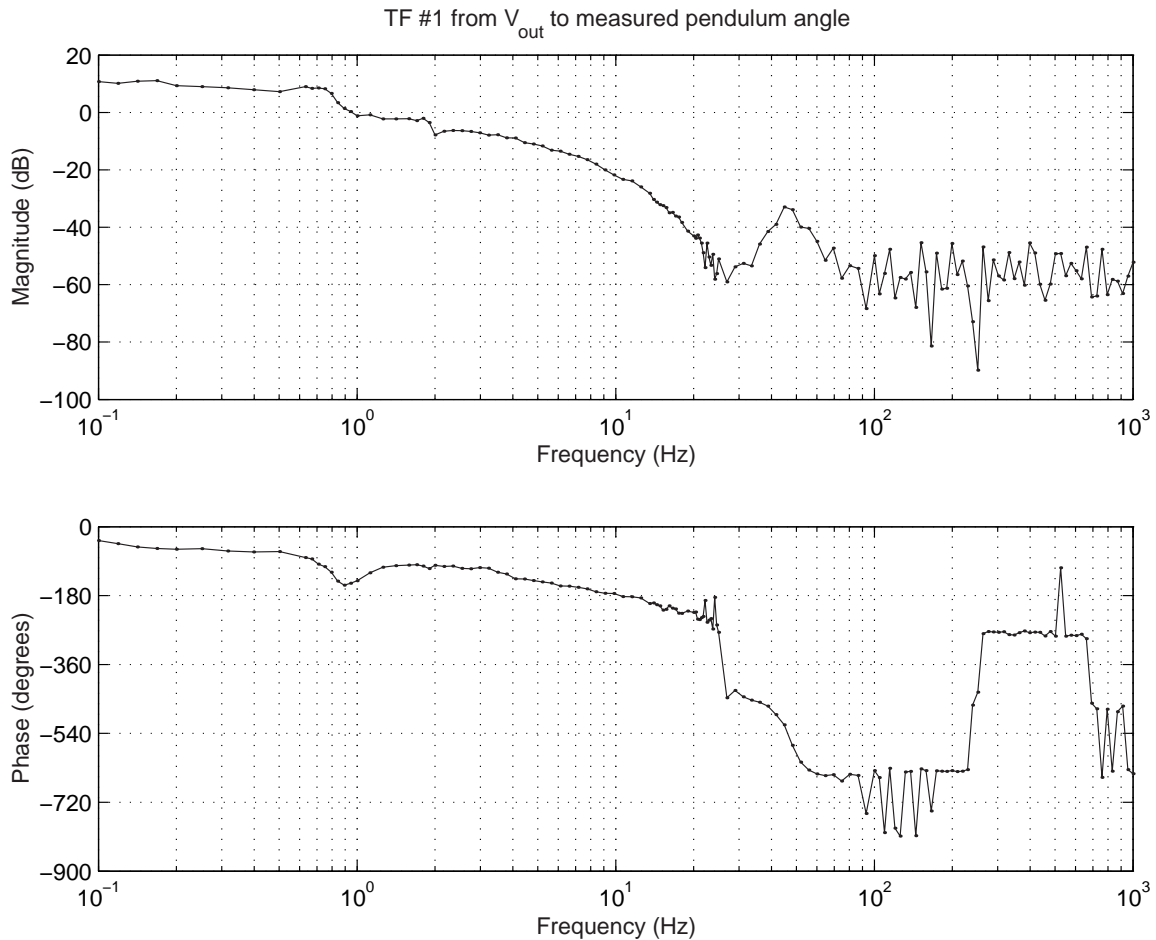
Figure 7-38: Experimental transfer function #3: $\dot{\theta}_w(s)/V_o(s)$. This is the transfer function from commanded voltage to the motor, $V_o(s)$, to measured wheel velocity, $\dot{\theta}_w(s)$ (in units of deg/sec). The angular velocity of the wheel is the difference between the measured velocities of the motor and pendulum: $\dot{\theta}_w = \dot{\theta}_m - \dot{\theta}_p$. The gyro signal is smoothed through low-pass filtering. The reciprocal of the time between successive encoder counts is proportional to motor velocity, $\dot{\theta}_m = K/\Delta t_{ct}$. This quantized estimate of motor velocity is then filtered (low-pass). The output of the transfer function above corresponds to the final, measured wheel velocity: it includes the effects of quantization, low-pass filtering and discretization. The controller for the robot consists of the sum of scaled versions of TF#1, TF#2, TF#3 and TF#4. The scaling factor for this transfer function (TF#3) is: $G = 0.05$
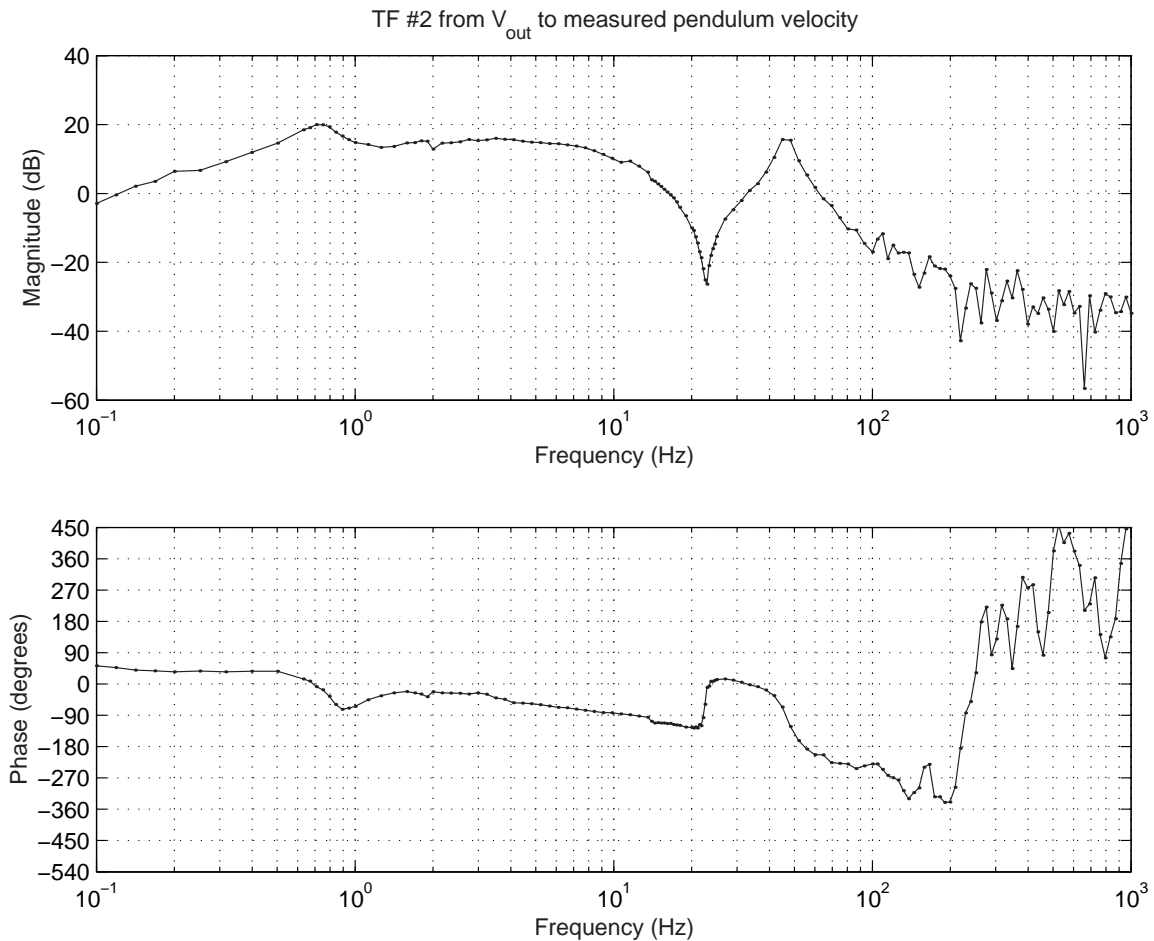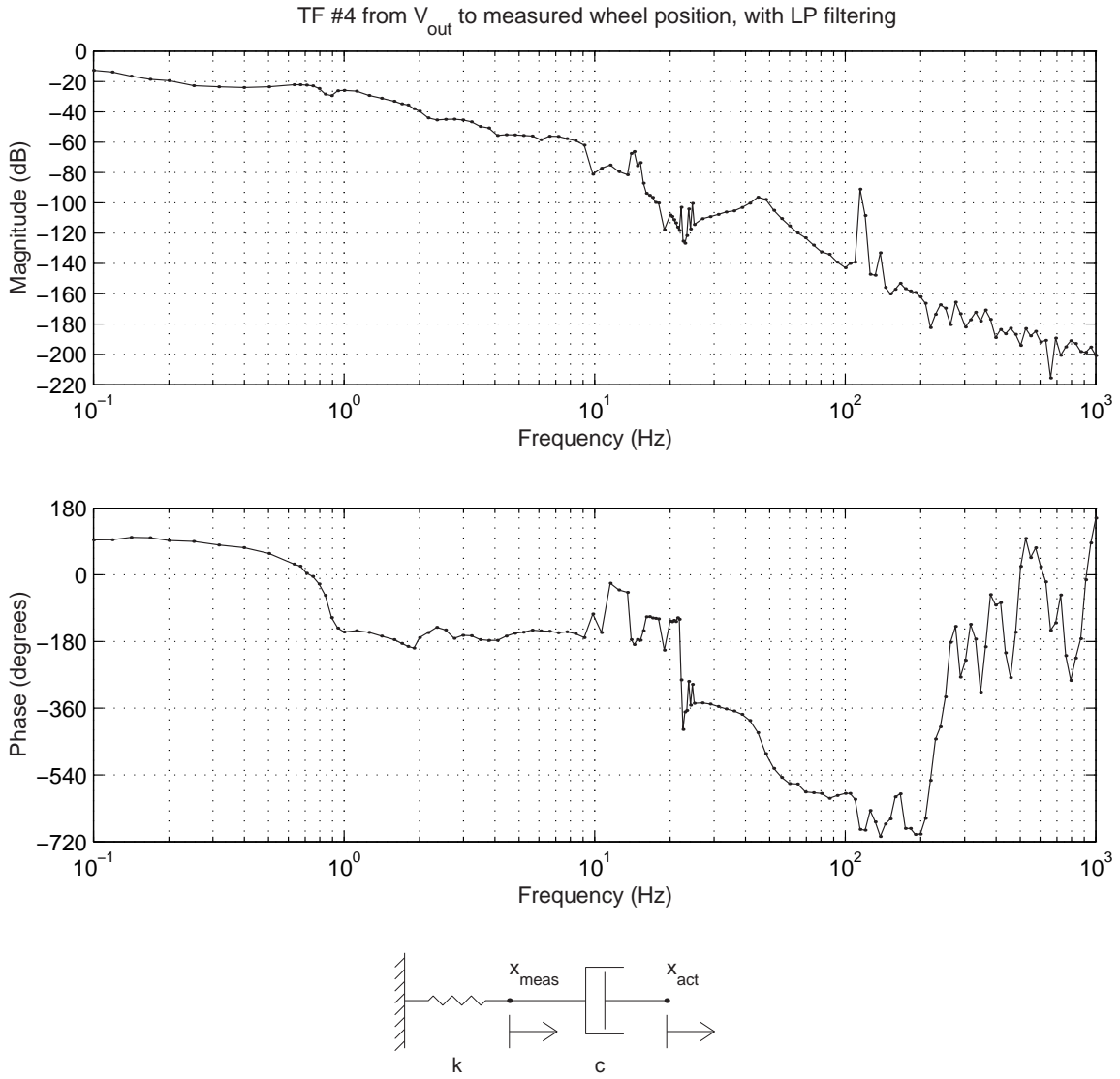
Figure 7-39: Experimental transfer function #4: $\theta_w(s)/V_o(s)$. This is the transfer function from commanded voltage to the motor, $V_o(s)$, to measured wheel position, $\theta_w(s)$ (in units of degrees). This term is included in the controller to prevent the robot from wandering. The *steering inputs* to the robot command *velocity*, however - not position. Therefore, the transfer function above filters wheel position with a first-order (high-pass) filter, so the DC measurement is zero. (The time constant is 5 seconds.) The schematic below the Bode diagram illustrates a mechanical analogy to the filtering used. If the actual wheel position (x_{act}) moves, the "measurement" at x_{meas} will die away with a time constant of $\tau = \frac{c}{k}$. $\left[\frac{x_{meas}(s)}{x_{act}(s)} = \frac{cs}{(cs+k)}\right]$ The scaling factor for this transfer function (TF#4) is small: $Kp \times G = 0.2 \times 0.05 = 0.01$
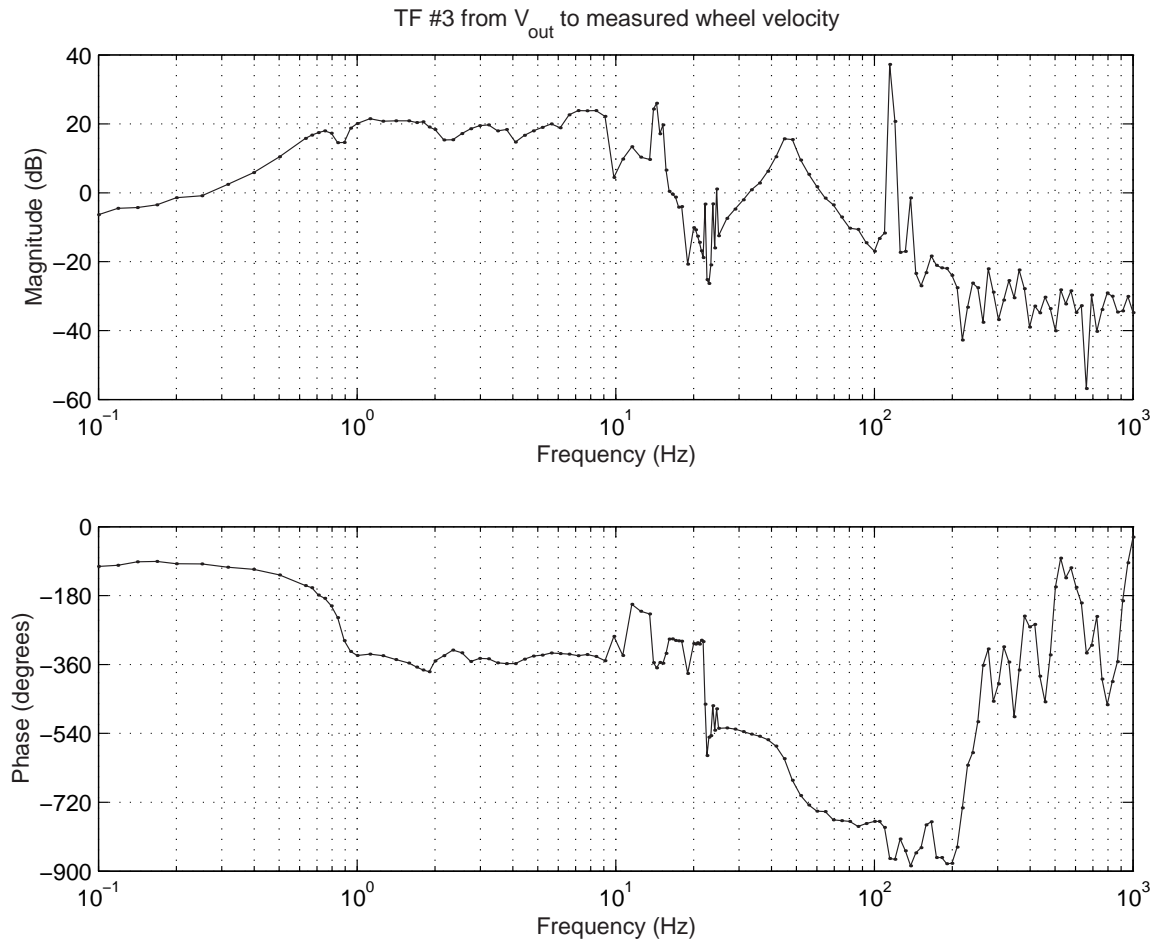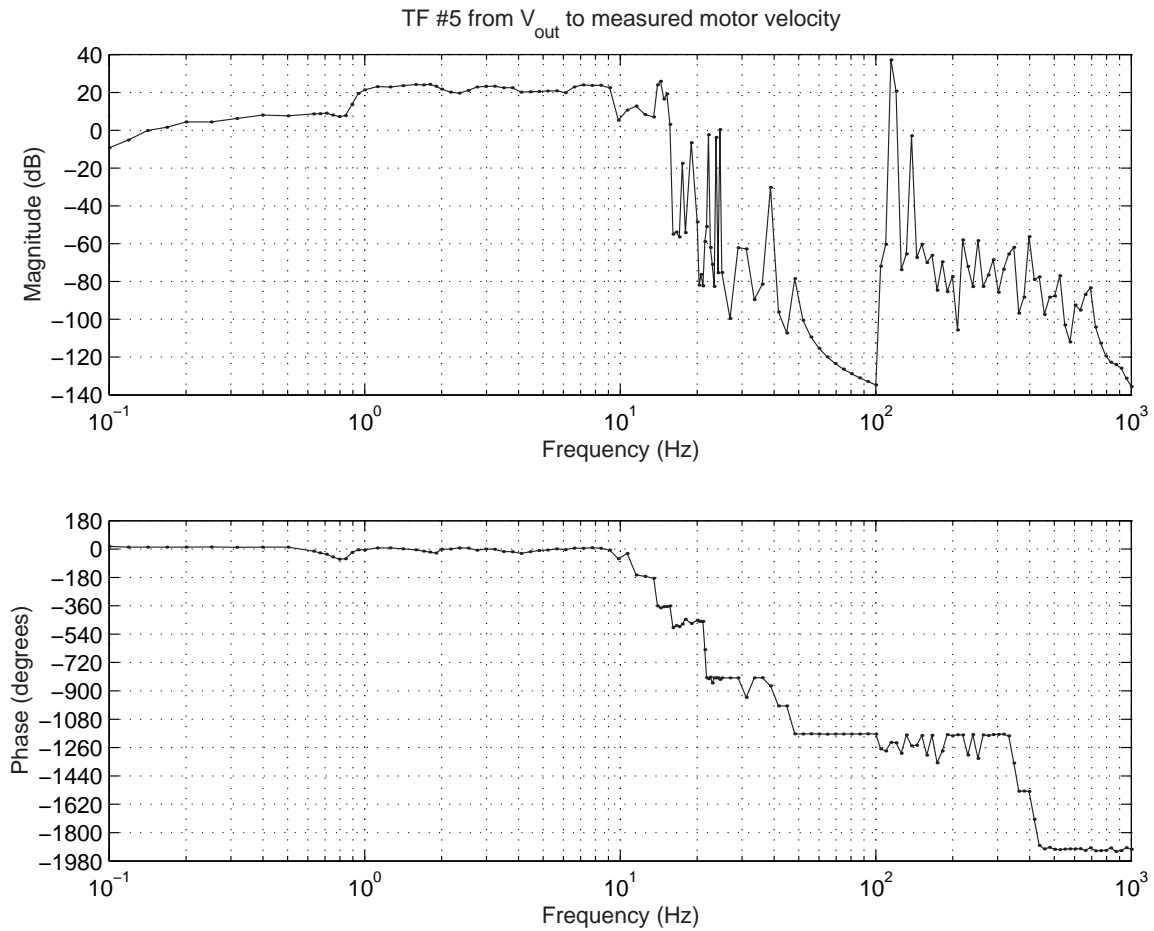
Figure 7-40: Experimental transfer function #5: $\dot{\theta}_m(s)/V_o(s)$. This is the transfer function from commanded voltage to the motor, $V_o(s)$, to measured motor velocity, $\dot{\theta}_m(s)$ (in units of deg/sec). This transfer function contributes to TF#3 (see Figure 7-38), and it is included primarily to illustrate how noisy this particular measurement is above 10 Hz. This transfer function is not as repeatable as the others, and it is also somewhat amplitude dependent! Obtaining a reasonable estimate of motor velocity is a significant challenge, due to the effects of quantization and backlash. These issues are described in detail in the text.

7.7 Controller Design

As previously mentioned, the controller for the robot was developed by forming an inner loop to command the wheel velocity and an outer loop on the pendulum angle. This approach was suggested by my advisor, Prof. Trumper, after my initial attempts at using state space methods to design the controller resulted in excitation of a significant resonance along the length of the pendulum.

With this logical structure in place, it was not difficult to tweak the gains to obtain a stable system. This then allowed me to obtain the experimental transfer functions which were presented on the preceding sections. I then used MATLAB to combine the transfer functions with appropriate weighting to simulate the dynamics of a number of controllers which were tested. The resulting controller is essentially a state space controller, although it was not designed using state space methods.

The transfer functions were particularly useful in explaining the resonance I was running into whenever I tried to push up the bandwidth of the controller. For example, Figure 7-38 on page 381 shows the transfer function from voltage to wheel velocity. There is a significant resonance at around 44 Hz which is seen in all four of the transfer functions to the state variables. This might plausibly represent a mode in the mechanical structure of the chassis.

More mysterious (and troubling) is a sharp peak just above 100 Hz, which was not entirely repeatable in magnitude. As this appears only in the transfer functions for the wheel (position and velocity), and not in those for the pendulum, it may be possible that this resonance is related to the quantization of the encoder measurement. This purely speculation, however.

I filtered the output to the motors through a discrete low-pass filter with an effective time constant of 0.05 seconds (3.2 Hz) to roll off the loop transmission to push the resonance near 100 Hz below unity. Figures 7-41 and 7-42 show Nyquist diagrams based on the loop transmission obtained by adding the transfer functions on the pages 379 through 7-39 with the weightings necessary to implement the state space controller.
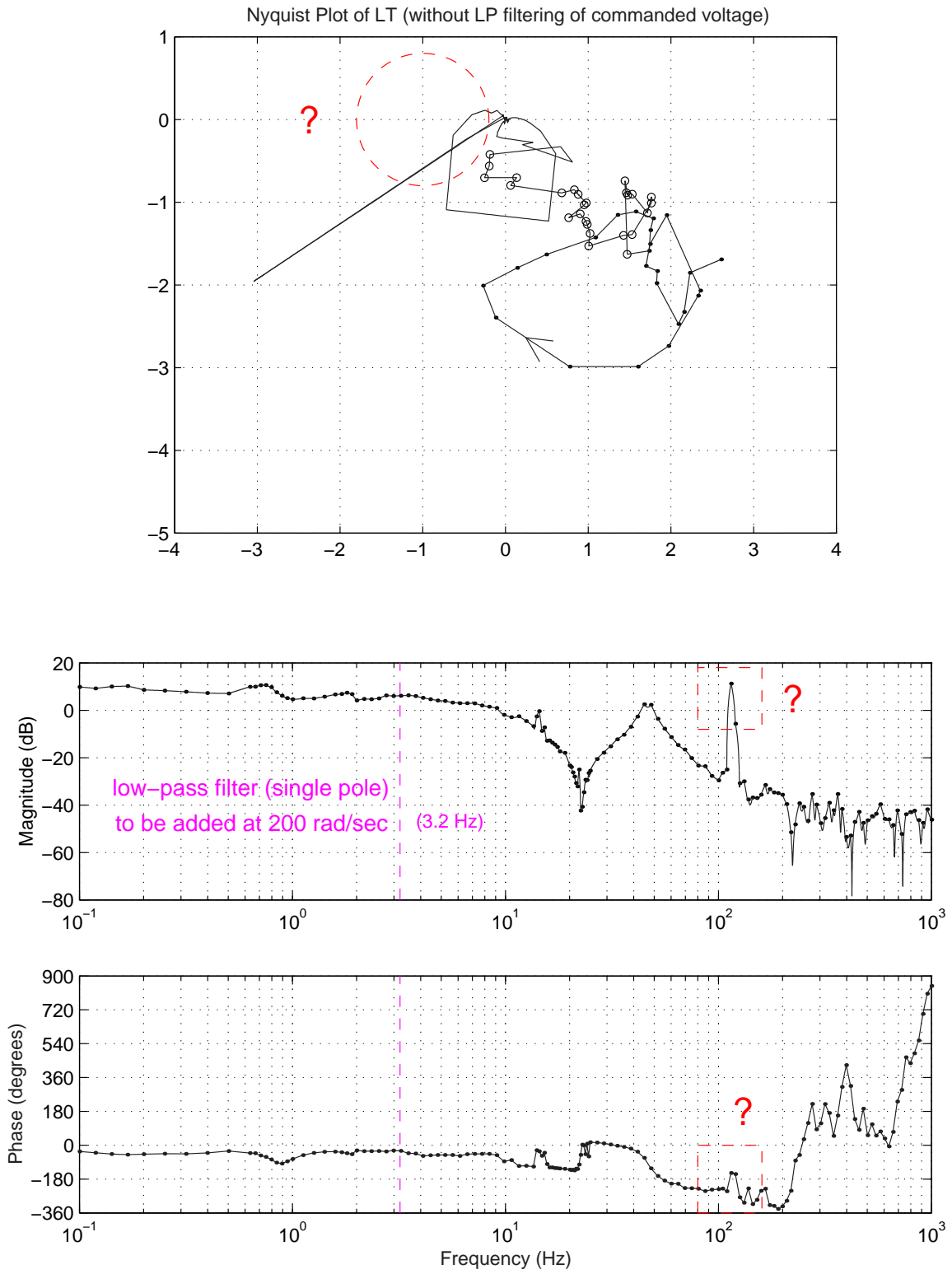
Figure 7-41: Nyquist and Bode plots for robot and controller (without LP filter)
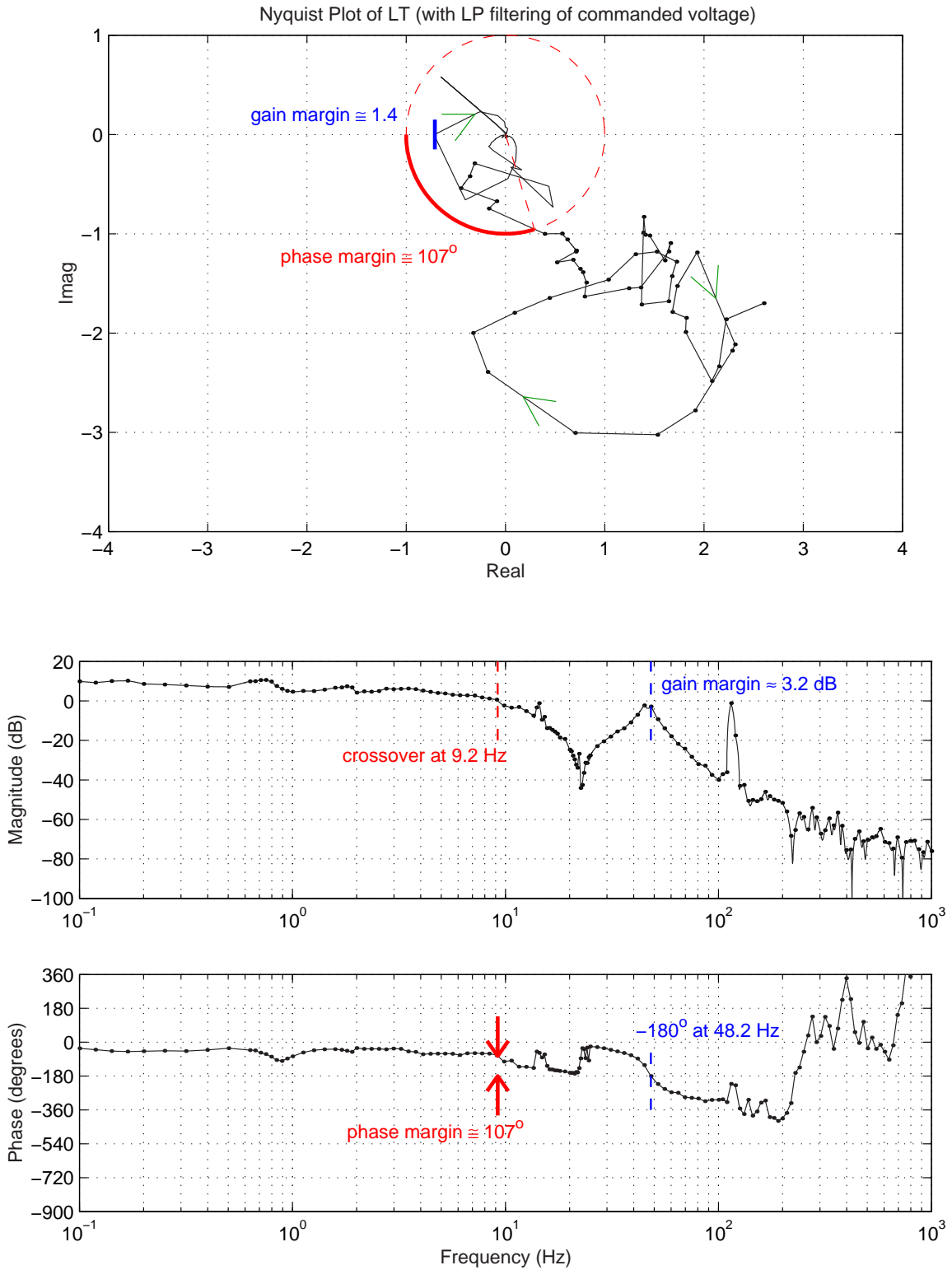
Figure 7-42: Nyquist and Bode plots for robot and controller (with LP filter). A 1st-order LP filter with a pole at 20.0 rad/s (3.2 Hz) is to be added here.

The Simulink model of the control is documented in Appendix H on page 433. One can derive the following state space equation from the inner and outer loop structures in this model:

$$V_{motor} = [\ .90 \quad .27 \quad .05 \quad .01\ ] \begin{bmatrix} \theta_p \\ \dot{\theta}_p \\ \theta_w \\ \dot{\theta}_w \end{bmatrix} \tag{7.97}$$

Figure 7-42 also shows a Bode plot of the measured loop transmission. The gain and phase margins of the system are labelled on the plot.

The system was much less prone to vibration after this low-pass filter was added. Both frequency and time response data for the controlled system are provided in next sections.

7.8 Experimental Closed-loop Performance

This section documents both the time (below) and frequency (p. 395) responses of the controlled inverted pendulum system. Data are also provided on pages 402 and fig:steppoke2b which compare the impulse responses of the current- and voltage-controlled systems.

7.8.1 Time Response Data

Figures 7-43 and 7-44 show impulse response data for the system in response to a sharp tap (by hand) applied near the pendulum tip and near the wheel axis, respectively. Figures 7-45 through 7-49 show step response data.

Each step response was generated by inputting a step to the reference angle for the pendulum. Theoretically, an offset in pendulum angle should correspond to a particular (constant) velocity for the robot, as discussed in first few pages of this chapter. The umbilical cords influence the dynamics of the system significantly, however, and do not allow the robot to roll freely. These bulky cords are quite problematic in the design, as previously mentioned.
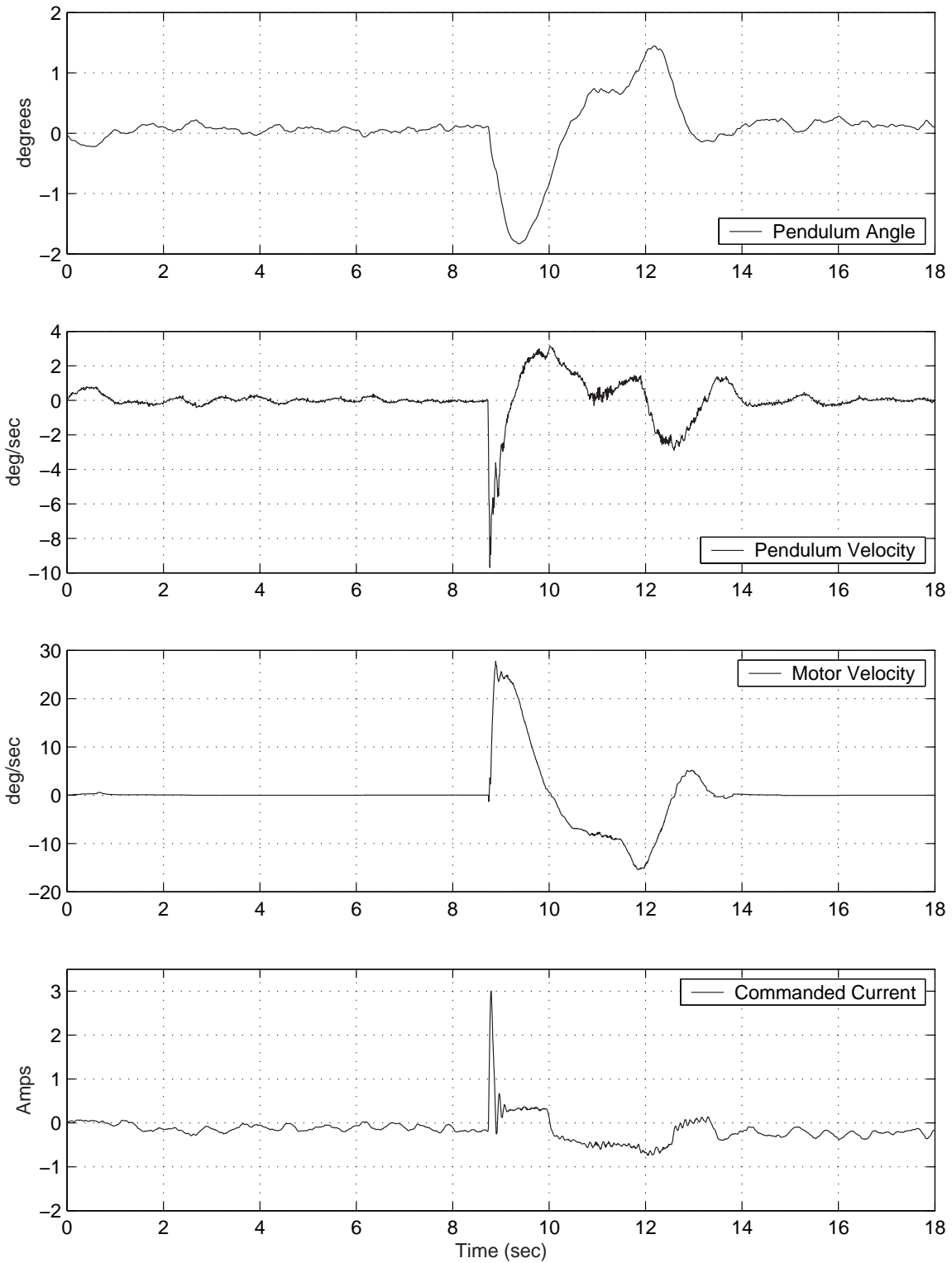
Figure 7-43: Transient response to impulse disturbance at pendulum tip (with excitation of mode near 0.6 Hz).
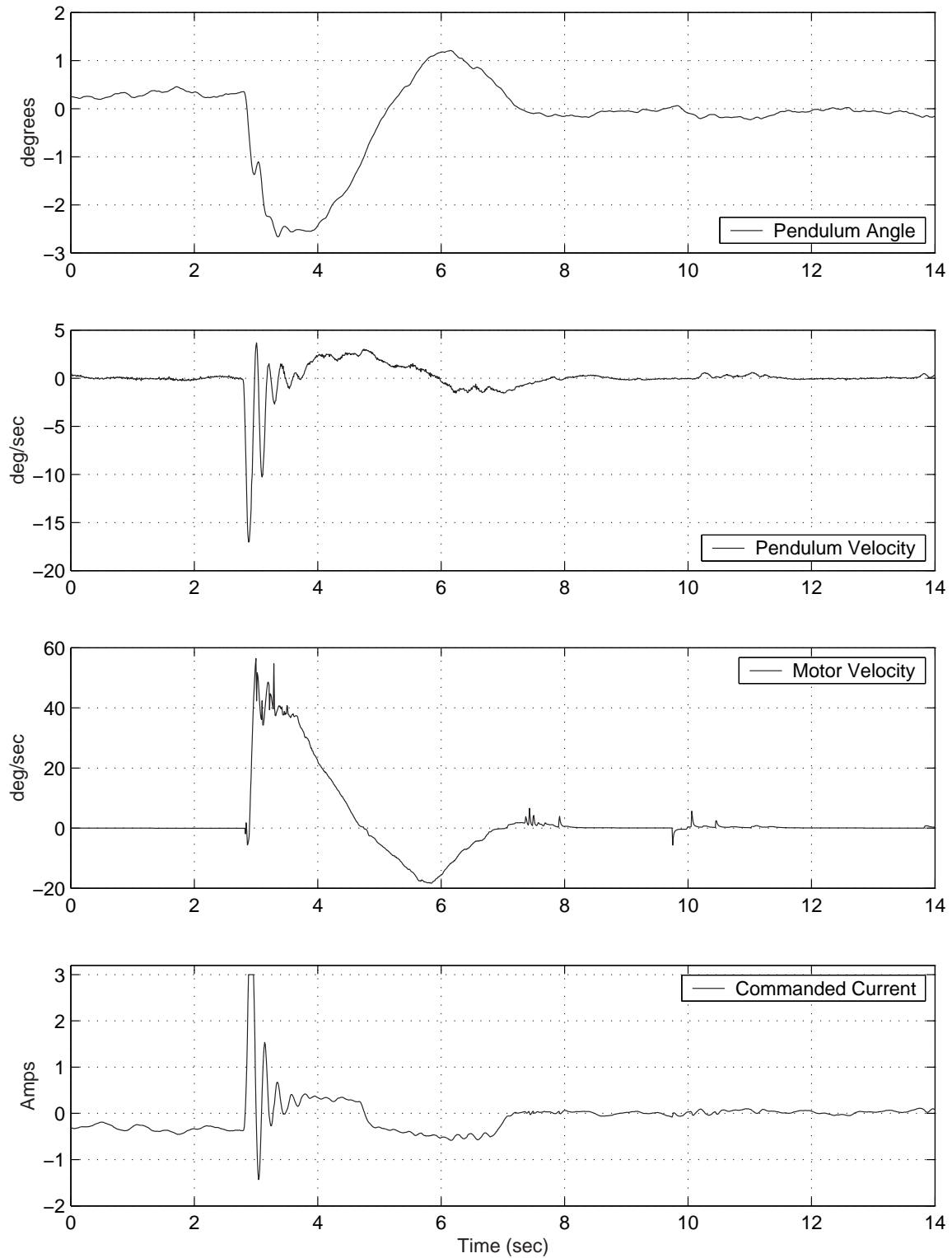
Figure 7-44: Transient response to impulse disturbance at pendulum tip (with excitation of mode near 5 Hz).
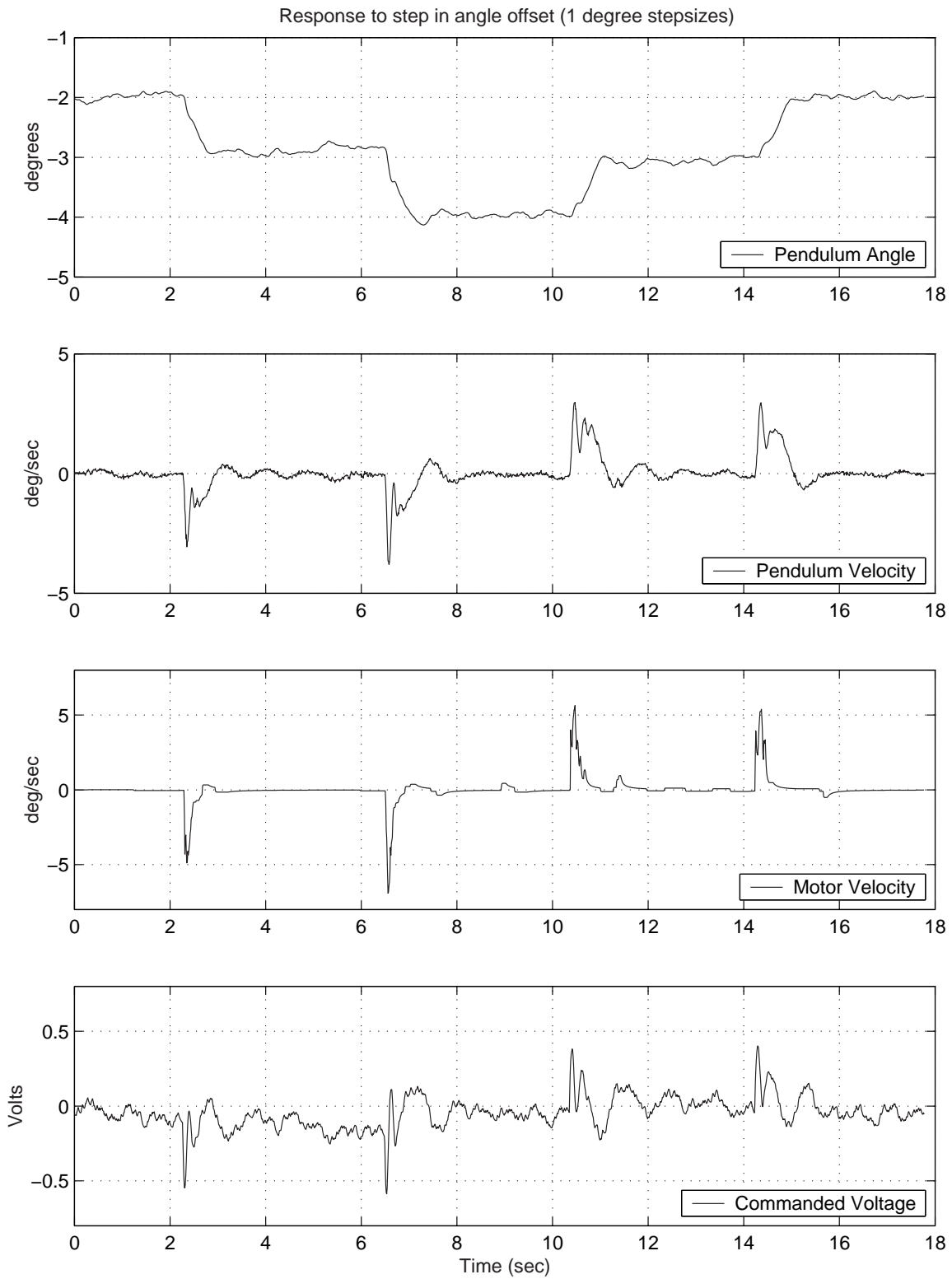
Figure 7-45: Experimental responses to a 1-degree step in offset angle.
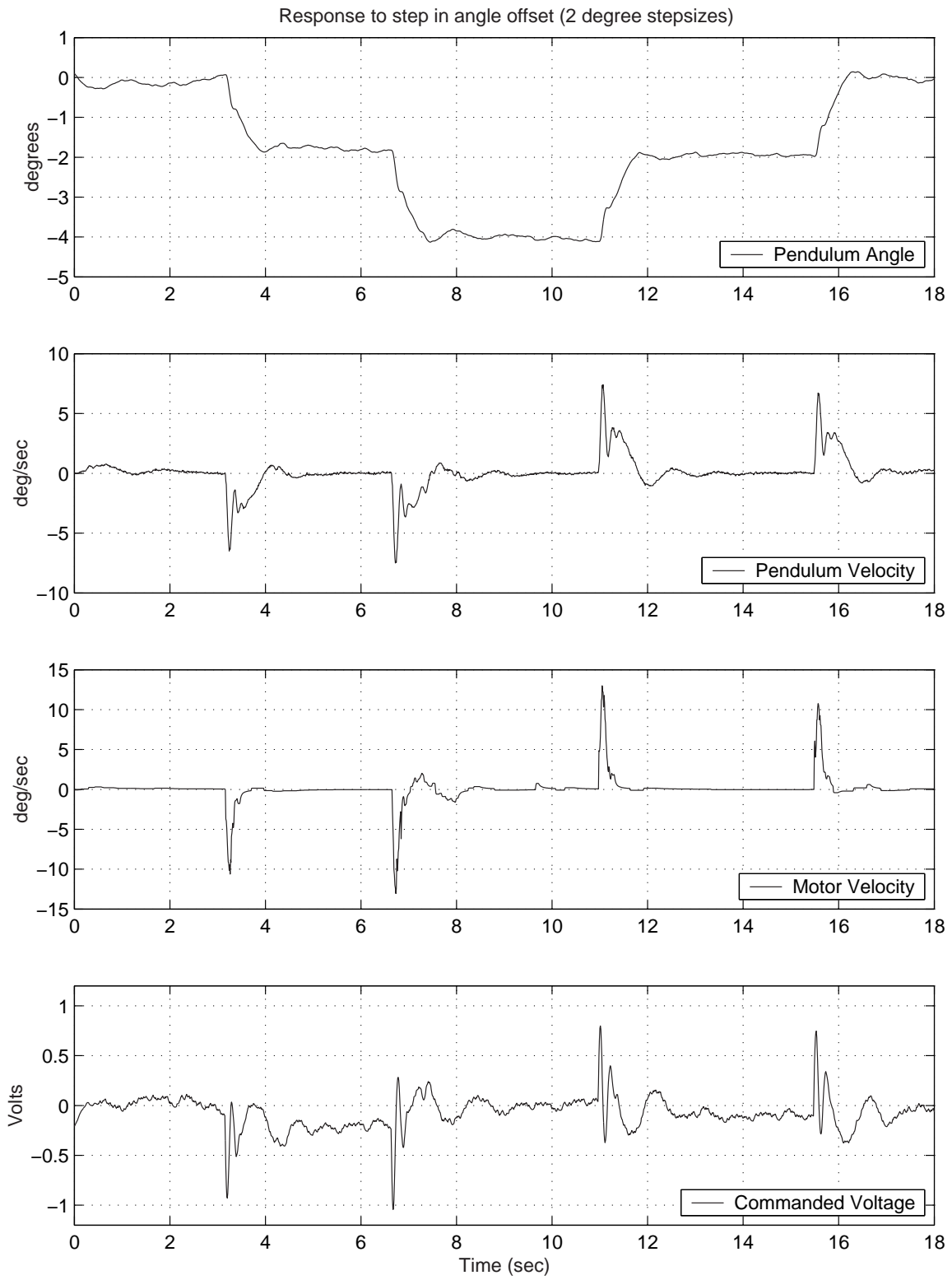
Figure 7-46: Experimental responses to a 2-degree step in offset angle.
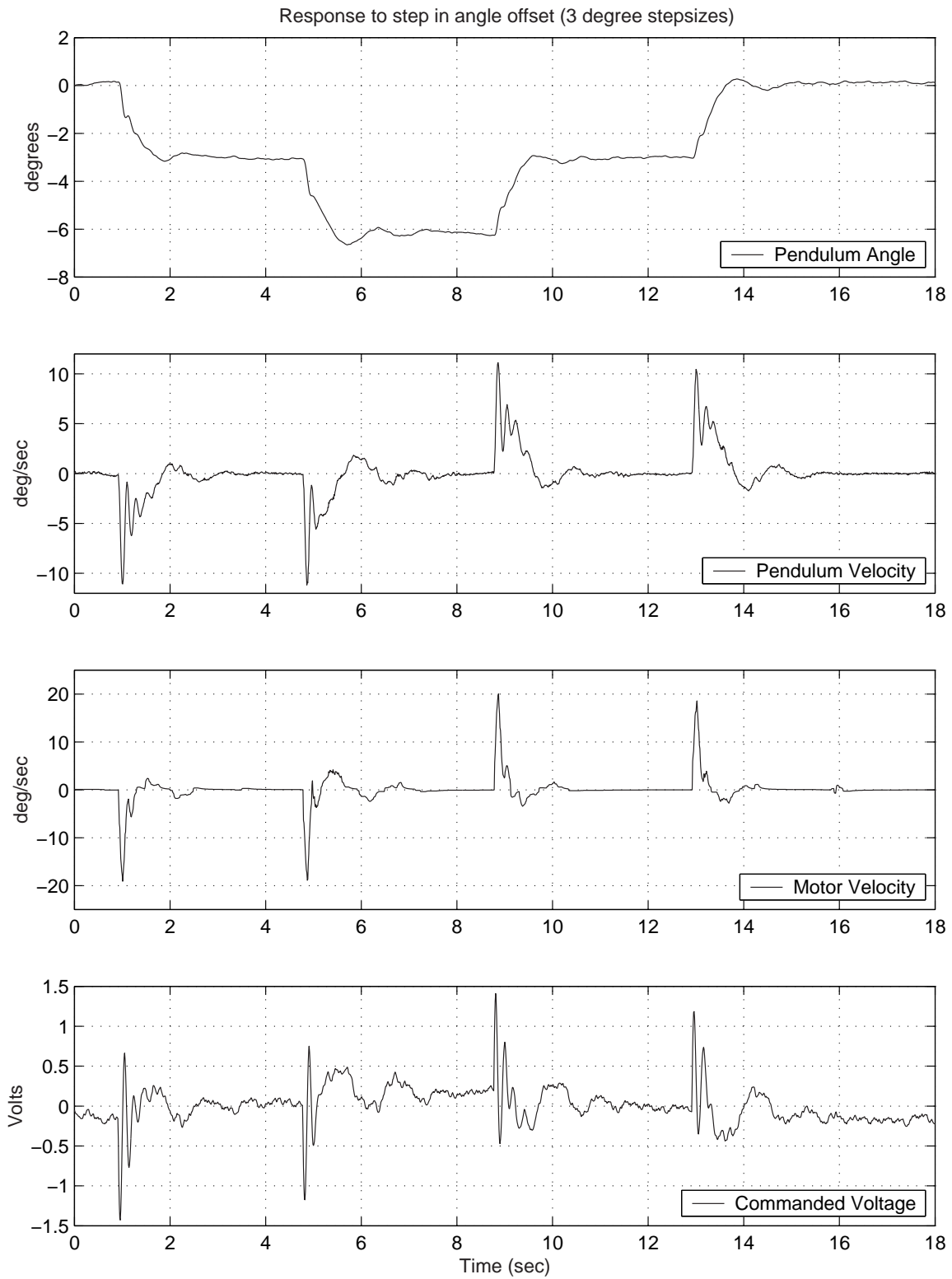
Figure 7-47: Experimental responses to a 3-degree step in offset angle.
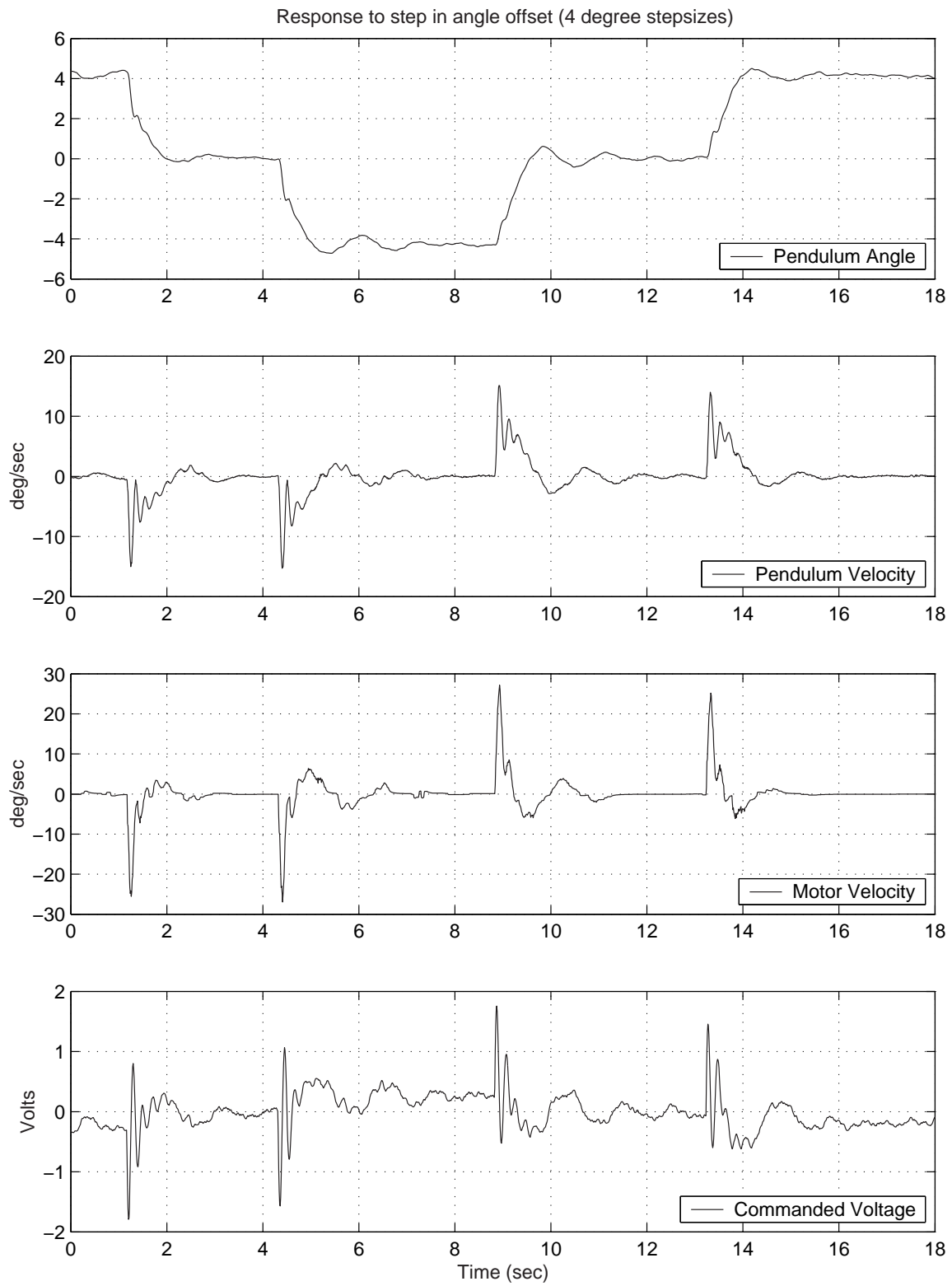
Figure 7-48: Experimental responses to a 4-degree step in offset angle.
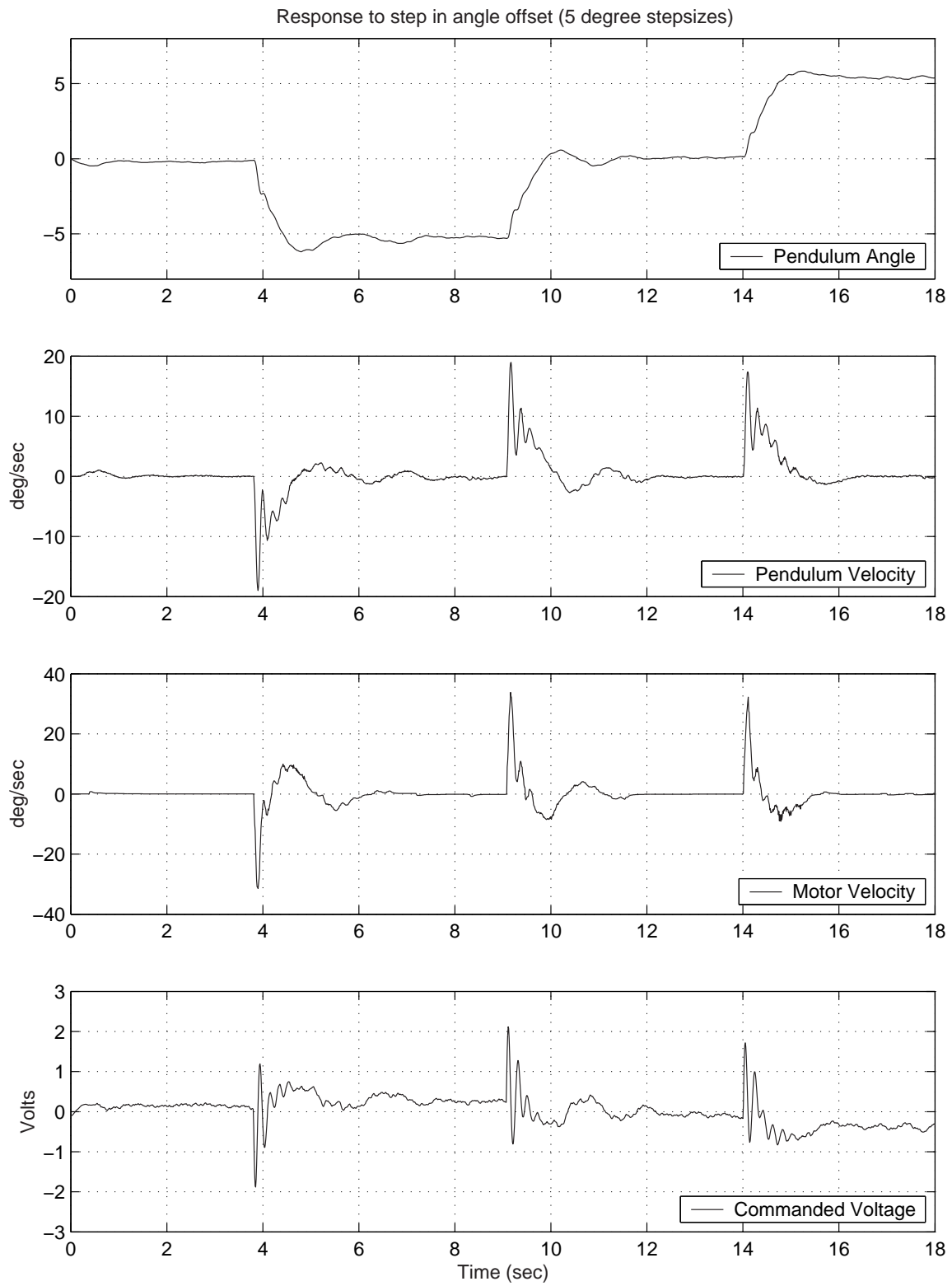
Figure 7-49: Experimental responses to a 5-degree step in offset angle.

394

7.8.2   Closed-Loop Frequency Response Data

The next few pages provide measured transfer functions of the controlled plant. This system has multiple outputs of interest, namely both pendulum angle and wheel velocity. The pendulum angle is of more importance in maintaining stability, and the controller begins to lose authority over the pendulum angle after about 0.5 Hz. (i.e. near the natural frequency of the free pendulum) Crossover for the loop transmission occurs near 7.5 Hz.

7.8.3   Data Comparing Current Control and Voltage Control

As mentioned in Section 7.5.4, the inertias involved in the system are large enough that one would expect little difference in performance when the system is run under current control rather than voltage control. Figure 7-56 on page 402 shows the transient response to a disturbance applied at the tip of the pendulum. Figure 7-57 on page 403 provides similar data for the voltage-controlled system.
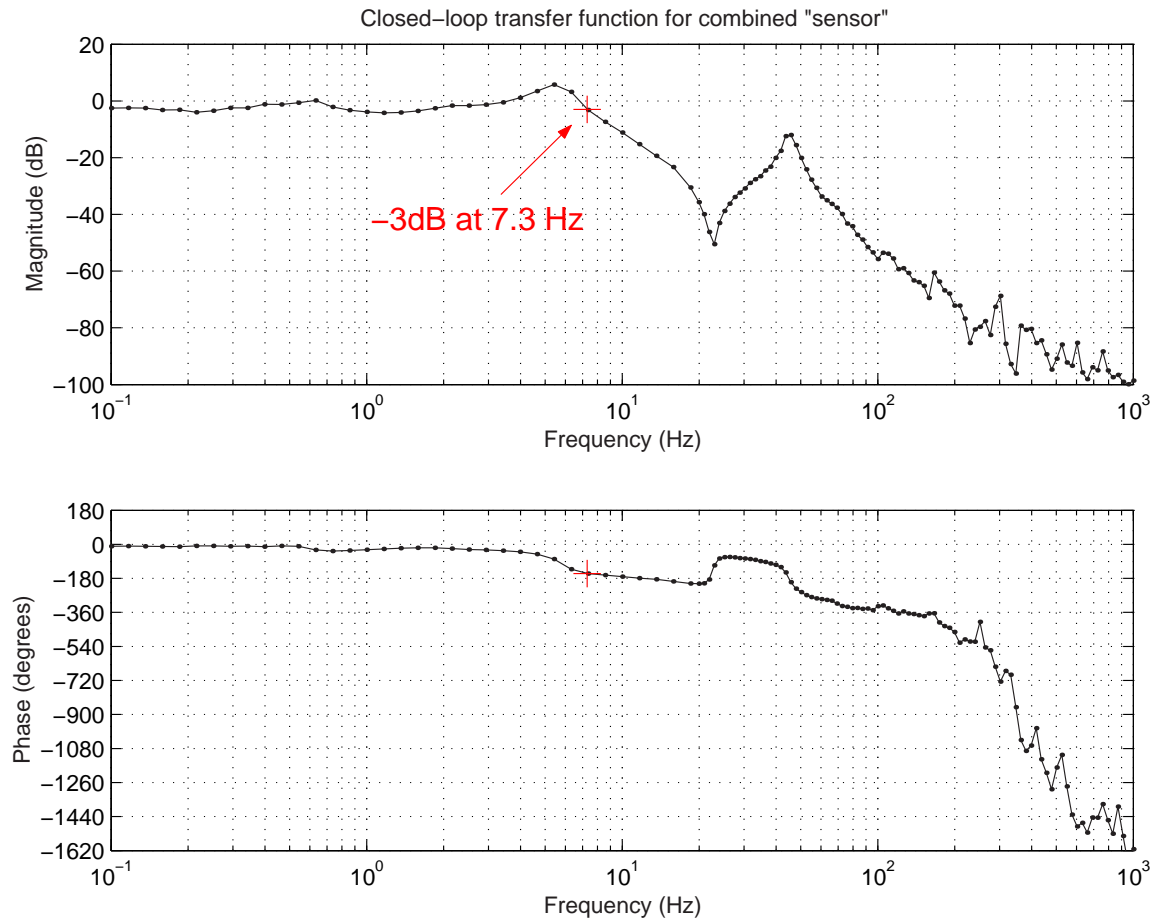
Figure 7-50: Experimental closed-loop transfer function for composite measurement signal: $M(s)/\theta_{des}(s)$. This is the closed-loop transfer function from commanded pendulum position, $\theta_{des}(s)$, to a so-called "composite measurement signal", $M(s)$. This composite measurement is the feedback signal, and it consists of the sum of the four filtered and scaled measurements (as described earlier in the text). The four measurements are the angle and velocity for both the pendulum and wheel, and their scaling factors are summarized in the equation that follows:

$$M(s) = 0.05 \times \left(18\left(0.3\,\dot{\theta}_p + \theta_p\right) + \dot{\theta}_w + 0.2\,\theta_w\right)$$

Note that this transfer function should look essentially like a controlled SISO system (as compared with the individual closed-loop responses to each individual measurements which follow). The -3dB crossover occurs at approximately 7.3 Hz, as shown.
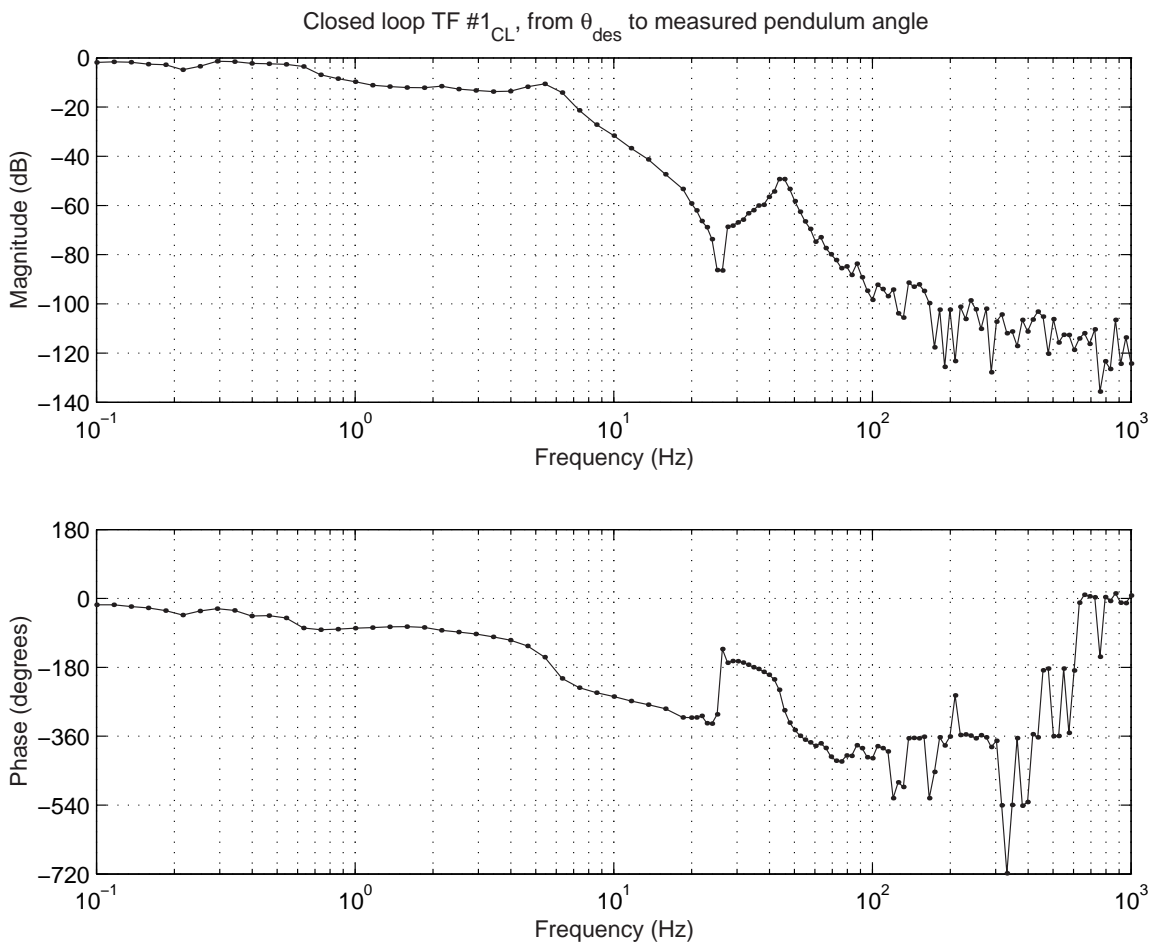
Figure 7-51: Experimental closed-loop transfer function #1_{CL}: $\theta_p(s)/\theta_{des}(s)$. This is the closed-loop transfer function from commanded pendulum position, $\theta_{des}(s)$, to measured pendulum angle, $\theta_p(s)$.
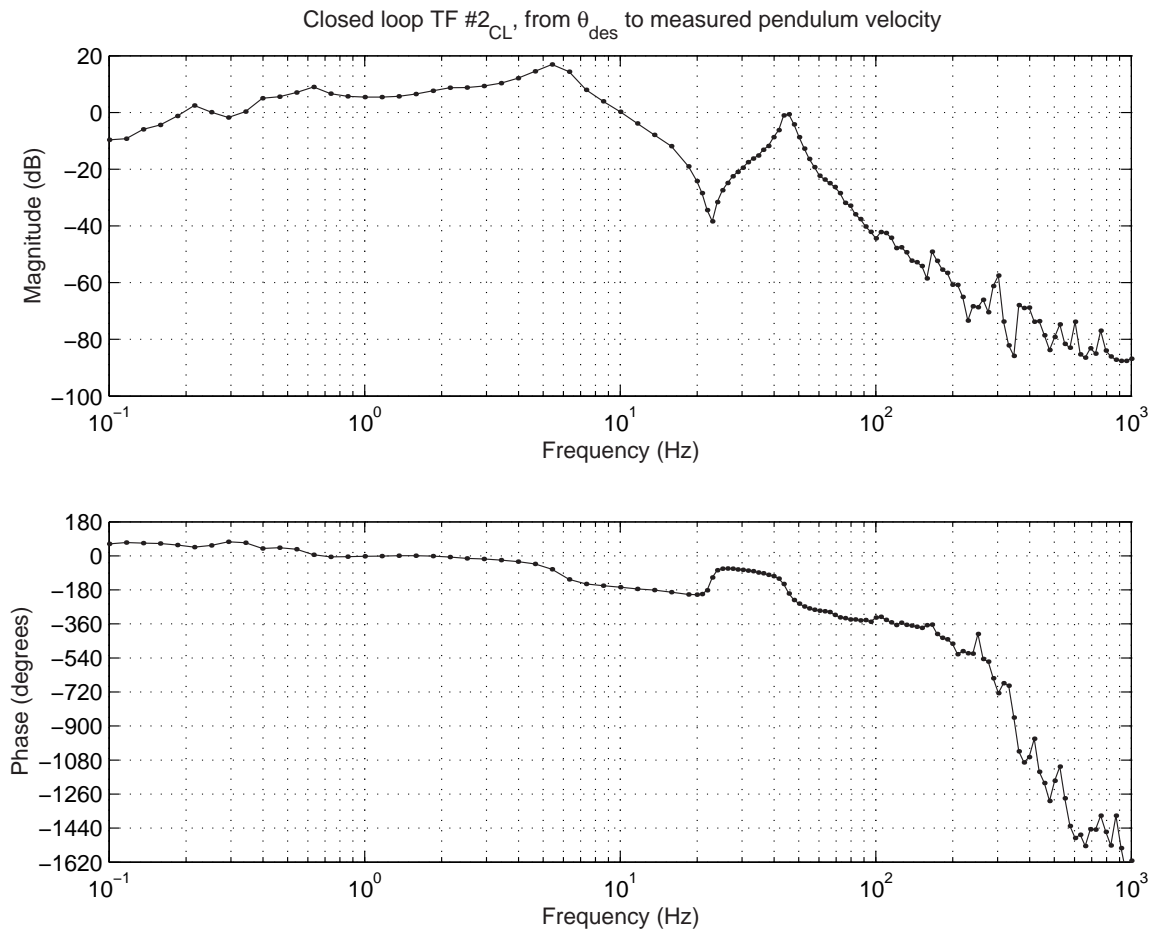
Figure 7-52: Experimental closed-loop transfer function $\#2_{CL}$: $\dot{\theta}_p(s)/\theta_{des}(s)$. This is the closed-loop transfer function from commanded pendulum position, $\theta_{des}(s)$, to measured pendulum velocity, $\dot{\theta}_p(s)$.
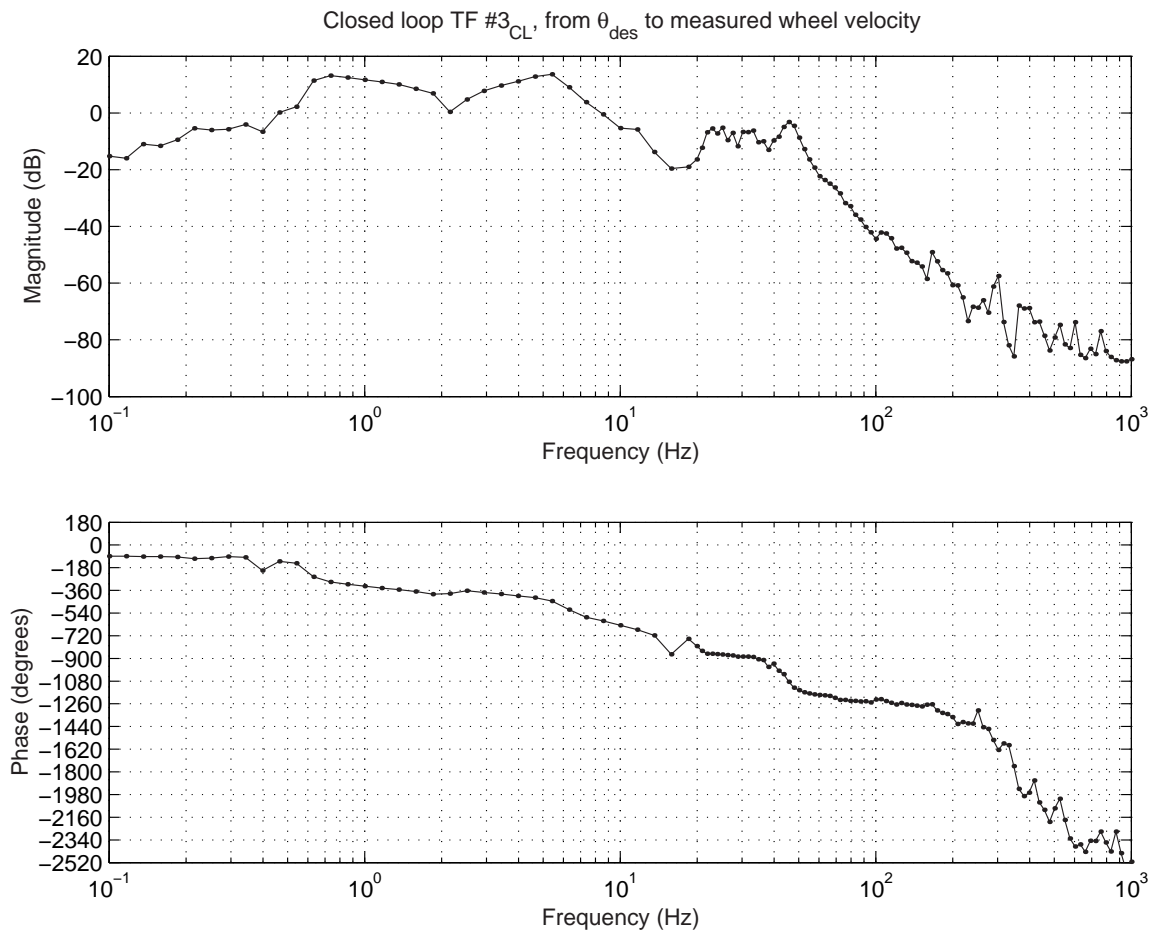
Figure 7-53: Experimental closed-loop transfer function $\#3_{CL}$: $\dot{\theta}_w(s)/\theta_{des}(s)$. This is the transfer function from commanded pendulum position, $\theta_{des}(s)$, to measured wheel velocity, $\dot{\theta}_w(s)$.
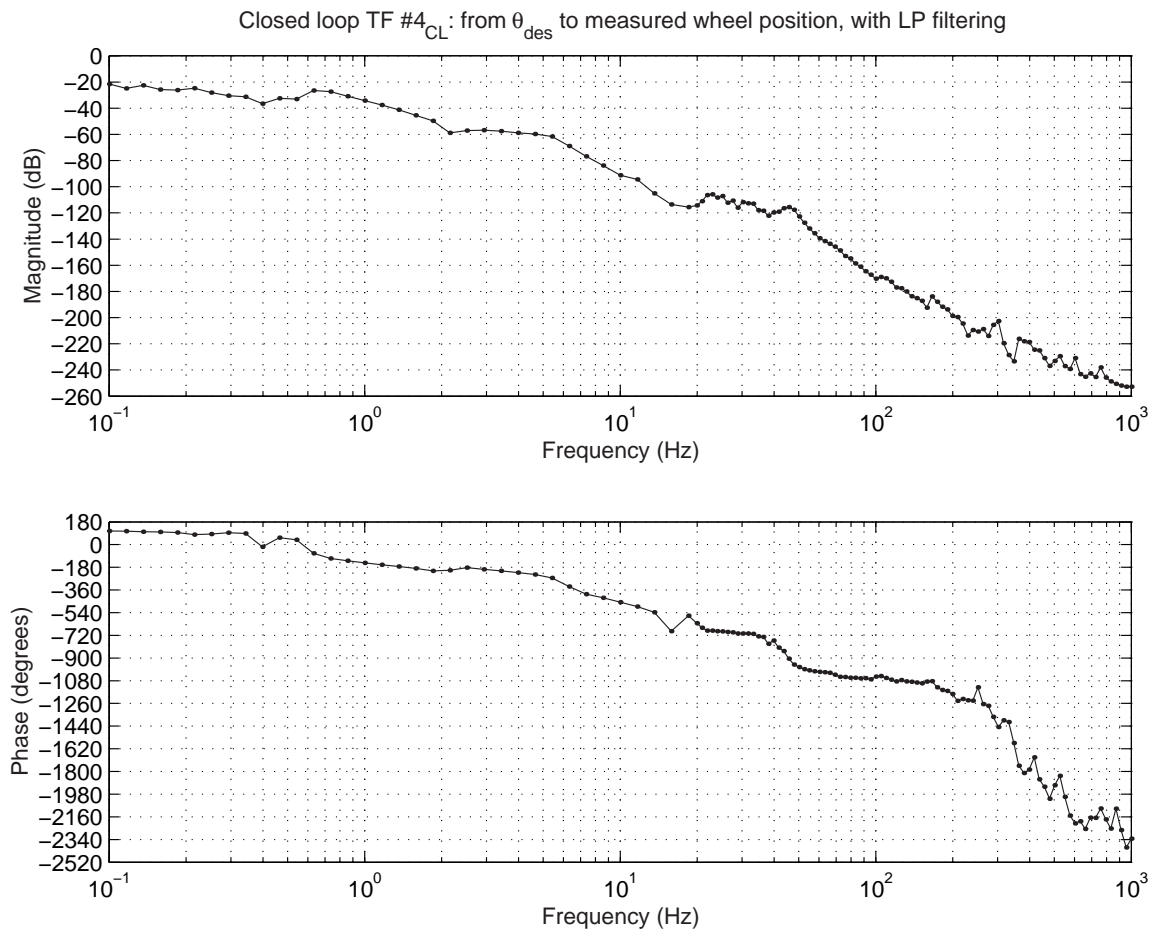
Figure 7-54: Experimental closed-loop transfer function $\#4_{CL}$: $\theta_w(s)/\theta_{des}(s)$. This is the transfer function from commanded pendulum position, $\theta_{des}(s)$, to measured wheel position, $\theta_w(s)$.
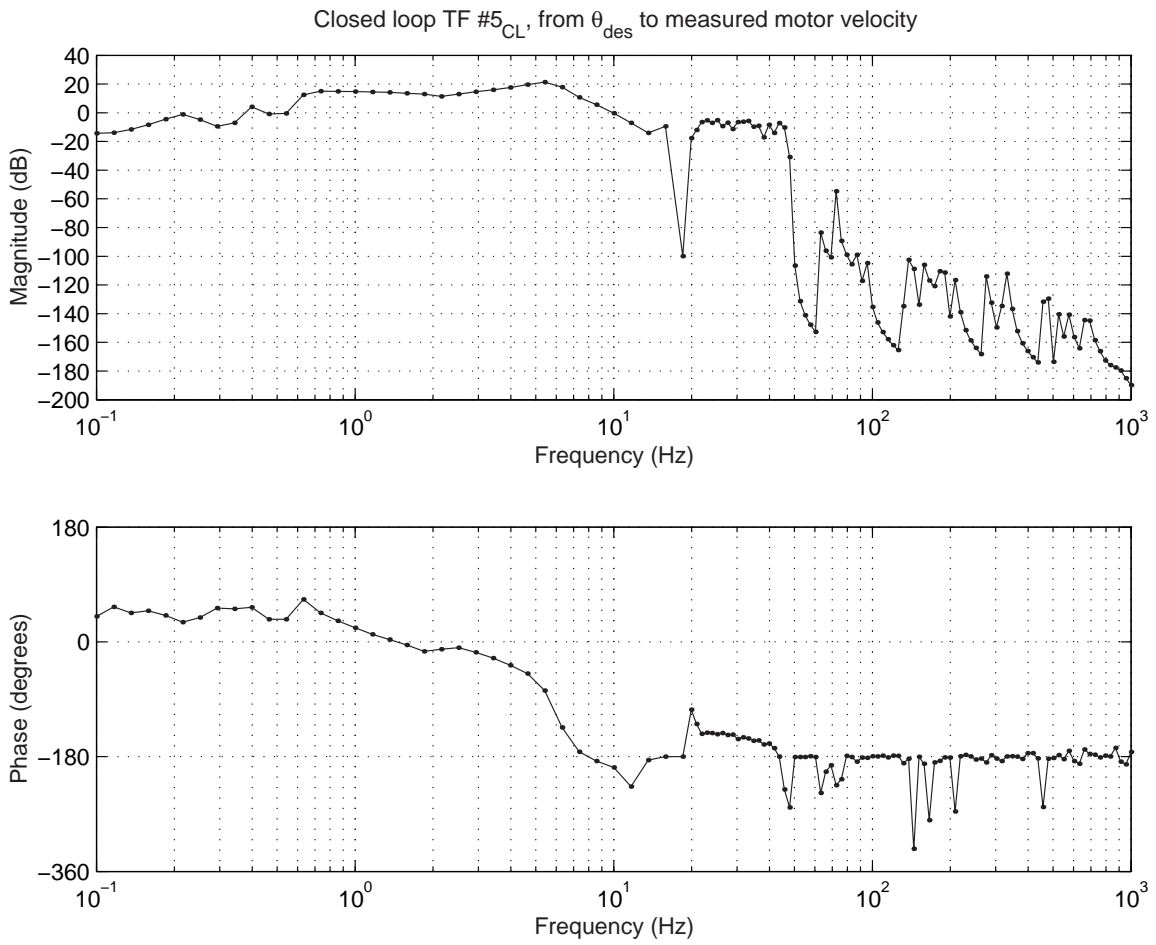
Figure 7-55: Experimental closed-loop transfer function $\#5_{CL}$: $\dot{\theta}_m(s)/\theta_{des}(s)$. This is the transfer function from commanded pendulum position, $\theta_{des}(s)$, to measured motor velocity, $\dot{\theta}_m(s)$.
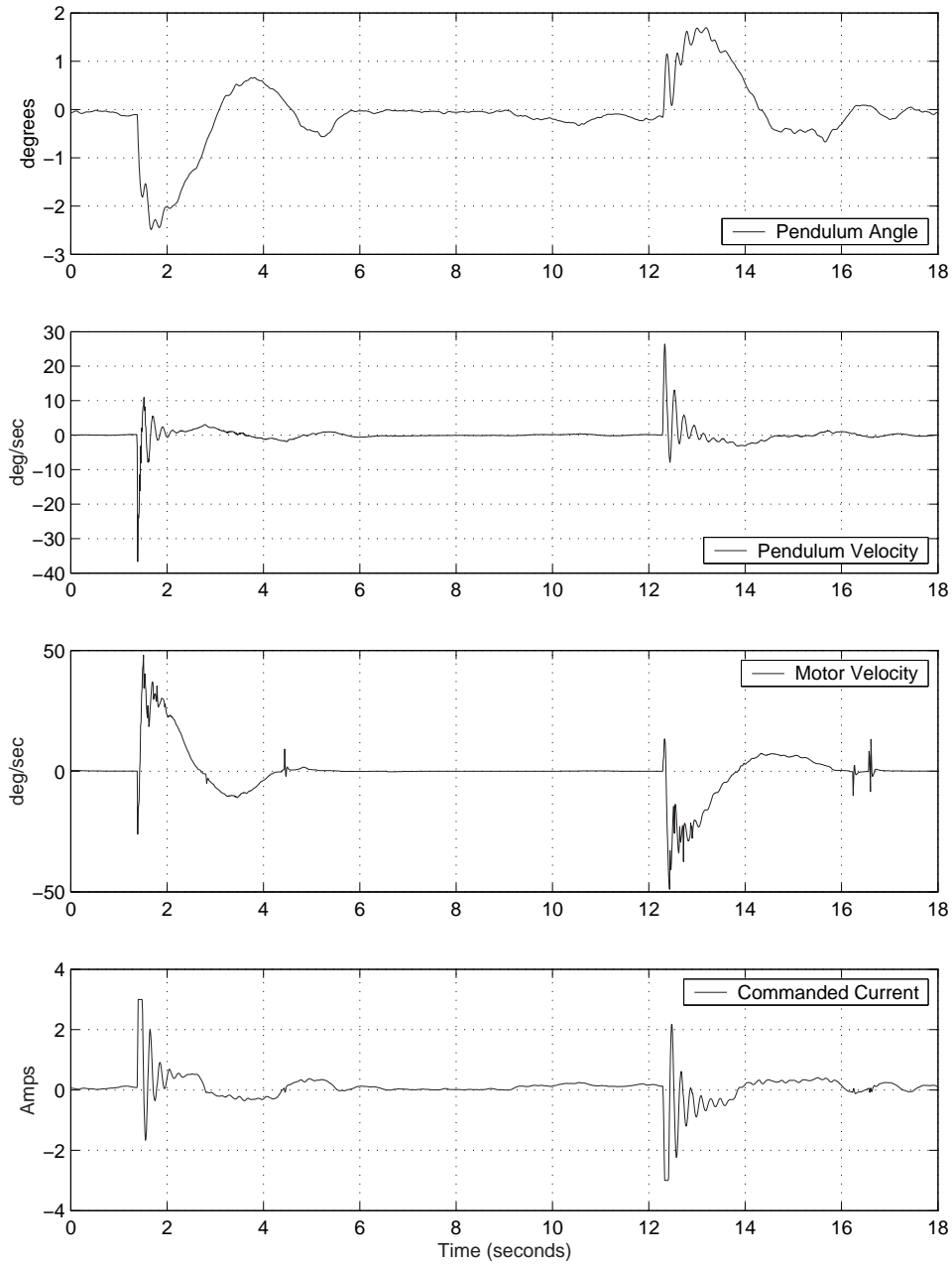
Figure 7-56: Current-controlled transient response to disturbance at pendulum tip. These data are provided to allow the reader to compare the transient response under current control with that obtain under voltage control. Figure 7-57 plots a similar impulse response obtained when the motors were under voltage control.
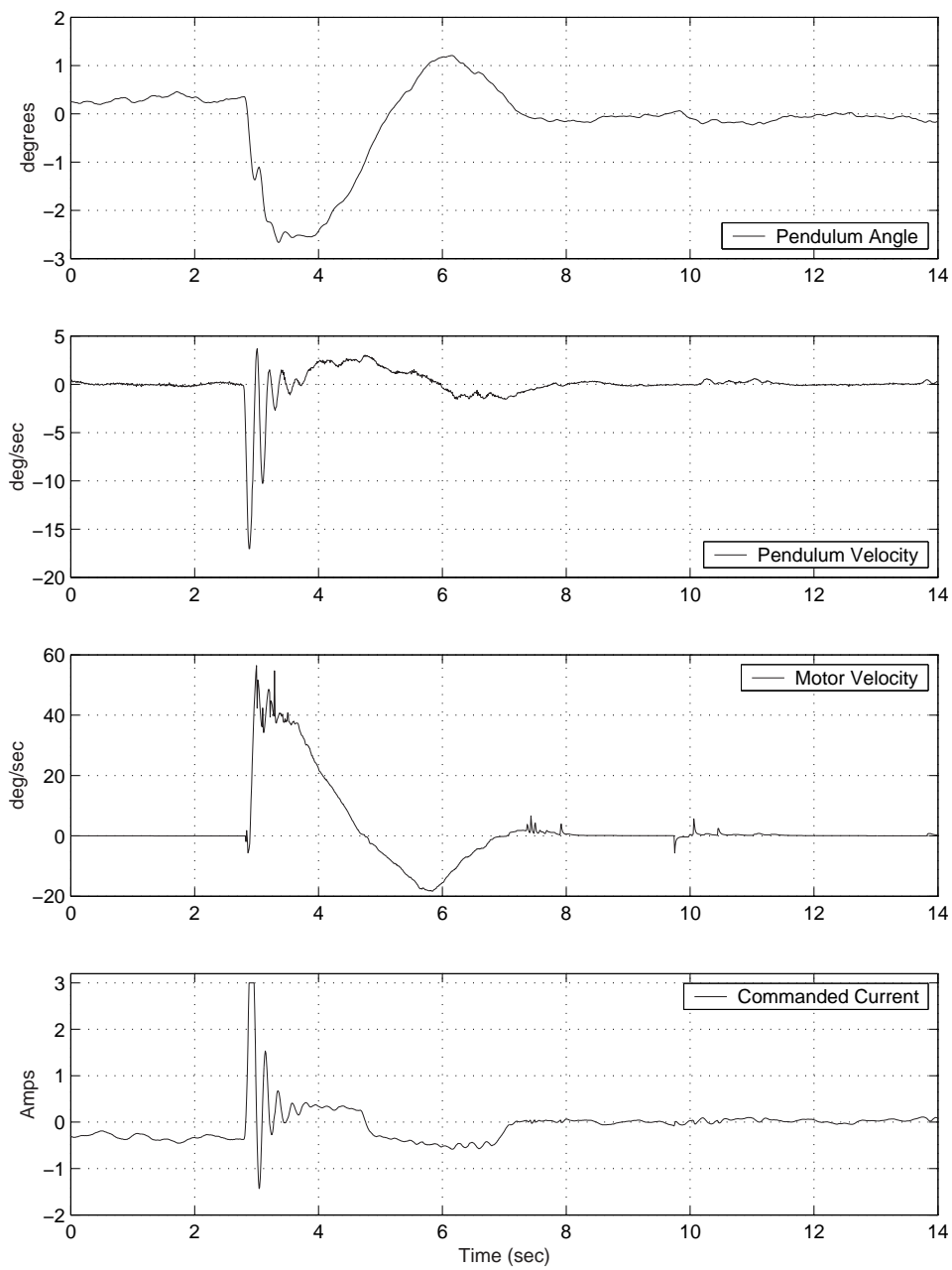
Figure 7-57: Voltage-controlled transient response to disturbance at pendulum tip. Same figure appears on page 7-44 and is included again here for comparison with the data at left.

403

7.9   Summary

The inverted pendulum robot discussed in this chapter was originally intended as an autonomous classroom demo for 2.003. It is not autonomous at this time, and the umbilical cords interfere significantly with the desired dynamics of the uncontrolled plant.

Most of the effort in creating the robot involved the design and manufacture of the hardware and appropriate sensor selection and filtering. Two sensor issues are of particular interest. The first is complementary filtering, which combines the measurements from a gyro and an accelerometer in order to compensate for drift, and the second is the estimation of motor velocity from the quantized encoder output.

We do not currently plan to use the robot as an in-class demo. The theoretical differences in dynamics between the cart-driven and Segway-type inverted pendulums are interesting, however, and might be presented in a recitation or lecture for the class.

Chapter 8

Conclusions and Recommendations

This thesis has two central goals, each of which relates to laboratory projects and/or classroom demos which demonstrate dynamics and introductory control. This work was all inspired by the recent revision of the sophomore-level course "2.003 Modeling Dynamics and Control I", which is a required course for undergraduates in the Department of Mechanical Engineering at MIT. The three central parts of this thesis are: (1) a description of a set of ActivLab experiments which we have designed to create weekly laboratory experiences, and (2) the development of an inverted pendulum robot (named the DIPR) intended as a classroom demo in dynamics and control.

To provide background for these two goals (the ActivLab projects and the IP robot), I have also compiled a survey of other projects which provide undergraduates with experiences in dynamics, controls and design. The survey covers a variety of laboratory projects, lecture demos, capstone projects, robot contests and other activities, described in Chapter 2, created by educators at MIT and other universities. Chapter 4 forms a second part of the survey, which focuses on additional laboratories and demos which are specifically appropriate for 2.003. The remainder of this chapter summarizes current status of and provides suggestion for future work on both the ActivLab project and the inverted pendulum robot.

8.1 ActivLab Conclusions and Recommendation

8.1.1 Brief Evaluation of ActivLab Projects

As of this writing, the ActivLab hardware has completed its fourth term in use. The equipment is designed to demonstrate first-, second- and higher-order system responses and to introduce controls. Much care has been taken to create systems which demonstrate nearly ideal first- and second-order responses. In particular, much of the hardware uses air bearings to virtually eliminate any Coulomb friction in the mechanical systems.

We have still observed a variety of anomalous behaviors in the course of teaching the class however, many of which are documented in Chapter 3. We feel it is important that any non-ideal behaviors are not "swept under the carpet" during the labs. Unexpected system behaviors can, in moderation, present an opportunity for students. During the labs, we encourage curiosity in the students. We hope that students will explore, experiment, and also propose and test hypotheses during lab sessions. The ability to engage hardware with an open-minded yet scientific outlook is a necessity for successful independent research.

8.1.2 Final Notes on the ActivLab Equipment and Website

The ActivLab projects are documented on the website for course 2.003 Modeling Dynamics and Control I at MIT. The current address for the ActivLab site is:

http://web.mit.edu/2.003/www/activlab/activlab.html

This website is also accessible through MIT's growing "OpenCourseWare" (OCW) project, which is described in Section 2.3.4 on page 119. The link to 2.003 can be found among the courses offered by the Department of Mechanical Engineering which currently participate in OCW. The OCW homepage is currently located at:

http://ocw.mit.edu/index.html

We encourage others to use or adapt any of the ideas we have documented in this thesis and on the ActivLab website.

The ActivLab hardware was designed to be robust, easy to assemble, and relatively transparent in operation. The equipment has proved to be fairly robust so far, and we have not experienced any significant hardware failures. The most notable issue with wear involves the cantilevers used in the second-order translational system described in Section 3.5 (page 170). We use lengths of thin welding rod, and these have a tendency to fatigue after a couple of terms of use because the second-order system is driven. The welding rod is cheap and easy to replace, however. (We got a few lengths for free from welders at MIT's Central Machine Shop.)

We have been particularly pleased with the decision to design the mechanical hardware in the ActivLab projects so that labs can be assembled on optical breadboard and then stored efficiently after disassembly. The Delrin adapter plates we manufactured which interface between the air bearings and the breadboard have been particularly useful in this respect. The design of this adapter plate is documented in Appendix D on page 419.

Overall, we have been pleased with the laboratories for 2.003, and there are no plans to modify the ActivLab projects significantly in the near future. We do hope to create some supplementary material for the class over the summer of 2003, however, primarily through the efforts of undergraduate (UROP) students who have previously taken the class.

Ross Hatton will be creating online materials which will describe a magnetic ball levitation demo. This demo was originally created by Prof. Trumper and has been subsequently modified to run under the dSPACE environment by Yi Xie as part of her MEng thesis. Ross is also creating an online tutorial explaining many of the key electromechanical components of a disk drive, and he will also be helping to format Prof. Trumper's course notes for the class with LATEX.

Larry Hawe II will be creating additional documentation for the cart-driven inverted pendulum demo described in Chapter 5. He also plans to add storage shelves beneath the laboratory benches which will help us store the optical breadboard out

of the way during the weeks when they are not used.

We may also create some additional hands-on projects and exercises for a weekly one-hour recitation session for the class. The recitations, if added to the class content, could provide tutorial coverage of topics such as: drawing and using free body diagrams, the fundamentals of Bode diagrams, introduction to MATLAB, and a review of complex exponentials. A particular recitation session might also present a more in depth examination of demos presented in lecture, or it could focus on problem solving and involve hardware exercises which are more loosely-structured that the three-hour weekly labs.

8.2 Inverted Pendulum Demo Summary

The inverted pendulum robot I designed which is described in Chapter 7 (the DIPR) is not practical as a classroom demo in its current state. The robot requires umbilical cords to carry power, sensor signals, and control commands for the robot. These cords interfere with the operation of the inverted pendulum, and the entire demo is quite bulky since it must include the off-board power supplies and a computer equipped with a dSPACE controller board.

At this time, there are no plans to adapt the DIPR into a fully autonomous robot, and we will instead continue to use the cart-driven inverted pendulum hardware described in Chapter 5 as a lecture demo for 2.003. The operation of the cart-driven system is documented in Andrew Stimac's bachelor thesis: "Standup and Stabilization of the Inverted Pendulum"[189]. As mentioned in the previous section, Larry Hawe plans to document this demo further over the summer of 2003.

One suggestion for future work is the development of a smaller, autonomous inverted pendulum robot, similar in scale and complexity to the Legway described on page 2.1.5, as a lecture demo. Another possible project is the development of a low-cost kit of parts which each student could assemble to create his or her own inverted pendulum. The device would more likely be a fixed base design instead of a two-wheeled robot, and it would be small enough to sit in the corner of a desktop.

Students would then be asked to complete a design project at home to stabilize the inverted pendulum with their own analog control circuits.

This type of project would give each student the opportunity to work on a design project and gain some experience in introductory controls. They would also have much more opportunity to interact with this demo than with a lecture demo version of an inverted pendulum demo and would be encouraged to explore the effects of "tweaking" the controller.

The actual hardware could also involve some other system, such a magnetic ball levitator, instead of an inverted pendulum. Hopefully, students would be inspired by the opportunity to build their own working desktop toy to keep at the end of the term, and this might also generate more interest in the content of the class. A design project of this type could also be useful for a class which focuses more directly on introductory control theory, such as 2.14 or 6.302.

Appendix A

Course Catalog Descriptions for 2.003 and 2.004

Below are the text descriptions of 2.003 and 2.004 from the *MIT Bulletin* (course catalog). Also included is a brief paragraph clarifying some details about 2.003.

2.003 Modeling Dynamics and Control I

Undergraduate Subject

Prereq.: 8.01, 8.02, 18.02, 18.03

Units: 4-3-8

URL: http://web.mit.edu/2.003/www/

First of two-term sequence on modeling, analysis and control of dynamic systems. Mechanical translation, uniaxial rotation, electrical circuits and their coupling via levers, gears and electro-mechanical devices. Analytical and computational solution of linear differential equations and state-determined systems. Laplace transforms, transfer functions. Frequency response, Bode plots. Vibrations, modal analysis. Open- and closed-loop control, instability. Time-domain controller design, introduction to frequency-domain control design techniques. Case studies of engineering applications. *D. Trumper, D. Gossard, N. Hogan*

Additional details about 2.003

Most subjects at MIT are 12-unit courses. 2.003 is a 15-unit class, meaning students should typically spend approximately 15 hours per week on their combined preparatory and in-class efforts. Each week, students are expected to attend two one-hour lectures, two one-hour recitations and a three-hour laboratory session. 2.003 is a required, sophomore-level course for mechanical engineering majors. The workload and content are by design similar to the EECS course *6.003 Signals and Systems.* Course prerequisites include *classical mechanics* (8.01), *electricity and magnetism* (8.02), *multi-variate calculus* (18.02), and *differential equations* (18.03).

2.004 Modeling Dynamics and Control II

Undergraduate Subject

Prereq.: 2.003, 18.03

Units: 4-3-8

Second subject of two-term sequence on modeling, analysis and control of dynamic systems. Kinematics and dynamics of mechanical systems including rigid bodies in plane motion. Linear and angular momentum principles. Impact and collision problems. Linearization about equilibrium. Free and forced vibrations. Sensors and actuators. Control of mechanical systems. Integral and derivative action, lead and lag compensators. Root-locus design methods. Frequency-domain design methods. Applications to case-studies of multi-domain systems.

T. R. Akylas, S. H. Crandall, N. Hogan

Appendix B

Programs in Mechatronics

Table B.1: Undergraduate Lab Programs in Mechatronics in the US - *Note the ‡ symbol indicates an introductory undergraduate dynamics course with a laboratory component.*

∘ University *website*	Undergraduate Course (or Program)
‡ Carnegie Mellon University *http://www.andrew.cmu.edu/course/24-352/syllabus.htm*	24-352 DYNAMIC SYSTEMS & CONTROL
• Carnegie Mellon University *http://www.ece.cmu.edu/ fedder/mechatronics/Syllabus.html*	16-879/18-879/24-700A Mechatronics Design
• Clemson University *http://ece.clemson.edu/crb/*	Undergraduate Integrated Systems Lab
• Colorado State University *http://www.engr.colostate.edu/d̃ga/me307.html*	ME307 Mechatronics and Measurement Systems
‡ Illinois Institute of Technology *http://weblab.iit.edu/*	WEBLAB Online Data Acquisition and Remote Control
• Johns Hopkins University *http://custer.me.jhu.edu/html/mechatronics.html*	ME 530.421 Mechatronics
• Massachusetts Institute of Technology *http://web.mit.edu/2.737/www/*	2.737 Mechatronics
• North Carolina State University *http://courses.ncsu.edu:8020/mae534/lec/001/*	MAE 534 Mechatronics Design

∘ University	Undergraduate Course (or Program)
website	
• Rensselaer Polytechnic Institute	MEAE-4490 Mechatronics
http://www.rpi.edu/ craigk/mech2002.html	
• Rice University	ELEC 201 Introduction to Engineering
http://www-ece.rice.edu/Courses/201/	
• San Jose State University	ME 106 Fundamentals of Mechatronics
http://www.engr.sjsu.edu/bjfurman/courses/ME106/ME106courseinfo.htm	
• Stanford University	SPDL Lab Courses
http://design.stanford.edu/spdl/	
• SUNY University at Buffalo	MAE 476/576: Mechatronics
http://www.eng.buffalo.edu/Courses/mae576/CourseInformation.html	
• University of California Berkeley	EE192 Mechatronics Design Lab
http://www-inst.eecs.berkeley.edu/ẽe192/	
• University of California Davis	EEC 194 MicroMouse Competition
http://www.ece.ucdavis.edu/umouse/	
• University of Illinois and Urbana-Champaign	UIUC College of Engineering Mechatronics Lab
http://robot0.ge.uiuc.edu/ spong/deere/	
‡ The University of Texas at Austin	ME 244L Dynamic Systems and Controls Lab
http://www.me.utexas.edu/ lotario/me244L/labs/ufresp/	
• University of Utah	ME3200/ME3210 Mechatronics
http://www.mech.utah.edu/ me3200/	
• University of Washington	Mechatronics Project
http://www.me.washington.edu/ dig/medesign/Mechatronics.htm	
• Virginia Tech	ME/ECpE 4734 Mechatronics
http://mechatronics.me.vt.edu/home.html	
• Wellesley College	CS115/PHYS115 Robotic Design Studio
http://nike.wellesley.edu/ rds/rds01/index.html	

Table B.2: International Undergraduate Programs in Mechatronics

○ University *website*	Undergraduate Course (or Program)
• Chemnitz University of Technology *http://www.tu-chemnitz.de/ifm/english/index.htm*	Institute of Mechatronics
• City University of Hong Kong *http://www.cityu.edu.hk/me/bengmte.htm*	Bachelor of Engineering in Mechatronic Engineering
• Griffith University (Australia) *http://www.gu.edu.au/school/mee/home.html*	School of Microelectronic Engineering
• Indian Institute of Technology Kanpur (India) *http://www.iitk.ac.in/robotics/general/about.html*	Center for Mechatronics
• James Cook University (Australia) *http://www.eng.jcu.edu.au/mech/info/mechatronics.html*	
• Johannes Kepler University of Linz (Austria) *http://www.mechatronik.uni-linz.ac.at/index.en.html*	Mechatronics Course Curriculum
• Loughborough University (UK) *http://www.lboro.ac.uk/research/mechatronics/*	Mechatronics Teaching Laboratory
• McGill (Canada) *http://www.mcgill.ca/mecheng/undergrad/curriculum/mechatronics/*	Mechatronic Option for Undergrads
• National University of Singapore (Singapore) *http://www.eng.nus.edu.sg/mpe/courses/me4244.html*	Mechatronics Electives for Undergrads
• Singapore Polytechnic (Singapore) *http://sspwb100.sp.edu.sg/schools/mm/courses/cm_ftdmec.htm*	Full-time diploma in Mechatronics
• The University of Adelaide (Australia) *http://www.mecheng.adelaide.edu.au/Courses/Bachelors/structure.html*	Bachelor of Engineering (Mechatronics)
• University of Delft (Netherlands) *http://dutera.et.tudelft.nl/Delft_Control/*	Advanced Mechatronics group

| ○ University | Undergraduate Course (or Program) |
| | |
website	
• University of Hannover (Germany)	Hanover Center of Mechatronics
http://www.mzh.uni-hannover.de/lehre_e.htm	
• University of Twente (Netherlands)	The Mechatronic Design Group
http://www.rt.el.utwente.nl/mechatronics/	
• The University of Waikato (New Zealand)	0773.415 Mechatronics
http://www.phys.waikato.ac.nz/	
• University of Waterloo (Canada)	Engineering Mechatronics Option for Undergrads
http://www.me.uwaterloo.ca/ mechatro/	
• University of Wollongong (Australia)	Bachelor of Engineering (Mechatronics)
http://www.uow.edu.au/ friso/mechatronics.htm	

Note that the lists in Tables B.1 and B.2 only sample a few particular types of programs in mechatronics. The emphasis is on courses and degree programs which (1) provide *undergraduate* preparation for design in mechatronics and (2) have publicly accessible materials from which others may survey the types of course work available. Even under these guideline, there are clearly a large number of notable programs left off of this list (because of time and space constraints or my own ignorance) that deserve note.

Appendix C

ActivLab Vendors and Prices

Below is a spreadsheet listing the vendors and prices for the most expensive equipment and materials purchased during the summer of 2001 to create the ActivLab hardware. Note that costs would be significantly higher if we had not already had a lab space with a dozen work stations already equipped with networked PC's (equipped with dSPACE controller boards), oscilloscopes, function generators and power supplies!

Item	Qty	Supplier	ea.	total
LVDTs (+/- .5in) and Signal Cond'rs	15	Schaevitz	$617	$9,255
Air Bearings and Pillow Blocks	50	New Way Machine Comp.	$260	$13,000
LA24-33 Voice Coil Actuators (30)	30	BEI-Kimco	$315	$9,450
Optical Baseplates (15)	15	OptoSigma	$375	$5,625
Digital PC Video Cameras	15	CDW-G	$300	$4,500
Angle Plates (to mount voice coils)	30	Suburban Tool Co.	$50	$1,500
Eliminizer Air Filters (for air lines)	15	iProcessSmart.com	$70	$1,050
Quick Disconnects, Tubing, Fittings	NA	Beswick	NA	$1,000
Airpot 2K95 dashpots	20	Airpot Corporaton	$40	$800

Figure C-1: Spreadsheet of high-cost materials

Appendix D

CAD Drawing of Delrin Air Bearing Mounting Plate
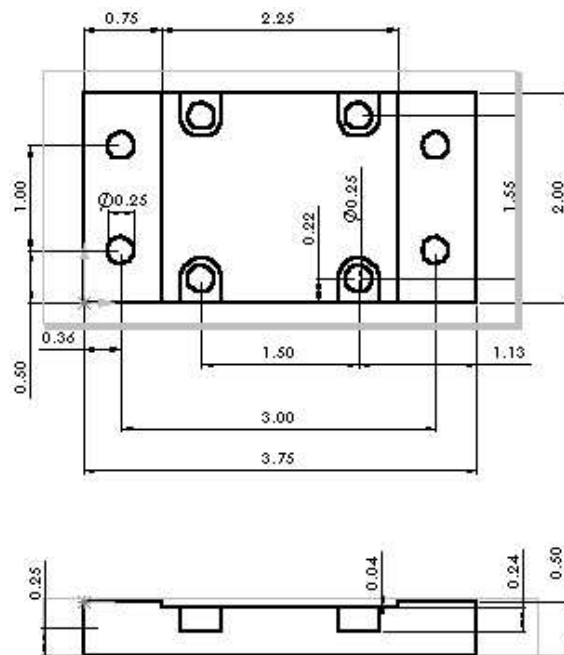
Figure D-1: CAD Drawing of Delrin adapter plate for air bearings.

Appendix E

MATLAB Valve Flow ODE Code

This appendix lists the MATLAB m-file used to simulate the cantilever-dashpot system described on page 139 and describes some of the dynamic assumptions used. The orifice is actually an annulus, formed by the tapered plug shown in Figure 3-5. The equation governing volume flow rate of a compressible gas through a valve (ISA S75.01 standard) is:

$$Q_v = Y C_v P \sqrt{\frac{\Delta P}{\rho P T}} \qquad (E.1)$$

where

Q_v = volume flow rate $[m^3/s]$

C_v = valve coefficient

T = upstream temperature $[K]$

P = pressure of gas upstream of valve $[Pa]$

ΔP = pressure differential across valve $[Pa]$

ρ = density of gas flowing through valve $[kg/m^3]$

Y = fluid expansion factor

The fluid expansion factor, Y, is a value between 2/3 and 1, defined as:

$$Y = 1 - \frac{\Delta P}{3P} \qquad (E.2)$$

421

Rearranging, the *mass* flow rate through a valve can be written as:

$$Q_m = K \cdot \left(\frac{P - \frac{1}{3}\Delta P}{P} \right) \sqrt{\frac{P \cdot \Delta P}{\rho T}} \tag{E.3}$$

where K is a constant that depends on the valve geometry. For the cantilever-Airpot lab, K is a variable that depends on how tightly the needle valve in the Airpot has been set.

The m-file that follows takes the following three state variables as inputs: (1) piston position, (2) piston velocity and (3) the mass of air currently inside the piston. To use "ode23()" or "ode45()" to calculate system response to some particular initial conditions, this m-file must output the derivative of each of these variables. The calculations involved simply match the piston geometry with that of the cantilever; apply the mass flow equation; explicitly relate velocity as the derivative of position; and then finally balance forces to apply Newton's law to calculate acceleration.

The m-file which performs these calculations is shown in Figure E-1. To calculate the response as the piston *compresses* the air, one can run MATLAB's ode45 solver as follows:

```
>> tfin = 5;

>> global Lrest = .015;

>> P = 101e3; A = 6.8e-5; R = 287; T = 300;

>> x1 = .016; v1 = 0; m1 = x1*(P*V)/(R*T);

>> [tout,yout] = ode45('airpot_ode',[0 tfin],[x1 v1 m1]);
```

```matlab
function [dy] = airpot_ode(t,y)
% function [dy] = airpot_ode(t,y)
% input variables defined by "y":
%   y(1): x, position in m
%   y(2): v, velocity in m/s
%   y(2): m_air, mass of air inside

global Lrest; %x position of cantilever at rest

isentropic=1;                    % (set to 0 for isothermal limit)
b=.0127; h=.00127; L=.205;       % cantilever dimensions
E=210e9; I=b*h^3/12;             % cantilever properties
k=3*E*I/(L*L*L);                 % cantilever spring constant
Pout=101e3;                      % Pa, atmospheric pressure
Tout=300;                        % room temp of air outside, Kelvin
R=287;                           % gas constant for air
mpot=1.8e-3;                     % mass of airpot piston
m=mpot+.24*b*h*L*8000;           % ..with effective mass of cantilever
x=y(1); v=y(2); m_air=y(3);
A=6.8e-5;                        % piston area
V_air=(Lrest+x)*A;               % volume now inside piston
if isentropic
    V1=m_air*R*Tout/Pout;        % volume this mass at STP
    Pin=Pout*(V_air/V1)^-1.4;    % isentropic relationship
    Tin=Pin*V_air/(R*m_air);
else                             % assume isothermal limit
    Pin=(m_air*R*Tout)/V_air;    % pressure in piston given T=Tout
    Tin=Tout;
end
K=.000000000005;                 % scaling coefficient for orifice size
dP=Pout-Pin;                     % driving pressure differential
if sign(dP)>0                    % check air flow direction...
    rho=Pout/(R*Tout);           % use density of air going thru orifice!
    Tair=Tout;
else
    rho=m_air/V_air;             % density of air in piston
    Tair=Tin;
 end


q = sign(dP)*K*((Pin-.33*dP)/Pin)*sqrt(Pin^2*abs(dP)*rho/Tin);


fr=.05*sign(v);                  % friction in piston, .002 to .1
c=1.5;                           % damping in piston
Fnet = -k*x - dP*A -fr -c*v;
dv = Fnet/m;                     % F = m*a
dy=[v; dv; q];                   % output all derivatives
% --- EOF ---
```

Figure E-1: MATLAB function airpot_ode() for orifice flow damping

Appendix F

Motor Specifications for the Inverted Pendulum Robot

Maxon DC Motor
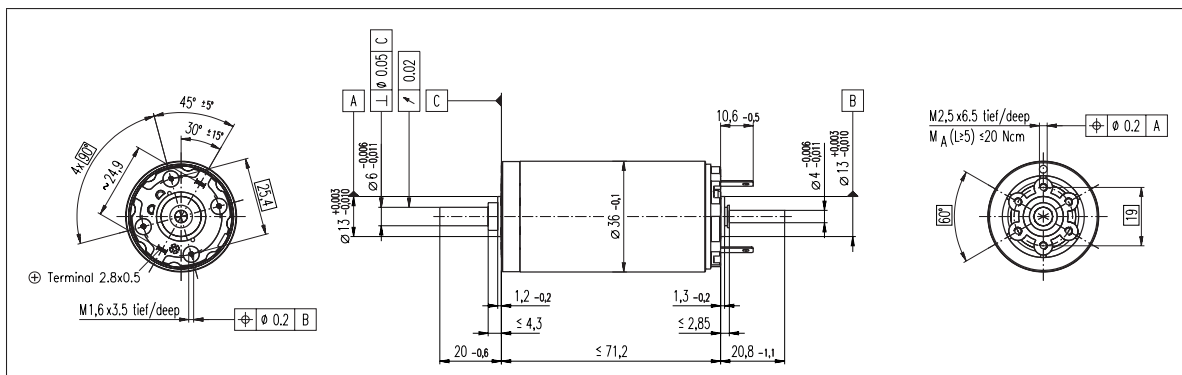
Figure F-1: Maxon RE 36 motor CAD drawing. (pt# 118797) Data below are reprinted from page 77 of the 2001 Maxon product catalog [129].

The two motors used to power the inverted pendulum robot are RE 36[1] DC motors. Each is outfitted with a Maxon GP 42C planetary gearhead with a single stage reduction ratio of 4.33 and a HEDS 55 digital encoder with line driver. Figure ?? gives an engineering drawing of the motor, taken from the Maxon product catalog [129].

---

[1]The name refers to ϕ 36 mm body

Table F.1 and Table F.2 list various motor and gearhead parameters, respectively.

Table F.1: Maxon RE 36 motor data. (pt# 118797) Data below are reprinted from page 77 of the 2001 Maxon product catalog [129].

Motor Data	Symbol	Specification Value	
Power rating	P	70	Watts
Nominal voltage	V_{nom}	18	Volts
Stall torque	T_p	0.73	Nm
Max. continuous torque	T_c	0.0824	Nm
Starting current	I_p	27.8	Amps
Max. continuous current	I_c	3.14	Amps
No load current	I_{NL}	0.147	Amps
Mass	m_m	0.35	kg
Rotor Inertia	J_m	62.0	gcm^2
Resistance	R_m	0.647	Ohms
Terminal inductance	L_m	0.100	mH
Max. efficiency	η_m	84	%
Torque constant	K_t	0.0263	Nm/Amp
Back emf constant	K_b	0.0263	Volt/rad/s

Planetary Gearhead

The planetary gearhead on each motor is constructed with straight, ceramic teeth. Each wheel on the inverted pendulum robot is mounted to the stainless steel output shaft via a fixture with a keyway and set screw, as described in Section **??**. The ball bearings in the gearhead are the only bearings for each wheel; no additional wheel bearings are used in the robot design.
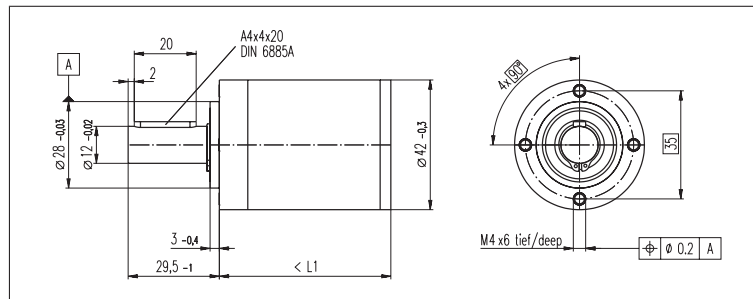
Figure F-2: Maxon GP 42 C planetary gearhead CAD drawing. (pt# 203114) Data below are reprinted from page 195 of the 2001 Maxon product catalog [129].

Table F.2: Maxon GP 42 C planetary gearhead data. (pt# 203114) Data below are reprinted from page 195 of the 2001 Maxon product catalog [129].

Gearhead Data	Symbol	Specification Value	
Gear reduction	N	13/3	-
Mass	m_g	0.26	kg
Rotor Inertia	J_g	9.1	gcm^2
Max. efficiency	η_g	90	%
No load backlash	-	0.3	degrees
Max. cont. torque output	T_{gc}	3.0	Nm
Peak torque output	T_{gp}	4.5	Nm
Max radial load at 12mm	-	120	N

Digital Encoder
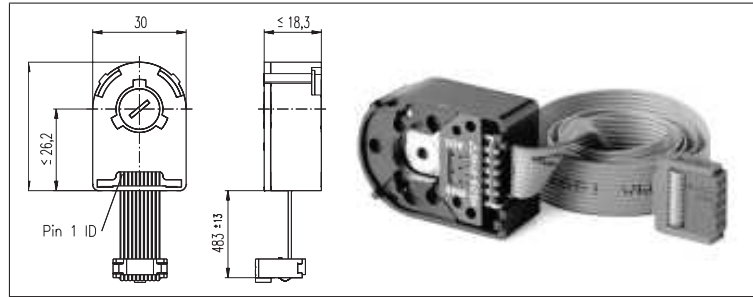
Figure F-3: Maxon HEDL 55 digital encoder with line driver. (pt# 110514) Data below are reprinted from page 206 of the 2001 Maxon product catalog [129].

The encoders used have quadrature, square pulse, line driven RS 422[2] outputs with a "resolution" of 500 counts per turn. The encoder measures the motor's angular position, not the angular position of the gearhead. Neglecting backlash, the rotation of each wheel is therefore measured in increments of 0.042°, as shown in Equation F.1.

$$\Delta_{angle} = \frac{360°}{4 \cdot 500} \cdot \frac{3}{13} = 0.0415° \tag{F.1}$$

Neglecting slip and assuming a 6" diameter wheel, this translate into an increment wheel position of about 0.004".

$$\Delta_{position} = 6'' \cdot \frac{\pi}{180°} \cdot 0.0415° = 0.00435'' \tag{F.2}$$

---

[2]Note that the DS1104 dSPACE board used to control the inverted pendulum robot accepts both TTL and differential (RS 422) inputs, while the older DS1102 dSPACE board used for the ActivLab experiments accepts only TTL input. The DS1102 can use one of the RS 422 differential signals as a single ended input, but the noise-reducing benefits of using a line driven signal would then be largely lost.

Appendix G

MATLAB Code Simulating IP Dynamics

This appendix contains MATLAB code that simulates an initial "stand-up" of the robotic inverted pendulum (described in Chapter 7). Figure G-1 shows the calculated performance for the robot as originally planned. Note this simulated robot is substantially smaller that the one actually built.

Figure G-1: Pendulum stand-up simulation from MATLAB code (planned design). 1 second simulation from at rest (horizontal) to upright. Pendulum positions (at left) are drawn at 0.1 second intervals. Current command as a function of time shown at right.

```
nmotor=2; mmotor=.35; mgears=.26;
m_stuff= 7;  % extra mass of batteries, wheel, et al
mp=.2;  mw=nmotor*(mmotor+mgears)+m_stuff; % kg
L=1; n=13/3; % gear ratio
Jp=1e-3;  Jbody=.14; Jm=nmotor*6.2e-6;  %kg-m^2
mass_one_wheel=1.25;  R=.15;  % 15 cm wheel radius
Jw=nmotor*.5*mass_one_wheel*R*R; % m_wheel= 1 kg
Kt=nmotor*.0263;  % Nm/A , 18 volt ref...
fr=5e-4;  eff=.75;  % friction, gear train efficiency

theta_p=zeros(10100,1); theta_w=theta_p; thetad_p=theta_p;
thetad_w=theta_p;  thetad2_p=theta_p;  thetad2_w=theta_p;
torque_val=theta_p;  u_was=theta_p;
theta_p(1)=-pi/2-atan2(.5*R,L);   theta_w(1)=-pi/2-atan2(.5*R,L);
dt=1e-4;     A=mp*L*L+Jp+Jbody+n*n*Jm;     g=9.8;
ustall=27.75;  % stall current
no_load_speed=671;  % rad/sec
Fe=0;   K=-10;   sum_pos=0;   K_control=40;  %20;
for i=2:length(theta_p)
    u=K_control*(theta_p(i-1)+thetad_p(i-1)*.2)-0*sum_pos;   % u is current
    umax=ustall*(1-abs(thetad_p(i-1)/no_load_speed));
    if abs(umax)>20
        umax=sign(umax)*20;
    end
    if abs(u)>umax
        u=sign(u)*umax;
    end
    u_was(i)=u;
    B=mp*R*L*cos(theta_p(i-1))-n*n*Jm;
    C=-mp*g*L*sin(theta_p(i-1));
    D=fr*(thetad_p(i-1)-thetad_w(i-1));
    E=(mp+mw)*R*R+Jw+n*n*Jw;
    F=-mp*R*L*sin(theta_p(i-1))*(thetad_p(i-1)^2);
    thetad2_w(i)=(A/(E*A-B*B))*((B*D+B*C+B*n*Kt*u)/A+D-F+n*Kt*u+Fe*R);
    thetad2_p(i)=(-1/A)*(n*Kt*u+B*thetad2_w(i)+C+D);
    thetad_w(i)=thetad_w(i-1)+dt*thetad2_w(i);
    thetad_p(i)=thetad_p(i-1)+dt*thetad2_p(i);
    theta_w(i)=theta_w(i-1)+dt*thetad_w(i);
    theta_p(i)=theta_p(i-1)+dt*thetad_p(i);
    sum_pos=sum_pos+theta_w(i)*R*dt;
end
t=dt*[1:length(theta_p)];   base_pos=R*theta_w;
pend_posx=base_pos+L*sin(theta_p);   pend_posy=R+L*cos(theta_p);
figure(1); clf;  a=2*pi*[0:.01:1];  i=1; nframe=11;
plot([-2 1],[0 0],'k'); hold on;
for j=1:nframe;
    if j==1
        plot(base_pos(i)+[R (-.5*R+L)]*sin(theta_p(i)),R+[R (-.5*R+L)]*cos(theta_p(i)),'b')
        patch(base_pos(i)+R*cos(a),R+R*sin(a),'b')
        patch(pend_posx(i)+.5*R*cos(a),pend_posy(i)+.5*R*sin(a),'b')
    elseif j==nframe
        plot(base_pos(i)+[R (-.5*R+L)]*sin(theta_p(i)),R+[R (-.5*R+L)]*cos(theta_p(i)),'r')
        patch(base_pos(i)+R*cos(a),R+R*sin(a),'r');
        patch(pend_posx(i)+.5*R*cos(a),pend_posy(i)+.5*R*sin(a),'r')
    else
        plot(base_pos(i)+[R (-.5*R+L)]*sin(theta_p(i)),R+[R (-.5*R+L)]*cos(theta_p(i)),'k')
        plot(base_pos(i)+R*cos(a),R+R*sin(a),'k');
        plot(pend_posx(i)+.5*R*cos(a),pend_posy(i)+.5*R*sin(a),'k')
    end
    i=i+1000;
end
axis image; axis([-1.5 0 -.05 1.5]); axis off
% --- EOF ---
```
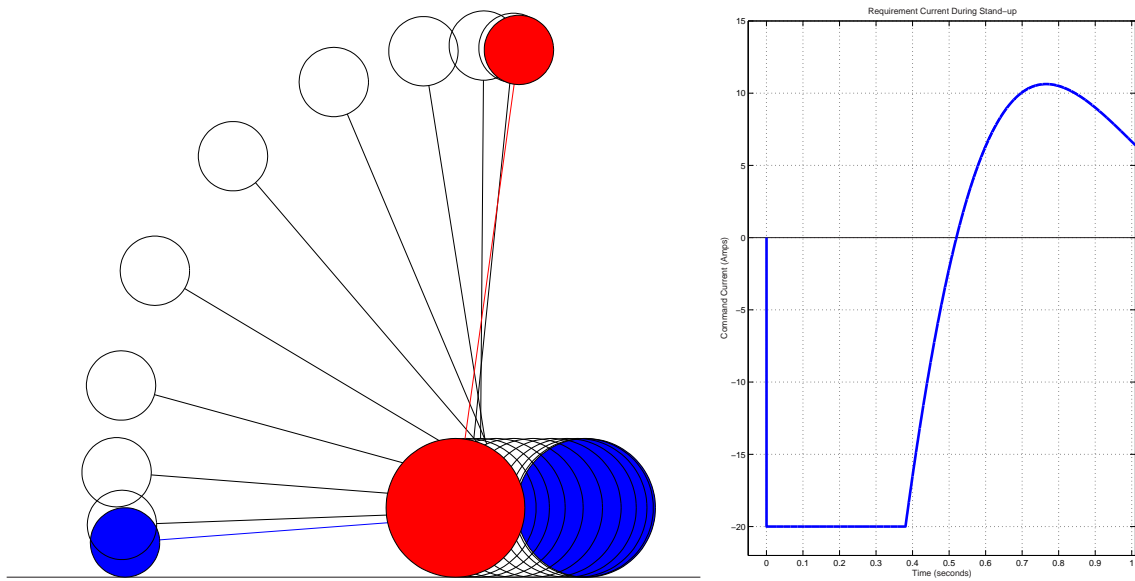
Figure G-2: MATLAB simulation code.

Appendix H

Simulink/dSPACE Controller

This appendix documents the main Simulink/dSPACE model used to control the inverted pendulum robot. There is a separate figure for each subsystem in the model. Table H lists the MATLAB variables used for the controller.

MATLAB variables for Simulink model

name and value	variable definition
dt = .5e-4;	time step size
Enc_cnt = 500;	(Quad) counts per revolution
I_max = 17.5;	[Amps] Peak supply current available (at 18 volts)
Ki_motor = 0.0263;	[Nm/A]
N_gearhead = 13/3;	Maxon Motor single-stage planetary gearhead ratio
R_wheel = 0.1525;	[meters]
accX_off = -0.2580;	X-dir acc offset (*added* to signal)
accX_gain = (1/.06245);	X-dir gain to set range -1 to +1 (for atan2)
accY_off = -0.2539;	Y-dir acc offset
accY_gain = (1/.06010);	Y-dir gain (for atan2 scaling)
ang_acc = -4.3;	correction for angle at which acc is mounted
enc_k = (360/Enc_cnt)(1/N_gearhead);	encoder gain, A/D to degrees
gyro_off = -0.025;	gyro offset, a/d input scaling
gyro_gain = 400;	output rate in deg/sec; nominal value is 400
i_limit = I_max;	max current request for D/A
signX = +1;	+/- for atan2 function (acc x)
signY = -1;	+/- for atan2 (acc y)
steer_dzforw = 0.05;	deadzone, forw (out of -1 to +1 ADC range possible)
steer_dzturn = 0.05;	deadzone, turning input
steer_Gforw = 1*5;	to command up to 1 meter per second
steer_Gturn = 20*5;	to command up to 20 degrees per second
steer_off_forw = -.25;	offset for forward vel input
steer_off_turn = -.25;	offset to be ADDED to turning input
tau_acc1 = .01;	accelerometer filtering time constant
tau_acc2 = .05;	additional acc filtering improved signal
tau_g1 = .0022;	gyro first-order filtering time constant
tau_drift = 1;	gyro drift time constant
Dval=0.3;	derivative action gain
PDval=18.0;	PD controller (outer loop) gain
Kp=0.2	Motor Position gain
G=0.05;	inner loop gain (for wheel velocity)
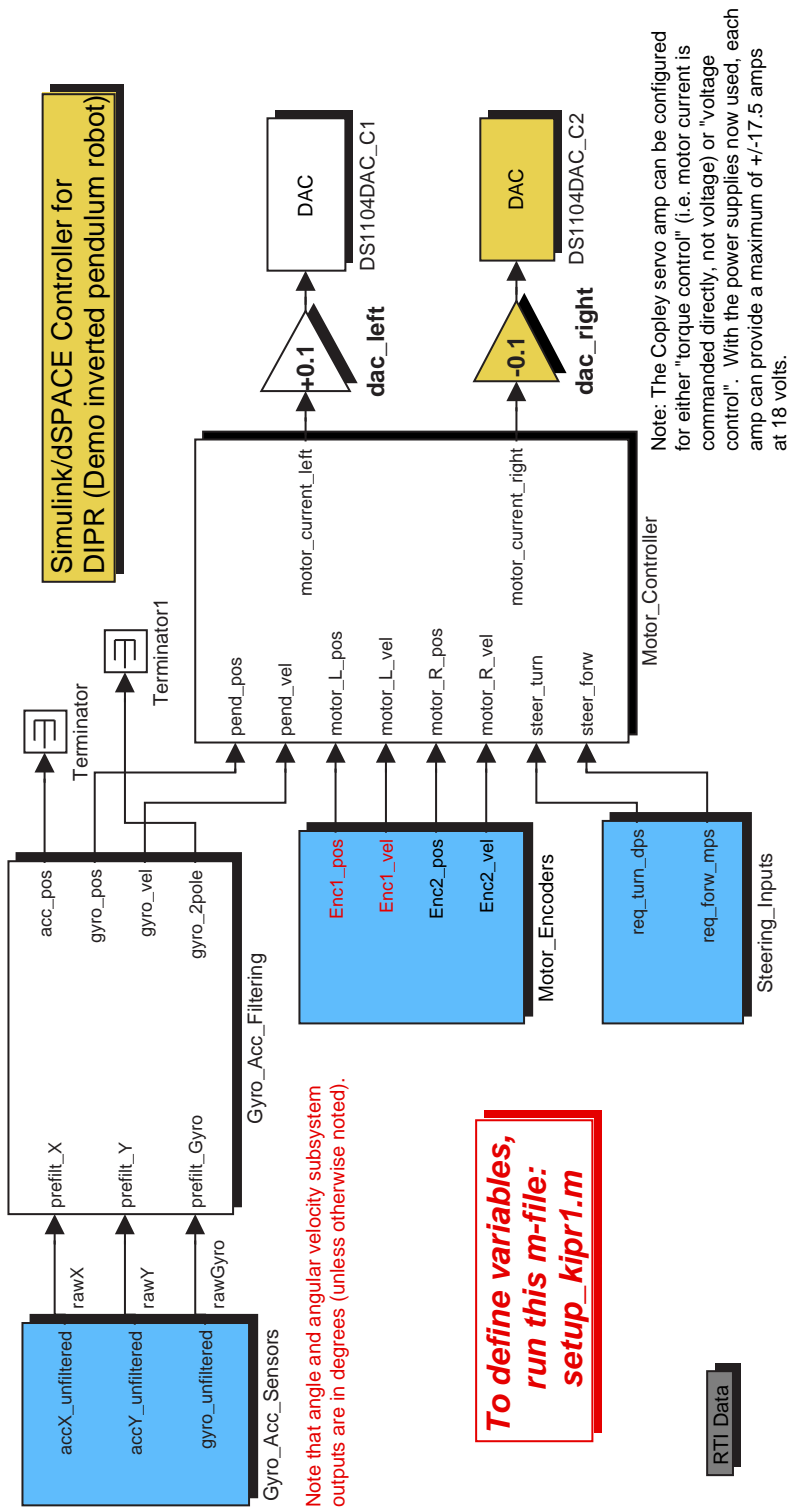
Figure H-1: Simulink controller mdl-file.

435
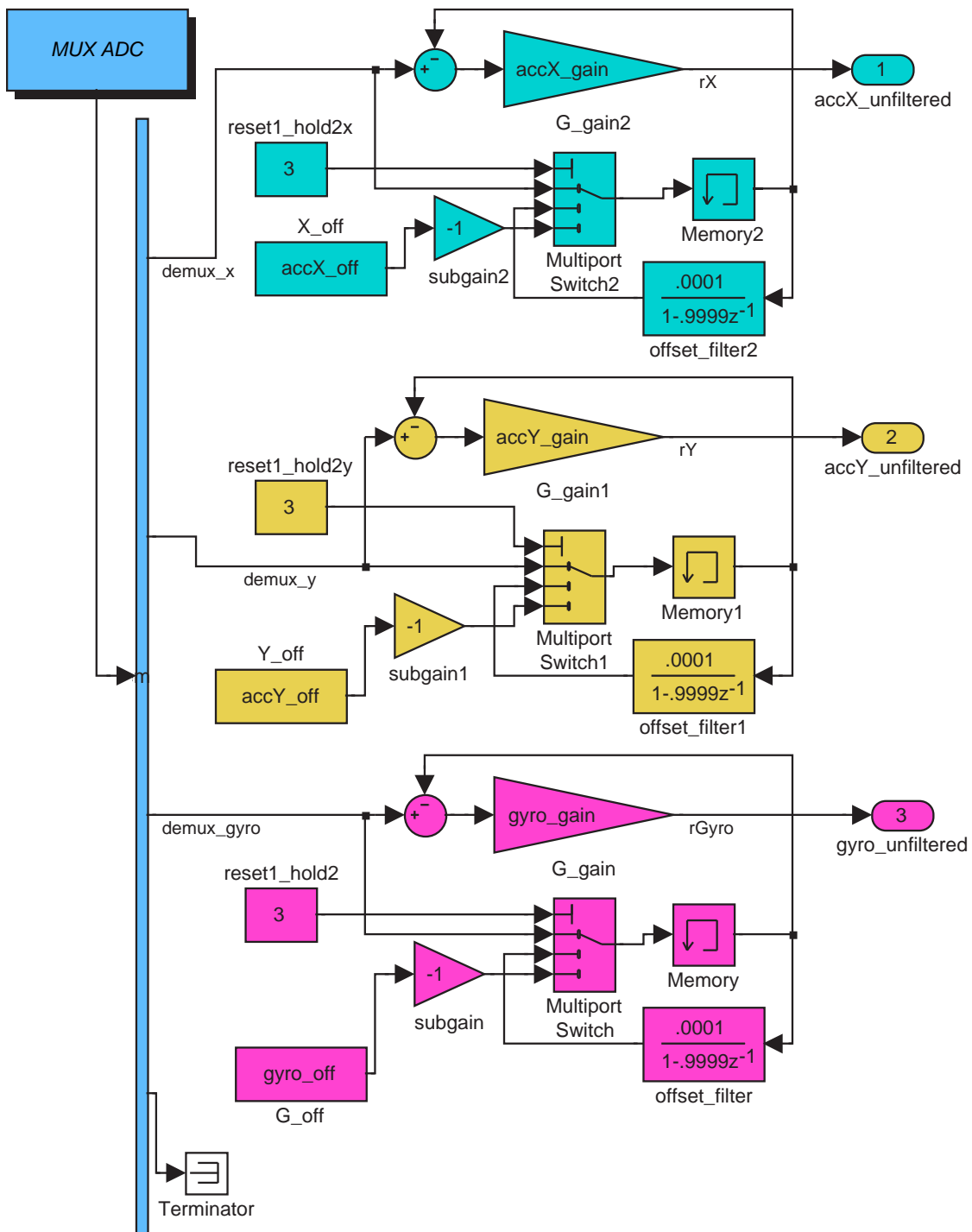
Figure H-2: Gyro_Acc_Sensors subsystem of Controller mdl-file.
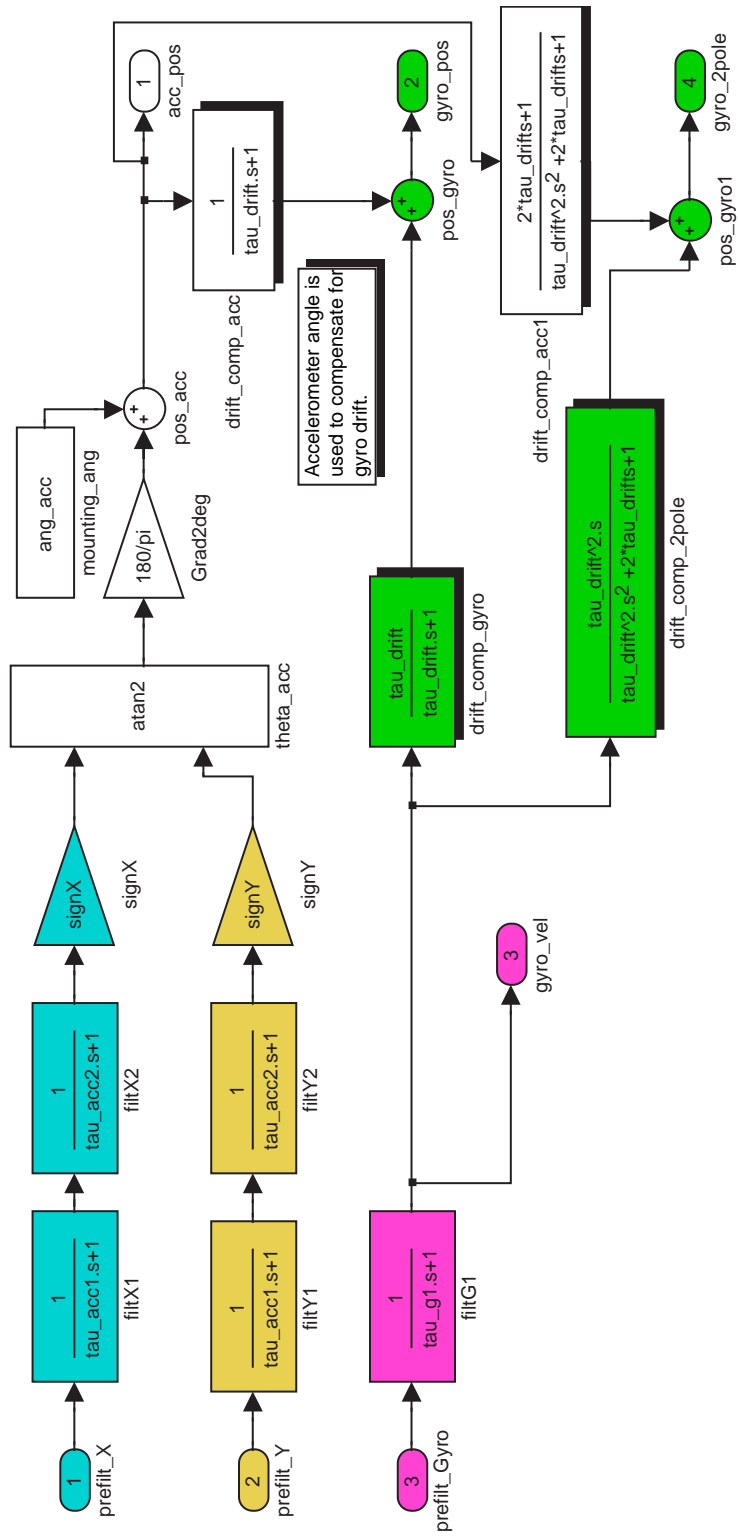
Figure H-3: Gyro_Acc_Filtering subsystem of controller mdl-file.
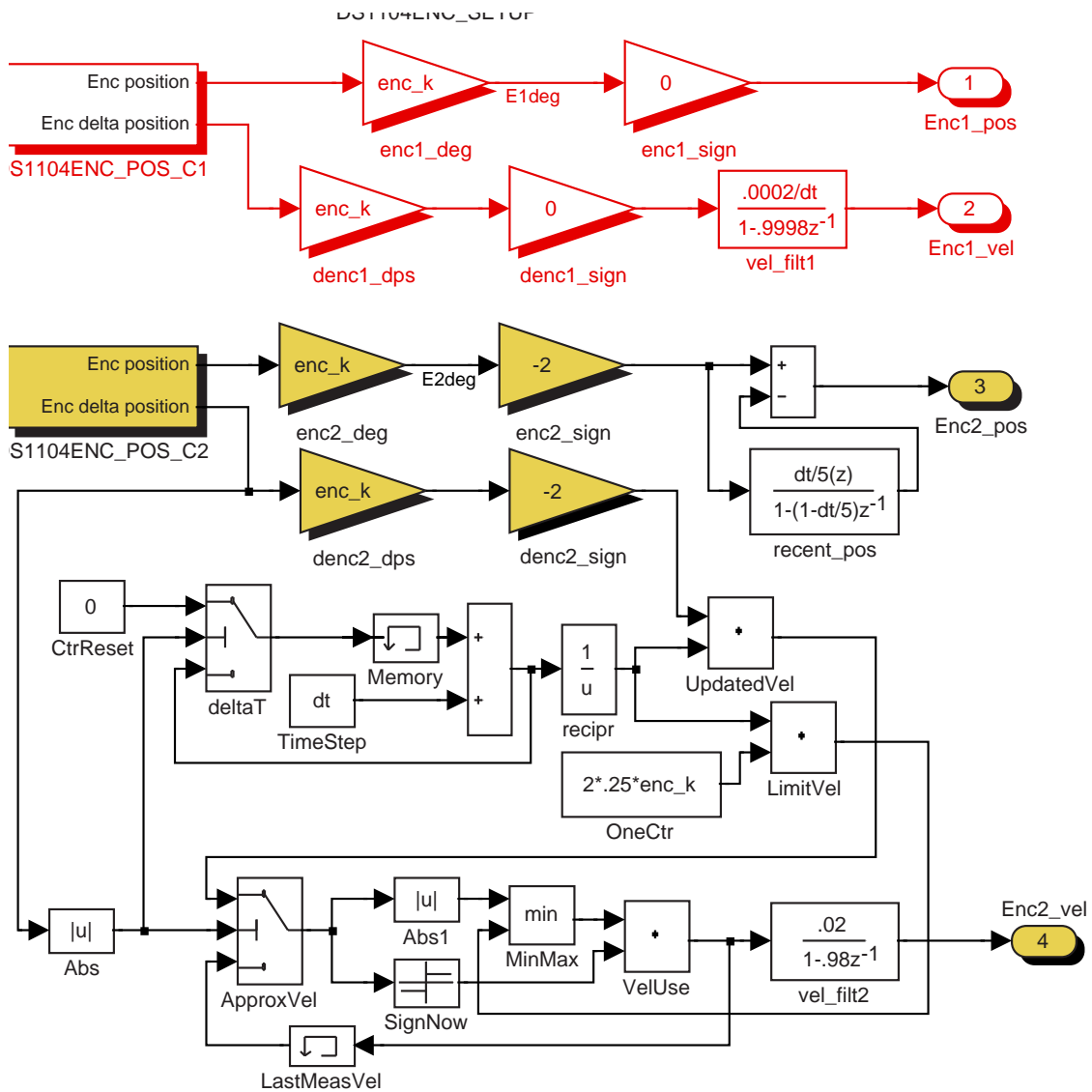
Figure H-4: Motor_Encoders subsystem of controller mdl-file.
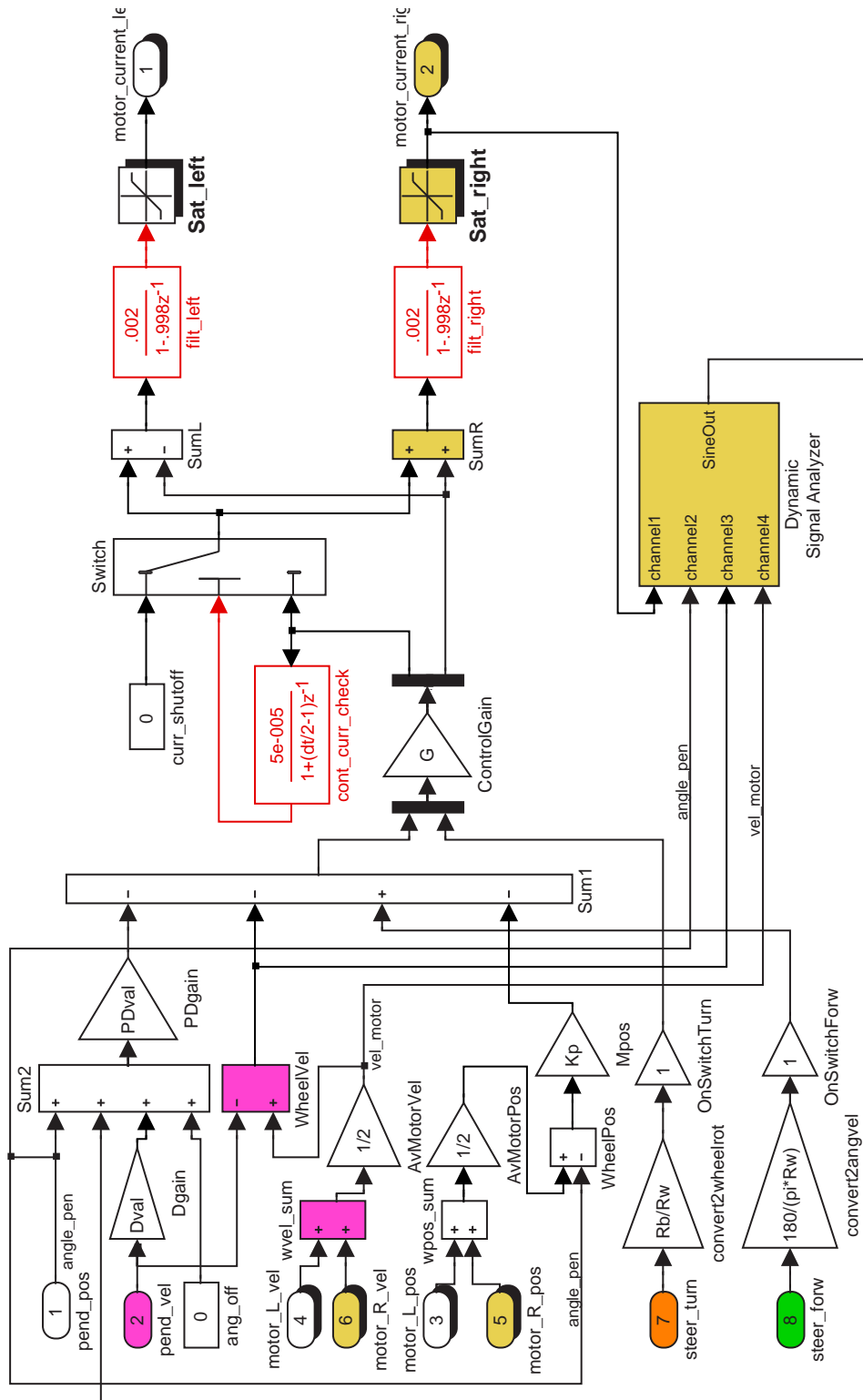
Figure H-5: Motor_Controller subsystem of controller mdl-file.

439

Potentiometers are use to provide
steering inputs [with deadzones].

steer_off_turn

turning_offset

ADC

DS1104ADC_C5

+ +

DeadZoneTurn

steer_Gturn

scale_turn

Requested turning speed
[degrees per sec]

1

req_turn_dps

steer_off_forw

velocity_offset

ADC

DS1104ADC_C6

+ +

DeadZoneForw

steer_Gforw

scale_forw

Requested forward speed
[meters per sec]

2

req_forw_mps
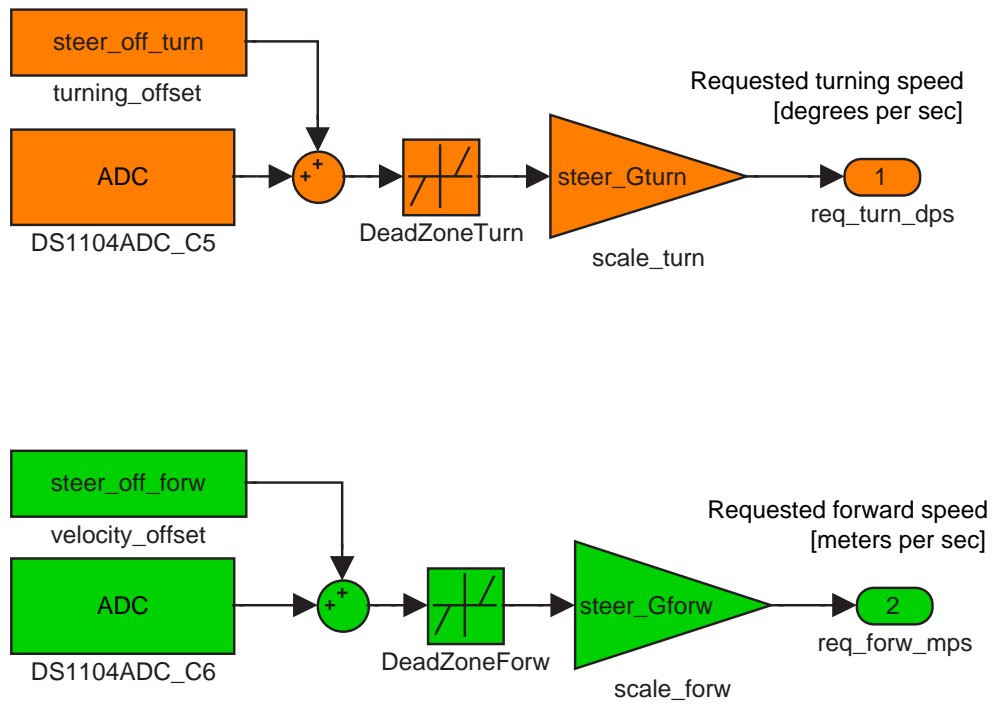
Figure H-6: Steering_Inputs subsystem of controller mdl-file.

Bibliography

[1] M. Acar. Mechatronics challenge for the higher education world. *IEEE Transactions on Components, Packaging, and Manufacturing Technology - Part C*, 20(1):14–20, 1997.

[2] M. Acar and R. M. Parkin. Engineering education for mechatronics. *IEEE Transactions on Industrial Electronics*, 43(1):106–112, February, 1996.

[3] Edith Ackermann. Piaget's constructivism, papert's constructionism: What's the difference? (publication in progress, 2001).
http://learning.media.mit.edu/content/publications/EA.Piaget%20_%20Papert.pdf.

[4] National Aeronautics and Space Administration. Hubble facts: Hubble space telescope servicing mission 3A (Gyroscopes), 1999. Fact sheet.
http://www.gsfc.nasa.gov/gsfc/service/gallery/fact_sheets/spacesci/hst3-01/hst_gyros.pdf.

[5] National Aeronautics and Space Administration. The Hubble project: Servicing mission 3B, 2002. Mission Update.
http://sm3b.gsfc.nasa.gov/mission-updates/mission/mar9.html.

[6] The Airpot Corporation. Airpot corporation home page. website, accessed July 2001. http://www.airpot.com.

[7] D. G. Alciatore and M. B. Histand. Integrating mechatronics into a mechanical engineering curriculum. *IEEE Robotics and Automation Magazine*, pages 35–38, June, 2001.

[8] Amazon.com. The science behind the segway. *Amazon.com: Electronics - Segway Human Transporter*, accessed March 2003. http://www.amazon.com/exec/obidos/tg/detail/-/B00007EPJ6/ref=segway_tn_left/104-4673826-9915947.

[9] American stirling company. mm-6 stirling engine. website, accessed January, 2003. http://www.stirlingengine.com/ecommerce/product.tcl?product_id=31.

[10] American Association of People with Disabilities. FDA backs stair-climbing wheelchair, Dec. 2002. http://www.aapd.com/docs/stairclimbwheelchair.html.

[11] Analog Devices, Inc. Low cost +/-2 g / +/-10 g dual axis iMEMS accelerometers with digital output. Product Specification Sheet, 1999.

[12] David P. Anderson. nBOT balancing robot. website, accessed February 2003. http://www.geology.smu.edu/ dpa-www/robo/nbot/.

[13] R. C. Arkin, K. Lee, L. F. McGinner, and C. Zhoe. The development of a shared interdisciplinary intelligent mechatronics laboratory. *Journal of Engineering Education*, pages 113–118, April, 1997.

[14] The Associated Press. The Associated Press photo archive. website, accessed August, 2002. http://photoarchive.ap.org/apdbs/Intl_Photos/views/mini/6068/6068441.jpg.

[15] D. M. Auslander. Meeting industrial needs in mechatronics and control. *Proceeding of the ASME Dynamic Systems and Control Division*, DCS-64:383–387, 1998.

[16] Autodesk. FIRST. website - Site design courtesy of Autodesk, accessed February, 2003. http://www.usfirst.org/.

[17] Tak Auyeung. Micromouse handbook, April 6, 2003. http://www.mobots.com/EeC194/book/book/.

[18] Farrokh Ayazi and Khalil Najafi. Design and fabrication of a high-performance polysilicon vibrating ring gyroscope. *Eleventh IEEE/ASME Intervational Workshop on Micro Electro Mechanical Systems*, Heidelburg, Germany, January 25-29 1998.

[19] Farrokh Ayazi and Khalil Najafi. A HARPSS polysilicon vibrating ring gyroscope. *Journal of Microelectromechanical Systems*, 10(2):169–179, June 2001.

[20] Richard Babyak. Servo surprise. *Appliance Manufacturer Magazine*, March 2002. http://www.ammagazine.com/CDA/ArticleInformation/features/ BNP_Features_Item/0,2606,72638,00.html - Note the underscores ("__") are two "_" wide, each.

[21] A.J. Baerveldt and R. Klang. A low-cost and low-weight attitude estimation system for an autonomous helicopter. *Proc. of the IEEE Int. Conf. on Intelligent Engineering Systems, INES '97*, September 1997.

[22] Albert-Jan Baerveldt and Robert Klang. A low-cost and low-weight attitude estimation system for an autonomous helicopter. *Proc. of the IEEE Int. Conf. on Intelligent Engineering Systems, INES 97, Budapest, Hungary*, Sep 1997. online at: http://www.geology.smu.edu/ dpa-www/robo/balance/inertial.pdf.

[23] Jens G. Balchen and Kenneth I. Mummé. *Process Control: Structures and Applications*. Van Nostrand Reinhold Company, New York, 1988.

[24] Neil Barbour and George Schmidt. Inertial sensor technology trends. *Proceedings of the 1998 Workshop on Autonomous Underwater Vehicles*, Cambridge, MA:55–62, August 20-21 1998.

[25] Larry Barello. Gyrobot - a balancing robotic platform. website, accessed February, 2003. http://www.barello.net/Robots/gyrobot/index.htm.

[26] Garrett Barter, Elie Krevat, and Dan Kwon. Team 33 - Dr. Whackenscore. MIT website, accessed January 2003, 6.270, January, 2001. http://robots6270.mit.edu/contests/2001/robots/33/www/.

[27] Robert J. Beichner. SCALE-UP project summary, 1999. online at the North Carolina State University website http://www.ncsu.edu/PER/SUPFIPSE.pdf.

[28] Robert J. Beichner, Jeffrey M. Saul, Rhett J. Allain, Duane L. Deardorff, and David S. Abbott. Introduction to SCALE-UP: Student-centered activities for large enrollment university physics. *Proceedings of the 2000 Annual meeting of the American Society for Engineering Education.*, 2000.

[29] John W. Belcher. Studio physics at MIT, Fall 2001. Physics Department News Letter.

[30] Steve Benkovic, Steven Uyetanaka, and Meng Cheng Hsieh. Micromouse - hints, ideas, inspiration. Personal website, accessed January, 2003. http://homepage.mac.com/SBenkovic/MicroMouse/index.html.

[31] C. F. Bergh, A. Kita, and C. Ume. Development of mechatronics course in the school of mechanical engineering at Georgia Tech. *Proceeding of the 1999 IEEE/ASME International Conference on Advanced Intelligent Mechatronics*, pages 459–465, September, 1999.

[32] Jonathan Bernstein. MEMS inertial sensing technology. *Sensors Magazine Online*, Feb. 2003. http://www.sensorsmag.com/articles/0203/14/main.shtml.

[33] Michael V. Berry. The levitron^{TM}: an adiabatic trap for spins. *Proceedings of the Royal Society of London: Mathematical, Physical and Engineering Sciences*, 452(1948):1207–1220, May 8, 1996.

[34] Beswick Engineering. Beswick engineering home page. website, accessed January 2003. http://www.beswick.com.

[35] David Black-Schaffer, Dave Chisholm, Ramji Srinivasan, and Tenbite Ermias. The Yellow Jacket robot project report. Stanford website, accessed May 2002, EE118, Winter, 2001. http://design.stanford.edu/spdl/EE118/YellowJacket/.

[36] Boston EMS. Technology at 106th Boston marathon. website, accessed July 2002. http://www.bostonems.com/GalSegway.htm.

[37] R. S. Bradbeer. An integrated studio approach to teaching basic electronics to first year mechatronics degree students. *2001 IEEE/ASME International Conference on Advanced intelligent Mechatronics Proceedings*, pages 1118–1123, July, 2001.

[38] E. Douglas Bradbury. Suspension fork for bicycles. U.S. Patent 5,445,401 - assigned to Manitou Mountain Bikes, Inc., August 29, 1995.

[39] E. Douglas Bradbury. Suspension fork for bicycles with dual, fluid-based dampers. U.S. Patent 5,509,677 - assigned to Manitou Mountain Bikes, Inc., April 23, 1996.

[40] British Aerospace Engineering Systems. VSG typical performance guide, 2001. http://www.baesystems-gyro.com/PDF/Vsg.pdf.

[41] Alison K. Brown, Mark A. Sturza, Franco DeAngelis, and David A. Lukaszewski. Fault tolerant GPS/inertial syste design. *ION Satellite Division 3rd International Technical Meeting*, pages 495–504, September 1990.

[42] Robert Grover Brown. *Introduction to Random Signals and Applied Kalman Filtering: with MATLAB exercises and solution*. John Wiley & Sons, 1997.

[43] Vic Caleca. Under wraps: How they kept the Segway secret. *USA Today online*, February 2002. http://www.usatoday.com/tech/techreviews/2002/1/30/segway-secret.htm.

[44] Andre Cardadeiro. Dre's 99gsx master tranny rebuild vfaq. Personal website, accessed January 2003. http://www.twingles.com/ideck/rebuild3/dretranny.htm.

[45] J. E. Carryer. Controller and components: Deciding what (and what not) to teach in mechatronics courses. *Proceeding of the ASME Dynamic Systems and Control Division*, DSC-64:377–382, 1998.

[46] J. E. Carryer. March madness: A mechatronics project theme. *Proceeding of the 7th Mechatronics Forum Internsational Conference: Mechatronics Education VI session*, September, 2000.

[47] J. F. Cham, B. Stafford, and M. R. Curkosky. See labs run: A design-oriented laboratory for teaching dynamic systems. *Proceedings of 2001 ASME International Mechanical Engineering Congress and Exposition*, November 11-16 2001.

[48] Edward Y. Chow and Alan S. Willsky. Analytical redundancy and the design of robust failure detection systems. *IEEE Transactions on Automatic Control*, AC-29(7):603–614, July 1984.

[49] Richard D. Christie. The disposable camera, June 1996. http://www.ee.washington.edu/conselec/CE/kuhn/labs/camera/fl.htm.

[50] Donna Coveney. Photo of seymour papert from mit's tech talk. copyright 2002. http://www.davidsonfilms.com/piafot01.htm.

[51] Kevin Craig. Mechatronics facilities at rensselaer. RPI website. http://www.rpi.edu/sincraigk.

[52] Kevin Craig. Mechatronics in university and professional education: Is there anything really new here? *Proceedings of the ASME Dynamic Systems and Control Division*, DSC-64:369–375, 1998.

[53] Kevin Craig. Mechatronics at rensselaer: a two-course senior-elective sequence in mechanical engineering. *Proceedings of the 1999 IEEE/ASME International Conference on Advanced Intelligent Mechatronics*, pages 452–458, September, 1999.

[54] Kevin Craig. Is anything really new in mechatronics education? *IEEE Robotics and Automation Magazine*, pages 12–19, June, 2001.

[55] Edward F. Crawley, Kenneth B. Lazarus, Jeffrey W. Moore, Douglas A. Simpson, Gerald F. Caron, and Farla M. Russo. Damper and valve. U.S. Patent 6,193,029 - assigned to Active Control eXperts, Inc., February 27, 2001.

[56] Martin L. Culpepper. 2.000 How and why things work - labs (MIT). http://psdam.mit.edu/2.000/lab.html.

[57] Davidson Films. Piaget, middle age, boating with friends. website copyright 1998-2002.
http://www.davidsonfilms.com/piafot01.htm.

[58] James C. Deckert, Mukund N. Desai, John J. Deyst, and Alan S. Willsky. F-8 DFBW sensor failure identification using analytic redundancy. *IEEE Transactions on Automatic Control*, AC-22(5):795–803, October 1977.

[59] John DeGaspari. Shake, rattle and roll - thanks to the airbag, MEMS accelerometers are getting to explore new territory. *Mechanical Engineering Magazine [online]*, 2001. Published by the American Society of Mechanical Engineers. http://www.memagazine.org/backissues/nov01/features/rattle/rattle.html.

[60] Richard C. Dorf and Robert H. Bishop. *Modern control systems*. Prentice Hall, Upper Saddle River, NJ, seventh edition, 1995.

[61] The dSPACE Corporation. dSPACE - solutions for control. website, accessed March 2002. http://www.dspaceinc.com.

[62] Christopher W. Dyck, James J. Allen, and Robert J. Huber. Parallel-plate electrostatic dual-mass oscillator. *Presented at the Society of Photo-Optical Instrumentation Engineers (SPIE) Micromachining and Microfabrication Symposium, Santa Clara, California*, Septempber 20-22, 1999. available online at http://www.sandia.gov/mstc/technologies/micromachines/biblog_summit.html.

[63] Samuel Earnshaw. On the nature of the molecular forces which regulate the constitution of the luminiferous ether. *Transactions of the Cambridge Philosophical Society*, 7:97–112, 1842.

[64] Imme Ebert-Uphoff, John F. Gardner, William R. Murray, and Ronald Perez. Preparing for the next century: The state of mechatronics education. *IEEE/ASME Transactions on Mechatronics*, 5(2):226–227, 2000.

[65] Edmunds.com, inc. manual transmission basics. website, accessed Jan. 2003. http://www.edmunds.com/ownership/techcenter/articles/46029/article.html.

[66] G. Engh, P. Nelson, and N. J. Roach. Numismatic gyrations. *Nature*, 408:540, 2000.

[67] Epistemology and Learning Group MIT Media Lab. The programmable brick FAQ. website, accessed March, 2002. http://el.www.media.mit.edu/groups/el/projects/programmable-brick/more.html.

[68] Louis J. Everett. Dynamics as a process, helping undergraduates understand design and analysis of dynamic systems. *1997 ASEE National Conference*, Session 2666, 1997.

[69] Ron Fearing. Ee192 mechatronics design lab, 2003. http://www-inst.eecs.berkeley.edu/˜ee192/.

[70] Richard M. Felder and Linda K. Silverman. Learning and teaching styles. *Engineering Education*, 78(7):674–681, April 1988.

[71] S. Field, S. Meek, and S. Devasia. Mechatronics education in the department of mechanical engineering at the University of Utah. *Proceedings of the 7th Mechatronics Forum International Conference: Mechatronics Education IV session*, September, 2000.

[72] J. F. Gardner. Two projects for undergraduate mechatronics class: Success and failure. *Proceedings of the 7th Mechatronics Forum International Conference: Mechatronic Education VI session*, September, 2000.

[73] Jerold P. Gilmore and Richard A. McKern. A redundant strapdown inertial system mechanization - SIRU. *Charles Stark Draper Laboratory publication*, pages 899–902, August 17-19 1970. Presented at the AIAA Guidance, Control and Flight Mechanics Conference, Santa Barbara, California.

[74] Felix Grasser, Aldo D'Arrigo, Silvio Colombi, and Alfred Rufer. JOE: A mobile, inverted pendulum, 2001. Unpublished paper, available online. http://leiwww.epfl.ch/publications/grasser_darrigo_colombi_rufer_mic_01.pdf.

[75] Felix Grasser, Aldo D'Arrigo, Silvio Colombi, and Alfred Rufer. JOE: A mobile, inverted pendulum. *IEEE Transactions on Industrial Electronics*, 49(1):107–114, February 2002.

[76] Donald E. Grove. The vertical integration of mechatronics at Virginia Tech. Master's thesis, Virginia Tech, Mechanical Engineering Department, February 2001.

[77] T. G. Habetler, J. Meisel, G. H. Ronald, and H. B. Püttgen. A new undergraduate course in energy conversion and mechatronics at Georgia Tech. *Proceedings of the 7th Mechatronics Forum International Conference: Mechatronics Education I session*, September, 2000.

[78] Blake Hannaford. Robust electronic circuits: The disposable camera flash, March 2001. Lab assignment for EE498 Consumer Electronics Design at the University of Washington.
http://www-brl.ee.washington.edu/Education/EE498/labs/lab_cam_1-2.html.

[79] Tom Harris. HowStuffWorks, Inc. Howstuffworks - how segways work. website, accessed August 2002. Copyright 1998-2003, HowStuffWorks, Inc.
http://www.howstuffworks.com/ginger.htm.

[80] Steve Hassenplug. Steve's LegWay. website, accessed February 2003.
http://perso.freelug.org/legway/LegWay.html.

[81] H. A. Haus and J. R. Melcher. *Electromagnetic Fields and Energy.* electronic text rights reserved by HTF (Hypermedia Teaching Facility) at MIT, online text edition, 1998. http://web.mit.edu/6.013_book/www/book.html.

[82] John Heilemann. Reinventing the wheel. *Time online edition*, December 2 2001.
http://www.time.com/time/business/article/0,8599,186660-2,00.html.

[83] Willem M. Hijmans. ActivLab. website, accessed August 2002.
http://web.mit.edu/2.003/www/activlab/activlab.html.

[84] HiTechnic Products. HiTechnic products and accessories. website, accessed
February 2003. http://www.hitechnic.com/products.htm.

[85] Ian D. Hopkins. Performance and design of a silicon micromachined gyro. *Rate
Sensor Application Note*, 2001. Silicon Sensing Systems
http://www.siliconsensing.com/acrobat/AN0199.pdf.

[86] Ian David Hopkins, Christopher Paul Fell, Kevin Townsend, and Timo-
thy Robert Mason. Vibrating structure gyroscope. U.S. Patent 5,932,804 -
assigned to British Aerospace Public Limited Company, August 3, 1999.

[87] HowStuffWorks, Inc. HowStuffWorks - learn how everything works! website.
Copyright 1998-2003, HowStuffWorks, Inc. http://www.howstuffworks.com.

[88] Jerwei Hsieh and Weileum Fang. A boron etch-stop assisted lateral etching pro-
cess for improved high-aspect-ratio silicon micro-machining and its applications.
Journal of Micromechanics and icroengineering, 12:574–581, June 2002.

[89] T. Hsu and J. Wang. A mechatronics curriculum stem for undergraduate
mechanical engineering education. *Proceedings of the 1999 IEEE/ASME In-
ternational Conference on Advanced Intelligent Mechatronics*, pages 577–584,
September, 1999.

[90] Kevin Hulsey. Mountain bike suspension fork. website, accessed January, 2003.
Copyright Kevin Hulsey Illustration, Inc.
http://www.khulsey.com/bikefork.jpeg.

[91] Immersion Corporation. Immersion Corporation homepage, copyright 2002.
http://www.immersion.com/.

[92] Fascinations Incorporated. Levitron - the amazing anti-gravity top. website,
accessed March, 2002. http://www.levitron.com.

[93] Institute of Electrical and Electronic Engineers (IEEE) U.C. Davis. What is Micromouse? http://www.ece.ucdavis.edu/∼ieee/umouse/umouse.html.

[94] Hong Jin and Hong Yue Zhang. Optimal parity vector sensitive to designated sensor fault. *IEEE Transactions of Aerospace and Electronic Systems*, 35(4):1122–1128, October 1999.

[95] Johnson & Johnson and DEKA. Independence Technology, a Johnson & Johnson company - iBOT(TM). website, accessed August 2002. http://www.independencenow-europe.com/ibot/index.html.

[96] Joseph L. Jones, Bruce A. Seiger, and Anita Flynn. *Mobile Robots: Inspiration to Implementation.* A K Peters, Ltd., Natick, Massachusetts, second edition, 1999.

[97] Dean L. Kamen, Robert R. Ambrogi, Robert J. Duggan, Richard K. Heinzman, Brian R. Key, and Susan D. Dastous. Control loop for transportation vehicles. U.S. Patent 5,791,425, August 11, 1998.

[98] Dean L. Kamen, Robert R. Ambrogi, Robert J. Duggan, Richard K. Heinzman, Brian R. Key, Andrzej Skoskiewicz, and Phyllis K. Kristal. Human transporter. U.S. Patent 5,701,965, Deceber 30, 1997.

[99] Dean L. Kamen, Robert R. Ambrogi, Richard Kurt Heinzman, Christopher C. Langenfeld, Marc A. Nisbet, Stanley B. Smith (III), and Thomas Alan Brindley. Mechanical improvements to a personal vehicle. U.S. Patent 6,405,816, June 18, 2002.

[100] Dean L. Kamen, Robert R. Ambrogi, John David Heinzmann, Richard Kurt Heinzmann, David Herr, and John B. Morrell. Control inputs for a balancing personal vehicle. U.S. Patent 6,415,879, July 9, 2002.

[101] Matt Kelly. MEMS for everyman? Analog gyro puts a new spin on price, October 1 2002. http://smalltimes.com/document_display.cfm?document_id=4732.

[102] Clive William Kilmister. *Lagrangian Dynamics: An introduction for students.* Plenum Press, New York, 1967.

[103] Mike Koss. Home page for mike koss. Personal website, accessed January 2003, 6.270, January, 2002. http://mckoss.com/6270/sozoomy.htm.

[104] Suzanne M. Kresta. Hands-on demonstrations: An alternative to full scale lab experiments. *Journal of Engineering Education*, 87(1):7–9, January 1998.

[105] T. Kurfess and J. G. Witzel. Using mechatronics in early design. *Proceedings of the 7th Mechatronics Forum International Conference: Mechatronics Education III session*, September, 2000.

[106] Thomas R. Kurfess. Mechatronics and early mechanical design. *IEEE/ASME International Conference on Advanced Intelligent Mechatronics Proceedings*, pages 990–993, July 8-12, 2001.

[107] Lauren E. LeBon. Students petition against TEAL. *The Tech*, 123(14), March 21 2003. http://www-tech.mit.edu/V123/N14/14802T.14n.html.

[108] Sangwoo Lee, Sangjun Park, Jongpal Kim, Sangchul Lee, and Dong il (Dan) Cho. Surface/bulk micromachined single-crystalline-silicon icrogyroscope. *TJournal Of Microelectromechanical Systems*, 9(4):557–567, December 2000.

[109] The LEGO Group. LEGO Mindstorms Robotics Invention System 2.0. website, last accessed February 2003.
http://mindstorms.lego.com/eng/products/ris/risdetails.asp.

[110] Walter Lewin. 8.01 fall 1999 lecture 30: Simple harmonic oscillations - energy considerations - torsional pendulum. MIT PIVoT online study materials, Recorded Nov. 24, 1999. (limited website access)
https://curricula2.mit.edu/servlet/pivot.pvservlet.Home?acode=0x0008000.

[111] John Lewis and Karen Auguston Field. An exclusive look at the engineering behind the Segway HT, with some never-before-published technical details. *Design News - Product Design and Development (online)*, March 25, 2002. http://www.manufacturing.net/dn/index.asp?layout=articleWebzine&articleid=CA200964.

[112] John H. Lienhard V. A heat transfer textbook: A free electronic textbook. Online letter to the public. http://web.mit.edu/lienhard/www/ahttproject.pdf.

[113] Katherine A. Lilienkamp. A simulink-driven dynamic signal analyzer. Bachelor's thesis, MIT, Mechanical Engineering Department, February, 1999.

[114] Katherine A. Lilienkamp and David L. Trumper. Dynamic signal analyzer for dSPACE. http://web.mit.edu/pmc/www/Links/dsa_paper.pdf, 1999.

[115] G. R. Luecke. "Muscletronics": Teaching mechatronics with fluid power systems. *Proceedings of the 1999 IEEE/ASME International Conference on Advanced Intelligent Mechatronics*, pages 466–471, September, 1999.

[116] Howard Lundberh. Linear dual inverted pendulum control. Master's thesis, MIT, Electrical Engineering Department, 1997.

[117] Jed S. Lyons, Jeffrey H. Morehouse, and Edward F. Young. Design of a laboratory to teach design of experiments. *Proceedings of the 1999 ASME Education Annual Conference*, Session 2566, June 20-23 1999.

[118] David Macaulay. *The Way Things Work*. Houghton Mifflin Company, 1988.

[119] David Macaulay and Neil Ardley. *The New Way Things Work: From Levers to Lasers, Windmills to Web Sites, a Visual Guide to the World of Machines*. Houghton Mifflin Company, 1998.

[120] R. Manseur. Development of an undergraduate robotics course. *1997 Frontiers in Education Conference*, Session F1C:610–612, 1997.

[121] Fred Martin. The handy board technical reference, accessed March, 2002. available online at http://handyboard.com.

[122] Fred Martin. Mindstorms information. website, accessed March, 2002. http://fredm.www.media.mit.edu/people/fredm/mindstorms/.

[123] Massachusetts Institure of Technology website. 6.270 - MIT's autonomous robot design competition. website. http://web.mit.edu/6.270/.

[124] *Massachusetts Institute of Technology. Bulletin*, volume 138. MIT, Cambridge, MA, 2002.

[125] Massachusetts Institute of Technology. OpenCourseWare -About OCW. http://ocw.mit.edu/global/about-ocw.html.

[126] Ben Massawir, Aren Sandersen, and Tenbite Ermias. Wilt - introduction. Stanford website, accessed May 2002, EE118, Winter, 2001. http://design.stanford.edu/spdl/EE118/Wilt/.

[127] The MathWorks, Inc. The MathWorks: Developers of MATLAB and Simulink for technical computing. website, accessed March, 2002. http://www.mathworks.com.

[128] Oliver Max. Ee192 stanford natcar, 2003. http://www.stanford.edu/group/natcar/index.html.

[129] Maxon Precision Motors, Inc. Maxon motor 2001: High precision drives and systems. Product Catalog, 2001. pp. 77, 195, and 206.

[130] Peter Maxwell, Jon Tessman, and Bruce Reichert. Design through to production of a MEMS accelerometer for seismic acquisition. *First Break*, 19(3):141–144, March 2001. published by the European Association of Geoscientists & Engineers. www.firstbreak.nl.

[131] S. W. McCuskey. *An Introduction to Advanced Dynamics*. Addison Wesley Publishing Company, Inc., Reading, Massachusetts, 1959.

[132] K. T. McDonald. Mcdonald's physics examples. website, accessed March 2002. http://www.hep.princeton.edu/~mcdonald/examples/.

[133] Ann McKenna and Alice Agogino. Integrating design, analysis, and problem solving in an introduction to engineering curriculum to high school students. *Engineering Education: Contributing to U.S. Competitiveness; Proceedings of ASEE '98*, Session 1280:1–14, June 28-July 1 1988. CD ROM.

[134] Ann McKenna and Alice Agogino. Integrating design, analysis, and problem solving in an introduction to engineering curriculum for high school students. *ASEE Annual Conference and Exposition, Charlotte, NC*, June 20-23, 1999. http://www.asee.org/conferences/annual99/assets/images/00308.pdf.

[135] Andrew McKinney and Mark Bessette, et al. MIT TEAL/Studio Physics Project. MIT TEAL tutorial visualizations, 2002. available through the MIT OpenCourseWare project at http://ocw.mit.edu/8/8.02/f02/index.html.

[136] James R. Melcher, Mark Zahn, and Harold Edgerton. *"Edgerton's Boomer" Demonstration 10.2.1 for 6.013*. electronic text rights reserved by HTF (Hypermedia Teaching Facility) at MIT, online video demonstration and numeric calculations edition, 1998. See Section 10.2 at http://web.mit.edu/6.013_book/www/book.html.

[137] MicroStrain, Inc. MicroStrain microminiature sensors: FAS-G inclinometer. website, accessed February 2003. http://www.microstrain.com/FAS-G.htm.

[138] Henry Minsky. Photo of marvin minsky from personal website. copyright 2002. http://www.ai.mit.edu/people/hqm/marvin1.gif.

[139] Marvin Minsky. *The Society of Mind*. Simon & Schuster, New York, 2nd edition edition, 1988.

[140] H. K. Moffat. Euler's disk and its finite-time singularity. *Nature*, 404:833–834, 2000.

[141] Francis C. Moon. *Applied dynamics with application to multibody and mechatronic systems.* John Wiley & Sons, Inc., New York, 1st edition edition, 1998.

[142] MSNBC Dateline. A revolutionary new wheelchair. website, accessed August 2002. http://www.msnbc.com/news/285231.asp.

[143] W. R. Murray and J. L. Garbini. Mechatronics: A thread in the mechanial engineering undergraduate curriculum. *Proceedings of the ASME Dynami Systems and Control Division*, DSC-Vol. 64:397–404, 1998.

[144] W. R. Murray and J. L. Garbini. Mechatronics capstone design projects at the University of Washington. *Proceedings of the 1999 IEEE/ASME International Conference on Advanced Intelligent Mechatronics*, pages 598–604, September, 1999.

[145] Yoav Naveh, Pinhas Z. Bar-Yoseph, and Yoram Halevi. Nonlinear modeling and control of a unicycle. *Dynamics and Control*, 9(4):279–296, Oct 1999.

[146] New Way Machine Components, Inc. Air bearings. website, accessed August 2001. http://newwaybearings.com.

[147] Newton Research Labs, Inc. Interactive C (IC). website, accessed February 2002. http://www.newtonlabs.com/ic/.

[148] Clark T.-C. Nguyen. Frequency-selective MEMS for miniaturized communization devices. *Proceedings of the 1998 IEEE Aerospace Conference (Snowass, Colorado)*, 1:445–460, March 21-28 1998.

[149] Steven Niemczyk. *An Adaptive Domain-Independent Agents-Based Tutor for Web-Based Supplemental Learning Environments.* PhD thesis, MIT, Department of Civil and Environmental Engineering, February, 2003.

[150] North Carolina State University. about the SCALE-UP project... Website accessed March 2003. http://www.ncsu.edu/per/scaleup.html.

[151] Hans Ohanian. *Physics.* W. W. Norton Publishing Co., 2nd edition edition, 1989. online text adapted by EspriTEC (not publically available) included on PIVoT website.

[152] Allison Okamura. The haptic paddle. website, copyright 1998. http://www-cdr.stanford.edu/Touch/previous_projects/paddle/.

[153] William J. Palm III. *Modeling, Analysis, and Control of Dynamic Systems.* John Wiley & Sons, Inc., New York, 2nd edition edition, 1999.

[154] Seymour Papert. *Logo Philosophy and Implementation - Introduction: What is Logo? Who needs it?* Logo Computer Systems, Inc, 1999.

[155] Seymour Papert. Papert on piaget. *Time Magazine: "The Century's Greatest Minds"*, page 105, March 29 1999.

[156] Parallax, Inc. Parallax: BASIC stamp microcontrollers. website, accessed March 2002. http://www.parallaxinc.com/.

[157] Antoónio M. Pascoal, Isaac Kaminer, and Paulo Oliveira. Navigation system design using time-varying complementary filters. *IEEE Transactions on Aerospace and Electronic Systems*, 36(4):1099–1114, Oct 2000.

[158] R. J. Patton and J. Chen. Review of parity space approaches to fault diagnosis for aerospace systems. *Journal of Guidance, Control and Dynamics*, 17(2):278–285, March-April 1994.

[159] Theresa M. Pease. Papert describes his philosophy of education. *Tech Talk*, May 16 1990. http://web.mit.edu/newsoffice/tt/1990/may16/23181.html.

[160] Arthur J. Pejsa. Optimum skewed redundant inertial navigators. *AIAA Journal*, 12(7):899–902, July 1974.

[161] A. J. Peyton, J. R. Burch, A. Bradshaw, and A. P. Dorey. The teaching of sensors and instrumentation to second year electronics/mechatronics students.

Technical report, Engineering Dept., Lancaster UK, 1996. (published by the Institution of Electrical Engineers).

[162] H. A. Pham, Y. S. Kua, and K. Salem. Having fun with muscle wires. *Proceedings of the 7th Mechatronics Forum International Conference: Mechatronic Education II session*, September 2000.

[163] Philips Electronics N. V. Philips employee appointed advanced mechatronics professor at Delft University of Technology. news release, accessed online March 2001. http://www.cft.philips.com/newscenter/newscenter_copy(3).htm.

[164] Lara C. Phillips. Control of a dual inverted pendulum system using linear-quadratic and H-infinity methods. Master's thesis, MIT, Electrical Engineering Department, 1994.

[165] Jean Piaget. *To understand is to invent: the future of education. [English translation by George-Anne Roberts].* Grossman Publishers, New York, 1973.

[166] J. E. Potter and M. C. Suman. Thresholdless redundancy management with arrays of skewed instruments. *Integrity in Electronic Flight Control Systems*, NATO Agardograph(225):15:1–25, April 1977.

[167] James E. Potter and James C. Deckert. Minimax failure detection and identification in redundant gyro and accelerometer systems. *Journal of Spacecraft and Rockets*, 10(4):236–243, April 1973.

[168] Derek Reamon. Mechanical dissection labs. Stanford University. http://www-adl.stanford.edu/labs.html.

[169] Christopher Richard, Allison M. Okamura, and Mark R. Cutkosky. Getting a feel for dynamics: Using haptic interface kits for teaching dynamics and controls. *ASME IMECE 6th Annual Symposium on Haptic Interfaces (Dallas, Texas)*, November 15-21 1997.

[170] Christopher Richard, Allison M. Okamura, and Mark R. Cutkosky. Feeling is believing: Using a force-feedback joystick to teach dynamic systes. *Proceedings of the 2000 ASEE Annual Conference and Exposition, Session 3668*, 2000.

[171] Rebecca Richkus, Alice Agogino, David Yu, and David Tang. Virtual disk drive design game with links to math, physics and dissection activities. *29th ASEE/IEEE Frontiers in Education Conference, San Juan, Puerto Rico*, Session 12c3:1–5, November 10-13 1999.

[172] Rebecca Richkus, Alice M. Agogino, David Yu, and David Tang. Virtual disk drive design game with links to math, physics and dissection activities. *29th ASEE/IEEE Frontiers in Education Conference, San Juan, Puerto Rico*, Nov. 10-13, 1999. http://best.me.berkeley.edu/ãagogino/papers/VIRTUAL.PDF.

[173] James K. Roberge. *Operational Amplifiers: Theory and Practice.* John Wiley and Sons, New York, 1975.

[174] James K. Roberge. Propogation of the race (of analog circuit designers). In Jim Williams, editor, *Analog Circuit Design: Art, Science, and Personalities*, pages 79–88. Butterworth-Heinemann, Boston, Massachusetts, 1991.

[175] Suzanne Rockwell. Eight more seated at the endowed 'table'. *Dateline U.C. Davis*, February 25, 2000.
http://www-dateline.ucdavis.edu/022500/Dl_chairs.html.

[176] Ely Sachs. personal communication, 2001.

[177] San Francisco Chronicle [online]. Dashing new device for delivering mail / postal service tries scooter on s.f. hills. website, accessed July 2002.
http://sfgate.com/cgi-bin/article.cgi?f=/c/a/2002/07/16/BA232425.DTL&type=news.

[178] Arnoldus Schoonwinkel. *Design and Test of a Computer-Stabilized Unicycle.* Ph.d. thesis, Stanford University, 1988. (Abstract only.).

[179] Marie A. Schroeder. Memorandum containing the review of p020033 - independence ibot 3000 mobility system by independence technology, l.l.c., October 24 2002. FDA document obtained online at:
http://www.fda.gov/ohrms/dockets/ac/02/briefing/3910b1_03_P020033.clinical.doc.

[180] Segway LLC. Segway. website, accessed August 2002. http://www.segway.com.

[181] SensAble Technologies. SensAble Technologies homepage, copyright 1996-2003. http://www.sensable.com/.

[182] Stephen D. Senturia. *Microsystem Design.* Kluwer Academic Publishers, Boston, Massachusetts, first edition, 2001.

[183] Katherine Shim. Edgerton, inventor, professor, dies at 86. *The Tech*, 109(58), January 10 1990. http://the-tech.mit.edu/V109/N58/edge.58n.html.

[184] Herbert A. Simon. What we know about learning. *Journal of Engineering Education*, 87(4):343–348, October 1998.

[185] Philip L. Skousen. *Valve Handbook.* McGraw-Hill, New York, 4th edition edition, 1998.

[186] Daniel Sorid. Hubble plagued by old, broken gyroscopes. *space.com*, November 15, 1999.
http://www.space.com/scienceastronomy/astronomy/hubble_gyroold_991115.html.

[187] Richard Spencer. Natcar homepage. http://www.ece.ucdavis.edu/natcar/.

[188] A. A. Stanislavsky and K. Weron. Nonlinear oscillations in the rolling motion of euler's disk. *Physica D*, 156:247–259, 2001.

[189] Andrew K. Stimac. Standup and stabilization of the inverted pendulum. Bachelor's thesis, MIT, Mechanical Engineering Department, June, 1999.

[190] Mark A. Sturza. Navigation system integrity monitoring using redundant measurements. *Navigation: Journal of The Institute of Navigation*, 35(4):69–87, Winter 1988-89.

[191] Salah Sukkarieh, Peter Gibbens, Ben Grocholsky, Keith Willis, and Hugh F. Durrant-Whyte. A low-cost, redundant inertial measurement unit for unmanned air vehicles. *The International Journal of Robotics Research*, 19(11):1089–1103, 2000.

[192] Swagelok Company. Swagelok home page. website, accessed June 2001. http://www.swagelok.com.

[193] Keith R. Symon. *Mechanics*. Addison Wesley Publishing Company, Inc., Reading, Massachusetts, third edition, 1971.

[194] Kaman Industrial Technologies. Kamandirect.com: Welcome. website, accessed January 2003. http://www.kamandirect.com/.

[195] Bradley A. Trago, Edward J. Byrnes, and Griff D. Neal. Injection molded motor assembly. U.S. Patent 6,020,661 - assigned to Pacific Scientific Company, February 1, 2000.

[196] Bradley A. Trago and Robert E. Lordo. Fault tolerant electric machine. U.S. Patent 5,929,549 - assigned to Pacific Scientific Company, July 27, 1999.

[197] David L. Trumper and Steven J. Ludwick. Development of 2.737 mechatronics at MIT. In *Development Conference on Advanced Intelligent Mechatronics*, pages 446–451, 1999. invited paper.

[198] David L. Trumper and Tsuyoshi Sato. A vibration isolation platform. *Mechatronics*, 12:281–294, 2002.

[199] Chin S. Tsai. Bicycle shock-absorbing apparatus. U.S. Patent 5,088,705 - assigned to Dan Ken Industrial Co., Ltd., February 18, 1992.

[200] Chin S. Tsai. Compression-adjustable bicycle shock-absorbing apparatus. U.S. Patent 5,284,352, February 8, 1994.

[201] Paul H. Turner. Bicycle with improved front fork wheel suspension. U.S. Patent 5,186,481 - assigned to Rockshox, Inc., February 16, 1993.

[202] University of Central Florida. The Student Centered Activities for Large Enrollment Undergraduate Programs (SCALE-UP) project. Website accessed May 2003. http://www.physics.ucf.edu/ peg/SCALE-UP/.

[203] H. M. J. van Brussel. Mechatronics - a powerful conurrent engineering framework. *IEEE/ASME Transactions on Mechatronics*, 1(2):127–136, June, 1996.

[204] Jesco von Puttkamer. Space flight 1999 - space sciences and astronomy. http://www.hq.nasa.gov/osf/1999/yearinrev/99science.html.

[205] David William Vos. Dynamics and nonlinear, adaptive control of an autonomous unicycle. Master's thesis, MIT, Department of Aeronautics and Astronautics, 1989.

[206] David William Vos. *Nonlinear control of an autonomous unicycle robot: practical issues.* PhD thesis, MIT, Department of Aeronautics and Astronautics, 1992.

[207] George Watson. Phys345 laboratory: Camera flash and transients in circuits, 1999. Lab assignent for PHYS345 Electricity and Electronics for Engineers at the University of Delaware.
http://www.physics.udel.edu/w̃atson/phys345/lab/camera.htm.

[208] William S. Watson. Vibrating structure gyro performacne improvements. *Product Report Paper*, September, 2001. Watson Industries, Inc.
http://www.watson-gyro.com/company_info/vsgrpt.pdf.

[209] Harvey Weinberg. Dual axis, low g, fully integrated accelerometers. Analog Dialogue 33-1, 1999.

[210] R. Weiss and I. Nathan. An ultrareliable sensing system for vehicles with limited sparing capability. *Journal of Spacecraft*, 4(9):1151–1158, September 1967.

[211] Glenn Weston-Murphy. Floppy drive dissection (Yale University).
http://www.eng.yale.edu/me185/floppy_dissection.htm.

[212] Whittet-Higgins company. Whittet-Higgins Company home page. website, accessed January 2003. http://www.whittet-higgins.com/.

[213] James C. Wilcox. Competitive evaluation of failure detection algorithms for strapdown redundant inertial instruments. *Journal of Spacecraft and Rockets*, 11(7):525–530, July 1974.

[214] James H. Williams. *Fundamentals of Applied Dynamics*. John Wiley and Sons, New York, 1996.

[215] John Williamson. Latest news! iBOT 3000 stair climbing balancing wheelchair! website, accessed August 2002.
http://www.dynopower.freeserve.co.uk/homepages/ibot3000/stairs.jpg.

[216] Alan S. Willsky. A survey of design methods for failure detection in dynamic systems. *Integrity in Electronic Flight Control Systems*, NATO Agardograph(225):5:1–14, April 1977.

[217] Jack M. Wilson. The CUPLE physics studio. *The Physics Teacher*, 32(9):518–523, December 1994.

[218] Jack M. Wilson. The CUPLE Physics Studio. *The Physics Teacher*, 32(9):518–523, December 1994.

[219] Donald R. Woods and Cameron M. Crowe. Characteristics of engineering students in their first two years. *Engineering Education*, 74(5):289–295, February 1984.

[220] Sarah Wright. Papert misses big ideas of the good old days in AI. *Tech Talk*, July 10 2002. http://web.mit.edu/newsoffice/nr/2002/papert.html.

[221] K. Yamazaki and S. Miyazawa. A development of courseware for mechatronics education. *International Journal of Engineering Education*, 8(1):61–70, 1992.

[222] S. Yurkovitch, Ü. Özgüner, and K. M. Passino. Control system testbeds and toys: Serendipitous or suspect. In *Proceedings of the 1997 American Control Conference*, pages 2692–2696, Albuquerque, NM, June, 1998.

[223] S. Zarabadi, T. Vas, D. Sparks, J. Johnson, Q. Jiang, M. Chia, and E. Borzabadi. A resonating comb/ring angular rate sensor vaccum packaged via wafer bonding. *SAE Technical Paper Series*, 199-01-1043, March 1-4 1999.